XXII TELEMAC-MASCARET User Conference

Daresbury Laboratory
15-16/10/2015

ARTELIA BAW Cerema EDF HR Wallingford Working with water Science & Technology Facilities Council

Editors
Charles Moulinec & David R. Emerson

Proceedings of the

XXII TELEMAC-MASCARET Technical User Conference

October 15–16, 2015

Organised by

STFC Daresbury Laboratory
Sci-Tech Daresbury Campus
Warrington
WA4 4AD
UK

Edited by

Charles Moulinec
David R. Emerson

ISBN 978-0-9574402-3-4

Printed in the UK

Table of Contents

Foreword of the XXII TELEMAC-MASCARET User Conference

Dear Participants,

STFC Daresbury Laboratory was host to the XXII TELEMAC-MASCARET Annual Technical User Conference (TUC2015) that highlights the latest developments and applications of the open-source hydrodynamic suite of solvers used to compute free-surface flow problems. TUC2015 was organised and chaired by SCD's Computational Engineering Group (David Emerson and Charles Moulinec) and held at Daresbury from 13 to 16 October 2015. The Annual User Conference ran for 2 days, with software training sessions taking place before the conference. This year, the conference welcomed 68 attendees, with international participants from academia and industry, the furthest coming from Uruguay. The XXII conference was also very important, because one of the main developers of the software, Jean-Michel Hervouet, would retire in 2016.

The training sessions were delivered by EDF, CEREMA and STFC over 2 days and saw 18 attendees taking part. For the first time in the conference series, hands-on tutorials with practical use of the software and a High End Machine were offered, as it was acknowledged by the consortium members that High Performance Computing is very important for the hydrodynamic community. Our main objectives were to train the current and new generation of scientists and engineers on using cutting edge software and supercomputers. The practical session involved the triple coupling between wave propagation, hydrodynamics, and sediment transport to simulate a zone located in the North of Normandy. All attendees were first introduced to running the TELEMAC software on one of the local machines of the Hartree Centre training room. The attendees could then submit larger models on the Centre's Blue Gene/Q (Blue Joule) supercomputer to simulate 90 days of the flow during a 6 hours overnight simulation. This was the first time any of the attendees had used a supercomputer and the feedback from the experience was extremely positive.

On behalf of STFC Daresbury Laboratory and of the TELEMAC-MASCARET Consortium, we would like to thank all authors and participants for their contributions to the TELEMAC-MASCARET User Conference.

C. Moulinec & D.R. Emerson
Co-chairs of TUC2015 Local Organising Committee

STFC Daresbury Laboratory
Sci-Tech Daresbury CampusWarrington
WA4 4AD, UK

Organisation

International Scientific Committee

Rebekka Kopmann BAW
Thomas Brudy-Zippelius BAW
Jacek Jankowski BAW
Jean-Michel Hervouet EDF R&D and Saint-Venant Laboratory
Nicole Goutal EDF R&D and Saint-Venant Laboratory
Chi-Tuan Pham EDF R&D and Saint-Venant Laboratory
Pablo Tassi EDF R&D and Saint-Venant Laboratory
Christophe Coulet Artelia
Olivier Bertrand Artelia
Sébastien Bourban HR Wallingford
Catherine Villaret HR Wallingford
Alan Cooper HR Wallingford
Michiel Knaapen HR Wallingford
Noémie Durand HR Wallingford
Patrick Chassé CETMEF
David Emerson STFC Daresbury Laboratory
Charles Moulinec STFC Daresbury Laboratory

Local Organising Committee

Robert Barber
David Emerson
Damian Jones
Shirley Miller
Charles Moulinec
Esme Williams
Yue Yin

Assessing the effects of modifications to river training structures using numerical modelling

Manuela Baron[1], Lars Backhaus[1]
[1]BAW, Kußmaulstr. 17, 76187 Karlsruhe
Corresponding author: Manuela Baron, manuela.baron@baw.de

Proposed session: *river, estuaries, maritime, coastal sediment processes*
Keywords: river modelling, training structures, modifications
Speaker: Manuela Baron

Abstract: To maintain and optimize the river training works on the 70 km long stretch of the Danube River between the cities of Straubing and Vilshofen (see Figure 1), modifications on the training structures are being investigated and planned. The effect of such modifications on the water level, river bed and flow distribution can only be quantified using complex Hydro-numerical modelling.

For this purpose, a 2D-HN model for the 70 km river stretch, including floodplains, was set up and calibrated and validated using field measurements. The computational grid contains 2.6 million elements, with a minimum grid resolution of 3 m in the fairway and a maximum resolution of 25 m on the floodplains. Telemac2D Version 6P3r2 is used for the numerical simulations. Using the numerical model, the effect of typical modifications of the different river training structures can be investigated and quantified for the aforementioned parameters. Different variations (e.g. training structure dimensions) of the planned modifications were investigated. Additionally, ecological measures such as the restoration or inclusion of river islands, bank vegetation and flood routing channels (see Figure 2) were investigated. With many of the modifications, also the computational grid is adapted. The modular setup of the model allows the systematic assessment of the influence of the separate modifications.

The results of these hydrodynamic simulations will form the basis for ship navigability, morphologic and ground water investigations. The project illustrates the broad scope of the typical applications considered at the BAW.

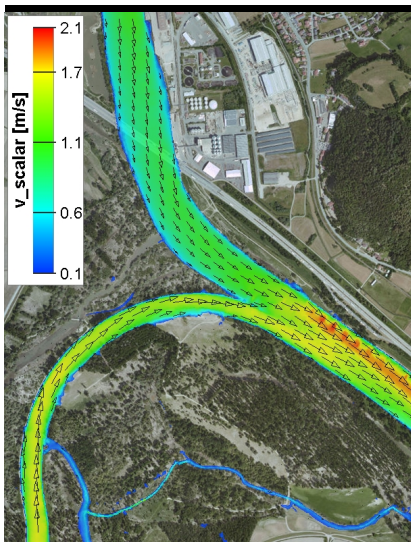

Figure 1: extract of the 2D-model near Deggendorf

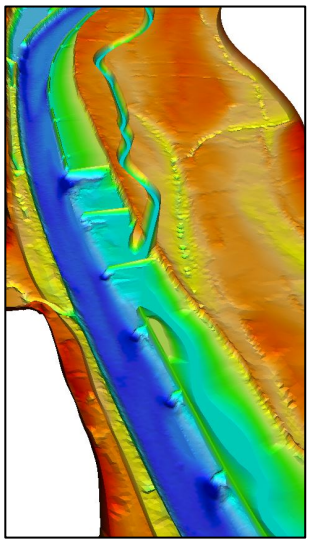

Figure 2: example of structures for river training

An End User Perspective on the Telemac Suite in Coastal Application

Lövstedt, Charlotta B., and Almström, Björn
Sweco Environment AB
Coasts and Rivers department
Malmö, Sweden
bjorn.almstrom@sweco.se

Abstract—**This paper focuses on an application of a three-way coupling of TELEMAC 3D, TOMAWAC and SISYPHE in order to understand the sediment transport patterns of the Skälderviken bay on the Swedish west coast. Ängelholm municipality, in the south of Sweden, experiences severe coastal erosion and is therefore planning for a beach nourishment. As part of the environmental impact assessment for the beach nourishment the characteristics of the sediment transport patterns in the Skälderviken bay were simulated with the aim of finding possible marine sand extraction sites. In addition, TELEMAC 2D was used to simulate the flood impact of a sand dune breach along the coast. This is the first case in Sweden where the TELEMAC suite has been used for such an applications.**

The model was run in four constant scenarios representing different wind directions.

Results from the model were used to determine accumulation areas where geological field surveys of the bottom were carried out. Furthermore, the TOMAWAC model was used to assess whether a dredging of the extraction area would influence wave propagation and risk exacerbating coastal erosion. The flood analysis of a sand dune breach was mainly used in communication with politicians to highlight the risk of not doing beach nourishment.

From the perspective of an end user the TELEMAC suite is being evaluated in respect to the investigated case. Moreover, general experiences from modelling with the TELEMAC are described and further developments, both in how to use the software and the software itself, are suggested.

I. Introduction

This Ängelholm municipality in the south of Sweden has had problems with beach erosion during the entire 20th century. In recent years three storm events, in 2011, 2013, and 2015, caused severe erosion on the beach dunes, which protect the hinterlands from flooding. The risk for flooding as well as the risk of losing their main beach to erosion has forced the municipality to act. In order to evaluate the usefulness of the Telemac-suite in a coastal consultancy business the cases of Ängelholm has been selected.

In Sweden each municipality has the responsibility to mitigate the coastal erosion. Moreover the municipalities are not allowed to apply for funding from national authorities. Their solitary role in this issue leads to that the mitigation methods for erosion must be very economical effective since the municipalities normally have a strengthened economy. Traditionally hard mitigation methods have been the only methods used against erosion in Sweden. Ystad municipality was in 2011 the first in Sweden to perform a beach nourishment project, but the project was preceded of almost a decade of legislation processes. In this legislation process many of the involved authorities expressed their anxiety against beach nourishment since it was regarded as a new technology in Sweden.

Ängelholm and Ystad are however not the only municipalities in Sweden needing to mitigate coastal erosion. The issue is rising in other coastal municipalities with sandy coast lines, who all are found in the southern part of Sweden. It is therefore necessary to find tools to better describe the physical processes involved in coastal erosion and to show the consequences of coastal mitigation measurements as well as the consequences of doing nothing.

II. Description of the site

The subject of the study is Skälderviken bay on the Swedish southern west coast (Fig. 1). The city of Ängelholm is situated in the inner part of the bay. The inner coastline of the bay consists of a 7 km long beach, whereas the sides of the bay mostly consist of solid rocks alternated by smaller pocket beaches. The inlet to the bay is about 15 km wide and 25 m depth.

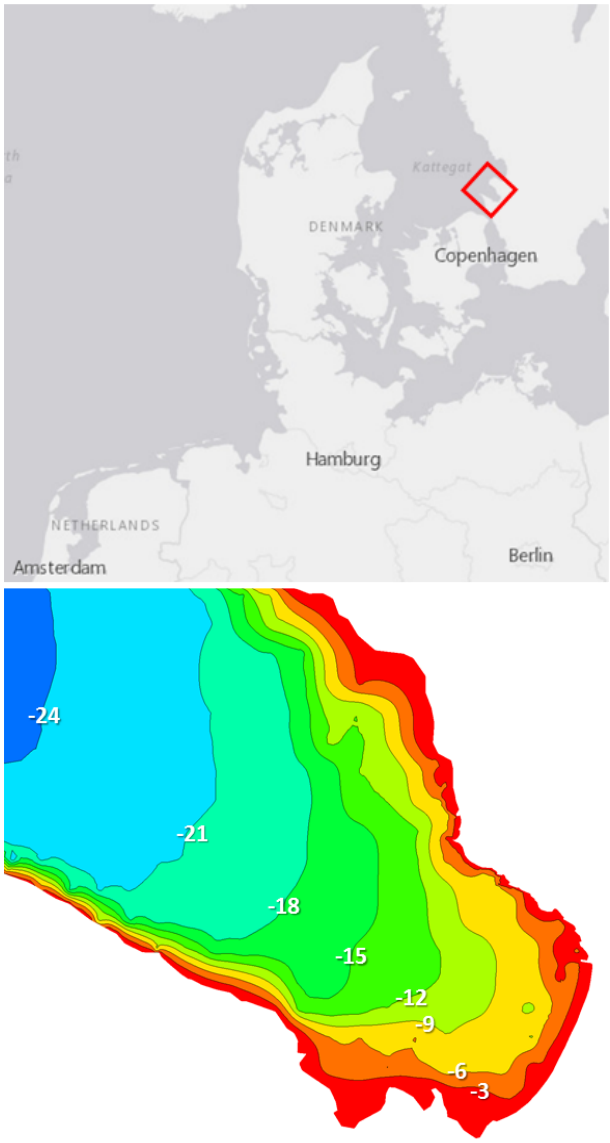

Figure 1. Top: Location of the Skälderviken Bay. Below: Bathymentry of the Skälderviken.

In this region tidal range is negligible and is not considered to be a driving force of the currents. Instead wind is the main force locally and in a larger scale sea water level variations are also an important. Close to the shore the incoming waves also affects the pattern of the currents. Two rivers discharge into the bay; Rönneå in the northern part of the inner beach, and Vegeå in the southern part of the same beach. Although the rivers affect the currents locally at their mouths they are not considered to be a significant force for the current pattern in the Skälderviken bay since the flow is quite low and the force from the wind are much superior.

Wind is measured since 1951 on an island (Hallands Väderö) directly north of the bay. The mean wind speed here is 7.4 m/s and the maximum measured wind speed is 38 m/s. The main directions for the strong winds are from west to southwest, but for moderate wind speed there is no dominant direction, see Fig. 2.

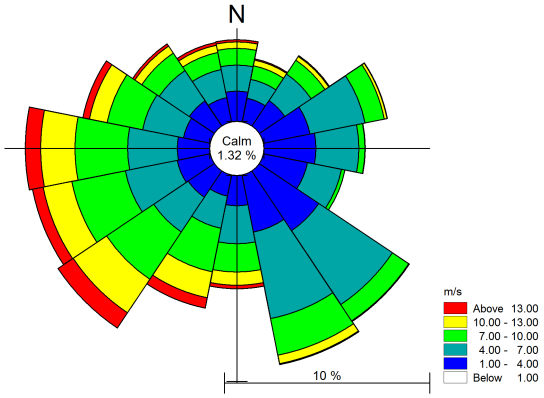

Figure 2. Wind rose from measurments at Hallands Väderö.

The water level normally varies between +1 m and -0.5 m from mean water level within a year. The water level never falls below -1 m and the highest measured level is about +1.75 m.

The salinity in the bay is about 18 psu in the surface water and around 30 psu in the bottom water at 20–25 m depth.

III. METHOD

First, the main current pattern had to be described. Since the inner part of the bay is shallow and sloping gentle, the currents were not only induced by winds but also by the waves. Therefore a coupled TELEMAC 3D and TOMAWAC model was set up. 3D was chosen due to that the main force for the currents are wind and not tidal currents. The wind should induce a surface current that is turned clockwise from the wind direction due to the coriolis force. Below a return current in the other direction should be induced.

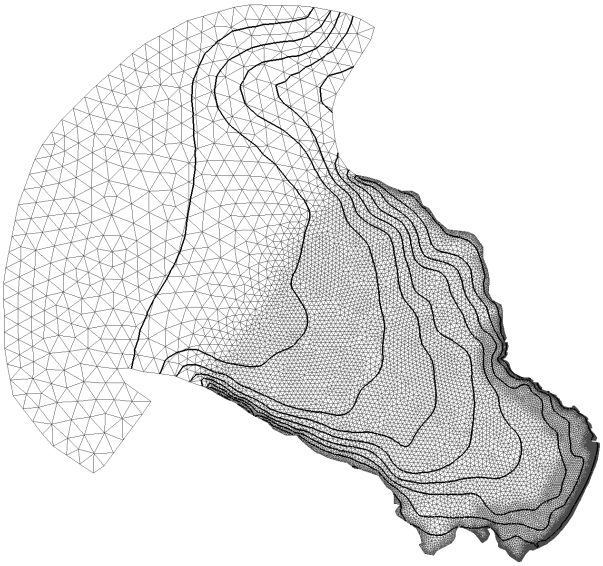

Figure 3. Model domain with mesh and depth curves at every 3rd meter.

To describe the sediment transport pattern and determine areas of erosion and accumulation SISYPHE was also directly coupled with TELEMAC 3D and TOMAWAC.

The model area was defined so that the outer boundary was quite far out into the sea to avoid potential numerical uncertainties at the boundary affecting the area of interest. The model domain is shown in Fig. 3. Near shore the sides of the elements are 10 m and are stepwise increasing in length to about 900 m in the open sea area near the boundary. The domain is reaching about 30 km from the inner beach to the outer boundary and contains about 800 000 elements in each layer.

The vertical resolution is defined so that there are five layers with a fixed depth above 5 m (3 layers of 1 meter below surface and thereafter a layer of 2 m). Below the fixed layers are 3 equal layers following the bottom curve.

The effects of vertical and horizontal salinity and temperature gradients were not taken into account since they were not considered to be significant compared to the effects of wind, waves and bathymetry.

Four constant scenarios were chosen to describe the main current, wave and sediment transport pattern in the bay altering the wind direction between the scenarios. The wind directions were SE, NE, SW and NW, since these wind directions are either along or across the Skälderviken bay.

Incoming wave heights were estimated from mean wind speeds and average fetch length. Fetch limited wave heights and wave period were calculated according to the Shore Protection Manual [1].

The main setup is described below:

- Boundary conditions: constant water level (0 m), waves with a boundary significant height of 1.07 m, peak frequency of 0.18 Hz and main direction 125˚.
- Type of boundary directional spectrum: 6 (parameterised Jonswap (Hm0, fp))
- Mean diameter of sediment: 0.2 mm
- Wave energy losses through: bottom friction, white capping and depth-induced breaking
- Wind speed: 7.4 m/s
- Turbulence models: Mixing length on the vertical and constant on the horizontal.

A wide range of parameters have been tested for different values including for example resolution, both horizontal and vertical, friction options, turbulence options, boundary options (both water level and waves), time step, wind options, and wave energy dissipation options.

Unfortunately, almost no measurements were available to validate the results except for water level measurements at two locations within the bay. Therefore, calibration has been done with respect to what was expected in terms in of main current pattern. Wave transformation has been calculated by hand to compare with the wave pattern within the bay. Sediment transport was validated against geological maps and a few observations of erosion and accumulation areas along the beach.

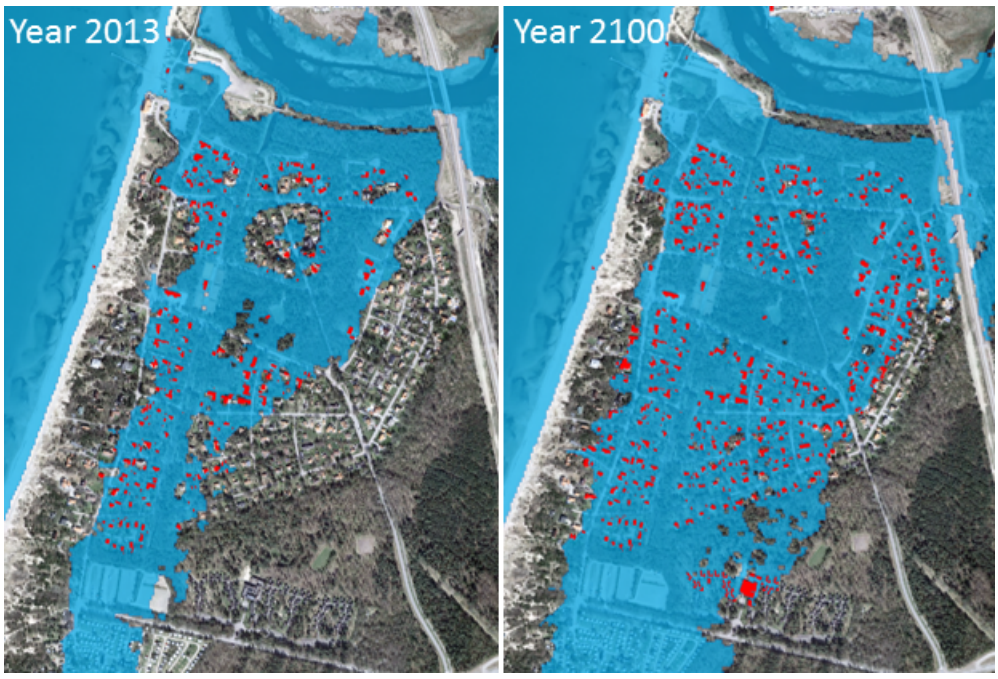

Figure 4. Results from the flood analysis

Furthermore a TELEMAC 2D-model was set up for the area behind the dunes. A DEM with a resolution of 2 m was used as bathymetry for the model. A breach of the dunes was simulated with the breach-function within TELEMAC 2D. Sea levels during the last major storm in 2013 was used for the present day scenario, and for the future scenario of year 2100, a mean sea level of one meter was added to the storm of 2013.

IV. RESULTS

The flood modelling clearly showed the importance of the sand dunes for the urban area behind the dunes. Results from the flood modelling are shown in Fig. 4. During the storm in 2013 no flooding occurred, but for the scenario where the dune breach a large flooding occurs. About 100 houses would be flooded if the dunes were not present.

Combining the storm of 2013 with a sea level 1 m above the present level the flooding becomes even larger and about 300 houses would be flooded. Even in the climate change scenario no houses would be flooded if the dunes is intact. This shows the importance of maintaining the dunes as a flood protection system.

Calculated main current patterns at the surface and near the bottom is shown in Figure 4 to 7. Bottom currents are of most interest since they show direction of sediment transport. For northerly winds the bottom currents are directed southwards, while the southern wind scenarios generates bottom current going northwards for southwestern winds and inwards for southeastern winds.

Results from TOMAWAC are shown in Fig. 9. The largest waves within the bay correlate, not surprising, with wind directions from north west (Fig. 9). The wave height

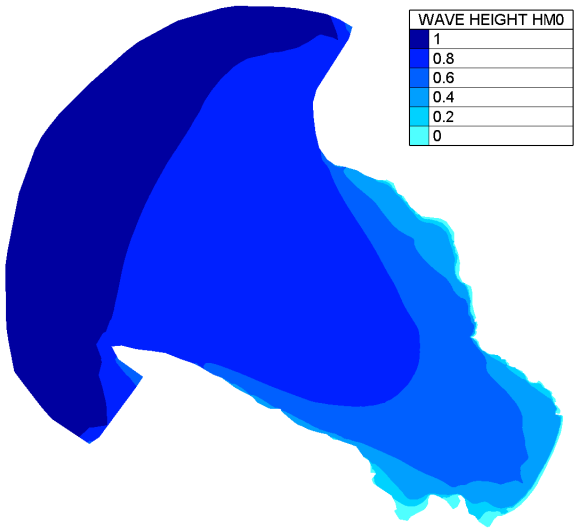

Figure 9. Wave heights (m) with winds from NW.

during the opposite wind direction (south east) results in wave heights in the middle of the bay of about 1/3 of the wave height during the north westerly winds. The wave height itself is not of main interest in this study, but the effect on the near shore currents and the bottom shear stress is of importance.

In Fig. 10 the results from SISYPHE showing the sediment flowrate is presented. The entire bottom of Skälderviken Bay is active in the sediment transport, and the results show distinct patterns for different wind directions. This indicates that there are no apparent accumulation zones.

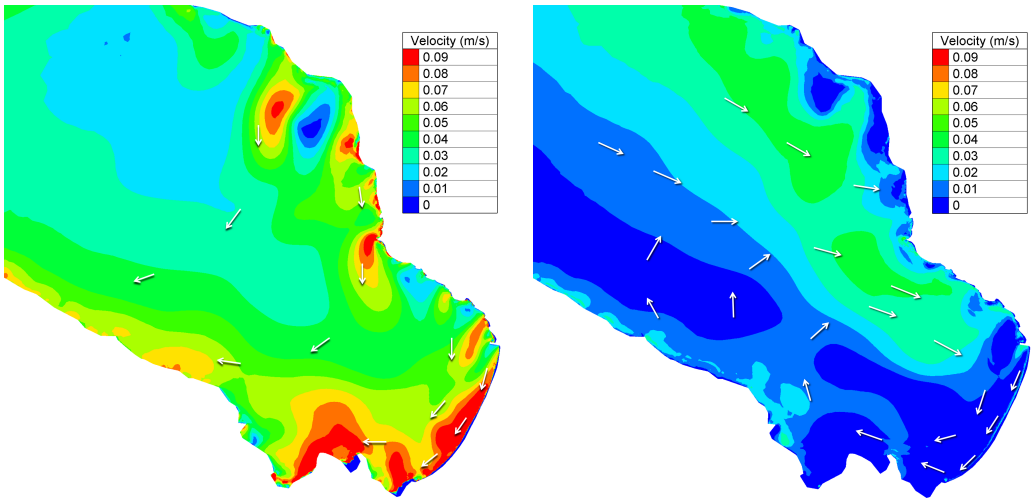

Figure 5. Main current pattern for winds from NE ; Left : Surface currents, right: bottom currents.

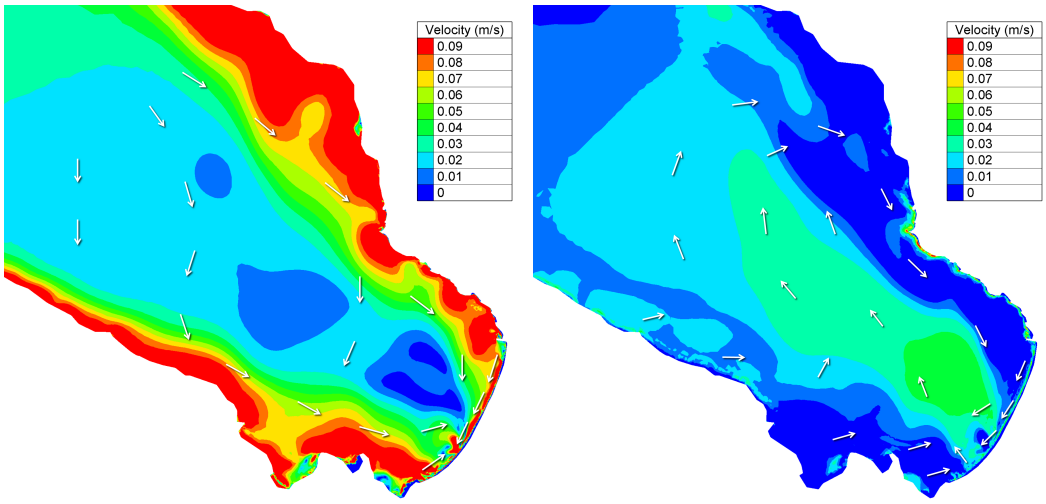

Figure 6. Main current pattern for winds from NW ; Left : Surface currents, right: bottom currents.

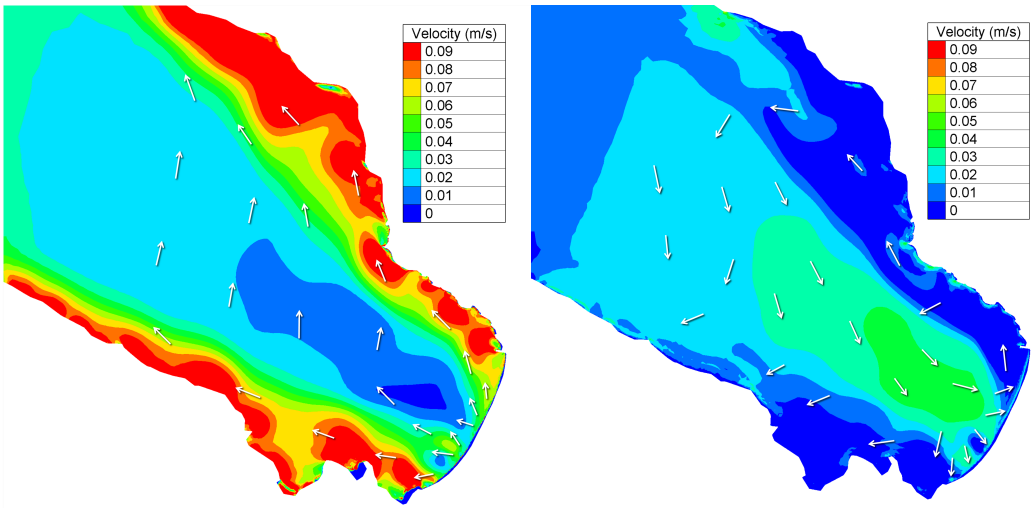

Figure 7. Main current pattern for winds from SE ; Left : Surface currents, right: bottom currents.

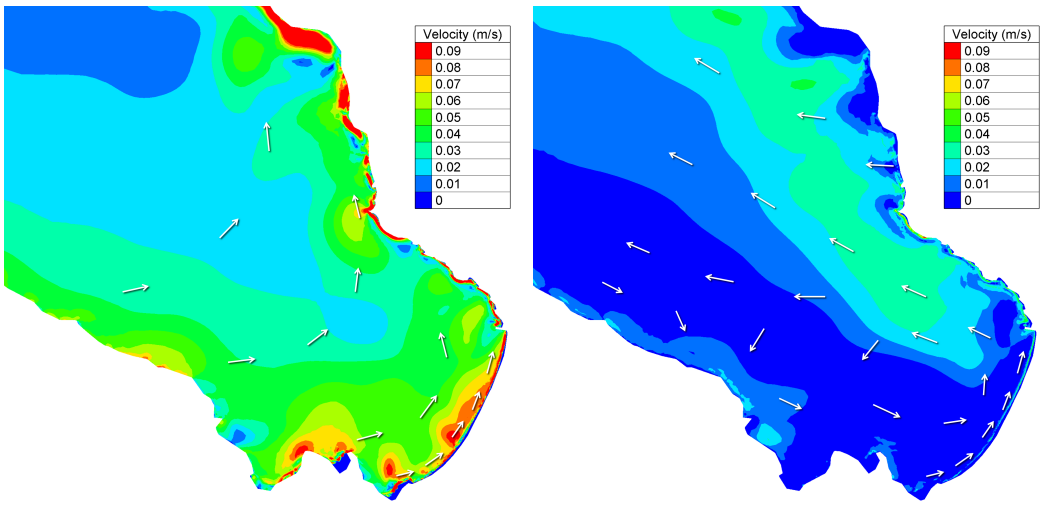

Figure 8. Main current pattern for winds from SW ; Left : Surface currents, right: bottom currents.

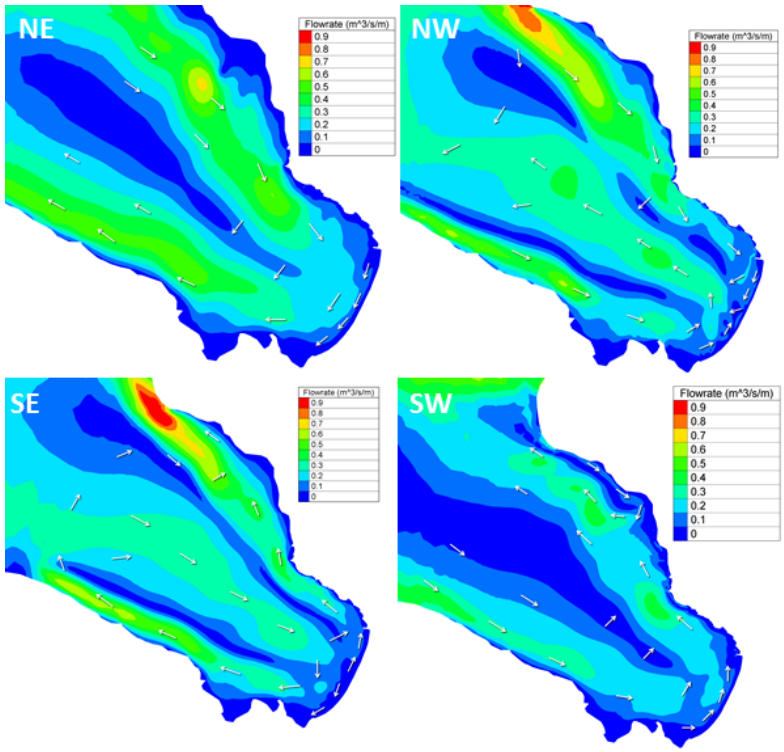

Figure 10. Sediment flowrate (m3/(s·m)) with winds from NE, NW, SE, and SW.

V. DISCUSSION AND CONCLUSION

The results so far have been used in presentations for politicians with the purpose to describe the importance of the sand dunes as flood protections. The bottom shear stresses have been used to determine were to investigate the bottom to find suitable areas for sand extractions.

Unfortunately all modeling work is not completed and further development of the model is ongoing and will be described in the next section. However, it has been shown in this project that the TELEMAC suit is useful for such an application.

A large part of the usability of the Telemac-suite can be found that it is open-source, compared to, for example DHI's software which normally is too expensive for clients such as small municipalities. The main argument for expensive software is usually that it includes professional support. This argument fails in comparison with TELEMAC, since the forum provides fast help that has solved many of the problems that we have faced during this project.

Some parts of the modelling have been more problematic than others and could be worth to develop in the future. These include:

- Varying boundary conditions: should be more standardized and not require additional fortran-files.
- Varying wind condition in TOMAWAC: it was quite tediously to first produce the wind in TELEMAC 2D or 3D. Could have been easier to direct use a time series as input in TOMAWAC.
- Visualization: the post processing tools Blue Kenue and Fudaa are quite limited in terms of visualization, which is often a quite important part for end users.

The main challenge in the project has, however, been the lack of measurements and observations to calibrate the model against.

VI. FURTHER DEVELOPMENT OF THE PROJECT

The upcoming developments of the model project are to

- Simulate storm conditions with input varying in time to reproduce the major storm in 2013. Some observations are available for this event that will be useful.
- Refine the model in the surf zone to better represent small scale sediment transport pattern.
- Include rivers to simulate local effects.

Combining results from the coupled model with other investigations, such as marine biology and geotechnical surveys, will result in a comprehensive knowledge base for the environmental impact assessment.

REFERENCES

[1] U.S. Army Corps of Engineers, "Shore Protection Manual," U.S. Army Corps of Engineers, Washington, D.C. (in 6 volumes), 1984.

Investigating the sediment transport processes in a river meander

Clemens Dorfmann[1], Matthias Redtenbacher[1], Gerald Zenz[1]
[1]Institute of Hydraulic Engineering and Water Resources,
Graz University of Technology,
Stremayrgasse 10/II, A-8010 Graz
Corresponding author: Clemens Dorfmann, clemens.dorfmann@tugraz.at

Proposed session: *River, estuaries, maritime, coastal sediment processes*
Keywords: Telemac-2D, Telemac-3D, secondary currents, suspended load transport modelling
Speaker: Clemens Dorfmann

Abstract: At the river Drau a river-hydro power plant has to confront severe sedimentation problems. In the river meander (Figure 1), which represents only a section of the reservoir, guide walls have been constructed as well as dredging activities have been carried out in order to facilitate the suspended load transport and to prevent the disordered deposition of sediments. However the bed elevation measurements carried out in recent years indicate that additional measures have to be adopted in order to reduce the sedimentation. The scope of the work presented herein is the evaluation of different construction measures in the river meander by means of numerical modelling. The numerical modelling is supported by high-resolution multibeam echosounding data and ADCP velocity measurements. To assess the performance of the different measures, one idea is, to run suspended load transport simulations using synthetic concentrations as well as sediment inflows and to evaluate the sediment outflows.

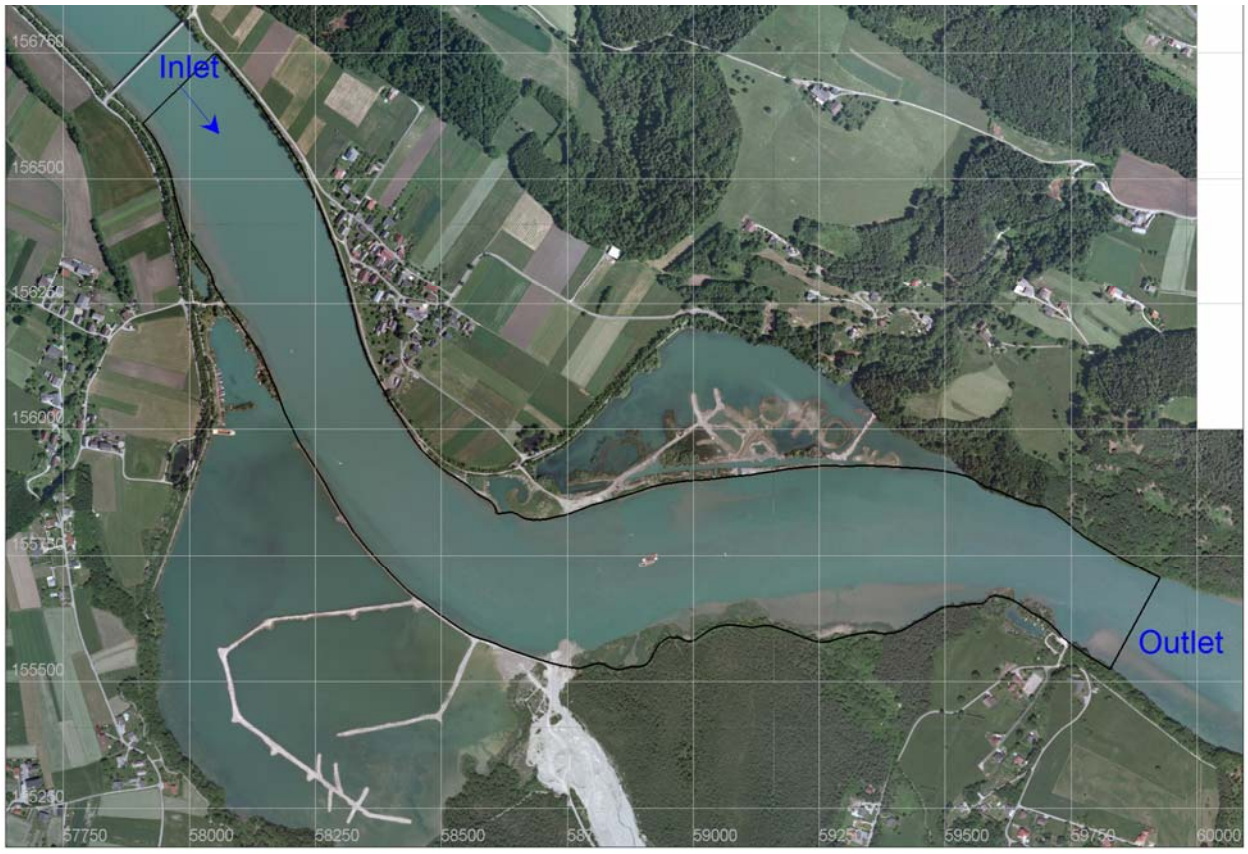

Figure 1 : Project area, (image source : Verbund VHP)

Large-scale morphodynamics structures in the Arc en Maurienne River (France)

Florian Cordier, Pablo Tassi & Magali Jodeau
EDF R&D - LNHE – Saint-Venant Laboratory
Chatou (France)
{florian.cordier;pablo.tassi;magali.jodeau}@edf.fr

Benoit Camenen
Irstea, UR HLL
Villeurbanne Cedex (France)
benoit.camenen@irstea.fr

***Abstract*—This work focuses on the morphodynamic study of alternate gravel bars in a engineered montainous alpine river, the Arc en Maurienne (France). The experimental site is a selected long reach, which evolved from a natural braided pattern into a single channel formed by two straight reaches, connected by a curve acting as a forcing point on the sediment motion. The channel's width variation also affected its morphology, leading to the formation of an alternate bar system. Numerical results shows that the Telemac-Mascaret modelling system is able to reproduce the morphodynamics behaviour observed in a gravel bar-scale reach (approx. 1 km) and the alternate bar patterns observed in a 8 km river reach of the Arc en Maurienne river.**

I. Introduction

Rivers generally evolve from an initial single thread into a configuration which is averagely in dynamic equilibrium, also called quasi-equilibrium state [12]. The mutual interaction between hydraulics and sediment transport processes controls the shape of these dynamic systems. The evolution of the channel pattern is therefore dominated by the sediment motion, through the erosion and deposition of the alluvial material [2].

Rivers are subjected to either natural perturbations (climatic and tectonic) or anthropic pressures (water retention, channel derivation, construction of groynes, *etc.*), conducting to variations of the solid transport rate. Such changes trigger the modification of the river bed, towards a new equilibrium state. In this way, the system's morphological response is adapted to the given perturbation type and magnitude. Since the industrial revolution, river engineering strongly developed as a response to special needs like land reclamation, flood control or water retention and distribution. Several effects of artificial structures on the dynamics of the river can be discerned, but can also lead to side (undesired) effects. Disturbances can be originated from hydrodynamics, by controlling the upstream discharge, from morphodynamics, by dragging or limiting the sediment supply, or finally because of geometric changes of the river course (channelization, deviation, *etc.*). Depending on the perturbation's importance, the river morphology adjustments in space can be limited to little areas or expanded to large ones, and evolving in time from weeks to several decades.

The Arc en Maurienne (France) is an alpine mountainous river located next to Sainte-Marie-de-Cuines, approximately at 35km of the confluence with the Isère river. This river has been subjected to a large number of training works during the last centuries, where the consequences of such human activities led to considerable changes of the river morphology and dynamics. As a response of land reclamation and flood control, a wide operation of channelization started from the 19^{th} century, by means of embankments. A succession of hydro-power dams was built during the 20^{th} century, regulating the flow discharge and reducing the sediment supply. Due to artificial embankments, this river has evolved from a natural braided pattern into a single channel formed by two straight reaches, connected by a curve acting like a forcing point on the sediment motion and presenting spatial width variations. In response to these perturbations, the channel evolved from a braided natural pattern into a single-thread river confined in a straight channel. Consequently, a sequence of alternating deeps and shoals developed, with impact on the navigation, flood control and ecosystem.

In the last few years, prediction of bar formation and development has been considerably improved through the application of analytical theories and empirical and physically-based models. Nevertheless, these models usually fail on predicting the behaviour of these macroforms for complex cases, wherein most of hypothesis become invalid. Therefore, the study of such bed forms has been promoted by the use of numerical models. Although these models have shown to successfully reproduce the formation and behavior of bars, *i.e.* straight channels [1], [4], [14], curved channels [3], [13], or width varing channels [5], their domain of applicability has been restricted to simple geometrical, hydrological and flow and sediment characteristics.

This work focuses on the numerical simulation of an alternate gravel bar system in a selected reach of the Arc en Maurienne river. Previous studies have been presented by Jodeau [11], Jaballah [8] and Jaballah *et al.* [9]. The aim of the present paper is twofold. First, the development and validation of a morphodynamic model at a gravel bar-scale reach of the order of 1 km, using data recorded during a dam flushing event; and second, the application of the model for the prediction of alternate bar patterns for a 8 km river reach. Numerical simulations were performed with the Telemac-Mascaret modelling system.

II. Mathematical modeeling of bar formation and propagation

A. 2D flow model

The hydrodynamics solver Telemac-2D is internally coupled to the sediment transport and bed evolution module Sisyphe in order to investigate the behaviour of bars in the

study site. The hydrodynamics module is based on the solution of shallow-water equations (SWE) obtained from several strong assumptions (hydrostatic pressure distribution, vertical acceleration negligible, *etc.*), wherein turbulence effects are took into account using a constant viscosity model:

$$\left\{\begin{array}{lcl} \partial_t h + \nabla hu = 0 & & \\ \partial_t u + u\partial_x u + v\partial_y u & = & -g\partial_x z_s + F_x + h^{-1}\nabla\cdot(h\nu_t\nabla u) \\ \partial_t v + u\partial_x v + v\partial_y v & = & -g\partial_y z_s + F_y + h^{-1}\nabla\cdot(h\nu_t\nabla v) \end{array}\right. \quad (1)$$

where g is the acceleration of gravity $= 9.81$ ms^{-2}, h is the water depth [m], $z_s = z_b + b$ the free surface [m], with z_b the elevation of the bottom topography above datum, u (resp. v) the fluid velocity along the Cartesian $x-$axis (resp. $y-$axis) [m/s], ν_t the depth-averaged eddy viscosity, and F_x (resp. F_y) the source terms along the Cartesian $x-$axis (resp. $y-$axis).

B. 2D morphodynamics model

By considering only bedload transport, the bed evolution is computed from the Exner's sediment mass balance equation:

$$\partial_t z_b + \frac{1}{\epsilon_0}\left(\frac{\partial q_{b_x}}{\partial x} + \frac{\partial q_{b_y}}{\partial y}\right) = 0, \quad (2)$$

where $\epsilon_0 = (1-\lambda)$ with λ the bed porosity ($= 0.40$), $(q_{b_x}, q_{b_y}) = q_b(\cos\alpha, \sin\alpha)$ are the bedload components in the $x-$ and $y-$ directions, respectively, with α the deviation angle between the sediment transport and the flow direction and q_b the sediment transport rate computed with the Meyer-Peter and Müller (MPM) formula:

$$\frac{q_b}{\sqrt{g\Delta d_m^3}} = \alpha\Big(\mu\theta - \theta_c\Big)^{\gamma}, \text{ with } \alpha = 8 \text{ and } \gamma = \frac{3}{2}, \quad (3)$$

with θ the non-dimensional Shields parameter, θ_c the critical Shields parameter ($= 0.047$), and μ a correction factor that depends on the ration between the total roughness and the skin roughness of the bed. Calibration of MPM formula for α and γ coefficients lead to other formulations popular in the literature [16]. The sediment transport model is parametrized in order to reproduce both relevant physical processes corresponding to (i) bed slope effects and (ii) secondary currents effects.

1) Bed Slope effects: Bed slopes causes the increase (decrease) of bed-load transport rate in the downslope (upslope) direction. In this work, bed slope effects are accounted using the Soulsby's expression for magnitude (1997) which allows the correction of the original critical shear stress θ_c. The non-dimensional critical Shield stress θ_{co} is modified as a function of the bed slope χ, the angle of repose of the sediment ϕ_s and the angle of the current to the upslope direction ψ:

$$\frac{\theta_c}{\theta_{co}} = \frac{\cos\psi\sin\chi + (\cos^2\chi\tan^2\phi_s - \sin^2\psi\sin^2\chi)^{0.5}}{\tan\phi_s}, \quad (4)$$

and the correction of sediment slide direction is implemented using Talmon *et al.* [15] formula:

$$T = \frac{1}{\beta_2\sqrt{\theta}}, \quad (5)$$

with β_2 a coefficient.

2) Secondary currents effects: Three-dimensional effects due to helical flows [17] generated in curves in 2D models can be parameterized with semi-empirical formulation [6], [18]. In this work, the Engelund formula is used. This expression is based on the assumption that the bed shear stress, the roughness and the mean water depth are constant in the cross-section, using the expression $\tan\delta = 7\frac{h}{r}$, where δ is the deviation angle between the main flow direction and bed load direction and r the radius of curvature of the bend.

III. Study sites presentation

A. Study reach

The Arc River is a mountainous river which springs from its headwaters in the French Alps, flowing until its confluence with the Isère River, through the narrow Maurienne watershed of 1957km^2 (Fig.1a,b). The economic importance of the valley has been shown since the industrial revolution, connecting France to Italy through a diversified transportation network and the implantation of a chain of hydroelectricity generating stations.

The experimental site is a 8km long reach, located next to Sainte-Marie-de-Cuines at downstream. The site is located at approximately 19km of the lower dam of S^{t} Martin-la-Porte (Fig.1b). Constraints due to steep engineered embankments around the channel led to the assumption that active width is equal to the river width (for more details, the reader is referred to [9]). The bed slope varies from 1.1% upstream to 0.5% at the downstream part, showing a transient behavior between sub- and super-critical flows and presenting a width variation from 35m upstream to 50m downstream. In this configuration, the reach can be divided in two channels connected by the curve located at the KP (Kilometer point upstream the confluence with Isère River) 36.22 (Fig.1d).

B. Hydrology of the reach

The Arc River shows common alpine river characteristics, with a nival hydrological regime which can heavily fluctuate following the seasons (*i.e.* storage and melting of water supply due to hot/cold seasons). Mean discharges recorded varies from 6-8m^3/s during autumn/winter and 15-20m^3/s during spring/summer. In addition to channel deviations, the stream discharge in the study reach is controlled and regulated by the sequence of dams located upstream. According to Hydratec and Cemagref [7], only 5% of the river remained with its natural flow and morphological conditions, highlighting the artificialization of the reach.

Due to the low dams storage capacity, water released from dam flushes do not exceed a one-year return period flood, so extremes floods statistics are hardly ever altered. The 10 and 100-year return-period floods monitored at S^{t} Michel-de-Maurienne (1b) were estimated equal to 300m^3/s and 660m^3/s respectively [7]. Every year, a dam flushing event is operated in the beginning of the spring season, in order to release fine sediments trapped by the dams. This artificial flood show high levels of concentrations of fine suspended sediments with a discharge equivalent to the 1-year return-period flood equal to 130m^3/s.

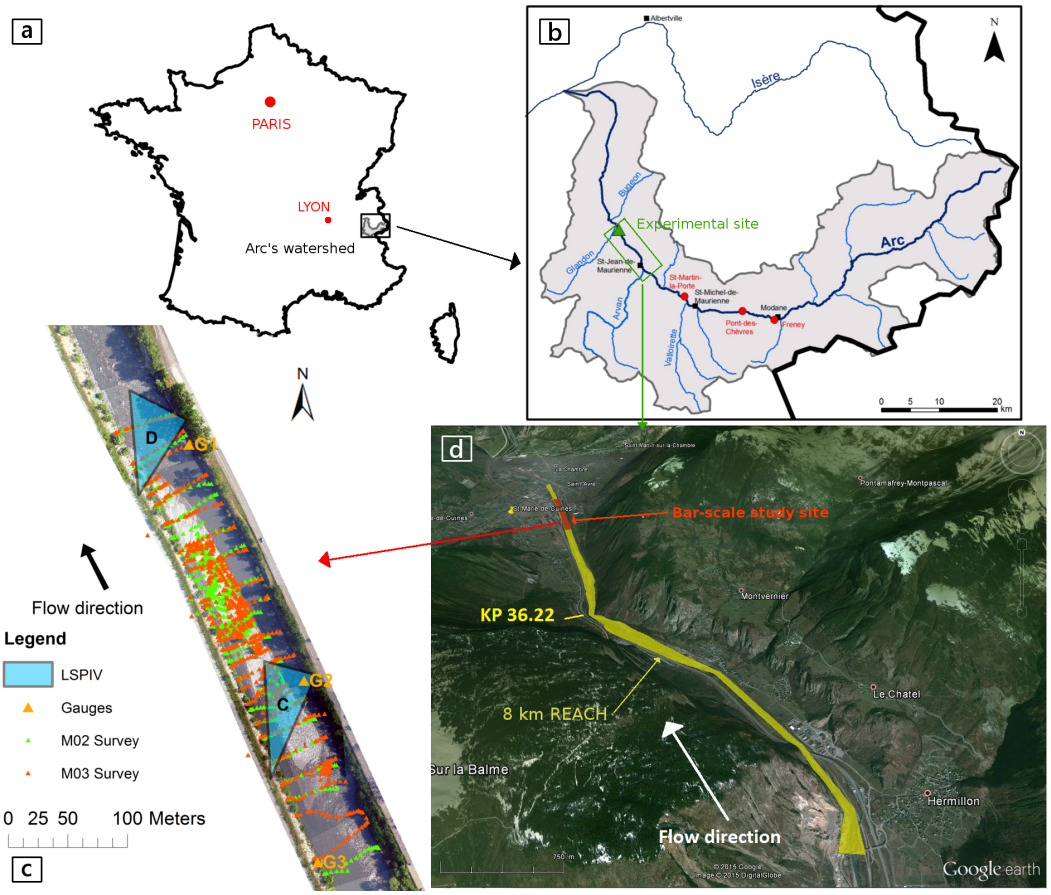

Fig. 1: Location of the Arc's watershed in France (a). Map showing the study reach location in the Arc river [11], with its affluents and the confluence with the Isère river, dams in red points (b). Aerial photograph of the gravel bar unit used for this research work, with the location of the topographic and hydrodynamic measurements (c). Position of the study sites (reach-scale and bar-scale) used in the current study (d).

C. River bed composition

The river bed sediment composition [11] is mainly composed of mountainous poorly sorted gravels, showing a bi-modal distribution of large boulders and significant amounts of sand. Although a large set of information is provided concerning the riverbed granulometry, the grain size distribution in the main channel remains a mere estimation (due to difficulties for leading measurements in this damped area). Field measurements lead to assumption that the main channel's bed is composed of large boulders (12.8-25.6cm). The riverbank composition is also roughly estimated, mostly composed of big boulders and sparse fine sediments, deposited after flooding events. The granulometry of the riverbed was divided into 9 classes of bed material of respectively [1;3;5;10;20;40;60;100;180] mm (Fig.2), in order to be spatializated for the morphodynamical study of the bar-scale reach (cf. IV.D.2).

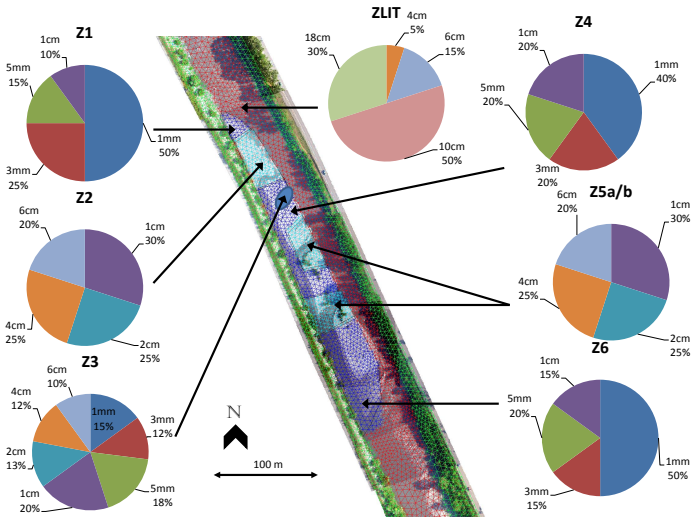

Fig. 2: Distribution of particle sizes composing the riverbed, which varies intensely over space. The distribution has been made using terrain measurements from Jodeau [11].

D. Experimental data

1) River bed topography: Two datasets were provided for the current study, corresponding to samplings before and after the dam-flushing event of 2006 (respectively the June 8th and the July 4th) gathered in the bar-scale study site (Fig.1c,d). In the current research, we call M02 and M03 the topographies

gathered respectively before and after the dam-flushing event according to Jaballah's surveys identification (2012) (Fig1c). M02 (resp. M03) is described using 664 points (resp. 839) with a mean point density of 0.03 (resp. 0.037), showing a diminution of the bar height from 2.40m to 2.25m, and a bar mean surface level decreasing of 19cm. Topography reconstitution from terrain measurements is obtained using the breakline method [8], [11], [19]. A set of cross-sections gathered in 2006 [9] with a sparse mean spatial step of 1km is used to describe the whole reach topography.

2) Hydraulic measurements: A full dataset of hydraulic measurements recorded during the dam flushing event is provided including discharges, water stages, and profile velocities using the LS-PIV (Large Scale Particle Image Velocimetry) technology [10], [11]. The discharge was measured at the stream gauging station of Sainte-Marie-de-Cuines monitored by Irstea [7]. The previous discharge associated a gauge measurement at the same location was useful to draw a rating curve linking stage to discharge. Three water stages (G1-G3) were measured using stream gauges and two LS-PIV cameras were set-up to survey water surface velocities over C and D areas (Fig.1c) at respectively two and four different stages of the event.

IV. 2D NUMERICAL SIMULATIONS AT THE GRAVEL BAR-SCALE REACH

In this section, the validation of the model is presented selected reach of the Arc en Maurienne river. The choice of the study zone was motivated by previous studies and the access to measurement data, see [8], [9], [11].

A. Model implementation

1) Boundary conditions and model parameters: The computational mesh B presented in IV.3 was used for the hydrodynamic model calibration. The 24h dam flushing event was simulated using a constant time-step of 0.25s using the finite-elements numerical solver of Telemac-2D. Spatialization of Strickler's roughness coefficient was used for the calibration of the model. Sensibility analysis were firstly carried out using uniform Strickler's K distribution in the range of [30;33;35;40;45] $\mathrm{m}^{1/3}\mathrm{s}^{-1}$.

Experimental measurements [11] showed the particularity of the reach to be subjected to subcritical and supercritical flows, depending on several parameters such as the bed slope and the input discharge. Therefore, it has been considered essential to investigate the reach's flow regime by building both subcritical and supercritical models and by imposing different formulations for the boundaries. The imposed upstream discharge was originally measured at the downstream part of the reach, at the stream gauging station of Sainte-Marie-de-Cuines monitored by Irstea [11]. Upstream and downstream discharges were supposed equal due to the small area of the domain and the negligence of source terms such as precipitation or infiltration. A rating curve linking stage to discharge is introduced as the downstream boundary condition of the subcritical model, allowing more flexibility by canceling the time-lag effect between the imposed upstream discharge and the downstream water elevation originally measured at the same location. Water stage G3 is chosen as the second upstream boundary condition of the supercritical model. For the subcritical one the boundary condition was extended of an approximate distance of 400m upstream, allowing more flexibility by flow stabilization.

The supercritical model was unable to generate a relevant stationary flow, showing the importance of the downstream boundary by the predominance of subcritical flow. The hotstart generation (uniform steady flow) using a constant discharge of $5\mathrm{m}^3/\mathrm{s}$ has been well reproduced by the subcritical model using a 20,000s simulated time. At this given discharge, only two areas of supercritical flows located close to the bar head show Froude values in the range [1-1.2].

2) Mesh generation: Bar-scale topographic datasets M02 and M03 (*cf* III.D.1) were used for this study. Several computational mesh grid were set-up to perform the numerical tests (*cf* IV.A.3). Previous studies showed that the mesh can efficiently capture the information with an average resolution of 2m, with a minimum cell size approx. 0.5m in steepest slopes areas regions. Therefore, the mesh size has been directly linked to the bed slope S_0 calculated with ArcMap. The operation was only led in the area of interest. Beyond this area, the cell size was kept constant at 2.5m. The mesh density $dens$ was determined by using the following linear-thresholded function:

$$dens = \begin{cases} -0.03.|S_0| + 2, & \text{for } |S_0| < 0.5 \\ 0.5, & \text{otherwise} \end{cases} . \qquad (6)$$

3) Mesh convergence analysis: In order to assess the ability of the model to reproduce the field data observations, a mesh convergence analysis was proposed. This operation consist on creating several meshes, by using a coarse reference mesh template and increasing its cell density by a factor of 2 at each step. This pre-processing was performed by using the module Stbtel of the TMS. A single triangle is divided into four small ones, where the centered corners are defined by the middle points of each the initial triangle sides (Fig. 3). Three meshes were created, where the coarsest mesh shows a maximal density of 10m (C), 5m for the medium one (B) and 2.5m for the finest one (A).

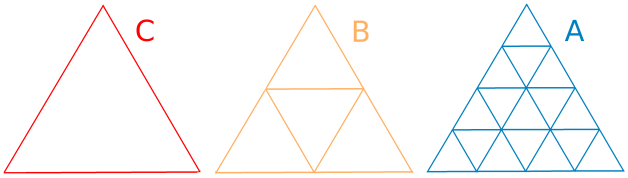

Fig. 3: Mesh creation process using the stbtel module. The mesh resolution is increased by a factor of 2 at each step.

Results of this convergence analysis were compared using the water stages G1-3 and the profile LS-PIV velocities C1,2 and D1-4. The simulations were launched using parallelism MPI library, with a 8-core processors Intel(R) Xeon(R) CPU E3-1240 v3@3.40GHz 3.39GHz.

According to the numerical results (Fig.4a,b), the coarsest mesh (C) showed overestimated water depths, whereas meshes (A) and (B) showed water depths in the same range. We can notice the general tendency of a general water stage decreasing when the mesh resolution increases. The cumulated

absolute error was calculated for each gauge where $err = \sum_{t=0}^{t=86400}(y_t - x_t)^2$ using x experimental data and y numerical results with time-step of 250s, showing the same conclusions as stated before.

Mesh	Density max.	Nb. nodes	Mean simul. time
A	2.5	17739	53 min 37 s
B	5	4556	20 min 59 s
C	10	1200	3 min 41 s

TABLE I: Main charecteristics of the meshes used for the convergency analysis, highlighting the fast growth of simulation time when the mesh quality increases.

Comparison between computed and observed velocity profiles (Fig.4c) was done for the medium (B) and the fine (C) meshes. The last comparison was made at the D-section, located at the bar's tail. The velocities distribution across the river's section justified the right bank erosion and the local deposits at the bar's tail. The velocity's curve can showed the difficulties of the model to reproduce the local variation due to the topographies changes during the flood and could arise from the model's limits, but on the whole the physical-mechanic process can be assumed to be well reproduced with both meshes. To conclude, the medium mesh (B) was clearly eligible to carry out sensitivity analysis and qualitative tests, giving a satisfactory compromise between the results obtained by a particular mesh and the computational time. The choice of the fine mesh (A) was advantaged to conduct quantitative processes and improve the accuracy of the (B) model's results.

B. Hydrodynamic model calibration

The horizontal spatialization process was handled by the Telemac-2D subroutine *corfon.f*, where Strickler's coefficient zones are defined using the polygon Fortran function `inpoly()`. Outcomes together with aerial photographs showing vegetated areas and granulometry maps were useful for the model calibration. Results of the model calibration are shown in Fig.4.

C. Pre-investigation of morphodynamics behavior

Numerical computations of the bed shear stress were performed for a preliminary analysis of the system behavior and its morphological response. Figure 2 shows the differences between the dimensional critical Shields parameter τ_c and the dimensional bed shear stress τ. The analysis was carried out for constant grain sizes of 2.5cm, 5cm and 10cm and for a grain size-distribution (Fig.2). For the high discharge values, the difference between $\tau_c - \tau$ can reach values up to 40Pa. The importance of sediment sorting along the domain, which is a characteristic of fluvial reaches presenting gravel-sanded bars, is illustrated in Figure 5). The finer sediment located over the bar surface are prone to erosion, even for medium discharges (Fig.5c).

D. Morphodynamics of the gravel bar unit

Sensitivity analysis were conducted to evaluate the response of the system in function of several parameters, such as the selected bedload transport formula, the activation of bed

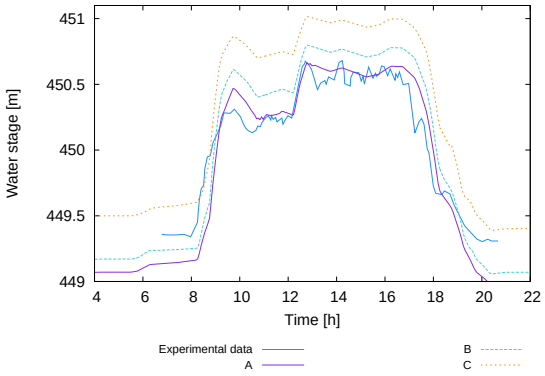

(a)

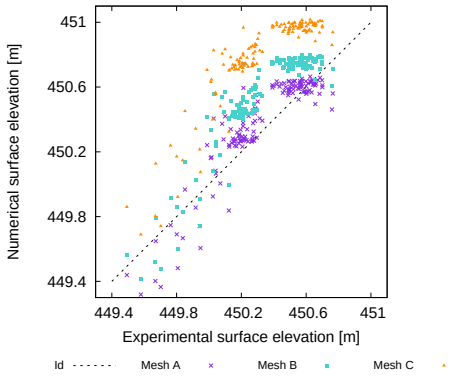

(b)

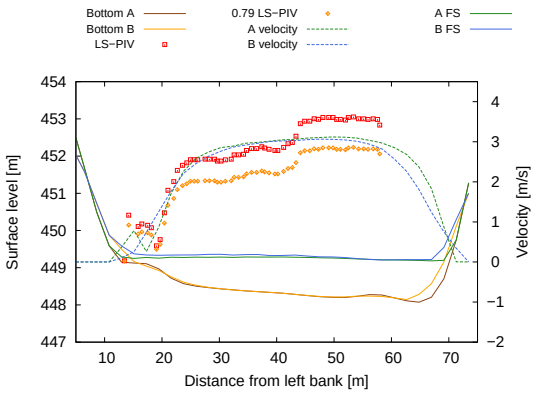

(c)

Fig. 4: (a) Results of mesh convergency analysis on water stages for the river bed M02 on Gauge 2, (b) on numerical surface elevation in function of experimental one on Gauge 2 and (c) on velocity profiles for meshes A and B along *D*-cross-section for the discharge D4=119m^3/s.

slope effect or even the sediment properties. Last step consisted on the calibration of the morphodynamic model to reproduce the 2006 dam flushing event.

1) Sensitivity analysis: A sensitivity analysis was performed to investigate the model response to the variation of different parameters. This investigation started by focusing on the bedload transport capacity (a), calculated with different

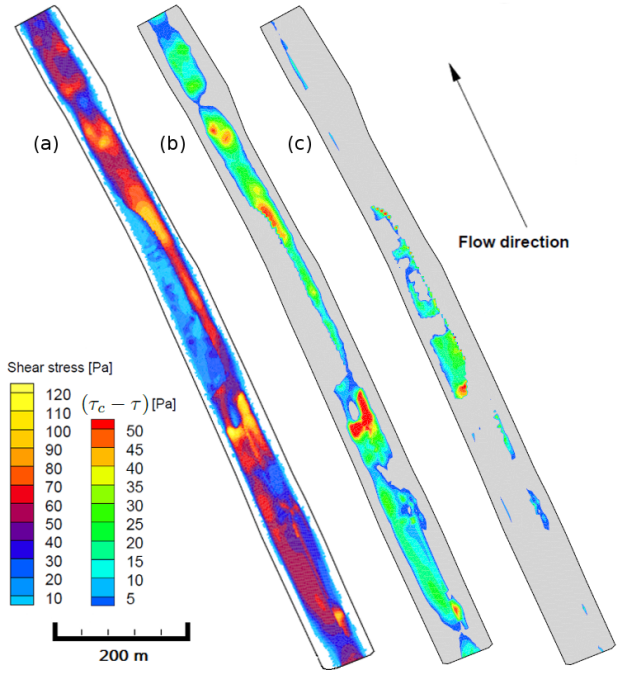

Fig. 5: (a) Shear stress map [Pa] at T=46000s. Difference (τ-τ_c) plotted at Q=120m^3/s (T=46000s) for (b) material diameter of 5cm and (c) spatialized sediment distribution.

sediment transport formulas (Meyer-Peter-Müller, Einstein-Brown, *etc.*) found in the literature. The granulometry effects (b) over the reach morphodynamics were studied by considering uniform and non-uniform sediment distributions, using various particle diameters. Last operations were done by considering the bed slope effect (c) induced by gravity and the secondary currents (d) activation, which allows the reproduction of helical flows induced by 3D effects in 2D-H models.

a) Bedload transport formula: Analysis of the reach morphodynamics evolution in function of the sediment transport capacity formula was done, using a uniform sediment distribution with a particle diameter equal to [1;3;5;7;10] cm. The choice of bedload transport capacity formula has a great

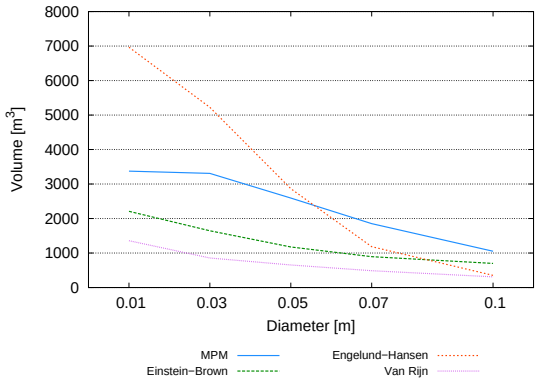

Fig. 6: Comparison of positive volumetric evolutions of the bar-scale domain using various bedload transport formulas.

impact on the volume of sediments eroded and deposited in the domain of interest (Fig.6). Einstein-Brown and Van Rijn formulas showed results in the same range in comparison with MPM one which slightly overestimated the phenomena of erosion/deposition (*e.g.* the computed q_b is greater). Engelund-Hansen formula is mostly useful to determine the total load transport.

Therefore, results differ from the previous ones, especially for particle diameters inferior to 5cm, showing more sensibility for the sediment diameter fluctuations. However, the erosion/deposition mechanic process was hardly ever perturbed, where locations of erosion and deposition remains quasi-identical.

A sensitivity analysis was done on the MPM α coefficient (*cf* II.B) for $\alpha = [2; 3; 4; 5; 6; 7; 8]$, using a uniform grain size distribution of 5cm. As expected, variation of α coefficient had an impact on the solid transport rate, which became greater when α increased (Fig.7c,d) and was also confirmed by the computation of positive and negative volumetric changes. MPM α coefficient had strong impacts on the riverbed evolution process, hence the coefficient is suitable to calibration.

b) Bed composition: The bed has been first described with an uniform sediment distribution. Particle diameters of [1;3;5;7;10] cm were considered using several sediment transport capacity formulas (*cf* IV.D.1.a). Fine sediments seems to be subjected to more transport (*e.g.* more erosion and deposition), whereas coarser gravels have the tendency to resist to the flow and stay unmoving. This physical phenomena is depicted by a diminution of erosion/deposition in amplitude, but also in space where differences can be mostly found over the bar close to transverse channels and zones of confluence (Fig.7b,c).

As a natural alpine river, the Arc is composed of a large mix of sediments. The river bed was described using a non-uniform distribution of sediments, where the particle diameters are in the range of [1;5;10] cm. Classes of sediments with their respective fraction were specified in the Sisyphe module. Riverbed evolution is calculated by calculating the solid transport discharge $q_{b,i}$ for each class of sediment i. Hence, the total computed solid discharge is equal to $q_b = \sum_{i=1}^{nclass} q_{b,i}$.

The bed-material mixture, described by the fraction of each sediment class, strongly affects the morphodynamic evolution of the reach both in space and amplitude. A poor-sorted granulometry (40% of 1cm - 20% of 5cm - 40% of 10cm) seems to increase the phenomena of erosion-deposition (Fig.7e). While the variation of the particle diameter has little impact in space on the evolution of an uniform bed, the mixture of sediments in non-uniforms riverbeds seems to alter stronger the morphodynamics in space. This can be mostly observed close to the bar's tail and close to the transverse channels.

c) Slope effect: The actual model seemed to be much more sensible to the deviation effects than the magnitude ones. This has been demonstrated using Soulsby's formulation for magnitude (Eq.4) and Talmon's *et al.* formulation for deviation (Eq.5). Deviation correction effects are controlled by the calibration of β_2. Low values of β_2 (Fig.7g) showed overestimated erosion of the bar and deposition in the main channel, whereas higher ones (Fig.7h) showed less sediment

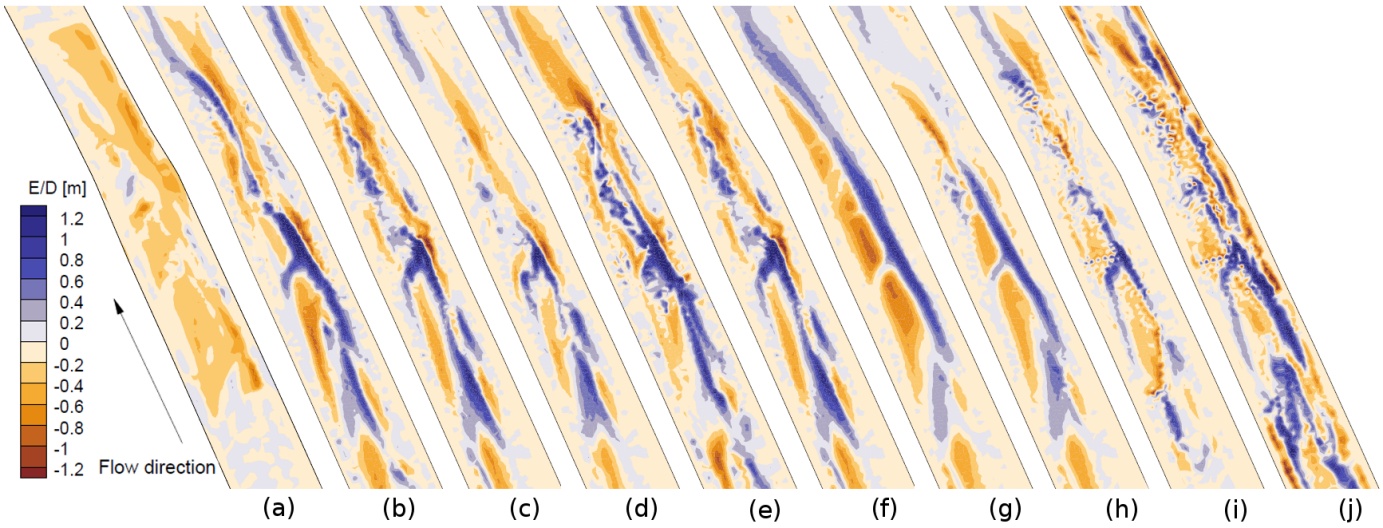

Fig. 7: Comparison of bed river evolution after the dam flushing event (erosion/deposition) using : (a) experimental data; uniform sediment distribution of (b) 1cm (c) 5cm (d) 5cm and α=5; (e) non-uniform sediment bimodal distribution; (f) secondary currents; bed-slope effects using β_2= (g) 1.6 (h) 3; non-uniform spatialized sediment distribution with α=5, β_2=2.5 and secondary currents for a main channel composed of (i) big boulders (j) mix of big boulders and sand.

motion. Using high values of β_2 diminished the bed slope effect, and tended to converge to the state without bed slope consideration (Fig.7c). However, values in the range [1;3] seems to provide a physically relevant compromise. A general smoothing of results can be noticed once the bed-slope effect is activated due to the diffusivity effects.

d) Secondary currents: We can notice the bedload movement deviation from the main flow direction, showing sharp differences over the middle part of the bar, where transverse channels connects the secondary and the main channel together (Fig.7f). Deposits fronts directions in this area were changed, taking into account to the helical flows together with gravitational effects.

2) Morphodynamic model calibration: Morphodynamic simulations presented here were performed for a time step $\Delta t = 0.25$s, with a MPM α coefficient $= 5$. At the inflow boundary condition, the equilibrium solid discharge is imposed. At the outflow boundary condition, a free or Neumann-type boundary condition has been imposed.

The non-uniform sediment distribution along the reach (*cf* III.D.1) is given by Fig.2. Horizontal spatialization process is handled by the Sisyphe subroutine called *init_compo.f*, using the Fortran polygon function `inpoly()` wherein zones composed of different fractions of each sediment class are defined.

Due to difficulties to conduct measurements in the depth-damped areas, the grain size distribution in the main channel remained a mere estimation [11], leading to assumption that the main channel's bed is composed of large boulders (12.8-25.6cm). The riverbank composition was also roughly estimated, mostly composed of bimodal distribution of boulders and sparse fine sediments deposited after flooding events. Several investigations of the morphodynamic response of the system were carried out, depending of the bed-material composition of the main channel and the riverbanks.

The main channel riverbed composition had a predominant effect on the final morphodynamic evolution of the reach. Indeed, large boulders (20% of 10cm - 80% of 18cm) were found to be more stable than a bed composed of finer sediments (50% of 1mm - 50% of 18cm). The bar was less eroded for the bed composed of finer sediments (Fig.2i,j), whereas the riverside at the opposite of the bar was strongly eroded and the main channel is filled of deposited sediments. Last investigations were done on the riversides. Although the morphological evolution of the reach was altered by the riversides composition, the amplitude seemed to be lessened compared to the effects induced by changes of the main channel granulometry. This was due to the rare contacts between the flows and the riversides, only triggered during highest flood-stages. This effect is non-negligible, where we observe a stronger erosion of the right riverside and the apparition of a deposit front located in the main channel for finer granulometry distribution. Higher flood-stages could play a major role on the reach planform evolution. This is subject of future investigations.

V. 2D NUMERICAL SIMULATIONS OF THE LARGE-SCALE REACH

In this section, preliminary simulations of alternate bars in a 8 km reach, subject to the influence of constant upstream discharges and constant sediment distribution are presented.

A. Model parameters

1) Mesh and bathymetry: The long-time morphodynamical evolution of the 8km long reach (Fig.1b) was investigated. The simulation started with an almost panform bed, enriched by the M02 bathymetric dataset in the downstream part describing the bar unit (*cf* III.D.1). The computational mesh-grid is composed of 37.330 nodes and was generated using a mesh size around 5m.

2) Hydrodynamic calibration: A uniform distribution of the Strickler coefficient was considered for the calibration of the model, using a value of K=35 $m^{1/3}s^{-1}$. The calibration process was carried out following a similar methodology as for the bar-scale model, by using the dam-flushing event of 2006.

3) Morphodynamic parameters: Numerical simulations were performed with a time step $\Delta t = 0.10$ s to prevent for instabilities due to higher velocities in consequence of higher discharges imposition. The MPM α coefficient was kept equal to 5. At the inflow boundary condition, the equilibrium solid discharge was imposed. At the outflow boundary condition, a free or Neumann-type boundary condition was set. The computational cells located in a range of aproximately 20 m from the boundaries were assumed as non-erodible. This operation was necessary to prevent for morphodynamical instabilities generally provoked by supercritical flows in the boundaries areas. A uniform constant sediment distribution of the riverbed was considered, using a bed-material diameter of 2cm.

B. Morphodynamics of the large-scale reach

Preliminary simulations were performed by imposing constant discharges of 90m^3/s, 150m^3/s and 200m^3/s at the upstream boundary. According to Jaballah *et al.* [9], it was observed that the higher discharge submerged the existing bars. In agreement with observations, the large-scale morphological features observed downstream of the reach was reproduced for the three imposed discharges, even for a constant sediment distribution and simplified hydrological conditions [8], [9], see Figure 8.

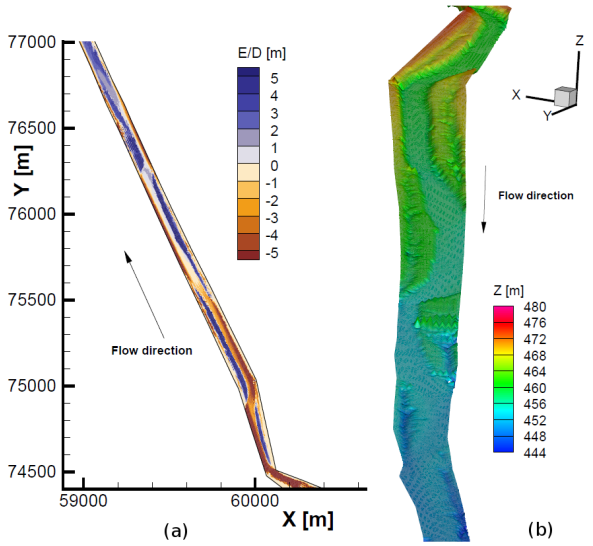

Fig. 8: (a) Morphological evolution of the downstream part of the reach and (b) resulting riverbed, leading to the formation of alternate bars. Forced bars are the results of the forcing effects of the curve. The simulation has been computed with a numerical time of 100 days with Q=100m^3/s.

VI. Conclusions

In this work, morphodynamic simulations were presented for two different spatial scale reaches of the Arc en Maurienne river in France. Firstly, a morphodynamic model at a gravel bar-scale reach (of the order of 1 km) was developed and validated with high resolution field measurements. Secondly, the capability of the model to reproduce the formation and propagation of alternate bars in a 8 km reach model was assessed. For the gravel bar-scale reach model, an exhaustive sensitivity analysis was performed for different model parameters and flow conditions. Preliminary results for the 8 km reach showed that the model was able to reproduce the formation of an alternate bar system, even for a constant sediment distribution and simplified hydrological condition. Future works include further comparisons of the dynamical characteristics of the large-scale morphodynamics structures with field data and observations (satellite images, aerial photographs) and the study of the influence of the initial conditions on the final or steady morphological patterns distribution. Finally, it is expected to perform a series of test of different scenarios of type what-if ? (anthropic influence), designed on the basis of discussions with engineers and practitioners.

Acknowledgments

We are grateful for the precious contribution of M. Jaballah (measurement data). Financial support for F. Cordier's internship through the Project PHE (EDF R&D) and the Institut Méditerranen du Risque, de l'Environnement et du Développement Durable (IMREDD) is gratefully acknowledged.

VII. References

[1] A. Bernini, V. Caleffi, and A. Valiani, "Numerical modelling of alternate bars in shallow channels," *Braided Rivers: Process, Deposits, Ecology and Management (Special Publication 36 of the IAS)*, vol. 21, p. 153, 2009.

[2] J. S. Bridge, *Rivers and floodplains: forms, processes, and sedimentary record*. John Wiley & Sons, 2009.

[3] D. Chen and C. Tang, "Evaluating secondary flows in the evolution of sine-generated meanders," *Geomorphology*, vol. 163–164, no. 0, pp. 37–44, 2012, meandering Channels. [Online]. Available: http://www.sciencedirect.com/science/article/pii/S0169555X12001833

[4] A. Crosato, F. B. Desta, J. Cornelisse, F. Schuurman, and W. S. J. Uijttewaal, "Experimental and numerical findings on the long-term evolution of migrating alternate bars in alluvial channels," *Water Resources Research*, vol. 48, no. 6, pp. 1–14, 2012, w06524. [Online]. Available: http://dx.doi.org/10.1029/2011WR011320

[5] G. Duro, A. Crosato, and P. Tassi, "Numerical study on river bar response to spatial variations of channel width," *Advances in Water Resources*, vol. Accepted, 2015.

[6] F. Engelund, "Flow and bed topography in channel bends," *Journal of the Hydraulics Division*, vol. 100, no. 11, pp. 1631–1648, 1974.

[7] Hydratec and Cemagref, "Etude hydraulique de l'Arc en Maurienne de Modane à l'Isére," Hydratec and Cemagref, Tech. Rep., 1999.

[8] M. Jaballah, "Alternate-Bar morphodynamics in an engineered mountains river," Theses, Université Claude Bernard - Lyon I, Nov. 2013. [Online]. Available: https://tel.archives-ouvertes.fr/tel-01145403

[9] M. Jaballah, B. Camenen, L. Pénard, and A. Paquier, "Alternate bar development in an alpine river following engineering works," *Advances in Water Resources*, vol. 81, pp. 103–113, 2015, fluvial Eco-Hydraulics And Morphodynamics. [Online]. Available: http://www.sciencedirect.com/science/article/pii/S0309170815000585

[10] M. Jodeau, A. Hauet, A. Paquier, J. Le Coz, and G. Dramais, "Application and evaluation of ls-piv technique for the monitoring of river surface velocities in high flow conditions," *Flow Measurement and Instrumentation*, vol. 19, no. 2, pp. 117–127, 2008.

[11] M. Jodeau, "Gravel bar morphodynamics in an engineered river during high flow events," Theses, Université Claude Bernard - Lyon I, Nov. 2007. [Online]. Available: https://tel.archives-ouvertes.fr/tel-00198125

[12] L. Leopold and M. Wolman, "River channel patterns," *Fluv Geom: Geom Crit Conc Vol*, vol. 1, p. 3, 1957.

[13] H. pei An, S. chin Chen, H. chuan Chan, and Y. Hsu, "Dimension and frequency of bar formation in a braided river," *International Journal of Sediment Research*, vol. 28, no. 3, pp. 358–367, 2013. [Online]. Available: http://www.sciencedirect.com/science/article/pii/S1001627913600463

[14] A. Siviglia, G. Stecca, D. Vanzo, G. Zolezzi, E. F. Toro, and M. Tubino, "Numerical modelling of two-dimensional morphodynamics with applications to river bars and bifurcations," *Advances in Water Resources*, vol. 52, pp. 243–260, 2013. [Online]. Available: http://www.sciencedirect.com/science/article/pii/S0309170812002928

[15] A. Talmon, N. Struiksma, and M. Van Mierlo, "Laboratory measurements of the direction of sediment transport on transverse alluvial-bed slopes," *Journal of Hydraulic Research*, vol. 33, no. 4, pp. 495–517, 1995.

[16] M. Wong and G. Parker, "Reanalysis and correction of bed-load relation of meyer-peter and müller using their own database," *Journal of Hydraulic Engineering*, vol. 132, no. 11, pp. 1159–1168, 2006.

[17] W. Wu, *Computational River Dynamics*, ser. NetLibrary, Inc. CRC Press, 2008. [Online]. Available: https://books.google.fr/books?id=EggiazLLXaYC

[18] M. S. Yalin, "Review of fluvial processes," *Journal of Hydraulic Engineering*, vol. 129, no. 2, pp. 169–169, 2003. [Online]. Available: http://dx.doi.org/10.1061/(ASCE)0733-9429(2003)129:2(169)

[19] C. Zi-Tan, *A method to modify interpolations for integration of break lines*, 1988.

Numerical modeling of sediment transfers at the catchment scale with TELEMAC

TACCONE Florent & ANTOINE Germain
Laboratoire National d'Hydraulique et Environnement
EDF R&D
Chatou, France
germain.antoine@edf.fr

***Abstract*— The aim of this work focuses on the extension of the 2D code TELEMAC-SISYPHE from the river bed to the catchment scale. Several formulae have been implemented into the code in order to take into account erosion processes due to the rainfall. Furthermore, a continuous model, which estimates the friction coefficient directly as a function of the water level, has been implemented. These new developments are tested first on two theoretical test cases, representing two different scales: the first one represents processes at the plot scale, and the second one models two hillslopes adjacent to a straight river bed. Then the model is validated and calibrated on field data from a real catchment (Draix, in the Southern French Alps). These first results are very promising, and open new perspectives on the way of applying TELEMAC.**

INTRODUCTION

The transfers of sediments and associated contaminants play an important role in catchment management. An excessive sediment yield from hillslopes to river channels can contribute to reservoir siltation, degradation of aquatic habitats and to the export of nutrients or contaminants to downstream water bodies. However, the dynamics of sediment and contaminant redistribution is highly variable in space and time due to the complex non-linear processes involved. Because of this complexity and the huge spatial and temporal scales of the processes, few numerical models are today able to reproduce this transfer dynamic.

One of the main difficulties consists in representing continuously the flow and the erosion processes that are involved in every compartments of the watershed. Especially, a continuity between river flow and sheet flow has to be defined. Furthermore, it is necessary to represent the rain effect on the hillslope erosion, and to model properly the moderating effect of the water level on this specific erosion. From the hillslope to the river bed, many erosion processes may be involved, such as splash effect, rain fall induced transport or rain detachment with flow transport. In order to reproduce the effective sediment transport at the catchment scale, each one of these erosion processes has to be represented with the right order of magnitude.

In this work, a continuous model of the friction coefficient, calculated as a function of the water depth, has been implemented in TELEMAC-2D. Four rain detachment formulas have been also implemented in TELEMAC-SISYPHE, in order to take into account the effect of the rain as an additional source term in the advection-dispersion equation for suspended sediment transport. These new developments of the code, presented in the first part of this paper, have been evaluated on two test cases: one simple plot with a slope break for representing the local scale, and one straight river bed with two adjacent hillslopes for an intermediate scale. Then, data from a real watershed have been used to evaluate their relevance on a large scale by comparing the simulated results and the measurements. These results are presented in the second part, and discussed in the last part.

MATERIALS AND METHODS

All the simulations have been performed with the V7P0 version of TELEMAC-SISYPHE. The suspension sediment transport is calculated with the 2D advection-dispersion equation in the conservative form, and the source terms for erosion and deposition depend on the considered sediments. In this study, we focused on non-cohesive sediments. From a defined value of sediment diameter, the default parameters of the suspension simulation have been used. For non-cohesive sediments, the erosion and deposition terms are calculated as:

$$E - D = V_s(C - C_{eq})$$

with E the erosion rate ($m.s^{-1}$), D the deposition rate ($m.s^{-1}$), V_s the settling velocity calculated with the Soulsby formula, C the concentration of sediment in the flow and C_{eq} the equilibrium concentration evaluated with the Zyserman and Fredsoe formula (see the manual [1] for more informations).

Friction coefficient estimation

To represent the bottom friction, the model presented here has been defined in [2]. The inundation ratio Λ is a dimensionless number which is defined by the following formula:

$$\Lambda = \frac{h}{k}$$

with h the water depth and k the representative height of the soil roughness.

Using this parameter, the Darcy-Weisbach coefficient *f* is characterized by the equation:

$$f = \begin{cases} \left(\frac{1}{1.64 + 0.803\ln(\Lambda)}\right)^2 \; if\ \Lambda \geq 10 \\ \frac{10}{\Lambda} \; if\ 1 \leq \Lambda < 10 \\ \frac{192}{\pi R_*} min\left(\frac{\pi}{4}, \Lambda\right) \; else \end{cases}$$

with R_* the Reynolds number associated to a particle.

Finally, the Chezy coefficient C ($m^{1/2}.s^{-1}$) is given by:

$$C = \sqrt{\frac{8g}{f}}$$

With g the gravity acceleration in $m.s^{-2}$.

We can notice that for very small values of Λ, the friction is representative of a sheet flow around spherical structures.

Rain erosion

Four formulas have been chosen from existing erosion codes (PSEM_2D [3], WESP [4], EUROSEM [5] and FullSWOF_2D [6]) in order to reproduce the detachment due to rain drop impacts:

- $E1 = \alpha_r R\left(1 - \frac{h}{6.69R^{0.182}}\right)$
  with α_r the erodability coefficient ($kg.m^{-2}.mm^{-1}$), R the rain intensity ($m.s^{-1}$) and h the water depth (mm).
- $E2 = K_i R^2$
  with K_i the erodability coefficient ($kg.m^{-4}.s^{-1}$) and R the rain intensity ($m.s^{-1}$).
- $E3 = \frac{k}{\rho_s}(8.95 + 8.44\log(R))\ e^{-2h}$
  with k the erodability coefficient ($g.J^{-1}$), ρ_s the density of sediments ($kg.m^{-3}$), R the rain intensity ($m.s^{-1}$) and h the water depth (m).
- $E4 = \alpha\frac{h_0}{h}R$
  with α the erodability coefficient ($kg.m^{-3}$), h_0 the minimal value of the water depth to drag sediments (m), h the water depth (m) and R the rain intensity ($m.s^{-1}$).

An important point to notice is that the moderating effect of the water level h on the rain drop impacts is taken into account in E1, E3 and E4 by different ways.

These equations are implemented into SISYPHE as an additional source term for erosion in the advection-dispersion equation for suspended sediment transport.

Hairsine and Rose model

Another complete model for erosion and deposition is tested. In the Hairsine and Rose model, described in [7], the continuity equations for suspension and for bed evolution are the same as in SISYPHE, with different source terms for erosion and deposition. In this model, a deposited layer is introduced and is governed by the equation:

$$\frac{\partial M}{\partial t} = D - E_{fd} - E_{rd}$$

where M is the mass of the deposited layer ($kg.m^{-2}$), D the deposition rate ($kg.m^{-2}.s^{-1}$), E_{fd} and E_{rd} ($kg.m^{-2}.s^{-1}$) the detachment of the deposited layer due to respectively the flow and the rain.

In addition to the three source terms representing the evolution of the deposited layer, there are two erosion terms that influence the original soil E_r and E_f. These 5 source terms for both original soil and deposited layer are detailed bellow:

- $D = Ch\left(1 - e^{\frac{-V_s dt}{h}}\right)$
- $E_r = (1 - H)\alpha R\frac{h_0}{h}$
- $E_{rd} = H\alpha_d R\frac{h_0}{h}$
- $E_f = (1 - H)\frac{F(\omega - \omega_c)}{J}$
- $E_{fd} = HF(\omega - \omega_c)\frac{\rho_s}{(\rho_s - \rho)gh}$

where C is the mass concentration ($kg.m^{-3}$), h the water depth (m), V_s the settling velocity ($m.s^{-1}$), dt the time step (s), α and α_d are erodability coefficients respectively for original soil and deposited layer ($kg.m^{-3}$), R is the rain intensity ($m.s^{-1}$), ω-ω_c the available stream power ($m^2.s^{-1}$), F a fraction, g the gravity acceleration ($m.s^{-2}$), ρ the water density ($kg.m^{-3}$) and ρ_s the sediment density ($kg.m^{-3}$). The high number of parameters is the main characteristic of this model, therefore its calibration might be difficult.

Theoretical test cases

To test these developments, a very intensive rain (100 $mm.h^{-1}$) is simulated on two domains (Fig. 1) during one hour.

The first test case is a 4×1 m parcel, with a 10% slope upstream, a slope break in the middle and a 1% slope downstream. The size of the mesh is 1 cm and a water height of 3 mm is imposed at the downstream boundary. The chosen constant value of the Chezy coefficient is 28.

The second one is a river with two adjoining 20 m hillslopes with a 10% slope. A discharge of 1 $m^3.s^{-1}$ is imposed upstream, then flowing over 50 m following a 1% slope, to a reservoir with a 3 m weir downstream. The river is considered as a non-erodible zone. The Chezy coefficient for the constant bottom friction model is 40 and the chosen size of the mesh is 15 cm.

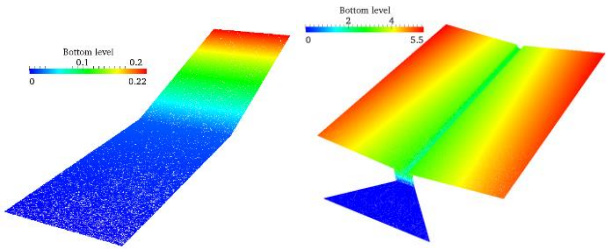

(a) : 4×1 m parcel (b) : River with adjacent parcels

Figure 1: Representation of the bottom level (m) for the two theoretical test cases

For both test cases, the size of the non-cohesive sediments in the model is 150 µm, this value is used as the representative height of the soil roughness. In every node of the mesh, a random number between -1 mm and 1 mm, following a uniform distribution, is added to the bottom elevation to create a disturbance in order to be more representative of a real soil.

Real case

Thanks to data provided by [8], it is possible to evaluate these new developments by comparing results from SISYPHE to measured discharges and suspended sediment concentrations from field campaigns on a real catchment.

The Laval watershed (Fig. 2) is a sub-catchment of the Bouinenc watershed, located on the Draix site in the Southern French Alps. Its total area is about 86.4 ha. The soil is mostly constituted of black marls and half of the surface is a bare soil. At the outlet of the catchment, the discharge and the associated sediment concentration are available for many rainfall events.

First the same constant one-hour rain is performed on the whole watershed in order to evaluate the model at this scale. Then two fast and intensive rainfall events are chosen in order to calibrate and validate the new developments. The hydraulic part of the model is calibrated using different size of the surface roughness, which is the k parameter in the inundation ratio used for the friction model. Indeed, the main river bed contains bigger irregularities, thus a specific value of k is defined in this zone.

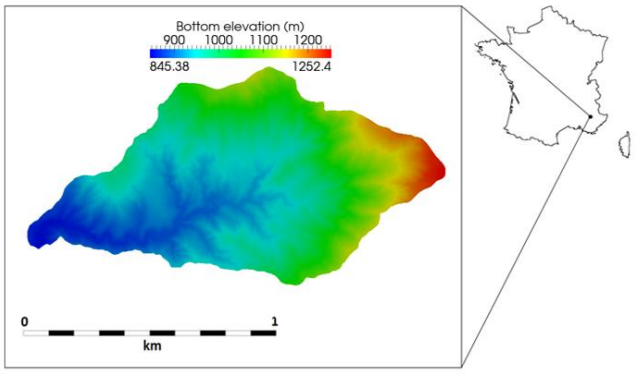

Figure 2 : Presentation of the Laval watershed

RESULTS

Plot scale erosion

For the first test case, the hydraulic results from TELEMAC-2D for a constant value of friction coefficient are presented on the Fig. 3. On this figure, the water depth and the Froude number are plotted. These results show a roll-wave phenomenon in the steep slope part of the domain. This phenomenon appears only under specific conditions of runoff flow. This is due to the soil disturbance when the Froude number is higher than 2. The waves reach a height of 2 mm when they are close to the break in slope and the water depth varies from 1 mm to 3 mm downstream. It is interessting to notice that the same roll-waves are observed with the variable friction model, but in this case, the wave period is higher.

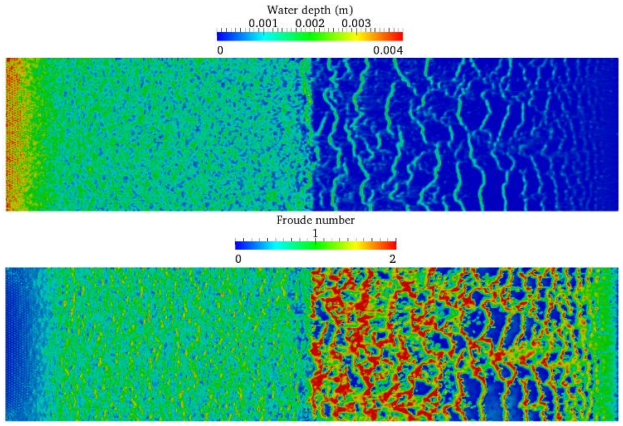

Figure 3 : Water depth and Froude number at the end of the simulation. The downstream boundary is on the left.

The main difference between the constant friction model and the variable one consists in estimating the bed shear stress. The Fig. 4 shows the calculated values of bed shear stress in the case of constant or variable friction coefficient. We can see higher values if the friction coefficient is calculated on each point, particularly in the upstream part. The maximal value of the shear stress is 1.35 Pa with the variable model, while it is only 0.93 Pa if the friction coefficient is constant.

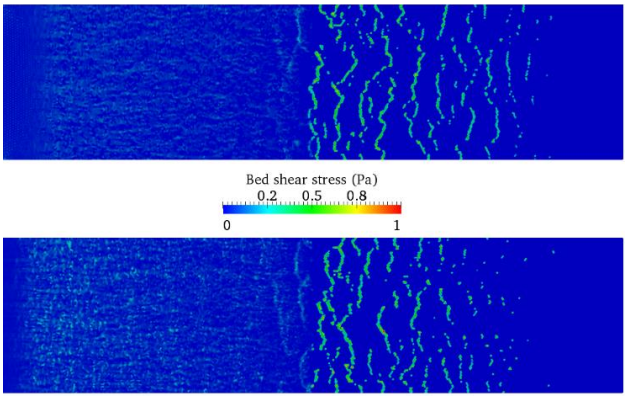

Figure 4 : Bed shear stress with the constant bottom friction model (at the top) and the variable one (at the bottom).

By coupling the model with SISYPHE, the bottom evolution is calculated and updated at each time step. The effects of the respective friction models on the bed evolution are compared on the Fig. 5. The models are compared first without adding specific terms for rain erosion. For both models, a rill erosion can be observed in the upstream part of the domain. In the case of a variable friction coefficient, the rills are deeper and visible even in the downstream part of the domain. This result is relevant regarding the previous conclusions on the bed shear stress values.

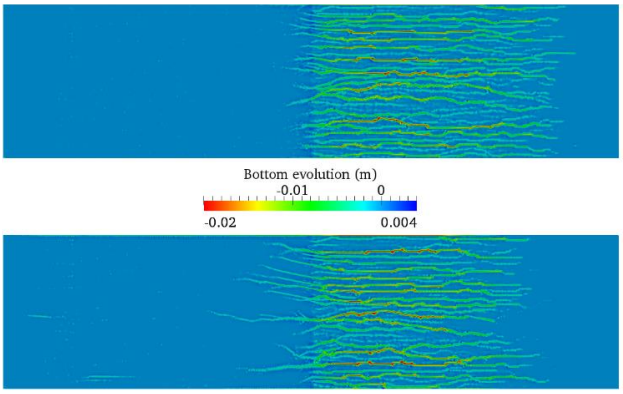

Figure 5: Bottom evolution without adding rain effect, using the constant friction model (at the top) or the variable one (at the bottom).

In order to test the four formulas defined in the part 1 for estimating the rain effect on the erosion term, a cross section is defined 20 cm upstream the break slope. On this cross section, the bed evolutions are compared after one hour of simulation for the four formulas (Fig. 6).

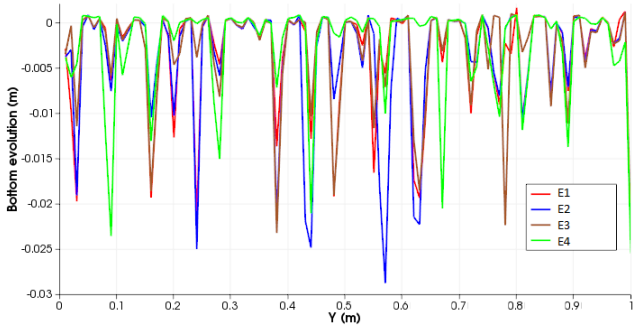

Figure 6 : Comparison of the bottom evolution between the rain detachment formulas on a cross section of the plot.

As a default set of parameters is available in FullSWOF_2D for the Hairsine and Rose model, the erodability parameters of each formula E1, E2 and E3 have been calibrated in order to obtain the same total volume with a constant friction value (at least the same order of magnitude). The Table 1 shows the computed volumes on the whole domain at the end of the simulation. Even if the computed volumes are comparable, the results of the Fig. 6 show that the rill formation is very different from one case to another.

An important point to notice is that the configurations SISYPHE+E4 and Hairsine & Rose evaluate the same rain effect with different source terms for flow erosion and deposition. In order to evaluate the impact of changing the flow detachment evaluation, these two configurations are compared on the same cross section (Fig. 7).

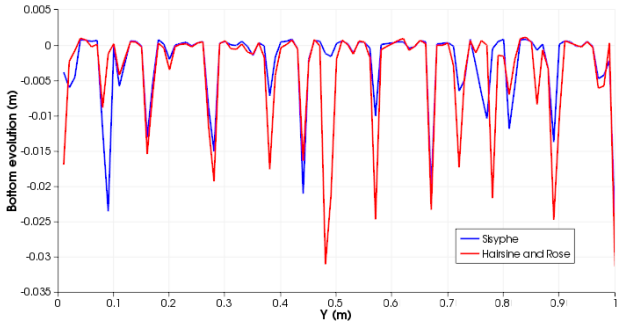

Figure 7 : Comparison between the SISYPHE+E4 and Hairsine and Rose models on a cross section of the plot

In this case, the rills are formed in the same place, even if their depth are frequently bigger with the Hairsine and Rose model. The effect of changing source terms for flow erosion and deposition is less significant than the one resulting of changing the rain effect at this scale.

The eroded and deposited volumes are presented in the Table 1 for all the tested combinations. We can notice that the use of a variable friction coefficient has no significant effect on the Hairsine & Rose model, but this effect is not negligible for the other configurations.

Especially, the configuration SISYPHE+E4 is very sensitive to the friction variations and this sensitivity not reliable with the other configurations. We can also notice that the rain detachment plays a significant role in the total erosion at this scale.

Model	Eroded volume	Deposited Volume	Total Volume
Constant friction			
SISYPHE	3.123	0.2545	-2.868
SISYPHE + E1	8.402	0.4717	-7.930
SISYPHE + E2	8.297	0.4725	-7.825
SISYPHE + E3	8.147	0.4719	-7.675
SISYPHE + E4	7.758	0.6283	-7.130
Hairsine and Rose	8.284	0.5234	-7.760
Variable friction			
SISYPHE	3.1490	0.3086	-2.840
SISYPHE + E1	10.51	0.3161	-10.19
SISYPHE + E2	10.38	0.3181	-10.07
SISYPHE + E3	10.34	0.3166	-10.02
SISYPHE + E4	5.064	0.1901	-4.874
Hairsine and Rose	8.105	0.4348	-7.671

Table 1 : Eroded and deposited volumes (10^{-3} m^3) computed at the end of the simulation for the first theoretical test case

River and adjoining hillslopes

In the second theoretical test case, the runoff causes roll-waves on the parcels when the Froude number is greater than 2, as it was observed in the first plot case. The Fig. 8 illustrates this result. Close to the river, the roll-waves reach about 1 cm height. In the channel, the flow is subcritical and it is slowed down by the flow conditions into the reservoir about 15 m before the entrance of the reservoir.

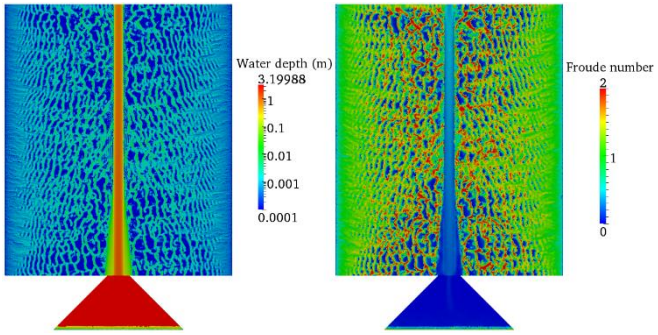

Figure 8 : Water depth and Froude number and the end of the simulation in the whole domain.

Depending on the chosen friction model (constant or variable), the Fig. 9 shows that the computation of the bed shear stress is this time again very different. Indeed, a homogenization is visible between the hillslopes and the river bed in the case of a variable friction coefficient. With a constant value of friction coefficient, the maximal value of the bed shear stress is 2 Pa on the hillslopes and 8 Pa in the river. If the friction coefficient depends on the water depth, it reaches a maximum value of 2 Pa in the river. We can also notice that the roll-waves period is higher with a variable coefficient, and that this phenomenon appears more upstream on the hillslopes.

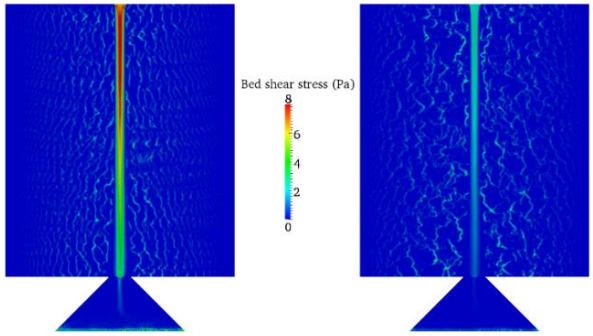

Figure 9 : Bed shear stress with the constant friction value (on the left) and the variable one (on the right)

The bottom evolution is first computed with the simple SISYPHE configuration (Fig. 10). We can observe that rills appear because of the runoff due to the rain on the hillslopes, and these rills are longer if the friction coefficient is variable. In terms of eroded volumes on the whole domain (Table 2), we can notice that the eroded volume is significantly higher with a variable friction coefficient. Concerning the deposition, whatever the characterisation of the friction coefficient is, it is located on the banks of the river, especially where the flow velocity starts slowing down.

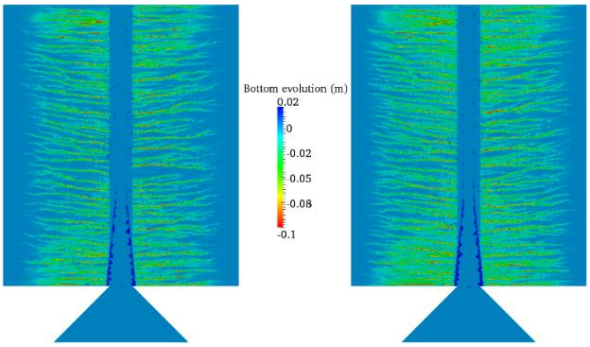

Figure 10 : Bottom evolution with the SISYPHE configuration, using the constant friction model (at the top) and the variable one (at the bottom).

As for the first test case, the four formulas Ei defined in the first part of this paper have been tested, using the same parameters than for the previous test case. The observed differences between SISYPHE+E1, E2 or E3 are very small (Table 2) and not significant with the simple SISYPHE configuration. This result can be explained by the dimensions of the eroded rills, which are much longer and deeper in this test case, and by the way more exposed to the flow erosion.

Because the main difference between the SISYPHE configurations and the Hairsine and Rose model consists in the erosion and deposition processes due to the flow, we can observe significant differences between these configurations in terms of global calculated volume (Table 2).

The Fig. 11 shows the bed evolution for the configurations SISYPHE+E4 and the Hairsine and Rose model, with a variable friction coefficient. The deposition appears to be more realistic with the Hairsine and Rose model, because it is very well correlated to the decrease of transport capacity. By using the Hairsine and Rose model, we can clearly observe a sediment transfer from the hillslopes to the reservoir. However, as it can be seen in the Table 2, the eroded volume is about two times bigger with the Hairsine and Rose model.

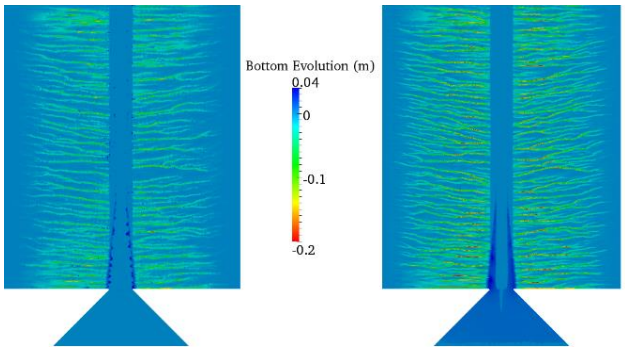

Figure 11 : Bottom elevation with the SISYPHE code (on the left) and with the Hairsine and Rose model (on the right)

For this test case, a last configuration has been tested. All the previous presented results are available by considering the main river bed as a non-erodible zone. The Fig. 12 presents the bed evolution obtained with the Hairsine and Rose configuration with an erodible river bed, by using a constant or a variable friction coefficient. These results show that the river bed erosion is higher when the friction coefficient is constant than when it is variable, as expected with the bed shear stress results in the Fig. 9. With the constant friction, the erosion in the river is about 1 m at the end of the simulation, while it is only 0.3 m with the variable friction model.

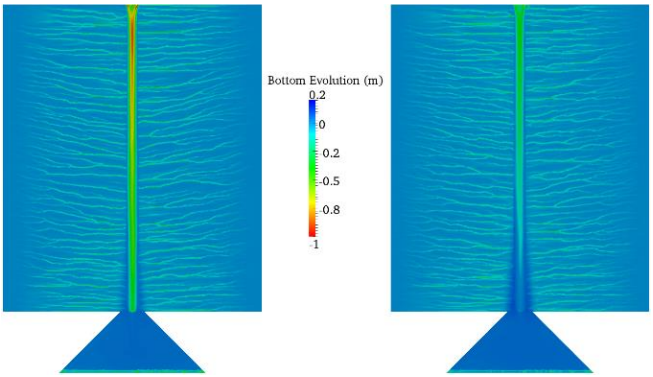

Figure 12 : Bed evolution obtained with the Hairsine and Rose configuration and an erodible river bed, with a constant friction on the left, and a variable one on the right.

The Table 2 summarizes the eroded volumes in the domain for the different tested configurations. The highest difference is visible between the Hairsine and Rose model and all the SISYPHE configuration. By using a variable friction coefficient, this difference tends to be decreased.

Model	Eroded volume	Deposited Volume	Total Volume
Constant friction			
SISYPHE	16.00	0.2969	-15.70
SISYPHE + E1	17.65	0.3794	-17.27
SISYPHE + E2	17.60	0.3812	-17.21
SISYPHE + E3	17.55	0.3769	-17.17
SISYPHE + E4	16.16	0.3078	-15.86
Hairsine and Rose	30.78	1.677	-29.11
River erosion	57.25	7.132	-50.12
Variable friction			
SISYPHE	20.58	0.3289	-20.25
SISYPHE + E1	21.82	0.4806	-21.34
SISYPHE + E2	21.89	0.4694	-21.42
SISYPHE + E3	22.02	0.4891	-21.53
SISYPHE + E4	20.72	0.3324	-20.38
Hairsine and Rose	28.63	3.438	-25.19
River erosion	50.03	9.126	-40.91

Table 2: Eroded and deposited volumes (m^3) calculated on the whole domain for the second theoretical test case

The Laval catchment

First a constant one-hour rain is applied on the whole watershed in order to evaluate the new developments by the same way than the two previous test cases. The Fig. 13 shows the results in terms of water discharge and suspended sediment concentration at the outlet of the catchment, for the constant and the variable friction coefficient model.

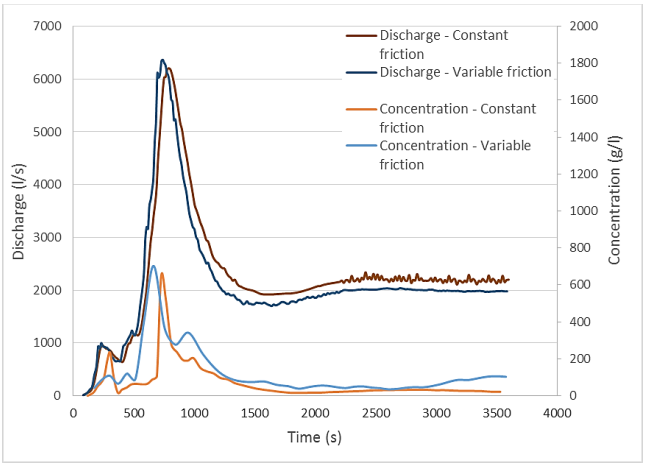

Figure 13 : Discharge and concentration at the outlet depending on the friction model

We can see on this figure that the variation of the friction coefficient does not have a significant effect on the discharge at the outlet. When the flow is stabilized, the flow rate is lower for the variable friction coefficient and presents no high-frequency variations.

On the opposite, the choice of the friction model has a significant impact on the suspended sediment concentration signal. The results on the Fig. 13 show that even if the magnitude of the maximum value is the same for both models, the shapes of the two signals are very different: with a variable friction coefficient, the arrival time of the maximum value is smaller, and the signal presents a second significant peak value.

The Fig. 14 shows the bed shear stress in the watershed at the end of the simulation, when the flow is stabilized. Unlike the results for the two theoretical test cases presented previously, a preferential flow is already created in the watershed.

Thus, the velocities are increasing along the river and its tributaries, as well as the bed shear stress values. In analogy to the second theoretical test case, the shear stress is smaller in the river bed with a variable friction coefficient than with a constant one.

Indeed, the value of the bed shear stress with the constant friction coefficient can exceed 100 Pa at some points and is globally around 50 Pa in the main river. With the variable friction model, the mean value of the bed shear stress in the main river is about 15 Pa and it can reach at most 30 Pa.

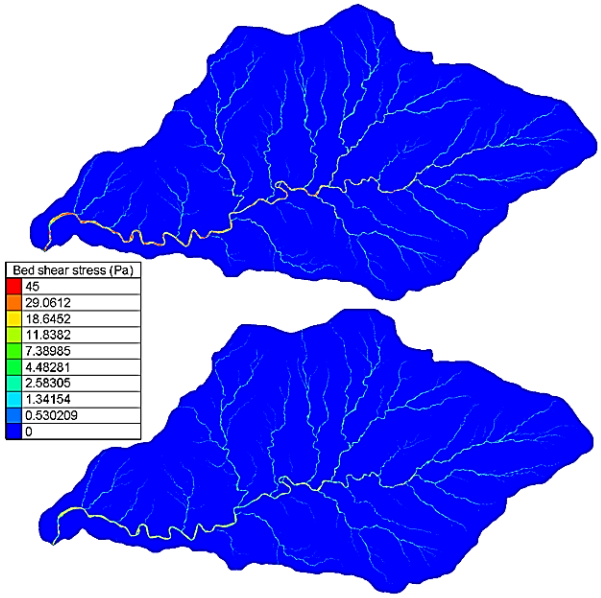

Figure 14 : Bed shear stress distribution in the watershed with constant friction coefficient (at the top) and with variable friction coefficient (at the bottom)

The bottom evolution, plotted on the Fig. 15, follows the bed shear stress results obtained in the domain. The main part of the erosion is located in the river network and the constant friction model gives the deepest erosion values.

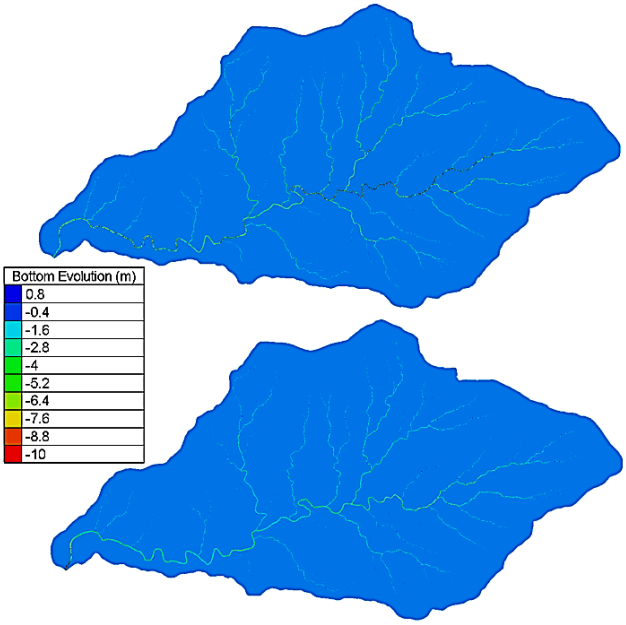

Figure 15 : Bottom evolution in the watershed with constant friction coefficient (at the top) and with variable friction coefficient (at the bottom)

The erosion is superior to 10 m in the main river for the first model and it is at most 4 m for the second. On the other hand, the erosion is quite similar in the tributaries with the two friction models, starting to be significant at the same points upstream and with a comparable depth.

The Fig. 16 shows the concentration at the outlet for the SISYPHE model, the SISYPHE model with the E4 formula and the Hairsine and Rose model. These simulations are performed with the variable friction coefficient model. The concentration are higher with the Hairsine and Rose model. The effect of the rain detachment formula is in this case negligible when the SISYPHE model is used.

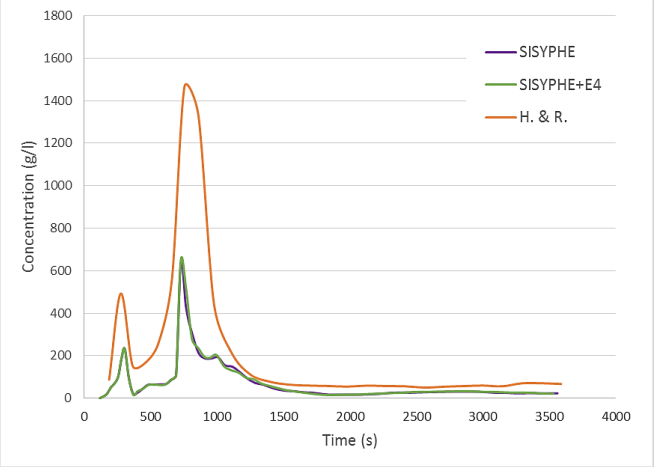

Figure 16 : Suspended sediment concentration at the outlet of the Laval watershed for the constant rain

The Table 3 gives the total eroded volume in the domain in function of the choice of the friction coefficient calculation (constant or variable), the rain detachment formula and the flow erosion/deposition model.

Model	Eroded volume	Deposited Volume	Total Volume
Constant friction			
SISYPHE	45214	280	-44934
SISYPHE + E1	45490	282	-44207
SISYPHE + E2	45514	283	-45230
SISYPHE + E3	45517	286	-45232
SISYPHE + E4	45530	282	-45248
Hairsine and Rose	35036	206	-34831
Variable friction			
SISYPHE	25278	366	-24912
SISYPHE + E1	28387	386	-28001
SISYPHE + E2	28495	381	-28113
SISYPHE + E3	28083	375	-27708
SISYPHE + E4	28628	382	-28246
Hairsine and Rose	28630	344	-28286

Table 3: Eroded and deposited volumes (m^3) calculated on the whole domain for the Laval watershed

The effect of the erosion terms due to the rain is negligible with the SISYPHE model when the friction coefficient is

constant. The models SISYPHE+Ei are more sensitive to the different formulas with a variable friction coefficient. But whatever the friction model is, the choice of the rain formula has not a significant impact on the results in terms of total eroded volume. In the two theoretical test cases, the erosion volumes increased with the variable friction model while it is the contrary at this scale.

The model has also been tested on two real hydrological events, and the water discharges and sediment concentrations have been compared at the outlet of the watershed with the field measurements. The calibration is realized with one event and the same parameters are used for the second one. For the hydraulic model, the variable friction model is used and the height of the soil roughness k is modified in function of the areas (river bed or hillslope).

The Fig. 17 shows as a function of time the hydraulic results of the model for the two rainfall events, compared with the measured hydrograph and presented with the associated rain signal.

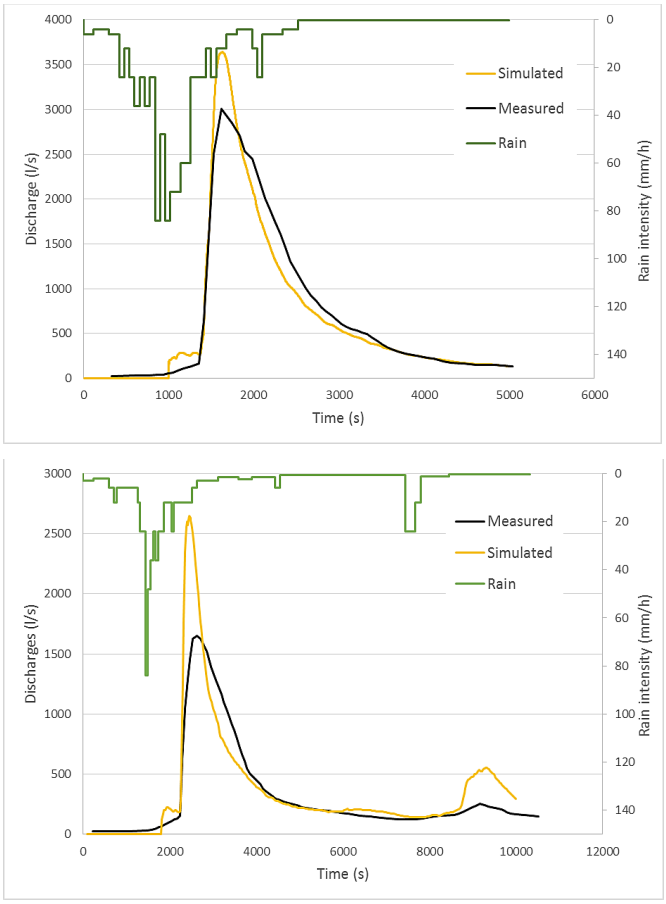

Figure 17 : Discharge at the outlet of the Laval watershed for the two rain event

We can see on this figure that the discharge peak is reproduced at the same time, but the maximum value is much higher than the measured ones for the two events. With SISYPHE, the calibration of the model has been done with the lateral and longitudinal dispersion coefficient of the convection-diffusion equation and the grain size. The respective calibrated values for these parameters are $K_x = 10\ m^2/s$, $K_y = 10\ m^2/s$ and $D_{50} = 70\ \mu m$.

Once this calibration completed, the four rain detachment formulas are tested with the same erodability coefficient as the previous test cases. In the Fig. 18, the outlet concentration are represented with the different models.

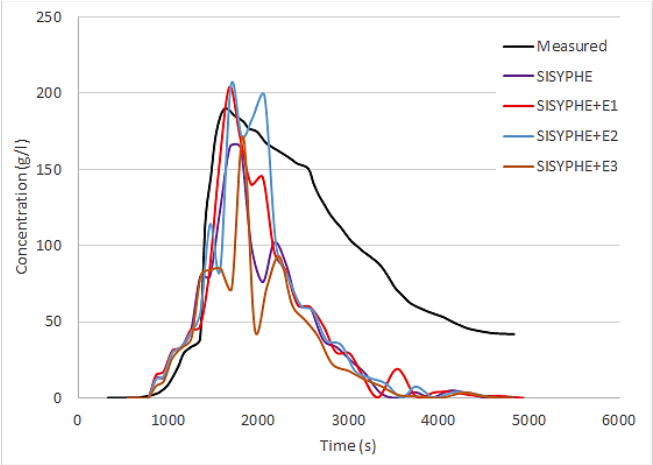

(a) SISYPHE + Ei, Event 1

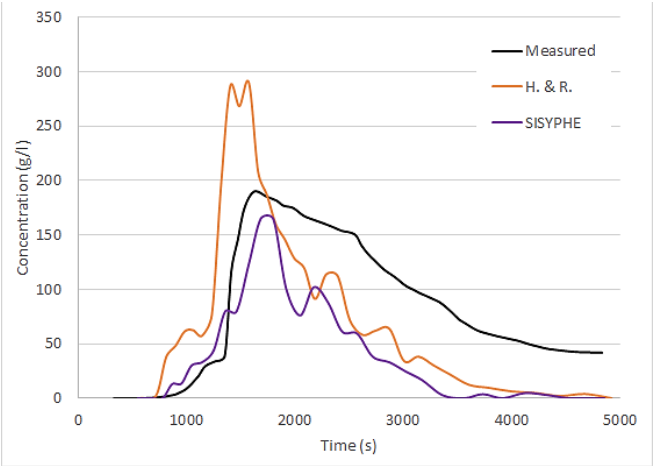

(b) SISYPHE+E4 and Hairsine and Rose, Event 1

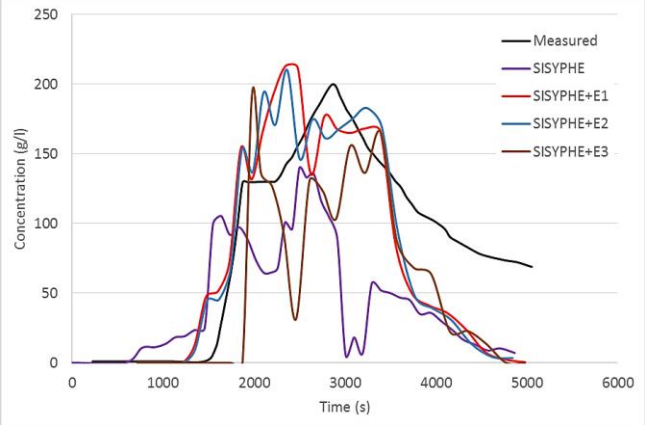

(c) SISYPHE + E1, Event 2

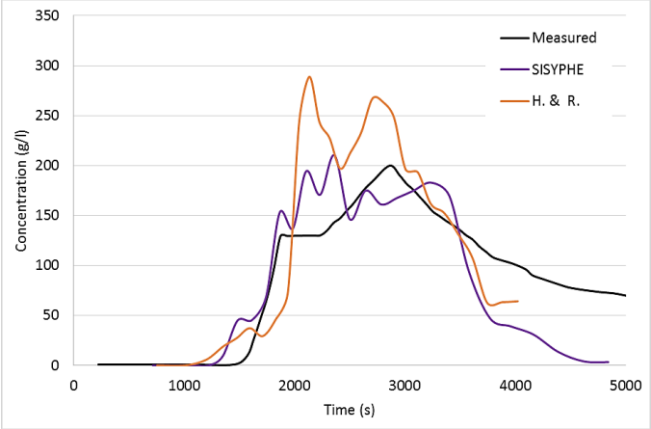

(d) SISYPHE+E4 and Hairsine and Rose, Event 2

Figure 18 : Sediment concentration at the outlet of the Laval watershed

The previous graphs show that:

- the choice of the rain-erosion formula is of a great importance for reproducing correctly the suspended sediment concentration signal. In this case, the formulas E1 and E4 appear to be the most relevant formulations. Without rain detachment formulas, SISYPHE is unable to reproduce correctly the concentration signals, especially for the second event;
- The parameters used for the formulas Ei at the plot scale allow reproducing the right order of magnitude for the suspended sediment concentration signal, with a calibrated value of sediment diameter which is low but still realistic;
- The erosion/deposition model for the flow part has a great impact on the concentration values. Both SISYPHE and Hairsine and Rose models are able to reproduce quite well the concentrations at the outlet, but the curves are decreasing too fast after the peak, whatever the parameter are modified. Furthermore, the Hairsine and Rose model overestimates the suspended concentration with this set of parameters, which is very complicated to change without losing the physical meaning of the whole set of parameters.

DISCUSSION

The great interest of the variable friction model is to reproduce continuously the flow and the erosion on a miscellaneous domain. Indeed, for an application on a real watershed, where the hillslope runoff, the river flow and the deceleration of the water in a reservoir are all observed, this approach allows a better representation of the different processes. Moreover, this friction characterization had been compared to a large number of existing models in [2], with similar results. Nevertheless, several studies ([9], [10]) show that for smaller range of inundation ratio (Λ), the model can be significantly improved. Furthermore, there are three equations to describe the Darcy-Weisbach coefficient depending on the inundation ratio, and the boundary between these equations can be different (see [11]). The highest difficulty is to give the best value of the size in the soil roughness, the k coefficient in the definition of the inundation ratio, especially in a large domain.

With the increasing scale, we observed in this work that the flow detachment becomes predominant over the rain detachment. The difference in the eroded volumes between the simulation of the SISYPHE flow detachment alone and SISYPHE with the rain erosion formulas becomes smaller (see Table 1 and Table 2). The fact that one class of non-cohesive sediments is used with a relatively small grain size (150 µm, and 70 µm for the calibrated value) can overestimate the erosion by the flow compared to the rain erosion. Another hypothesis is that the the rain drop impact adds mass in the deposited layer, which is easily detached by the flow, like it is presented in the Hairsine and Rose model. In this case, the SISYPHE erosion/deposition system does not represent this indirect effect of the rain detachment. Another simulation choice that could be responsible of this results is that the mesh size enlarge with the scale (1cm, 15 cm and 1 m). Indeed, the disturbance of ± 1 mm at each node of the mesh is distributed with a different gap and may have a different effects. With a very small mesh at the larger scale, the cumulative differences observed with the different rain formulas may give a higher importance to the choice of the rain detachment formula.

In addition, many phenomenon are not represented in the simulations. As the matter of fact, the infiltration, exfiltration and evapotranspiration are not taken into account. It could explain the excess of maximum discharge in the calibration of the hydraulic model of the Laval catchment (Fig. 16). In order to have better results and for other rainfall events, it could be essential to represent these processes, that are usually not defined at the mesh scale. Furthermore, the influence of the vegetation on both erosion and runoff is not represented, despite its predominant impact (see [12]). The effect of

vegetation may better improve the diffusion or retention effect observed on suspended sediment concentration. Some other phenomenon like debris flow or landslide which could transport substantial amount of sediment are also not described. These kind of rare events are difficult to predict, so their modeling is very complicated.

CONCLUSION

The V7P0 version of TELEMAC-SISYPHE contains mostly equations adapted to the river or coastal erosion. Inspired by existing codes used for modeling plot erosion, some implementations have been realized in this code in order to simulate the sediment transport in an entire watershed and create a continuity between the hillslopes and the river bed. Three test cases have been chosen or defined for analyzing the effect of these new developments at different scales.

A variable friction model, depending on the water depth at each point of the mesh, has been tested. The main interest of this model is the homogenization created between the hillslope and the river erosion, with a low impact on the total eroded volumes. Its main effect is to moderate the river erosion which becomes more realistic, and to allow a better transfer from the plots to the outlet.

Four rain detachment formulas have also been added to the SISYPHE flow detachment. At the local scale, where the power of the flow is low, the effect of the rain detachment is considerable, so the choice of the rain formula significantly impacts the erosion results. However, at a largest scale, the choice of the rain detachment formula is less influent in term of erosion volumes, but is still very important in terms of shapes of the suspended sediment concentration signal.

At the same time, an erosion model designed for plot, the Hairsine and Rose model, has been carried out to be compared with the erosion/deposition terms of SISYPHE. The erosion results are very different, especially in the cases with a flow strong enough to be preponderant. For example, the H&R model overestimates the suspended concentration at the outlet of the Laval watershed. The parameter set, which is very large, is complicated to calibrate, especially for a complex and heterogeneous real case.

A large variety of options to model erosion at the watershed scale has been given in this paper, but there are still further ways to explore. The question of chosing the best numerical schemes, for both hydraulic and sediment transport, is still open. The infiltration and evapotranspiration processes, as well as the influence of the vegetation on runoff and erosion should also be represented. Finally, representing only one class of suspension transport may not be enough to describe all the processes existing on a real watershed, and the evaluation of the bed load transport appears to be also an important issue. With a better description of these still-missing processes, the code will be able to be used in the future for preventing the erosion on a watershed and finding up-front solution, like hillslopes management in area with dam protection issues.

REFERENCES

[1] P. Tassi, C. Villaret, “Sisyphe V6P3 User’s Manual”, Note EDF LNHE ref. H-P74-2012-02004-EN, January 2014.

[2] D. S. L. Lawrence, “Macroscale surface roughness and frictional resistance in overland flow”, Earth Surface Processes and Landforms, Vol 22, Issue 4, pp. 365–382, April 1997.

[3] G. Nord, M. Esteves, “PSEM_2D: A physically based model of erosion processes at the plot scale” Water Resources Research, Vol. 24, Issue 13, pp. 1766–1780, June 2010

[4] C. A. G. Santos, V. S. Srinivasan, K. Suzuki, M. Watanabe, “Application of an optimization technique to a physically based erosion model” Hydrological Processes, Vol. 17, Issue 5, pp. 989–1003, April 2003.

[5] R. P. C. Morgan, J. N. Quinton, R. E. Smith, G. Govers, J. W. A. Poesen, K. Auerswald, G. Chisci, D. Torri, M. E. Styczen, “The European Soil Erosion Model (EUROSEM): a dynamic approach for predicting sediment transport from fields and small catchments”, Earth Surface Processes and Landforms, Vol. 23, Issue 6, pp. 527–544, June 1998.

[6] M. H. Le, “Modélisation multi-échelle et simulation numérique de l’érosion des sols de la parcelle au bassin versant”, Université d’Orléans, <tel-00838947>, November 2012, French.

[7] P. B. Hairsine, C.W. Rose, “Rainfall Detachment and Deposition: Sediment Transport in the Absence of Flow-Driven Processes”, Soil Science Society of America Journal, Vol. 55 No. 2, pp. 320-324, March 1991.

[8] C. Le Bouteiller, S. Klotz, F. Liébault, M. Estèves, Observatoire hydrosédimentaire de montagne Draix-Bléone, Irstea, 2015, http://dx.doi.org/10.17180/OBS.DRAIX.

[9] D. S. L. Lawrence, “Hydraulic resistance in overland flow during partial and marginal surface inundation: Experimental observations and modeling”, Water Resources Research, Vol. 36, Issue 8, pp. 2381–2393, August 2000.

[10] V. Ferro, “Flow resistance in gravel-bed channels with large-scale roughness”, Earth Surface Processes and Landforms, Vol. 28, Issue 12, pp. 1325-1339, November 2003.

[11] N. Roche, “Modélisation du ruissellement sur surfaces rugueuses” Hydrology. Université Joseph-Fourier - Grenoble I, <tel-00121568>, December 2006.

[12] N. Claude, “Interactions entre végétation, processus hydro-sédimentaires et morphodynamique des cours d'eau : état de l'art et principes de modélisation”, Note EDF LNHE ref. H-P73-2014-05213-FR, January 2015.

Numerical study of the influence of waves and tidal currents on the sediment dynamics in the vicinity of the Somme Bay area (France)

Meng Jia[1,2], Pablo Tassi[2], Nicolas Huybrechts[3]

[1]Université de Nice-Sophia Antipolis (Erasmus Mundus)
Nice, France
[2]Laboratoire Saint Venant
EDF - Research & Development
Chatou Cedex, France

[3]Roberval Laboratory of Numerical Hydraulic
(joint Research Unit CETMEF-UTC)
UMR CNRS 7337
Compiègne, France

***Abstract*—In this work, a depth-averaged coastal morphodynamic model (2DH) is developed on the basis of the Telemac-Mascaret modeling system. The model is implemented and validated in the Somme Bay zone (France), which suffers severe sediment deposition problems. Tides and waves are considered as the main driving forces for the sediment transport and offshore bathymetry. Therefore three different models are implemented to simulate tides, waves and morphodynamic conditions. Firstly a tidal and a waves model are developed and validated. Secondly, a coastal morphodynamic model is established by internally coupling the validated tidal and waves model to a sediment transport and bed evolution model. Finally, the validation of the sediment transport processes is performed in the Somme bay area for different scenarios.**

I. INTRODUTION

Beach and nearshore sediments are continually responding to interactions between waves, wave-induced littoral currents, currents induced by wind and tides, and the wind directly [1], [2]. However, the dominant factors that drive the sediment dynamics and beach shaping are usually the direct wave action and the wave-induced littoral currents, except near coastal inlets, where tide-induced flows can typically dominate.

The presence of a headland or a structure such a groyne or a jetty, oriented normal to the shoreline and attached to the shore will strongly interact with the active waves and currents and the resulting sediment transport in the vicinity of the structure [3]. In consequence, a shoreline harbor or a jettied inflow channel entrance will trap the sediment being transported down coast. To alleviate the resulting unwanted deposition in a harbor or a power station cooling water inlet, it become necessary to artificially deepen the water depth by dredging the sediment accumulated in the channel inlet or by mechanically bypass sediment deposited at the channel entrance.

Both sediment dredging and bypassing are, in general, costly operations that must be repeated several times over a project life. Therefore, it is of crucial importance to anticipate the forcing effects on the sediment and morphodynamic behavior in the vicinity of harbors or cooling water inlets to accurately predict the impact of coastal structures on the study area to efficiently optimize sediment dredging and bypassing operations. From the last few years, numerical coastal models are widely used to study this process.

The major goal of this work is to develop numerical models for the reliable prediction of the sediment dynamics and morphological evolution of coastal areas subject to the interaction of waves and tide-induced currents. These models, with appropriate waves, tides, bathymetric and sediment information, would allow the prediction of the behavior of the sediment dynamics and offshore bathymetry over a given period of time. Furthermore, future application of the models would be to evaluate the impact of coastal structures, such as jetties placed at the water intake channel, over any period of time. It is expected that the resulting validated models would also be used as a predictive tool for analyzing and evaluating dredging and sediment deposition management subject to different climate and forcing scenarios [4], [5].

II. MODEL APPROACH

Generally speaking, there are two types of coastal models: (i) *physical models*, which are normally smaller scale versions of the real (prototype) situation, and (ii) *equation-based models* involving the solution of the governing equations. The latter includes numerical models, used to predict both the spatial and temporal variation of the wave, current and sediment transport fields and analytical models which, although simpler, provide conceptual tools for analysis and understanding.

Traditionally, three types of numerical models have been developed [6], [7]: (i) *coastal profile models*, focuses on cross-shore processes and longshore variability neglected; (ii) *coastline models*, where the cross-shore profiles are assumed to retain their shape when the coast advances or retreats; (iii)

coastal area models, where variations in both horizontal dimensions are resolved. The latter can be further subdivided into two-dimensional horizontal (2DH) models, which use depth-averaged equations, and three-dimensional (3D) models, which solve the vertical variations of flow and transport.

In this work, 2DH coastal area models are implemented. The general setup of the three-way processes model (wave, currents and sediment transport) is presented below and schematized in Fig.1:

i. Give initial bathymetry and initial conditions.

ii. Give boundary conditions for waves and flow, the coupled hydrodynamic process is computed.

iii. The sediment transport field is computed, based on the flow and wave fields, the bathymetry and the sediment properties.

iv. The bathymetry is updated based on the sediment transport gradients.

v. Back to [ii] and repeat process until final time.

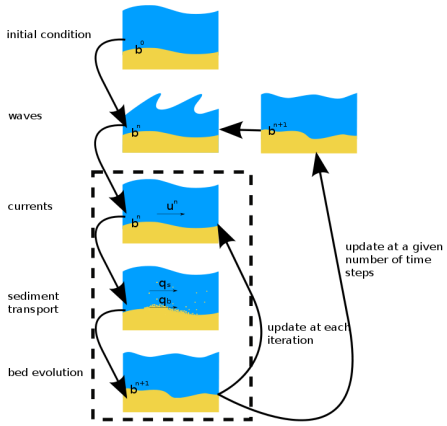

Figure 1. Schematic representation of the modelling coupling strategy used in this work

The Telemac-Mascaret modelling system (TMS) is selected as the modelling suite to simulate coastal processes. In particular, the version 7.0 of TELEMAC-2D (currents), TOMAWAC (waves) and SISYPHE (sediment transport and bed evolution) modules of the TMS will be used (released in December 2014).

III. GOVERNING EQUATIONS

In this section, the mathematical models for the description of tidal currents, waves, and sediment dynamics are presented.

A. Currents

The hydrodynamic processes are described by the shallow water equations. These equations obtained by depth-averaging the Reynolds-Averaged Navier-Stokes, consisting of one continuity equation (1) and two momentum equations (2) and (3), are written in non-conservative form as follows [8]:

$$\frac{\partial h}{\partial t} + \mathbf{U}\cdot\nabla(h) + h\cdot div(\mathbf{U}) = S_h \quad (1)$$

$$\frac{\partial U}{\partial t} + \mathbf{U}\cdot\nabla(U) = -g\frac{\partial h}{\partial x} + S_x + \frac{1}{h}div(hv_t\nabla U) \quad (2)$$

$$\frac{\partial V}{\partial t} + \mathbf{U}\cdot\nabla(V) = -g\frac{\partial h}{\partial y} + S_y + \frac{1}{h}div(hv_t\nabla V) \quad (3)$$

where h is the water depth, t is the time; $\mathbf{U}$ is the depth-averaged velocity vector, with components U and V in the x and y Cartesian coordinates respectively, v_t is the diffusion coefficient, g is the gravity acceleration, S_h is a source or sink term in the continuity equation. The source or sink term S_x and S_y in the dynamic equations represent the wind and the atmospheric pressure, the Coriolis force, the bottom friction and additional sources or sink of momentum within the domain in the two directions x and y.

For the astronomical tides, the water level ζ can be computed by means of a superposition of different tidal components [9]:

$$\zeta = \sum_{n=1}^{N} f_n A_n \cos\left[\omega_n t - G_n + (V_n + u_n)\right] \quad (4)$$

where t is the time referred to 0 hour at Greenwich Me an Time (GMT), n is the index of the tidal constituent, A_n is the amplitude of the tidal constituent, f_n is the nodal fact or of the tidal constituent, ω_n is the frequency of the tidal c onstituent, G_n is the phase lag of the tidal constituent behin d the phase of the corresponding constituent at Greenwich, $V_n + u_n$ is the value of the equilibrium argument of the tidal constituent, V_n is the uniformly changing part of the phase of the constituent at the Greenwich meridian, and u_n is the n odal adjustment of the tidal constituent [10].

The values calculated according to Equation (4) can be used to define the water depth h in the shallow water equations at the open boundaries of the domain.

B. Waves

Statistical approach is used to describe the wave activity as a large amount of random parameters are contained in the wave field.

In the general case of wave propagation in an unsteady medium (sea currents and/or levels varying in time and space), a common way of describing the wave field is wave action, which is conserved during propagation [11]. The action balance equation governing the wave evolution in Cartesian coordinates in the following forms:

$$\frac{\partial \mathbf{N}}{\partial t}+\frac{\partial(\dot{x}\mathbf{N})}{\partial x}+\frac{\partial(\dot{y}\mathbf{N})}{\partial y}+\frac{\partial(\dot{k}_x\mathbf{N})}{\partial k_x}+\frac{\partial(\dot{k}_y\mathbf{N})}{\partial k_y}=S_{tot} \quad (5)$$

where $\mathbf{N}(k_x,k_y,x,y,t)$ is the wave action density, t is time, the position vector $\mathbf{x}=(x,y)$ for spatial location in a Cartesian coordinate system, the wave number vector $\mathbf{k}=(k_x,k_y)=(k\sin\theta,k\cos\theta)$ for directional spectrum discretization, θ denoting the wave propagation direction, S_{tot} is total source term.

For the propagation equations:

$$\dot{x}=\frac{\partial\Omega}{\partial k_x}\quad \dot{y}=\frac{\partial\Omega}{\partial k_y}\quad \dot{k}_x=-\frac{\partial\Omega}{\partial x}\quad \dot{k}_y=-\frac{\partial\Omega}{\partial y} \quad (6)$$

where Ω results from the Doppler relation applied to the wave dispersion.

The term S_{tot} includes wind input S_{in}, dissipation S_{ds} and non-linear wave-wave interactions S_{nl}. In deep water the main dissipation process is due to whitecapping S_{wc} [12]. Reducing water depth, a considerable amount of wave energy is also dissipated by wave-bottom interaction S_{bf} [13]. In extreme shallow water, depth-induced wave breaking S_{bk} dominates over all other dissipating processes [14].

C. Sediment transport

The transport rate due to the combined action of waves and current is provided by Soulsby-van Rijn formula [15]:

$$Q_{b,s}=A_{b,s}U\left[\left(U^2+2\frac{0.018}{C_D}U_0^2\right)^{0.5}-U_{cr}\right]^{2.4} \quad (7)$$

This formula can be used to estimate the components for total sediment transport rate (bed load Q_b and suspended load Q_s)

The bed load coefficient A_b and suspended load coefficient A_s are computed as:

$$A_b=\frac{0.005h(d_{50}/h)^{1.2}}{((s-1)gd_{50})^{1.2}} \quad (8)$$

$$A_s=\frac{0.012d_{50}D_*^{-0.6}}{((s-1)gd_{50})^{1.2}} \quad (9)$$

where U is the depth-averaged current velocity, U_0 is the RMS orbital velocity of waves, and C_D is the quadratic drag coefficient due to current alone. The critical entrainment velocity U_{cr} is given by the expression:

$$U_{cr}=\begin{cases}0.19d_{50}^{0.1}\log_{10}\left(\frac{4h}{D_{90}}\right) & if\ 0.1mm\le d_{50}\le 0.5mm\\ 8.5d_{50}^{0.6}\log_{10}\left(\frac{4h}{D_{90}}\right) & if\ 0.5mm\le d_{50}\le 2.0mm\end{cases} \quad (10)$$

The validity range for the Soulsby-van Rijn formula is h = (1 – 20) m, U = (0.5 – 5) m/s, and d_{50} = (0.1 – 2.0) mm.

D. Bed level updating

The bed level updating module is described as:

$$(1-n)\frac{\partial Z_f}{\partial t}+\nabla\cdot Q_b=0 \quad (11)$$

where n is the non-cohensive bed porosity, Z_f is the bottom elevation, and Q_b (m^2/s) is the bedload transport per unit width, with components Q_{bx} and Q_{by} in the x and y Cartesian coordinates respectively.

IV. Study Site and Available Data

A. Study Area

The Somme Bay is located between Hourdel in the south and Saint-Quentin-en-Tourmont in the north (Fig. 2). It covers an area about 70 km^2 and comprises the Somme river, with a yearly average flow rate of about 30 m^3/s, controlled by a lock at Saint Valery sur Somme [16]. Within a distance of about 20km to the North, the Authie Canche bay is located, with a yearly average flow rate of about 10 m^3/s. The Somme bay is covered by a high percentage of tidal flats and salt marshes. From several years, this area endures severe sedimentation issues, with an increasing of the mean bed level of about 1.3 cm/year.

The domain is chosen to cover a large coastal area, about 60km offshore and along shore, to include Somme Bay and also some other areas of interest for EDF as the Penly and Paluel nuclear plants and the Fécamp offshore wind farm (Fig.2). The model can be profited to possess a large number of observation points in different zones of the domain, and it is expected that the validated model can be used as a predictive tool and applied directly in the other interesting areas of the same domain.

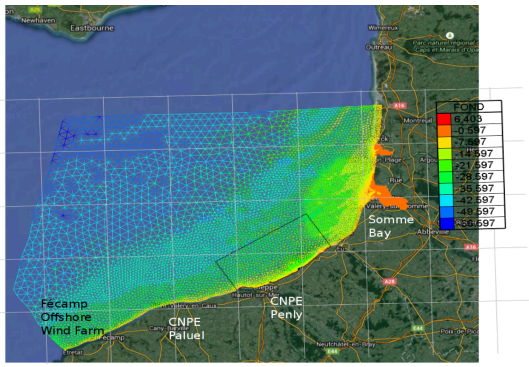

Figure 2. Location of the Somme Bay and extension of the numerical model

B. Bathymetry Data

The bathymetric data are taken from the following sources:

- In the intertidal part of the Bay of Somme, Light Detection and Ranging (LiDAR) data (1 sampling point/1m) have been acquired in June 2012 by the CLAREC operational team (M2C Lab, University of Caen).
- Field surveys Mosag07& Mosag08 on Thalia vessel [17], occurred about 30km South-West from the bay mouth in 2007 and 2008, and high resolution bathymetric data (1 sampling point/3m) were collected offshore during these surveys.
- Elsewhere bathymetric data collected by the "Service Hydrographique et Océanographique de la Marine" (SHOM) are used with a resolution of 2km offshore to 25m at some locations

C. Validation Data

During the Mosag07& Mosag08 [17] surveys, tide levels, flow velocities, wave height and period were measured for a neap spring cycle (~15days) [16]. Acoustic Doppler Current Profiler (ADCP) measurements occurred at locations C1 - C2 in 2007 and at C3 in 2008 (Fig.3).

The validation data for wave model comes from the Candhis database (National Center for Archiving Swell Measurements) in the location of Cayeux. Candhis refers to the coastal national network of in situ measurements provided by CETMEF (Centre d Etudes Techniques Maritimes et Fluviales).

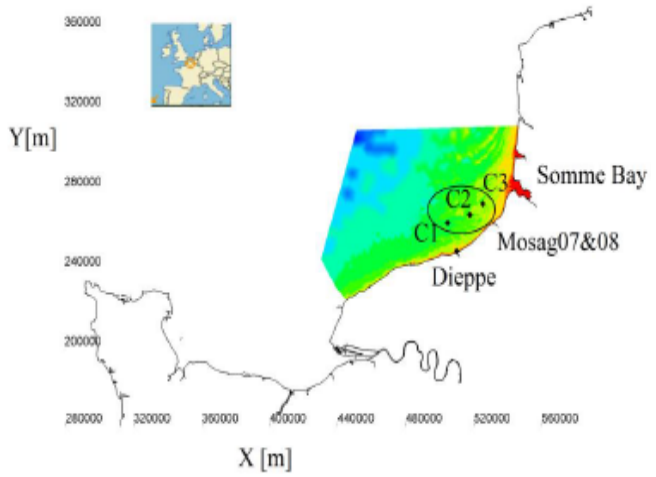

Figure 3. Mosag07&08 field survey

LiDAR data in Somme Bay acquired from CLAREC team is used here to validate the morphodynamic model. The evolution of the bottom in Somme bay is presented in Fig. 4.

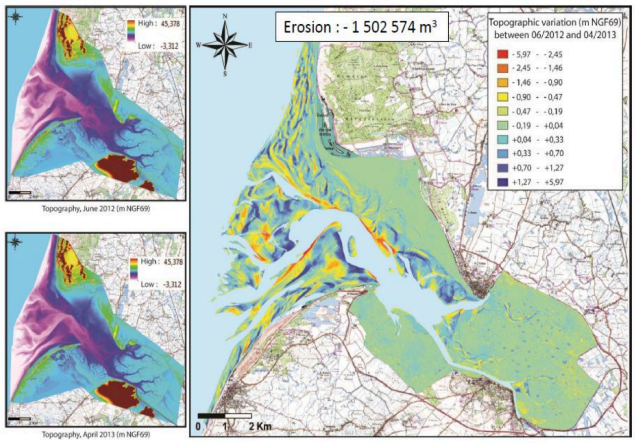

Figure 4. Measured LiDAR data for morphodynamic evolution (C. Michel M2C Rouen unpublished work)

D. Numerical Data

The wind data (wind velocity component at 10 m height and atmospheric pressure) used in the hydrodynamic model were obtained from the database of ERA Interim supplied by European Centre for Medium-Range Weather Forecasts (ECMWF). Each six hours a new set of U wind velocity and V wind velocity is given and the wind data is applied to the whole domain uniformly.

For the tidal level and velocities on offshore boundary the imposed values are calculated from harmonic constants provided by global or regional tidal model. 4 databases of harmonic constants are interfaced with TELEMAC-2D [18]. In this study domain, the global TPXO database and its regional and local variants are applied.

For the open boundary of wave module, the parameters of significant wave height, peak frequency, main direction and directional spread are given from the datasbase of Anemoc-2 (Atlas Numérique d'Etats de mer Océanique et Côtier) developed by EDF - LNHE (Électricité de France - Laboratoire National d'Hydraulique et Environnement) with support of CETMEF.

V. Numerical Results

A. Accuracy criteria

The comparison between the computation outputs and observation data is evaluated based on a quantitative criterion, the Relative Mean Absolute Error RMAE [19]. The RMAE is given by the expression:

$$RMAE = \frac{\left\langle \left| Y_c - X_c \right| \right\rangle}{\left\langle \left| X_c \right| \right\rangle} \qquad (11)$$

where $\mathbf{X}_c$ ($\mathbf{x}_1$, ..., $\mathbf{x}_N$) is a set of observations and $\mathbf{Y}_c$ is the model predictions. The mean value noted $\langle\ \rangle$ is defined by the expression:

$$\langle |X| \rangle = \frac{1}{N} \sum_{i=1}^{N} |x_i| \qquad (12)$$

The quality criteria associated with RMAE criteria is given in Table Ⅰ.

TABLE I. QUALITY CRITERION

	RMAE
Excellent	<0.2
Good	0.2-0.4
Reasonable	0.4-0.7
Poor	0.7-1.0
`Bad	>1.0

B. Tidal model

The module TELEMAC-2D is used as the numerical tool to develop and validate the hydrodynamic model with tides as driving force.

The tidal model is initialized with a constant water surface elevation and still water level equal to 5m over the whole domain. An alignment of the different temporal conditions of the boundary condition datasets was made to match the initial conditions as closely as possible to those observed.

The boundaries along the coast are treated as solid boundaries, in which no flux transfer is allowed. Constant flow rates imposed for the Somme and Authie rivers are ignored for validation of the model.

The Nikuradse formulation is chosen to impose the bed friction coefficient with a value of 0.5 m in the whole domain, in order to incorporate into the model the effects of skin friction and the presence of bed forms. For the tidal model, a constant eddy viscosity equal to 1 m^2/s is chosen for the numerical simulations. The inertia effect of the Coriolis force is also taken into account with a Coriolis coefficient equal to 0.000112 rad/s.

According to the field data, two time periods are chosen to test the tidal model under different wave (with higher or lower value) conditions. The basic information is summarized in Table Ⅱ. Δt_{T2D} is time step for TELEMAC-2D model.

TABLE II. SCENARIOS FOR TIDAL SIMULATION

Scenarios	***From***	***Durations [Days]***	Δt_{T2D} ***[s]***	***Description***
1	2007/07/27	5	10	Higher waves
2	2007/08/01	5	10	Lower waves

The measurement velocity and water level in C2 are available for the model validation. In Fig.5, The cross marks represent the measured data, and the red lines represent the numerical results.

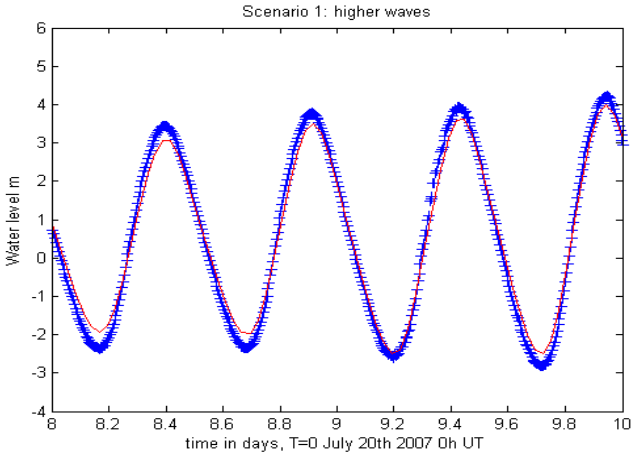

(a)

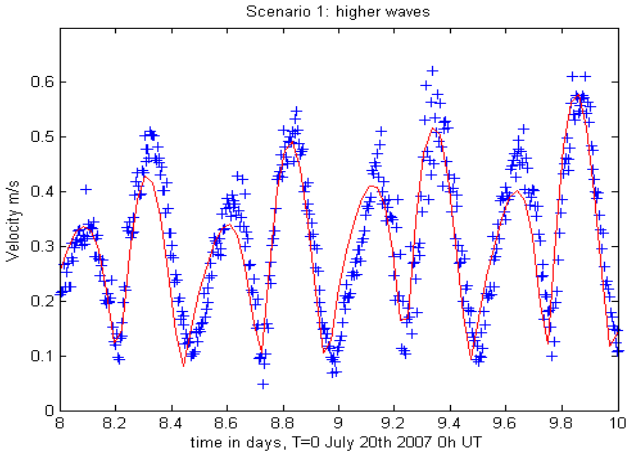

(b)

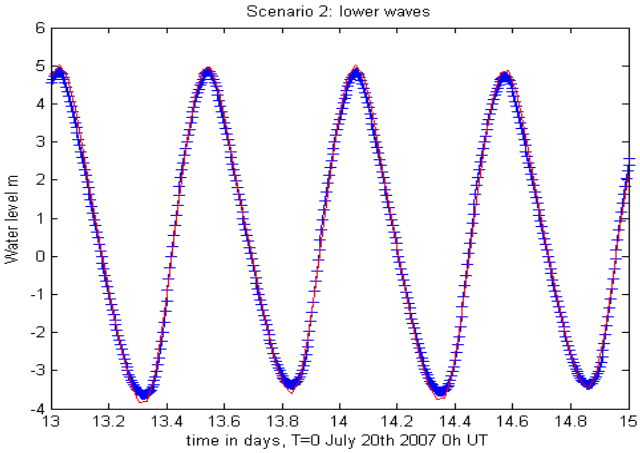

(c)

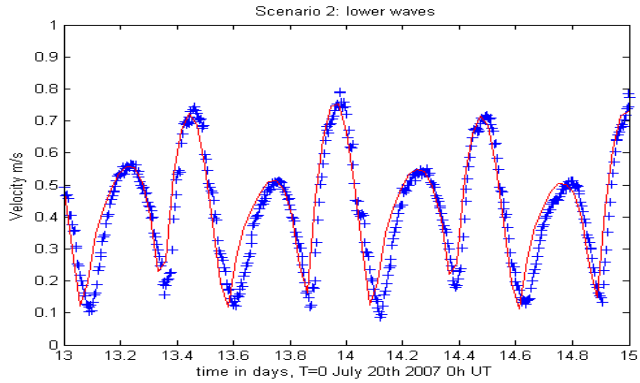

(d)

Figure 5. Validation of tidal model: (a) Tides with higher waves: water level; (b) Tides with higher waves: velocity; (c) Tides with lower waves: water level; (d) Tides with lower waves: velocity;

To quantitatively assess the tidal behavior under different wave conditions, RMAE scores are computed for each parameter in each scenario as well as the mean value, and a summary is presented in Table III as below.

TABLE III. RMAE SCORES FOR TIDAL MODEL RESULTS

Scenarios	*Velocity C1*	*Velocity C2*	*Water level C2*	*Average*
1	0.1586	0.1685	0.0996	0.1114
2	0.1484	0.1437	0.0617	0.1179

From the comparison of 2 scenarios, it can be found that the average RMAE values for the output parameters during the tidal period, characterized with lower waves, show in general a better accuracy level than the RMAE values evaluated during the tidal period corresponding higher waves. This is reasonable because without taking waves into account, the tidal model shows a poor performance during the period presenting a significant wave activity. However, both Fig.5 and RMAE results show a good agreement between simulated results and observation data are achieved for both scenarios.

C. Wave model

In this section, the module TOMAWAC is coupled to the module TELEMAC-2D to take into consideration of the driving force of waves.

To initialize the model, the significant wave height is set to be 0.99m, peak frequency 0.15 s^{-1}, main direction 140 °, and direction spread to be 0.6.

The Anemoc-2 data is used as input of boundary condition. The model includes energy loss due to white capping dissipation, non-linear quadruplet interactions, wave breaking dissipation and bottom friction. Bottom friction was applied uniformly across the domain with a coefficient value of 0.038m^2/s^3.

Two simulations are launched from September 12th, 2010 with a duration of 8 days. The time step in TELEMAC-2D is set to be 10s, and the model is coupled internally with TOMAWAC with a coupling period of 10, which means the time step in TOMAWAC is 100s. Wind is only considered in the second simulation to study the influence of wind on the numerical model.

The simulation results are compared and presented in Figure 6. The cross marks represent the measured data and the red lines represent the numerical results (significant wave height and mean frequency). The green line represents the discrete peak frequency.

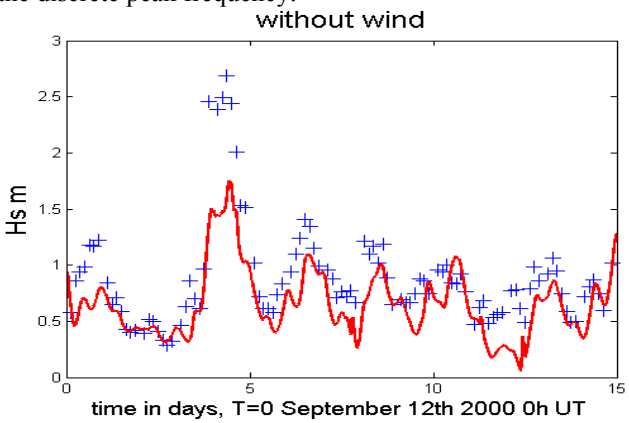

(a)

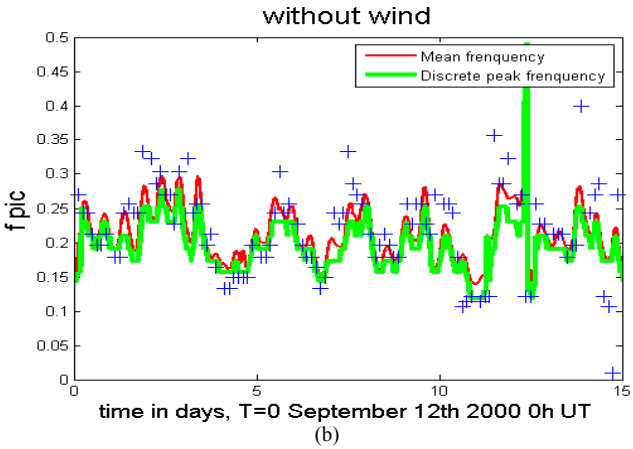

(b)

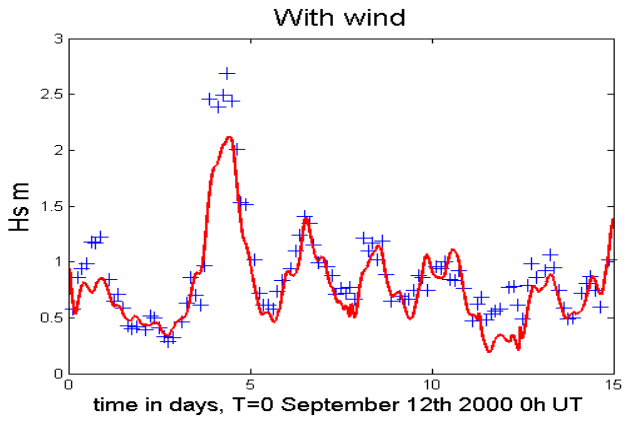

(c)

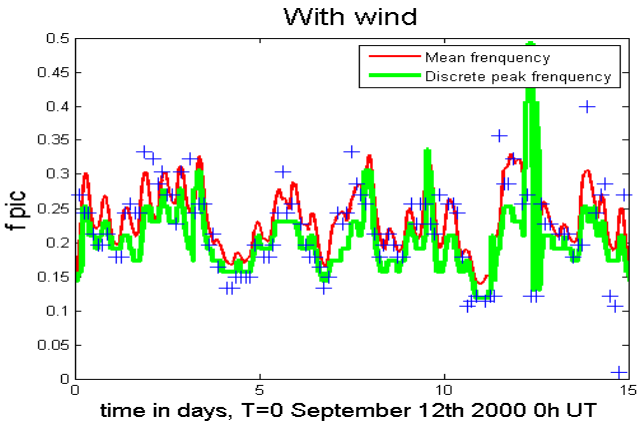

(d)

Figure 6. Validation of wave model: (a) Without wind: significant wave height; (b) Without wind: wave frequency; (c)With wind: significant wave height; (d) With wind: wave frequency.

From the simulation results and the comparison with the observation data, it is showed that for both simulations, the numerical results match well with the measured data. However, for the first simulation without the consideration of wind, the modeled results underestimate the values of the significant wave height for the highest peak the interval day 4 - day 5, with a difference of about 1 m.

By considering the influence of the wind, the model result is improved largely, especially for significant wave height, where the first peak is better captured with only a slightly underestimation of 0.5 m. It also appears a better agreement for the significant wave height for the interval day 5 - day 10.

RMAE scores of the two simulations are summarized in Table IV.

TABLE IV. RMAE SCORES FOR WAVE MODEL RESULTS

Scenarios	*Significant wave height*	*Mean frequency*	*Discrete peak frequency*	*Average*
1	0.3014	0.1289	0.1563	0.1955
2	0.1818	0.1346	0.1529	0.1564

From the results presented in Table IV, it can therefore be concluded that the wave model provides better predictions for significant wave height when the influence of the wind is considered in the numerical simulations. For both simulations, the average RMAE scores reach the excellent level according to the quality criterion.

D. Morphodynamic model

In this study, the sediment transport and bed evolution module SISYPHE is coupled with TELEMAC-2D and TOMAWAC. A uniform, non-cohesive sediment distribution is used for the numerical simulations, with a median diameter equal to 0.2mm. The bed porosity is set to be 0.4. Only bed load transport is considered in this study and Soulsby-van Rijn formula is used.

Long-term simulations are launched from June 2nd, 2012 to April 6th, 2013, when the LiDAR data is acquired (Fig.4). The topography evolution will be used as reference for the model validation.

In order to assess the separate impact of tidal and wave action, two different scenarios are carried out and compared by considering the driving force of tidal currents only (SISYPHE coupling with TELEMAC-2D), and tidal currents plus waves (SISYPHE coupling with TELEMAC-2D and TOMAWAC).

The time step is set to be 60s in TELEMAC-2D and SISYPHE, and 3600s in TOMAWAC.

The bathymetry evolutions from simulations under different force scenarios are shown in Fig. 7.

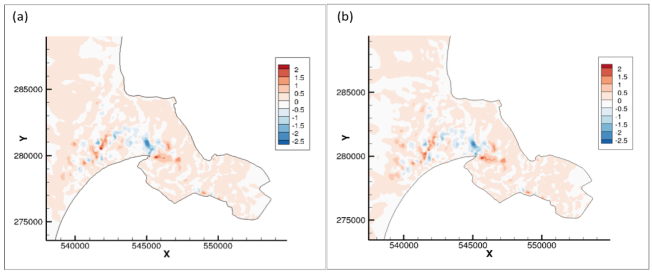

Figure 7. Bathymetry evolution from the morphodynamic simulation results by considering the effects of (a) tides (b) tides and waves.

From Fig.7, we can find that compared with the LiDAR survey, the simulation results show a good agreement with the observation according to the sediment erosion and deposition locations. Though a relatively lower estimation is obtained from the morphodynamic model, which is reasonable because suspension load is not taken into account, the magnitude of the bed evolution in Somme Bay from the model matches well with the observations.

An extra scenario is also developed based on a finer mesh to evaluate the influence of the mesh size on the morphodynamic model.

The comparison of the simulation results based on coarse and fine meshes are shown in Fig. 8.

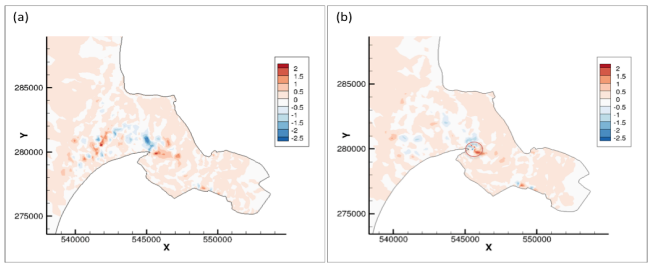

Figure 8. Bathymetry evolution from the morphodynamic simulation results by using (a) coarse mesh (b) fine mesh

With the refinement of the mesh, it can be seen that the sediment deposition and erosion are more concentrated in a corner in the left bank marked in the red circle in Fig. 8(b)

with higher deposition and erosion values than the results in coarse mesh.

VI. CONCLUSIONS

In this contribution, the coastal morphodynamic model is developed by coupling well validated tidal and wave models to a sediment transport and bed evolution model. The assessment of the separate impact of tides and tides plus waves on the sediment dynamic of Somme Bay is implemented using this model. In a near future, Improvement of the morphodynamic model is necessary in order to get a better representation of the simulated phenomena with the following considerations:

- Use of a finer mesh to better capture the characteristics of the bed of the study domain.
- Consider graded sediment in the model based on the material sample collected during the field survey Mosag07&08 and SHOM database.
- To include the suspension load as an additional sediment transport process.
- To include the boundary conditions from the Somme and Authie Canche rivers.

ACKNOWLEDGEMENTS

The Research and Development division of Electricity of France (EDF R&D - LNHE National Hydraulics and Environment Laboratory) and Laboratory for Hydraulics Saint-Venant is gratefully appreciated for their financial support to this study. Antoine Joly and Amélie Laugel-Joly (EDF R&D) are thanked for providing Anemoc-2 numerical data used for the numerical simulations. Thanks to Robert Lafite, Sophia le Bot and Charotte Michel (M2C, Rouen) for the provision of field surveys Mosag 07 &08, ADCP, wave and bathymetric data. Thanks to Olivier Monfort (M2C Lab, University of Caen) for sharing the LiDAR data used in the study.

REFERENCES

[1] D. Reeve, A. Chadwick and C. Fleming, "Coastal engineering: processes, theory and design practice," 2nd edition. Spon Press, 2012.

[2] R.G. Dean and R.A. Dalrymple, "Coastal processes with engineering applications," Cambridge University Press", 2002.

[3] S. Kristensen, N. Dronen, R. Deigaard and J. Fredsoe, "Hybrid morphological modelling of shoreline response to a detached breakwater," Coastal Engineering, vol.71, pp.13-27, 2013.

[4] P.E. Robins, A.G.Davies, "Application of TELEMAC-2D and SISYPHE to complex estuarine regions to inform future management decisions", Proceedings of the XVIIIth Telemac-Mascaret User Club, October, 2011.

[5] J. Bacon, L. Fernand and F. Luxford, "Overview of Telemac Hydrodynamic and Sediment Transport modelling at Sizewell", Internal Report EDF, November, 2012.

[6] D. Roelvink and A. Reniers, "A guide to modeling coastal morphology: Advances in Coastal and Ocean Engineering," Vol. 12. World Scientific Publishing Co, 2012.

[7] Y. Qinghua, "An approach towards generic coast geomorphological modeling with applications," PhD thesis, 2012

[8] J.M. Hervouet, "Hydrodynamics of free surface flows: modeling with the finite element method," Wiley, 2007

[9] J.J. Dronkers, "Tidal computation in rivers and coastal waters," North Holland Publishing Co., Amsterdam, pp.245, 1964

[10] C.S. Yu, "Modelling shelfs sea dynamics and estuarine circulations," PhD thesis, Katholieke Universiteit Leuven, Leuven, 1993.

[11] O.M. Phillips "The dynamics of the upper ocean, volume 2nd edition," Cambridge University Press, pp.366, 1977.

[12] K. Hasselmann, "On the spectral dissipation of ocean waves due to whitecapping," Boundary Layer Metereology, pp.107–127, 1974

[13] G.J. Komen, L. Cavaleri, M. Donelan, S, Hasselmann, K. Hasselmann, and P.A.E.M Janssen, "Dynamics and modelling of ocean waves," Cambridge University Press, Cambridge, pp.532, 1994.

[14] J.A Battjes and J.P.F.M. Janssen, "Energy loss and set-up due to breaking of random waves," Proceedings 16th International Conference Coastal Engineering, pp.569–587, 1978.

[15] R.L. Soulsby, "Dynamic of marine sands," Thomas Telford, London, pp1–249, 1997.

[16] N. Huybrechts, H. Smaoui, A. Ouahsine, S. Le Bot, Y. Ferret, C. Michel and R. Lafite, "Prediction of the bed friction coefficient using either high resolution bathymetric data or granulometry samples," Proceedings of the XXth Telemac-Mascaret User Club, October, 2013.

[17] Y. Ferret, S. Le Bot, B. Tessier, T. Garlan and R. Lafite, "Migration and internal architecture of marine dunes in the eastern English Channel over 14 and 56 year intervals: the influence of tides and decennial storms," Earth Surf. Process. Landforms, 35 (12), pp1480-1493, 2010.

[18] R. Ata, C. Goeury, J.M. Hervouet, "Telemac-2d User's Manual v7.0," 2014.

[19] J. Sutherland, D.J.R. Walstra, T.J. Chester, L.C. van Rijn and H. N. Southgate, "Evaluation of coastal area modelling systems at an estuary mouth," Coastal Engineering. 51: 119-142, 2004.

First-Order uncertainty Analysis using AD 2D Application

Catherine VILLARET[1,2], Cedric Goeury[1],
[1]EDF-LNHE, Chatou
[2]Saint-Venant Laboratory for Hydraulics, Chatou

Catherine.villaret@edf.fr

Michiel Knaapen[3], Jan Riehme[4], Uwe Merkel[5], Uwe Nauman[4]
[3]Hydraulic Research, Wallingford, UK
[4]RWTH Aachen, Germany
[5]UHM river engineering company, Germany

***Abstract*—We present here an efficient method to quantify uncertainty in morphodynamic models. The FOSM/AD method is applied to a complex 2D test case: the long term morphodynamic evolution of a tidal inlet. The sensitivity to grain size and bed roughness has been quantified as well as various model parameters including slope effect and secondary currents using the tangent linear model (TLM) of the Sisyphe/Telemac-2d model for the 7.0 release. The TLM was developed using the AD-enabled Nag Fortran compiler. However the duration of simulation is still limited due to the use of a scalar version. The method needs to be extended to study the effect of mesh size.**

I. INTRODUTION

The uncertainty associated with morphodynamic simulations is difficult to quantify given the number of variable input parameters and CPU time associated to each simulation. This is particularly true in complex process-based models like the Telemac-2d/Sisyphe morphodynamic model.

An efficient first-order second moment method using Algorithmic Differentiation (FOSM/AD) developed by Villaret et al. (2015) can be applied to quantify uncertainty/sensitivities in morphodynamic models. Changes in the calculated bed evolution with respect to variable flow and sediment input parameters are estimated with machine accuracy using the technique of Algorithmic Differentiation (AD).

The FOSM/AD method has been previously applied and validated in a simple 1D application. Results were found to be consistent with Monte Carlo (MC) simulations for a significant gain in CPU time. Only one run of the Tangent Linear Model (TLM) is required per variable input parameter against hundreds for the MC method even with the use of stratified sampling techniques.

In this paper, the FOSM/AD method is applied to a complex 2D simulation using a recently developed TLM model of the Telemac-2D/Sisyphe model for the 7.0 release (Goeury, 2015). TLM and Adjoints codes were developed using the NAG-enabled Fortran compiler, following a procedure developed for the 6.2 release (Riehme et al., 2010).

The test case selected here is a schematic representation of a tidal inlet which was developed initially by Marciano et al. (2005) in order to represent the typical conditions of the Dutch Warden Sea, and later reproduced by Baaren (2011).

The objectives of the present study are:

1. To provide a new validation test case for the Telemac-2d/Sisyphe morphodynamic model.
2. To apply the FOSM/AD method to identify the key processes and most sensitive input parameters
3. To quantify the total uncertainty
4. To discuss the present limitations and provide guidance for future work

The outline of this paper is as follows: Part 2 gives a brief literature review on the tidal inlet processes and existing models. In Part 3, we describe the test case and Telemac-2D/Sisyphe model. In Part 4, the model is applied to medium term simulations (up to 100 years). This part includes a brief discussion of the model set-up and CPU time. In Part 5, we present a sensitivity and uncertainty analysis using the FOSM/AD method. We finally draw some conclusions on the feasibility of the method for in-situ applications and discuss the present limitations.

.

II. LITERATURE REVIEW

Tidal inlets are morphodynamic features commonly observed around the world. Despite numerous observations, theoretical and numerical studies, the key processes governing the ebb delta formation offshore and the development of a complex multi-channel pattern inside the inlet are still unknown.

There are many examples of well developped branching channels in natural inlets where the main characteristic of the channel inlets depend on the geometrical dimensions of the barrier and tidal forcing. The Arcachon Basin in France, the tidal inlets in the Dutch Warden Sea and the Humber estuary in the UK are some examples of the diversity of the features which can be encountered in nature (cf. Stefanon et al., 2010).

In addition to theoretical and experimental studies, there have been a few attempts to model the medium to long term evolution of such complex systems using morphodyamic process-based models. Cayocca (2001) developed a 2D morphodynamic model of the Arcachon Bay, whereas Marciano et al. (20005) developed a 2D model of a schematic inlet using Delft3D. The same test case was later reproduced by Baaren (2011) using the ELCOM 3D model. A more realistic 2D model using Delft 3D is presented in Dessanayake et al. (2009) to represent the tidal network formation in the Ameland inlet (Dutch Warden Sea) including tidal asymmetry and higher harmonics and long shore current. Both 2D and 3D models were able to reproduce the ebb delta formation offshore and the branching system with features typically observed in short basins.

According to previous limited sensitivity analysis (Marciano et al., 2005 and van Baaren, 2011), the effect of the initial bathymetry is essential and tidal forcing and geometrical constraints govern the channel final equilibrium pattern. The effects of secondary currents and bottom slope are expected to play a minor role, whereas the sediment mobility and initial bed perturbation have a major influence on the development and equilibrium pattern. Model results are expected to be also sensitive to the limiting erosion depth. The effect of the mesh size has not yet been examined and is expected to play a major role.

III. MORPHODYNAMIC MODEL

A. *Schematic Test Case*

The test case proposed by Marciano et al. (2005) and Baaren (2011) represents a short tidal embayment, with conditions typically encountered on the Dutch Warden Sea. The model geometry, shown in Figure 1, covers an area of 12x16 km^2 with an offshore area extending 4 km seaward and an inner basin of 8x16 km^2. The two areas are separated by a barrier island of 2.5 km width. In the offshore area the bed slope increases linearly from -8 m below MSL to -6 m at the inlet. Inside the inlet, the bed profile increases from -6 m at the inlet to +1 m at the landward boundary. The initial bathymetry does not have any shoal pattern but small perturbations of +/-0.15 m height are randomly distributed at each node. As in the original simulation (Baaren, 2011), a Chezy friction coefficient is imposed for the long term simulations using a value of 65 m$^{0.5}$/s.

Different grids have been tested. In Figure 1 we show the initial coarse mesh with 32 500 elements and a triangular mesh size of 100 m. Another refined mesh around the inlet (with mesh size down to 30 m and 52 000 elements) was also included to test the sensitivity of the model to the mesh size.

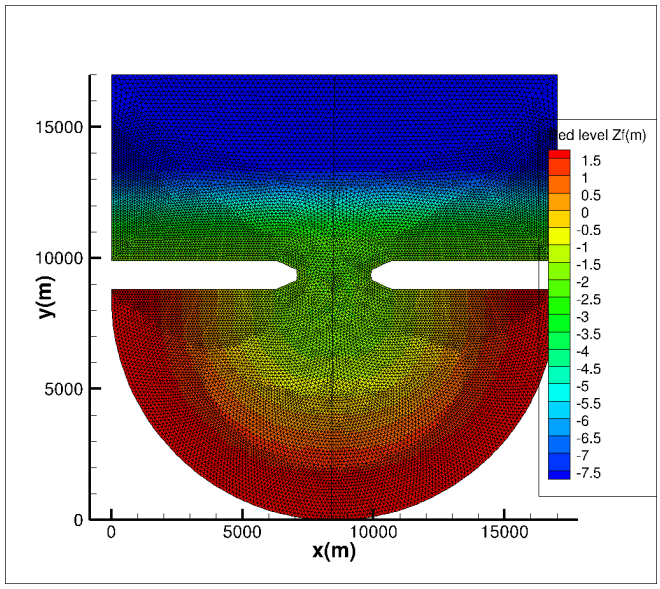

Figure 1. Geometry and bottom variation. The coarse grid (mesh size of 100 m) is also represented.

B. *Hydrodynamic Model*

On the seaward boundary, a sinusoidal variation of the water level is imposed with an amplitude of 1 m. At the inlet, the flow velocity reaches its maximum of 0.8 m/s approximately 3 hours before Low Water (LW). As shown in Figure 2, the tidal currents at the tidal inlet are ebb dominant leading to a global loss of sediment from the inlet offshore. Hydrodynamic results obtained with different meshes and using different numerical schemes are found to give the same flow results. This test case shows very little sensitivity to numerical parameters. Diffusion coefficients from 10^{-6} to 10^{-2}, slip or no slip conditions have no effects on the hydrodynamic model results and velocity pattern. Two different advection schemes have been tested: the N-edge based Residual Distributive (NERD) scheme (13) and the recently developed Locally Implicit Psi Scheme (LIPS) second-order predictor corrector scheme which is 10 times less diffusive than the NERD scheme (Hervouet et al., 2015). Both schemes are found to give the same results for a significant increase in the CPU time (35%).

The N-edge scheme No13 which is well adapted to represent tidal inlet has been used in the morphodynamic simulations with a time step Dt=10 s.

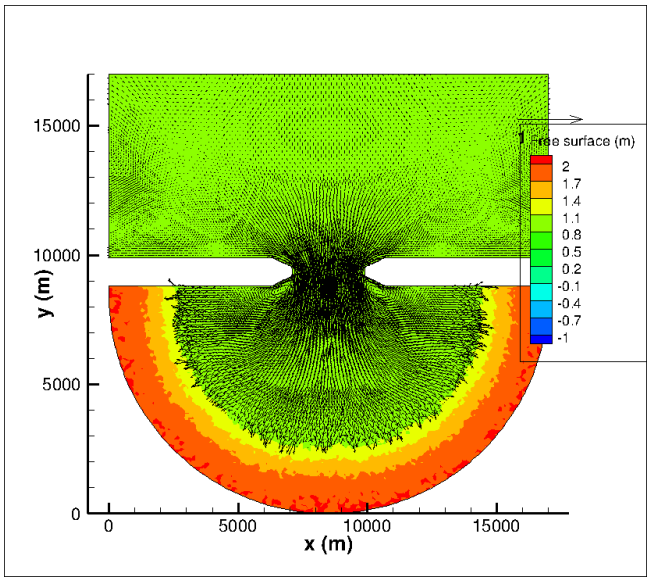

Figure

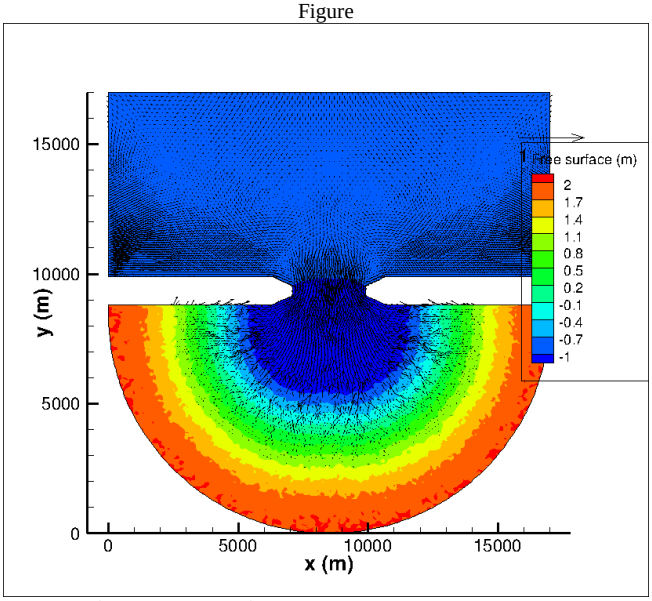

2: Free surface and velocity field at high tide (top) and at low tide (bottom)

C. *Sediment Transport Processes*

The sediment is made of uniform sand with mean diameter D_{50}=150 µm. The Coriolis force is neglected while the effect of secondary currents and sloping bed effects are parameterized.

The model has been run using the Engelund and Hansen (1967) total load formula (N° 30):

$$Q_s = 0.01 \sqrt{g(s-1)d_{50}{}^3}\ \theta^{5/2} \qquad (1)$$

Where θ is the adimensional bed shear stress, s the relative sand density, g gravity and d_{50} the sediment grain size.
Following Baaren (2011), we added the Kirwan and Murray (2007) sloping bed effects; the current induced sediment transport is modified by adding a slope driven component:

$$Qs = \alpha \nabla Z_f \qquad (2)$$

Where α is a dimensional empirical coefficient (α=1.15 10^{-5}m^2/s). The slope driven transport only occurs if the slope is greater than 0.01.

We also included the secondary current parameterization in Sisyphe. Following the empirical method of Engelund (1974) the near bed angular deviation is proportional to h/R, where h is the water depth and R the radius bend:

$$\tan\delta = \beta \frac{h}{R} \qquad (3)$$

with the adimensional coefficient β =7.

IV. LONG TERM EVOLUTION

A. *Morphodynamic Factor*

For long term simulation (up to 100 years), we used a morphodynamic factor (MF) to reduce the CPU time. This classical method is equivalent to multiplying the hydrodynamic time step (Dt=10s) by the MF factor in the morphodynamic model. In all simulations, the coupling period is set to 1.

Results obtained for different values of the MF factor from 10 up to 50 are compared in Figure 3. The bed evolution pattern obtained after 30 years are very similar and therefore we used in the simulations MF=25.

B. *Long term evolution – Coarse mesh*

The bed obtained after 100 years are shown in Figure 4. The ebb delta forms during the first 10 years and then the channel pattern develop rapidly in the next 30 years and continue to extend and deepen more slowly after 100 years.

In the morphodynamic model results shown below, there is no limiting depth to erode. After 100 years, the bed is eroded locally down to 50 m which is rather unrealistic, since in nature the presence of a rigid bottom would limit the depth of erosion.

C. *Influence of the Mesh size*

The effect of the mesh size after 10 years of bed evolution – including sloping bed effects – is shown on Figure 5. The refined mesh on the right provides a more detailed channel pattern. The mesh size has an important effect on the results whereas the slope effect does not make any difference for the coarser grid and modifies slightly the results for the refined grid.

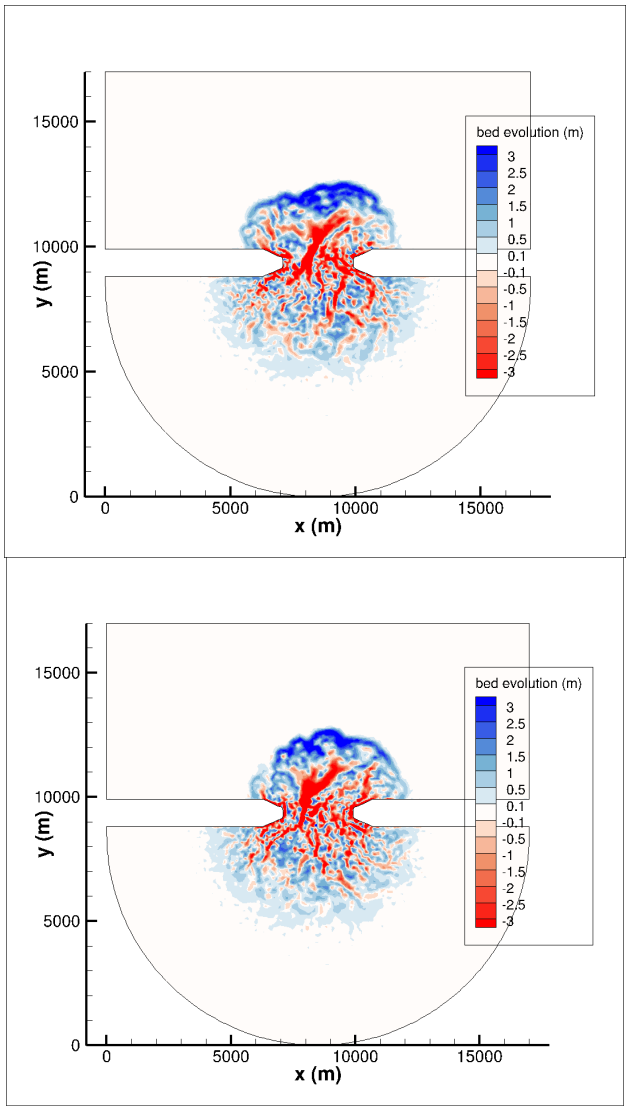

Figure 3: Bed evolution obtained after 30 years for a morphodynamic factor MF =10 on top and MF = 50 on the bottom

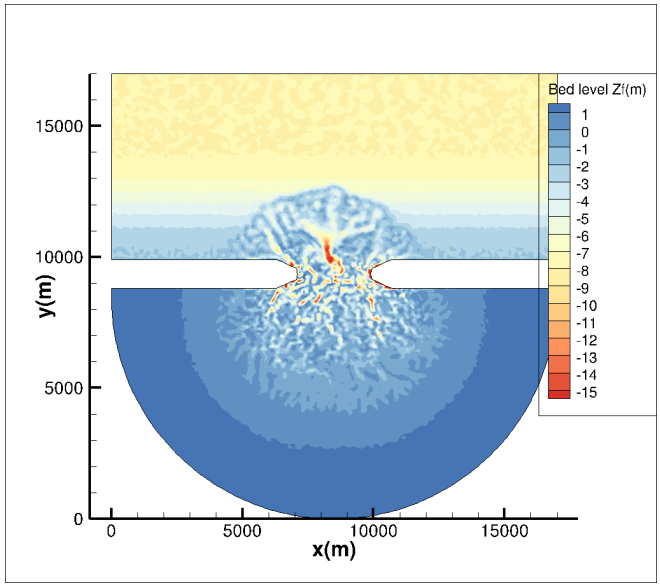

Figure 4: Bottom after 100 years for the coarse mesh – For 8 processors on a linux Z 600 station, the CPU time is about 1 day 13 hrs.

Variable input parameters	Mean Value	Standard deviation
k_s (m)	0.05	0.005
d_{50}(m)	$1.5\ 10^{-4}$	$1.5\ 10^{-5}$

Table 1: Variable input parameters – mean values and standard deviations

Variable Input parameters	Mean Value	Standard deviation
Secondary current parameter β	7	0.7
Sloping bed parameter α (m^2/s)	$1.15\ 10^{-5}$	10^{-6}

Table 2: Variable input model parameters- mean values and standard deviations

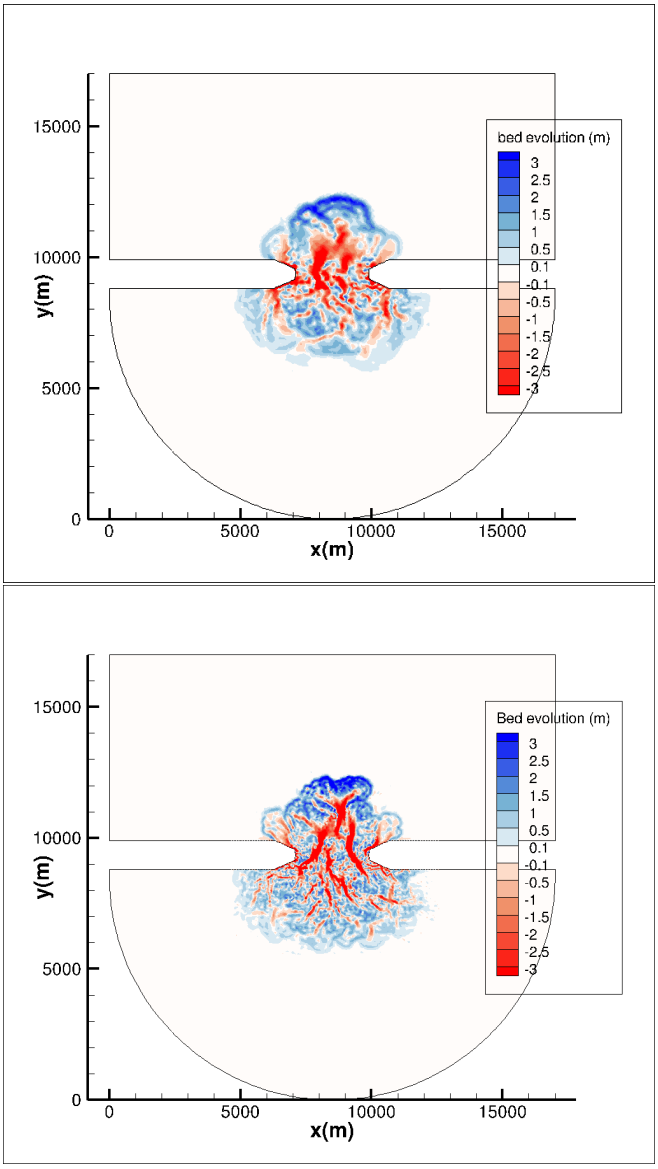

Figure 5: Bottom evolution after 10 years for the 2 meshes with sloping beds included. The top figure is obtained for the coarse grid and the bottom one, with the refined grid.

V. Uncertainty and Sensitivity Analysis using AD

A. *Presentation of the FOSM/AD Method*

The First-Order Second Moment Method using Algorithmic Differentiation (FOSM/AD) presented in Villaret et al. (2015) is applied here to quantify sensitivities and uncertainty in the Telemac-2D/Sisyphe morphodynamic model.

Assuming first-order Taylor expansion and independent input variables X_i, the variance of the model output variable can be expressed as a function of partial derivatives of the morphodynamic model function F according to:

$$Var(Zf) \simeq \sum_{i=1}^{n} \left[\frac{\partial F}{\partial X_i}\left(E(X)\right)\right]^2 \cdot Var(X_i) \qquad (4)$$

Where $Zf = F(X_i)$ is the calculated bed evolution, and n is the number of variable inputs, $E(X)$ is the best estimates or mean values of X. Partial derivatives in Eq. 4 can be calculated exactly up to machine accuracy using Algorithmic Differentiation (AD).

The AD-generated Tangent Linear Model of the Telemac-2D/Sisyphe model (TLM) computes in addition to the bed evolution, a projection of the Jacobian (matrix of partial derivatives). The partial derivatives $\frac{\partial Zf}{\partial X_i}$ of the calculated bed evolution $Zf = F(X_i)$ with respect to each individual uncertain variables X_i for $1 \leq i \leq n$ are obtained by evaluating the TLM $\dot{F}$ repeatedly. Eq. (4) can then be evaluated easily from the stored partial derivatives $\frac{\partial Zf}{\partial X_i}$ to obtain the total variance $Var(Zf)$.

B. *Sensitivity Analysis to variable grain size and bed roughness*

For the FOSM uncertainty, we use a Nikuradse friction law and variable bed roughness with mean value k_s=0.05 m.

Sediment transport formulas embedded in morphodynamic models are highly sensitive to both grain size $d_{50}$and bed roughness k_s input parameters. Here we assume 10% for the standard deviation of each input parameter.

The TLM model has been applied twice to calculate the partial derivatives with respect to both grain size and bed roughness. Variations of the bed evolution are then obtained by multiplying the calculated partial derivatives by the standard deviation of each input parameter.

Variations of the bed evolution with respect to both grain size and bed roughness after one year of bed evolution are shown in Figure 6. The pattern obtained for both parameters is overall similar but with opposite signs. An increase in grain size is expected to reduce the transport rates and resulting bed evolutions, which is qualitatively similar to a decrease in bed roughness.

Quantitatively, the effects of both grain size and bed roughness are maximum where the bed evolutions are higher, e.g. at the mouth of the inlet and in the delta where it is about +/-20 cm, which represents overall less than 10 % of the bed evolution.

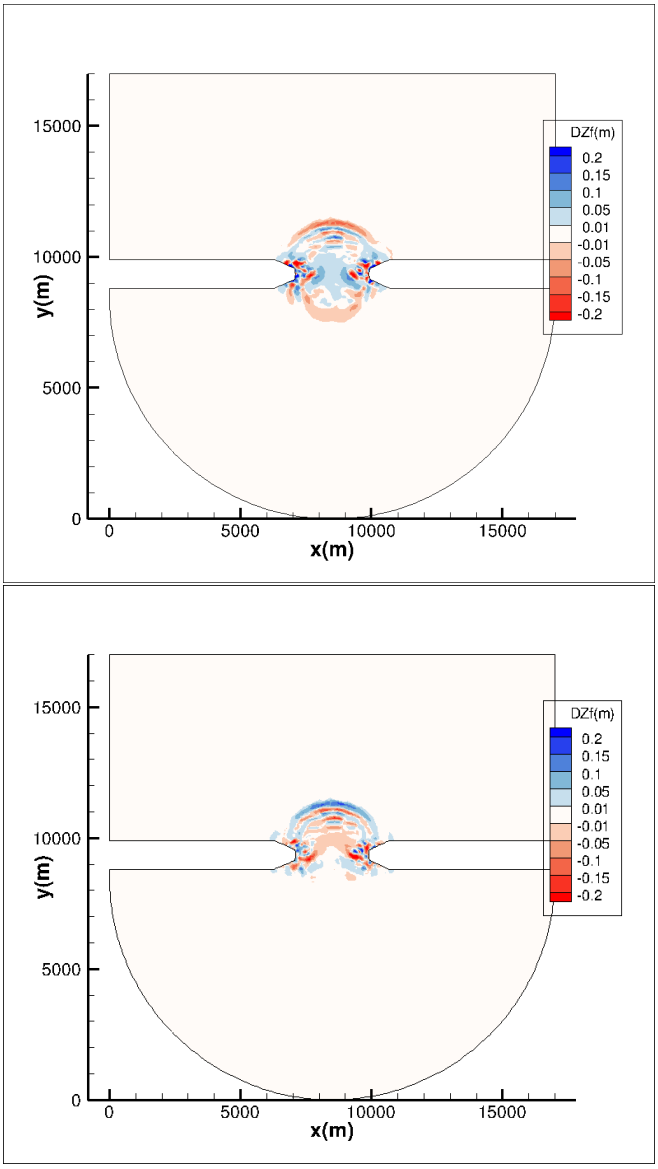

Figure 6: Sensitivity to grain size (top) and bed roughness (bottom) after 1 year of simulation (130 000 NIT with Dt = 10s and MF=25). In scalar version each run of the TLM model takes approximately 10 to 15 hours on a Linux station

C. Sensitivity Analysis to Model parameterization

Sediment transport models rely on empirical formulations for complex sediment transport processes (bed load formulae, sloping bed effects, secondary currents…). In addition to the set of physical input parameters, a set of semi-empirical coefficients can be also considered as variable input model parameters.

Here we are interested in the sensitivity of model results to sloping bed and secondary currents. Again we assume 10% of variation for the standard deviation of both coefficients α in the sloping bed formula (eq. 2) and β in (eq. 3).

According to the TLM model results shown in Figure 7, both secondary currents and sloping bed effects are found to have only a minor influence on the results, in comparison to the grain size and bed roughness parameters. Sloping bed effects are more important at the mouth of the inlet where gradients in the bottom slope are higher. The effect of secondary currents is found to have a very local influence inside the inlet. Quantitatively their effect is less than 2% of the bed evolution.

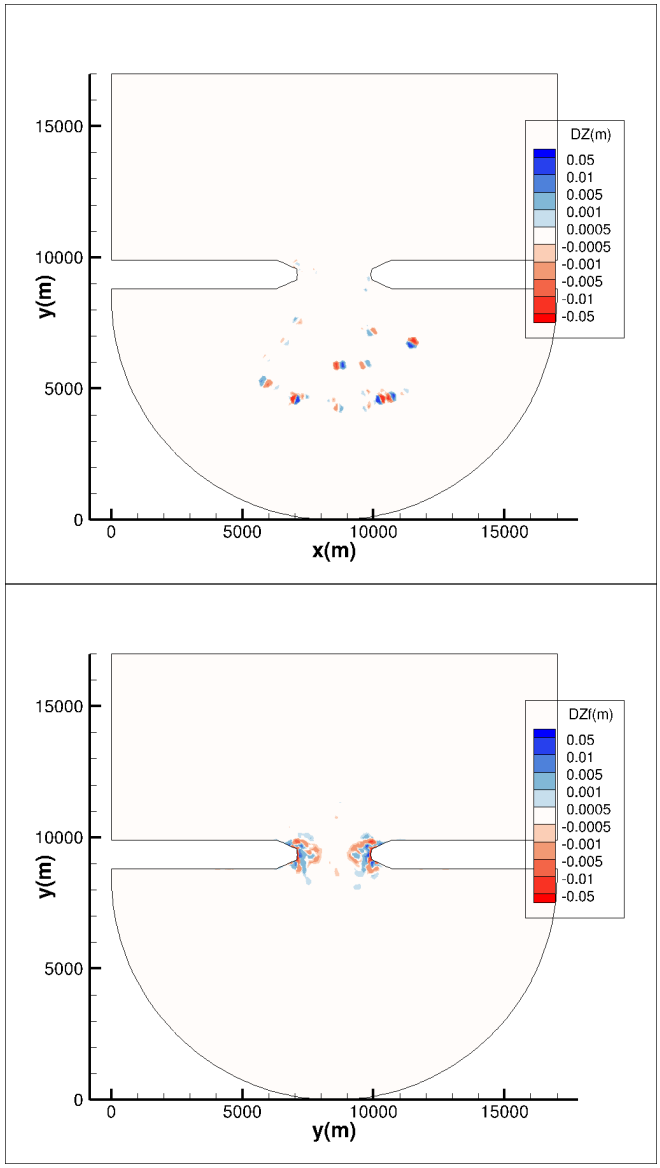

Figure 7: Sensitivity to secondary current (top) and sloping bed (bottom) after one year of simulation

D. Uncertainty Analysis

The effects of both bed roughness and grain size are dominant and only those two terms have been retained to calculate the total variance. Equation (4) reduces to:

$$Var(Z_f) \simeq \left[\frac{\partial Zf}{\partial D_{50}}\right]^2 \cdot Var(D_{50}) + \left[\frac{\partial Zf}{\partial k_s}\right]^2 \cdot Var(k_s) \quad (5)$$

The total variance has been calculated by post processing results of the TLM results presented in Figure 6. The final results obtained after 1 year of bed evolution are shown in Figure 8 (top figure). Again the uncertainty is larger where the bed evolution (bottom figure) is larger, i.e. at the inlet side boundaries and at the position of the ebb delta offshore. The global uncertainty represents approximately 10 % of the bed evolution.

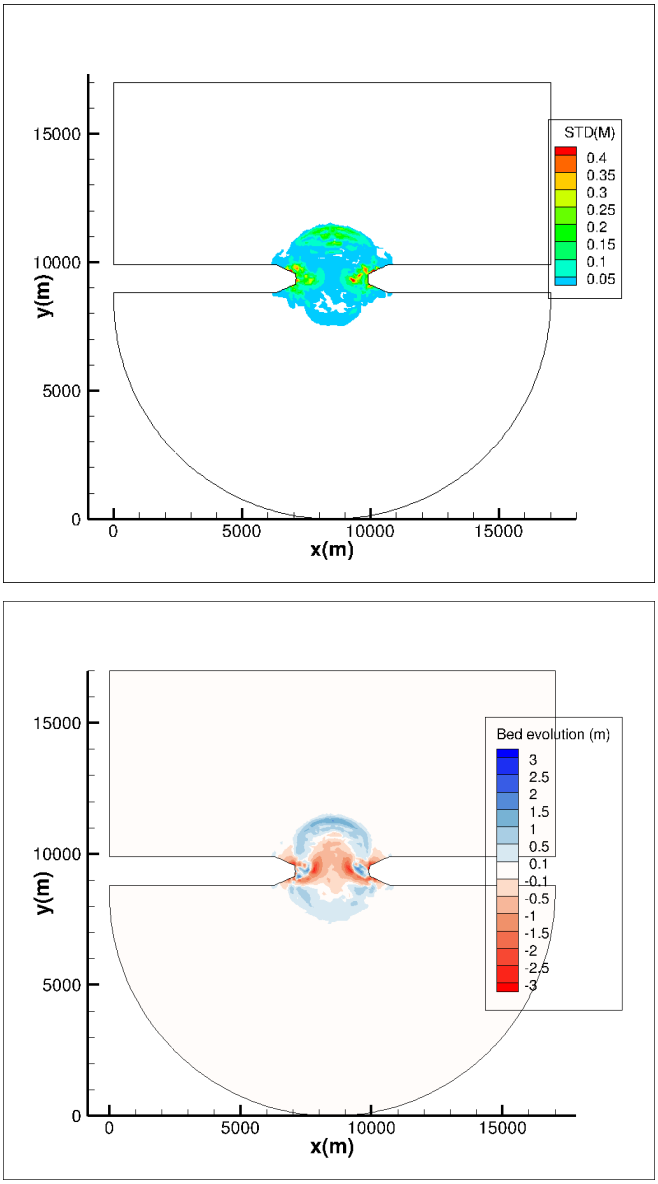

Figure 8: Uncertainty analysis. The standard deviation of the bed evolution (m) as a result of variability in the grain size and bed roughness is shown on the top. The corresponding bed evolution after one year is shown on the bottom.

CONCLUSIONS

The FOSM/AD method has been applied to quantify uncertainty and sensitivities in a complex 2D application: the formation of an ebb delta and channel pattern in a schematic tidal inlet. Here we used a recently developed TLM model of the Telemac-2d/Sisyphe model using release 7.0 and the AD-enabled NAG Fortran compiler.

The effects of secondary currents and sloping beds are found to make only a small local contribution to the total uncertainty whereas the sensitivities to both bed roughness and grain size are dominant. The partial derivatives obtained with respect to grain size and bed roughness are similar but with opposite sign.

Assuming 10 % for the standard deviation of each input parameters, the uncertainty due to both bed roughness and grain size represents approximately 10% of the bed evolution after one year. Uncertainty is larger where the bed evolution is larger, i.e. at the mouth of the inlet along the side boundaries as well as offshore where the ebb delta starts to form.

Despite its efficiency – only one TLM run per variable input parameter – the FOSM/AD method is here limited by the use of a scalar version. A parallel version is under development and needs to be applied to study uncertainties at morphodynamic time scales (10 to 100 years). The effect of other parameters – like the rigid bed level - is expected to be important for the channel pattern formation observed after 30 years.

The mesh dimension is shown to have a major influence on the model results and determine the channel pattern characteristic scales (extension and width). The FOSM/AD method needs to be extended to study the sensitivity to mesh size.

The sensitivity of the bed evolution to the initial bathymetry needs also to be further investigated.

REFERENCES

[1] Engelund, F., and Hansen, E., 1967. A Monograph on Sediment Transport in Alluvial Streams. Teknisk Forlag, Copenhagen, 62 pp.

[2] Cayocca, F, 2001: Long-term morphological modeling of a tidal inlet: The Arcachon Basin, France Coastal Engineering (Impact Factor: 2.06). 02/2001; 42(2):115-142. DOI: 10.1016/S0378-3839(00)00053-3

[3] Dissanayake, D.M.P.K., Roelvink, J.A., and van der Wegen, M., 2009. Modelled channel patterns in a schematized tidal inlet. Coastal Engineering 56, 1069-1083.

[4] Goeury C., 2015: Differentiation automatique de TELEMAC v7p0 par surcharge d-operateur: Rapport EDF-LNHE H-P73-2015-05312-FR.

[5] Hervouet JM, Pavan S., Ata R., 2015: Distributive advection schemes and dry zones; new solutions: Telemac User Club, 2015.

[6] Marciano, R., Wang, Z.B., Hibma, A., de Vriend, H.J., and Defina, A., 2005. Modeling of channel patterns in short tidal basins. Journal of Geophysical Research 110, F01001

[7] Kirwan, ML and Murray, B., 2007: A coupled geomorphic and ecological model of tidal marsh evolution, Proceedings of the National

Academy of Sciences of the USA 104, 6118-6122. vol. 104, no. 15, www.pnas.org/cgi/content/full/ 0700958104/DC1.

[8] Knaapen, M: "Multiscale Morphodynamics," H.R. Wallingford Report, DDY0465-RT001-R01, 2014.

[9] Riehme, J., Kopmann, R., Naumann, U., 2010: Uncertainty quantification based on forward sensitivity analysis in Sisyphe, Proceedings of the Vth European Conference on Computational Dynamics, ECOMAS CFD 2010 (on CDROM).

[10] van Maaren B., 2011: Modelling the long-term morphological evolution of tidal embayments, Ph. D Thesis, University of Waikato.

[11] Villaret, C., Kopmann, R., Wyncoll, D., Riehme, J., Merkel, U. Naumann,U.: "First-order Uncertainty Analysis using Algorithmic Differentiation of the Telemac-2D/Sisyphe Morphodynamic Model", accepted for publication in Computers and Geosciences, 2015.

UNCERTAINTY QUANTIFICATION ON A REAL CASE WITH TELEMAC-2D

C. Goeury[1], T. David[1], R. Ata[1,2], S. Boyaval[2], Y. Audouin[1], N. Goutal[1,2], A.-L. Popelin[3], M. Couplet[3], M. Baudin[3], R. Barate[4]
[1]EDF R&D National Laboratory for Hydraulics and Environment (LNHE)
[2]Saint-Venant Laboratory for Hydraulics
[3]EDF R&D Industrial Risks Management (MRI)
[4]EDF R&D Neutronic Simulation and Information Technology (SINETICS)
6 quai Watier, 78401 Chatou, France
e-mail: cedric.goeury@edf.fr

***Abstract*— In this study the software TELEMAC-2D (www.opentelemac.org) is used with the OpenTURNS library (www.openturns.org) to quantify the uncertainty on a real hydraulic case. The used approach is based on the chaining of OpenTURNS and TELEMAC-2D using the SALOME platform (www.salome-platform.org) in order to implement a Monte Carlo-like algorithms. Each uncertain parameter (inlet discharge, friction coefficient) is associated to a statistical distribution (defined using OpenTURNS). A sufficient number of TELEMAC-2D runs are achieved with respect to the pre-defined random entries in order to guarantee the convergence of the studied Monte Carlo-like algorithms. EDF's cluster has been used to run the simulations.**

Indeed, to handle the uncertainty with the Monte Carlo method, it is important to run a lot of simulations in order to have reliable results. The obtained results are analysed twofold: On one hand, the effect of variability of random inputs is assessed at some specific points (assumed to be around a fictive point of interest). On the other hand, a global statistical analysis all over the domain is done. A spatial distribution of the mean water depth and its variance is obtained. These results are of utmost importance for dimensioning of protecting dykes. Furthermore, they are very useful when establishing scenarios for flood managing.

However, Monte Carlo technique that while generic and robust is also computationally expensive. Ways to lower the cost typically require to replace the pure random sampling that form the backbone of the Monte Carlo method by alternative sampling methods such as the Latin Hypercube Sampling approach and the quasi-Monte Carlo method based on low discrepancy sequence. The present work aims to compare the behavior of these Monte Carlo-like algorithms.

This work shows that, thanks to the availability of important computer resources and to an optimized software, we are able to consider Monte Carlo-like algorithms for uncertainty quantification of real hydraulic models. This critical conclusion was, even an unfeasible dream, couple of years ago.

I. INTRODUTION

Water resource management and flood forecasting are crucial societal and financial stakes that require a solid capacity of flow depth estimation that is often limited by uncertainties in hydrodynamic numerical models. In order to overcome these limits, uncertainties should be analyzed. Uncertainty analysis means the quantification of the uncertainty in the model outputs due to uncertainty in the input data, parameters, model structure and modelling assumptions.

In this study, we investigate the effect of two uncertainty sources on water level calculation for extreme flood event, the roughness coefficient and the upstream discharge. Indeed, the hydraulic roughness is uncertain because flow measures are not available or reliable for calibration and validation. Discharge is also uncertain because it results from extrapolation of discharge frequency curves at very low exceeding probabilities.

A variety of statistical methods can be used to propagate input uncertainties through the model into output uncertainties. Most classical method to propagate the uncertainty through the dynamical model is the Monte Carlo technique. This approach requires random generation of the ensemble of inputs from their probability distributions and successive deterministic model simulations to generate a lot of realizations of the output. The main drawback of this is the computational cost. A way to lower the computationally demanding is to replace the pure random sampling that form the backbone of the Monte Carlo method by alternative sampling methods such as the Latin Hypercube sampling approach and the quasi-Monte Carlo method based on low discrepancy sequence of Sobol. The present work aims to compare the behaviour of these Monte Carlo-like algorithms.

This work has been carried out using the SALOME platform in which the hydraulic software TELEMAC-2D is coupled with the uncertainty library OpenTURNS.

The paper is organized as follows: in the first section, the numerical tools used during the study are presented. In section 3, the model is presented with a description of the study area, the hydraulic model and the uncertainty study. Then the results of the simulations are described in the section 4. Finally, in the last section we discuss the results and we draw some conclusions.

II. NUMERICAL TOOLS

As already mentioned, this study was performed by coupling the hydrodynamic model TELEMAC-2D and the uncertainty library OpenTURNS in the SALOME platform. These numerical tools are presented in this section.

A. *Hydraulic modelling system TELEMAC-2D*

The modeling system TELEMAC is a hydro-informatic software developed by the LNHE (National Laboratory for Hydraulics and Environment) from the research and development department of EDF. It is an open source software (www.opentelemac.org) which can be used to perform numerical simulation in two and three dimensions. Several modules can be used to solve different problems such as tidal wave (Artemis, Tomawac), current (TELEMAC-2D, TELEMAC-3D), sediment transport (Sisyphe) and water quality (Delwaq, developed by Deltares).

In this work, hydrodynamic is provided using TELEMAC-2D depth-averaged hydrodynamic model. It solves the shallow water equations in two dimensions. In each point of the mesh, TELEMAC-2D gives the water depth and the vertically average horizontal velocity field [4].

B. *Uncertainty treatment library OpenTURNS*

OpenTURNS is an open source library for uncertainty treatment coded in C++ (www.openturns.org) used through python scripts. OpenTURNS stands for "Open source initiative to Treat Uncertainties, Risks'N Statistics". It is co-developed since 2005 by EADS IW, EDF R&D and PHIMECA Engineering. It is used according the uncertainty method describes as follow by EDF R&D (see Fig. 1) [8].

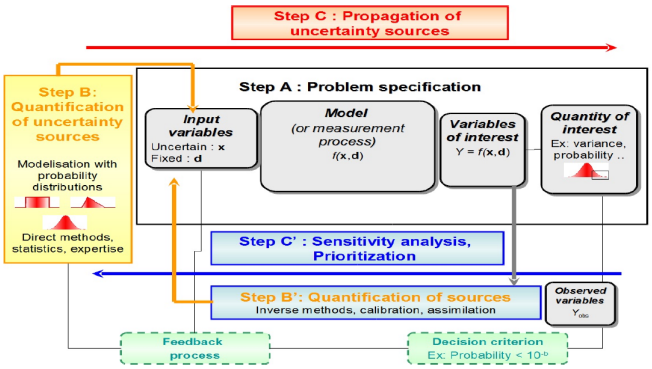

Figure 1. Steps for an uncertainty study [8]

C. *The SALOME platform*

Salome is an open source software (www.salome-platform.org) which is a platform for pre and post processing for numerical simulation and where it is possible to define a chain or a coupling of computer codes. It is based on an open and flexible architecture with reusable components. SALOME is developed by EDF, the CEA and OPENCASCADE S.A.S. with the GNU LGPL license as the source code can be downloaded and modify from the website. All the components within SALOME can be used together with the YACS module which build a computation scheme and call each module and make them communicate. In our case TELEMAC-2D and OpenTURNS are working together within this platform as shown in Fig. 2.

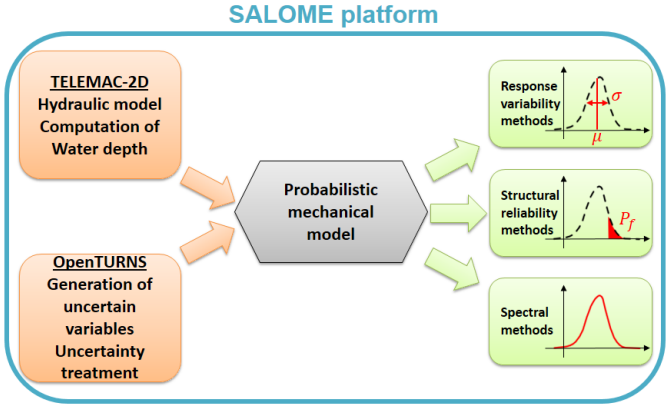

Figure 2. The SALOME principle for uncertainty quantification (inspired from [9])

III. PROBLEM SPECIFICATION

In this part the study area is presented with its global location and general overview of the situation. Then the model itself with its input parameters are introduced to bring the uncertainty study. Finally the method used to propagate and quantify the uncertainty are presented.

A. *Study area*

The area chosen for this study extends over a reach of the Garonne river measuring about 50 km, between Tonneins (upstream), downstream of the confluence with the Lot river, and La Réole (downstream) (see Fig. 3).

Figure 3. Study area of the Garonne [1]

This part of the valley was equipped in the 19th century with infrastructure to protect against floods of the Garonne river which had heavily impacted local residents. A system of longitudinal dykes and weirs was progressively built after that flood event to protect the floodplains, organize submersion and flood retention areas. This configuration is also similar to the characteristic of other managed rivers such as the Rhone and the Loire.

B. *The hydraulic model*

1) *Boundary conditions*

The 2D Telemac model, constituted by a triangular mesh of some 41 000 nodes with an extremely small mesh size around the dykes, has a constant discharge upstream imposed at Tonneins and downstream, a stage-discharge relationship corresponding to the stream gauge at La Réole. This model has been realized by Besnard and Goutal (2008) [1].

In this work, the upstream discharge is set up to 8 790 m^3/s corresponding to a very low exceeding probabilities (a thousand return period discharge) in order to model an extreme flood event with points affected around the floodplain.

2) Roughness coefficient

The models were calibrated in [1] using steady-state water surface profiles at high discharge, from bank-full discharge in the main channel (2 500 m^3/s) to bank-full discharge in the overbank flow channel between dykes.

For the main channel, the Strickler roughness coefficient was split into three different areas:

- Tonneins – upstream of Mas d'Argenais: 45
- Upstream of Mas d'Argenais – upstream of Marmande: 38
- Upstream of Marmande – La Réole: 40

In floodplain, the roughness coefficient is selected as an area with cultivated fields all around the river with a Strickler coefficient of 17.

C. Uncertainty study

1) Variable of interest

As already mentioned, the quantity of interest considered in this study is the flow depth all over the computational domain.

2) Uncertainty quantification

In this study, we investigate the effect of two uncertainty sources on water level calculation for extreme flood event, the roughness coefficient and the upstream discharge. In fact, the hydraulic roughness is uncertain because flow measures are not available or reliable for calibration and validation. Discharge is also uncertain because it results from extrapolation of discharge frequency curves at very low exceeding probabilities. The quantification of these uncertainty sources is given the following subsections.

a) Probability density function of roughness coefficient

Classically, according to the available expert knowledge, the friction coefficient is contained in an interval bounded by physical values depending on the roughness of soil material. Consequently, using the principle of maximum entropy [9], the distribution of the bounded Strickler roughness coefficient is uniform. The boundaries of the uniform distribution are arbitrarily chosen ± 5 from the calibrated value given in the section B.2). Fig. 4 shows the probability density function of the Strickler coefficient in the floodplain.

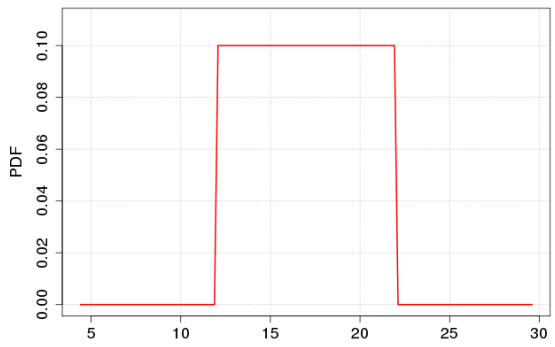

Figure 4. Probability density function of the Strickler coefficient in the floodplain

b) Distribution of the discharge

As already mentioned, the upstream discharge is estimated using an extrapolation of discharge frequency curves at very low exceeding probabilities corresponding to a thousand year return period event. Confidence intervals on the extrapolated value can be derived. In that case, when the mean value (discharge of the thousand year return period) and the standard deviation (extrapolated from the confidence intervals) are known, the maximum entropy distribution is Gaussian [9]. The mean and standard deviation are set to, respectively, 8 490 m^3/s and 900 m^3/s. Moreover, to avoid too high or too low values, the probability density function is truncated at 5 790 m^3/s and 11 190 m^3/s which means the probability to have a discharge outside these boundaries is zero (see Fig. 5).

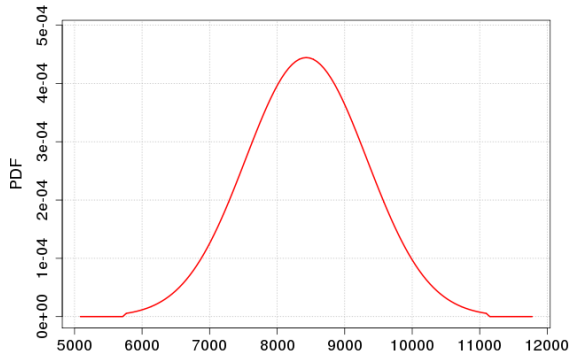

Figure 5. Probability density function of the upstream discharge

3) Uncertainty propagation methods

a) The Monte Carlo method

The Monte Carlo method requires random generation of the ensemble of input random variables from their probability distributions. The resulted sampling form a matrix composed by n (number of simulations) $\times s$ (number of variables). Each row of the matrix represents a configuration that is used as an input for the hydraulic simulation. A lot of realizations of the output is generated by

successive deterministic model simulations corresponding to each configuration of the sampling matrix. Then, some statistical estimators can be computed on the output sample. For example, the mean value $\overline{\mu_Y}$ and the standard deviation $\overline{\sigma_Y}$ of a response quantity $Y = f(x_k)$ are given by (1) and (2).

$$\overline{\mu_Y} = \frac{1}{n}\sum_{k=1}^{n} f(x_k) \quad (1)$$

$$\overline{\sigma_Y}^2 = \frac{1}{n-1}\sum_{k=1}^{n}[f(x_k) - \overline{\mu_Y}]^2 \quad (2)$$

With x_k the input sample of uncertain variables.

The statistics computed on sample sets are random quantities in nature. Therefore, confidence intervals on the results should be provided. Monte Carlo method easily give a confidence intervals for the estimation by using the central limit theorem.

It implies that if a random variable Y have a mean μ_Y and a variance ${\sigma_Y}^2$ which are finite, then the distribution of the mean of n independent realizations Y_i converge toward a Gaussian distribution when n tends towards infinity. More precisely, if $n \to \infty$,

$$\frac{\overline{\mu_Y} - \mu_Y}{\sigma_Y/\sqrt{n}} \xrightarrow{\mathcal{L}} \mathcal{N}(0,1). \quad (3)$$

As show in (3), the convergence speed of the method is then, on average, $o(\sqrt{n})$ independent of the dimension s of the problem. The Monte Carlo method is theoretically applicable whatever the complexity of the deterministic model or the desired statistical estimator. However, its computational cost makes it rather impracticable when the computational cost of each run of the model is non negligible and when the statistical estimator requires a lot of realization to be converged. One way to lower the computationally demanding is to replace the pure random sampling that form the backbone of the Monte Carlo method by alternative sampling methods such as the Latin Hypercube sampling approach and the quasi-Monte Carlo method based on low discrepancy sequence of Sobol. These sampling methods are developed in the next two sections. In these sections, it is assumed that the sampling space is the unit cube $I^s = [0,1]^s$. In fact, even if each uncertain parameter can take values in a certain finite range, it is always possible to rescale them appropriately to obtain a unit cube.

b) The Latin Hypercube sampling

The Latin Hypercube Sampling (or LHS) is a sampling method enabling to better cover the domain of variations of the input variables, thanks to a stratified sampling strategy.

The sampling procedure is based on dividing the domain of each variable into several intervals of equal probability. A unique random value is chosen in each interval and then the values obtained for the variables x_i and x_j are randomly combined. This step is repeated for all the random variables to give a $n \times s$ matrix which can be used as an input sample.

Fig. 6, extracted from [2], shows the comparison between the two sampling methods of two random variables (x_1, x_2) taken from a uniform distribution in the interval $[0,1]$. This figure demonstrates the sampling strategy of the LHS as each row and column are filled with points instead of the Monte Carlo sampling in which some rows and columns does not have points.

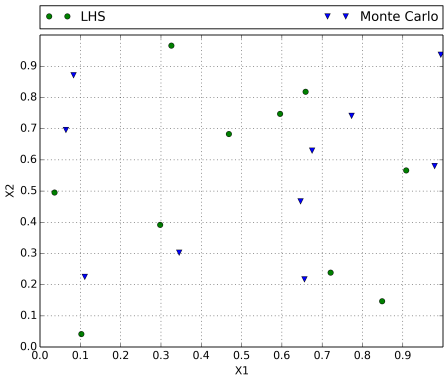

Figure 6. Comparison between Latin Hypercube and Monte Carlo sampling with 10 values [2]

According to [7], if the function f is monotonic in each of its arguments, then the variance of the estimator of the LHS is lower than the Monte Carlo one given by (4).

$$Var(\bar{\mu}_{Y_{LHS}}) \leq Var(\bar{\mu}_{Y_{MC}}) \quad (4)$$

The expression of the estimator is defined by (1) where the input samples x_k are generated according the LHS and Monte Carlo techniques.

Therefore, by (4) the LHS technique is supposed to be more efficient in term of convergence rate than the Monte Carlo method.

c) The quasi-Monte Carlo method

Quasi-Monte Carlo (or QMC) techniques are deterministic methods that have been designed by analogy with Monte Carlo simulation. In quasi-Monte Carlo, the random sample of Monte Carlo is replaced by a sequence of well distributed points called a low discrepancy sequence [7]. Fig. 7 presents the comparison between the sampling from the Sobol sequence and Monte Carlo. It demonstrates that the Monte Carlo does not fill the domain as the Sobol sequence does.

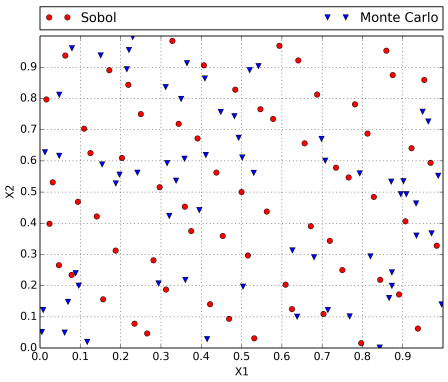

Figure 7. Comparison between low discrepancy sequence and Monte Carlo sampling with 64 values

A low-discrepancy sequence is a sample whose points are in a way that approximates the uniform distribution as close as possible. The discrepancy is a measure of deviation

from uniformity of a sequence of points in $D = [0,1]^s$. The discrepancy of a quasi-Monte Carlo sampling is known and given by (5).

$$D^*(Pn) \leq c\frac{[\ln(n)]^s}{n} \quad (5)$$

With c a constant which depends on the sequence used.

Moreover, the discrepancy contributes to the error in quasi-Monte Carlo methods. The deterministic error bounds, through the Koksma-Hlawka theorem, can be estimated by (6).

$$\left|\frac{1}{n}\sum_{i=1}^{n} f(u_i) - \int_{I^s} f(u)\,du\right| \leq V(f)D^*(Pn) \quad (6)$$

With $V(f)$ the variation in the sense of Hardy and Kraus of the f function in the mono dimensional case on $I = [0,1]$ given by (7).

$$V(f) = \sup_{P\in \mathrm{P}} \sum_{i=0}^{n_p-1} |f(u_{i+1}) - f(u_i)| \quad (7)$$

Where P is a set of all the partitions P of $I = [0,1]$ and P_n a low discrepancy sample.

Thus, when $V(f) < \infty$ and $P_n = \{\boldsymbol{u}_1, \boldsymbol{u}_2, \dots\}$ is based on a low discrepancy sequence, the control of the variance of the approximation is about $o\frac{[\ln(n)]^s}{n}$ [7]. Comparing this with the probabilistic Monte Carlo error that is in $o\frac{1}{\sqrt{n}}$, one can argue that for a fixed dimension s, the quasi-Monte Carlo method converges faster than with Monte Carlo. So, for function that are smooth enough and if you are willing to take n sufficiently large, the error with quasi-Monte Carlo technique will be smaller than the Monte Carlo one.

d) Quantity of interest

The objective of an uncertainty study is to assess some characteristics of interest of the uncertain output variable distribution, such as, probability of exceeding a threshold, quantile, or expectation and variance. In this study, the considered characteristics of interest are the first four statistical moments (mean, variance, skewness and kurtosis) of the water depth.

To ensure the relevance of the comparison of the different Monte Carlo-like algorithms, the "bootstrap" method is used to estimate confidence intervals on the Monte Carlo results.

CONFIDENCE INTERVAL BY BOOTSTRAP

The "bootstrap" method is the practice of estimating properties of an estimator (such as its variance) by measuring these properties when sampling from an approximating distribution. This technique is easily implemented and rely on few hypothesis [5]. In this work, the non-parametric bootstrap is used.

Let $x = (x_1, \dots, x_n)$ denote a sample of n independent realizations and identically distributed according to the probability density function F. The statistical estimator $\theta = T(F)$ (mean, variance…) is sought. To estimate θ, $\hat{\theta} = T(\hat{F}_n)$ is calculated where $\hat{F}_n$ is the empirical cumulative density function defined by (8).

$$\hat{F}_n(x) = \frac{1}{n}\sum_{i=1}^{n} 1_{u_i \leq x} \quad (8)$$

The idea of the non-parametric bootstrap is to simulate data from the empirical cumulative density function $\hat{F}_n$. Here $\hat{F}_n$ is a discrete probability distribution that gives probability $\frac{1}{n}$ to each observed value $x_1, \dots, x_n$. A sample of size n from $\hat{F}_n$ is thus a sample size n drawn with replacement from the collection $x_1, \dots, x_n$. Once the bootstrap samples done, the properties of the estimator $\hat{\theta}$ can be determined as shown in Fig. 8.

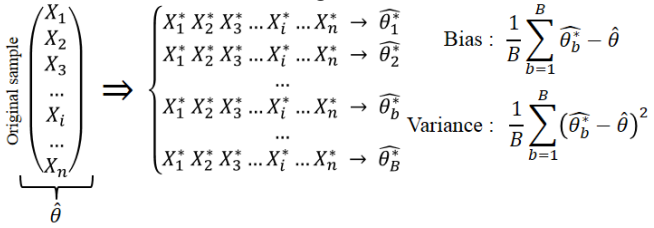

Figure 8. Bootstrap algorithm [5]

IV. RESULTS

Firstly, in this section, results induced by the Monte Carlo technique are presented. In fact, a sufficient number of TELEMAC-2D runs has been carried out with respect to the pre-defined random entries in order to guarantee the convergence of the method. The obtained results provide the reference statistical estimators used to compare the efficiency of the Monte Carlo-like methods which constitute the second part of this section.

A. Monte Carlo results

To handle the uncertainty with the Monte Carlo technique, it is important to run a lot of simulations in order to have reliable results. In this work, around 70 000 Monte Carlo computations have been carried out. EDF's cluster has been used to run these simulations. MPI library was used for launching and managing the uncertainty quantification study. Post-processing of the huge amount of results files is tackled through some Python scripts specifically developed within OpenTURNS.

The obtained results are analyzed twofold: On one hand, the effect of variability of random inputs is assessed at some specific points (assumed to be around an industrial plant, for example). On the other hand, a global statistical analysis all over the domain is done, as shown in Fig. 9.

A spatial distribution of the mean water depth and its variance is obtained. These results are of utmost importance for dimensioning of protecting dykes. Furthermore, there are very useful when establishing scenarios for flood managing.

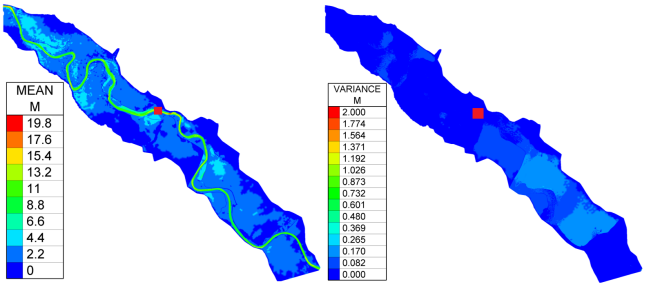

Figure 9. Mean and variance all other the domain (■ node 37 242)

To be sure that the obtained results are reliable, it is important to verify the convergence of them, especially by plotting the graph of the dispersion coefficient (σ/μ) as a function of N: if the convergence is not visible, it is necessary to increase N or if needed to choose another propagation method to estimate the uncertainty [8].

Fig. 10 shows the convergence of the dispersion coefficient and the mean of the water depth at the node number 37 242 located on Fig. 9.

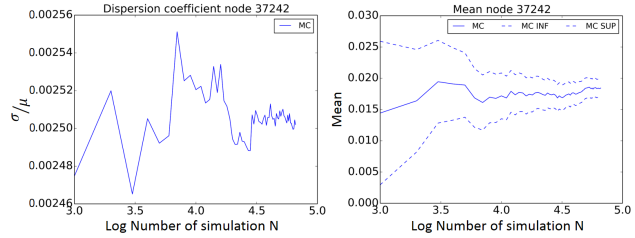

Figure 10. Convergence graphs of the dispersion coefficient and the mean according to the logarithm of the number of simulations

These graphics shows that the convergence of results are guaranteed from 30 000 simulations of Monte Carlo Technique. These results are then used to provide reference statistical estimators in the comparison of the efficiency of the Monte Carlo-like methods.

B. Comparison of Monte Carlo-like algorithms

As shown in IV.A, thanks to the availability of important computer resources and to an optimized software, we are able to consider Monte Carlo uncertainty propagation algorithm for real hydraulic models. This conclusion was, even an unfeasible dream, couple of years ago.

However, the growing complexity of studies (such as coupled waves and hydrodynamics or hydro-sedimentological simulations, for instance) and the ever-greater needs in terms of precision in results (very fine mesh simulations) tend to encourage the use of techniques requiring less computation time.

As mentioned previously, a way to lower the computationally demanding of the Monte Carlo method is to replace the pure random sampling by alternative sampling methods such as the Latin Hypercube sampling approach and low discrepancy sequences. The section presents the comparison of Monte Carlo, quasi-Monte Carlo and Latin Hypercube Simulation on fourth first statistical estimators (mean, variance, skewness and kurtosis) of the distribution of the water depth.

The characteristic of interest of the output distribution is considered as stabilized when its variation are contained in the confidence interval of the reference solution. This confidence interval is calculated using the bootstrap technique, described in III.C.3)d), on the 70 000 Monte Carlo simulation results. The comparison was carried out at some points all over the computational domain. Since the obtained results are similar to each other, only one node results (node 37 242) are presented in Fig. 11. Firstly, the response variability limited to the mean value and the variance is studied. This constitutes the central part of the model response. In that case, the quasi-Monte Carlo algorithm has a faster convergence rate than the others techniques. In fact, from the beginning (about 1 024 runs), the mean value and the variance estimates are in the reference confidence

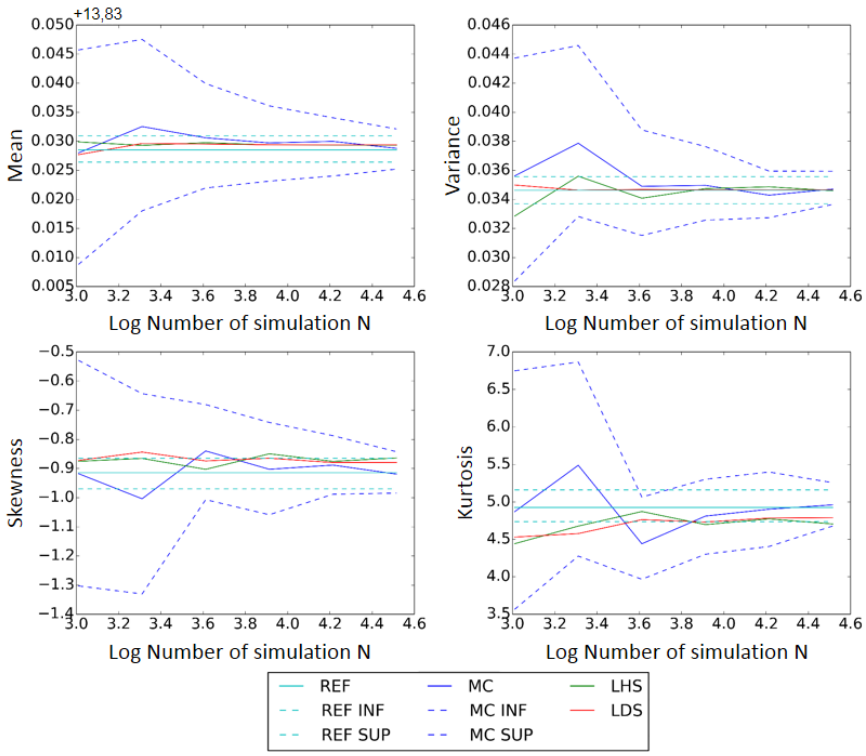

Figure 11 Comparison of the first four statistical moments on the node 37 242

intervals in contrary of the Latin Hypercube simulation and the Monte Carlo technique. The Latin Hypercube Sampling technique is more efficient than the Monte Carlo technique. Respectively, these techniques needs 2 000 and 4 000 simulations in order to obtained results contained in the reference confidence intervals.

The computation of higher order moments (skewness and kurtosis) do not converge as fast as for the mean and standard deviation since the variation of the related estimators of these moments is large. However, as observed for the central part of the model response, the quasi-Monte Carlo is the technique more efficient to determine these moments. In fact, about 4 000 runs are sufficient to reach the reference interval with the quasi-Monte Carlo method. It is more complicated for the Monte Carlo and Latin Hypercube simulation. In fact, the skewness estimated by the Monte Carlo converge as fast as the quasi-Monte Carlo whereas the estimation provided by the Latin Hypercube Sampling is oscillating at the upper bound of the reference confidence interval. At the opposite, the kurtosis estimation based Latin Hypercube Sampling has the same behavior that the low discrepancy sequence of Sobol and the Monte Carlo estimation needs more runs (about 10 000 runs).

As expected, sampling techniques, with their better exploration of the uncertain variable domain of variation, are more efficient than the brute random sampling. However, among the two techniques tested in this work, the quasi-Monte Carlo method is more effective. In fact, according to [3], unlike the quasi-Monte Carlo method, the LHS does not control the quality of the joint distribution of samples when the dimension is higher than two.

V. Conclusion and Discussion

In this paper, the feasibility of an uncertainty propagation with the Monte Carlo method on a two dimensional real case with TELEMAC-2D has been presented. In order to improve the converge speed of the Monte Carlo method, the Latin Hypercube Sampling and the quasi-Monte Carlo method are tested. In all cases, the more efficient technique is the quasi-Monte Carlo method. The improvement of the convergence speed induced by this method opens the doors of uncertainty studies with more complicated cases and bigger meshes where the computation time is crucial. However one of the drawbacks of the quasi-Monte Carlo method is that it does not possess a confidence interval of the results which is essential in practice. In fact, the error estimation, possible in theory using (6), is intractable in practice in contrary of the Monte Carlo method which easily provides a statistical confidence intervals [11]. In order to get the error estimates, the randomized quasi-Monte Carlo method can be used. This method, which constitutes an outlook of the current study, applies a randomization technique to the low discrepancy sequence [7].

Moreover, in the spirit of decreasing the computation cost of uncertainty studies, some techniques can be applied on the sensibility analysis too. The sensibility analysis intends to quantify the relative importance of each input

parameter of a model. The variance-based methods aim at decomposing the variance of the output to quantify the participation of each variable. Generally, these techniques compute sensitivity indices called Sobol indices. In practice, these sensibility indices are calculated using the Monte Carlo simulation. However, as for the uncertainty propagation, this technique requires a lot of computation time. So, in order to decrease the computational cost, some techniques such as the polynomial chaos method and derivative-based global sensitivity measures can be tested:

- The polynomial chaos method is a spectral method which gives a representation of the random response of the experiment. Based on this technique, it is possible to obtain sensitivity indices [10].
- When the derivatives of a computer program are known (Adjoint code for example), it is possible to apply the derivative-based global sensitivity measures (DGSM) [6] to perform sensitivity analysis.

These methods reduce drastically the number of runs needed for the sensitivity indices estimation and should be applicable to more complicated studies. Therefore, in the same way as this work, the sensitivity analysis can be optimized as well with further research.

REFERENCES

[1] A. Bernard and N. Goutal, “Comparison between 1D and 2D models for hydraulic modeling of a floodplain : case of Garonne river”,proceedings of River Flow conference, 2008, in press.

[2] EDF-EADS-PHIMECA, “Reference guide”, OpenTURNS version 1.1, 2013.

[3] R. Faivre, B. Iooss, S. Mahévas, D. Makowski, H. Monod, “Analyse de sensibilité et exploration de modèles”, 2013, éditions Quæ, pp.67.

[4] J-M. Hervouet, “Hydrodynamics of Free Surface Flows”, Wiley, 2007, pp. 83–130.

[5] M. Kadiri Ottmani, “Traitement statistique d’un échantillon”, 2002, Technical report of CEA.

[6] M. Lamboni, B. Iooss, A.-L Popelin, F.Gamboa, “Derivative-based global sensitivity measures: General links with sobol’ indices and numerical test”, ELSEVIER, Febuary 2014, in press.

[7] C. Lemieux, “Monte Carlo and Quasi-Monte Carlo Sampling”, 2009, Edition Springer Series in Statistics, pp. 201–203.

[8] A. Pasanisi, M. Couplet and A-H. Dutfoy Lebrun, “Guide méthodologique pour le Traitement des Incertitudes”, Note EDF-MRI, reference H-T57-2013-02207-FR, 2013.

[9] B. Sudret, “Uncertainty propagation and sensitivity analysis in mechanical models. Contributions to structural reliability and stochatstic spectral methods”, Accreditation to supervise research report, 2007.

[10] B. Sudret, “Global sensitivity analysis using polynomial chaos expansions, Reliab. Eng. Sys. Safety, in press.

[11] B. Tuffin, “Randomisation of quasi-Monte Carlo methods for error estimation: survey and normal approximation”, in press.

Using algorithmic differentiation for uncertainty analysis

Mai Trung Hieu, Wolfgang Nowak
University of Stuttgart
IWS/LS^3 - Pfaffenwaldring 5a
Stuttgart, Germany
mai.trunghieu.vn@gmail.com
Wolfgang.nowak@iws.uni-stuttgart.de

Rebekka Kopmann
Bundesanstalt für Wasserbau
BAW - Kußmaulstr. 17
Karlsruhe, Germany
rebekka.kopmann@baw.de

Abstract— **Although numerical modelling is state of the art and has been very helpful in river engineering for a long time, it should not be neglected that uncertainties are unavoidable in numerical modelling. Uncertainty analysis can help to identify which model parameters cause the largest share of overall simulation uncertainty, and to find the locations and time periods or system states that are subject to the largest predictive uncertainties. Three methods for uncertainty analysis of numerical simulations with TELEMAC-2D have been used and compared: The Monte Carlo method (MC), the First-Order Second Moment method based on numerical differentiation (FOSM/ND) and the same based on algorithmic differentiation (FOSM/AD). The methods have been compared on an application to a laboratory experiment with groynes. With an in-situ application of the uncertainty methods to a 10 km long stretch of River Rhine between Neuss and Düsseldorf, the practical applicability in river engineering could be shown.**

I. INTRODUTION

Numerical modelling is state of the art and has proven very helpful in river engineering. However, numerical modelling is subject to inevitable sources of uncertainty such as deficient descriptions of physical processes, estimated initial/boundary conditions and uncertain model parameters. The latter are uncertain due to measurement errors, natural variability or due to unsatisfactory parameterization. These sources of uncertainty may have serious influence on simulation results and subsequent engineering decisions. Therefore, it is necessary to quantify the resulting uncertainty of model results in order to appraise their reliability. Uncertainty analysis reveals the locations and time periods or system states that are subject to the largest predictive uncertainties. Furthermore, it can identify the model parameters causing the largest share of overall simulation uncertainty. So-called sensitivities can be used to describe the influence of uncertain parameters to model predictions, and can guide efforts of model refinement or data collection.

This study applies and compares three methods for uncertainty analysis of TELEMAC/2D simulations: The Monte Carlo method (MC) and the First-Order Second Moment method with numerical differentiation (FOSM/ND) and with algorithmic differentiation (FOSM/AD). The application scenarios are a laboratory experiment with groynes and a 10 km stretch of River Rhine between Neuss and Düsseldorf.

MC is a very general uncertainty quantification tool that requires no assumptions on linearity of the parameter-to-prediction relations in models and poses no restrictions on allowable probability distributions of input parameters. However, MC requires a huge number of model runs for statistically robust uncertainty estimates. In waterways engineering, a typical single model run can take days or weeks even in modern parallel computing environments. Therefore, MC is only partially feasible for real-world projects.

It is well known that FOSM methods can be much faster than MC, as we will illustrate in Section III/A. Thus, they are better applicable to real-world problems. However, for FOSM the parameter-prediction relations in models must be linear (or at most weakly non-linear) due to the first-order approximations taken. Additionally, FOSM can provide probability distributions of model output only if all uncertain model inputs follow Gaussian distributions.

FOSM/ND calculates the sensitivities required for the first-order approximation numerically using finite differences. Therefore, the number of required model runs is the number of uncertain parameters plus one (simple differences) or two times the number of parameters plus one (central differences for better precision).

In FOSM/AD, the sensitivities are computed based on so-called adjoint states or related concepts, which require simulation runs with a modified numerical model. The required modified model is obtained through a special AD compiler for algorithmic differentiation. Thus, FOSM/AD avoids numerical differentiation and yields sensitivities accurate to machine precision (more accurate than central differences) with a number of modified model runs equal to only the number of uncertain parameters. One model run with the AD compiler is nearly 2 times slower than a normal model run, so that AD provides more accurate sensitivities than ND in less computing time than central differences.

In section II, a short introduction to the used uncertainty analysis methods is given. Section III presents two applications of the uncertainty methods, featuring simulations of a laboratory experiment for comparing the methods, and simulations of a 10 km long stretch of River Rhine for showing the engineering relevance of uncertainty analysis. Section IV provides discussion and conclusions.

II. Uncertainty Analysis Methods

Three methods were applied for analysing the uncertainty due to uncertain input parameters of two TELEMAC-2D models: The well-known Monte-Carlo method and the First-Order Second Moment method based on numerical differentiation or based on algorithmic differentiation. With all methods, the influence of uncertain input parameters to the output variables could be investigated.

A. Monte-Carlo Method (MC)

Following the MC principle, a large number N of randomly generated input values for all uncertain input parameters p_i are generated according to their (joint) probability distributions. For each of these sets of input values, simulation runs must be conducted. The results are analysed statistically to obtain mean values, variances, probability distributions and confidence intervals for all output variables of interest. The latter include in our case the water depth $H_k=H(x_k,p_i)$, which depends on the uncertain input parameters p_i. The variance, for example, is approximated by MC as:

$$Var(H_k) \simeq \frac{1}{N-1}\sum_{i=1}^{N}(H_k(p_i) - \overline{H_k})^2 \qquad (1)$$

For this study, N=1000 simulation runs were assumed to be sufficient. There exist some techniques to reduce the number of model runs while preserving the same accuracy (e.g. Latin Hypercube Sampling [1], Monte Carlo CL method [2], meta modelling [3]), but they are not taken into account here. In all these improved techniques, the approximation error of the statistical analysis remains proportional to the square root of N, which is typical for all sampling-based uncertainty analysis methods like MC.

B. First-Order Second Moment method (FOSM)

FOSM is an adequate method for linear or slightly non-linear problems with assumed Gaussian distributions for the uncertain parameters as well as for the output variables. Applying a Taylor expansion for the output variables $H_k=H(x_k,p_i)$, FOSM approximates their variance as

$$Var(H_k) \simeq \frac{\partial {H_k}^T}{\partial p_i} \cdot Cov(p_i) \cdot \frac{\partial H_k}{\partial p_i} \qquad (2)$$

where $\partial H_k/\partial p_i$ is the vector of partial derivatives ("sensitivitiy") of H_k with respect to all parameters p_i. The covariance matrix $Cov(p_i)$ between all uncertain parameters has to be chosen from measurements or literature values. When assuming that p_i are not correlated, the variance simplifies to:

$$Var(H_k) \simeq \sum_{i=1}^{n}\left(\frac{\partial H_k}{\partial p_i}\right)^2 \cdot \sigma_{p_i}^2 \qquad (3)$$

where $\sigma_{p_i}^2$ is the variance of parameter p_i. Based on the Gaussian assumption, confidence intervals for the output variables can be derived. For example, the 95% confidence interval is the mean value plus/minus two times the standard deviation.

FOSM with numerical differentiation (FOSM/ND)

The sensitivities $\partial H_k/\partial p_i$ can be calculated numerically with finite differences. For central differences, two simulation runs, e.g., with $(\overline{p}_i \pm \sigma_i)$ for each uncertain parameter are needed. Only if the parameter-to-prediction relation is linear, there is no effect of different values of σ_i. For strongly non-linear functions, the choice of a proper parameter difference between the two simulation runs becomes essential to get the useful local derivatives.

FOSM with algorithmic differentiation (FOSM/AD)

Algorithmic differentiation (AD) is a method for computing derivatives of functions implemented as numerical simulation programs in a semi-automatic manner. Often, only minimal manual adaption of the computing code is needed. New model versions can be differentiated easily by reapplying the compiler. Here, the so-called tangent-linear or forward mode of AD is used. For our case, this is more efficient than the adjoint mode as the number of uncertain input variables is relatively small compared to the number of output variables. Further information about AD methods can be found elsewhere (e.g., [4], [5], www.autodiff.org). A tangent-linear version of TELEMAC-2D and SISPYHE [6] has been created with the AD-enabled NAG Fortran compiler [7].

Using an AD version of TELEMAC-2D, the sensitivities $\partial H_k/\partial p_i$ can be calculated directly and up to machine precision. For each uncertain parameter, one simulation run with the AD code is needed.

III. Applications

We use two application cases for comparing the three methods. A first comparison between the three methods has been done with a fast simulation model for the laboratory experiment Schönberg (see Section III/A). The second application is based on simulations of an actual river stretch of River Rhine (see Section III/B) and demonstrates exemplarily the possibilities of uncertainty analysis for numerical simulations in river engineering.

A. Schönberg model

The laboratory model Schönberg (see figure 1) was conducted at BAW for groyne investigations in the project "ecological optimisation of groynes in River Elbe" [8]. The model geometry was oriented at the stretch of River Elbe near Schönberg (El-km 439.3 – 446), which is representative for the lower Middle Elbe. The numerical model we use was built up in that project [9]. Due to the slight bend and the groynes, the flow characteristic is adequately complex as in natural rivers. The experimental setup is relatively small (about 30 m long and 9 m wide). As the numerical model was built with a triangular mesh of 5127 nodes and 10179 elements and executed in parallel mode on 32 cores, the simulations ran sufficiently fast for in-depth comparison of the three uncertainty quantification methods.

Figure 1. Laboratory model Schönberg

The comparison is performed for two hydraulic conditions: steady flow and transient flow with a roof-shaped hydrograph as uncertainty scenario. The Nikuradse roughness coefficients in two zones (one mostly in the main channel and one in parts of the groyne fields) were considered uncertain. For both parameters, a Gaussian probability distribution was assumed with mean values of 3 mm (in the main channel) and 2 mm (in the groyne fields) and with standard deviations of 10 % of the corresponding mean values. The spatial arrangement of the zonation is shown in figure 2.

a. Numerical experiment in steady flow

For the steady-state case, we applied a low water flow condition known from the experimental studies with a constant inflow discharge of 22 l/s and a constant water level at the outflow. With the resulting flow rate and water levels, vortexes develop in the groyne fields, but the groynes themselves are not submerged. For all three methods, we computed the mean values and standard deviations of the water depth and of the velocities for each cell of the triangular mesh. FOSM/ND took 5 simulation runs, while FOSM/AD required only two and MC was performed with 1000 simulation runs. FOSM/AD was 1.25 times faster than FOSM/ND and 250 times faster than MC.

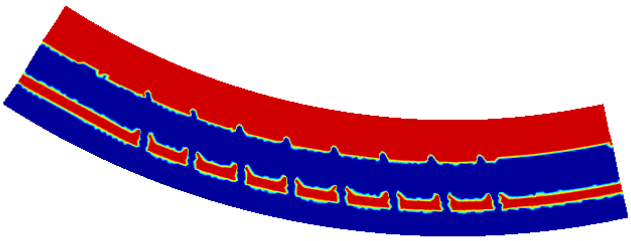

Figure 2. Zonation of the Nikuradse roughness coefficient (here: mean values) in the Schönberg model (red: 3mm, blue: 2mm for the mean value)

Figure 3 presents the close agreement between the three methods for the standard deviations of the water depth and the scalar velocity (the absolute value of the velocity vector). The uncertainty of water depth is high at the inflow and decreases gradually to zero at the outflow, because the water depth is given there as boundary condition. The uncertainty of scalar velocity concentrated mostly in the second groyne field. The standard deviation in the main channel is small (< 1mm/s) and nearly constant along the flow length. Due to the absence of groynes in the inflow and outflow cross sections, the flow direction is not parallel to the bend anymore. This leads to higher uncertainties at the outflow.

To quantify agreement between the three methods, we introduced a similarity index based on a threshold of accuracy (*ta*). The similarity index is defined as a triangle fuzzy number with base (*-ta, ta*). It is zero if the difference between two values is larger (smaller) than the upper (lower) threshold *ta* (*-ta*) and increases to one if the two values are exactly equal. The threshold value depends on the accuracy of available data and the scale of the problem. For this case, a threshold of 1mm for the water depth seems to be feasible. Figure 4 proves the good agreement between the methods, as the similarity index of FOSM/ND to MC and FOSM/AD to MC is mostly around one except for the second groyne field. This disagreement between the linear FOSM method and MC indicates highly non-linear effects in the affected region.

To verify the linearity assumption in the FOSM approach, we conducted a test for normality: Only if the parameter-to-prediction relations in a model are linear, the assumed Gaussian distribution for input parameters results in Gaussian distributions for all model predictions. The result of the normality test is the probability for each grid cell that the respective 1000 Monte-Carlo values could in fact originate from a Gaussian distribution (see figure 5). For the water depth, all probabilities to be Gaussian are near one, which validates the applicability of FOSM methods. For the scalar velocity, Gaussianity (and hence linearity) is only present in the main channel. Small probability values in the groyne fields show the non-linearity in these regions.

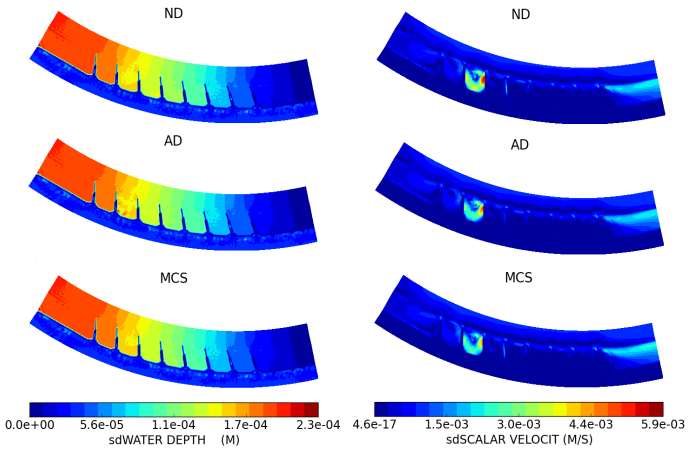

Figure 3. Comparison of standard deviation of water depth (left) and scalar velocity (right) in the domain computed by FOSM/ND (top), FOSM/AD (middle), MC (bottom)

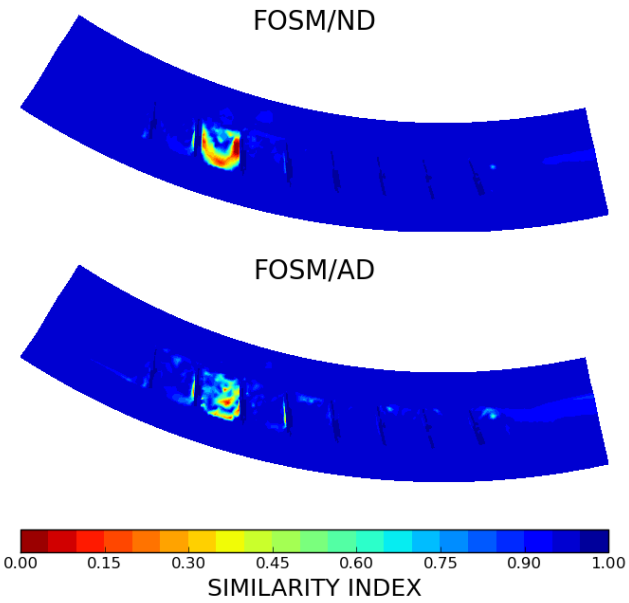

Figure 4. Distribution of similarity index for comparison of FOSM/ND to MC (top) and FOSM/AD to MC (bottom)

Although the velocities in the groyne fields have little agreement with a Gaussian distribution, our results indicate that the variance or standard deviation still can be estimated with satisfying results by FOSM methods – at least for the degree of uncertainty in the roughness coefficients considered here.

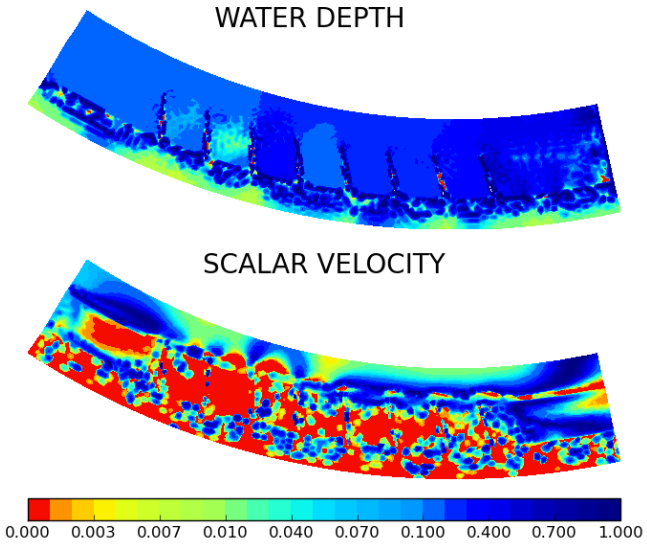

Figure 5. Map of the probabilities that the Monte-Carlo results indicate a Gaussian probability distribution

b. Numerical experiment in transient flow

For the comparison on time-dependent problems, we implemented an artificial flood hydrograph for three hours. The inflow discharge increased over 1.5 hours from 22 l/s to 156 l/s and then decreased back to the initial value.

In order to compare FOSM/ND and FOSM/AD with MC, we averaged the similarity indices of the standard deviation over the whole domain in each time step. Figure 6 presents the resulting averaged similarity indices for water depth and scalar velocity over time. Again, only minor differences between FOSM/ND and FOSM/AD can be seen. All similarity indices lay above 0.88, which we interpret as indication of linear or only weakly non-linear behaviour. As expected, the velocities show smaller similarity (i.e. more pronounced non-linear behaviour). The most non-linear periods occur when the height of the groynes equals the water level. Due to thresholds for wetting and drying procedures, the numeric solution is less smooth for this state. We conclude that FOSM provides satisfying results also for time dependent problems for the uncertainties of water levels and velocities – at least for the degree of uncertainty in the roughness coefficients considered here.

B. *River Rhine model*

The central reach of the Lower Rhine between Neuss and Düsseldorf (Rh-km 739-749) was chosen as in-situ application. In the project “artificial grain-feeding of bed material on the central Lower Rhine”, a two-dimensional numerical sediment transport model for this region was developed by the BAW. The aim of the project was to enhance the efficiency of future hydrological design and to optimise the measures economically. Further model details can be found in [10].This part of the river is characterised by strong meandering, dynamic bed load transport and an intensive bed load management. For this study, the dredging and supplying measures were not taken into account.

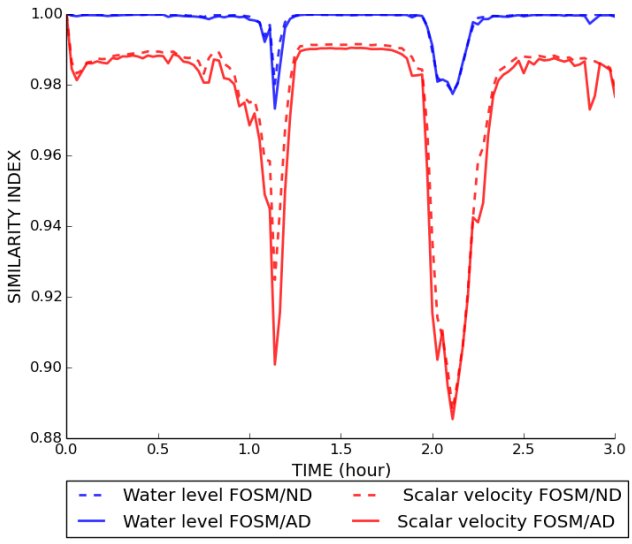

Figure 6. The average similarity index (FOSM/ND to MC, FOSM/AD to MC) for the flood period

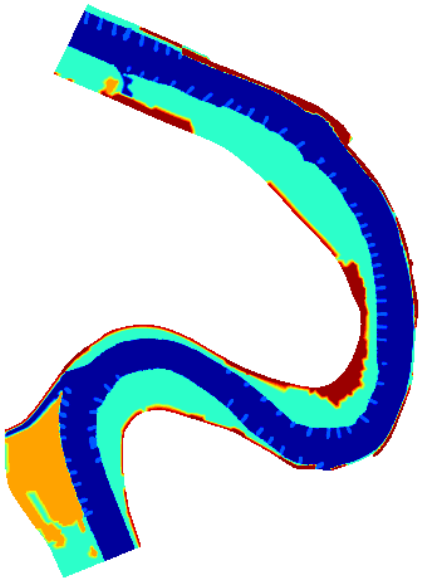

Figure 7. Distribution of mean values for the Nikuradse roughness coefficients in the Rhine model. Dark blue: 0.1 m (main channel), light blue: 0.3m (groynes), green: 0.5 m (floodplains), orange: 0.8 m (forest), red: 1.0 m (building area)

TABLE I. MEAN VALUES AND STANDARD DEVIATIONS OF THE UNCERTAIN PARAMETERS

Uncertain parameters	Mean value [m]	Standard deviation [m]
Roughness coefficient main channel	0.01	0.001
Roughness coefficient groynes	0.03	0.003
Roughness coefficient floodplains	0.5	0.05
Roughness coefficient forest	0.8	0.08
Roughness coefficient building area	1.0	0.1
Grain size class 1	$0.38\ 10^{-3}$	$0.038\ 10^{-3}$
Grain size class 2	$0.75\ 10^{-3}$	$0.075\ 10^{-3}$
Grain size class 3	$1.5\ 10^{-3}$	$0.15\ 10^{-3}$
Grain size class 4	$3.0\ 10^{-3}$	$0.3\ 10^{-3}$
Grain size class 5	$6.0\ 10^{-3}$	$0.6\ 10^{-3}$
Grain size class 6	$12.0\ 10^{-3}$	$1.2\ 10^{-3}$
Grain size class 7	$23.75\ 10^{-3}$	$2.375\ 10^{-3}$
Grain size class 8	$38.25\ 10^{-3}$	$3.825\ 10^{-3}$
Grain size class 9	$50.5\ 10^{-3}$	$5.05\ 10^{-3}$
Grain size class 10	$59.5\ 10^{-3}$	$5.95\ 10^{-3}$

As boundary condition, an artificial flood wave for 25 days with a peak value of 7020 m^3/s was simulated (see figure 8). We performed all three methods for uncertainty quantification on the Rhine model. For brevity, we only report here results of the FOSM/AD method.

Figure 9 shows the globally most sensitive parameter to the evolution over time (i.e. the change of mean river bed level over time) for the main channel. For each grid node in the main channel, the most sensitive parameter for a specific time was determined. It is the one parameter to which the river bed level has the largest sensitivity in the FOSM/AD method. Then, the number of occurrences as most sensitive parameter was

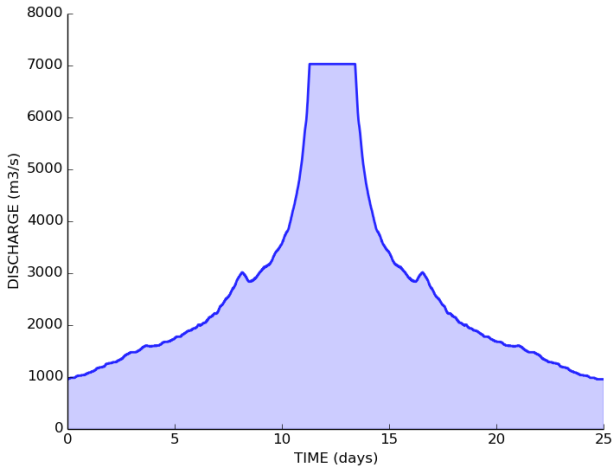

Figure 8. Artificial flood used for the Rhine study

counted for each parameter at each time step. Besides the initialising phase, the grain size of the 6^{th} class is most sensitive. This grain class is nearest to the mean grain diameter and has the biggest part of the total bed load discharge for most of the simulation time. Together, the 6^{th} and 7^{th} grain class provide nearly 50 % of the initial grain distribution, which explains their high sensitivities.

The simulation started from a fully developed flow field, but with a uniform grain size distribution at the river bed. Therefore, in the beginning, the grain classes sorted due to the flow situation. Smaller grain sizes are more mobile but much less available in the bed composition. This resulted in a high sensitivity of the 4^{th} grain class and also of the roughness parameter of the main channel shortly after startup.

Figure 10 shows the evolution at a selected point in the main channel and its confidence interval. During 10 days of increasing flood level, the mean river bed was rising and the confidence interval was comparably small (< 5 cm). Together

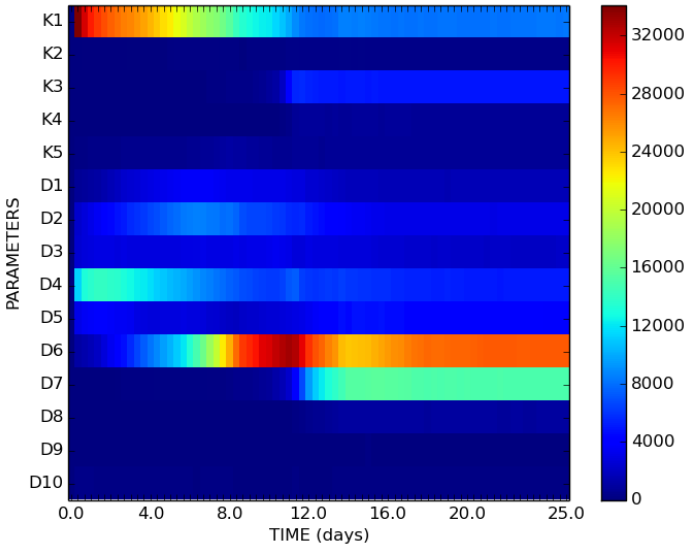

Figure 9. Number of occurency of the most sensitive parameter to the evolution in the main channel

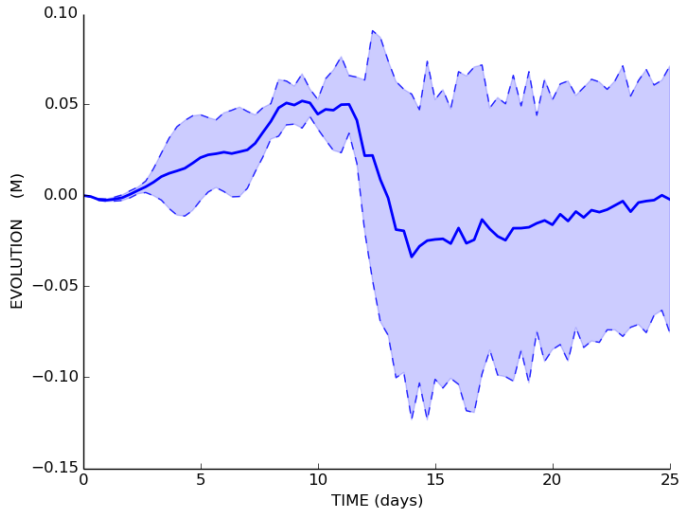

Figure 10. Evolution and its confidence interval for the flood event at a significant grid point in the main channel

with the stronger growth of discharge (see figure 8), the uncertainty increased rapidly and the mean river bottom decreased. In the decelerating flood, the confidence interval decreases again slowly. Interestingly, the variability in the uncertain parameters could lead to an eroded or accumulated river bottom after the flood period. The disclosure of such interesting results demonstrates the advantage of uncertainty quantification, as they investigate the range of possible outcomes.

IV. Conclusion

In this study, we compared uncertainty quantification for TELEMAC simulations with three different methods (FOSM/ND, FOSM/AD and MC) A first comparison was been done on simulations of a laboratory experiment. All methods are in good agreement for standard deviations and sensitivities for both steady-state and transient simulations. Even though an analysis of the MC results indicated that the considered model equations are non-linear (especially for velocities), both FOSM methods provided good approximations to standard deviations of water level and velocities – at least in the range of uncertainty investigated here. At acceptable accuracy, the computational time with FOSM/AD was 250 times faster than for an MC simulation with 1000 model runs. We conclude that, if only standard deviations are of interest and the variations of the uncertain parameters are small as in our case, FOSM/AD is a feasible and reasonably accurate choice.

The three methods were also applied successfully to a 10 km long stretch of the River Rhine and show very interesting results. Exemplarily, two results from FOSM/AD have been presented here. The effect of 15 uncertain parameters (five roughness coefficients and 10 grain sizes) to the evolution of river bed level during a 25-day artificial flood event was investigated. The analysis allowed identifying the most sensitive parameters for the evolution in the main channel: in the initialisation phase, the main channel roughness coefficient was most sensitive, while later the grain class with the largest part of the bed load discharge was more important. Small confidence intervals of the evolution in the main channel during the first 10 days of the flood event indicate comparably reliable simulation results. The highest uncertainty was detected at peak flood, which decreased slowly with decelerating flood. These kinds of results can be wealthy contributions for calibration processes or final interpretation and evaluation of simulation results. Overall, the study demonstrates the possibilities and the benefit of uncertainty analysis for numerical simulations in river engineering.

Acknowledgement

The authors would like to thank Backhaus L., Brudy-Zippelius T. for the calibrated model of river Rhine.

References

[1] Stein, M., “Large Sample Properties of Simulations Using Latin Hypercube Sampling,” Technometrics 29, 143–151, 1987.

[2] Nikitina, L., Nikitin, I. Stefes-lai, D., Clees, T. “Studie Zuverlässigkeitsanalyse morphodynamischer Modelle. Abschlussbericht der Zuverlässigkeitsanalyse für stark nichtlineare Funktionen y(x) mittels einer speziellen, durch RBF-Metamodellierung beschleunigten Monte-Carlo-basierten Methode zur CL-Berechnung,“ Fraunhofer Institut Algorithmen und Wissenschaftliches Rechnen, 2010.

[3] Clees, T., Nikitin, I., Nikitina, L., Kopmann, R., “Reliability analysis of river bed simulation models,” EngOpt 2012 – 3rd International Conference on Engineering Optimization, Rio de Janeiro, Brazil, 01 - 05 July 2012

[4] Naumann, U., “The Art of Differentiating Computer Programs”, SIAM, 2012.

[5] Griewank, A., Walther, A., “Evaluating Derivatives. Principles and Techniques of Algorithmic Dierentiation (Second Edition),” SIAM, 2009.

[6] Riehme, J., Kopmann, R., Naumann, U., “Uncertainty quantification based on forward sensitivity analysis in Sisyphe,” Proceedings of the Vth European Conference on Computational Dynamics, ECOMAS CFD 2010, 2010.

[7] Naumann, U., Riehme, J., “A differentiation-enabled Fortran 95 compiler,” ACM, 2005.

[8] Hentschel, B., Anlauf, A. “Ökologische Untersuchungen of Buhnen in der Elbe”, in: Weitbrecht, V., Mazijk, A.V. (eds) report for Workshop at UFZ Leipzig-Halle, Magdeburg, 22./23.10.2001, pp 121-133, Technical University Delft, University of Karlsruhe, 2001.

[9] Walzer, A., “Numerische Untersuchungen einer neuartigen Buhnenform, Diploma thesis, Bauhaus-University Weimar, 2000.

[10] Backhaus, L., Brudy-Zippelius, T., Wenka, T., Riesterer, J., “Comparison of morphological predictions in the Lower Rhine River by means of a 2-D and 3-D model and in situ measurements”, Proceedings of River Flow conference, Lausanne, 2014.

[11] Kopmann, R., Merkel, U., Riehme, J., “Using Reliability Analysis in Morphodynmic Simulation with Telemac2D/Sisyphe,“ Proceedings of the XIXth Telemac-Mascaret User Conference, Oxford, 2012.

IMPLEMENTATION OF A NEW TURBULENCE MODEL IN TELEMAC2D/3D : MODIFIED SPALART-ALLMARAS :

Adrien Bourgouin Riadh ATA

LNHE-EDF R&D

This model is a RANS turbulence model which solves one transport equation for a viscosity like variable. As it was designed for aerodynamic flows[1], the set of constants has been adapted for free surface cases, in order to stabilize it and to get more coherent results. It has been implemented in Telemac-2D and Telemac-3D and tested with several examples, such as « pildepon ».
Obtained results have been compared to the experimental results of Negretti [2] for the case of a flow around a cylindrical obstacle (figure 1). The chaarcterization of eddy detachment was achieved using a non-dimensional number. This non dimensional numer links the effects of lateral boundary and bottom friction with the geometrical property of the domain/obstacle. Encouraging results are obtained with this new model. Obtained results are compared to those obtained with K-eps model and some measurements as well.

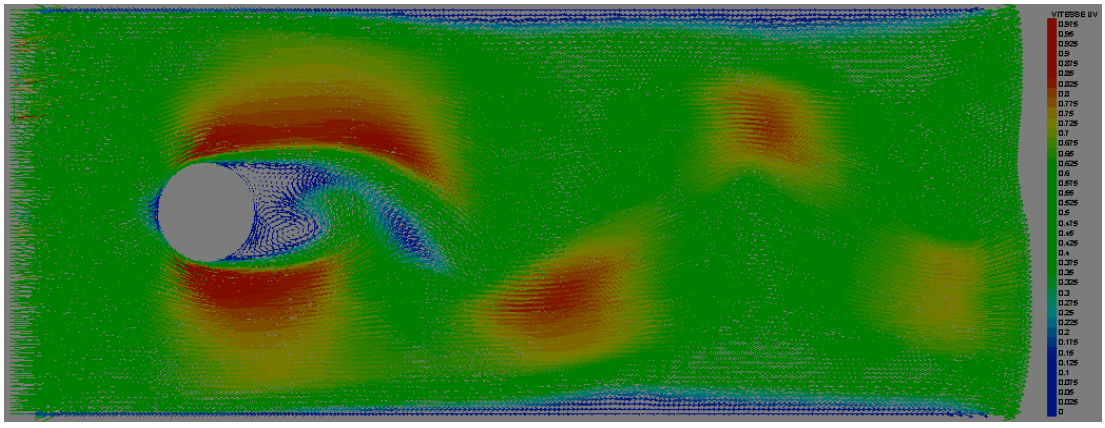

Référence :

[1] : P. R. Spalart, S. R. Allmaras :One-Equation Turbulence Model for Aerodynamic Flows.
[2] : M. E. Negretti, G. Vignoli, M. Tubino, M. Brocchini : One Shallow-water Wakes : an analytical study.

Wall-Adapting Local Eddy-Viscosity Turbulence Model for TELEMAC3D

Yue Yin
School of Engineering,
University of Liverpool
Liverpool, UK
yue.yin@stfc.ac.uk

Ming Li
School of Engineering,
University of Liverpool
Liverpool,UK
Mingli@liverpool.ac.uk

Charles Moulinec
Science and Technology Facilities Council,
Daresbury Laboratory,
Warrington, UK
charles.moulinec@stfc.ac.uk

David R. Emerson
Science and Technology Facilities Council,
Daresbury Laboratory,
Warrington, UK
david.emerson@stfc.ac.uk

Abstract—TELEMAC3D offers the user several options for turbulence modelling, including Reynolds-Averaged Navier-Stokes modelling and Large Eddy Simulation based on the Smagorinsky constant model. Complex turbulent flow problems can be computed using various levels of approximation, yielding a more or less detailed description of the flow state. The aim of this work is to implement the Wall-Adapting Local Eddy-Viscosity (WALE) turbulence model from the existing TELEMAC3D code and to compare it to the Smagorinsky constant model. There are two major advantages associated with the choice of the WALE model: firstly, the invariant of the symmetric part of $\bar{S}_{ij}$ is related to both the strain rate of the turbulent structure and the rotation rate. Secondly, it offers a proper wall-scaling to get a good prediction of the friction coefficient. The aforementioned advantages will help improve the representation of the complex turbulent flow. Numerical results are benchmarked against two experiment tests including the flow around a circular cylinder test case and the flow in a U-shape bend channel.

I. INTRODUTION

Turbulent flows are commonly encountered in engineering and are of considerable interests in a variety of industrial applications. In coastal engineering, to resolve the combined tides and waves induced by constant changes in flows around offshore structures, using a computer model is particularly important to coastal protection and development.

The 3-D module of the TELEMAC suite, i.e. TELEMAC3D [1] offers the user several options for turbulence modelling. The most widely used approximation is based on the Reynolds-averaged Navier-Stokes equations (RANS) which has one main drawback: i.e. the fact that all the scales are modelled in the same way dispite the fact that the small scales tend to depend only on the viscosity whereas the large ones are very strongly affected by the boundary conditions.

An alternative to RANS is Large Eddy Simulation (LES). It is based on the assumption that the large eddies of the flow are dependent on the geometry while the smaller scales more universal. The turbulent flow is split into large and small parts by a filtering process based on an energy cascade. The large eddies are simulated by the calculation, while the small eddies are ignored by using a sub grid-scale model. However there are two major drawbacks associated with to the choice of the Smagorinsky constant model, for instance: firstly, the invariant of the symmetric part of $\bar{S}_{ij}$ is only related to the strain rate of turbulent structure but not the rotation rate. Secondly, it does not offer a proper wall-scaling to get a good prediction of the friction coefficient.

To overcome the aforementioned drawbacks, the Wall-Adapting Local Eddy-Viscosity (WALE) turbulence model has been developed by Ducros et al. [2] and implemented in TELEMAC3D. In order to investigate the behaviour of the new turbulence model and examine potential factors which affect the results, the Smagorinsky constant and WALE models are compared with two laboratory scale cases, including the flow around a circular cylinder test case of Roulund et al [3] and the flow in a U-shape bend channel [4].

II. NUMERICAL MODEL

A. Governing Equations

The calculations are performed using the open source hydrodynamic suite TELEMAC and more specifically its 3-D module, TELEMAC3D. It is a three-dimensional computational code solving either the hydrostatic or non-hydrostatic equations. In this work the hydrostatic approximation is used for both the circular cylinder test case and the U-shape bend channel case. The code solves the three-dimensional mass and momentum conservation equations [5] :

$$\frac{\partial U}{\partial x}+\frac{\partial V}{\partial y}+\frac{\partial W}{\partial z}=0 \quad (1)$$

$$\frac{\partial U}{\partial t}+U\frac{\partial U}{\partial x}+V\frac{\partial U}{\partial y}+W\frac{\partial U}{\partial z}=-g\frac{\partial Z_s}{\partial x}-\frac{\partial \tau}{\partial x}+F_x \quad (2)$$

$$\frac{\partial V}{\partial t}+U\frac{\partial V}{\partial x}+V\frac{\partial V}{\partial y}+W\frac{\partial V}{\partial z}=-g\frac{\partial Z_s}{\partial y}-\frac{\partial \tau}{\partial y}+F_y \quad (3)$$

$$p=p_{atm}+\rho_0 g(Z_s-z)+\rho_0 g\int_Z^{Z_s}\frac{\Delta\rho}{\rho_0}dZ \quad (4)$$

where U, V and W are the three-dimensional components of velocity; τ is the stress tensor; Z_s is the free surface elevation and F_x, F_y are source terms. The pressure is calculated in Eq. 4 where ρ_0 and $\Delta\rho$ are the reference density (1024kg/m3) and the variation of density respectively. The stress tensor is computed as $\tau=-\nu\nabla U$, in which ν is the effective viscosity that needs to be computed by a turbulence model.

B. Turbulence Models

In order to obtain a better representation of complex turbulent flows, numerical model is computed using Large Eddy Simulation employing two turbulence models including the constant Smagorinsky model [6] and the 'Wall-Adapting Local Eddy-Viscosity (WALE)' model [2].

Using the Smagorinsky model, the viscosity is computed as:

$$v_t=C_s{}^2\Delta^2\sqrt{2S_{ij}S_{ij}} \quad (5)$$

where C_s is a dimensionless coefficient to be calibrated and Δ is the mesh size derived in 2-D or 3-D from the surface or from the volume of the element. The value of C_s is set to 0.1 for after calibration. More details of the constants can be found in User Manual [1].

In LES, the eddy-viscosity v_t must not change when the frame of reference is changed. Clearly the velocity gradient tensor $\bar{g}_{ij}=\partial\bar{u}_i/\partial x_j$ is a good choice to represent velocity fluctuations at the length scale Δ. The Smagorinsky model is based on the second invariant of the symmetric part $\bar{S}_{ij}$ of this tensor. However there are two major drawbacks associated with this choice:

- This invariant is only related to the strain rate of the turbulent structure but not the rotation rate.
- It does not offer a proper wall-scaling to get a good prediction of the friction coefficient.

For the aforementioned reasons, Ducros et al. uses a better operator with the traceless symmetric part of the square of the velocity gradient tensor as follows:

$$S_{ij}^d S_{ij}^d=\frac{1}{2}\left(\bar{g}_{ij}^2+\bar{g}_{ji}^2\right)-\frac{1}{3}\delta_{ij}\bar{g}_{kk}^2 \quad (6)$$

where $\bar{g}_{ij}^2=\bar{g}_{ik}\bar{g}_{kj}$ and δ_{ij} is the Kronecker symbol. Einstein summation is used here. If $\bar{\Omega}$ is used to represent the anti-symmetric part of $\bar{g}$:

$$\bar{\Omega}_{ij}=\frac{1}{2}\left(\frac{\partial\overline{u_i}}{\partial x_j}-\frac{\partial\overline{u_j}}{\partial x_i}\right) \quad (7)$$

the tensor S_{ij}^d can be rewritten in terms of $\bar{S}$ and $\bar{\Omega}$:

$$S_{ij}^d=\bar{S}_{ik}\bar{S}_{kj}+\bar{\Omega}_{ik}\bar{\Omega}_{kj}-\frac{1}{3}\delta_{ij}[\bar{S}_{mn}\bar{S}_{mn}-\bar{\Omega}_{mn}\bar{\Omega}_{mn}] \quad (8)$$

By construction, the trace of S^d is zero and its second invariant remains finite and proportional to $S_{ij}^d S_{ij}^d$. By using the relation above and making use of the Cayley-Hamiltion theorem of linear algebra, this quantity can be developed as:

$$S_{ij}^d S_{ij}^d=\frac{1}{6}(S^2S^2+\Omega^2\Omega^2)+\frac{2}{3}S^2\Omega^2+2IV_{S\Omega} \quad (9)$$

with the notations:

$$S^2=\bar{S}_{ij}\bar{S}_{ij},\ \Omega^2=\bar{\Omega}_{ij}\bar{\Omega}_{ij},\ IV_{S\Omega}=\bar{S}_{ik}\bar{S}_{kj}\bar{\Omega}_{jl}\bar{\Omega}_{li}$$

From the last relation, a LES model based on $S_{ij}^d S_{ij}^d$ will detect turbulence structures with either strain rate, rotation strain or both. In the case of pure shear (e.g., $\bar{g}_{ij}=0$, except $\bar{g}_{12}$), it yields $S^2=\Omega^2=4\bar{S}_{12}$ and $IV_{S\Omega}=-\frac{1}{2}S^2S^2$, so that the considered invariant, $S_{ij}^d S_{ij}^d$, is zero. This point is in agreement with the fact that the shear zones contribute to energy dissipation to a smaller extent than convergence zones and eddies. Moreover, this means that almost no eddy viscosity would be produced in the case of wall-bounded laminar flow. Thus the amount of turbulence diffusion would be negligible in such a case and development of linearly unstable waves would be possible. This is a great advantage over the Smagorinsky model. The expression for v_t is computed as:

$$v_t=\frac{\left(s_{ij}^d s_{ij}^d\right)^{3/2}}{\left(\bar{s}_{ij}\bar{s}_{ij}\right)^{3/2}+\left(s_{ij}^d s_{ij}^d\right)^{5/4}} \quad (10)$$

III. CASE I: FLOW AROUND A CIRCULAR CYLINDER

Both the constant Smagoringsky turbulence model and the WALE model are used in the simulation of the flow around a circular cylinder and their results compared to the laboratory measurement of Roulund et al [3].

A. Model Setup

Following Roulund et al [3], the simulation domain is set to be 50 m long by 4 m wide. The bed is assumed to be flat with a constant depth of 0.54 m. A cylinder with a diameter of 0.53 m (D) is placed at 13 m downstream the inlet as in Fig. 1. The computational mesh is generated by the software Bluekenue using 47,546 triangle elements in the 2-D horizontal plane and 20 non-equally distributed vertical layers across the water depth.

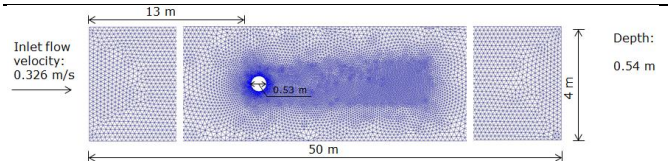

Figure 1. Model mesh layout for the validation test (top view)

The boundaries of the computational domain include inlet, outlet and walls. At the inlet, the flow rate Q is specified to 0.68 m^3/s following similar flow settings in Roulund's experiment. At the outlet, prescribed elevation is given to 0 m. The walls of the flume and pile are set as solid walls. Sidewall friction is not applied in this study, therefore all the walls are smooth. The bottom friction is modelled by the Nikuradse law and the friction coefficient k_s is set to 0.01.

B. Results

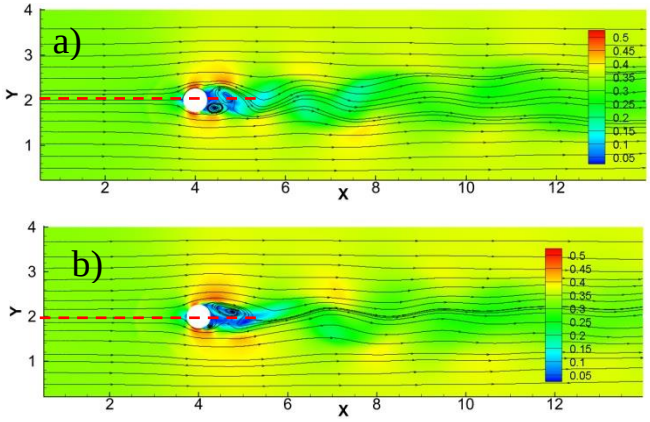

Figure 2. Instantaneous velocity field around a circular pile in a flume a) WALE model, b) LES Smagorinsky model.（01:00:00）

Figure 2 illustrates the instantaneous velocity distribution around a circular pile using the constant Smagorinsky model and the WALE model respectively. Similar flow patterns can be found with a decrease in velocity in the wake of the cylinder and flow acceleration at the side of the pile. The vortex shedding is clearly noticeable in both turbulence model results, although the vortex size in WALE model test seems smaller than it in the constant Smagorinsky model results.

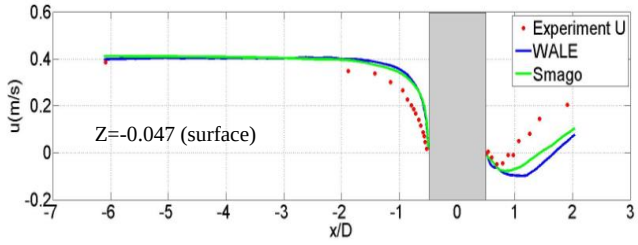

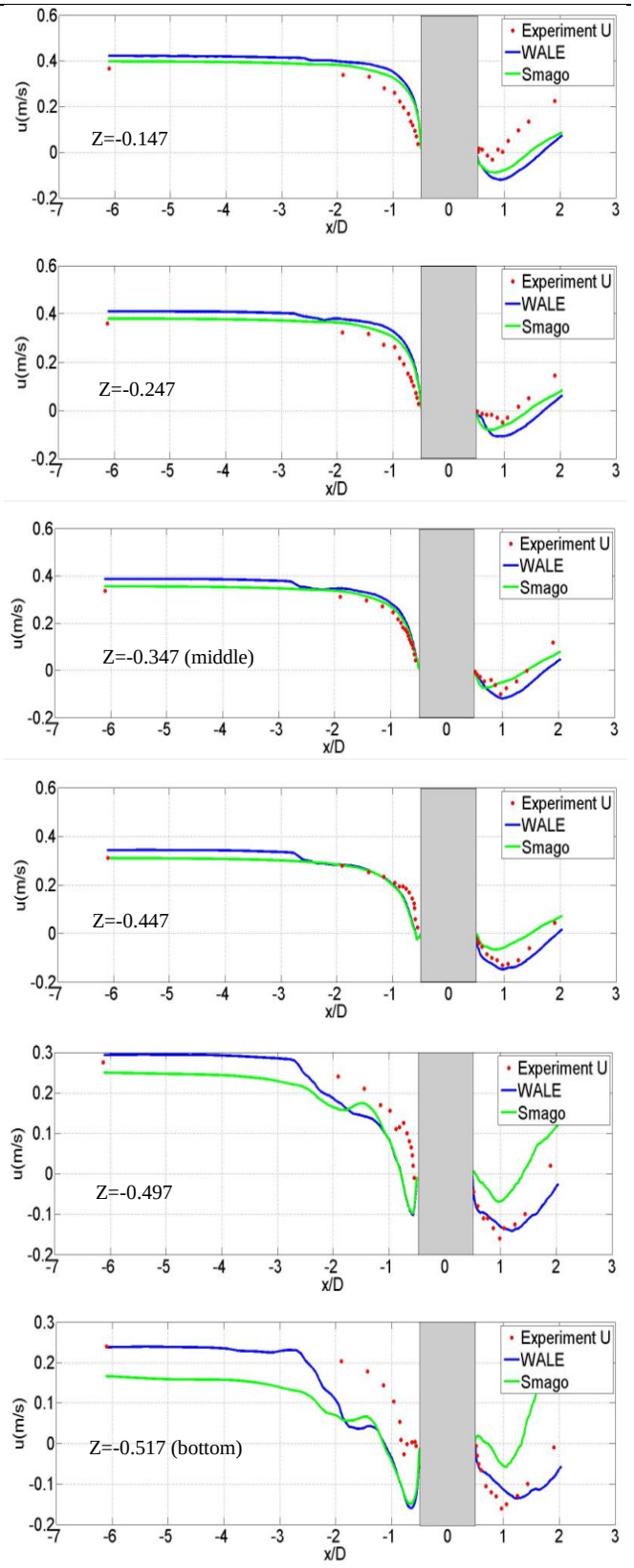

Figure 3. Mean horizontal velocity in the plane of symmetry at different distances from the bed obtained by both turbulence models.

To further illustrate the velocity distribution around the circular cylinder, instantaneous velocities are averaged over 10,000 time steps after ensuring flow development. Time-averaged horizontal velocity at different levels above the bed over the stream-wise centre plan of symmetry (the red broken line in Fig. 2) are compared with experimental data for one of the Roulund et al [3] experimental condition in Fig. 3. The red dots denote the experimental data obtained by Roulund et al. [3]. The blue and green curves represent the numerical results obtained using the Smagorinsky model and the WALE model respectively. Generally, both turbulence models show good agreement comparing with the experiment data. Although a slight over-prediction is found at levels close to the surface (z=-0.047 m and -0.147 m), the velocities at bottom levels are under-estimated by the numerical models. In the wake part, all the results show flow recovery, however the WALE model show better agreements at Z= -0.447m, -0.497m and -0.517m (which are close to the bottom) than the Smagorinsky model.

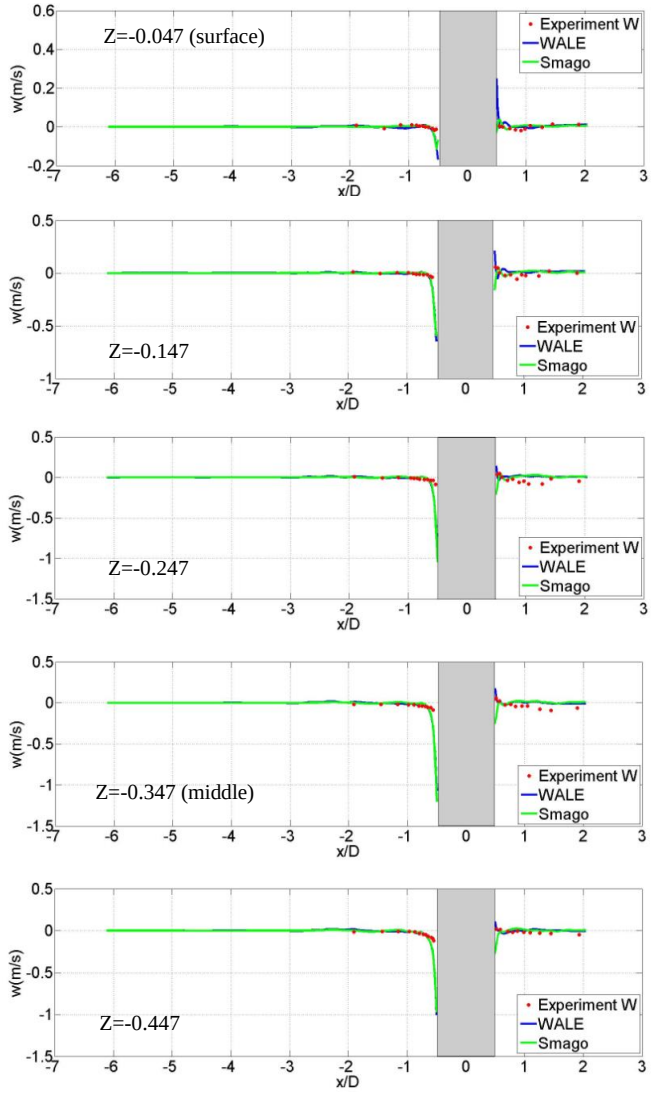

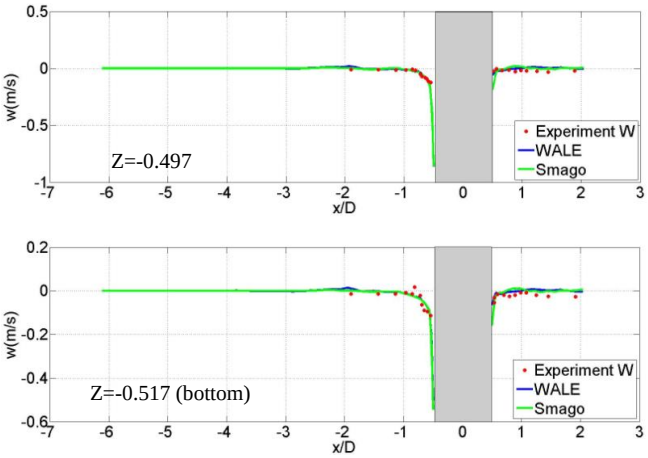

Figure 4. Mean vertical velocity in the plane of symmetry at different distances from the bed obtained by both turbulence models.

Figure 4 compares the averaged vertical velocity along the centre line at different levels. It is clear that, the vertical velocity profiles obtained by both the Smagorinsky model and the WALE model show very good agreement comparing with the experimental data. Small deviations are only found in the wake part which is very close to the cylinder wall and water surface. The Smagorinsky model shows negative velocities in this area, however positive velocities are obtained by the WALE model.

IV. CASE II: FLOW IN A U-SHAPE BEND CHANNEL

To further investigate the capability of the two turbulence models, the flow in a U-shaped bend channel is simulated. Numerical results are benchmarked with flow measurements in a curved rectangular channel made by H.J. de Vriend 1979 [4].

A. Model Step

The simulation domain of numerical model (shown in Fig. 5) matches the experiment of H.J. de Vriend [4]. The test flume is composed of two straight channels and one curved channel. The whole channel maintains a uniform width of 1.7 m. The inner radius of the curved channel is 0.34 m and its outer radius is 0.51 m. In De Vriend's experiment, both straight channels connecting with inlet and outlet are 6 meters long. However in the numerical model, the straight channel at outlet side is extended to 56 meters to reduce the impact of the outlet boundary setting.

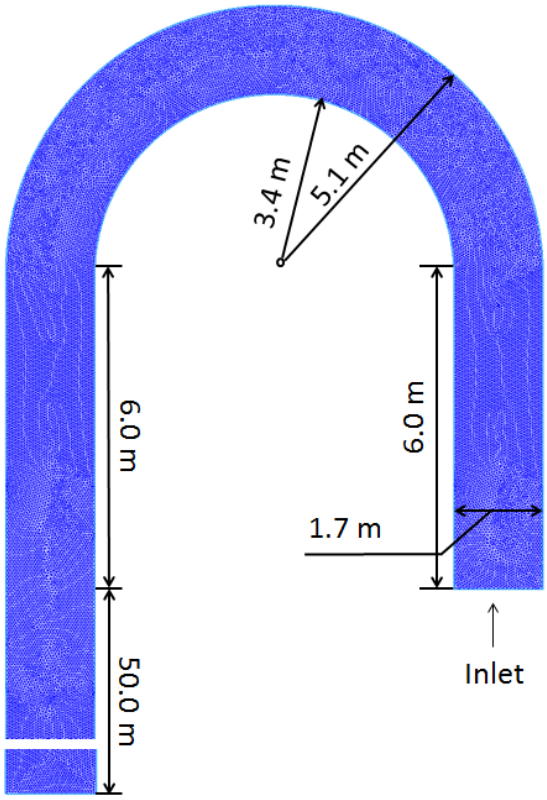

Figure 5. The geometry of U-shaped bend Channel.

The computational mesh was generated by software Bluekenue containing 117,664 elements in 2-D. Thirty non-equally distributed layers are used in the vertical direction.

For the boundary conditions, a constant flow rate of 0.184m/s at inlet boundary is specified and a prescribed water elevation of 0.18m is given at outlet. The walls of the flume are set as solid walls.

B. Results

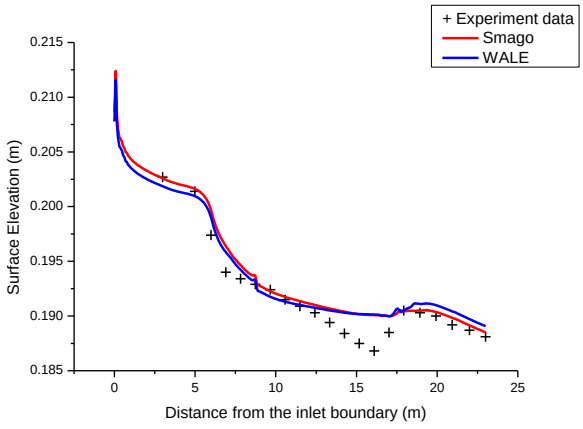

Figure 6. Comparsion between measured surface elevation and numerical results along channel at the inner bank.

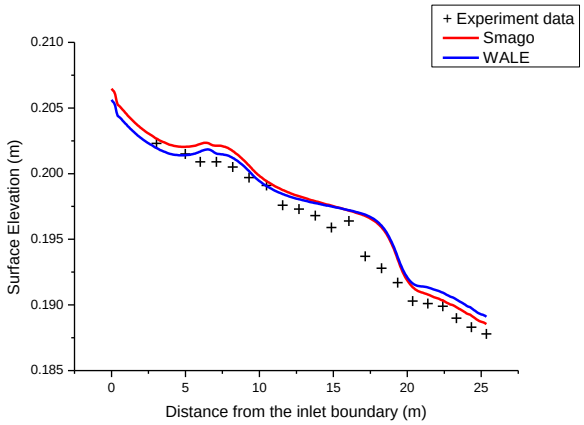

Figure 7. Comparsion between measured surface elevation and numerical results along channel at the centre.

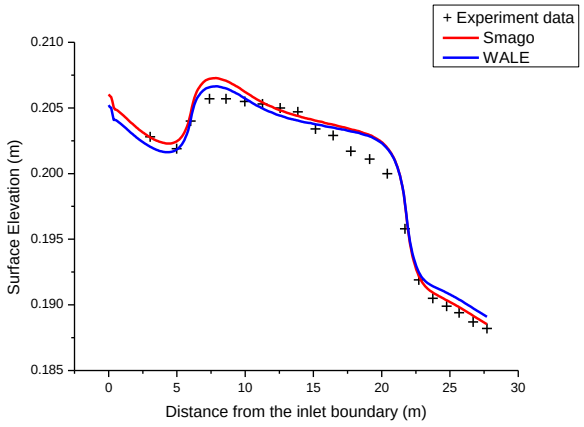

Figure 8. Comparsion between measured surface elevation and numerical results along channel at the outer bank..

Figures 6, 7 and 8 compare measured free surface elevations with numerical results along the channel at the inner bank, the centre and the outer bank respectively. Experiment data are represented by '+' and the numerical results obtained by the constant Smagorinsky model and the WALE model are displayed by red and blue curves respectively. According to the figures, free surface elevations show decrease trends from the inlet boundary to the outlet boundary throughout the channel. However a small increase can be found at the beginning of the curved channel at the centre and outer bank.

Comparing with two numerical results, all three figures show a similar feature: the free surface elevation obtained by WALE model is slightly lower than that of the constant Smagorinsky model at the inlet straight channel (0 m-6 m downstream the inlet) and first half of the curved channel (6 m -12.5 m downstream the inlet). Although both models

show similar results at the second half of the curved channel (12.5 m – 18 m downstream the inlet), small differences are still found at the outlet part. The surface elevation obtained by the constant Smagorinsky model is lower than that of the WALE model at 18 m-25 m downstream the inlet.

According to the comparison between numerical results and experiment data, the WALE model has a better representation of the surface elevation than the constant Smagorinsky model at the first half of the test channel (0 m-12.5 m downstream the inlet). Over-predicted surface elevation is found at 12 m – 18 m downstream the inlet by both two models, however it thes difference at outer bank is smaller than that at inner bank. At the outlet part (18 m-25 m downstream the inlet), both Smagorinsky and WALE models show good agreement. Lower surface elevation obtained by the constant Smagorinsky model matches experiment better.

V. CONCLUSIONS – FUTURE WORK

In this study, the behaviour of two turbulence models including the constant Smagorinsky model and the WALE model is investigated against two laboratory scale cases: the flow around a circular cylinder and the flow in a U-shape bend channel. In the circular cylinder test case, good agreement is observed for both turbulence models in front of the cylinder. However behind the cylinder, the result of the WALE model is clearly better than that of the constant Smagorinsky model. In the U-shaped bend channel case, the results of the WALE model match experimental data better in the first half of the est channel however the constant Smagorinsky model demonstrates a slightly better agreement at the outlet part.

Generally, the WALE model is a good turbulence model for the type of flows investigated here, according to the results of the benchmarks. Big improvement can be found when simulating complex turbulent flow close to structure walls.

The U-bend channel test case will be investigated further with a focus on the velocity field, to assess both turbulence models.

ACKNOWLEDGEMENT

The current study is supported by EPSRC and EDF Energy through an iCASE studentship. The technical supports from Computing Services of the University of Liverpool and from the Hartree Centre are also greatly appreciated.

REFERENCES

[1] The TELEMAC system. http://www.opentelemac.org

[2] Ducros F, Nicoud F, Poinsot T. Wall-adapating local eddy-viscosity models for simulations in complex geometries. In: Baines MJ, editor. ICFD; 1998. p. 293–300.

[3] Roulund, A., Sumer, B.M., Fredsøe, J., Michelsen, J. "Numerical and experimental investigation of flow and scour around a circular pile," Journal of Fluid Mechanics, 534, 2005, pp. 351-40

[4] D. J. De Vriend, "Flow measurements in a Curved Rectangular Channel", Laboratory of Fluid Mechanics, Department of Civil Engineering, Delft University of Technology, Internal Report No. 9-79, 1979

[5] Hervouet J-M.. Hydrodynamics of free surface flows: modelling with the finite element method, Wiley. 2007

[6] Smagorinski, J., "General circulation experiments with the primitive equations". I. The basic experiment. Monthly Weather Review, 91,99-164

TELEMAC-3D and Hydrostatic Inconsistency

A. J. Cooper, K. Day
HR Wallingford Ltd
Wallingford, UK

a.cooper@hrwallingford.com

***Abstract*—Not many simulations of ocean currents and deep sea hydrodynamics have so far been made using TELEMAC-3D. Ocean circulation models represent stochastic phenomena due to temperature and salinity variation and wind, so the models developed for this purpose have some important differences compared to those developed primarily to solve the shallow water equations.**

In some cases spurious currents may appear as a result of the phenomenon of "hydrostatic inconsistency". The consequence of this is that even when then density gradient only has a vertical component and the water is initially at rest and should remain at rest, it may start to move spontaneously because of the appearance of unreal horizontal pressure gradients caused by the density variation when the model planes are not completely horizontal. It is important to find ways of overcoming this problem so TELEMAC-3D can be used confidently to model ocean currents. Note, however, that this issue may also arise in 3D simulations when the water is not deep.

I. INTRODUCTION

In the first part of the paper the differences between the phenomena of ocean currents and tidal flows will be described. The consequent different scope of tidal and ocean circulation models will be reviewed. An application of TELEMAC-3D for a model of a small area of the California Current *(an ocean current?)* will be described and the issue of hydrostatic inconsistency illustrated as well as potential ways to overcome it.

II. DIFFERENT NATURE OF OCEAN CURRENTS

The following Table 1 illustrates some of the differences between tidal currents (which TELEMAC is mostly used for in marine applications) and ocean circulations. The main forces driving ocean currents are density differences and Coriolis force rather than water surface gradient.

TABLE I. TIDAL AND OCEAN CURRENTS - CHARACTERISTIC DIFFERENCES

Tidal Current	Ocean Current
Water flows down the slope high to low	Water flows around a high or low area (like in meteorology, Buys-Ballots Law, geostrophy, Coriolis)
Predictable for centuries ahead	Predictable for only a few days ahead (like the weather)
Currents result from location of sun and moon	Currents result from temperature, salinity, wind and the earth's rotation
Current varies during the course of hours	Current varies during the course of days
Initial conditions soon forgotten	Initial conditions affect subsequent solution (chaos theory), butterfly effect
Data assimilation not normally required	Data assimilation often required
Tidal current weakly varying through depth	Ocean current strongly varying through depth (e.g. opposite directions)
Current deducible from tidal constituents	Surface current largely deducible from water level measurements

Geostrophic flow balances pressure gradient with Coriolis force creating a flow along the water surface level contours instead of down the gradient (Fig 1).

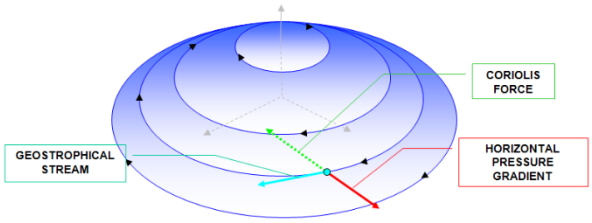

Figure 1. Geostrophic flow

As shown in Fig 2 an ocean circulation model includes extra parts not usually included in a tidal flow model (Met data,

data assimilation and possibly ice model and full thermodynamic model).

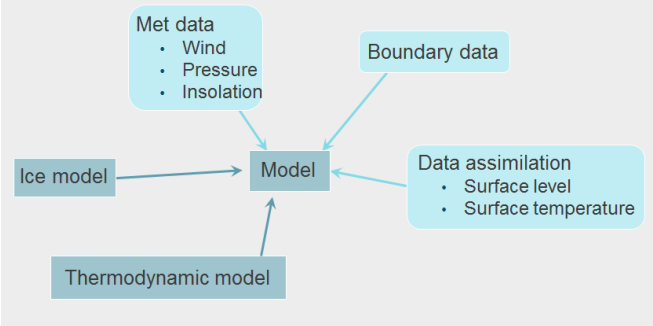

Figure 2. Ocean circulation model

Global circulation models with resolution of 1/12 degree (about 7km) are detailed in Table 2 below. The HYCOM model [1], [2] is often used for regional modelling as reanalysis data are available for a large number of years.

TABLE II. GLOBAL CIRCULATION MODELS

	HYCOM	**Mercator (MyOcean)**	**NOC NEMO**
H-resolution	1/12°	1/12°	1/12°
V-resolution	33 levels	50 levels	75 levels
Processes	Atmospheric forcing. *Data assimilation* of satellite and in-situ temperature, salinity, geopotential and current velocity. No tide	3-hourly atmospheric forcing. Louvain sea-ice model. *Data assimilation* of satellite sea level and in-situ temperature and salinity profiles. Uses NEMO. No tide	Drakkar Forcing Set, which is a consistent global forcing dataset based on a combination of ECMWF analyses and reanalysis and observed flux data. No tide. *No data assimilation*
Output period	19/9/2008 to present, plus 7-day forecast	01/01/2013 to present, plus 7-day forecast	1978-2010
Output times	Daily snapshot at 0 hour	Daily average	Five-day average
Output variables	11 variables including sea surface height, salinity, potential temperature, u and v-velocity	Temperature, salinity, currents, sea level and ice parameters	U, V, sea surface height, potential temperature, salinity

III. TELEMAC-3D LOCAL MODEL OF PART OF THE CALIFORNIA CURRENT

The study area was on the west coast of N America. This is a region which is influenced by a large-scale oceanic current – the southwards flowing California Current – as opposed to tidal currents. The California Current flows southwards along the Pacific coast of America, beginning off the coast of British Columbia in Canada and ending off the coast of the southern tip of Baja California in Mexico.

Bathymetry for this model has been obtained from GEBCO (General Bathymetric Chart of the Oceans) and the vertical datum is relative to Mean Sea Level (MSL).

The model bathymetry can be seen in Fig 3. The model domain covers an area around 58 km alongshore and 50 km offshore and the horizontal resolution is about 1km. There are 21 layers in the vertical. Maximum depth in this model domain is around 100 m below MSL.

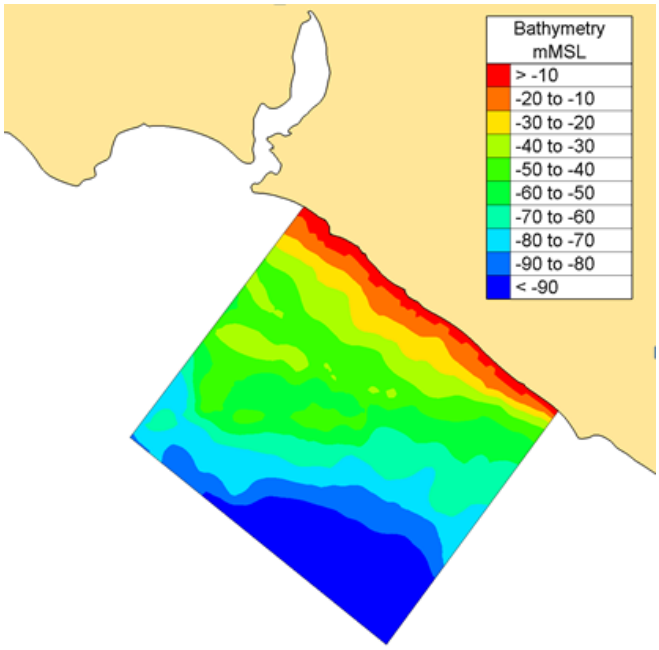

Figure 3. Model bathymetry

The HYCOM global model data (approx. 7km resolution) is used across the model domain as an initial condition at the beginning of a model run, and then HYCOM data is applied as forcing along the model open boundary for the duration of the model run.

HYCOM data supplied for the initial condition is free surface elevation, temperature and salinity. For the rest of the model duration the HYCOM data applied at the model open boundary is eastward and northward velocity components (U component and V component) and free surface elevation. HYCOM velocity is applied at the entire open sea boundary, but free surface elevation has only been applied at the north-west section of the open boundary.

The HYCOM velocity, temperature and salinity are applied as a vertical profile along the TELEMAC-3D model boundary.

A. Flow modelling results

The TELEMAC-3D model was run for an 87 day period. Time-series comparisons of temperature, salinity, free surface elevation and current speed and direction can be seen in Figs 4-8.

The time series plots show good agreement for the temperature, the salinity and the free surface. There is better agreement at the bed than at the surface.

Unfortunately, there is only approximate agreement for the speed and direction. The TELEMAC-3D current speeds tend to be lower than the HYCOM speeds at the surface.

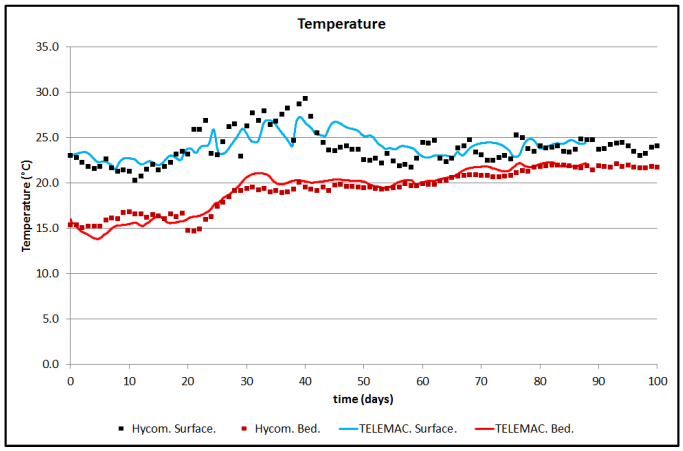

Figure 4. TELEMAC/HYCOM temperature comparisons at model centre point

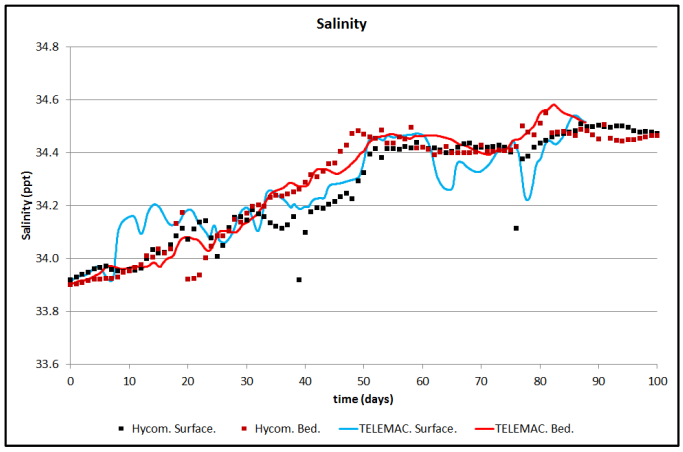

Figure 5. TELEMAC/HYCOM salinity comparisons at model centre point

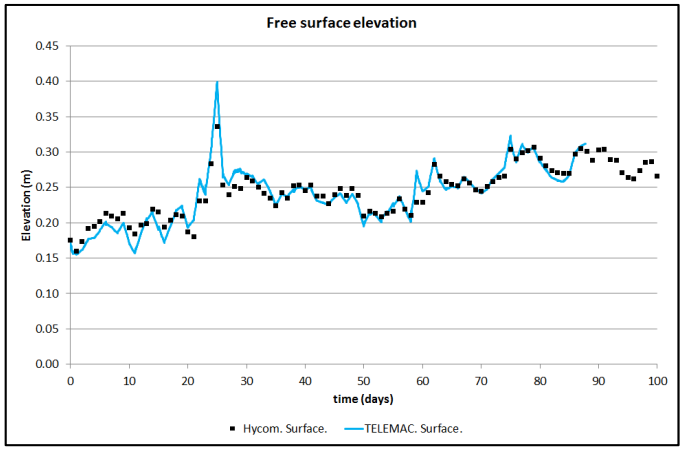

Figure 6. TELEMAC/HYCOM free surface elevation comparisons at model centre point

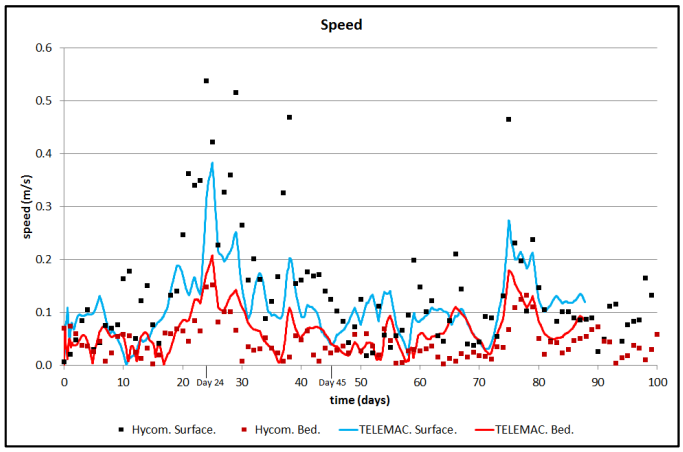

Figure 7. TELEMAC/HYCOM speeed comparisons at model centre point

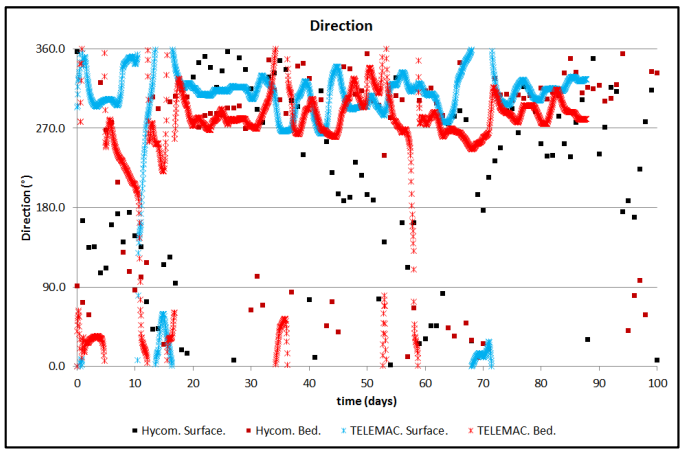

Figure 8. TELEMAC/HYCOM direction comparisons at model centre point

The global ocean model data from HYCOM includes flow from large-scale oceanic currents, and when this is applied as boundary input to TELEMAC-3D it has been shown that the flow structure has been maintained across the model domain. For example, stratification of the flow has been shown to be preserved in the centre of the TELEMAC-3D model domain. However, it is highlighted that the TELEMAC-3D model extent remains very small and that it does not demonstrate the ability of TELEMAC-3D to develop its own internal ocean currents.

IV. HYDROSTATIC INCONSISTENCY

Hydrostatic inconsistency is a phenomenon that occurs if the grid planes in a 3D flow model are not horizontal. When the model is computing the hydrostatic pressure gradient it has to estimate the horizontal gradient of density. With grid planes that are not horizontal it is usual to compute this density gradient as a combination of the variation of density in the vertical direction and the variation along a model grid plane. Depending on how far from horizontal the model grid planes are, the horizontal density gradient (which may be small or even zero if the water is nearly stationary) can become the small difference of two much larger terms and therefore quite inaccurate.

The well-known consequence of this is that if a model with non-horizontal grid planes is initialised with water at rest and a density variation only in the vertical direction, the water may begin to move. Under these conditions the water should remain stationary as there is no horizontal pressure gradient. In fact, even if horizontal grid planes are selected in TELEMAC-3D and the model has sloping sides, it is likely that the water will move.

The following criterion related to the geometry of the sigma grid has been considered [3] to apply for hydrostatic inconsistency not to occur (however many have found that this condition may not be necessary even if it is sufficient).

$$\left|\frac{\sigma}{H}\frac{\delta_x H}{\delta\sigma}\right| < 1$$

H is water depth, σ is a vertical co-ordinate varying from 0 at the surface to -1 at the bed, $\delta_x H$ is the horizontal change in depth of adjacent grid cells and δσ is the vertical cell size of a sigma grid cell. At the bed σ is -1 so this condition places a strong requirement there that gets less in the upper layers and disappears at the surface where σ is zero.

With 20 layers the horizontal change in depth $\delta_x H$ can be only a 20^{th} of the water depth which is a strong requirement on the bed slope. Sometimes bed smoothing is applied and this can help with the criterion if it reduces the bed gradient.

Clearly the criterion can be satisfied by refining the horizontal grid size as long as the vertical grid is not also refined. On the other hand, if the horizontal grid size is kept the same while refining the vertical grid size near the bed in order to model near bed sediment processes the criterion will rapidly be violated.

The criterion also indicates that the highest node at the bed in a cell should be lower than the lowest node of the next model layer above the bed. This is the criterion TELEMAC-3D uses to invoke the "Hydrostatic Inconsistency Filter". The result of using the filter is to switch off the horizontal gradient of density in the pressure calculation. In some cases this will falsify the result (e.g. where there is a uniform horizontal density gradient across the model) but often it will reduce the issue of hydrostatic inconsistency.

Hydrostatic inconsistency can be a cause of failure of a model to simulate real flows correctly as the velocities that it creates may be as large as the currents that are being simulated or may even create instability so no simulation can be produced. So it is important to have strategies to deal with it.

A quantity of simulations have been carried out with different layering approaches in TELEMAC-3D and different parameter selections. In particular the "Hydrostatic Inconsistency Filter" key-word has been selected as this has been introduced to counter inconsistency problems. The keyword means that elements whose geometry involves one node of the lower layer (layer n) in the element being higher than another node of the layer above (layer n+1) in the same element then the horizontal gradient of density is set to zero. This criterion selects elements that have a high slope of the grid planes and large horizontal element size. By refining the mesh horizontally an element can always be resolved into a larger number of elements that do not violate this criterion.

It is found that with an initial vertical density variation that is linear through depth it is possible, by invoking the hydrostatic inconsistency filter, to remove the hydrostatic inconsistency. However this does not happen if the vertical density variation is even slightly non-linear. Although the water should still remain stationary in this case, if the vertical density variation is slightly non-linear then a comparatively small current is produced, but not zero.

This was found to be the case both with classic sigma layers (equally spaced) and also with horizontal planes. In the case of horizontal planes with a sloping boundary there will always be slopes in the last element before the wall (Fig 9). This is where the currents begin. See Figs 10 and 11 for the current speed after 17 days for a slightly non-linear vertical density profile for classic sigma co-ordinates and for horizontal planes. The horizontal planes solution is seen to create less unreal currents, especially near the bed where inconsistency is large with sigma co-ordinates.

Fig 12 shows a start condition with a sharp step in the density which varies only in the vertical. The mesh is flat planes but at the edges they cannot be wholly flat. After 17 days (Fig 13) the density step has largely been eroded as a result of hydrostatic inconsistency flows. In the case of a step density profile the hydrostatic inconsistency is clearly creating much larger and more disruptive currents than with the only slightly non-linear profile.

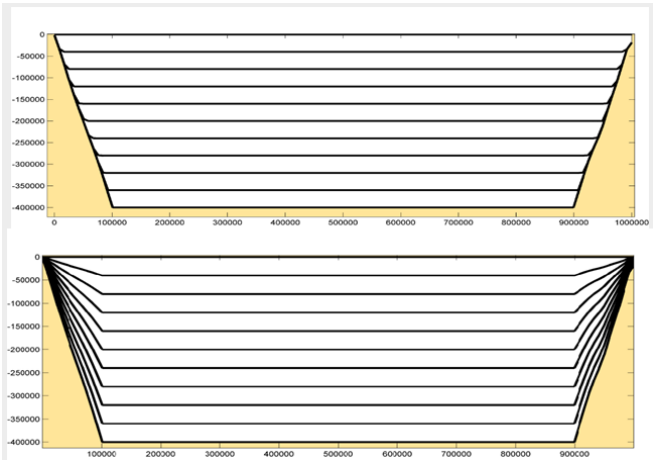

Figure 9. Meshes using flat planes (above) and sigma coordinates (below) note the depth is 1000m – exaggerated x400 for figures

Another strategy that is often available in cases where the density varies mostly in the vertical (as in the cases depicted here) is to compute the average vertical density at each level over the entire domain. As a variation of density in the vertical alone has no effect on the flow, this average density at each node location can be subtracted leaving small density values everywhere (and zero values if the density gradient is only in the vertical direction). This can greatly reduce (or remove) the hydrostatic inconsistency.

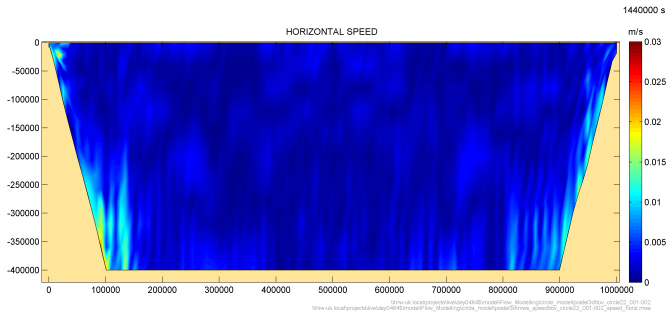

Figure 10. After 17 days sigma coordinates, slightly non-linear density profile

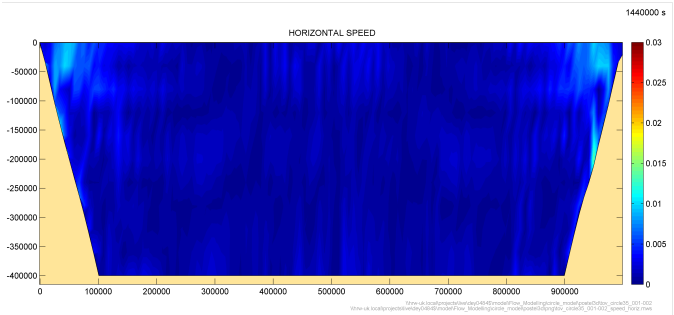

Figure 11. After 17 days flat planes, slightly non-linear density profile

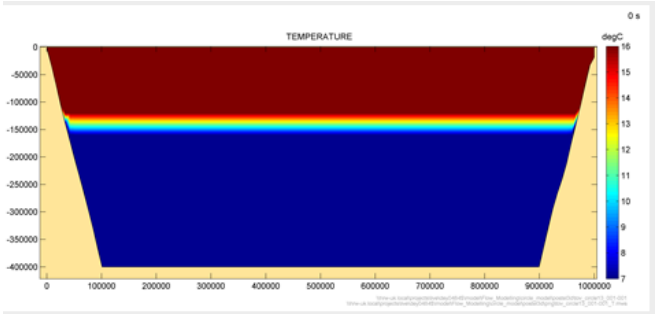

Figure 12. Initial condition (step profile) with flat planes

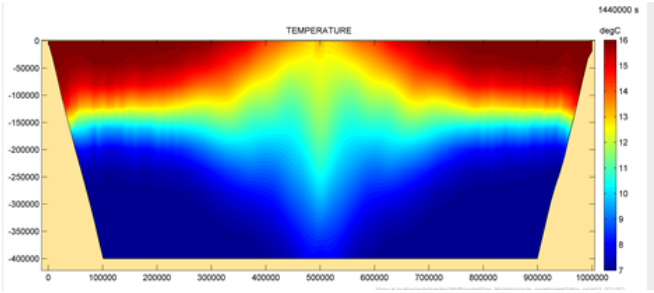

Figure 13. After 17 days initally step density profile with flat planes

V. CONCLUSIONS AND FUTURE WORK

Hydrostatic inconsistency is a problem that is likely to occur in TELEMAC-3D with non-linear vertical density profiles. However ways of reducing the effect have been described.

The future work will include modelling the flow past a schematic seamount (a submerged mountain) and proceed to modelling a larger area of coastal current including the use of sponge layer boundary conditions.

REFERENCES

[1] R. Bleck, “An oceanic general circulation model framed in hybrid isopycnic-cartesian coordinates,” Ocean Modelling, vol. 4, pp. 55–88, 2002.

[2] E. P. Chassignet, H. E. Hurlburt, O. M. Smedstad, G. R. Halliwell, P. J. Hogan, A. J. Wallcraft, R. Baraille and R. Bleck, “The HYCOM (Hybrid Coordinate Ocean Model) data assimilative system,” Journal of Marine Systems 65 (1-4), pp.60–83, 2007.

[3] G. L. Mellor, T. Ezer and L.-Y. Oey, “The pressure gradient conundrum of sigma coordinate ocean models,” in Journal of Atmospheric and Oceanic Technology, vol. 11, pp 1126-1134, 1993.

Adding boundary conditions on the bed for Telemac-3D simulations

Antoine Joly & Agnès Leroy
EDF R&D LNHE / LHSV
6 quai Watier, 78401 Chatou, France
Email: antoine.joly@edf.fr

***Abstract*—Telemac-3D has been developed to work on a two dimensional mesh that has been extruded along the z-axis. Ongoing work is done by the development team to move away from this structure. The work presented here, and available in version 7.1 of Telemac-3D, is the first step of this process as it will extend the available external boundary conditions to the bed. The impact of imposing a flow rate on the bed on the equations solved by Telemac-3D and on the hypotheses chosen will be developed. The use of these new boundary conditions in a Telemac-3D simulation will then be explained. These boundary conditions will then be illustrated through a simple test case through a comparison with source terms, which was the only available method in the previous versions of Telemac-3D to model inflow near the bed.**

I. Introduction

Historically, Telemac-3D has been developed to work on a two dimensional mesh that has been extruded along the z-axis. Work is ongoing within the Telemac-Mascaret development team to move away from this concept. The first step chosen was to work on the boundary conditions, with a focus on liquid boundary conditions on the bed. Aside from the structural modifications in the code, this has affected the hypothesis used to solve the Navier-Stokes equations.

Therefore, a brief description of the modified equations will be given, followed by an explanation of how to use this new functionality of Telemac-3D. To finish a simple validation case will be given illustrating the advantages of these new boundary conditions.

II. Reminders of the equations solved in Telemac-3D

The time-discretisation, from time t^n to $t^{n+1} = t^n + \Delta t$, of the Navier-Stokes equations is done following the sequence below:

$$\frac{\tilde{\boldsymbol{U}}^{n+1} - \boldsymbol{U}^n}{\Delta t} = -\boldsymbol{U}^n \cdot \mathbf{grad}\,\boldsymbol{U}^n + \boldsymbol{F}^{visc^{n+1}} + \tilde{\boldsymbol{F}}^{n+1} \quad (1a)$$

$$\frac{\eta^{n+1} - \eta^n}{\Delta t} = -\mathrm{div}_{2D}\left(\int_b^\eta \tilde{\boldsymbol{U}}_{2D}^n dz\right) \quad (1b)$$

$$\mathrm{div}\left(\frac{1}{\rho}\mathbf{grad}\, p_d^{n+1}\right) = \frac{1}{\Delta t}\mathrm{div}\,\tilde{\boldsymbol{U}}^{n+1} \quad (1c)$$

$$\frac{\boldsymbol{U}^{n+1} - \tilde{\boldsymbol{U}}^{n+1}}{\Delta t} = -\frac{1}{\rho}\mathbf{grad}\, p_d^{n+1} \quad (1d)$$

Where:

- $\boldsymbol{U}$ is the three-dimensional velocity vector
- $\boldsymbol{U}_{2D}$ is the horizontal velocity vector
- W is the vertical velocity vector
- η is the free surface
- $\boldsymbol{F}^{visc}$ are the viscous forces, i.e.:

$$\boldsymbol{F}^{visc} = \frac{1}{\rho}\mathbf{div}\left(\mu\left[\mathbf{grad}\,\boldsymbol{U} + (\mathbf{grad}\,\boldsymbol{U})^T\right]\right) \quad (2)$$

- $\tilde{\boldsymbol{F}}$ are external forcing terms, including buoyancy effects and hydrostatic pressure terms
- p_d is the dynamic pressure and p_h is the hydrostatic pressure, i.e. total pressure $p = p_d + p_h$

To solve for the fluid velocities, the momentum equation is usually separated into different stages (depending on the scheme used), which is the viscous forces are written under the symbol $\boldsymbol{F}^{visc}$.

III. Considering flux on the bed

Considering flow on the bed will affect how the continuity equation can be used to solve for the free surface. Indeed to solve for equation 1b, one starts by integrating the continuity equation from the bed to the free-surface:

$$\int_b^\eta \mathrm{div}\,\boldsymbol{U} dz = 0 \quad (3)$$

If we develop equation (3) to separate the horizontal and vertical directions, we get:

$$\begin{aligned}\int_b^\eta \mathrm{div}\,\boldsymbol{U} dz &= \int_b^\eta \mathrm{div}_{2D}\boldsymbol{U}_{2D} dz + \int_b^\eta \frac{\partial W}{\partial z} dz \\ &= \int_b^\eta \mathrm{div}_{2D}\boldsymbol{U}_{2D} dz \\ &\quad + W(z=\eta) - W(z=b)\end{aligned} \quad (4)$$

Where $z = \eta$ is the plane at the free surface, and $z = b$ is the plane at the bed.

Leibniz's theorem then gives:

$$\begin{aligned}\int_b^\eta \mathrm{div}_{2D}\boldsymbol{U}_{2D}dz =& \mathrm{div}_{2D}\left(\int_b^\eta \boldsymbol{U}_{2D}dz\right)\\ &- \boldsymbol{U}_{2D}|_{z=\eta}\cdot\mathbf{grad}_{2D}\eta\\ &+ \boldsymbol{U}_{2D}|_{z=b}\cdot\mathbf{grad}_{2D}b\end{aligned} \tag{5}$$

Using equation (5) to rewrite equation (4) we get:

$$\begin{aligned}&\mathrm{div}_{2D}\left(\int_b^\eta \boldsymbol{U}_{2D}dz\right)\\ &- \boldsymbol{U}_{2D}|_{z=\eta}\cdot\mathbf{grad}_{2D}\eta\\ &+ \boldsymbol{U}_{2D}|_{z=b}\cdot\mathbf{grad}_{2D}b\\ &+W(z=\eta)-W(z=b)=0\end{aligned} \tag{6}$$

The kinematic condition on the free-surface states that [1]:

$$\frac{d}{dt}(z-\eta)=0 \qquad \text{on} \quad \Gamma_\eta \tag{7}$$

Where Γ_η is the free surface boundary. This boundary condition can be rewritten as:

$$W(z=\eta)-\frac{\partial\eta}{\partial t}-\boldsymbol{U}|_{\Gamma_\eta}\cdot\mathbf{grad}\,\eta=0 \qquad \text{on} \quad \Gamma_\eta \tag{8}$$

Since the free surface ($z=\eta$) is only dependent on x and y, $\mathbf{grad}\,\eta=\mathbf{grad}_{2D}\eta$. Therefore, using (8), equation (6) can be rewritten as:

$$\frac{\partial\eta}{\partial t}+\mathrm{div}_{2D}\left(\int_b^\eta \boldsymbol{U}_{2D}dz\right)=F_b \tag{9}$$

Where the right-hand side of equation (9) is defined as the conditions on the bed boundary:

$$F_b = W(z=b)-\boldsymbol{U}_{2D}|_{z=b}\cdot\mathbf{grad}_{2D}\{b\} \tag{10}$$

If the bed boundary is fixed, and because the bottom plane ($z=b$) is only dependent on x and y then:

$$F_b = -\boldsymbol{U}|_{z=b}\cdot\boldsymbol{n}_b \tag{11}$$

Where $\boldsymbol{n}_b$ is the normal of the bed boundary pointing away from the domain.

IV. Solving for the bed flux term in finite elements

In a finite element framework, let us define the domain as Ω, its boundary as Γ, and Ψ is the basis function.

The term describing the bed fluxes F_b will also appear when the divergence of the velocity is necessary:

$$\begin{aligned}\int_\Omega \mathrm{div}\,(\boldsymbol{U}\Psi)d\Omega &= \int_\Omega \mathrm{div}\,(\boldsymbol{U})\Psi d\Omega+\int_\Omega \boldsymbol{U}\cdot\mathbf{grad}\,(\Psi)d\Omega\\ &= \int_\Omega \boldsymbol{U}\cdot\mathbf{grad}\,(\Psi)d\Omega-\int_\Gamma \boldsymbol{U}\cdot\boldsymbol{n}\Psi d\Gamma\end{aligned} \tag{12}$$

Where the last part of equation 12 found using Gauss' divergence theorem. Therefore, when using finite elements, the bed flux term F_b will be written as:

$$F_b = -\int_\Gamma \boldsymbol{U}\cdot\boldsymbol{n}\Psi d\Gamma \tag{13}$$

In telemac-3D bed fluxes will therefore be added when solving free surface (equation 1b), also when solving the Poisson equation for the dynamic pressure (1d).

When solving for the momentum equation (equations 1a and 1c), F_b can be thought of as an additional source term. This become clear from the fact that:

$$\begin{aligned}\boldsymbol{U}\cdot\mathbf{grad}\,(U) =& \mathrm{div}\,(U\boldsymbol{U})-U\mathrm{div}\,(\boldsymbol{U})\\ =& \mathrm{div}\,(U\boldsymbol{U})\end{aligned} \tag{14}$$

Which can be solved in a finite element notation in the same way as equation 12:

$$\begin{aligned}\int_\Omega \mathrm{div}\,(U\boldsymbol{U}\Psi)d\Omega &= \int_\Omega \mathrm{div}\,(U\boldsymbol{U})\Psi d\Omega+\int_\Omega U\boldsymbol{U}\cdot\mathbf{grad}\,(\Psi)d\Omega\\ &= U\left[\int_\Omega \boldsymbol{U}\cdot\mathbf{grad}\,(\Psi)d\Omega+F_b\right]\end{aligned} \tag{15}$$

This last part will be solved differently according to the advection scheme chosen.

V. Imposing a flux on the bed in Telemac-3D

To take into account the velocity on the bed, a choice has been made to create additional keywords which will allow the user to define a flow rate per boundary on the bed. This is done by adding the following keywords to the steering file:

```
/-------------------------------------------------/
/        OPTION FOR BED FLUXES
/-------------------------------------------------/
OPEN BOUNDARY CONDITIONS ON THE BED = YES
PRESCRIBED FLOWRATES ON THE BED = <Enter Flowrates>
```

The values following the keyword PRESCRIBED FLOWRATES ON THE BED follows the same structure as for other prescribed flowrates in a Telemac-Mascaret system code, it should be a list of numbers separated by a semi-colon. One number per liquid boundary on the bed must be given.

Furthermore, as the BOUNDARY CONDITIONS FILE only deals with horizontal boundaries the user has to define the liquid boundary on the bed by hand. This can be done by modifying the subroutine LIMI3D in the user fortran. For example to add a circular boundary of radius 50 m centred around coordinate $(2000, 2000)$ m, the following modifications can be done:

```
...
!      BOUNDARY CONDITIONS ON VELOCITIES
!      *********************************
!
!      BOTTOM
!      ======
!
!      DEFAULT: IMPERMEABILITY AND LOG LAW
!
       IF(BC_BOTTOM.EQ.1) THEN
!
         DO IPOIN2 = 1,NPOIN2
           LIUBOF%I(IPOIN2) = KLOG
           LIVBOF%I(IPOIN2) = KLOG
           LIWBOF%I(IPOIN2) = KLOG
!          USEFUL ? SHOULD NOT BE USED ANYWAY
           UBORF%R(IPOIN2)  = 0.D0
           VBORF%R(IPOIN2)  = 0.D0
           WBORF%R(IPOIN2)  = 0.D0
           IF(SQRT((X(IPOIN2)-2000.D0)**2
      &       +(Y(IPOIN2)-2000.D0)**2)
      &       .LE.50.D0)THEN
             !5: IMPOSED FLOW RATE
             LIUBOF%I(IPOIN2) = 5
             LIVBOF%I(IPOIN2) = 5
             LIWBOF%I(IPOIN2) = 5
             NLIQBED%I(IPOIN2) = 1
             PRINT*, '========================'
             PRINT*, 'FOR POINT ',IPOIN2
             PRINT*, 'BEDFLO',BEDFLO(1)
           ENDIF
         ENDDO
!
...
```

It should be noted that since NLIQBED%I(IPOIN2) = 1 this is only applied to the first liquid boundary defined in the steering file.

This is all that needs to be defined by the user to deal with fluxes on the bed. The developments added to version 7.1 of Telemac-3D, will then calculate the velocity imposed on the bed from the imposed flowrate and the area of the liquid nodes. At the moment, only a constant velocity profile is available. The term F_b will then be calculated and added to the relevant steps.

VI. Validation of the implementation through a simple test case

A new test case has been added to the Telemac-3D examples. It is known as bottom_bc. The configuration of this test case is simple, it is a square box of sides 4000 m. The depth is constant, and initially set to 500 m. A discharge Q of 10 000 m^3s^{-1} will be imposed inside a circle with diameter D

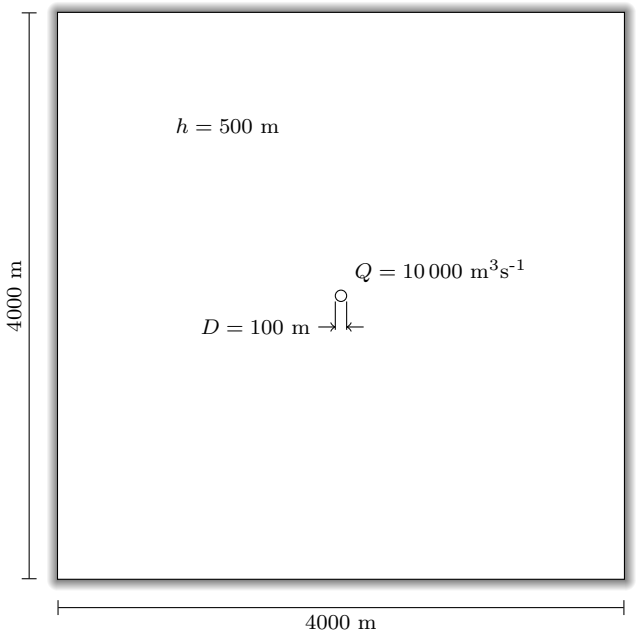

Fig. 1: Geometrical parameters of the test case.

of 100 meters placed at the centre of the box. The geometry of the test case is shown in figure 1.

This test case is solved in three different manners, two of which are given by steering file in bottom_bc and an additional method used to validate.

1) t3d_bottom_inlet.cas: This file launches a simulation where an inlet is imposed on the bed as a liquid boundary with an imposed flow rate.
2) t3d_bottom_source.cas: This file launches a simulation where the inlet is imposed as a source discharge.
3) bottom_inlet_equiv_source: This simulation is not present in the example folder. It is a reference solution where an inlet is imposed on the bed as a liquid boundary, but the fortran user file has been modified so that F_b is calculated to be equivalent to the source terms, and once it is calculated the velocity on the bed is fixed to zero, as source terms do not cancel the impermeability of the bed.

In essence, the simulation launched by file bottom_inlet_equiv_source should give the same results as t3d_bottom_source.cas and it is used to validate the fact that no bug has been introduced in the development of the liquid bed boundary conditions.

Furthermore, two different meshes will be used, a fine mesh and a coarse mesh. Since source terms are imposed on a node the coarse mesh is used to impose the inflow on a single node, and it will be used for t3d_bottom_source.cas and bottom_inlet_equiv_source. Since applying a flowrate can be imposed on several nodes on the bed, the finer mesh will be compared to the coarse mesh for t3d_bottom_inlet.cas simulation results. The coarseness of the mesh is also present for the distribution of the

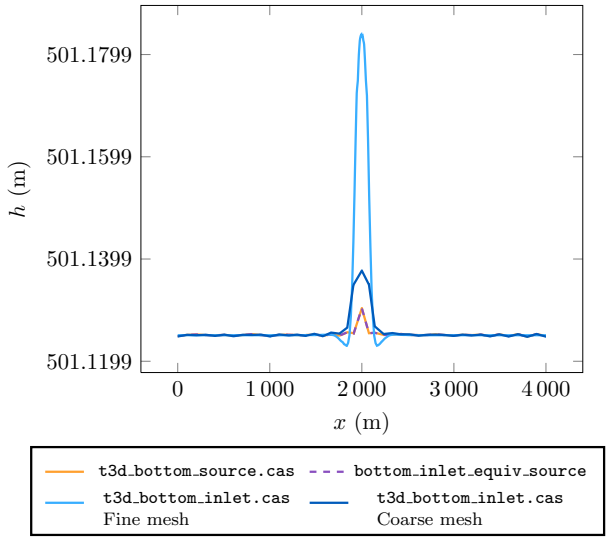

Fig. 2: Water depth profiles plotted along the along the line $y = 2\,000$ at $t = 1\,800$ s.

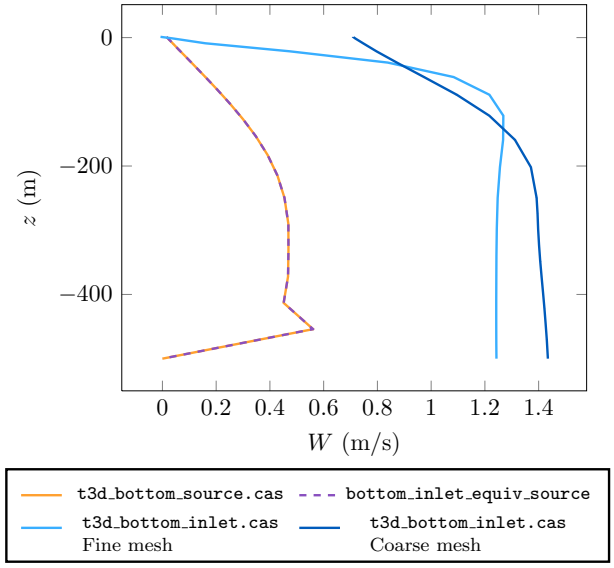

Fig. 3: Vertical velocity profiles plotted along the line $x = 2\,000$ and $y = 2\,000$ at $t = 1\,800$ s.

planes in the simulation. The fine mesh has a smaller plane spacing near the bed and the free surface, whereas the coarse mesh has the same number of planes, but these are distributed evenly on the bottom half of the domain and the plane spacing decreases towards the free-surface.

Finally, simulation results of the imposed flowrate on the bed will be compared to a point discharge imposed through source terms because the use of F_b is close to those source terms, and great care was taken in previous versions of Telemac-3D to ensure that these source terms did not introduce any unphysical effects (see Telemac-3D release notes 5.7 [2]).

The simulation results will be shown in three figures. Firstly, profiles of the water depth will be plotted along the line $y = 2\,000$ at $t = 1\,800$ s in figure 2. Secondly, profiles of the vertical velocity will be plotted along the line $x = 2\,000$ and $y = 2\,000$ at $t = 1\,800$ s in figure 3. Finally, contour plots of this vertical velocity will be plotted along the plane $y = 2\,000$ at $t = 1\,800$ s in figure 4.

The first thing to observe when looking at figures 2 and 3 is that, as expected, the simulation results for `bottom_inlet_equiv_source` are equivalent to `t3d_bottom_source.cas`. This shows that one can expect to have results that are at least as good when imposing a flow rate on the bed than when using a source discharge. Furthermore, this is why the velocity contour plots for `bottom_inlet_equiv_source` are not shown in figure 4.

Looking in greater detail at the water depths presented in figure 2, it is shown that the correct volume of water has been introduced (i.e. a mean increase of depth of 1.125 m is expected). Furthermore, even though the differences may look big on the graph between the different simulation results, they are of the order a few centimetres (compared to a depth of 500 m). Furthermore, no method gives unphysical results (such as a dip in the free surface above the inlet). In conclusion, when looking at depths only all the methods appear to be equivalent and can introduce the correct volume.

However, when looking at figure 3 the differences between a source discharge and an imposed flow rate on the bed become apparent. When applying a source discharge the impermeability condition of the bed is maintained. This explains why the vertical velocity is 0 at the bed for those results. A quick calculation shows that a velocity of 1.27 m/s is expected towards the inlet ($4Q/(\pi R^2)$). These values are close to what is calculated with the imposed flowrate on the bed. The coarse mesh has a value that is slightly greater, but this is because the velocity imposed on the bed is the flowrate divided by the area of the node (i.e. a third of the surface of the connected elements) which is not equal to $\pi D^2/4$. Aside from the differences of the bed velocity, the results from `t3d_bottom_inlet.cas` maintain this velocity almost throughout the bottom two thirds of the depth, whereas the result from the source discharge (`t3d_bottom_source.cas`) never reach more than half of this value (0.6 m/s). Therefore, for processes where the vertical velocity is important, an inlet should be modelled as a flowrate on the bed instead of through a discharge source.

Furthermore, refining the mesh in three dimensions will allow the vertical velocity calculated from source terms to be much more accurate than a coarse mesh, as the velocity on the free surface is close to 0, which was not the case for a coarse mesh. Figure 4 shows that the column of water with a high velocity is larger with a refined mesh, which also leads to a slightly higher water depth directly above the inlet, but more importantly there is a small drop of the water depth around the inlet and the water depth is a lot more stable away from the inlet (see figure 2).

VII. Conclusion and Recommendation for Use

In the beginning of this article, it was shown that imposing a velocity on the bed will only affect Telemac-3D by introducing a new term, F_b, to the several equations solved by the code. However, from a user point of view this is done by

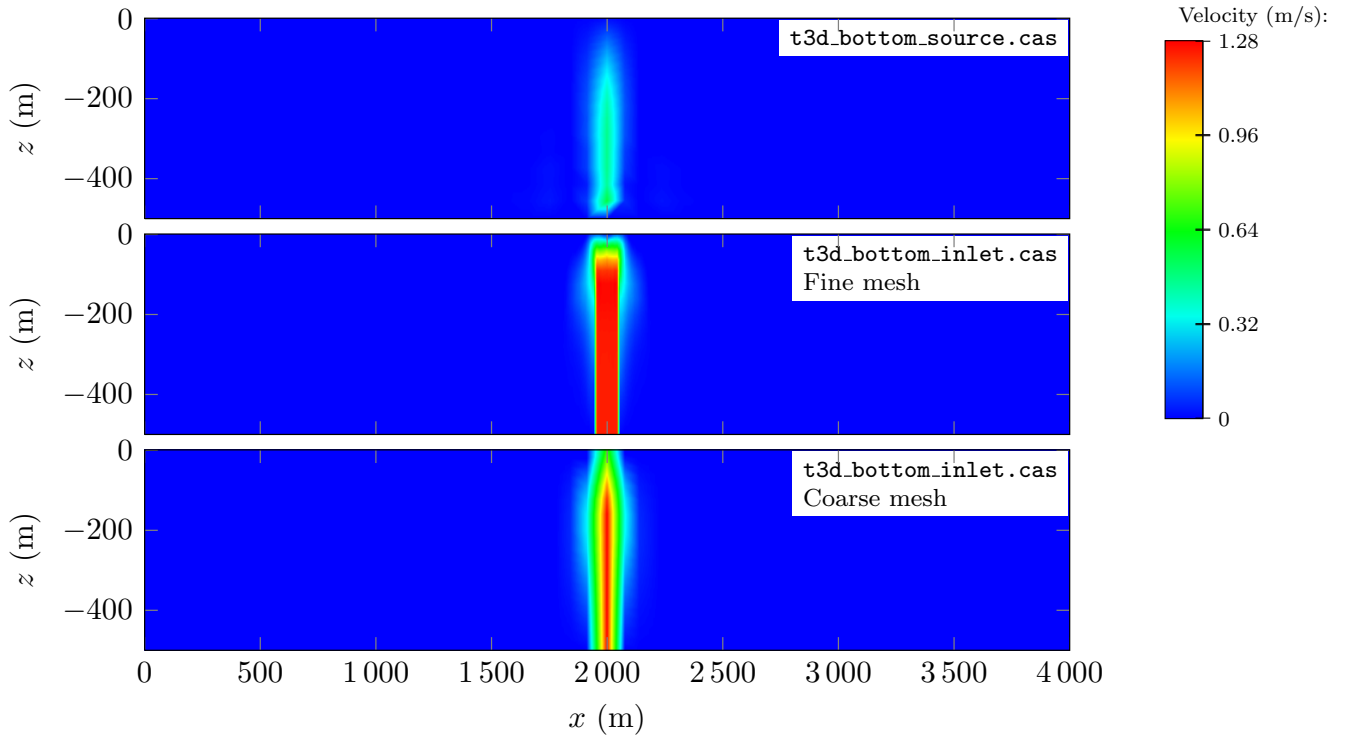

Fig. 4: Vertical velocity contours plotted along the plane $y = 2\,000$ at $t = 1\,800$.

the use of keywords OPEN BOUNDARY CONDITIONS ON THE BED and PRESCRIBED FLOWRATES ON THE BED in the steering file and through the modification of LIMI3D in the user fortran.

The validation of these developpements through a simple test case have shown that introducing liquid boundaries on the bed will not affect greatly the free surface of the flow when compared to a source discharge, which was the only method available in previous versions to impose inflows or outflows near the bed. However, imposing a flow rate on the bed has a great impact on the vertical velocities modelled. In addition, these boundary conditions are a lot more flexible for the user than source terms close to the bed, as it is possible to spread the flowrate over an area covering several nodes. As such, it is recommended to properly impose liquid boundaries on the bed, rather than using source terms.

Nonetheless, these boundary conditions may still be improved. At the moment, it is not possible to specify the fluid density on these liquid boundary, and therefore it has not been tested on stratified flows. The same is true for turbulence.

Nonetheless, several tests have been done with these new boundary conditions. They have been tested in parrallel and in scalar implementations with minimal differences. These boundary conditions have been tested with all advection schemes. The mass losses are of the order of the machine precision if the ACCURACY FOR PROPAGATION is set to small enough value. It is also possible to add the DYNAMIC PRESSURE IN WAVE EQUATION, but this requires the keyword VELOCITY PROJECTED ON BOTTOM to be set to no.

In addition, when using these new liquid boundaries, these recommendations should be followed:

- Use the non-hydrostatic version of the code (it will work for hydrostatic flows, but a lot of the errors will be reported on the vertical velocities).
- Use a sigma transformation of the mesh, i.e. setting MESH TRANSFORMATION to 1 or 2.
- Refining along the bed and the free surface will help produce correct vertical velocity profiles.
- The time step needs to be chosen so that the CFL condition is also valid along the vertical.

Finally, it should be noted that when imposing a flowrate it will always be converted into a velocity along the normal of each node and that these conditions will work for outflows as well.

REFERENCES

[1] J.-M. Hervouet, *Hydrodynamics of free surface flows*. Chichester: Wyley, 2007.

[2] J.-M. Hervouet and C.-T. Pham, "Telemac version 5.7, release notes. Telemac-2D and Telemac-3D," EDF R&D LNHE, Tech. Rep., 2007.

Distributive advection schemes and dry zones, new solutions

Jean-Michel Hervouet [(1)], Sara Pavan [(1,2)], Riadh Ata [(1,2)]
[(1)] Laboratoire National d'Hydraulique et Environnement, Electricité de France
[(2)] Laboratoire d'Hydraulique Saint-Venant
6 Quai Watier, 78400 Chatou, France
Email of corresponding author: j-m.hervouet@edf.fr

***Abstract*—This paper is a continuation of "Ongoing research on advection schemes", published in 2014 in this series of proceedings. It is restricted to distributive schemes and comes after the description of the new predictor-corrector introduced in the previous paper. The developments and tests were done with Telemac-2D but can be easily applied also to 3D. First a second order in time version of this predictor-corrector is developed. Then a new criterion for proving monotonicity is coined, which allows to perform as many correction steps as we want, with an arbitrary predictor which is just maintained within a given range and is not even subjected to mass conservation. With 4 extra correction steps the rotating cone grows from 0.5331 to 0.75. At this level the problem of dry zones still remains. To solve it, it is first shown that a fully implicit distributive scheme is unconditionally stable, even on dry zones. However the numerical diffusion is largely increased, losing all the benefits previously gained. Then a locally implicit predictor-corrector scheme is designed, with full implicitation only in the dry zones. An unexpected consequence of this new scheme is that we can choose an arbitrary time-step, and this allows to use the distributive schemes in conditions where they perform better, e.g. the rotating cone height after one rotation is now 0.79 in the latest tests. This is much larger than the 0.39 of the NERD scheme which was before the only distributive scheme working with tidal flats. A new test case with bridge piers and an island treated as a dry zone is presented. Monotonicity is well preserved and mass conservation is obtained at machine accuracy.**

I. Introduction

Mass conservation, monotonicity and dry zones are now fairly well handled in the Telemac system, so that the numerical diffusion of advection schemes becomes the new frontier where progress is necessary to improve the quality of studies. For example the study of pollutants in rivers, the stability of stratifications, and the numerical simulation of non linear waves are highly dependent on the quality of advection schemes, and on the space and time orders. Improving on this topic is not an easy task, since on one hand a couple of theorems show that simple linear schemes cannot do the job, and on the other hand this subject has been already heavily investigated by many teams. Moreover we face additional problems due to the free-surface flows, like the depth-averaged or moving grid context, and still the treatment of tidal flats, that at first sight precludes most existing solutions, since divisions by the depth appear in many solution procedures.

In the 2014 Telemac User Club we presented several improvements. In finite volumes an approximate Riemann solver, the Harten-Lax-van Leer-Contact scheme (HLLC, see [12]) with 1^{st} and 2^{nd} order was presented. In finite elements, the classical N and PSI distributive schemes could be improved by adding the derivative in time in the upwinding process. It was done in a predictor-corrector procedure, after the recent publication by Mario Ricchiuto [11]. The predictor gives an approximation of the derivative in time of the tracer, which is then used in the corrector step. Three test cases were presented: a pollutant plume in a steady state river, the transport of a stain, and the rotating cone. The height of the cone after one rotation, which should theoretically be 1, was 0.2136 for the classical PSI scheme, 0.4710 for the HLLC second order scheme, and 0.5331 for the new predictor-corrector PSI scheme. The conclusion of this first paper announced: "We now work on tidal flats, which could be dealt with by an implicit predictor-corrector distributive scheme, as shown by preliminary tests not treated here. Another promising issue is the possibility of iterating the corrector step, which would give even less numerical diffusion, which is also shown by preliminary tests". The present paper will now detail in a sequence the three main improvements obtained since the first paper: a second order in time predictor-corrector scheme, then the possibility of iterating the corrections, and in the end a new approach, a locally implicit predictor-corrector distributive scheme. The rotating cone test and a new test case with bridge piers and an island will show the new features. All the developments and tests are done with Telemac-2D but the theory applies also to 3D, as the varying volumes around points in 3D play the same mathematical role as the varying depth in 2D.

II. A second order in time predictor-corrector distributive scheme

In the previous paper we reported theoretical mass conservation problems to get a second order in time predictor-corrector scheme in the depth-averaged context, as was done in a simpler context by Ricchiuto in his original paper. We now have found a correct derivation, with boundary and source terms now always taken into account in all the steps. We start from the same predictor step, which is the classical PSI scheme:

$$\frac{S_i h_i^{n+1} C_i^* - S_i h_i^{n+1} C_i^n}{\Delta t} =$$

$$-\sum_j \min(\Phi_{ij}^{psi}(C^n), 0)\left(C_j^n - C_i^n\right) \quad (1)$$

$$-\min(b_i, 0)\left(C_i^{boundary} - C_i^n\right)$$

$$+\max(Sce_i, 0)\left(C_i^{sce} - C_i^n\right)$$

We recall that h_i^n and h_i^{n+1} are respectively the depths at point i at the beginning and at the end of the time step, S_i is the integral of the test function, Φ_{ij}^N and Φ_{ij}^{psi} are the fluxues between points given by respectively the N and PSI scheme. C_i^n is the initial value of the tracer at point i, C_i^{n+1} the final value, and C_i^* the value at the predictor step. Δt is the time step, b_i is the boundary flux if i is on a boundary and Sce_i a possible source term inside the domain, while $C_i^{boundary}$ is the prescribed value of C at the boundary, and C_i^{sce} the value of the tracer at a source.

The rather long derivation of the corrector step will not be given here, it is obtained with the construction of a fully implicit and a fully explicit scheme, and then by blending them with the implicitation coefficient θ. When C_i^{n+1} is involved in the fluxes, it is replaced by C_i^*, which does not spoil the mass conservation if this is correctly done at the level of the conservative form. We eventually find the following equation, which is by construction mass conservative:

$$S_i h_i^{n+1}\left(C_i^{n+1} - C_i^*\right) =$$

$$-\theta\overleftarrow{S_i h_i^n\left(C_i^* - C_i^n\right)} - (1-\theta)\overleftarrow{S_i h_i^{n+1}\left(C_i^* - C_i^n\right)}$$

$$-\theta\Delta t\overleftarrow{\sum_j \min(\Phi_{ij}^{psi}(C^*), 0)\left(C_j^* - C_i^*\right)} \quad (2)$$

$$-(1-\theta)\,\Delta t\overleftarrow{\sum_j \min(\Phi_{ij}^{psi}(C^n), 0)\left(C_j^n - C_i^n\right)}$$

$$+Sce_i\ \Delta t\left(C_i^{sce} - (1-\theta)\,C_i^n - \theta C_i^*\right)$$

$$-b_i\ \Delta t\left(C_i^{boundary} - (1-\theta)\,C_i^n - \theta C_i^*\right)$$

Backward arrows are put on terms which are treated altogether with upwinding, at element level, in the same way that leads from N to PSI scheme. At element level derivatives in time are first equally shared between the 3 points of the triangle, this is considered to be the equivalent of a N scheme, then the PSI limitation is applied to the whole contribution that includes the fluxes. Mass conservation is rather easy to prove, with the help of the discretised continuity equation, but a proof of monotonicity was impossible to find, unless some restrictions are applied to C^*, namely that C^* is not too far from C^n, and this idea will be also used for iterating the corrector. A very important point is that the mass conservation is ensured whatever the mass of C^*, because it is both in the left- and righ-hand side and can be cancelled, except in fluxes that do not contribute to a change of mass. The monotonicity proof can thus be done with an arbitrary C^*. We write the corrector in the following way, as already done in the previous paper:

$$S_i h_i^{n+1} C_i^{n+1} = S_i h_i^{n+1} C_i^* - f_i S_i h_i^{n+1-\theta}\left(C_i^* - C_i^n\right)$$

$$-(1-\theta)\Delta t\sum_j \mu_j\left(C_j^n - C_i^n\right)\min(\Phi_{ij}^{psi}(C^n), 0)$$

$$-\theta\Delta t\sum_j \mu_j\left(C_j^* - C_i^*\right)\min(\Phi_{ij}^{psi}(C^*), 0) \quad (3)$$

$$+\Delta t\max(Sce_i, 0)\left(C_i^{sce} - (1-\theta)\,C_i^n - \theta C_i^*\right)$$

$$-\Delta t\min(b_i, 0)\left(C_i^{boundary} - (1-\theta)\,C_i^n - \theta C_i^*\right)$$

All f_i and μ_j are in the range [0,1] to account for the upwinding limitation. $h_i^{n+1-\theta}$ is a notation for $(1-\theta)\,h_i^{n+1} + \theta h_i^n$. Note that if $C^* = C^n$ we fall back to the classical N or PSI scheme, which is stable, so we can expect to keep this stability if C_i^* is chosen not too far from C_i^n. We now want to have positive coefficients for all values of C in the right-hand side. Only the coefficients of C_i^* and C_i^n are questionable. They are:

Coefficient of C_i^*:

$$a^* = S_i h_i^{n+1} - f_i S_i h_i^{n+1-\theta}$$
$$+\theta\Delta t\sum_j \mu_j \min(\Phi_{ij}^{psi}(C^*), 0) \quad (4)$$
$$-\theta\Delta t\left(\max(Sce_i, 0)\ - \min(b_i, 0)\right)$$

Coefficient of C_i^n:

$$a^n = f_i S_i h_i^{n+1-\theta}$$

$$+(1-\theta)\Delta t\sum_j \mu_j \min(\Phi_{ij}^{psi}(C^n), 0) \quad (5)$$

$$-(1-\theta)\,\Delta t\left(\max(Sce_i, 0)\ - \min(b_i, 0)\right)$$

a^* or a^n may be negative but the positivity of $a^* + a^n$ is largely ensured by the stability condition of the predictor, as we have:

$$a^* + a^n = S_i h_i^{n+1} + \theta\Delta t\sum_j \mu_j \min(\Phi_{ij}^{psi}(C^*), 0)$$

$$+(1-\theta)\,\Delta t \sum_j \mu_j \min(\Phi_{ij}^{psi}(C^n),0) \tag{6}$$

$$+\Delta t\,[-\max(Sce_i,0)\ +\min(b_i,0)]$$

As a matter of fact, we can take $\mu_j = 1$ (worst case scenario), and replace the $\Phi_{ij}^{psi}(C^*)$ and $\Phi_{ij}^{psi}(C^n)$ by Φ_{ij}^{N}, and we fall back to the classical stability condition.

We now write:

$$C_i^* = C^{\min} + \alpha\left(C^{\max} - C^{\min}\right) \tag{7}$$

$$C_i^n = C^{\min} + \beta\left(C^{\max} - C^{\min}\right) \tag{8}$$

with α and β in the range [0,1]. $C^{\min}$ and $C^{\max}$ are the local extrema that should not be trespassed, computed with the neighbouring values of C^n and C^*. We want to find the solutions under which:

$$a^* C_i^* + a^n C_i^n = (a^* + a^n) C_i^{average} \tag{9}$$

with: $C_i^{average} = C^{\min} + \gamma\left(C^{\max} - C^{\min}\right)$, and γ in the range [0,1]. In fact there is not always a solution, even with very small time steps, and we had to change the strategy. Choosing $\theta = \frac{1}{2}$ and under the stability condition of the first order in time of the predictor-corrector, we looked for a condition on α as a function of β, and it gave:

$$2\beta - 1 \leq \alpha \leq 2\beta \tag{10}$$

$$\frac{\beta}{3} \leq \alpha \leq \frac{2}{3} + \frac{\beta}{3} \tag{11}$$

which is equivalent to:

$$2C_i^n - C^{\max} \leq C_i^* \leq 2C_i^n - C^{\min} \tag{12}$$

$$\frac{2C^{\min}}{3} + \frac{C_i^n}{3} \leq C_i^* \leq \frac{2C^{\max}}{3} + \frac{C_i^n}{3} \tag{13}$$

Our solution resorts to imposing these conditions to every C_i^*, which, as we have said, does not spoil the mass conservation even if we change the mass of C^*. In some severe conditions, when the restrictions apply, the second order will simply not be reached.

III. Iterating the corrections

We have shown in the previous section that any predictor value can be used in the corrector step, provided that it remains within a certain distance from the initial value C^n. The corrector can thus be applied as many times as we want, taking every time as new predictor the value of the last iteration. The same principle can be applied also to the first order in time predictor-corrector scheme, but the condition appears to be different:

$$C_i^n + \frac{C^{\min} - C_i^n}{2} \leq C_i^* \leq C_i^n + \frac{C^{\max} - C_i^n}{2} \tag{14}$$

It can also be shown that this condition is naturally ensured by the PSI scheme which is our predictor, so the limitation does not need to be applied at the first iteration. Iterating the corrector proves to be very efficient, as shown by the rotating cone test. We recall that in this case the mesh is a 20.1 m x 20.1 m square composed of 4489 squares of side 0.3 m, each one split into two triangles. With the first order scheme we find after one rotation:

number of corrections	cone height after one rotation
0	0.21 (PSI scheme)
1	0.53
2	0.69
3	0.74
4	0.75
21	0.75

It seems that we have rapidly a dramatic improvement, after very few iterations of the corrector. The state-of-the-art obtained last year, 0.53, is boosted to 0.75. Comparing order 1 and order 2 of the N predictor-corrector with corrections scheme yields:

corrections	cone height, order 1	cone height, order 2
0	0.18 (N scheme)	0.18 (N scheme)
1	0.50	0.48
2	0.68	0.60
3	0.74	0.63
4	0.75	0.64
5	0.76	0.64
6	0.77	0.65

Figure 1, for order 1 and Figure 2 for order 2 show the cone after one rotation of the N predictor-corrector with six corrections. The shape is different but there is no clear advantage of order 2 in this case. However the convergence tests, not shown in this paper, show the gain in order, though order 2 is not exactly achieved, as was already found with unstructured meshes.

IV. Dry zones: a locally implicit predictor-corrector scheme

It can be shown that when the tracer is semi-implicited in the fluxes with a coefficient θ, the stability criterion on the time is divided by $1-\theta$ and becomes:

$$\Delta t < \frac{1}{1-\theta}\frac{S_i h_i^n}{\left(\sum_j \max\left(\Phi_{ij},0\right) + \max\left(b_i,0\right) - \min\left(Sce_i,0\right)\right)} \tag{15}$$

A fully implicit distributive scheme becomes unconditionnally stable, even on dry zones. However tests show that such a scheme is far too diffusive. This is why we looked for a

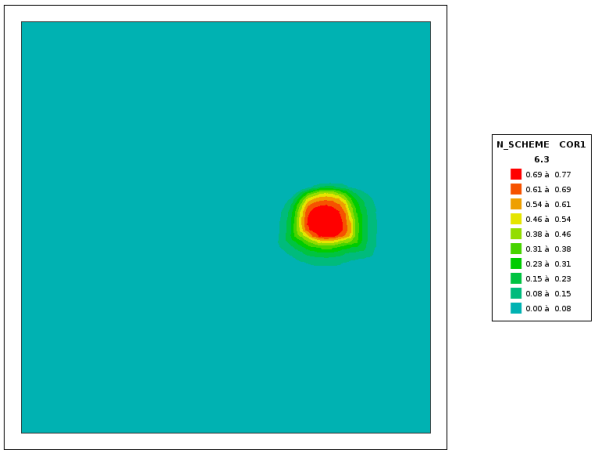

Fig. 1. Rotating cone test, cone after one rotation. N predictor-corrector with 6 corrections, order 1.

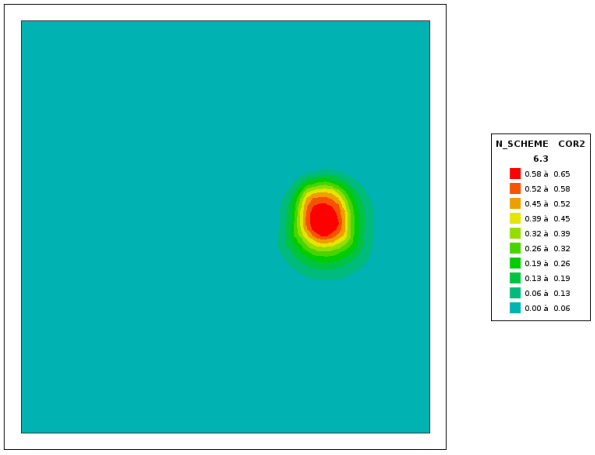

Fig. 2. Rotating cone test, cone after one rotation. N predictor-corrector with 6 corrections, order 2.

scheme that would be locally implicit, with full implicitation only on dry zones.

A. Semi-implicit predictor

We choose to solve in the predictor step the following equation:

$$S_i h_i^{n+1-\theta_i} C_i^* - S_i h_i^{n+1-\theta_i} C_i^n =$$

$$-\Delta t \sum_j \left(\theta_j C_j^* + (1-\theta_j)\, C_j^n\right) \min\left(\Phi_{ij}^N, 0\right)$$

$$+\Delta t \sum_j \left(\theta_i C_i^* + (1-\theta_i)\, C_i^n\right) \min\left(\Phi_{ij}^N, 0\right) \qquad (16)$$

$$+\Delta t \max\left(Sce_i, 0\right) \left(C_i^{sce} - \left(\theta_i C_i^* + (1-\theta_i) C_i^n\right)\right)$$

$$-\Delta t \min\left(b_i, 0\right) \left(C_i^{boundary} - \left(\theta_i C_i^* + (1-\theta_i) C_i^n\right)\right)$$

B. Corrector

Now that we have an approximation C_i^* of the final concentration, we can write the original derivative in time in the form:

$$S_i h_i^{n+1-\theta_i} \left(C_i^{n+1} - C_i^* + C_i^* - C_i^n\right) \qquad (17)$$

where the term $S_i h_i^{n+1-\theta_i} \left(C_i^* - C_i^n\right)$ can be transfered in the right-hand side. Separating the contribution of fluxes between explicit and implicit terms, we get:

$$S_i h_i^{n+1-\theta_i} \left(C_i^{n+1} - C_i^*\right) = -S_i h_i^{n+1-\theta_i} \left(C_i^* - C_i^n\right)$$

$$-\Delta t \sum_j \left(\theta_j C_j^{n+1} - \theta_i C_i^{n+1}\right) \min\left(\Phi_{ij}^N, 0\right)$$

$$-\Delta t \sum_j \left(\left(1-\theta_j\right) C_j^n - \left(1-\theta_i\right) C_i^n\right) \min\left(\Phi_{ij}^N, 0\right) \qquad (18)$$

$$+\Delta t \max\left(Sce_i, 0\right) \left(C_i^{sce} - \left(\theta_i C_i^{n+1} + (1-\theta_i) C_i^n\right)\right)$$

$$-\Delta t \min\left(b_i, 0\right) \left(C_i^{boundary} - \left(\theta_i C_i^{n+1} + (1-\theta_i) C_i^n\right)\right)$$

We now want to add upwinding to the derivative in time, and we also include in the upwinding the explicit part of the flux contributions. It gives, still using our backward arrays notation:

$$S_i h_i^{n+1-\theta_i} \left(C_i^{n+1} - C_i^*\right) = \overleftarrow{-S_i h_i^{n+1-\theta_i} \left(C_i^* - C_i^n\right)}$$

$$-\Delta t \sum_j \left(\theta_j C_j^{n+1} - \theta_i C_i^{n+1}\right) \min\left(\Phi_{ij}^N, 0\right)$$

$$\overleftarrow{-\Delta t \sum_j \left(\left(1-\theta_j\right) C_j^n - \left(1-\theta_i\right) C_i^n\right) \min\left(\Phi_{ij}^N, 0\right)} \qquad (19)$$

$$+\Delta t \left(\max\left(Sce_i, 0\right) \left(C_i^{sce} - \left(\theta_i C_i^{n+1} + (1-\theta_i) C_i^n\right)\right)\right)$$

$$-\Delta t \min\left(b_i, 0\right) \left(C_i^{boundary} - \left(\theta_i C_i^{n+1} + (1-\theta_i) C_i^n\right)\right)$$

Note that a tentatively second order upwinded contribution should be:

$$\overleftarrow{-S_i h_i^{n+1-\theta_i} \left(C_i^* - C_i^n\right)}$$

$$\overleftarrow{-\Delta t \sum_j \left(\theta_j C_j^* + (1-\theta_j) C_j^n\right) \min\left(\Phi_{ij}^{psi}, 0\right)} \qquad (20)$$

$$\overleftarrow{+\Delta t \sum_j \left(\theta_i C_i^* + (1-\theta_i) C_i^n\right) \min\left(\Phi_{ij}^{psi}, 0\right)}$$

but it is not what is naturally given by the derivation, the reason being that this would lead to mass errors, because Φ_{ij}^{psi} is built with C^n and can replace Φ_{ij}^N safely only when used with C^n, not with C^*.

C. Monotonicity

As the mass is correct by construction, the only remaining question is the monotonicity. We now rewrite our corrector step so that only positive coefficients of values of C appear. We also introduce coefficient f_i and μ_{ij} as before to account for the PSI reduction of the upwinded terms, it yields:

$$\begin{aligned}
&\left(S_i h_i^{n+1-\theta_i} - \theta_i \Delta t \sum_j \min\left(\Phi_{ij}^N, 0\right)\right) C_i^{n+1} \\
&+\theta_i \Delta t \left(\max\left(Sce_i, 0\right) - \min\left(b_i, 0\right)\right) C_i^{n+1} = \\
&\Delta t \left(\max\left(Sce_i, 0\right) C_i^{sce} - \min\left(b_i, 0\right) C_i^{boundary}\right) \\
&-\Delta t \sum_j \theta_j C_j^{n+1} \min\left(\Phi_{ij}^N, 0\right) \\
&-\mu_{ij} \Delta t \sum_j \left(1-\theta_j\right) C_j^n \min\left(\Phi_{ij}^N, 0\right) \\
&+C_i^* \left(1-f_i\right) S_i h_i^{n+1-\theta_i} + C_i^n f_i S_i h_i^{n+1-\theta_i} \\
&+(1-\theta_i) C_i^n \Delta t \sum_j \mu_{ij} \min\left(\Phi_{ij}^N, 0\right) \\
&-(1-\theta_i) C_i^n \Delta t \left[\max\left(Sce_i, 0\right) - \min\left(b_i, 0\right)\right]
\end{aligned} \tag{21}$$

With this form we see that the only risk of negative coefficients happens with C_i^n. The coefficient of C_i^{n+1} is positive thanks to the stability condition that has been previously chosen. Without the extra derivative in time, we would have to ensure the positivity of:

$$B_{ii} = S_i h_i^{n+1-\theta_i} - \Delta t (1-\theta_i)\ flux(i)$$

Denoting:

$$flux(i) = \max\left(Sce_i, 0\right) - \sum_j \min\left(\Phi_{ij}^N, 0\right) - \min\left(b_i, 0\right) \tag{22}$$

which leads to the condition:

$$\Delta t < \frac{1}{1-\theta_i} \frac{S_i h_i^n}{\left(flux(i) + \sum_j \Phi_{ij} + b_i - Sce_i\right)} \tag{23}$$

Now we see that there is a risk of negative coefficient of C_i^n, unless we consider a limitation of C_i^*. As the terms depending on μ_{ij} are negative in the coefficient of C_i^n we remain on the safe side by choosing $\mu_{ij} = 1$. As before, we now introduce:

$$C_i^* = C^{\min} + \alpha \left(C^{\max} - C^{\min}\right) \tag{24}$$

$$C_i^n = C^{\min} + \beta \left(C^{\max} - C^{\min}\right) \tag{25}$$

We are left with proving that:

$$\begin{aligned}
&C_i^* \left(1-f_i\right) S_i h_i^{n+1-\theta_i} + C_i^n f_i S_i h_i^{n+1-\theta_i} \\
&+(1-\theta_i) C_i^n \Delta t \sum_j \min\left(\Phi_{ij}^N, 0\right) \\
&-(1-\theta_i) C_i^n \Delta t \left(\max\left(Sce_i, 0\right) - \min\left(b_i, 0\right)\right) = \\
&S_i h_i^{n+1-\theta_i} C_i^{average} \\
&+(1-\theta_i) \Delta t \sum_j \min\left(\Phi_{ij}^N, 0\right) C_i^{average} \\
&-(1-\theta_i) \Delta t \left(\max\left(Sce_i, 0\right) - \min\left(b_i, 0\right)\right) C_i^{average}
\end{aligned} \tag{26}$$

we denote:

$$\begin{aligned}
\gamma &= S_i h_i^{n+1-\theta_i} \\
&+(1-\theta_i) \Delta t \sum_j \min\left(\Phi_{ij}^N, 0\right) \\
&-(1-\theta_i) \Delta t \left(\max\left(Sce_i, 0\right) - \min\left(b_i, 0\right)\right)
\end{aligned} \tag{27}$$

It eventually yields:

$$\begin{aligned}
\gamma C_i^{average} &= C_i^* \left(1-f_i\right) S_i h_i^{n+1-\theta_i} \\
&+C_i^n \left(f_i S_i h_i^{n+1-\theta_i} + \gamma - S_i h_i^{n+1-\theta_i}\right)
\end{aligned} \tag{28}$$

or:

$$\begin{aligned}
&\gamma C_i^{average} = \\
&\left(\gamma - S_i h_i^{n+1-\theta_i}\right) \left(C^{\min} + \beta \left(C^{\max} - C^{\min}\right)\right) \\
&+S_i h_i^{n+1-\theta} \left(C^{\min} + \alpha \left(C^{\max} - C^{\min}\right)\right) \\
&-\left(f_i S_i h_i^{n+1-\theta_i} \left(C^{\min} + \alpha \left(C^{\max} - C^{\min}\right)\right)\right) \\
&+\left(f_i S_i h_i^{n+1-\theta_i} \left(C^{\min} + \beta \left(C^{\max} - C^{\min}\right)\right)\right)
\end{aligned} \tag{29}$$

which is:

$$C_i^{average} = C^{\min}$$

$$+\frac{\beta\left(\gamma - S_i h_i^{n+1-\theta_i}\right)}{\gamma}\left(C^{\max} - C^{\min}\right) \quad (30)$$

$$+\frac{\alpha\left(1-f_i\right)S_i h_i^{n+1-\theta_i} + \beta f_i S_i h_i^{n+1-\theta_i}}{\gamma}\left(C^{\max} - C^{\min}\right)$$

We see that need to have:

$$0 < \beta\gamma + (\alpha - \beta)\left(1 - f_i\right) S_i h_i^{n+1-\theta_i} < \gamma \quad (31)$$

If $\alpha > \beta$: positivity is ensured and then the worst situation happens when $f_i = 0$, in which case we get the condition:

$$\beta\gamma + (\alpha - \beta) S_i h_i^{n+1-\theta_i} < \gamma \quad (32)$$

which also reads:

$$\alpha S_i h_i^{n+1-\theta_i} < \gamma\left(1 - \beta\right) + \beta S_i h_i^{n+1-\theta_i} \quad (33)$$

We now assume that the time step was chosen so that:

$$\Delta t < \frac{1}{2\left(1-\theta_i\right)} \frac{S_i h_i^n}{\left(flux(i) + \sum_j \Phi_{ij} + b_i - Sce_i\right)} \quad (34)$$

which gives the property:

$$\gamma > \frac{S_i h_i^{n+1-\theta_i}}{2} \quad (35)$$

Our most demanding condition for α is then (the smallest γ is to be considered):

$$\alpha < \frac{1}{2} + \frac{\beta}{k} \quad (36)$$

If $\alpha < \beta$: only the positivity gives a condition and again the worst condition is $f_i = 0$ and we get the condition:

$$0 < \beta\gamma + (\alpha - \beta) S_i h_i^{n+1-\theta_i}$$

where the stronger condition, again obtained with the minimum γ, is:

$$\frac{\beta}{2} < \alpha \quad (37)$$

We end up with the general condition:

$$\frac{\beta}{2} < \alpha < \frac{1}{2} + \frac{\beta}{k} \quad (38)$$

which is also:

$$C_i^n + \frac{1}{2}\left(C^{\min} - C_i^n\right) < C_i^* < C_i^n + \frac{1}{2}\left(C^{\max} - C_i^n\right) \quad (39)$$

Now the next question is: is this property ensured by C_i^* when we use a semi-implicit predictor? We have:

$$S_i h_i^{n+1-\theta_i} C_i^* - S_i h_i^{n+1-\theta_i} C_i^n =$$

$$\Delta t\left(\max\left(Sce_i, 0\right)\left(C_i^{sce} - (\theta_i C_i^* + (1-\theta_i) C_i^n\right)\right)$$

$$-\Delta t \sum_j \left(\theta_j C_j^* + (1-\theta_j) C_j^n\right) \min\left(\Phi_{ij}, 0\right) \quad (40)$$

$$+\Delta t \sum_j \left(\theta_i C_i^* + (1-\theta_i) C_i^n\right) \min\left(\Phi_{ij}, 0\right)$$

$$-\Delta t \min\left(b_i, 0\right)\left(C_i^{boundary} - (\theta_i C_i^* + (1-\theta_i) C_i^n)\right)$$

which is equivalent to:

$$\left[S_i h_i^{n+1-\theta_i} + \theta_i \Delta t\left(-\min\left(\Phi_{ij}, 0\right)\right)\right] C_i^*$$

$$+\theta_i \Delta t\left(\max\left(Sce_i, 0\right) - \min\left(b_i, 0\right)\right) C_i^*$$

$$-\left[S_i h_i^{n+1-\theta_i} + \theta_i \Delta t\left(-\min\left(\Phi_{ij}, 0\right)\right)\right] C_i^n$$

$$-\theta_i \Delta t\left(\max\left(Sce_i, 0\right) - \min\left(b_i, 0\right)\right) C_i^n = \quad (41)$$

$$\Delta t\left(\max\left(Sce_i, 0\right)\left(C_i^{sce} - C_i^n\right)\right)$$

$$-\Delta t \sum_j \left(\theta_j C_j^* + (1-\theta_j) C_j^n - C_i^n\right) \min\left(\Phi_{ij}, 0\right)$$

$$-\Delta t \min\left(b_i, 0\right)\left(C_i^{boundary} - C_i^n\right)$$

Denoting:

$$\lambda = \Delta t\left(\max\left(Sce_i, 0\right) - \min\left(\Phi_{ij}, 0\right) - \min\left(b_i, 0\right)\right)$$

and remarking that in the right-hand side all terms C_i^n are balanced by a $-C$ of some sort, we can write:

$$C_i^n + \frac{\lambda}{\left(S_i h_i^{n+1-\theta_i} + \theta_i \lambda\right)}\left(C_i^{\min} - C_i^n\right) < C_i^* \quad (42)$$

and:

$$C_i^* < C_i^n + \frac{\lambda}{\left(S_i h_i^{n+1-\theta_i} + \theta_i \lambda\right)}\left(C_i^{\max} - C_i^n\right) \quad (43)$$

The maximum of $\frac{\lambda}{\left(S_i h_i^{n+1-\theta_i} + \theta_i \lambda\right)}$ is obtained with the maximum of λ. Under the condition 34 this maximum is $\frac{1}{2+\theta_i}$ which is less than $\frac{1}{2}$. So we get indeed the property:

$$C_i^n + \frac{1}{k}\left(C_i^{\min} - C_i^n\right) < C_i^* < C_i^n + \frac{1}{k}\left(C_i^{\max} - C_i^n\right) \quad (44)$$

which is the condition found for the explicit predictor, and which could be even stricter if we impose a non zero minimum of θ_i.

With $k = 2$ we arrive at:

$$C_i^n + \frac{1}{2}\left(C_i^{\min} - C_i^n\right) < C_i^* < C_i^n + \frac{1}{2}\left(C_i^{\max} - C_i^n\right) \quad (45)$$

which is identical to the property found for the explicit predictor. This long derivation shows that the locally implicit scheme basically behaves like the explicit option. However, we have so far only half of the monotonicity proof, because a new and unexpected problem occurs: the sum of the coefficients of values of C is no longer correct after PSI reduction. This problem is addressed in the next paragraph.

D. A correct sum of coefficients

It is easy to see that our final linear system is in the form $S_i h_i^{n+1-\theta_i} C_i^{n+1} = S_i h_i^{n+1-\theta_i} C_i^* +$ other terms which all contain well balanced differences of values of C, for example $\Delta t \left(\max\left(Sce_i, 0\right)\left(C_i^{sce} - C_i^n\right)\right)$. It can be deduced by this that we have in the end $C_i^{n+1} =$ a correct interpolation of values of C, with the sum of coefficients equal to 1. This is however not the case if such balanced terms are reduced by a PSI limitation in an unbalanced way. In what precedes it is the case with the term:

$$\overleftarrow{-\Delta t \sum_j \left(\left(1-\theta_j\right) C_j^n - \left(1-\theta_i\right) C_i^n\right) \min\left(\Phi_{ij}^N, 0\right)}$$

The balance of $\left(1-\theta_j\right) C_j^n - \left(1-\theta_i\right) C_i^n$ is ensured by terms $-\theta_j C_j^{n+1} - \theta_i C_i^{n+1}$ and this is no longer the case after PSI reduction of only the explicit part. We are thus doomed to reduce only true differences of C values. In the case of term:

$$\overleftarrow{-\Delta t \sum_j \left(\left(1-\theta_j\right) C_j^n - \left(1-\theta_i\right) C_i^n\right) \min\left(\Phi_{ij}^N, 0\right)} \quad (46)$$

a solution consists in not upwinding all the terms, but only those that can be balanced in the PSI reduction, denoting:

$$\min\theta(i,j) = \min(1-\theta_j, 1-\theta_i) \quad (47)$$

we replace our term by:

$$-\Delta t \sum_j \left(\left(1-\theta_j - \min\theta(i,j)\right) C_j^n\right) \min\left(\Phi_{ij}^N, 0\right)$$

$$+\Delta t \sum_j \left(\left(1-\theta_i - \min\theta(i,j)\right) C_i^n\right) \min\left(\Phi_{ij}^N, 0\right) \quad (48)$$

$$\overleftarrow{-\Delta t \sum_j \min\theta(i,j) \left(C_j^n - C_i^n\right) \min\left(\Phi_{ij}^N, 0\right)}$$

This can be done at the element level when doing the PSI reduction.

E. Choosing the local semi-implicitation

Assuming that the classical condition of the explicit N scheme gives the limitation:

$$\Delta t_{stab}(i) < \frac{S_i h_i^n}{\left(flux(i) + \sum_j \Phi_{ij} + b_i - Sce_i\right)} \quad (49)$$

which is the condition 23 with $\theta = 0$, and prescribing a number of n steps into a time step Δt we now want for the implicit predictor-corrector:

$$\frac{1}{1-\theta_i}\frac{\Delta t_{stab}(i)}{2} = \frac{\Delta t}{n} \quad (50)$$

which yields:

$$\theta_i = \max(0, 1 - \frac{n\Delta t_{stab}(i)}{2\Delta t}) \quad (51)$$

To get the same implicitation as the one step semi-implicit N we thus just need to multiply the number of time steps by 2.

Choosing the N scheme, a number of corrections of 5, the height of the rotating cone after 1 rotation, depending on the number of substeps n, gives:

n	1	2	3	4	5	6	7
height	0.09	0.12	0.14	0.16	0.18	0.20	0.24

n	8	9	10	11	12	13	14
height	0.28	0.33	0.41	0.46	0.53	0.59	0.64

n	15	16	17	18	19	20	21
height	0.69	0.72	0.75	0.77	0.77	0.78	0.78

After $n = 20$ it gradually decreases, so 20 is an optimum. With $n = 20$, if we now vary the number of corrections we get:

corrections	1	2	3	4	5	6
cone height	0.54	0.71	0.76	0.77	0.78	0.79

corrections	7	8	9	10	11	12
cone height	0.79	0.79	0.79	0.79	0.79	0.79

Six iterations here already give an optimum result. It is noteable that we get a slightly better result than the previous predictor-corrector approach. It is due to the fact that we can now look for the better time stepping, independently of any stability condition.

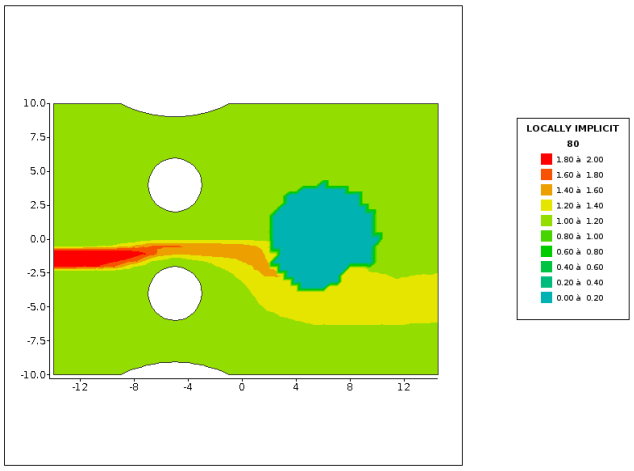

Fig. 3. The bridge pier test case with a tracer and an island.

V. A TEST CASE WITH DRY ZONES

The test case called "pildepon", a flow around bridge piers, in the portfolio of examples has been chosen, but the bottom has been modified so that a part of the domain is dry, thus forming an island. To achieve this a disc of radius 4 m has been carved out around the point of coordinates (6,0), by setting the bottom elevation at 5 m instead of 0. In Figure 3 the tracer on the island has been artificially set to 0 after the computation, to visualise the island. Otherwise the values are between 1 and 2, according to the initial and boundary conditions. The island contour is uneven due to the mesh roughness. Being a steady state, this case is not really meant for the predictor-corrector approach since the derivative in time is 0, but we show the ability of the locally implicit scheme to cope with dry areas. For this case the number of corrections is 0 and there is no sub-stepping.

VI. CONCLUSION

Thanks to a local semi-implicitation depending on the local stability condition we could eventually build a distributive advection solver with a number of interesting properties:

- Mass conservation
- Monotonicity
- Low numerical diffusion
- Ability to cope with dry zones
- Unconditional stability

The height of the cone after one rotation is now more than 3 times higher than what we get with the original PSI scheme, also higher than the method of characteristics. There is no extra problem with domain decomposition parallelism. The only drawback so far is the fact that there are linear systems to solve. Given the fact that the algorithm is potentially unconditionnally stable, the number of sub-steps, which was originally given by the stability analysis, is now a tuning parameter yielding more or less numerical diffusion. The number of corrections after the predictor step is also a parameter, but it seems that no more than 5 to 6 iterations is enough to get optimum results. A problem remains: the locally implicit scheme is only a first order scheme, because so far we could not get 2^{nd} order without getting non linear terms in the final system.

We shall now try to apply these ideas to 3D. It should not be too difficult, as we already know that the varying depth is replaced in 3D by the varying volumes around points, so that all our theory is readily applicable.

A potential improvement would be to avoid solving too many linear systems. In the corrector steps, taking advantage of the fact that a good predictor mass is not a problem, except for the last correction, it could be possible to downgrade the accuracy, or every correction could be considered as an iteration in a Newton-Raphson process, this is left for further researches.

REFERENCES

[1] HERVOUET J.-M., PHAM C.-T.: Telemac version 5.7, release notes. Telemac-2D and Telemac-3D. 2007.
[2] HERVOUET J.-M., RAZAFINDRAKOTO E., VILLARET C.: Telemac version 5.8, release notes. Telemac-2D, Telemac-3D and Sisyphe. 2008.
[3] HERVOUET J.-M.: Telemac version 5.9, release notes. Bief, Telemac-2D, Telemac-3D and Sisyphe. 2009.
[4] HERVOUET J.-M.: Telemac version 6.0, release notes. Telemac-2D and Telemac-3D. 2010.
[5] HERVOUET J.-M., RAZAFINDRAKOTO E., VILLARET C.: Telemac version 6.1, release notes. Telemac-2D, Telemac-3D and Sisyphe. 2011.
[6] ATA R., HERVOUET J.-M.: Telemac version 6.2, release notes. Telemac-2D, Telemac-3D. 2012.
[7] HERVOUET J.-M., PAVAN S.: Telemac version 6.3, release notes. Telemac-2D, Telemac-3D. 2013.
[8] http://www.opentelemac.org/
[9] HERVOUET J.-M.: Hydrodynamics of free surface flows, modelling with the finite element method. Wiley & sons. 2007.
[10] ABGRALL R., MEZINE M.: Construction of second order accurate monotone and stable residual distribution schemes for unsteady flow problems. Journal of Computational Physics. 188:16-55. 2003.
[11] RICCHIUTO M.: An explicit residual based approach for shallow water flows. Inria Research Report n°8350, Project-Team Bacchus, September 2013.
[12] TORO E.F.: Riemann Solvers and Numerical Methods for Fluid Dynamics. Springer, 2009.

QGIS as a pre- and post-processor for TELEMAC: mesh generation and output visualization

P. Prodanovic
Hydrotechnical Engineer
Riggs Engineering Ltd.
London, Ontario, Canada
pprodanovic@riggsengineering.com

Abstract— **This paper presents a summary of scripts named pputils that link QGIS to tasks common in numerical modeling of free surface flows, such mesh generation and visualization of model output. QGIS is an open source Geographic Information System under active development and supported under all major platforms. The scripts in pputils are written in the Python programming language relying on libraries Matplotlib, Numpy, and the Python parser scripts that are part of the TELEMAC source code. Mesh generation is accomplished by developing skeleton geometry within the QGIS environment (model boundary, constraint lines, islands, nodes, etc.) and exporting it to a WKT (well known text) format. The WKT format is then used by pputils to generate steering files for Triangle and Gmsh mesh generation programs. The meshing programs are then executed, and produce a mesh respecting user specified constraints. The bottom elevation and spacially varying friction attributes in the generated mesh are created and final output saved for further TELEMAC simulations. After the simulations are complete, the scripts in pputils take the TELEMAC output files and generate a set of gridded files (with a user specified resolution), thus allowing snapshots of the model output to be visualized within the QGIS environment. The same also applies to display of vector variables. Having model output available in the QGIS environment allows the user to create publication quality output of the TELEMAC simulation results.**

I. INTRODUTION

Increasing development of open source Geographic Information Systems (GIS) has had a marked impact in how spacial data is managed. By being open source, current GIS applications provide individual users with a real alternative to commercially available GIS packages. In recent years open source GIS has matured that it now allows users to perform a wide variety of spacial data management tasks using both vector and raster data. For example, open source GIS applications provide numerical modeling specialist a useful set of tools for vector based geometry manipulation (such as importing and editing shoreline features, creating model boundaries, adding constraint lines, islands, re-sampling polylines, etc.). Tasks that in the past would require a Computer Aided Design (CAD) packages, nowadays need only an open source GIS package. The open source GIS package relied upon in this work is QGIS [1]. Alternative open source GIS applications include SAGA [2] and GRASS GIS [3], GDAL [4] although there are others as well.

A typical free surface flow modeling project requires the user to collect, assemble, merge, and edit geometric data like topographic and bathymetric surveys, lidar data (masspoints and breaklines), digital elevation models, etc. Free surface modeling projects are defined here as those that study river or coastal hydraulics, sediment transport, wave climate analysis, water quality assessments, and others using 2D or 3D numerical modeling codes. Typical projects of this kind also require one to manage large data sets like aerial images, land use data, and other spacial databases. Such data sets are used in numerical modeling projects where the user is required to define model boundary, construct internal constraint lines, delineate islands or holes, and include other geometric features in the domain. Following geometrical edits, the next step is to apply a meshing algorithm to: i) construct terrain models (or digital surfaces) that are used as the basis for interpolating or assigning elevations, and ii) construct a quality model mesh for use in numerical simulations. After the input meshes are assembled, and bottom elevations and friction or other attributes are assigned to the mesh, the numerical simulations take place. Following completion of the numerical simulations, results of the models need to be conveyed, often to those not familiar with intricacies of numerical analysis. High quality graphical outputs are thus required to include in reports and provide the reader with a graphical summary of simulated behaviour under study.

Given the rapid development of open source GIS applications (QGIS in particular), the near future will likely allow all tasks typical in free surface modeling projects to be completed within a GIS environment. This means it would likely be possible to open a GIS package, import the necessary topographic and bathymetric data, build terrain models to represent surfaces, produce a quality mesh of a domain for use in simulations, interpolate the quality mesh from the generated surface, write model steering files, execute the numerical simulations, view model outputs, and prepare publication ready figures of the desired output.

No doubt, creating an interface envisioned above will require significant effort by many in the user community, but tools are now available that make this possible. There has been progress to date in the regard. Existing developments include the following projects:

- Lutra Constulting's Crayfish project [5], which allows visualization of hydraulic model output within the QGIS environment,
- ETH Zurich's BASEMENT hydraulic modeling system [6], and in particular its BASEmesh QGIS plugin that allows the user to create terrain surfaces, develop quality model meshes, perform necessary data interpolations, and prepare model geometry files all within QGIS,
- Uwe Merkel's TELEMAC Selafin Reader for QGIS [7], that allows visualization of TELEMAC model output within QGIS.

Each of the above projects has advanced use of using open source software in free surface modeling projects. They have served as both an inspiration and motivation for the development of pputils that are the focus of this paper. The main objective of pputils is to continue the trend in using open source software as both pre- and post-processors for use in free surface flow modeling projects.

One of the guiding principles that lead to the development of pputils was driven by the need to efficiently complete tasks typical in environmental flow modeling projects, and the desire to do so entirely using open source software. Use of commercially available software, or software that is free but not in open source, was not further considered.

The guiding criteria that was set when developing pputils were the following:

- All code must be entirely in open source,
- It must work on all common platforms,
- It must have absolute minimal dependencies and easy installation,
- It must be computationally efficient with minimal execution times, and
- All scripts must be executed using standard command line.

It is believed that if the above criteria are met, the tools developed could easily be incorporated in a future graphical user interface, and be integrated within an open source GIS environment like QGIS.

A. Scope of paper

This paper presents a summary of command line tools collectively named pputils that provide its users with an ability to complete all aspects of a typical environmental flow modeling project while using only open source software. Background information is provided on the open source software used, including QGIS, Triangle [8,9] and Gmsh [10] meshing programs, as well as Numpy [11] and Matplotlib [12] libraries part of the Python programming language. An illustration of the process used in the construction of meshes used in numerical simulations is presented, and includes geometric input preparation using QGIS (boundary definition, specifying mesh constraints, re-sampling polylines, etc.), development of Triangulated Irregular Networks (TIN) for terrain surfaces using Triangle, quality mesh generation using Gmsh, interpolation of quality mesh from a previously developed TIN, and creation of Selafin files for use in simulations using the TELEMAC modeling system. Visualization of the TELEMAC model output within QGIS is also illustrated, using both field and vector variables.

II. BACKGROUND

This section of the paper presents a brief overview of the tools relied by pputils. For example, open source QGIS application is required with which the user performs all geometrical edits, and prepare input files used by scripts in pputils. In this regard, QGIS is not used out of necessity, but simply out of convenience. It is possible for the user to create manually (in a simple text editor) all of the inputs required for say, mesh generation using Triangle and Gmsh. However, tasks like drawing and re-sampling polylines, joining, breaking, merging and otherwise editing polygons can be accomplished with relative ease using QGIS, that it becomes simply easier to use a graphical user interface than a text editor. As noted earlier, QGIS is used in this work, although no doubt the same tasks could be carried out using other GIS packages. Given the wide spread development of open source software, other users may find ways to accomplish same tasks differently, and perhaps more efficiently than is presented in this paper.

A. Open source GIS

The focus on this paper is on using QGIS on pre- and post-processing tasks associated with typical free surface flow modeling projects using the TELEMAC modeling system. QGIS is a free and open source Geographic Information System application that, in the most general sense, provides its users with editing, viewing and analysis of spacial data. QGIS has reached a mature status in its evolution, having a large number of volunteer developers who provide regular updates and bug fixes to the program. The application has been translated in approximately 50 languages, and is freely available on Windows, Mac and Linux operating systems.

QGIS also interfaces with other open source GIS packages, including GRASS, SAGA, GDAL and others, and thus provides its users with access to a wide range of geospacial tools all within one application. QGIS Plugins, which are commonly written in the Python programming language act to further customize and extend capabilities of QGIS. The Crayfish, BASEmesh and Selafin reader for QGIS projects are all plugins written to work inside QGIS.

B. Mesh generation for TELEMAC

Mesh generation for use in the TELEMAC modeling system requires high quality triangular meshes. A number of tools currently exist that accomplish this task. Perhaps the most popular in the TELEMAC user community is the BlueKenue application [13], developed by researchers at the National Research Council in Ottawa, Canada. BlueKenue is a pre- and post-processor for TELEMAC, with features to generate and interpolate meshes, and read and view model output. BlueKenue is free, but not in open source. It is available only on the Windows platform.

Another set of pre- and post-processors for TELEMAC (and other models) are Gismo, Janet, and Davit, developed by Smile Consult GmbH [14]. Gismo, Janet, and Davit allow their users highly advanced pre- and post- processing capabilities. The programs from Smile Consult are commercial applications and are available for Windows, Mac, and Linux platforms.

Open source mesh generation for TELEMAC is perhaps not as common as above applications. Triangle [8, 9] mesh generator, developed by JR Shewchuk at the University of California at Berkley, is available in its entirety as C source code from the author's website. Further, description of Triangle is given in [8]:

"Triangle is a C program for two-dimensional mesh generation and construction of Delaunay triangulations, constrained Delaunay triangulations, and Voronoï diagrams. Triangle is fast, memory-efficient, and robust; it computes Delaunay triangulations and constrained Delaunay triangulations exactly. ... Features [of Triangle] include user-specified constraints on angles and triangle areas, user-specified holes and concavities, and the economical use of exact arithmetic to improve robustness" p. 203.

After compiling Triangle, the program is executed from the command line, with the user specifying a number of parameters and input files. The BASEmesh QGIS plugin, is one variant of pre- and post-processor to the Triangle mesh generator. Another is pputils script (gis2triangle.py), described in the subsequent section of this paper.

Another open source triangular mesh generator is Gmsh [10], developed by Christophe Geuzaine and Jean-François Remacle, at the Université de Liège, Belguim. Gmsh is an all purpose 2D and 3D finite element mesh generator (more than just triangular meshes are included), with a built-in GUI CAD engine for pre- and post-processing. Gmsh's GUI is developed using FLTK GUI toolkit, making it extremely fast, light while at the same time providing its users advanced graphical input and visualization features. The Gmsh program is available as open source, and is supported in Windows, Mac and Linux. The GUI has four different modules: geometry, mesh, solver and post-processing. Geometry for Gmsh can be generated interactively using its GUI, or be imported from external files using a number of different formats. Geometry can also be developed using Gmsh's text based steering files.

Previously, Dr. Olivier Gourgue at the Flanders Hydraulic Research developed a set of post-processing scripts using Matlab named PUG [15] that are able to convert Gmsh output to the Selafin format for use in TELEMAC simulations. The PUG scripts also produce the TELEMAC *.cli boundary conditions files.

C. Python programming language

In order to create a link between QGIS and mesh generation programs Triangle and Gmsh, a script is needed to convert GIS geometry and create a steering file understood by each respective meshing algorithm. Further, scripts are also needed to extract TELEMAC simulation output and port it back to QGIS.

Package Numpy, used for scientific computing on the Python language was heavily used in the development of pputils scripts. Numpy's vectorized implementation of common functions ensured that tasks involving numerical calculations are executed extremely efficiently, with minimal waiting times for the user. Using Numpy, rectangular grids can be generated using tens of millions of cells in a matter of seconds using just today's desktop computers.

The Python library Matplotlib was also heavily relied upon in pputils, specifically its triangulation and gridding algorithms. Matplotlib is a plotting library and is a numerical extension of Numpy. Using Matplotlib triangulation algorithms allowed scripts in pputils to carry out conversion tasks (such as converting TELEMAC's simulation output to a gridded format used by QGIS).

Python provides functionality of a general scripting language with excellent libraries used for numerical analysis, thereby making it an extremely useful tool for general scientific analysis of data. Since Python programming language is used by both QGIS and TELEMAC, it seems natural that it also be used as a scripting language to link QGIS and TELEMAC.

III. Mesh Generation

There are at least two different types of meshes commonly used in free surface flow modeling projects. One deals with the generation of digital terrain surfaces or Triangulated Irregular Networks (TINs) from topographic, bathymetric, lidar and other digital data. TINs are used to represent digital surfaces of table lands, rivers or sea beds, and are used for, among other things, as a basis for interpolating (and assigning elevations) to the quality mesh to be used in numerical simulations. The other kind of mesh is the quality mesh on which numerical simulations are carried out. Regardless of the type of mesh the user wishes to generate, input data preparation is very similar. A skeleton geometry (meaning boundary polygon, constraint lines, islands or holes, and/or embedded nodes) must be prepared first.

A. Input preparation using QGIS

This section illustrates how to use the open source QGIS application to develop skeleton geometry used for mesh generation. The scripts in pputils will take the skeleton

geometry, do some format conversions, and then generate steering files for both Triangle and Gmsh mesh generation programs. It will be up to the user to launch these programs, and generate triangular meshes. More on this process is provided below.

The logic in how data management is used in pputils parallels the data management structure used by the BASEmesh QGIS plugin. There are some differences, of course. First, the user is required to define a polyline representing the boundary of the mesh domain. A required condition is that the boundary polyline be a closed shape, implying that the same coordinate be used as starting and ending point. Second and optional, internal constraint lines are developed, and can be either closed or open polylines. Third and optional, islands (or holes) in the domain are defined using closed polylines. Finally, the user must define a master nodes file, which contains vertices of all of the boundary, constraint, and island (if any) files. Creation of the master nodes files in QGIS is rather simple, as the user is required to merge all of the polylines, extract their vertices as individual nodes, and save the file as a text based xyz format. If there are to be embedded nodes in the mesh (as would be the case in the generation of digital surfaces or TINs), the nodes file must include these, in addition to the vertices of the boundary polyline, lines and islands. The inherent assumption in the above procedure is that all of the polyline vertices must snap (within a reasonable horizontal tolerance) to the coordinates of the master nodes file. Note that only the master nodes file contain xyz attributes), while the boundary, line constraints, and holes files contain shapeid,x,y attributes. The scripts that generate the mesh generation steering files for Triangle and Gmsh use sophisticated searching algorithms that look up the z value from the master nodes file for all boundary, lines, and island files (if any).

The user is required to save within QGIS individual files, according to the formats specified. For the master nodes file, an xyz, comma separated file suffices. For the boundaries, lines, and hole files, the easiest is to save each as a WKT (well known text) format within QGIS. A script within the pputils named wkt2csv.py takes the files in WKT format, and converts them to a shapeid,x,y comma separated format used by pputils.

In summary, before going to mesh generation, the user prepares nodes.csv (required), boundary.csv (required), lines.csv (optional) and holes.csv (optional) files.

B. Triangulated Irregular Network (TIN) using Triangle mesh generator

As a note of completeness, pputils use a slightly different format for specification of holes for use in the Triangle mesh generator. Simply by virtue of the requirements of the Triangle's steering file, the boundary of the holes should be included as closed lines in the lines file, and point coordinates (holeid,x,y) within hole boundary must be included in the holes file. Examples provided with the pputils source code explain this further.

In order for the user to generate a TIN surface using the Triangle mesh generator, the following files are required:

1. nodes.csv (containing a list of all nodes in xyz format, comma separated),
2. boundary.csv (containing comma separated node listings of mesh boundary, specified as shapeid,x,y),
3. lines.csv (optional, containing comma separated constraint lines or breaklines, specified as shapeid,x,y). If there are holes, they should be specified as closed lines in the lines file.
4. holes.csv (optional, containing comma separated point file with holeid,x,y attributes). x,y coordinates should be placed inside the hole closed polyline.

After creating the above files, the user creates the Triangle steering file by executing the following Python script:

```
python gis2triangle.py -n nodes.csv -b
boundary.csv -l lines.csv -h holes.csv -o
out.poly
```

If there are no lines or holes files needed, the user simply enters 'none', without the quotes as the -l and -h argument to the script.

The file out.poly is generated that is a steering file for Triangle. To generate the TIN mesh, the user executes the Triangle mesh generator using previously compiled binary program:

```
triangle_64 out.poly
```

Where triangle_64 is the Linux 64 bit version of the Triangle mesh generator. The compiled binaries in pputils also provide triangle_32 and triangle_32.exe, and represent Linux 32 bit and Windows 32 binaries.

The above command generates out.1.node, out.1.ele and out.1.poly text based files. A script in pputils takes these and creates an Adcirc based mesh:

```
python triangle2adcirc.py -n out.1.node -e
out.1.ele -o out.grd
```

Where the out.grd is the TIN in Adcirc mesh format. The Adcirc format was selected for use in pputils as it is a simple text based mesh file.

Suppose the user wishes to convert the out.grd TIN file to a regular *.asc gridded file (often referred to as the digital elevation model or DEM), the following would be executed:

```
python adcirc2asc.py -i out.grd -s 10 -o
out.asc
```

Where the out.grd is the Adcirc TIN file generated above, -s parameter is the output grid spacing in meters (10 m in above example), and -o parameter is the resulting output DEM file. The Matplotlib library is used to read the triangulation from the TIN file, and create a gridded DEM file. The *.asc file can easily be loaded into QGIS, or be used in input to other gridded based numerical simulation applications (like the SWAN wave model for example).

Testing was done by reducing the grid resolution and producing a DEM with tens million grid points. The processing for this task took in the order of seconds on a desktop computer due to vectorized Numpy and Matplotlib functions.

Lastly, should the user wish to display the mesh within the QGIS environment, the following script should be used:

```
python adcirc2wkt.py -i out.grd -o
outWKT_e.csv outWKT_n.csv
```

Where the outWKT_e.csv and out WKT_n.csv files are WKT (well known text) format output of the elements (as polygons) and nodes (as points) that can be easily loaded into QGIS.

Alternatively, the following script could be used to create a *.dxf file of the Adcirc file:

```
python adcirc2dxf.py -i out.grd -o out.dxf
```

Where -i represents the input Adcirc file and -o is the output file written in *.dxf format.

An example output of the TIN model of the bathymetry of Lake Manitouwabing, located in northern Ontario, Canada is shown in Figure 1 (global view) and Figure 2 (zoomed in view).

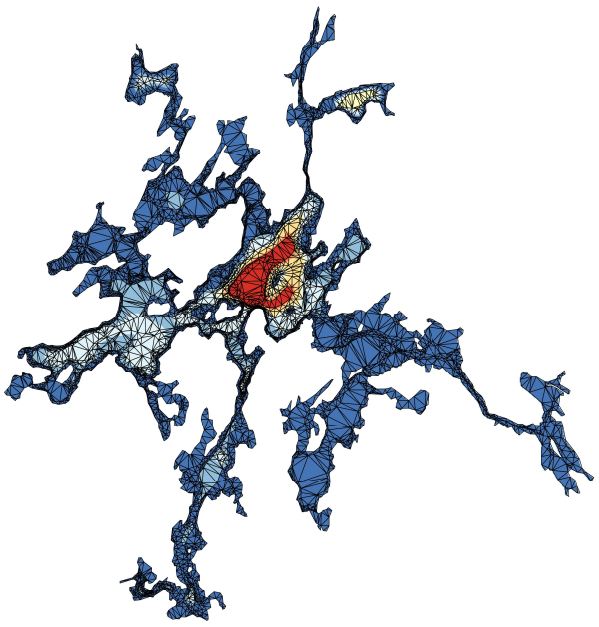

Figure 1: Lake Manitouwabing TIN generated by Triangle

Even though this section uses the Triangle mesh generator to generate a TIN, Triangle can also be used to create a quality mesh for use in numerical simulations. The interested user is thus directed to documentation of Triangle which covers command line flags and input parameters used to produce a quality based mesh. Note the same steering file generated by gis2triangle.py would be used as a starting point towards this task.

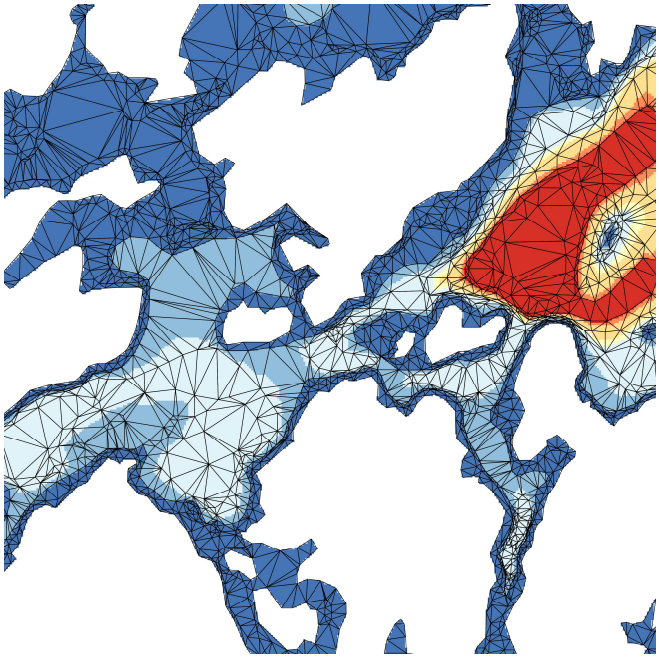

Figure 2: Close up of Lake Manitouwabing TIN

C. Quality mesh generation using Gmsh mesh generator

As an alternative to Triangle, the user is also given the option to use the Gmsh mesh generator. In the same way as Triangle, the user is expected to prepare the following input files:

1. nodes.csv (containing a list of all nodes in xyz format, comma separated),
2. boundary.csv (containing comma separated node listings of mesh boundary, specified as shapeid,x,y),
3. lines.csv (optional, containing comma separated constraint lines or breaklines, specified as shapeid,x,y). The lines can be either open or closed lines,
4. holes.csv (optional, containing comma separated hole or island closed polylines specified as holeid,x,y).

To generate a steering file for use in Gmsh, the user would use the following script:

```
python gis2gmsh.py -n nodes.csv -b
boundary.csv -l lines.csv -h holes.csv -o
out.geo
```

As before, if there are no lines or holes files the user simply enters 'none' without the quotes as the -l and -h flags in the script. pputils assumes the refinement of the Gmsh mesh (i.e., how mesh grows from small to large elements) is controlled by the spacing of the nodes in the boundary, lines and/or hole files. This is only one way of specifying mesh growth in Gmsh. There are others as well. The interested user is directed to the Gmsh model documentation for more information on this subject.

The file out.geo is a steering file for Gmsh. To generate the quality mesh using the command line, the user could execute the following:

```
gmsh -2 out.geo
```

Where the -2 option specifies that the 2d triangular mesh is to be generated. Alternatively, the user is also given the option to launch the Gmsh GUI (which is available in Linux, Mac and Windows) and open the out.geo steering file. Immediately upon opening the Gmsh GUI, the user will see the skeleton geometry (that was originally created in QGIS). Once in the Gmsh GUI, the user can further edit the meshing parameters (select how mesh grows, place attractors, etc.). Please refer to the Gmsh user documentation for further details.

Execution of the Gmsh program produces the out.msh file, which is a Gmsh formatted mesh file. The following script in pputils converts it to the Adcirc mesh file:

```
gmsh2adcirc.py -i out.msh -o out_gmsh.grd
```

Where out.msh is the Gmsh generated mesh file, and the out_gmsh.grd is the same mesh in the Adcirc format.

Once the mesh is in the Adcirc format, the user can use adcirc2wkt.py script (see above) to create WKT format of the element polygons and node points for viewing the mesh within QGIS. Alternatively, the user can convert the Adcirc format to a *.dxf file using adcirc2dxf.py for mesh visualization using existing CAD based packages.

An example of using Gmsh is shown in Figure 3, where the generated mesh was used in the simulations nearshore sediment transport at Wheatley Harbour, Lake Erie.

D. Interpolation of quality mesh from a TIN

Suppose now that we have a TIN file (generated by Triangle), and converted to an Adcirc format (tin.grd) and also the quality mesh generated by Gmsh, also in Adcirc format (mesh.grd). The task now is to assign elevations to every node of the mesh.grd file from the tin.grd file.

The following script in pputils does just that:

```
python interp.py -t tin.grd -m mesh.grd -o
mesh_interp.grd
```

Where the mesh_interp.grd is the quality mesh with node z values interpolated from the TIN file. Matplotlib library is used to recreate the triangulation of the TIN, and assign the z values to quality mesh. Note that the mesh must entirely be within the boundary of the TIN. If this is not the case, a warning message is displayed at the prompt informing the user of this fact.

Of course, the user could easily have used Fudaa [16] or BlueKenue to carry out the task of interpolation as well.

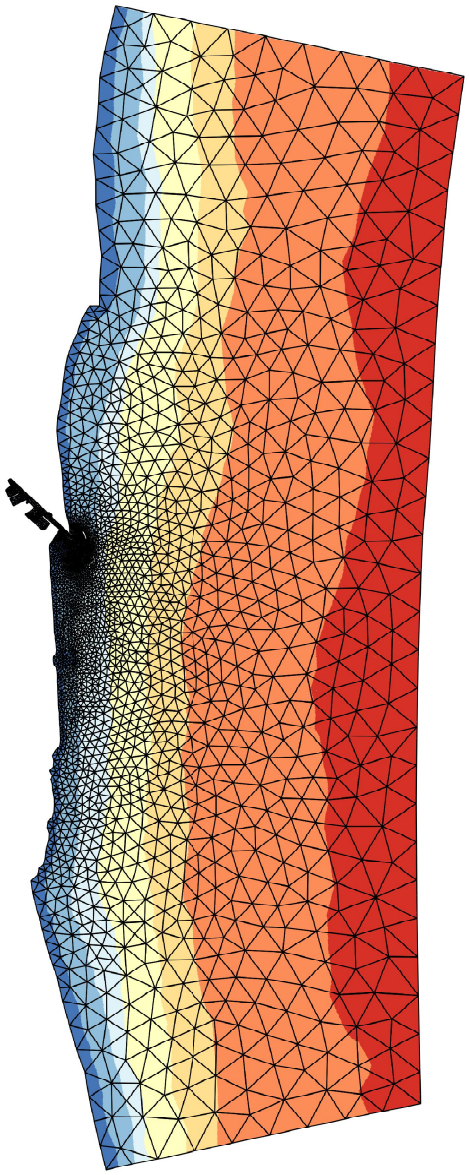

Figure 3: Nearshore mesh around Wheatley Harbour, Lake Erie, Ontario, Canada

E. Creation of Selafin files for use in TELEMAC simulations

Once the mesh_interp.grd Adcirc file is generated, the last step in the procedure is for the user to convert the Adcirc file to the Selafin format. There are at least three of the existing tools available to the TELEMAC user community that will do this. The user can:

1. Use Fudaa pre-processor, and convert Adcirc to Selafin mesh,
2. Use BlueKenue to import the Adcirc mesh, and save the imported mesh to Selafin format.
3. Use STBTEL program (part of the TELEMAC source code) to convert Adcirc to Selafin format.

There is an example in the validation cases on how to convert Adcirc mesh to Selafin mesh. After generating the Selafin files, the user then proceeds with numerical simulations using the TELEMAC modeling system.

IV. TELEMAC OUTPUT VISUALIZATION USING PPUTILS

Following completion of the numerical simulations using the TELEMAC system the user can port the output to QGIS using scripts in pputils. Please note however, that pputils output visualization is never intended to replace visualization that is typically done with BlueKenue, Fudaa, Davit, etc. At present time scripts in pputils are only meant to take select TELEMAC output (at key time steps), and generate publication style graphical output for use within the QGIS environment. Simulation output can then be overlaid with aerial photos, and annotated with labels, arrows, etc.

In order to get the TELEMAC output to QGIS, pputils relies on the Python parser scripts that are already part of the TELEMAC source code. For easy portability, the Python parser scripts (used for reading and writing TELEMAC data) have been copied and are included in the pputils distribution. The disadvantage of this is that a TELEMAC user will have these scripts in two places (one part of TELEMAC and one part of pputils). However, the advantage of including the Python parser scripts provides for easy installation, allows use of pputils without the need to update system path variables. A further advantage of including a copy of the Python parser scripts is that pputils can act as a standalone set of utilities, and could be open to more than just TELEMAC users. For example, those using Adcirc and/or SWAN could also benefit from them as well.

A. Displaying field variables

Displaying TELEMAC field variable (such as depths, velocity magnitudes, wave heights, etc.) with pputils is achieved by first probing the TELEMAC result file (assumed as result.slf) with the probe.py script, as follows:

```
python probe.py -i result.slf
```

Where -i represents the input file to probe. The output of the probe.py script simply tells the user what variables are saved in the result file, and what time steps are included. Most importantly, the probe.py script outputs the index of the variables and index of the time steps in the result file. An example of execution of the probe.py script on an existing output of the Telemac-2d simulation would be as follows:

```
The input file being probed: result.slf
Variables in result.slf are:
--------------------------------
     v     variable name
--------------------------------
0 --> VELOCITY U
1 --> VELOCITY V
2 --> WATER DEPTH
3 --> FREE SURFACE
4 --> BOTTOM
5 --> WIND ALONG X
6 --> WIND ALONG Y
7 --> COURANT NUMBER
number of records in input file : 25
--------------------------------
t        time (s)
--------------------------------
0 -->       0.0
1 -->    3600.0
2 -->    7200.0
3 -->   10800.0
     ......
24-->   86400.0
```

Suppose that the user wishes to display in QGIS the field variable free surface (-v index of 3) one hour into the simulation (-t index of 1 corresponding to simulation time 3600 s). The following pputils script would be executed:

```
python sel2asc.py -i result.slf -v 3 -t 1 -s
2.0 -o output.asc
```

Where -s parameter represents the grid spacing in meters (2 m grid spacing in above example). The sel2asc.py script parallels the adcirc2asc.py script, where Matplotlib reads the triangulation from the TELEMAC output file, and creates a gridded DEM file of the specified output variable for a specified time step using specified grid spacing.

B. Displaying vector variables

In order to display the vector variables within QIGS, the Field Renderer plugin [17] developed by Chris Crook out of New Zealand is used. The Field Renderer plugin requires the position (x and y) along with u- and v- components of the vector variable to be loaded as points within QGIS. In other words, it needs x, y, u, v points file. The pputils script extract.py is used to write this data from the TELEMAC results file. Suppose the user wishes to display within QGIS the velocity vectors for time step 24 (corresponding to simulation time 86,400 s), the following would be required:

```
python extract.py -i result.slf -v 0 1 -t 24
-o output.txt
```

Where -i is the Selafin result file to extract from, -v 0 1 are the indexes of the u- and v- component of the velocity vector (see output of probe.py above), -t is the time step to extract, and -o is the resulting text based output file containing x, y, u, v for each node in the Selafin file of the model results. The output.txt file is then loaded into QGIS, and the Field Renderer plugin is used to display the vector field within the QGIS.

An example of using the sel2asc.py and QGIS Field Renderer is shown in Figure 4 to display flood depths and velocity vectors during for a simulation of a flood wave of an urban area in London, Ontario, Canada using Telemac-2d.

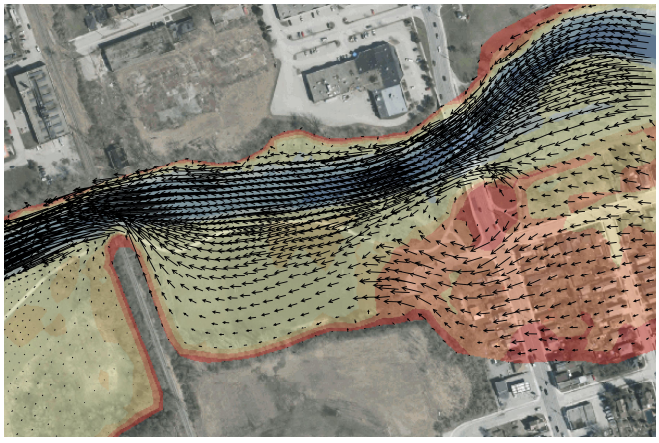

Figure 4: Flood depths and velocity vectors of an urban flood simulation using Telemac-2d at London, Ontario, Canada

C. *Future developments*

The post-processing of TELEMAC output using pputils are able to display single snapshots of field and vector variables for use in QGIS. At the present time, the intent of the post-processing features within pputils is to facilitate select graphical output for in QGIS for the preparation of reports and publication quality figures. To that end, having a small number of plots, overlaid with aerial photos and annotated with text, suffices.

Future developments may include different ways of visualizing 2d simulation model output in QGIS, and could include a full fledge post-processor with full animation control, extraction of cross sections, time series displays at select nodes, etc.

Note that pputils is work in progress, and will continually be refined and updated. The files included in the distribution also include a number of examples, which will assist the user in applying the code to their domains. pputils can be downloaded from the following links:

https://drive.google.com/open?id=0B7ZAQzSQW0q-NDlwbXBnbm1weUU

V. CONCLUSIONS

This paper presents a set of tools named pputils intended to be used for pre- and post-processing used in typical free surface flow modeling projects (mesh generation, digital surface creation, interpolation of mesh, display of model output). The main goal of the pputils project is to present the interested user with a set of tools that will allow the completion of an entire free surface flow modeling project from start to finish using only open source software. With this respect, pputils are able to achieve just that.

REFERENCES

[1] QGIS Development Team. QGIS Geographic Information System. Open Source Geospatial Foundation Project, 2015. http://qgis.osgeo.org.

[2] O. Conrad et al. “System for Automated Geoscientific Analyses (SAGA) v. 2.1.4”, Geoscientific Model Development, vol 8, pp. 1991-2007.

[3] GRASS Development Team, Geographic Resources Analysis Support System (GRASS) Software. Open Source Geospatial Foundation Project, 2015. http://grass.osgeo.org.

[4] GDAL. Geospatial Data Abstraction Library: Version 2.0.0, Open Source Geospatial Foundation, 2015. http://gdal.osgeo.org.

[5] Lutra Consulting Development Team, Crayfish QGIS plugin, 2015. http://www.lutraconsulting.co.uk/products/crayfish.

[6] D. Vetsch et al. “System Manuals of BASEMENT, Version 2.5”. Laboratory of Hydraulics, Glaciology and Hydrology (VAW), ETH Zurich, 2015. http://www.basement.ethz.ch.

[7] Uwe Merkel Consulting Engineers, TELEMAC Selafin Reader for QGIS, 2015. http://www.uwe-merkel.com/wordpress.

[8] J.R. Shewchuk, “Triangle: Engineering a 2D Quality Mesh Generator and Delaunay Triangulator”, in “Applied Computational Geometry: Towards Geometric Engineering” (M.C. Lin and D. Manocha, editors), volume 1148 of Lecture Notes in Computer Science, Springer-Verlag, Berlin, 1996, pp. 203-222.

[9] S.W. Cheng, T.K. Dey, and J.R. Shewchuk, Delaunay mesh generation, CRC Press, 2012.

[10] C. Geuzaine and J.F. Remacle, “Gmsh: a three-dimensional finite element mesh generator with built-in pre- and post-processing facilities”, International Journal for Numerical Methods in Engineering, 2009, vol 79, no 11, pp. 1309-1331.

[11] S. van der Walt, S.C. Colbert and G. Varoquaux, “The NumPy Array: A Structure for Efficient Numerical Computation”, Computing in Science & Engineering, 2011, vol 13, pp. 22-30.

[12] J.D. Hunter, “Matplotlib: A 2D Graphics Environment”, Computing in Science & Engineering, 2007, vol 9, pp. 90-95.

[13] National Research Council of Canada, BlueKenue: software tool for hydraulic modelers, Ottawa, Ontario, Canada, 2015, http://www.nrc-cnrc.gc.ca/eng/solutions/advisory/blue_kenue_index.html.

[14] Smile Consult GmbH, Janet, Gismo and Davit pre- and post processors for free surface numerical models, 2015, http://smileconsult.de.

[15] O. Gourgue, Pre- and post-processing of Unstructured Grids (PUG), 2015, http://www.oliviergourgue.net/pug.

[16] Fudaa, Object Oriented and Distributed Integration Platform For Scientific Codes, 2015, http://sourceforge.net/projects/fudaa.

[17] C. Crook, QGIS Vector Field Renderer plugin, 2013, https://github.com/ccrook/QGIS-VectorFieldRenderer-Plugin.

The TELEMAC's automated management and continuous integration and validation system

Dr Sébastien E. Bourban [1]
s.bourban@hallingford.com

Juliette C. Parisi [1]
j.parisi@hallingford.com

Alain Weisgerber [1]
a.weisgerber@hallingford.com

[1] HR Wallingford, Howbery Park, Wallingford, UK, OX10 8BA

Abstract— Testing and validation of scientific codes is time consuming but critical and even more so for industrial uses. It is paramount that TELEMAC follows a strict testing and validation programme for every release to maintain its quality standard. An automated continuous integration system (CIS) has been put in place by HR Wallingford to allow continuous testing, validation and monitoring of TELEMAC. The CIS is constituted of a myriad of python scripts compiling, running and verifying the performance of TELEMAC. These scripts are run across several virtual computers for over two hundred cases. They extract time series, values, cross-sectional data, generate figures, assemble table data, and validate extracted data against criteria to produce validation reports packaged into archive files for upload on the distribution website. This allows testing and validation to be carried out natively on each operating system, ensuring maximum compatibility and performance with known industry uses.

I. INTRODUCTION

TELEMAC is a suite of scientific codes developed as interconnected modules, each representing one or more aspects of the real world of free surface environmental hydraulics. Wave, sediment and hydraulic modules are available independently or combined as complex 2D or 3D systems, applicable to a wide range of real challenges such as coastal evolution, urban inundations, river mitigation, thermal and desalination outfalls, harbour wave agitation, renewable energy resource assessment, ports layout and dredging master planning to name only a few. These scientific codes are entirely written in standard Fortran.

Surrounding TELEMAC, and also distributed as open source codes, an ensemble of pre- and post-processing scripts entirely written in standard Python have been developed by HR Wallingford over the last 5 years. While users can add their own Fortran code to TELEMAC for particularly tricky simulations, they are likely to use – without necessarily noticing – the Python scripting codes to run their simulations, extract data or create figures. The principal objective of this Python initiative was to provide: (a) a robust and simple platform-independent scripting interface to TELEMAC users; (b) a first building block for future plugins to existing graphical user interfaces such as QGIS [7]; and last but not least (c) a library of generic scripting tools for the validation of TELEMAC.

The latter is the main subject of this article. Testing and validating scientific codes is time consuming but critical to maintain quality standards for industrial, commercial and research uses. An automated continuous integration system (CIS) has, therefore, been put in place by HR Wallingford to allow continuous testing, validation and monitoring of TELEMAC. Over the last 5 years, the CIS has grown to be one of the principal purposes of the Python scripting codes, and now groups scripts compiling, running and verifying the performance of TELEMAC across several virtual computers for over two hundred test cases.

However, because writing a Fortran or Python program for the analysis of each test case would be unnecessarily complex and result in duplication of codes, the simpler mark-up language XML was chosen to steer and define actions and procedures. Similarly to the role taken by the simpler CAS file (steering a TELEMAC simulation based on a list of keywords and values), the XML file steers what analysis is to be carried out during the validation procedure based on a list of tags and value fields. From the design stage, it was critical to develop definitions of analyses that were sufficiently generic to be applicable to as many test cases as possible – enabling the system to grow in number of test cases – and to develop a system that was sufficiently generic to include as many types of analysis as possible – enabling the system to grow in number of analyses. The XML files fulfil these roles, keeping the obscure Python scripting codes transparent to users.

This article describes in detail the procedure put in place to monitor any given modification to the TELEMAC source code. Specifically, Chapter II explains the terminology, illustrated by the types of verification and validation tests carried out for TELEMAC. Chapter III distinguishes the components of the automated system and the automation itself. Chapter IV details several examples of the XML steering files and possible uses of these by users outside the validation system. It should be emphasised, that the number and nature of test cases widen continuously, and that the examples presented here are not meant to form an exhaustive list.

II. A VALIDATION SYSTEM

A. Terminology

To start with, it must be stressed that the TELEMAC automated validation system developed and maintained by HR Wallingford aimed not only at its validation but also at the verification of its implementation and at measuring its accuracy. Because TELEMAC is applied to a wide range of problems including environmental assessment, industrial designs and civil engineering, it was critical to design a system continuously checking that TELEMAC does the right thing and that it does things right. For clarity, the definitions are introduced below.

1) Accuracy

Accuracy is a mathematical measure based on the numerical analysis of convergence, whether and how, discrete solutions (unstructured mesh) converge to known solutions when the space discretisation tends to the continuum (infinitely small triangles). Further, the rate of convergence defines the order of accuracy of the numerical code, where higher order codes would conserve more properties (such as energy) and be capable of larger and longer predictions.

2) Verification

Verification of a numerical code establishes whether it accurately implements what it is supposed to do (does things right), from a developer viewpoint.
For reference, Roaches [1] details and opposes various definitions of accuracies and associated errors and ties order accuracy to the verification process, or solving the equation right, whether or not the equation and its solutions bear any relation to a real world problem.
The verification of TELEMAC, therefore, includes verifying the quality of the code implementation and its reproducibility on computing platforms as well as measuring its accuracy against analytical solutions. Analytical solutions are often developed under particular assumptions (hydrostatic pressure, linearity of the operators) departing them somewhat from the real world applications.

3) Validation

The validation of a numerical code establishes whether the code accurately represents the real world (does the right thing) from a user viewpoint.
The validation of TELEMAC, therefore, includes validating simulation results against observations from physical modelling experiments or from real world events at specific sites, or against measures of know quantities such as mass and energy extracted at points or integrated over volumes of cross-sections.
Having said that, the rest of this article describes the validation of TELEMAC in a loose sense to include all notions, based on a variety of over two hundred test cases, continuously growing in number.

B. Illustrations

As mentioned previously, each test case of the system undergoes several validating (and verifying) analyses. Some analyses are applicable to all test cases (on the side of verification) while some are applicable only to a few test cases (on the side of validation). The following introduces the types of analyses carried out automatically by the validation system as detailed in Chapter III. Chapter IV provides examples of how these analyses are implemented.

1) Platform independent (verification)

The development of TELEMAC is subject to a long list of programing and quality standard rules, one of which is that it should remain platform independent. The user is free to choose any hardware, networking architecture, any operating system or any Fortran compiler.
The TELEMAC automated validation system has, thus, been setup to run simultaneously the same analyses on multiple computing architectures, under multiple operating systems and for multiple compilers. Chapter III explains how this is done, and how this is done automatically.

2) Reproducibility if not improvement (verification)

Another rule guiding the development of TELEMAC is that any new changes to its source code should at best improve the overall quality and robustness of TELEMAC (faster computation, closer comparison against experimental data, smaller numerical diffusion, etc.) or at worst keep previous results and execution time unchanged.
For this purpose, for every test case, there exists a reference result file created from a previously validated version of TELEMAC, which is compared against new results produced following changes to the source code.
The TELEMAC automated validation system has been setup to warn the developers if the results have changed by more than the machine accuracy, or to fail the validation if these have changed by more than a specified small value. Chapter IV provides an example of this sort of verification as XML code.

3) Parallel compatibility (verification)

Yet another rule guiding the development of TELEMAC is that any new changes to its source code should be compatible with execution in parallel – based on domain decomposition – whether on a network of computers or within a High Performance Computer facility.
For this purpose, virtually all test cases are set as pairs, of which one case runs on one compute core and the other runs on multiple compute cores.
Similarly to the reference file, the TELEMAC automated validation system warns the developers if the results between parallel and serial modes are different by more than the machine accuracy, or fails the validation if these are different by more than a specified small value. Chapter IV provides an example of this sort of verification as XML code.

4) Analytical solutions / approximations (verification)

Under certain circumstances (say wave oscillations in a tank), assumptions can be made (say 1D problem, linearized shallow water equations) to sufficiently simplify the problem (underlying differential equations) and develop an analytical solution. The analytical solution could be explicit or implicit. As long as the simplified problem is a valid approximation of the original problem, a comparison can be made with the

analytical solution.
The TELEMAC automated validation system has, thus, been designed and setup to include directly in the XML steering file the implementation of these analytical solutions and their comparison with data extracted from TELEMAC results. Chapter IV provides an example of this sort of verification as XML code.
Alternatively, the analytical solution could also be computed with the Fortran codes of TELEMAC, when it exists over the entire temporal and spatial domains. Its output together with the simulation results can then be exploited by the XML steering file.

5) Experimental comparison (validation)

Thanks to measurements made during physical modelling experiments and published by several research laboratories, a comparison can be made with TELEMAC under controlled environments at the appropriate physical scale. The purpose of physical modelling experiments is usually to validate specific aspects of a physical process by controlling the properties of the materials or the driving forces or the initial state of the experiment, thus limiting the number of possible unknowns influencing the outcome.
The TELEMAC automated validation system has, therefore, also been designed to include these sorts of comparisons. The XML file includes first a task to load the experimental data file, then to run the TELEMAC simulation of the experiment, to extract results at the same locations and time step and to report the comparisons. Chapter IV provides an example of this sort of validation as XML code.

6) In-situ observations (validation)

Similarly to measures obtained from physical modelling experiments, measures from in-situ observations can be made available, for instance when the project assessing the site is not commercially sensitive or confidential. However, the real environment is more complex with inputs and forces driven by external factors that are either less predictable or not measureable.
The same XML steering file developed for data obtained from physical experiment could be re-used for in-situ data. The sole difference is in choosing a less stringent target comparison accuracy or even only assess the agreement visually on the basis of a comparative figure to account for uncertainties in the model inputs.

7) Other analyses (verification)

The continuous integration and validation of TELEMAC is based on a large number of test cases, where each test case undergoes a large number of analyses. All validation test cases and their XML steering file are provided as open source with the rest of TELEMAC.
Several other analyses, also carried out automatically by the automated continuous integration and validation system, will not be detailed in this article as they do not show more features than what is already presented. A few are listed here:

a) Integrated quantities. The system is designed to test integrated quantities such as the conservation of quantities (water, tracers, sediments, wave energy).

b) Numerical processes. Numerical convergence (through mesh and time step refinement) can also be tested by the system, as well as the numerical properties of certain schemes, e.g. numerical diffusivity and order of accuracy.

c) Code quality. Python scripting codes have been developped to check whether changes to the Fortran of TELEMAC follows the standard programming rules.

d) Packaging. The automated management system is also designed to package releases of TELEMAC once the validation has been completed. Whilst the source code is accessible to all through the subversion site, pre-compiled binaries for various operating systems can be compiled and zipped as one file to be published through the ftp site. The packaging of TELEMAC also includes the automated PDF-ing of its user documentation and the automated generation of its source code documentation site.

III. AN AUTOMATED SYSTEM

A. Setting up a network of websites

While preparing for an open source distribution, one of the ambitions of the TELEMAC consortium was to increase the number of users from a few hundreds to a few thousands – something that was achieved within two years. Another ambition was to facilitate the integration and validation of developments carried out by organisations outside the TELEMAC consortium. As a consequence, it was clear that the management of TELEMAC had to be streamlined, optimised and automated from logging and documenting changes in the scientific and scripting codes to distributing public releases.

With that said, HR Wallingford took the responsibility to put in place and host a number of websites, including:

- The source code repository (svn.opentelemac.org) to establish the traceability of the source code based on Subversion SVN [2];
- The participative user and developer documentation site (wiki.opentelemac.org) based on dokuwiki [3];
- The code documentation site (docs.opentelemac.org) based on the processing tool doxygen [4]; and
- The project management site (cue.opentelemac.org) based on the framework RedMine [5], to track feature developments, to plan eventsand foster exchanges of ideas, peer reviews and trace communications between organisations.

Furthermore, HR Wallingford carried out a review of available open source technologies and eventually decided on the development of yet another website to automate most of the TELEMAC management tasks. Inspired by other open source software engineering and management platforms, a continuous integration system (CIS) based on the framework Jenkins [6] was eventually put in place for TELEMAC (cis.opentelemac.org).

Although each website can be access independently from another by users and developers, all the websites are linked. The CIS continuously monitors the repository (svn) and generates the doxygen documentation (docs) for tagged versions. It is also designed to link up with the wiki for the production of validation sheets. The management website (cue) also helps track bug corrections and development plans, which are linked to the subversion (svn) and the CIS reports.

B. Setting up computing resources

Figure 1 below shows a schematic of the types activities and interactions the CIS (a.k.a. Jenkins) has with the internal systems put in place and with the outside.

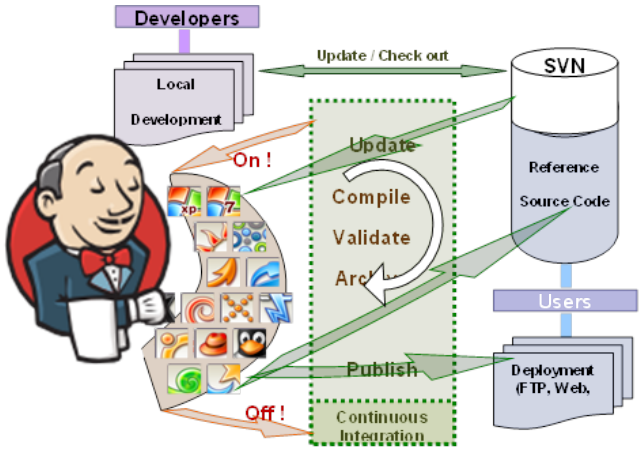

Figure 1 The CIS (a.k.a. Jenkins) does all tasks, routinely, as prescribed

Jenkins provides the TELEMAC consortium with:

- An automated system monitoring the entire source code repository of the TELEMAC scientific and scripting codes, including the main trunk and all branches of development, as well as all releases;
- An automated system managing communications to a number of virtual computers, each pre-configured with different computing architectures, operating systems and Fortran compilers; and
- An automated system capable of triggering several series of actions, including a promotion process for interdependent tasks and an email service reporting on the progress, and eventually success or failure of these tasks.

By design, the CIS is extendable as additional resources (say a new version of an operating system) or configurations (say debug or parallel modes) can easily be provided to Jenkins. Its actions can also be customised to fit any re-ordering requirements or changes in the validation procedure.

C. Defining the CIS principal functions

Jenkins has been taught to carry out specific actions for specific parts of the TELEMAC source code repository. For instance, for the main trunk of development, Jenkins will automatically monitor activities and do nothing until changes are made. When that is the case, it will choose the best time at night (when the available computing resources are less busy) to carry out a thorough validation of the entire system on several types of computers, for several Fortran compilers and configurations. For any other branch of development, Jenkins will only trigger the validation, for a limited number of configurations, when explicitly asked by the developer.

The validation (whether of the main trunk or of branches) is split in several sub-actions including a compilation of the system, running of the test cases, checking that the results achieve targets, generating the documentation and associated binaries and publishing of the validated version. A promotion process defines dependencies between these sub-actions, whereby the test cases are not checked if they have not been completed and they are not run if the compilation was not successful. Therefore, if any part of Jenkins's activities fails, a blaming report will be sent to the managers of that part of the repository by email as well as the developers who last modified it. If on the main trunk, the validation process will be re-attempted every night and a reminder will be sent by email to the developer until the validation is successful again. If on a branch, the validation process will remain a manual process for the developer concerned.

For illustration purposes, Figure 2 shows a snapshot of the validation of the tagged version v7p0r1 as captured from the website (cis.opentelemac.org).

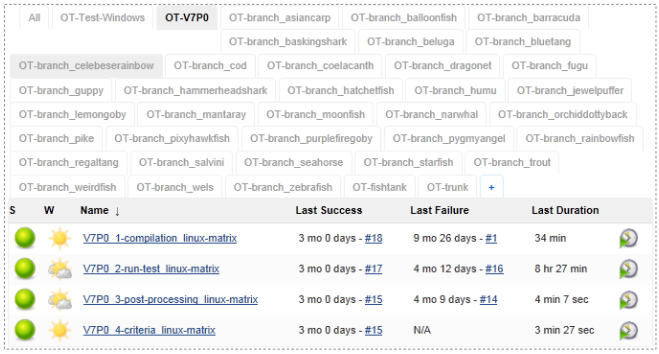

Figure 2 The CIS reports the outcome of the validation for all branches

One can check the status of any branch or of the main trunk of development. Two series of traffic light icons (left columns) summarise the status and the stability of each sub-task. The colour of the spheres varies from grey (the task has been suspended), red (the task has failed), orange (the task is a success but unstable) to green (the task is a success). The stability of the task is computed over the previous 5 attempts, and pictured by a weather pattern from a lightning storm (20% success or less) to a bright sunshine (80% success or more).

Finally, it must be highlighted that, because running all test cases lasts longer than 24 hours, Jenkins distinguishes weekdays as a validation based on "only" 80% of the test cases, from weekends when it does run the whole set.

D. Coding the CIS core tasks

While the Jenkins framework includes a number of pre-defined actions applicable to most continuous integration

systems (sending emails, monitoring a repository, turning on and off virtual computers, etc.), the tasks related directly to TELEMAC (such as, compilation and validation, packaging and documentation) are not included, for obvious reason. Instead, these procedures have been developed over the last 5 years by HR Wallingford within the Python scripting codes and are simply executed as terminal command on the virtual computers by Jenkins. For instance, Jenkins executes the following commands for the compilation of TELEMAC calling the Python script "compileTELEMAC.py":

```
python  ${WP}/scripts/python27/compileTELEMAC.py
-f ${WP}/configs/systel.cis-${NODE_NAME}.cfg
-r ${WP}/
-m system
```

where Jenkins replaces automatically the variable "${WP}" by the appropriate local copy of the trunk or the branch on a particular virtual computer, and the variable "${NODE_NAME}" by the name of the virtual computer (i.e. hydra, opensuse, debian, fedora, ubuntu, windows7). In fact, TELEMAC is distributed with several examples of configuration files for various operating systems. These are all used continuously by Jenkins.

Another example relevant to this article is the execution of the Python script "validateTELEMAC.py", for the validation of TELEMAC:

```
python  ${WP}/scripts/python27/validateTELEMAC.py
-f ${WP}/configs/systel.cis-${NODE_NAME}.cfg
-r ${WP}  --version ${SVNREVISION}
-k 6    -b    --clean
--report "ValidationSummary"
```

where, Jenkins replaces the variable "${SVNREVISION}" by the appropriate (and unique) repository versioning number starting the validation procedure, which gets then associated to the name of the report produced by the validation script and sent by email by Jenkins.

In the above command, we note the "-k" option, defining the rank of the test cases to be executed. Rank 6 covers 80% of the test cases (the weekday execution). Another execution with rank 0 is setup for the weekend to cover all test cases.

Finally, it must be reminded that the execution of the Python scripts by Jenkins is identical to the execution of the same scripts by users, hence allowing any user to run these on their own local copy and installation of TELEMAC.

E. Driving the CIS validation

As mentioned previously, the validation of TELEMAC is driven by the content of a myriad of XML files. The Python script "validateTELEMAC.py" (called by Jenkins) interprets these XML files and executes a number of actions defined within those. Chapter IV provides examples of actions implemented within the current state of the validation scripts.

In summary, the validation process plays as follows:

a) Jenkins. Executes various Python scripts stored within TELEMAC, in particular "validateTELEMAC.py"

b) Python. Interprets the action lists from various XML files found throughout the library of test cases.

c) XML files. Simply define a list of actions to be carried out for a specific test case, including compilation of the user code, running of the test case, comparative plotting and checking against targets and reporting to Jenkins.

d) Scientific and scripting codes. The codes that are being validated, including both the Fortran and the Python.

IV. A COMPREHENSIVE SYSTEM

As mentioned previously, every test case is associated to one XML file at least, containing a list of actions defining the validation procedure for that test case. The XML format was chosen for its simplicity and allows users to avoid python programing (although Python programing remains possible within the XML file itself).

In order to achieve this, a library of generic python scripts was developed to interpret a set of possible actions within those XML files. These include compile, run, compare, plot, save, extract data, check against targets, compute analytical solutions, report on success and failures.

This Chapter details examples of how to add various types of actions into an XML file as well as lists those available actions most used in the validation of TELEMAC by Jenkins.

A. Introductionary definitions

An XML file contains a series a tags, each associated to key-value pairs (also called tree leafs) or grouping other tags (also called tree branches). A tag defining a tree leaf starts with the symbol "<" closely followed by the name of the tag (say "action") and ends with "/>". A tag defining a tree branch (say "cast") starts with "<cast>" and ends with "</cast>", between which other tags can be inserted. The key-value pairs associated to a tag are inserted between the two symbols "<" and ">".

As an example of a tree leaf, the following extract from the XML file associated to the TELEMAC-2D test case called "bumpflu" shows the tag "action":

```
<action xref="1"
   do="translate;run;princi"
   code="telemac2d" target="t2d_bumpflu.cas"
/>
```

where the key "xref" is associated with the value string "1", the key "do" with the value "translate;run;princi", the key "code" with "telemac2d" and the key "target" with the value "t2d_bumpflu.cas".

The above tag is interpreted by the Python scripting codes to "translate" the CAS file in both English and French, to report a differentiation of the user "princi" file with the standard TELEMAC Fortran code and to "run" "telemac2d" for the CAS file "t2d_bumpflu.cas". The value "1" of the key "xref" is used as a reference for subsequent tags, for instance

to compare the results against a reference file. The value of the key "code" can be changed to any other TELEMAC code.

As an example of tree branch, the following extract from the same XML file shows the tag "plot2d" within which the tree leaf "layer" is set:

```
<plot2d xref="fig1" size="(12;3)" deco="default">
   <layer vars="FOND:map" target="1:T2DGEO" />
</plot2d>
```

where, similarly, the key "xref" is associated with the value string "fig1", etc.

The above tag is interpreted by the Python scripting codes to create and save to file (portable network graphic format) the content of Figure 3.

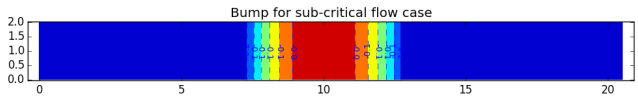

Figure 3 Plotting a coloured map of the bathymetry from a GEO file

One last example of tree branch is the following extract showing the tag "cast" within which the tree leafs "v1" and "v2" are set:

```
<cast xref="d" time="[0:-1]" type="2d:">
   <v1 vars="SURFACE:map" target="1:T2DRES" />
   <v2 vars="FOND:map" target="1:T2DRES" />
</cast>
```

where similarly, the key "xref" is associated with the value string "d", etc.

The above tags are interpreted by the Python scripting codes to compute / store for future reference two 2D variables, "v1" for the "SURFACE" and "v2" for the "FOND" both extracted from the result file "T2DRES" referred in the simulation "1" (as defined in the tree leaf example above), for all "time" step from the first "[0" to the last ":-1]". In this example, the variables "v1" and "v2" can be later on matched against a reference file, for instance.

B. *General coding principles*

To simplify the usability of the XML code by all users, whether for the validation of TELEMAC or more generally for the production of figures or the extraction of data, the development of the Python scripting codes associated to the interpretation of the XML files followed four coding principles:

1) *Re-usability of tags and keys*

In order to cover the definition and interpretation of all possible actions (as tags and their associated key-value pairs) within the XML files, only a limited number of purpose keys are used and the same keys and tags are re-used within different tags. For instance the key "target" (in all three example above) is the only key referring throughout to a file or another variable previously calculated. Similarly, the key "xref" is the only key referencing a variable or action item.

2) *Re-usability of references and names*

In order to be able to copy and re-use parts of XML codes from one test case to another, referencing to files and specific names is organised through the mnemonics of these file in TELEMAC. For instance, in the examples above, the names "T2DRES" and "T2DGEO" refer to the result and geometry files respectively, for a TELEMAC-2D simulation. Only a few specific metadata (and the specifics of the list of actions) can distinguish the XML file from one test case with another. Of course, outside the validation process, users are free to use their own names and references.

3) *The wheel shall not be re-invented*

When the key-value pairs of the XML file are used to drive the native Python directly (as opposed to drive specific TELEMAC related actions) for instance as parameters of native plotting packages, these are completely ignored by the TELEMAC scripting codes and transferred over directly for interpretation by the appropriate package. This allows the native Python installation to evolve independently of the scripting codes developed by HR Wallingford, which become extremely flexible in accepting all sorts of native key-value pairs.

For instance, another example of tree branch is the following extract showing the tag "deco" referred to as "default" in the previous "plot2d" example:

```
<deco xref="default">
   <look cmap="Blue.xml" linewidths="1.0" />
</deco>
```

where the keys "cmap" and "linewidths" are genuine keys of the popular matplotlib (1D and 2D) plotting package. Similar keys can also be passed directly to the mayavi (3D) plotting package, without the TELEMAC scripting codes having to interpret any of these.

4) *Simplicity without compromising on complexity*

While the XML file and its associated python scripting codes have to remain user-friendly with as fewer tags and keys as possible, it is critical not to prevent more advanced uses of the XML file whether as a validation procedure or not. For this reason, HR Wallingford has also implemented a way to insert python scripts and commands directly within the XML file. Moreover, an interface has crated between the variables created through the XML code (such as "v1" and "v2" above) and their uses within the inserted Python script.

For instance, a slightly extended extract of the tag "cast" shown above writes as follows:

```
<cast xref="d" time="[0:-1]" type="2d:">
   <python>
def diff(a1,a2):
   return a1.support,a2.values-a1.values
   </python>
   <v1 vars="SURFACE:map" target="1:T2DRES" />
   <v2 vars="FOND:map" target="1:T2DRES" />
   <v3 vars="diff(v1,v2)" />
</cast>
```

where the added variable "v3" is the water depth, or the result of the difference between "v1" and "v2" both extracted

from the result file, or the execution of the Python command "diff(v1,v2)", having defined the function "diff" within the tag "<python>"-"</python>". Of course, the variable "v3" can subsequently be saved to a file or plotted. Moreover, the inserted python script can be as complex as the user wishes it to be, including for the computation of analytical solution.

One interesting point to highlight is the use of ".support" (the unstructured mesh of "v1" in this case) and ".values" (the free surface and bottom for "v1" and "v2" in this case) to access various parts of "v1" and "v2". A thorough discussion of these fields (or the interface mentioned above) will be presented on the wiki website (wiki.opentelemac.org). We note also that "v3" is defined (result of "diff(v1,v2)") as both a mesh support and the difference of values at all times. This enables "v3" to be self-contained and later saved to a file or plotted.

C. Reporting to back Jenkins

The validation procedure (through its call to the Python script "validateTELEMAC.py") gradually assembles a report (so far a tabulated ASCII file) as it goes through the entire set of test cases. One or more entry can be made for every check implemented within the XML file, where checks are carried out through the tree leaf "return" of a tag "cast".

For instance, a slightly modified extract of the tag "cast" shown above writes as follows:

```
    <cast xref="d" time="[0:-1]" type="2d:">
   <python>
def diff(a1,a2):
   return a1.support,a2.values-a1.values
   </python>
   <v1 vars="SURFACE:map" target="1:T2DRES" />
   <v2 vars="SURFACE:map" target="1:T2DREF" />
   <v3 vars="diff(v1,v2)" />
   <return title="Reference file comparison."
      fail="max(v3.values.ravel()) > 1.e-6"
      warn="max(v3.values.ravel()) > 1.e-12"
      value="max(v3.values.ravel())" />
</cast>
```

where the added tree leaf "return" includes three keys, "fail", "warn" and "value", the computed values of which are written in the validation report. It is noted that the "fail" and "warn" values return true or false statements, and that "T2DRES" and "T2DREF" are used to refer to the result and the reference file respectively.

In this specific case, the validation will return a warning if the difference in more than machine accuracy, and will fail if the difference is more than 1D-6, which is a very stringent validation target.

D. Example: reference file comparison

This sort out comparison is carried out for all test cases. The so-called "bumpflu" test case of the TELEMAC-2D code is here chosen as an example, where the XML code shown below are extracted from.

1) Refering to a simulation

The XML file first defines an action to run the test case:

```
<action xref="1"
   do="run" code="telemac2d" target="t2d_bumpflu.cas"
/>
```

where "1" is the reference name for future uses of the simulation settings.

2) Comparison and reporting to Jenkins

The difference between the result and reference files is then computed and the fail-warn-value statements reported to Jenkins. The associated XML code has in fact been presented as the slightly modified extract of the tag "cast" above. By removing the name "SURFACE" from "v1" and "v2", the scripting code will infer a comparison for all variables.

In order to augment the information provided to Jenkins (and ultimately to the developer), the following modifications can be made first to the "value" key of the "return" tree leaf:

```
      value="maxdiff(v3)"
```

where the following function "maxdiff" is added within the tag "<python>"-"</python>" of the same "cast":

```
def maxdiff(d0):
   a0 = max(np.ravel(d0.values))
   a1 = np.argwhere(d0.values == a0)[-1]
   return "for instance value="+str(a0)+
   " at time: " +str(a1[0])+" for variable: "
   +str(a1[1])+" at node: "+str(a1[2])
```

and where the function "maxdiff" returns a character string composed of a node number, a variable name and a time frame for which the value is the maximum difference.

E. Example: paralel and serial mode comparison

This sort out comparison is carried out for all test cases. Again, the so-called "bumpflu" test case is chosen.

1) Refering to another simulation

The XML file first defines an action to run the test case:

```
<action xref="2"   ncsize="4"
   do="run" code="telemac2d" target="t2d_bumpflu.cas"
/>
```

where "2" is the reference name for future uses of that simulation carried out in parallel over "4" processors defined by the new key "ncsize".

2) Comparison and reporting to Jenkins

Thanks to its re-usability, only a slight modification to the "cast" shown so far is required to carry out a comparison between the results of the serial and parallel simulation: the variable "v2" should target "2:T2DRES" instead of "1:T2DREF".

F. Example: Comparion against measured data

This sort out comparison is carried out when physical modelling or other measured data has been obtained for that particular test case. The so-called "breche" test case of the ARTEMIS code is here chosen as an example. The example below focuses the illustration to comparative plotting.

1) Refering to a simulation

The XML file first defines an action to run the test case:

```
<action xref="1"
   do="run" code="artemis" target="art_breach.cas"
/>
```

where "1" is the reference name for future uses of the simulation settings.

2) Refering to external data

The XML file then defines an action to read the data:

```
<cast xref="Experiment" type="1d" >
   <v1 vars="H" target="experiment.csv" />
</cast>
```

where the variable "H" (values and associated support) is read from the external file "experiment.csv".

3) Spline interpolation

In order to augment the information provided on the figure, a spline interpolation is defined as follows:

```
<cast xref="Interpolation" type="1d:v-section" >
   <python>
def interp(x1,y1,x2):
  from scipy.interpolate import interp1d
  f = interp1d(x1,y1,kind=3)
  ExpInterp = f(x2[10:])
  return x2[10:], ExpInterp
   </python>
   <v2 vars="wave height:line" target="1:ARTRES"
     extract="(0;915)(1800;915)" time="[0]" />
   <v3 vars="interp(v1.support,v1.values,v2.support)" />
</cast>
```

where the variable "v1" is the experiment and "v2" is extracted along a cross section defined between the points "(0;915)" and "(1800;915)" from the result file "ARTRES". It is noted that the code within the tag "<python>"-"</python>" includes reference to the popular scipy scientific package.

4) Plotting

Finally, the creation of the (1D) plot is as follows:

```
<deco xref="line">
   <look color="green" />
</deco>
<deco xref="dots">
   <look color="red" marker='o' linestyle='None' />
</deco>
<plot1d xref="fig" type="1d:v-section" size="(10;7)" >
   <layer vars="v1:line"
     target="Experiment:v1" deco="dots" />
   <layer vars="v3:line"
     target="Interpolation:v3" deco="line" />
   <layer vars="wave height:line"
     extract="(0;915)(1800;915)"
     target="1:ARTRES" time="[0]" />
</plot1d>
```

where three layers are plotted one after the other, two of which referring to specific "deco" (decoration) tags for the transfer of key-value pairs directly to the matplotlib package.

It is noted that because the variable "v2" had been computed previously, it is not necessary to extract it once more within the "plot1d" tag. The result of the above is shown in Figure 4, where the red dots are associated with the experimental data and the (default) blue line with the computed wave height across the domain.

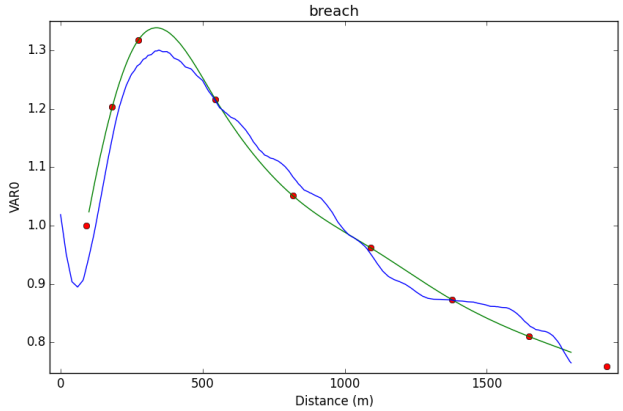

Figure 4 Plotting experimental data against computed wave height

G. Example: Comparison against analytical solution

This sort out comparison is carried out when an analytical solution can be computed for that particular test case. The so-called "criterion" test case of the Python scripting code validation is here chosen as an example.

Similarly to what has been presented previously, a "cast" tag is used to compute the analytical solution of the propagation of a dam break on dry bed:

```
<cast  xref="ana"  type="1d:v-section"  time="[0:-1:10]">
   <python>
def analytics(a0):
   x0 = a0.support
   at = a0.function[-2]
   nt = len( a0.values[0] )
   h0 = 4.0
   g = 9.81
   hn=np.zeros((1,nt,1,len(a0.support)),dtype=np.float)
   for ix in range( len(x0) ):
     if 10.5 > x0[ix]: hn[0][0][0][ix] = h0
   for it in range( nt )[1:]:
     for ix in range( len(x0) ):
       arg1=math.sqrt(h0*g)-(x0[ix]-10.5)/(2.0*at[it])
       hn[0][it][0][ix]=max(0.0,arg1)
       hn[0][it][0][ix]=h0*(hn[0][it][0][ix])**2/g/9.0
       hn[0][it][0][ix]=min(hn[0][it][0][ix],h0)
   return x0,hn
   </python>
   <s0 vars="free surface:line"
     type="1d:v-section" time="[0:-1:10]"
     extract="(0;10):(21;10)"
     target="f2d_dambreak.slf" />
   <a1 vars="analytics(s0)" />
</cast>
```

where the script within the tag "<python>"-"</python>" is complex and computed based on a physical support extracted from the file "f2d_dambreak.slf" (as opposed to be referring to a simulation), along a cross section defined between the points "(0;10)" and "(21;10)".

Of course, the variable "a1" can be subsequently saved to a file or plotted and checked against the results produced by the equivalent TELEMAC-2D test case. For instance, the following XML extract would create Figure 5.

```
<plot xref="comparison" type="1d:v-section" >
   <layer vars="a1:line" target="ana:a1" deco="red" />
   <layer vars="s0:line" target="ana:s0" deco="green" />
</plot>
```

where the reference to "ana" is the "cast" above.

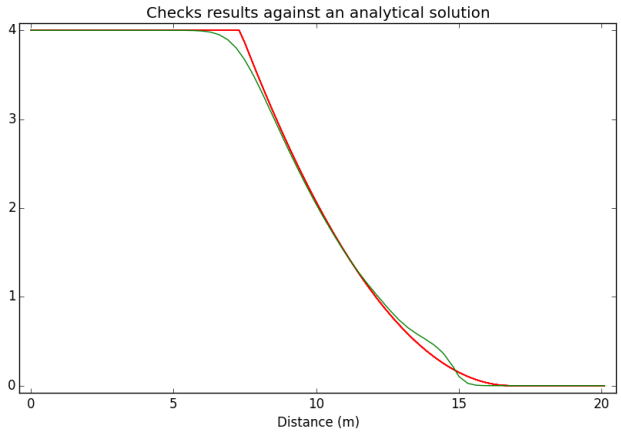

Figure 5 Plotting analytical solution against computed free surface

H. Example: 3D graphic rendering

To conclude this list of examples with nice pictures demonstrating the combined use of the XML codes and Python scripting codes in a reporting context, the following extract has been inspired from the TELEMAC-3D test case "lock-exchange", using the detailed results of the test case as published by Bourban in his thesis [8].

```
<deco xref="ver1">
   <look size="(10,5)" xtick.major.size="8"
      aspect="3" roi="(10;-0.6)(22;0.6)"
      title="Detailed lock-exchnage case" />
</deco>
<plot2d xref="fig1" type="v-section" deco=" ver1"
   extract="(0;0)(32;0)" time="[71]" >
   <layer vars="tracer:map" target="r3d-amr.slf" />
</plot2d>
```

where the key "roi" is the region of interest zooming in that interesting part of the lock 32 m long otherwise and where the key "aspect" defines the vertical to the horizontal aspect ratio.

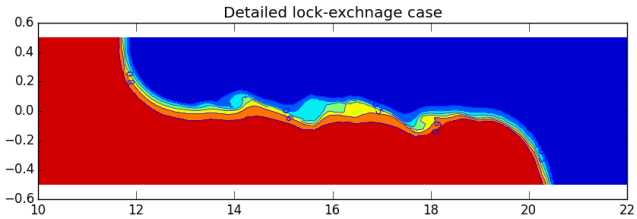

Figure 6 Only two XML tags required to plot a slice through a 3D result

Figure 6 shows the result of the XML code shown above, as a plot of coloured ":map" of "tracer" concentration through a vertical section of the 3D domain defined between the two points "(0;0)" and "(32;0)"m extracted at the time "[71]" from the 3D TELEMAC file "r3d-amr.slf".

It is noted that the extraction of the vertical section data through the 3D domain is computed by the TELEMAC scripting codes. As an alternative, one can also let the native mayavi Python package do the graphical slicing through the 3D domain. The following plots have been produced with very little XML code on the standard lock-exchange test case, to which streamlines have been added recently. The XML code associated to these plots can be found in the TELEMAC release v7p1.

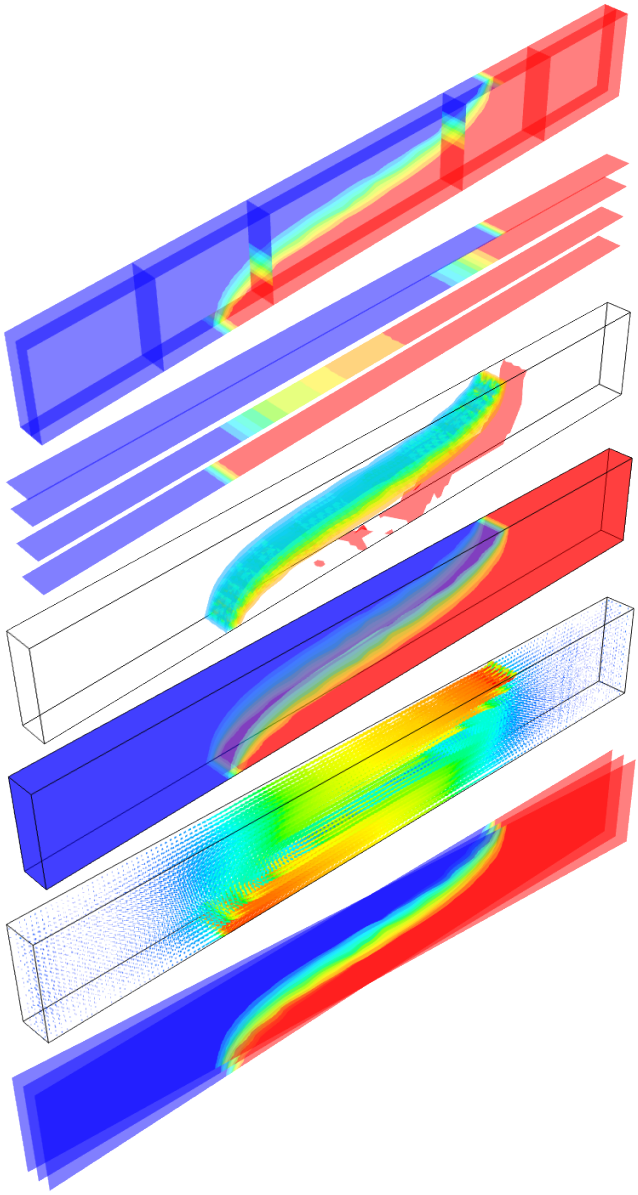

Figure 7 Examples of posisble uses of the XML to generate 3D plots

CONCLUSIONS

An automated continuous integration system (CIS) has been put in place and developed over the last 5 years to allow continuous testing, monitoring, verification and validation of all TELEMAC scripting and scientific codes.

The CIS is based on the so-called framework Jenkins and accessible through a website (cis.opentelemac.org) hosted at HR Wallingford. Several other websites have been linked to the CIS for greater interoperability and automation of the entire validation process, including the TELEMAC source code repository (svn.opentelemac.org), the TELEMAC wiki documentation (wiki.opentelemac.org) and the item tracking and project management site for members of the TELEMAC consortium.

In a general context, Jenkins enables automated tasks such as monitoring of all parts of the source code repository, management of an ensemble of virtual computers, promotion of successful validation, email of validation reports, and packaging of binaries. The ensemble of virtual computers allows testing and validation to be carried out natively on each operating system, ensuring maximum compatibility and performance with known industry uses.

Specifically for TELEMAC, Jenkins relies on a myriad of Python scripts compiling, running and verifying simulation results for over two hundred test cases. These scripts are part of TELEMAC and are themselves validated by the CIS. They are used to extract time series, values, cross-sectional data, generate figures, assemble table data, and validate extracted data against target criteria to produce validation reports. The validation procedure is defined by an ensemble of XML files, user-friendly and accessible to all.

This article also introduced numerous examples of XML code snippets to illustrate HR Wallingford strategic coding principles: (a) Re-usability of XML tags and keys throughout action items; (b) Re-usability of references and variables using mnemonics instead of hardcoded file names; (c) Not re-inventing the wheel through direct use of native python packages; and (d) Keeping the XML syntax as simple as possible while allowing advance users to input complex python code within the XML files.

Testing and validation of scientific codes is time consuming but critical and even more so for industrial uses. It is paramount that TELEMAC follows a strict testing and validation procedure for every release to maintain its quality standard. HR Wallingford believes that the CIS developed and documented here fulfils this role.

Looking forward, HR Wallingford shall continue its development of the TELEMAC Python scripting codes (including those related to the TELEMAC validation) to attempt a link with other environments such as QGIS [7], a community driven graphical user interface, which could become the default user interface to the TELEMAC system. Support from the open TELEMAC community is welcomed.

ACKNOWLEDGEMENT

Sébastien Bourban and his co-authors Juliette and Alain would like to thank Yoann Audoin from Laboratoire National Hydraulique et Environment, EDF-R&D, France, Clemens Dorfmann from the Graz University of Technology, Austria and Leopold Stadler from the Bundesanstalt fuer Wasserbau, Germany, for their own testing of the validation system and for their participation the testing and tweaking of the python scripting codes in general.

REFERENCES

[1] P. J. Roaches, “Verification and validation in computetional science and engineering,” Albuquerque: Hermosa Publishers, 1998.

[2] Subversion SVN, subversion.apache.org

[3] Dokuwiki, www.dokuwiki.org

[4] Doxygen, www.stack.nl/~dimitri/doxygen/

[5] Redmine, www.redmine.org

[6] Jenkins, www. jenkins-ci.org/

[7] QGIS, www.qgis.org/

[8] S.E. Bourban, “Stratified Shallow Flow Modelling”, Ph.D thesis, The Open University, UK, 2013.

Modelling suspended sediment transport due to helical flow in TELEMAC-2D

Gregor Petkovsek
HR Wallingford
Wallingford, UK
g.petkovsek@hrwallingford.com

***Abstract*— A helical flow is a type of secondary currents that develops in addition to the primary flow pattern in a river bend. It produces transversal fluxes of suspended sediment due to the fact that sediment concentration is not uniform through the vertical. Therefore, while vertically averaged transversal flow of water is zero, the average sediment flux is not.**

This paper presents development of a module that reproduces this effect of secondary flow in a river bend for suspended sediment transport. The module is integrated into TELEMAC-2D model. TELEMAC-2D already takes into account the effect of secondary flows on flow pattern and bed load transport. The present development therefore completes the modelling of secondary effects in TELEMAC-SISYPHE for two dimensions.

The model has been tested against field data collected at Kapunga intake (Tanzania) in early 1990s. five cases have been tested for different river flows, extracted flows, sediment concentrations and water levels. Exclusion performance (reduction of concentration flowing into intake compared to concentration in the river upstream) was of interest. This preliminary testing shows promising results both in terms of total suspended sediment as well as individual fractions.

I. INTRODUTION

Sedimentation is often a serious challenge in hydraulic engineering. The most obvious example of this are reservoirs. It has been estimated that about 1% of total worldwide storage is lost every year due to sedimentation [1]. Thus the potential of reservoirs to store water for irrigation, power production, etc. is decreased. Water intakes may also suffer from sediment related problems if the amount of sediment in the flow is high. The associated problems are, for example, siltation of canals branching from the intake or abrasion of power machinery in the case of electricity generation. Engineers have proposed various sediment management solutions for excluding sediment from intakes, one of them being sitting of the intake in the outer side of a river bend to take the advantage of helical flow that develops in a bend.

Efficiency of these options can be estimated with physical or numerical models. Physical models are more reliable for general hydrodynamic studies than the modelling of water flow only. However for water and sediment flows, the downside of physical models is that appropriate scaling for all processes is difficult to achieve and the required time and costs are also large. This is why numerical modelling is currently the preferred option to study sedimentation processes.

Numerical modelling can be done in one, two or three dimensions. Each approach has its advantages and disadvantages. While 1D models are very practical for long-term simulations (say 50 or 100 years), they cannot properly simulate details of complex flow patterns around structures. 3D models are most suitable for this. However in the vertical direction, the nature of sediment processes is such that they are concentrated near river bed or reservoir bottom [2]. A high modelling resolution and thus computational cost is necessary for numerical solution in these types of models. Furthermore, the physical knowledge of many sediment transport processes is largely based on mean flow parameters rather than details of vertical flow distribution. For these reasons, 2D models are often most suitable for solving practical engineering problems in relation to sediment. However, certain 3D effects, an example of which is helical flow, should be reasonably depicted by 2D models. This paper presents development of a module that takes into account the effects of helical flow on transport of suspended sediment, as well as its application to sediment exclusion at intakes.

II. METHOD

The change of flow direction in a river bend causes a phenomenon which is known as helical flow and is a type of a secondary current that develops in addition to the primary flow current. Flow on the surface has a higher inertia and tends to continue flowing towards the outer bend, while flow close to the bed turns towards the inner bank. Thus a secondary circulation is formed (Fig. 1).

Helical flow has been analysed by several authors (e.g. [3]) who have proposed different approaches towards its modelling. Recently, these formulae have been implemented into 2D numerical models (e.g. [4]). TELEMAC already has a module for evaluation of the effect of secondary currents on bed-load transport. In TELEMAC version 7, the effect of secondary flows on average (primary) flow field was also added. This paper presents developments of a module that evaluates the effect of secondary currents on the transport of suspended sediment.

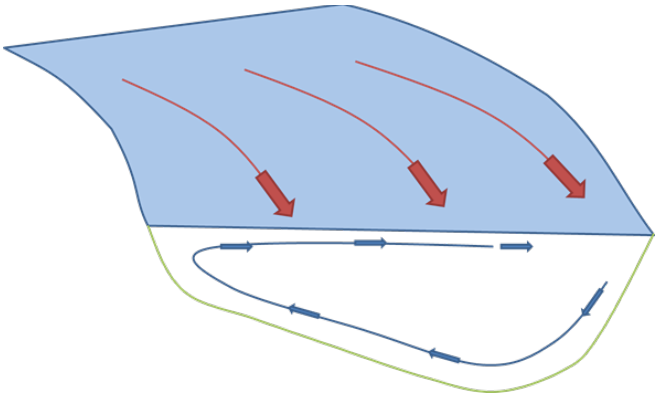

Figure 1. Primary (red) and secondary (blue) current in a river bend

The first parameter specific to secondary circulation in bend is the radius of bend curvature. Several authors have proposed stable methods for its computation from velocity field (e.g. [2], [5]). Here the radius of curvature r is computed as follows:

$$\frac{1}{r} = \frac{1}{(u^2+v^2)^{3/2}}\{u(uv_x - vu_x) + v(uv_y - vu_y)\} \quad (1)$$

The symbol u denotes velocity in x direction, v is velocity in y direction and subscripts denote the derivatives in the respective directions.

Next, vertical profile of transversal velocity must be calculated. The approach proposed by Olesen [6] is used as it has the advantage of taking into account no-slip conditions at bed. The downside of this approach is its rather complex computational procedure. Therefore a simplification with a curve fit was applied in the proposed model. A comparison between the exact and curve fit solution is show in Fig 2.

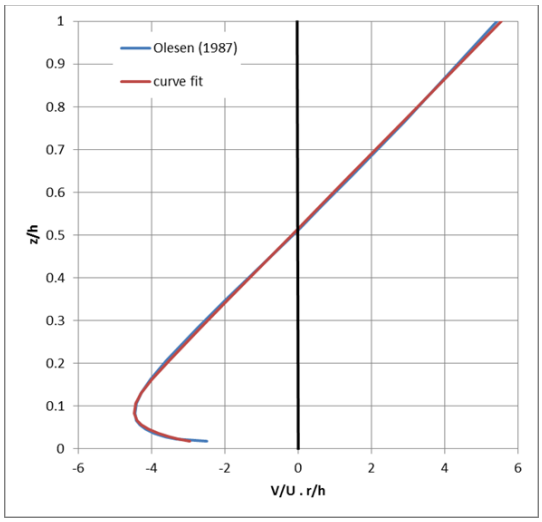

Figure 2. Comparison of vertical profile of a transversal velocity according to Olesen and the curve fit used in the proposed model.

Transversal flux of suspended sediment Qss,t is then calculated by integrating the product of concentration and transversal velocity:

$$Qss,t = \int_0^h C(z)V(z)dz \quad (2)$$

where $C(z)$ is sediment concentration at elevation z above bed calculated according to formula of Lane and Kalinske [7], $V(z)$ is transversal velocity computed as discussed above and h is the flow depth.

III. TEST CASE

The helical flow model was applied to simulate the sediment exclusion at Kapunga intake located in a river bend. The Kapunga Rice Project is located in Tanzania [8]. The water is derived from the Great Ruaha River from behind a weir structure. Typical water flows in the river in the wet season are between 15 and 50 m^3/s. The capacity of the water intake is 4.6 m^3/s. In addition to that, part of water extracted in the bend also flows towards the sluice channel and returns to the river below the weir. Typical extraction in the bend is thus between 5 and 10 m^3/s. All observed river discharges Q_{inflow} and discharges extracted in the bend Q_{ext} that were used for model verification are show in Table I. Layout of Kapunga intake is shown in Fig. 3.

Field measurements were taken by HR Wallingford in 1991 and 1992 [8]. Sediment concentrations and discharges were measured in the river about 160 m upstream from the weir, in the sluice channel and in the irrigation canal just below intake. Sand was measured separately from finer sizes. The latter were not critical to the operation of the irrigation system. Typical sand sizes in suspension were d_{35} = 0.135 mm, d_{50}=0.19 mm and d_{100} = 1 mm. Concentrations of sand ranged from 0.010 to 0.316 g/l.

For each measurement, a performance ratio, PR, was calculated as:

$$PR_{canal} = 1 - C_{canal} / C_{inflow} \quad (3)$$

Where C_{canal} is the concentration measured at the canal intake and C_{inflow} is the concentration in the river upstream. This ratio was found to be around 0.5 but varied substantially (at least between 0.2 and 0.8) depending on flow and sediment conditions. Concentration C_{sluice} and water flow Q_{sluice} was also measured at the sluice channel. Thus it was possible to calculate performance ratio PR_{ext} of the bend:

$$PR_{ext} = 1 - \frac{C_{canal}\,Q_{canal} + C_{sluice}\,Q_{sluice}}{C_{inflow}(Q_{canal} + Q_{sluice})} \quad (3)$$

A comparison the results of field observations to a numerical model, PHOENICS, is shown in [9] as well as in [10], where SSIIM was used. Both models are 3D models.

TABLE I. LIST OF RIVER AND EXTRACTED DISCHARGES USED IN MODELLING

Date	Discharge	
	in river, Q_{inflow}	*extracted, Q_{ext}*
25/2/1991	30.0 m^3/s	8.23 m^3/s
27/2/1991	23.5 m^3/s	9.07 m^3/s
1/3/1991	18.2 m^3/s	7.57 m^3/s
29/2/1992	40.7 m^3/s	11.07 m^3/s
23/4/1992	38.0 m^3/s	7.76 m^3/s

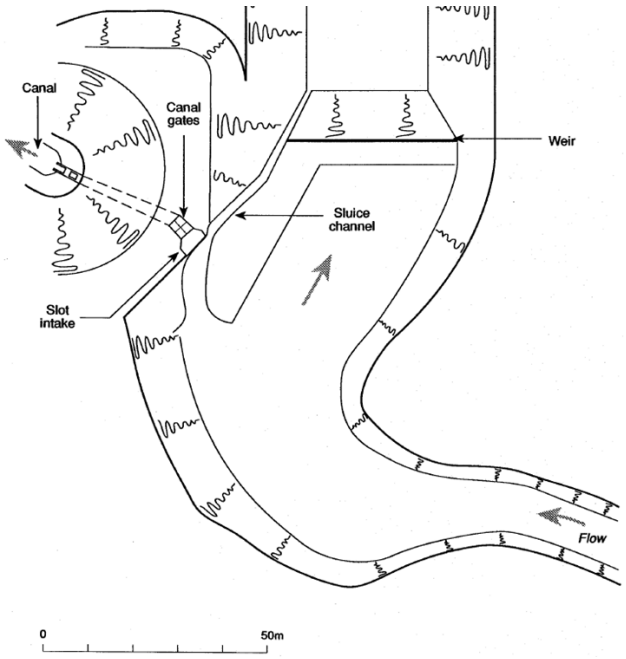

Figure 3. Layout of Kapunga intake

TELEMAC-2D 7.0 and its sediment module SISYPHE were used to perform simulations. TELEMAC-2D flow model already simulates the effect of secondary flows on the flow field and the bed load transport, but no module for simulating the effect of secondary flows on suspended sediment is available. Therefore the following improvements were made with respect to standard version 7.0:

- Ackers and White formula [11] was used to estimate sediment transport capacity;
- Improvements as described in chapter Method were coded and the executable file recompiled to take into account the effect of secondary currents on suspended sediment.

The modelled area was composed of 2465 elements with side lengths ranging from 1 to 2 m. The model mesh is shown in Fig. 4.

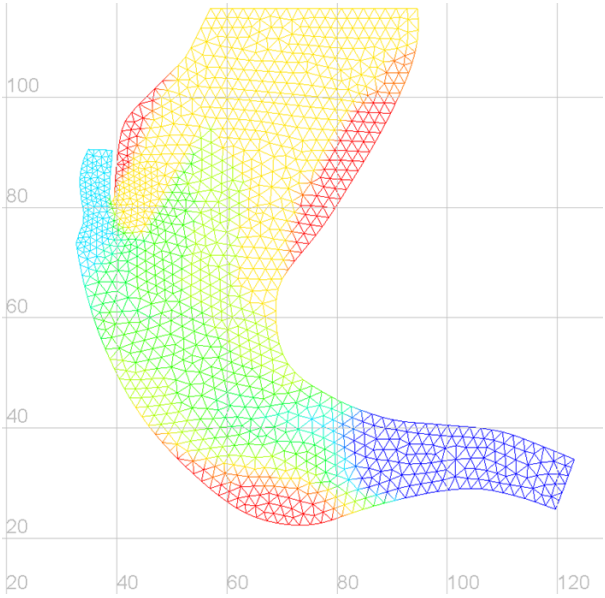

Figure 4. Numerical mesh for simulations. Different colours represent different bed elevations. The values on the axes scales are in metres

Table II lists the runs that were performed.

TABLE II. TABLE TYPE STYLES

Run name	*Q_{inflow} (m^3/s)*	*Water level at intake (m)*	*Conc.of sand in inflow (g/l)*	*Model description*
Q38o	38.0	1058.47	0.100	no secondary flows one sediment fraction
Q38f	38.0	1058.47	0.100	secondary flows in HD[a] one sediment fraction
Q38s	38.0	1058.47	0.100	secondary flows in SS[b] one sediment fraction
Q38sf	38.0	1058.47	0.100	secondary flows in SS & HD, one sediment fraction
Q41sf	40.7	1058.9	0.088	as above
Q30sf	30.0	1058.44	0.088	as above
Q23sf	23.5	1058.3	0.050	as above
Q18sf	18.2	1058.3	0.040	as above
Q38sf6	38.0	1058.47	0.100	secondary flows in SS & HD, six sediment fractions
Q41sf6	40.7	1058.9	0.088	as above
Q30sf6	30.0	1058.44	0.088	as above
Q23sf6	23.5	1058.3	0.050	as above
Q18sf6	18.2	1058.3	0.040	as above

a. HD = hydrodynamic module

b. SS = suspended sediment module

The first four runs were performed to see how the proposed improvements for secondary currents change the results of the model. The remaining runs were performed to see how the proposed model behaves at different discharges and sediment concentrations compared to observations.

The *Q**sf6* runs were run to investigate how the model performs if several sediment fractions are taken into account. Performance ratio for individual fractions was compared with observations for runs *Q30sf6* and *Q23sf6* where these observed data were available [12].

For one fraction model run, a representative sediment size of 0.135 mm was used, corresponding to sediment diameter d_{35}. This is deemed to be the representative size in Ackers and White formula in the case of mixtures [13]. For the six fractions runs, the sand sizes as showed in [12] were used (0.075 mm, 0.115 mm, 0.17 mm, 0.27 mm) in addition to two larger fractions to represent the whole spectre of sediment sizes at Kapunga (0.6 and 2 mm).

IV. RESULTS

Fig. 5-8 show the concentrations for the *Q38** family of runs after one day. It can be seen that when the proposed modification is not taken into account (*Q38o*), the concentration is very much uniform through the flow field. When the flow expands, the flow velocities decrease in particular along the edges of the flow field and where the transport capacity is no longer sufficient to carry the 100 g/l of sediment, some deposition occurs. This is manifested by the decrease of concentration. Using the option of considering secondary currents in the flow model only (*Q38f*) does not change the results much. In the case when the proposed modifications are used in the simulations (*Q38s* and *Q38sf*), the distribution of sediment concentration across the stream changes from high along the inner side of the bend to low on the outer side.

Table III shows the performance ratios predicted by different runs of the *Q38* family compared to the observed value. It can be seen that the runs where the proposed modification was used (*Q38s* and *Q38sf*) performed similarly well while the other two (*Q38o* and *Q38f*) significantly underestimated the performance ratio.

A direct comparison with the PHOENICS and SSIIM models is not possible as these studies ([9] and [10]) only reported the performance ratio of the intake, while this study only modelled the performance ratio of the extraction in the bend (as the flow split between intake and sluice channel is a 3D problem and cannot be modelled by a 2D model). Nevertheless, a comparison is shown in Table IV.

TABLE III. OBSERVED AND PREDICTED PERFORMANCE RATIOS FOR Q38 FAMILY OF RUNS

Observed	***Q38o***	***Q38f***	***Q38s***	***Q38sf***
0.61	0.32	0.31	0.57	0.57

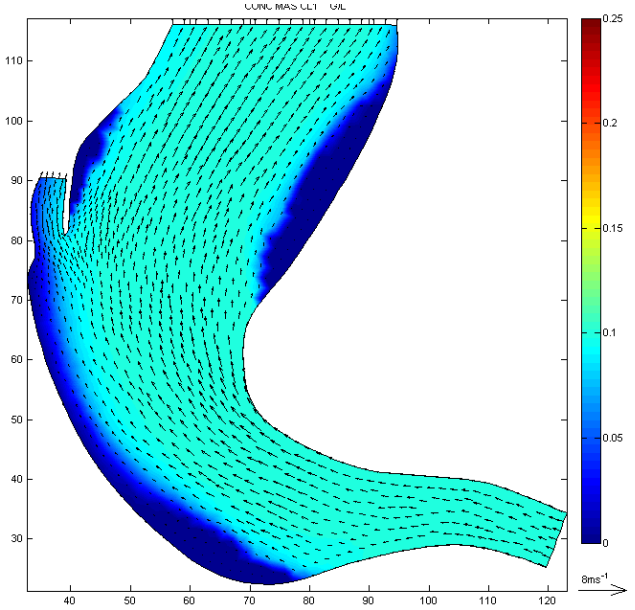

Figure 5. Flow field (arrows) and distribution of concentration for run Q38o

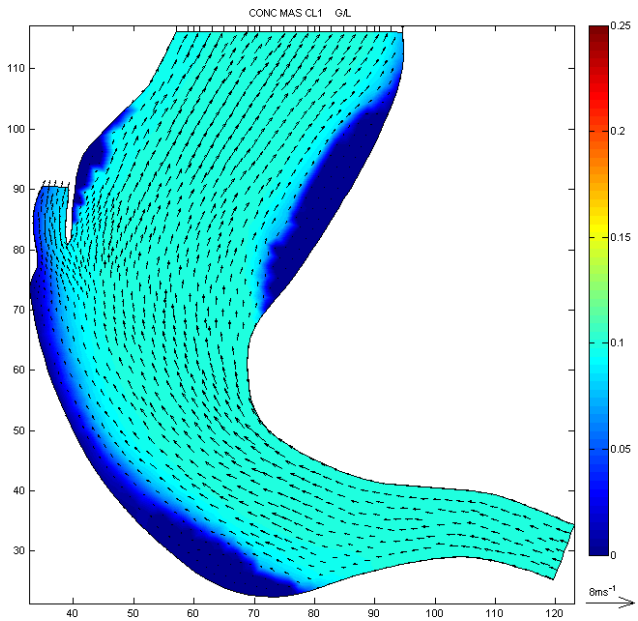

Figure 6. Flow field (arrows) and distribution of concentration for run Q38f

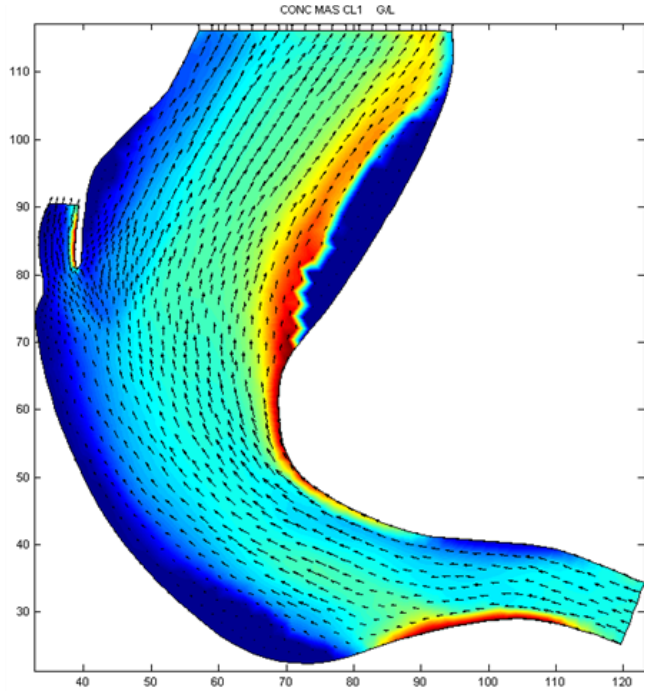

Figure 7. Flow field and distribution of concentration for run Q38s

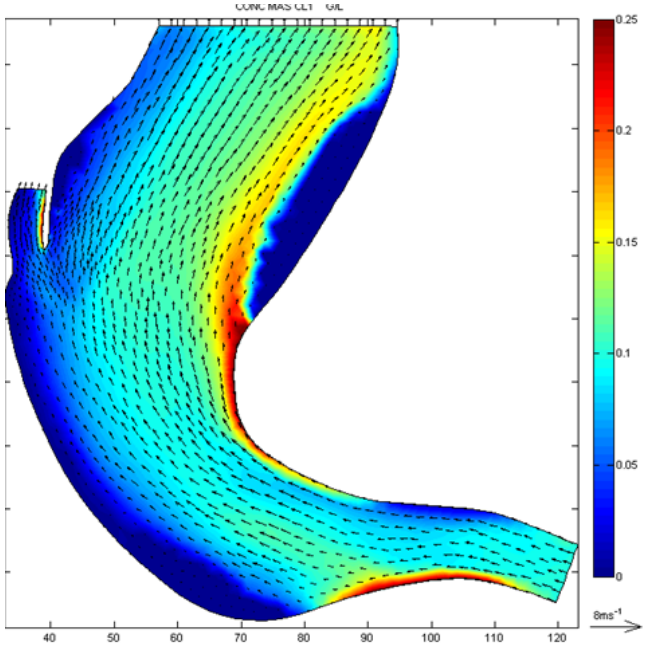

Figure 8. Flow field and distribution of concentration for run Q38sf

TABLE IV. PREDICTIONS OF PERFORMANCE RATIO OF DIFFERENT MODELS

Model	*Location*	*PR-observed*	*PR-predicted*
PHOENICS [8]	canal intake, PR_{canal}	0.65	0.54
SSIM [9]	canal intake, PR_{canal}	0.65	0.44
TELEMAC with SF	extracted flow, PR_{ext}	0.61	0.57

From these results it would appear that the improvements introduced in TELEMAC perform well. However, further validation with real data must be considered. Table V shows a comparison between observed and predicted values for all cases simulated with secondary flow model.

TABLE V. OBSERVED AND PREDICTED PERFORMANCE RATIO FOR ALL RUNS WITH SECONDARY FLOW MODEL

Model setup	**Performance ratio by discharge**				
	Q18*	***Q23****	***Q30****	***Q38****	***Q41****
Observed	0.40	0.51	0.67	0.61	0.31
*Q**sf*	0.72	0.50	0.59	0.57	0.47
*Q**sf6*	0.78	0.64	0.70	0.63	0.68

It can be seen that the model results for the *Q**sf* model setup are in similar range as the observed values. The observed variation in performance ratio with water discharge is between 0.31 and 0.67, while modelled variation is between 0.47 and 0.59 with an outlier at 0.72.

For *Q**sf6* model setup, matching between the observed and predicted values is not always good. The discrepancies can be attributed to the fact that the bathymetry (based on surveyed cross sections in the dry summer period, while data for modelled cases were taken from the high flow period between February and April) and the sediment composition are not well known for each case. Both will have an influence on performance due to deposition as well as due to net vertically averaged transversal sediment flux. The performance ratio increases if there is more sediment deposition before sediment reaches the bend, which occurs if sediment is coarser or the flow area is larger. Regarding the net vertically averaged transversal sediment flux, it increases in particular with coarser sediment. Changes in bathymetry may result in a different flow path and thus radius of curvature and therefore, have an influence on the magnitude of secondary currents.

When six sediment fractions were used (*Q**sf6*) instead of only one (*Q**sf*) the model gave higher performance ratios in all cases. This could be either due to sediment grain size composition being in each individual case different than the average composition that was used for modelling. Unfortunately, inflow compositions for individual runs were not available. The available field information is shown in Fig. 9.

The performance ratios for individual observations were however available in [12] for two modelled cases, *Q23sf6* and *Q30sf6*. A comparison of observed and modelled performance ratio for a known sediment size was thus possible. The results are shown in Fig. 10. It can be seen that for each individual size the model performs quite well.

Nevertheless further comparisons with real data are recommended to verify the performance of the model under different flow and sediment conditions.

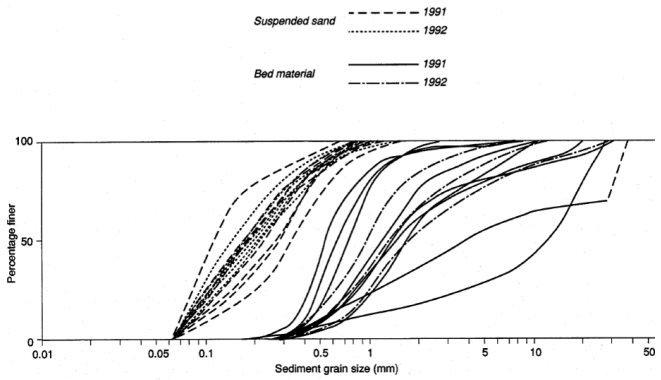

Figure 9. Variation in composition of bed and suspended sediment [11].

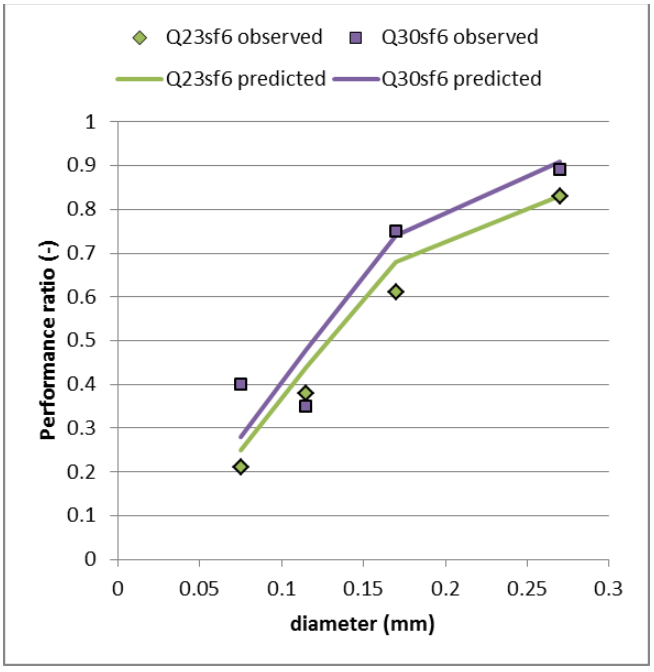

Figure 10. A comparison of observed and modelled performance ratio for different sediment sizes and two different flow conditions.

V. CONCLUSIONS

The paper describes the proposed methodology for inclusion of the effect of helical flows on suspended sediment into TELEMAC modelling suite. The method was successfully coded and applied to compute the Kapunga intake performance ratio in terms of sediment exclusion. Testing of the model with one (representative) sediment fraction on this case showed promising results. When used with multiple fractions the overall results were not as good, although the predicted performance ratios for individual fractions were satisfactory. There were however some uncertainties related to the initial bathymetry and sediment composition that might have impacted these results. A set of runs were performed to understand their potential impact. Nevertheless further validation of the proposed model is recommended.

The code has been prepared for the advection schemes no 3 and no 13 of the existing TELEMAC-SISYPHE code of Version 7.0. Both are conservative N-schemes with the first one being point based while the second one is flux-based, thus enabling flooding and drying simulations as well.

ACKNOWLEDGEMENT

The author wishes to express his thanks to J-POWER Business Service Corporation of Tokyo, Japan for their support of this research, in particular to Dr Yuichi Kitamura, Mr Muneo Sato and Mr Eiji Kobayashi.

REFERENCES

[1] R. White, Evacuating sediments from reservoirs. London: Thomas Telford, 260 pp, 2001.

[2] L. Begnudelli, A. Valiani and B.F. Sanders, “A balanced treatment of secondary currents, turbulence and dispersion in a depth-integrated hydrodynamic and bed deformation model for channel bends,” Advances in Water Resources 33, pp 17–33, 2010

[3] J. Odgaard, “River meander model. I: Development,” Journal of Hydraulic Engineering, Vol. 115, No. 11, pp 1433-1450, November 1989.

[4] Ch. Fang, J. Mao and W. Lu, “2D Depth-Avergaed Sediment Transport Model Taken Into Account of Bend Flows”, Proc. of US-China Workshop on Advanced Computational Modelling in Hydroscience & Engineering, Oxford, Mississippi, USA, 8 pp, 2005.

[5] Y. Shimizu and T. Itakura, “Calculation of flow and bed deformation with a general non-orthogonal coordinate system,” Proc. of XXIV IAHR Congress, Madrid, Spain, C-2, pp.41-48, 1991.

[6] K.W. Olesen, Bed topography in shallow bed rivers. PhD Thesis, TU Delft, 265 pp, 1987.

[7] E.W. Lane and A.A. Kalinske, “Engineering calculations of suspended sediment,” Trans Am Geophysical Union, 22, 1942.

[8] E. Atkinson, Measurements at the Kapunga Curved Channel Sediment Excluder. HR Wallingford report OD/TN67, 46 pp, 1994.

[9] E. Atkinson, The design of sluiced settling basins. HR Wallingford report OD124, 96 pp, 1992

[10] N. Ruether, J.M. Singh and N.R.B. Olsen, E. Atkinson, “3-D computation of sediment transport at water intakes,” Proceedings of the Institution of Civil Engineers, Water Management 158 Issue WM1, pp 1–8, 2005.

[11] HR Wallingford. Sediment Transport: Theory of Ackers and White Updated. SR237, 34 pp, 1990.

[12] E. Atkinson, Measurements at the Kapunga Curved Channel Sediment Excluder: Interim report. HR Wallingford report OD/TN60, 56 pp, 1991.

[13] A.L. Prashun, Modification of the Ackers-White Procedure to Calculate Sediment Transport by Size Fractions. USACE, Contract Report HL-93-4, 67 pp, 1993.

Calculating correct water and sediment fluxes in TELEMAC2D and SISYPHE

Leopold Stadler
Bundesanstalt für Wasserbau (BAW)
Federal Waterways Engineering and Research Institute,
Karlsruhe, Germany
leopold.stadler@baw.de

***Abstract* — This paper describes the fluxline method – a new method to compute water and sediment fluxes in TELEMAC2D and SISYPHE. The method uses the edge fluxes of the positive depth routine to calculate mass fluxes through a user-defined line. The approach of the method is presented and tested with the Yen test case of SISYPHE. The comparison of the calculated fluxes and the change of mass inside the domain show that the method is extremely accurate.**

I. INTRODUTION

The computation of water and sediment fluxes over a line (e.g. a cross section) is an important task for many engineering problems, which allows developers to verify local mass balances for numerical schemes. In this paper we present a new fluxline method that allows a correct and detailed flux computation for all TELEMAC2D and SISYPHE schemes that use the positive depths routine. The method was implemented and tested with the TELEMAC2D/SISYPHE version v6p3r2.

At a first glance, the computation of discharges may seem simple, especially when the geometry and relevant flow parameters like water depth and velocities are available as inputs. However, the numerical flux depends on the numerical scheme and cannot be obtained by a simple integration. It is also extremely important to consider the fact that the potential fluxes may be limited if not enough water or sediment is available. Finally, the only way to compute correct sediment and water fluxes over a section is to use the numerical flux of the numerical scheme. The new method could be a good tool to study sediment transport because the fluxes of all sediment fractions are calculated accurately.

II. FLUXLINE METHOD

In the following section the approach of the fluxline method and its application are explained. The idea behind the method is well-known and often used for mixed Finite Element / Finite Volume Methods (e.g. DuMu^x [1]).

A. Approach

Figure 1 shows a single finite element and the edge fluxes for this element. The edge fluxes of some SISYPHE and TELEMAC2D schemes are calculated by the subroutine 'positive depths' and stored in a data structure (FLODEL). The flux over a line (fluxline) inside a computational domain can be easily calculated by summing up all edge fluxes which intersect with the fluxline for each time step (see Fig. 3). Once all intersecting edges of each fluxline have been calculated, they are stored in a list to speed up the later computation.

Detailed information about water discharge and the discharge of each sediment fraction are calculated. The actual flux, accumulated flux and the actual time are printed into the listing for each fluxline. This makes the fluxline method very useful for investigating local and global sediment discharges. The length of each fluxline must be limited by a bounding box. Only element edges inside the box are taken into account for the flux computation. This allows the user to restrict the fluxline to local parts of the domain.

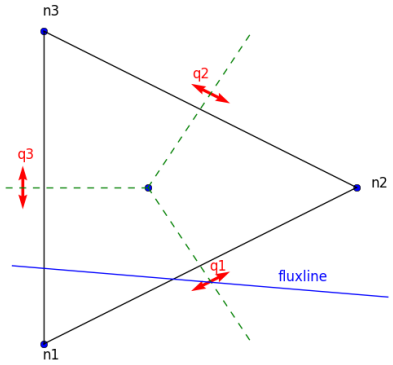

Figure 1. Finite element with edge fluxes (red) and fluxline (blue)

B. Using the fluxline method

In this section we will show how the method can be used to study sediment fluxes. The method is tested with the Yen test case of SISYPHE. Figure 2 shows the mesh of the Yen test case with five user defined fluxlines and the bounding box for each fluxline. Fluline 1 is near the inflow boundary and fluxline 4 near the outflow boundary.

The user must set the keyword FLUXLINE = YES and specify the input file (e.g. FLUXLINE INPUT FILE = fluxline.dat) to run TELEMAC2D/SISYPHE with the fluxline option. The fluxline method was tested with the serial version of TELEMAC/SISYPHE but should also work with the parallel version.

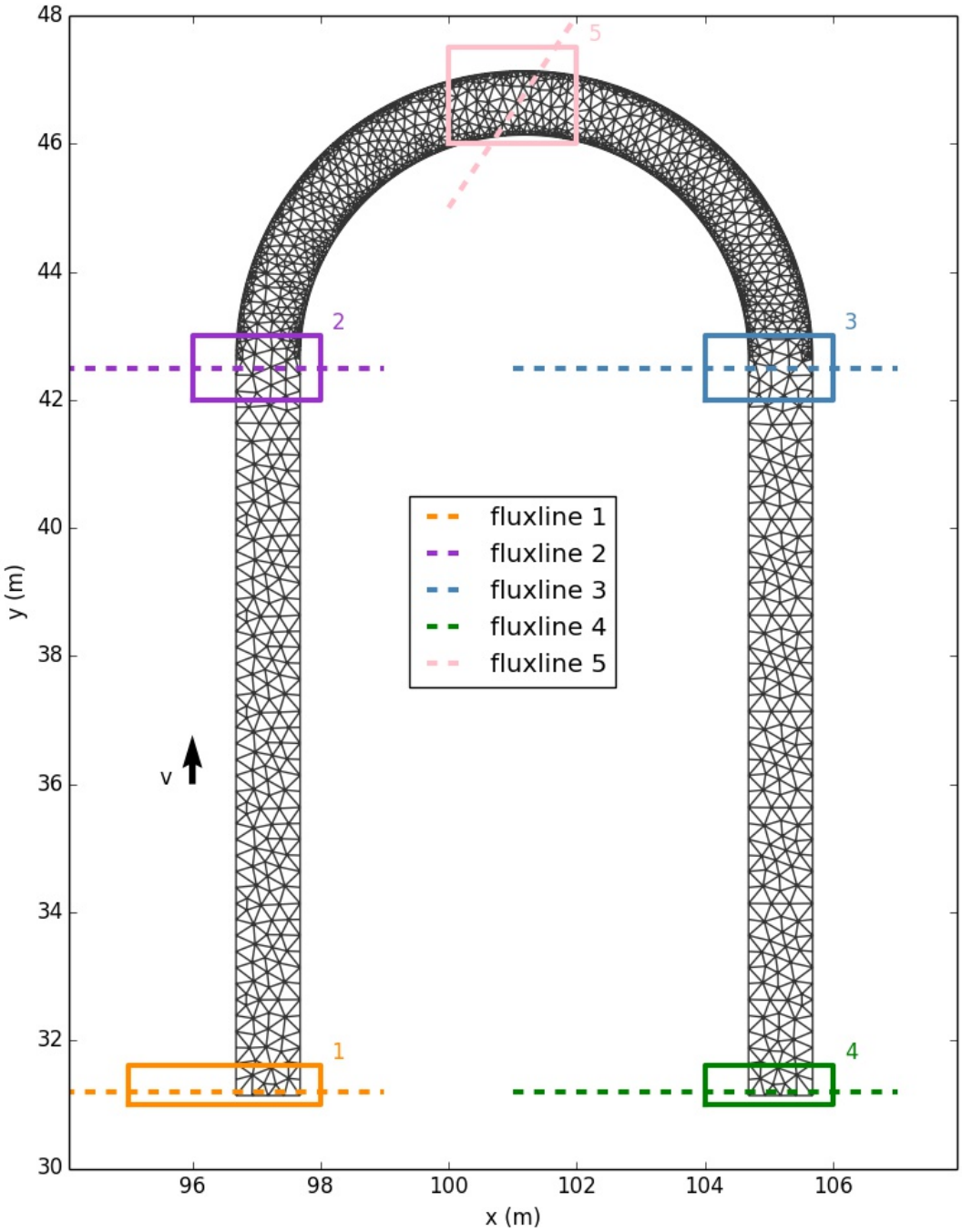

Figure 2. Yen test case with fluxlines

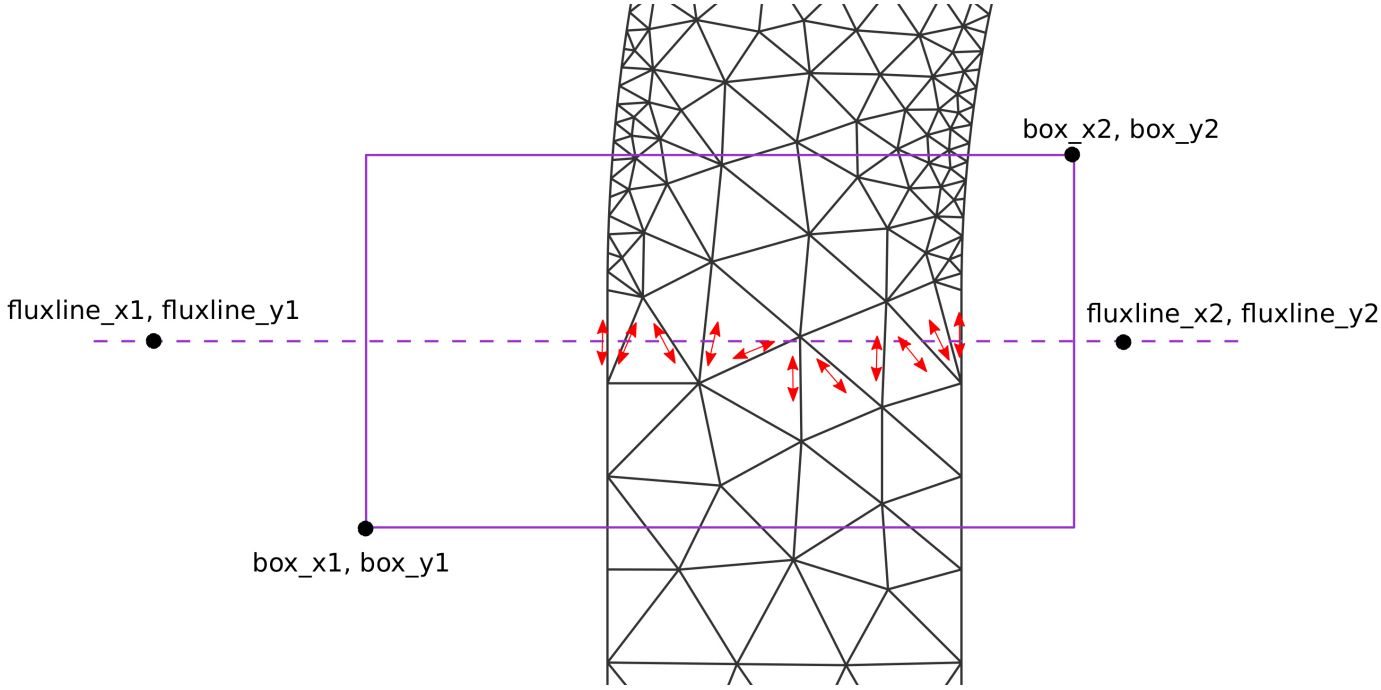

Figure 3. Description of a single fluxline and edge fluxes (red)

The fluxline input file includes the following content:

- The number of fluxlines (integer) is given in the first line of the file.
- All following lines contain the information needed to define a single fluxline (see Figure 3). The line starts with the definition of two points of the fluxline fluxline_x1, fluxline_y1, fluxline_x2, fluxline_y2, followed by the definition of a bounding box box_x1, box_y1, box_x2, box_y2 and ends with an integer which is not used so far.

TELEMAC2D/SISYPHE can be started as usual and the output of the fluxline method are printed into the listing file of TELEMAC2D/SISYPHE. Figure 3 shows the edge fluxes of the edges which intersect with the fluxline.

III. Application and Validation

The original grid and parameters used for this study are taken from the Yen example provided by the TELEMAC-SUITE. The example describes the bed evolution in a U-shaped channel and is often used to study the effect of secondary currents on the bed evolution. Further details about the Yen example can be found in [2]. In the present work we concentrate on the validation of the fluxline method. For this purpose, no details about the morphological results are discussed.

A. Boundary conditions

The domain has two boundaries. The first boundary is at the lower left where a discharge is defined (Figure 4). The second boundary is at the lower right where a water level is defined as boundary condition (Figure 5). Sediment transport will mainly occur during the increased flow rate.

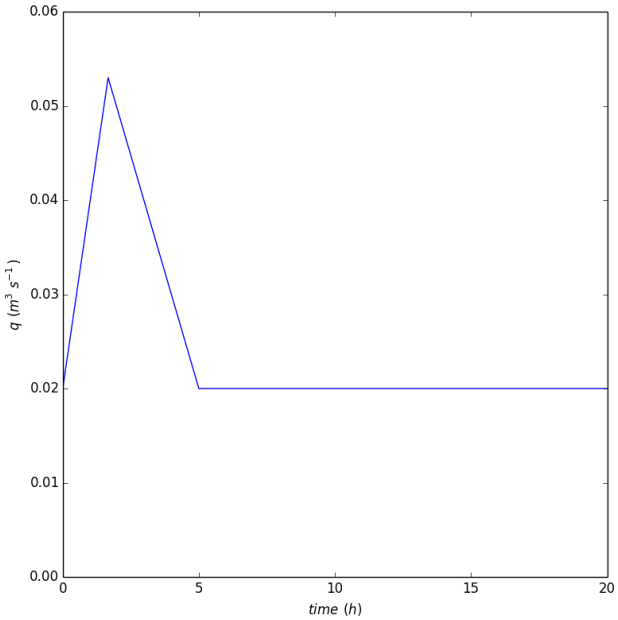

Figure 4. Discharge at the inflow boundary

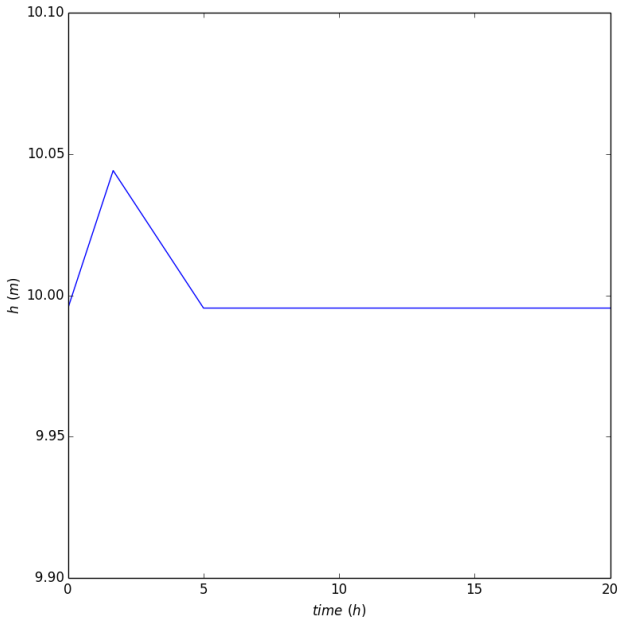

Figure 5. Water level at the outflow boundary

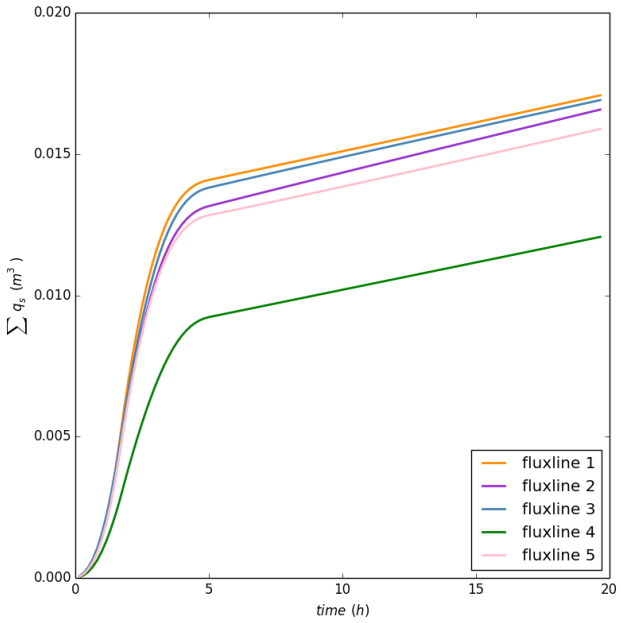

Figure 6. Cummulative discharge for all fluxlines

B. *Numerical results*

The cumulative sediment discharge curves (Fig. 6) for the fluxlines show that sediment transport occurs mainly during the increased flow rate. The highest sediment discharge occurred at the inflow (fluxline 1), the lowest sediment discharge near the outflow (fluxline 4). Figure 8 shows the initial bottom elevation and evolution after 5 h. The largest differences occur inside the bend and after the bend.

A comparison with the evolution after 10 h and 20 h (Fig. 9) shows that the bottom continues to evolve. The results show that local changes in the bottom height can also develop during low flow rates. This is in agreement with the cumulative sediment discharge curves (Fig. 6). The discharges are nearly constant after 5h.

The total sediment volume inside the domain and the sediment volume between fluxline 1 and fluxline 4 were nearly constant during the simulation (Figure 7). The total volume changed about 0.005 m^3 during the simulation.

C. *Validation of the fluxline method*

For the validation of the presented fluxline method the development of the bottom evolution between fluxline 1 and fluxline 4 was compared with the discharges through both fluxlines.

The differences should be theoretically zero, or at least in the order of the numerical accuracy. This accuracy depends on the compiler options and the machine. A difference of $1.2 \cdot 10^{-11}$ m^3 was observed, which is only slightly higher than expected. Nevertheless, this result illustrates the high accuracy of the new fluxline method.

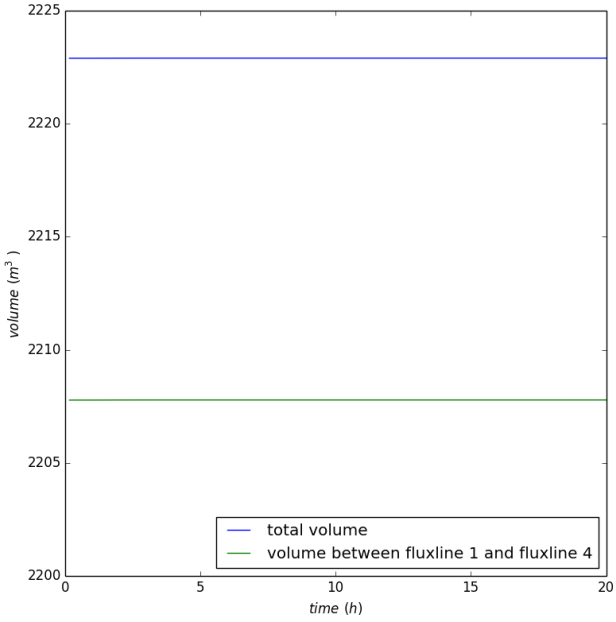

Figure 7. Sediment volume

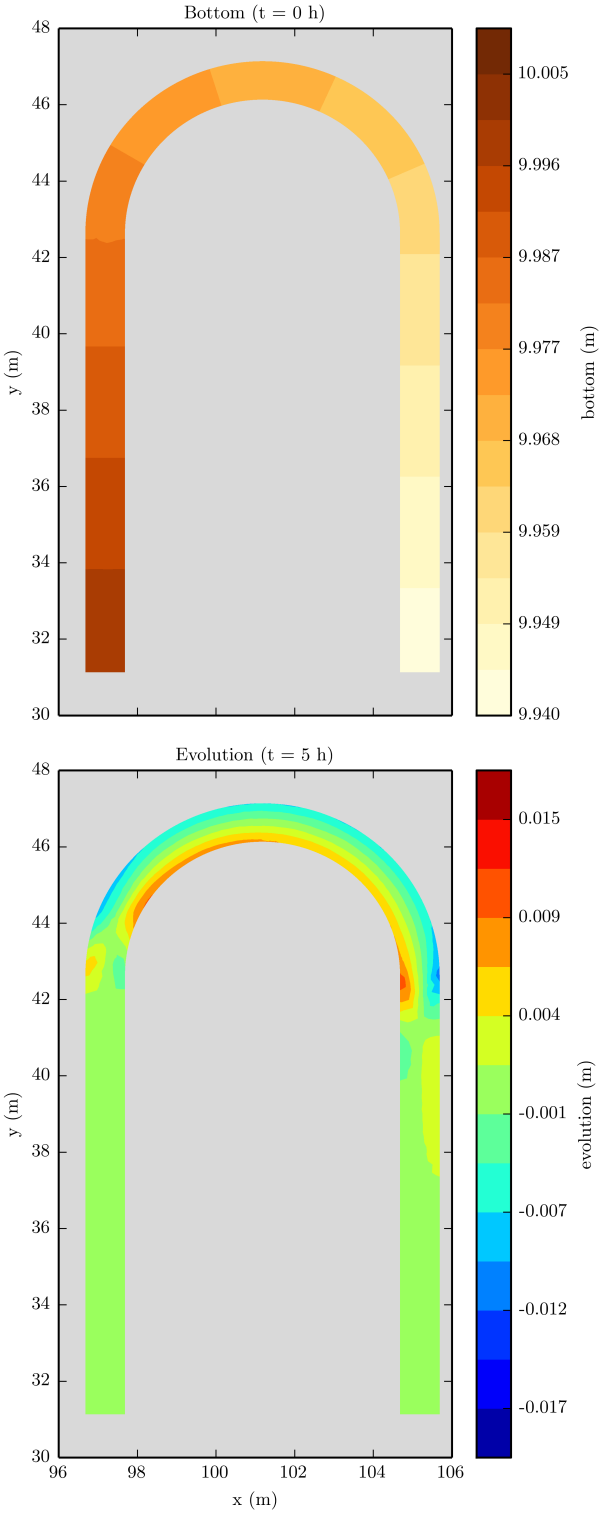

Figure 8. Initial bottom (top) and bottom evolution after 5 h (bottom)

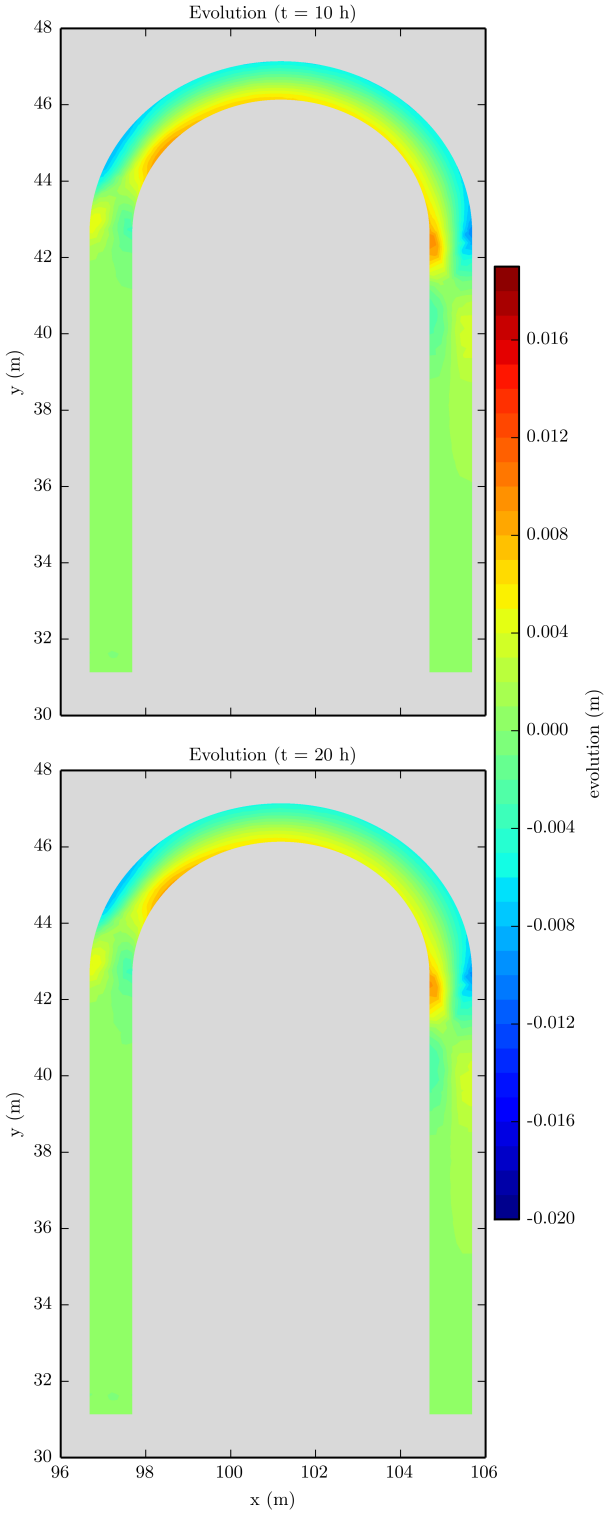

Figure 9. Simulated bottom evolution after 10 h (top) and 20 h (bottom)

IV. Conclusions And Perspectives

The new fluxline method allows the accurate computation of water and sediment discharges for all TELEMAC2D and SISYPHE schemes that use the positive depth subroutine. In this paper we presented the mathematical approach and showed how the method can be used in practice.

The calculated sediment discharges for Yen example of SISIYPHE are in agreement with the simulated bottom evolution. The computed difference between the calculated discharges and the calculated bottom evolution between two fluxlines was extremely small ($1.2 \cdot 10^{-11}$ m^3). The accuracy of the developed fluxline method is promising.

The presented method can not only be used to study local and global sediment discharges. It is also possible to ensure the global and local conservation of the water balance and sediment transport equation of TELEMAC2D and SISYPHE.

References

[1] B. Flemisch, M. Darcis, K. Erbertseder, B. Faigle, A. Lauser, K. Mosthaf, S. Müthing, P. Nuske, A. Tatomir, M. Wolff and R. Helmig, DuMux: DUNE for Multi-{Phase, Component, Scale, Physics, ...} Flow and Transport in Porous Media. Advances in Water Resources, vol. 34 (9), pp. 1102-1112, 2011.

[2] Yen, C. and K. Lee, Bed Topography and Sediment Sorting in Channel Bend with Unsteady Flow, Journal of Hydraulic Engineering, vol. 121 (8), pp. 591-599, 1995.

Modelling the sediment dynamics in the Chambon Reservoir with Telemac 3D

Magali Jodeau
EDF R&D LNHE
France
magali.jodeau@edf.fr

Abstract—**The Chambon Reservoir on the Romanche River has a high rate of sedimentation. In order to help identifying a sustainable sediment management strategy, a modelling of sediment dynamics in this reservoir was built. Numerical simulations were performed according to a comprehensive understanding of sediment transport in this lake based on a large set of in situ data. Suspended sediment concentration monitoring upstream the dam leads to the identification of the main contributing hydrological events. Downstream monitoring demonstrates that specific operating conditions (reservoir level, discharge) allow sediment routing throughout the reservoir. In order to elaborate a clear comprehension of sediment processes, field surveys have also been performed in the reservoir. Bathymetry, Velocity field, sediment concentration were monitored. An innovative device has been built in order to identify sediment and flow dynamics inside the reservoir. Calculations using TELEMAC3D allow to well reproduce the three dimensional patterns of suspended sediment transport in this large reservoir. Turbidity currents due to upstream erosion of sediments are observed in the reservoir and are reproduced with the model. Calculations are compared to in situ measurements, the global sediment dynamics is well reproduced, but there are some differences in the quantitative values.**

I. INTRODUTION

As it has been observed in many countries [9], sedimentation in reservoirs is unavoidable and may have several consequences: (i) loss of capacity, (ii) siltation near bottom gates, (iii) large sediment releases during reservoir emptying...

In order to define long-term management of reservoir sedimentation, deposition in existing reservoirs needs to be mitigated by using appropriate measures for sediment release. The management of sedimentation in large reservoirs is a major issue. Indeed, large amount of fine sediments and gravels could deposit. In the case of large dams, flushing operations (opening of dam gates) could only venture turbidity current or erode a limited part of the sediment bed near the gates. It could require research works to define the appropriate way of dealing with sediments in large reservoirs.

For example, [2] studied turbidity current in Luzzone lake comparing 3D numerical calculations with in situ measurements ; using laboratory experiments and numerical simulation [11] suggests to use geo-textile or underwater obstacle to deal with turbidity current, some numerical calculation were performed using Grimsel reservoir geometry, or [10] analyze the flow patterns and suspended sediment movement in pumped-storage facilities.

Before defining sediment operation, the main processes involved in sediment transport should be identified owing to measurements (bathymetric surveys, concentration monitoring, velocity measurements...). They may help to identify the locations of deposition and the propagating ways (turbidity currents or homogeneous suspension).

EDF stock of facilities accounts for approximately 200 large dams and more than 600 water intakes linked to run off river schemes. In several cases, sedimentation must be dealt with to avoid loss of storage or siltation near the bottom gates.

We focus on the Chambon Reservoir, located in the Alps Mountains. In order to understand the dynamics of sediment, the sediment propagation through this large reservoir has been analyzed, first measuring sediment output and input, then we analyze the internal dynamics using in situ monitoring [15]. Some preliminary numerical simulation of sediment dynamics in the reservoir using TELEMAC2D and SISYPHE have been presented [15], they give a good simulation of the global pattern of sediment dynamics. A 3D model is essential to reproduce the vertical stratification in the lake. Therefore the present paper details the 3D calculations. First the Chambon Reservoir and the sediment monitoring are described. Then the 3D model is introduced and the numerical results are analyzed.

II. SEDIMENTATION IN THE CHAMBON RESERVOIR

A. Description of dam and reservoir

The Chambon dam is located on the Romanche River in the French Alps, Figure 1. The watershed area at the dam is 254 km^2 and the elevation of the area is around 990 m. The Romanche River and a small water derivation flow into the

reservoir, the Ferrand derivation. This derivation enters the reservoir as a water fall, Figure 2 (b).

The hydropower facility, St Guillerme II, has been in activity since 1935, the head is 293 m and the electric power 110 MW.

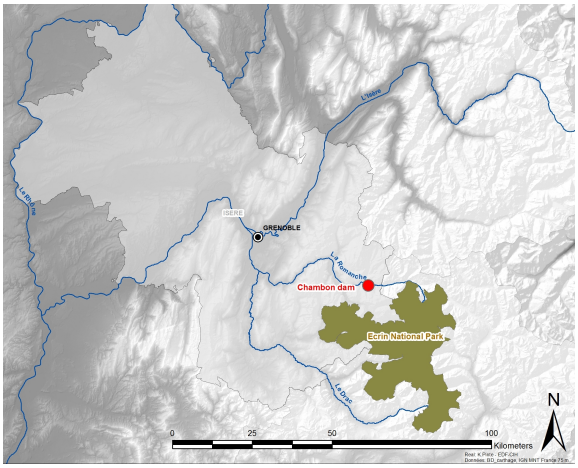

Figure 1. Location of the Chambon Dam.

(a)

(b)

Figure 2. (a) aeriel picture of the Chambon Reservoir (Geoportail). (b) Water fall of the Ferrand derivation.

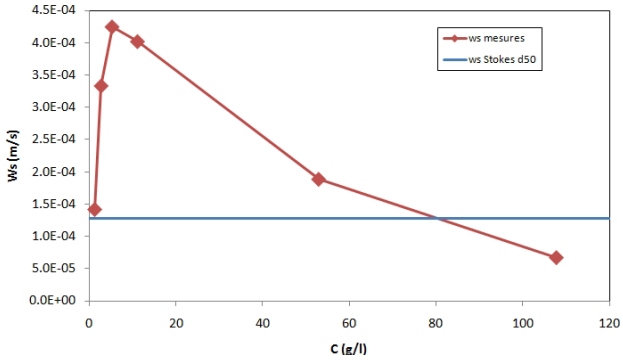

Figure 3. Settling velocity measurement of Chambon sediments.

The volume of water in the reservoir is estimated to be 47.5 10^6 m^3 and the reservoir is 3.5 km long at the highest water level. The water elevation varies depending on seasons, the water level fluctuations could be up to 60 m. Since the beginning of its use, the reservoir has undergone a high rate of sedimentation, it is due to the watershed geology, made of different areas of crystalline rocks but also metamorphic schist. The fine sediment deposition rate in the reservoir is around 100 000 m^3/year. In 2005, in order to protect the bottom gate of the dam, a dredging of 25 000 m^3 of sediments was performed. The sedimentation in the reservoir is studied to find the best sustainable way to manage sediments.

B. Bathymetric and sediment monitoring

A large set of data is available to understand the sediment dynamic in the lake. A comprehensive description of the measurements and their analysis is given in [15].

From the bathymetric data, we could conclude that the reservoir bed evolution is strongly impacted by the water level in the reservoir and its geometry: sediment are eroded in the upstream part of the reservoir where the water flows with high velocities and low water depths; sediment are deposited in the downstream part of the reservoir where the water is still and where the water depth could be high.

Sediment were sampled from the bed in 2004, d50 is around 50 µm, and the concentration of the bed varies from 900 to 1200 g/l. The content of organic matter is low (around 2 %). Due to their small grain size, these sediments are cohesive. Sediment fall velocity measurements have been performed in the laboratory on a representative sample of suspended sediments (d10 =3.7µm, d50 =10.9 µm, d90 =37.9 µm). Settling velocity have been measured owing to an Andreasen pipette, a sediment weight device [8] and a SCAF device [14]. The data from three devices indicate the same trend, figure 3: the settling velocity is the highest, 0.4 mm/s, for a concentration of 10g/l, this value is much higher than the one that could be calculated owing to Stokes formula, 0.12 mm/s. For concentrations higher than 10 g/l a hindered regime is measured [3].

The monitoring of sediment input and output shows that the output of sediment from the reservoir is strongly correlated to the water level in the reservoir, figure 3 shows

that: (i) above 985 m, sediment deposit in the upstream part of the reservoir; (ii) below 985 m, sediment are eroded and they could be transported to the water intake.

In order to have a better insight to the internal sediment dynamics, an innovative device has been designed. Its goal is to give continuous measurement of sediment concentration and flow velocities in the lake at a specific location and for two depths, near the surface and near the bottom of the lake. The data are used in the 3D calculations.

III. DESCRIPTION OF THE 3D NUMERICAL MODEL

Numerical modeling could be a relevant tool in order to test sediment management strategies. In the specific case of large reservoirs, 1D models have been used to predict the sediment concentration during lowering operations [6]. But due to the complex geometry of the large reservoirs, and stratification processes, 2D or 3D model could be required. 3D numerical modeling is now used to study reservoir sedimentation [10, 11]. First the results of some preliminary 2D calculations were studied [15] and in the following we show the 3D results.

TELEMAC 3D from the open source Telemac system (www.opentelemac.org) is used.

A. Description of the model

The geometry of the model is based on the last bathymetry (2011, 1 point/m), the area of the model is the area under water for a water level of 1018 m (maximal operating level during the last years).

The horizontal mesh is made of triangular elements with a size of 5m everywhere but in the talweg where there have a size of 2m and near the bottom gate and the water intake. In order to focus on the sediment processes near the dam, only the area located 1km upstream the dam is included in the model, Figure 4. HYPACK [5] and BLUEKENUE [1] softwares were used to build the horizontal mesh. Two vertical meshes were tested, a z-layer with 22 planes at constant elevations and a σ-layer with 10 planes, Figure 5.

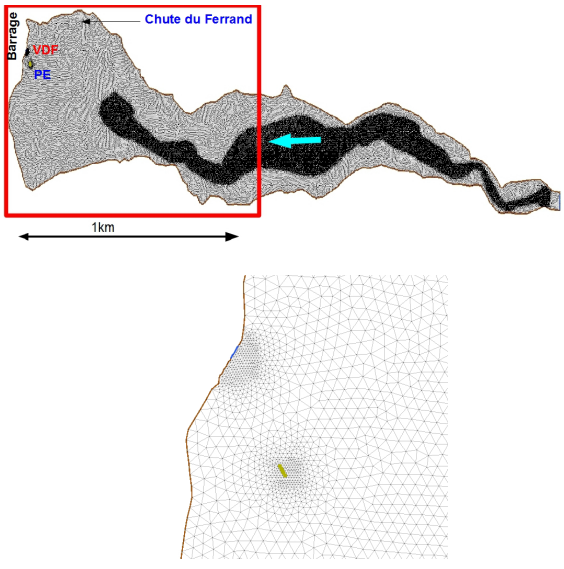

Figure 4. Horizontal mesh.

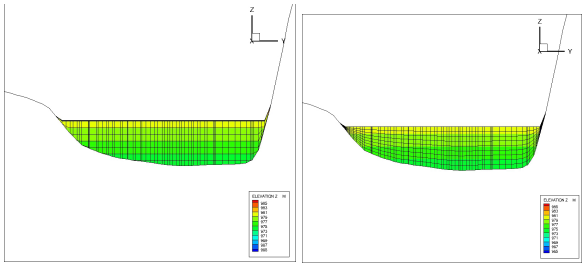

(a) (b)

Figure 5. View of the vertical mesh. (a) z-layer with 22 planes at constant elevations (b) σ-layer with 10 planes.

The upstream hydraulic condition is a varying discharge and the downstream condition could be an imposed water level or an output discharge. The concentration of sediment is chosen on the upstream boundary and it is a free condition on the downstream boundary. The water intake which is not at the boundary line, is represented by a sink.

No data is available to calibrate the friction coefficient, therefore the Strickler coefficient is chosen equal to $52 m^{1/3} s^{-1}$. The turbulence chosen model is a constant viscosity ($D = 10^{-3} m^2 s^{-1}$). In these first calculations, a simple configuration is designed according to the measurements, the sediment bed is made of 2m of uniform cohesive sediments, concentration of the bed is fixed to 900 g/l, fall velocity is 0.4 mm/s. Due to a lack of measurements, other parameters are chosen by analogy with other similar studies [13], that is to say : lateral and longitudinal diffusivity ; critical shear stress for erosion τ_{CE} = 1 Pa ; Partheniades coefficient $M = 10^{-2}$ $kgm^{-2}s^{-1}$; and critical shear velocity for deposition v_{CD} = 0.01 m/s, equivalent to a critical shear stress of 0.1 Pa.

IV. NUMERICAL RESULTS

A. Sensitivity tests

Several sensitivity tests have enabled to choose the numerical parameters and the unknown physical parameters.

Calculations were performed for a time step from 0.1 to 1s. Results are compared for a calculation with constant water elevation at the dam, constant input discharge and concentration. The results show that above 0.2s significant discrepancies are observed. Therefore all the calculations are performed with a 0.2s time step. The calculation time is twice the simulated duration with 192 cores.

The σ-layer vertical mesh is chosen because it shows a longer propagation of sediment in the reservoir.

Four turbulence models were tested (2 values of constant viscosity, kε, and Nezu Nagakawa mixing length model). Figures 6 and 7 show respectively the concentration in the lake and the bathymetric evolution after 22400s (constant elevation 980m, constant input discharge and concentration $20 m^3/s$ and 50g/l) for the kε model and (b) horizontal 10^{-3} m^2/s constant viscosity and vertical Nezu Nagakawa mixing length model. There are some significant differences

between both calculations, the pattern of sediment propagation in the lake for the kε model indicates that the sediments reach the dam and its gates whereas for the other model the sediment are directed towards the right bank. As the measurements at this water elevation and discharge show an output of sediment. All the calculations are performed with the kε model.

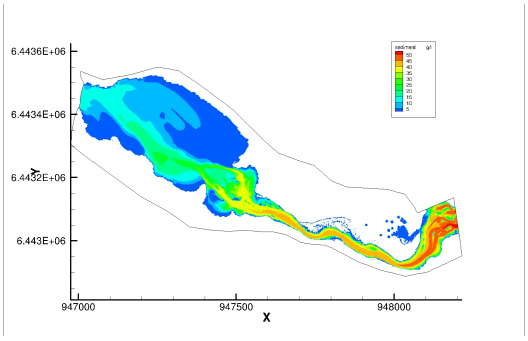

(a)

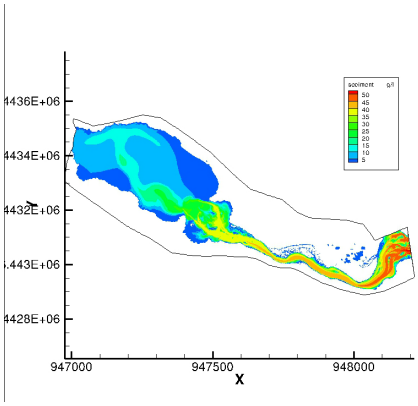

(b)

Figure 6. Concentration in the lake after 22400s (constant elevation 980m, constant input discharge and concentration 20m./s and 50g/l). (a) kε model and (b) horizontal 10^{-3} m^2/s constant viscosity and vertical Nezu Nagakawa mixing length model.

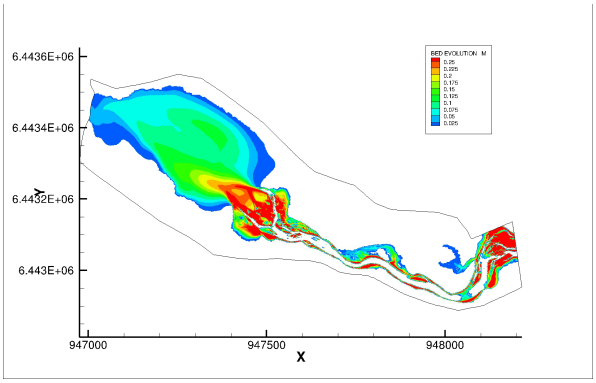

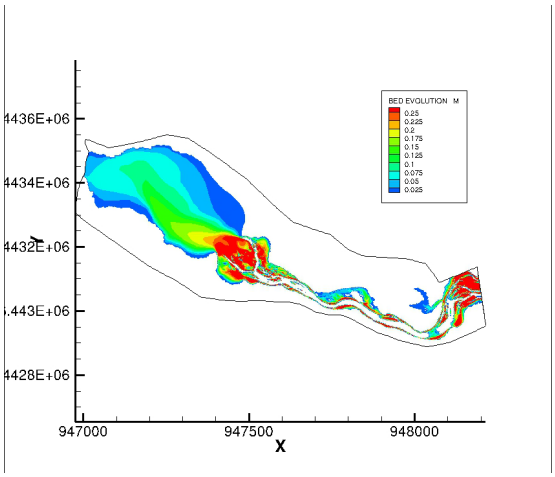

Figure 7. Bathymetric evloution in the lake after 22400s (constant elevation 980m, constant input discharge and concentration 20m^3/s and 50g/l). (a) kε model and (b) horizontal 10^{-3} m^2/s constant viscosity and vertical Nezu Nagakawa mixing length model.

B. Calculation of sediment dynamics for a real event

In order to test the model on a real event, we simulate the period from May 17th to the 20th. The upstream discharge is nearly constant around 17m^3/s, the upstream concentration is lower than 0.5g/l, and there is a lowering of the water level in the reservoir which induced erosion in the reservoir. Consequently the data show that the downstream concentration increases, Figure 8. The concentration measured by the upstream platform in the lake is chosen as the upstream boundary condition.

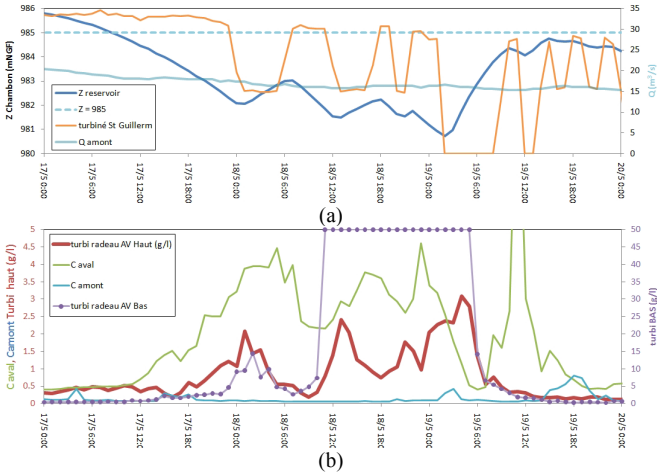

Figure 8. Hydraulic and sediment conditions around May 17th 2013. (a) Water elevation at the dam, input and output discharge; (b) input and output concentrations.

Figure 9 shows the concentration in the lake during the event. A plunging effect of the current can be observed, and the sediments reach the dam. Figure 10 shows a comparison between the concentrations measured downstream the dam and the concentrations calculated at the dam outlet. The order of magnitude and the dynamic is well reproduced but a

temporal lag exists between measured and calculated values. This could be due to several reasons:

- A downstream lag between the dam and the measurement point ;
- An upstream lag between the measurement station (discharge and concentration) and the upstream boundary of the model;
- A simplified description of the sediment bed;
- The fact that the hydrodynamics has not been calibrated (friction and turbulence);
- Etc…

Further measurements would help to better reproduce the sediment dynamics in the lake.

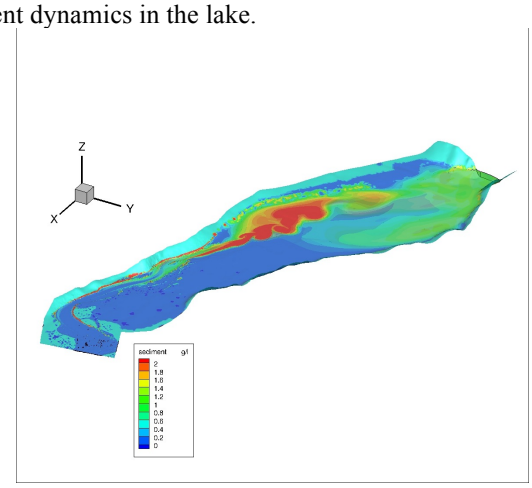

Figure 9. Concentration in the lake for the real event after 50 000s.

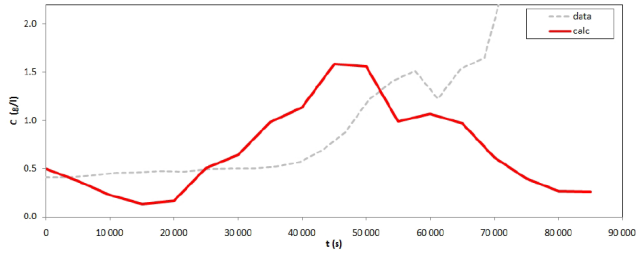

Figure 10. Measured and calculated concentration near the dam outlet for the real event of May 17th 2013.

C. *Effect of the water fall*

The previous monitoring indicates that the water fall near the dam, on the right bank, has an effect on the water velocities in the lake. Some simple tests are performed to try to simulate this effect. The water fall is reproduced with a discharge source on a node.

Figures 11 and 12 show the differences without and with the water fall. The water fall has an effect on the sediment propagation in the lake. The vertical stratification is changed near the dam.

Further measurement would be necessary to calibrate and to analyse the effect of the water fall more deeply.

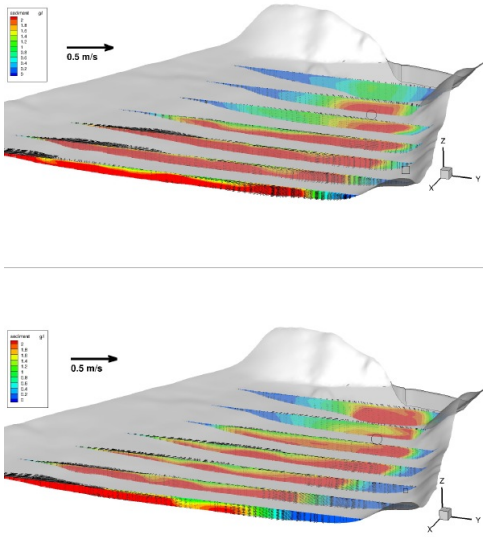

Figure 11. Tests to simulate the effect of the water fall. Top : concentarion in the lake without the water fall and Bottom : concentration in the lake with water fall. The water fall is represented by a “o” on the bottom picture.

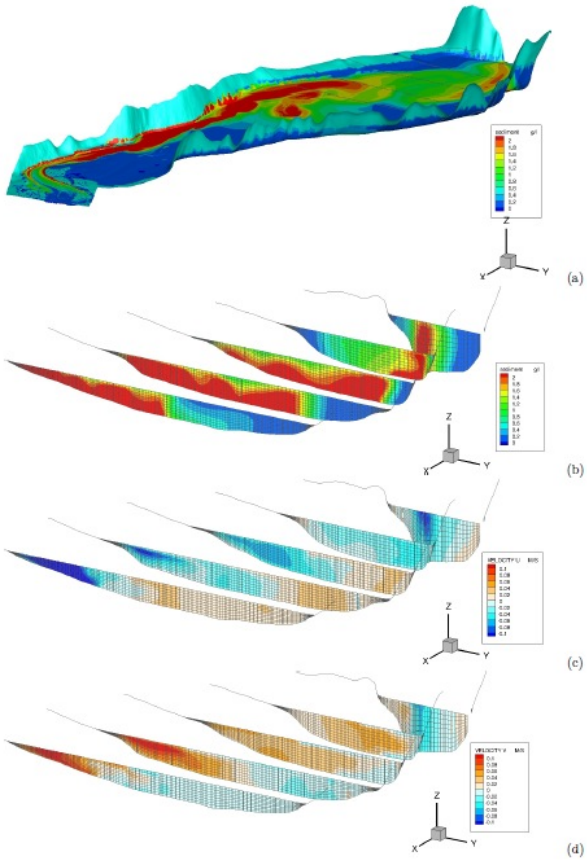

Figure 12. Calculation with the water fall, (a) surface concentration (b) ceoncentration in the lake (c) and (d) vx and vy components of the velocity vector.

V. Conclusion and Prespectives

3D calculation of sediment propagation in the Chambon reservoir were performed with Telemac 3D. Sensitivity tests enabled to choose the numerical parameters and the unknown physical parameters.

The calculations allow to reproduce the main trend of the sediment dynamics in the lake but some differences between the measurements and the numerical results are observed.

Identifying the source of the discrepancies is not easy but additional data could be a way to improve the calculations. The code could also be tested on experiment data in order to determine the best parameterization to simulate turbidity currents. Besides, the modelling of the turbidity currents in reservoirs will help to find ways to manage the sedimentation.

Acknowledgement

The author would like to thank DTG for the monitoring, Marion Cormier and Quentin Monnoyer for the settling velocity measurements.

[1] Blue kenue: Software tool for hydraulic modellers, http://www.nrc-cnrc.gc.ca, 2013.

[2] G. De Cesare. Alluvionnement des retenues par courants de turbidit. PhD thesis, EPFL, 1998.

[3] N. Gratiot, H. Michallet, and M. Mory. On the determination of the settling flux of cohesive sediments in a turbulent fluid. Journal of Geophysical Research, 110, 2005.

[4] J.M. Hervouet. Hydrodynamics of free surface flows, modelling with the finite element method.Wiley, 2007.

[5] Hypack. Hydrographic survey software. Technical report, Hypack Inc., http://www.hypack.com, 2013.

[6] M. Jodeau and S. Menu. Sediment transport modeling of a reservoir drawdown, example of Tolla reservoir. In River Flow Conference, 2012.

[7] V. Mano, J. Nemery, and A. Poirel. Assessment of suspended sediment transport in four alpine watersheds (France): influence of the climatic regime . Hydrological Processes, 23, 2009.

[8] A. Mantovanelli and P. V. Ridd. Devices to measure settling velocities of cohesive sediment aggregates : A review of the in situ technology. Journal of Sea Research, 56 (3):199–226, 2006.

[9] G. L. Morris and J. Fan. Reservoir Sedimentation Handbook . McGraw-Hill, 1997.

[10] M. Muller. Influence of in- and outflow sequences on flow patterns and suspended sediment behavior in reservoirs. PhD thesis, EPFL LCH, 2012.

[11] C.D. Oehy, G. De Cesare, and A.J. Schleiss. effect of inclined jet screen on turbidity current. Journal of Hydraulic Research, 48:81–90, 2010.

[12] P. Tassi, C Villaret, and D. Pham Van Bang. Sisyphe, release 6.2, user manual H-P73-2010-01219, available on www.open-telemac.org. Technical report, EDF, 2013.

[13] E. Valette, P. Tassi, M. Jodeau, and C. Villaret. St Egrve Reservoir - Multi-dimensional modelling of flushing and evolution of the channel bed . In River Flow, 2014.

[14] V. Wendling, Gratiot, C. N. Legout, I.G. Droppo, A.J. Manning, G. Antoine, H. Michallet, and M. Jodeau. A rapid method for settling velocity and flocculation measurement within high suspended sediment concentration rivers. In Intercoh, 2013.

[15] M. Jodeau,M. Cazilhac, A. Poirel, P. Negrello, K. Pinte, JP. Bouchard and C. Bertier Innovative in-situ measurements, analysis and modeling of sediment dynamics in Chambon reservoir, France. In River Flow, 2014.

Hydrodynamic and fine sediment transport numerical modelling, application to the Río de la Plata and Montevideo Bay

Pablo Santoro, Mónica Fossati, Ismael Piedra-Cueva
Instituto de Mecánica de los Fluidos e Ingeniería Ambiental
Universidad de la República
Montevideo, Uruguay
psantoro@fing.edu.uy, mfossati@fing.edu.uy,
ismaelp@fing.edu.uy

Pablo Tassi, Michel Benoit
Saint Venant Laboratory for Hydraulics
EDF R&D
Chatou, France
pablo.tassi@edf.fr, michel.benoit@edf.fr

Nicolas Huybrechts
Roberval Laboratory, LHN (UTC)
CEREMA
Compiègne, France
nicolas.huybrechts@cerema.fr

Damien Pham Van Bang
Saint Venant Laboratory for Hydraulics
CEREMA
Chatou, France
damien.pham-van-bang@cerema.fr

***Abstract*— The objective of this work is to develop a high resolution wave-current-sediment transport model to simulate the flow field and sediment transport processes of the Río de la Plata estuary and specifically at Montevideo Bay area. Numerical results using the depth-averaged modules of the TELEMAC-MASCARET Modelling System show excellent agreement when compared with observed sea surface elevation, currents, and wave parameters at several stations in the estuary. Preliminary results show a good representation of the suspended sediment concentration series near Montevideo Bay.**

I. INTRODUCTION

Montevideo Bay hosts the main port of Uruguay along with a large industrial development. Nowadays there are many maritime engineering projects in the area, including the construction of new breakwaters, land reclamation for container terminals, navigation channels deepening, etc. All these projects need a reliable characterization of the hydrodynamics in the area and also for some of them the sediment dynamics. Numerical modelling is a powerful tool in that sense, not only for the design of these projects but also to assess their impact on the whole area.

In this work the open source TELEMAC-MASCARET Modelling System (TMS) is implemented for the Río de la Plata estuary with special attention to Montevideo Bay in order to study the fine sediment dynamics. Previous studies of our group have been focused on the general hydrodynamic and fine sediment dynamics for the whole estuary [1],[2]. By using the finite elements/volumes technique the TMS works with non-structures meshes allowing to cover big domains increasing the resolution on the areas of interest which can have complex geometries e.g. harbours. As a first approach we started to work using the depth averaged modules of the TMS. Although we know the limitations of this approach for an estuarine application, it aims to be an efficient tool in terms of computation times, which is very important for example during the evaluation of several "what-if" scenarios for engineering projects.

II. STUDY AREA

The Río de la Plata is located on the east coast of South America. Its axis runs from NW to SE and is approximately 280 km long. Its surface area is approximately 35,000 km2, and its width varies from 20 km at the innermost part to approximately 220 km at its mouth (Fig. 1). The river communicates freely with the ocean and experiences seasonal freshwater discharge from its two major tributaries (the Paraná and Uruguay rivers), with annual average discharge of approximately 16,000 m3/s and 6,000 m3/s, respectively. Two main regions can be identified based on the morphology and dynamics of the Río de la Plata. A shallow area located along the Punta Piedras-Montevideo line separates the inner region from the outer region. The inner region has a fluvial regime, with no stratification or preferential flow direction. In the outer region, the increase in river width generates complex flow patterns. This outer region is formed by brackish waters of variable salinity that are influenced by the tides, the winds, and the contribution of fresh water from the river basin.

The tidal regime is dominated by the M2 component, followed by the O1 component which is responsible for the diurnal inequality. The tidal amplitude is greater along the Argentinean coast (order of 1 m), while it is about 0.4 m along the Uruguayan coast. The meteorological tide (storm

surge events) is of great importance being of the same order of magnitude as the astronomical tide [2]. Currents at the estuary are controlled by the oceanic tides that penetrate the river mouth. Although the amplitude of the tides is small, the very large river mouth generates a tidal prism that can dominate the flow regime despite the significant discharge received from the tributaries.

The outer Rio de la Plata and the adjacent continental shelf are covered with sands, while silty clays, clayey silts and silts, are confined to the upper and the middle portions of the estuary. The suspended sediment load is mainly carried by the Paraná river in amounts up to 160 million tons/year of fine sand, silt, and clay. Fine sands mostly settle in the innermost part of the Río de la Plata and are responsible for the Paraná Delta Front progradation. Fluvial fine cohesive sediments are further advected to the inner part of the estuary.

Montevideo Bay covers an area of approximately 12 km2 and is part of the Río de la Plata (Fig. 2c). The water depth reaches 5 m in the outer part of the bay and between 1 m and 1.5 m in the inner area. The navigation channels are approximately 11 m deep. The bay receives two urban streams, Pantanoso and Miguelete. Water circulation in the bay mainly occurs due to the sea level variations along the bay mouth and due to shear induced by the outer flow and the local winds.

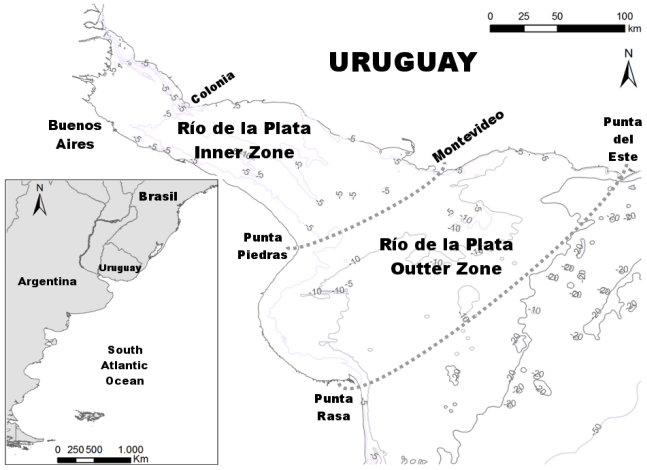

Figure 1. Río de la Plata location and bathymetry.

III. HYDRO-METEOROLOGICAL DATA

A. Meteorological data

Data from the European Centre of Medium Weather Forecast was used, in particular the ERA-Interim product [3] with a 0.125° spatial resolution and 6 hours temporal resolution.

B. Sea surface elevation data

Sea surface elevation (SSE) measurements at eight mareograph stations were used in this work, named Mar del Plata (MP), La Paloma (LP), Punta del Este (PE), Montevideo (MVD), Torre Oyarvide (TO), Pilote Norden (PN), Colonia (COL) y Buenos Aires (BA). Fig. 2a shows the location of each one of these stations.

Particularly for this work the analysed periods were the years 2004 and 2009. During the first one there is available information in the eight stations (with some missing gaps). During 2009 we have only available information at MP, MVD y PN stations. In all cases we worked with hourly sea level series.

C. Currents data

Current data from ADCPs (Acoustic Doppler Current Profiler) instruments are available at two locations near to Montevideo coast referred as Punta Brava (PB) and Punta Yeguas (PY) (see Fig. 2c). These instruments were installed at the end of 2003 and were measuring until the end of 2009 (with several gaps due to maintenance). These instruments provided simultaneous data of currents direction and intensity at different depths in the water column. The instruments were set to save a register each 30 minutes.

D. Wave data

Two wave database were used in this work. The first one correspond to PB ADCP time series of significant wave height, mean period, peak period and peak direction. The available period is 2007 to 2009 with several gaps, the temporal resolution of this series is 3 hours.

The second dataset comes from a wave rider buoy here called Hidrovia (HV), (see Fig. 2a). There is available data from 1996 to 2006 with several gaps, the temporal resolution is variable but it is close to 1 hour.

E. Suspended sediment data

Suspended sediment concentration data was obtained indirectly from the backscatter intensity from PB ADCP. The backscatter-SSC calibration was done using water samples taken at two different water depths during the initial deployments [4].

IV. MODEL SETUP

A. Domain and computational mesh

The modelled domain includes the Rio de la Plata and its maritime front zone approximately until the 200 m depth on the continental shelf (Fig. 2a). The main freshwater inflows are included, rivers Paraná and Uruguay at the west boundary (Fig. 2b). As it was mentioned before the TMS works with finite elements based on triangular meshes. The mesh elements size ranges from approximately twelve kilometres at the oceanic boundary to ten meters in the vicinity of the Montevideo Bay, it has 30059 nodes and 58594 elements. Fig. 2c shows in more detail the mesh at Montevideo Bay zone and includes its bathymetry. It can be seen the navigation channel which gives access to Montevideo's harbour and the harbour basins and internal channels in the bay.

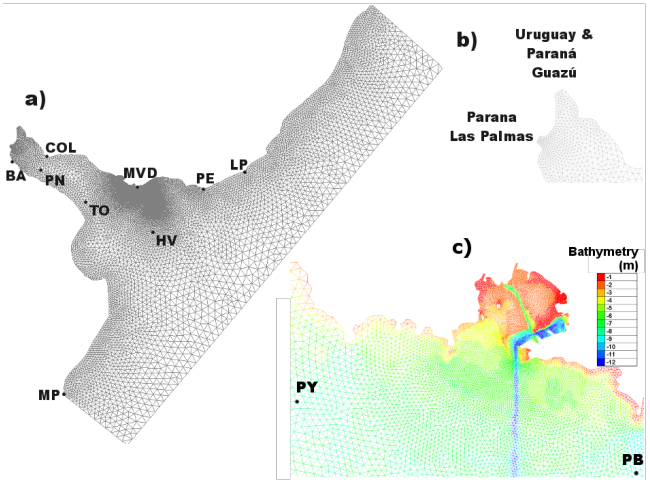

Figure 2. (a) Río de la Plata unstructured mesh, (b) detail of river discharges, (c) Montevideo Bay zone including its bathymtery.

B. Circulation model:

The hydrodynamic model Telemac 2D (T2D) takes into account the fluvial discharges of Paraná and Uruguay rivers, tides at the oceanic boundary (astronomical and meteorological from a regional model), and wind and sea level pressure from ERA-Interim ReAnalysis. The model takes into account the effect of the salinity horizontal gradients.

The daily flow information of the Parana and Uruguay rivers was provided by the Argentinean National Water Institute. Fig. 2b shows the two sections of stream flow contribution defined in the inner region of the Rio de la Plata, one corresponds to the income flow of Uruguay and Parana-Guazu rivers and the other to the Parana Las Palmas river.

Relevant tidal waves, both astronomical and meteorological, are imposed at the oceanic open boundary. Sea surface elevation values provided by a regional tidal model [5] are prescribed at oceanic boundary nodes.

For the bottom friction computation the Manning formulation was chosen and the Manning coefficient was considered as a calibration parameter.

On the free surface, wind and sea level pressure forcings are considered. For the wind surface stress an aerodynamic bulk formula is employed with a constant drag coefficient. This drag coefficient was the other calibration parameter.

After several tests the final configuration solves the quasi-bubble approximation of the primitive form of the shallow water equations [6] using a time step of 60s. The characteristics method is applied as advection scheme for the velocity computation and the distributed PSI method is used for the free surface elevation.

As it was mentioned before the chosen calibration parameters are the Manning coefficient, and the drag coefficient in the surface wind stress formulation. It was carried out a set of simulations varying these parameters in a wide range of reasonable values. The simulation period for the calibration was January – June 2004, while the validation period was January - May 2009. In order to evaluate the quality of the results, the simulated sea level series were compared against the observed values in the mareographs stations presented in Fig. 2a. Also the depth averaged currents at PB and PY were compared.

C. Wave propagation model:

The third generation spectral wave model TOMAWAC (TWAC) is forced with 10m wind from the European Centre of Medium Weather Forecast ERA-Interim Reanalysis. At the oceanic boundary the model is forced by wave statistics from a regional model [7]. A Jonswap spectrum is constructed at each boundary node based on the significant wave height, peak period, mean direction, and directional spread given by the regional model with a temporal resolution of 3 hours.

The model was configured to takes into account the following processes: white capping, bottom friction, depth breaking, and quadruplets interactions.

Model results were validated against observed data at PB and HV stations.

D. Coupled Circulation and Wave model

The TMS allows to perform a two way coupling between T2D-TWAC to represent wave current interactions: T2D transfers to TWAC the updated values of current velocities and water depths, while TWAC solves the wave action density conservation equation with reference to those current and water depth values and returns to T2D the updated values of the wave driving radiation forces acting on the current.

As mentioned before the time step for both models is 60s, the selected coupling period is 60 which means both models communicate with each other every 1h.

E. Sediment transport model

SISYPHE (SIS) was coupled with the circulation model T2D. Even though it is possible to implement a three way coupling including the wave model (SIS+TWAC+T2D), the wave model increases the computation time considerably. For this reason for sensitivity analyzes and preliminary calibration we modified the SIS code in order to read the wave results of the coupled wave and circulation model. Having read the wave results the wave bottom stress was computed using the Swart formulation [8] for the friction factor considering a bed roughness of 0.1mm and using the peak period for the orbital velocity computation.

Only one sediment class is considered, which is defined as cohesive. Our main interest is to study the fine sediment dynamics and specifically at Montevideo Bay zone the non-cohesive sediment fraction is negligible. The model computes the erosion flux using the Partheniades classical formula and the deposition flux using the Krone formula [9]. Based on these equations the parameters to be defined are: the settling velocity, the Partheniades coefficient, and both the critical shear stress for deposition and erosion. In SIS the settling velocity is considered as a constant value given by the user. In order to represent indirectly the effect of

flocculation in settling we modified the code and made the settling velocity proportional to the SSC. So it is needed to define both a settling velocity and the SSC associated to it.

The bottom bed is uniform all over the domain, however areas where non-cohesive sediments are predominant were set as non-erodables. As it was said before only the fine sediment fraction is being modelled in this implementation. The consolidation process is not taken into account yet.

The SSC imposed at the boundaries is null except for the two sections corresponding to Uruguay and Paraná Rivers (see Fig. 2b). At Paraná Las Palmas boundary the imposed SSC is 47mg/L, while at Uruguay and Paraná Guazú boundary it is 154 mg/L. These are annual mean values for the fine sediment fraction from [10].

By the time being it was made a sensibility analysis to the parameters mentioned before and a preliminary calibration procedure comparing the SSC results against the PB observations.

V. RESULTS

A. *Circulation model*

After the calibration process the wind drag coefficient showed to be the main parameter to adjust the meteorological tide events representation. The Manning coefficient influence is also noticeable, especially on the astronomical tide presentation. After comparing the results against SSE series and currents series at the stations mentioned before, it was selected the configuration with drag coefficient equals 3e-6 and Manning coefficient 0.02.

In order to illustrate the sensibility of the model results to these parameters, Figs. 3 and 4 show Taylor diagrams of the sea surface elevation series at Montevideo station. This diagram allows to summarize three statistics for a set of simulated series: the Pearson correlation between the observed and simulated series (blue), the standard deviation of each series (black), and the centred root mean squared error of the simulated series (green). Fig. 3 shows the results corresponding to nine simulations varying the wind drag coefficient (Cd) from 1e-6 to 5e-6 with step 0.5e-6. It can be seen that simulation 5, corresponding to a wind drag coefficient equals 3e-6, gives the best results.

Fig. 4 shows the results of seven simulations where the Manning coefficient (n) took these values: 0.015, 0.018, 0.019, 0.020, 0.021, 0.022, 0.025. Simulation 4, corresponding to a Manning coefficient equals 0.020, gives the best results.

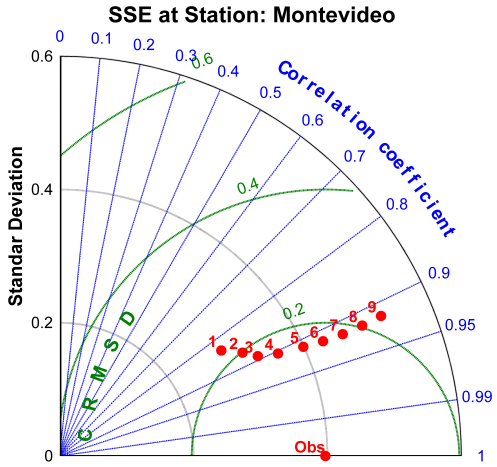

Figure 3. Taylor diagram of sea surface elevation series for different wind drag coefficients (1 correspond to Cd=1e-6 and 7 to Cd=5e-6).

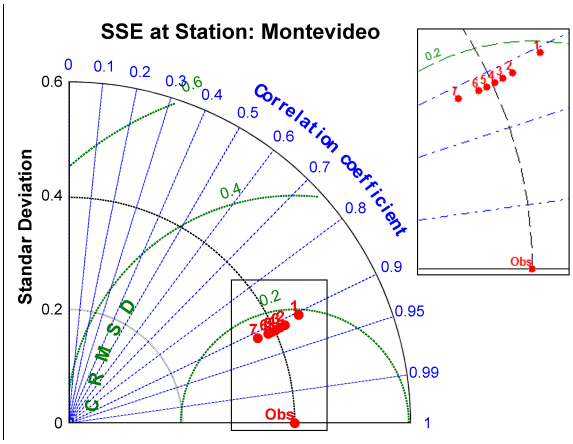

Figure 4. Taylor diagram of the sea surface elevation series for different Manning coefficients (1 correspond to n=0.015 and 7 to n=0.025).

Fig. 5 shows the SSE series at MVD and PN stations during Feb-Mar 2009. It can be seen that the model is able to properly represent both the astronomical tide oscillations and the meteorological tide events.

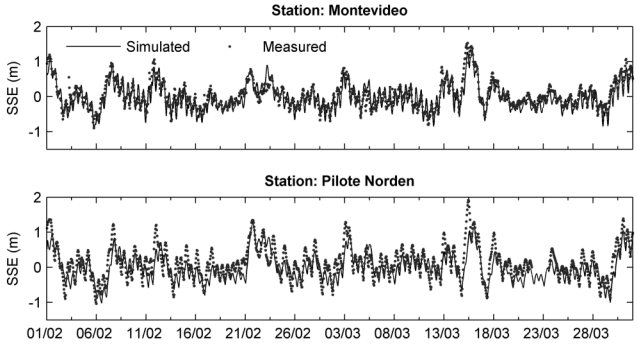

Figure 5. SSE time series comparison during Feb-Mar 2009 at MVD and PN stations.

Table 1 shows a summary of statistics resulting from comparing the simulated and measured SSE series. It includes the Normalized Standard Deviation (NSDV)

(modelled SDV / measured SDV), Centred Root Mean Squared Error (CRMSE), and Pearson Correlation (Corr). Finally the amount of data employed for the calculation is showed.

TABLE I. SSE STATISTICS.

Period	Station	NSDV	CRMSE (m)	Corr	# Data
2004 (Jan to Jun)	MP	0,80	0,21	0,87	4209
	LP	1,08	0,19	0,81	3287
	PE	0,97	0,17	0,86	3935
	MVD	1,01	0,19	0,87	4367
	TO	0,89	0,28	0,81	4367
	PN	0,95	0,25	0,84	4367
	COL	0,95	0,27	0,81	4367
	BA	0,93	0,28	0,84	4367
2009 (Jan to May)	MVD	0.97	0.19	0.89	3060
	PN	0.90	0.26	0.84	3234

Fig. 6 shows a comparison of the simulated and measured currents series during different periods of 2004 at PB and PY stations. The results show a good agreement between the model results and observed values. Table 2 shows the statistics for the depth averaged currents series.

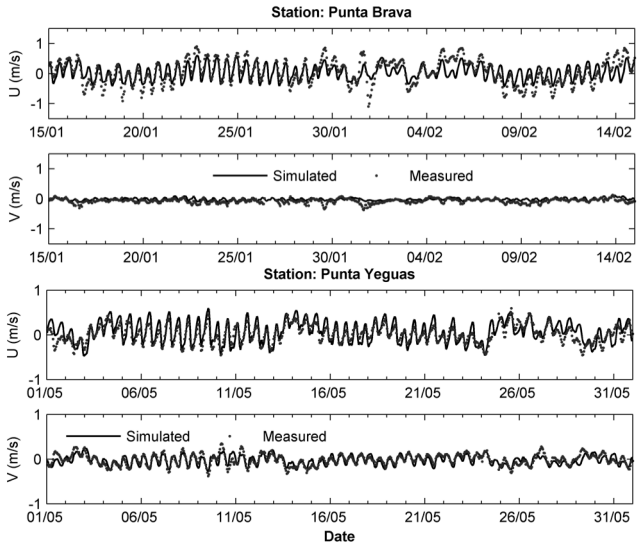

Figure 6. Depth averaged currents comparison at PB and PY stations during 2004.

TABLE II. DEPTH AVERAGED CURRENTS STATISTICS.

Station	NSDV	CRMSE (m/s)	Corr	# Data
PB U	0.66	0.26	0.73	3772
PB V	0.71	0.06	0.38	3772
PY U	1.08	0.17	0.71	2815
PY V	0.89	0.09	0.70	2815

B. Wave propagation model

Figs. 5 and 6 show a comparison of the wave parameters time series at HV and PB during 2006 and 2009 respectively. At both stations the significant wave height (Hs) is well represented. The mean period (TM02) is underestimated specially at PB, which is probably related to the frequency discretization chosen in the model. The peak period (TP) and direction (Dp) are reasonably well represent by the model at both locations.

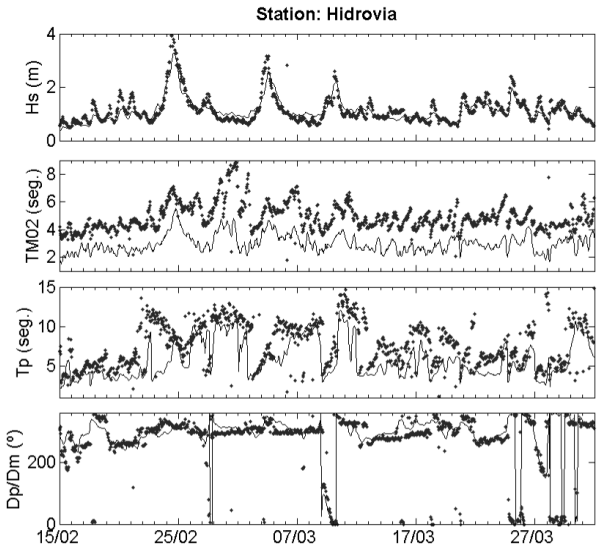

Figure 7. Wave parameteres time series comparison at Hidrovia station during Feb - Mar 2006.

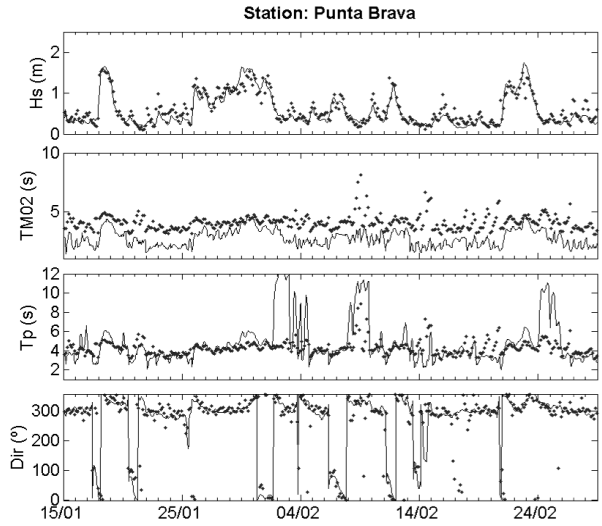

Figure 8. Wave parameters time series comparison at PB station during Jan – Feb 2009.

Table 3 shows a summary of statistics for the significant wave height and peak period time series, including the Root Mean Squared Error (RMSE), the Mean Error (ME), and Pearson Correlation (Corr). These two variables are of most interest as they will be used for the wave bottom stress shear computation.

TABLE III. WAVE PARAMETERS STATISTICS.

Wave Parameter	Statistic	PB 2009	HV 2006
Hs	RMSE (m)	0.16	0.21
	ME (m)	-0.02	-0.002
	Corr	0.89	0.86
Tp	RMSE (s)	2.4	3.9
	ME (s)	0.5	3.4
	Corr	0.34	0.42
# Data		916	2180

To evaluate the relative importance of the oceanic boundary conditions (swell waves) and the local wind effect (sea waves), two idealized simulations were made. One considering only the wind as forcing, and other taking into account only the oceanic boundary conditions propagation. The results (Fig. 7) show that at PB station the local wind is the main forcing.

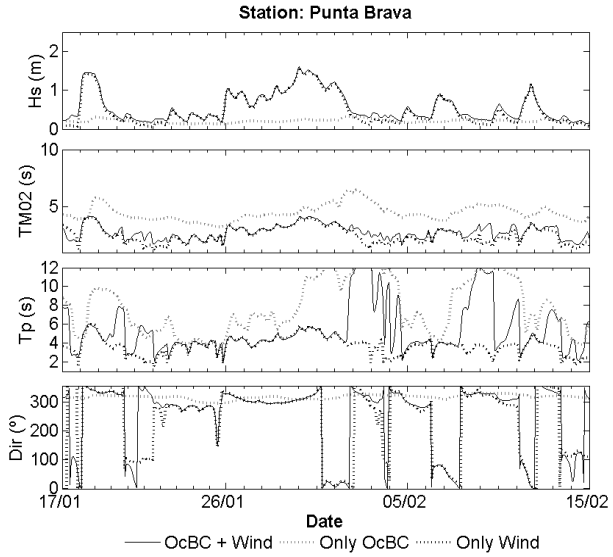

Figure 9. Wave boundary conditions influence. Comparison at PB station during Jan – Feb 2009.

However at HV stations it can be seen that the oceanic boundary conditions play a more important role (Fig. 8).

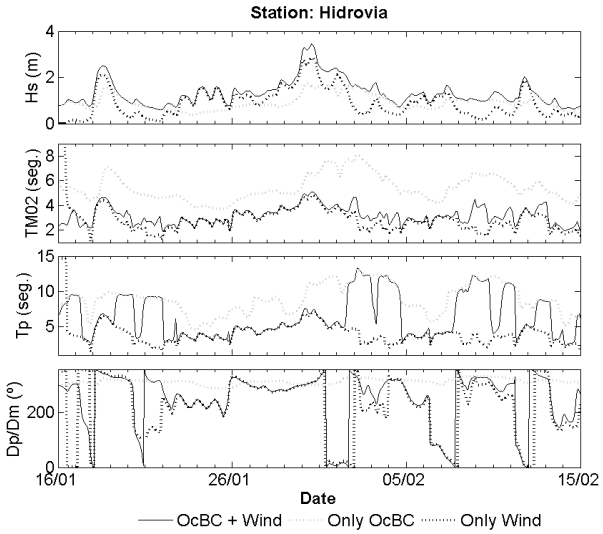

Figure 10. Wave boundary conditions influence. Comparison at HV station during Jan – Feb 2009.

C. *Sediment transport model*

The sensitivity analysis showed that all the parameters have a great impact on the sediment transport model results. The critical shear stress for deposition was set at a very high value (10e4 Pa). It means we are considering the simultaneous deposition-erosion paradigm, where deposition take place continuously at a rate D=Ws.SSC. This configuration has been proposed for engineering applications at low-concentration cohesive sediment suspensions [11].

After a preliminary calibration based on the SSC observed at PB, the selected parameters are: settling velocity 1e-4m/s, reference concentration for settling velocity 0.1kg/m3, critical shear stress for erosion 0.1 Pa, Partheniades coefficient 2e-6 kg/m/s.

Fig. 11 shows the model results during May 2009 at PB station. The first two panels show some of the main hydrodynamic variables, the current intensity and significant wave height. The third panel shows the simulated total bottom stress; wave and current bottom stresses are also included. It is clearly seen that the highest values of bottom stress are related to strong waves which are associated to storm conditions at the Río de la Plata. Finally the last panel shows the suspended sediment concentration series. It can be seen that the model reproduce the general behaviour of the SSC series. During calm conditions (small wave heights) the model seems to overestimate the SSC. It represented reasonably well the re-suspension during the two storm events that took place in the presented period.

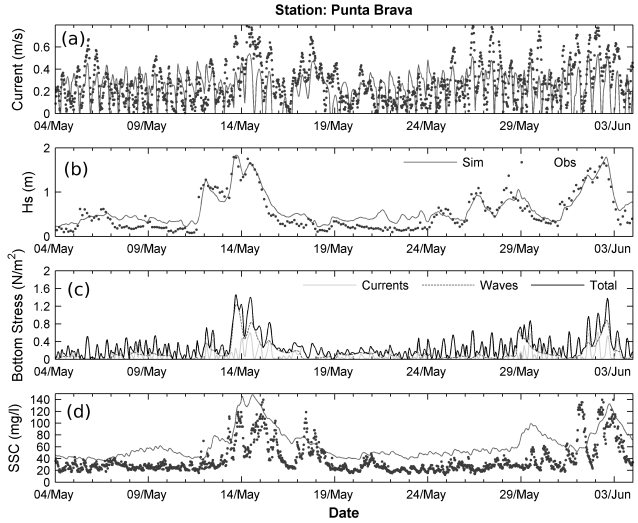

Figure 11. Time series of: (a) current intensities, (b) significant wave height, (c) simulated bottom stress, and (d) suspended sediment concentration, at PB station during May 2009.

Finally Fig. 12 shows the simulated bed evolution at Montevideo Bay area for the period May-June 2009. The model is able to reproduce the deposition of material in the navigation channel and harbour basin. Data about the sediment volume that is dredged from this channel will be compared against these results soon.

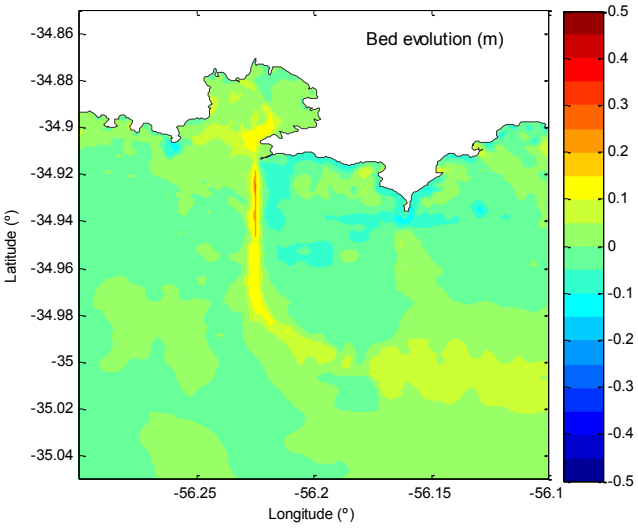

Figure 12. Simulated bed evolution during May - June 2009.

VI. CONCLUSIONS AND FUTURE WORK

A high resolution bidimensional depth averaged hydrodynamic and sediment transport model was implemented for the Río de la Plata and Montevideo Bay. Hydrodynamic numerical results show excellent agreement with observed sea surface elevation, currents, and wave parameters at several stations in the estuary. During the circulation model calibration process the wind drag coefficient showed to be a key parameter to simulate properly the meteorological tide events, while the Manning coefficient influence is especially noticeable on the astronomical tide presentation. Idealized simulations with the wave model showed that at Montevideo Bay area the oceanic boundary condition plays a secondary role and local waves are dominant during the main events.

After a preliminary calibration the sediment transport and bed evolution model was able to reproduce the general behaviour of the suspended sediment concentration at Montevideo Bay area. The results show the importance of both currents and waves for the induced bottom stress computation and its role in the reproduction of the main resuspension events.

Work in progress includes a finer calibration of the bidimensional sediment transport model including more field data and depositions rates at Montevideo Bay. Also we are currently working on the implementation of the three dimensional model TELEMAC 3D including the fine sediment transport module SEDI3D.

These numerical tools will help to study the fine sediment dynamics at Montevideo Bay and evaluate the impact of different human interventions on it (navigation channel deepening, breakwaters, etc.).

ACKNOWLEDGMENTS

This work was conducted within the research project ANII FMV_3_2011_1_680 and the Uruguayan - French cooperation project ECOS-Sud U014U01.

REFERENCES

[1] M. Fossati, F. Cayocca, I. Piedra-Cueva I., "Fine sediment dynamics in the Río de la Plata". Adv. Geosci., vol. 39, pp. 75-80, 2014.

[2] P. Santoro, M. Fossati and I. Piedra-Cueva, "Study of the meteorological tide in the Río de la Plata". Continental Shelf Research, vol. 60, pp. 51-63, 2013.

[3] D. P. Dee, and 35 co-authors, "The ERA-Interim reanalysis: configuration and performance of the data assimilation system". Q.J.R. Meteorol. Soc., vol. 137, pp. 553–597, 2011. doi: 10.1002/qj.828

[4] F. Pedocchi, M. Fossati, R. Mosquera, D. Bellón, I. Piedra-Cueva, "Waves, currents, and suspended sediment measurements in the Río de la Plata in front of Montevideo, Uruguay". Salt Lake City, Utah. Proceedings Internacional, Hydraulic Measurements and Experimental Methods; 2012.

[5] C. Martínez, J.P.Silva, E. Dufrechou, P. Santoro, P. Ezzatti, I. Piedra-Cueva, M. Fossati, "Towards a 3D Hydrodynamic numerical modeling system for long term simulations of the Río de la Plata dynamic". 36th IAHR World Congress, Delft-The Hague, 2015.

[6] J. H. Atkinson, J. J. Westerink and J. M. Hervouet, "Similarities between the quasi-bubble and the generalized wave continuity equation solutions to the shallow water equations". Int. J. Numer. Meth. Fluids, vol. 45, pp. 689–714, 2004. doi:10.1002/fld.700

[7] R. Alonso, "Evaluación del potencial undimotriz de Uruguay". MSc. Thesis, Universidad de la República, Uruguay, 2012, 278 pp.

[8] D.H. Swart, "Offshore sediment transport and equilibrium beach profiles". Delft Hydraulics Publication 131, Delft University, The Netherlands, 1976.

[9] P. Tassi and C. Villaret, "Sisyphe v6.3 User's Manual". EDF R&D Report N° H-P74-2012-02004-EN, http://www.opentelemac.org/, 2014.

[10] FREPLATA, "Estudio de la dinámica hidrosedimentológica del Río de la Plata: observación y modelación numérica de los sedimentos finos". FREPLATA-FFEM Project N° CZZ 1268.01, 2011.

[11] J.C. Winterwerp and W.G.M. van Kesteren, "Introduction to the physics of cohesive sediments in the marine environment", Elsevier, Developments in Sedimentology, 56, 2004.

Horizontal flow field modelling in a channel mouth

Dr. Regina Patzwahl *(Author)*
Federal Waterways Engineering
and Research Institute
76227 Karlsruhe, Germany
regina.patzwahl@baw.de

Tugba Güngör *(Author)*
Institute for Hydrodynamics
KIT Campus Süd
76131 Karlsruhe, Germany

***Abstract*—A large re-circulation zone in the mouth of the Elbe Side Channel leads to constant sedimentation and dredging of the fairway. Investigations are being carried out at the Federal Waterways and Research Institute concerned with constructive technical solutions. These investigations comprise scaled and numerical modelling. In-situ measurements are available. The three together make an exceptional data set. Little experience is available in the numerical modelling of such a large re-circulation zone in 2D and 3D. Only with the two measurement data sets at hand the set-up and calibration was possible. The paper points out the crucial aspects, shows calibration results for both the 2D- and 3D-Telemac model and provides insight in dependencies between calibration parameters.**

I. INTRODUCTION

The Elbe Side Channel (ESK) is located about 70 km upstream the town of Hamburg and links the Elbe River to the Midland Canal (Fig. 1). The mouth into the Elbe River can be regarded as large widening in the otherwise trained river. A typical re-circulation in the channel mouth accompanied by deposition of sediment in the river bed and suspended matter in the channel mouth is the consequence. The deposition mainly takes place in the fairway and needs dredging. In order to reduce the costs for maintaining the fairway the Federal Waterways Engineering and Research Institute (BAW) was tasked with analysing the problem and, when indicated, developing a technical solution.

Figure 1. Elbe River with inlet of the Elbe Side Channel (ESK) into the Elbe River.

II. PROJECT CONCEPT

As transport and deposition of sediment and suspended matter is involved, a combined scaled model/ numerical model approach was envisaged for the project. The numerical hydraulic model was tasked to help with optimisation steps within the global evolutionary steps of technical options. Additionally, the numerical model provided information on the effects of certain measures on their surrounding areas The scaled model was to comprise hydraulic aspects as well as transport of matter into the mouth, an important issue in the assessment of the efficiency of the different constructive variants.

A welcomed, important side-effect of the dual model approach is that it can be used for the further improvement of the applied numerical modelling technique and our understanding of river flow conditions beyond those we commonly model.

III. GEOMETRICAL SETTING

The channel mouth (see Fig. 2) has a width of about 480 m where the channel meets the bank of the Elbe River. Both sides of the channel and the transitions to the river bank on the eastern, up-stream part and the western, down-stream part are secured by standard sheet pile walls.

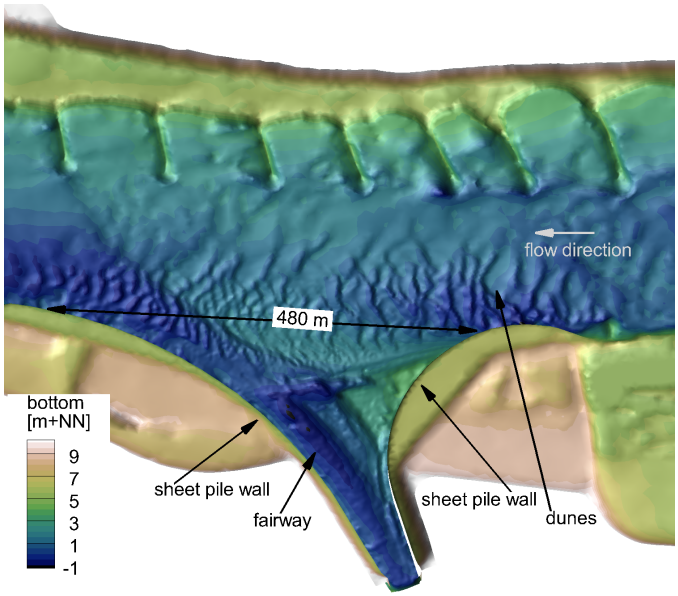

Figure 2. Topography of the channel mouth and adjacent river stretches

The maintained fairway is located on the left side of the channel (Fig. 2) and has to provide a width of 40 – 80 m and a minimum water depth of 3.30 m. The material dredged on the down-stream side within the channel mouth consists of fine

sand. It comprises little cohesive share. The material deposited on the up-stream side of the channel consists of a mixture of sand and silt. The river bed consists of fine and coarse sand. The transport takes place via dunes (see Fig. 2).

IV. FIELD DATA

A. Description

In order to guarantee good calibration and validation of both model types a series of field measurements took place. The measurements include 2D-depth-averaged velocity fields in the area of the channel mouth processed from a 3D-ADCP dataset and ADCP-cross profiles in the Elbe River and in the channel mouth. Four measurement campaigns took place between October 2007 and September 2010. Two flow conditions were covered: bank-full (2MQ) and a mean high water (MHQ) discharge.

Also dredging material and soil samples from the river bed and the channel mouth were analysed.

B. Results

The processed measurements (for 2MQ), presented in Fig. 3, top, show two main features: reduced flow velocities in the Elbe River where the channel meets the river and a distinguished large eddy in the channel mouth itself, accompanied by a secondary and third eddy deeper into the mouth.

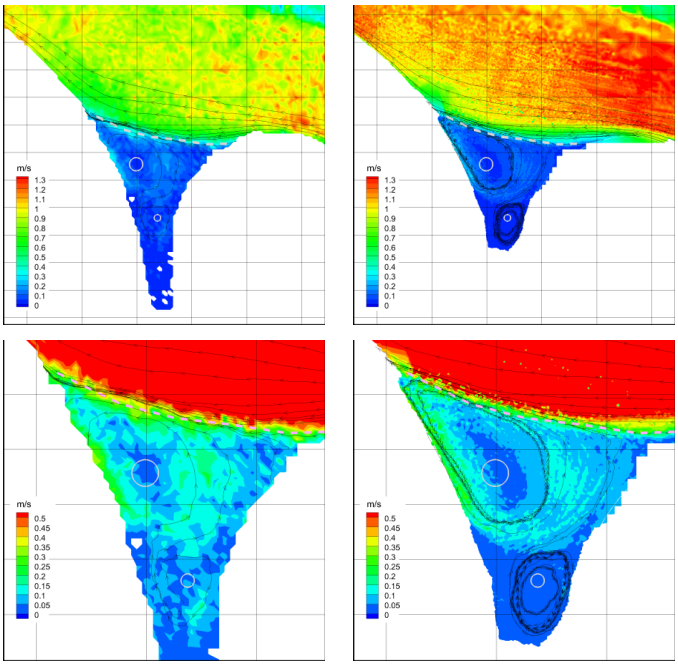

Measurements at 2MQ Scaled model at 2MQ

Figure 3. Measured depth-averaged velocity field near channel mouth (top left) and up-scaled PTV-field of surface flow velocity in scaled model (top rigth) and close-up on channel mouth (bottom) for 2MQ. The inner bound of the separation zone is marked as well as the centres of the eddy and the second eddy. Streamlines indicate flow characteristics.

The measurements show no discharge dependent behaviour of the eddy apart from increasing velocities with increasing discharge. The position and size of the eddy remain "unchanged". From the measurements it was concluded that the eddy is mainly two-dimensional. Mean velocities in the river amount to about 1.1 m/s up- and downstream the mouth and 1 m/s at the channel mouth at 2MQ and maximum speed to about 0.3 m/s in the eddy.

V. THE SCALED MODEL

A. Model description

The laboratory model has an overall length of 60 m and covers about 4 km of the Elbe River from El-km 571,1– 574,9 (see Fig. 4). It is downscaled by 1:60 in the horizontal direction and 1:30 in the vertical direction (Froude model). The river bed is made of a non-movable gravel-bed. Additional roughness was introduced during the calibration process, with the help of a system of riffles crossing the model river bed (Fig. 4). The sheet pile walls were geometrically exact down-scaled. Surface flow velocities were measured via Particle Tracking Velocimetry (PTV) and vertical velocity distribution with the help of Acoustic Doppler Velocimetry (ADV). Fig. 4 shows all applied measurement techniques.

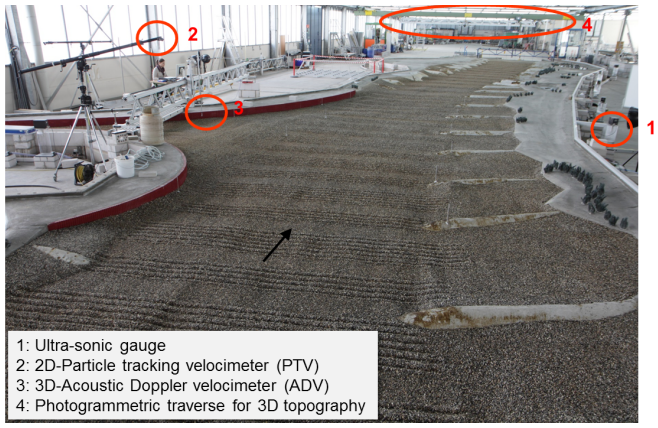

Figure 4. Scaled model of the Elbe River including channel mouth.

B. Results

1) Velocity Distribution in the Elbe River and the channel mouth

Fig. 3, right side shows the measured (PTV) surface velocities. Velocities in the scaled model might therefore be higher as the ones measured on-site, especially for the river part of the model. Still, the important features, namely decreased velocities in the channel mouth area (top right), position of the shear zone and velocity distribution in the eddies in the channel mouth are well reproduced (bottom right).

2) The sheet pile wall

In the course of the project the sheet pile wall and its impact on the eddy came into focus when setting up the numerical model. In order to investigate the impact of its hydraulic roughness, the sheet pile walls on the downstream side of the mouth in the scaled model were covered with smooth metal plates in order to reduce the wall roughness significantly. Fig. 5 shows the result of this experiment. The smooth wall (left side) lets the re-circulating flow enter deeper into the mouth then the rough wall (right) does. It appears that

the flow velocities in the eddy do not differ significantly from each other. From this, it was concluded, that the wall roughness controls how far into the mouth the flow can enter and the bottom friction which mainly controls flow velocities.

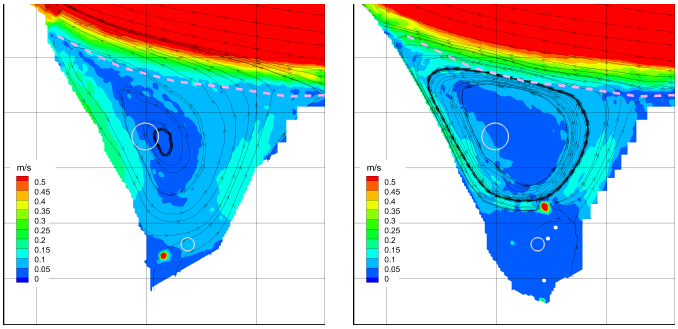

Measurements at 2MQ Scaled model at 2MQ

Figure 5. Left: PTV-surface velocities in the channel mouth with smooth wall (metal plate) covering the left border. Right: PTV-surface velocities in the channel mouth with rough wall (scaled sheet pile wall).

VI. THE 2D-TELEMAC MODEL

A. *Model description*

The computational grid for the 2D-Telemac model (El-km 571 – 575) was set up using edge constraint for all hydraulic relevant structures along the river stretch such as groynes. The domain is subdivided into two sections. The river stretch itself is discretised with elements of a mean edge length of 7 m whereas the area around the channel mouth is covered with elements with mean edge length of 2 m. The grid resolution in the river is high enough to resolve dunes. In Fig. 6 coarse and fine parts of the computational grid as well as the distribution of Nikuradse roughness height k_s values are shown. The red inset zooms into the region of the channel mouth and clarifies the grid concept. The grid boundary is plotted in red. The model was calibrated by fitting computed water levels to water level measurements by adjusting k_s–values. All numerically relevant details can be taken from Table 1. The Nikuradse roughness height k_s over the model domain after calibration is given in Table 2 [3].

TABLE I. NUMERICAL PARAMETERS OF THE 2D-TELEMAC MODEL

No. Of elements	**Min. edge length [m]**	**Max. edge length [m]**	**Time step [s]**	**Type of advection**
136 446	0.86	20.77	1.0	MURD[1]
Turbulence modell	**Hor. Viscosity [m²/s]**	**Wall friction [m] (k_s-value)**	**Roughness Model**	**Telemac Version**
Const. horizontal viscosity	0.0001	Nikuradse ($k_{s,Wall}$)	Nikuradse ($k_{s,\ Zone}$)	V6p3

1. the Multi-dimensional Upwind Residual Distributive scheme

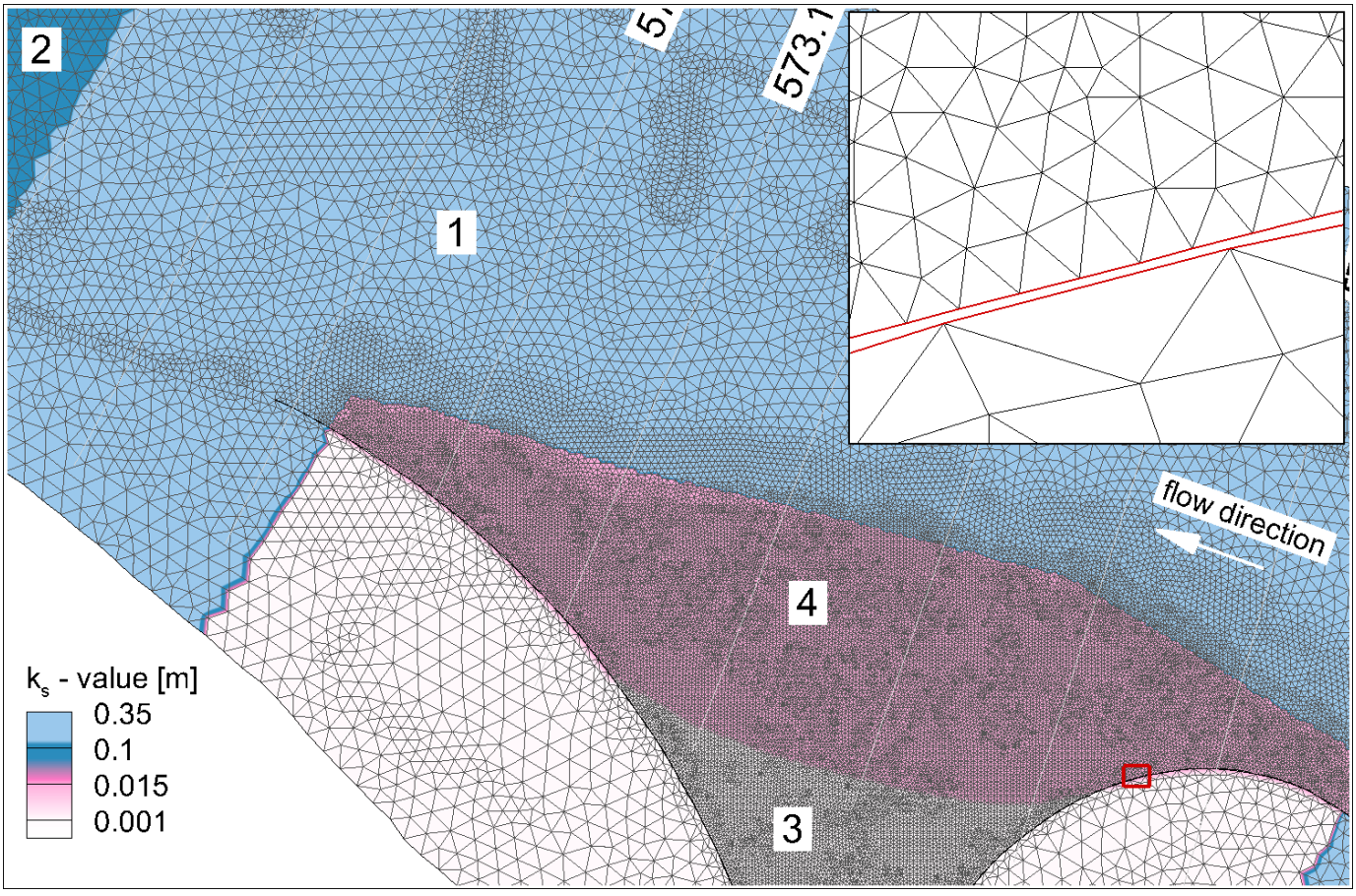

Figure 6: Computational grid and distribution of k_s-values in the numerical model

B. Modelling the sheet pile wall

The most challenging part of the grid design was to adequately account for the sheet pile wall. Such a wall construction, often used in waterways, is a vertical and hydraulically rough border between wet and dry elements. Its steepness is a problem in itself for finite element codes such as Telemac. The roughness and its impact on the flow field, as discussed in section « Scaled model » posed an additional challenge. Tests showed that defining the sheet pile wall sections via constraint edges as grid border (see inlet Fig. 6) and using the possibility of modelling wall friction led to the best results over the discharge spectrum. The $k_{s,Wall}$–value for the wall was adjusted in such a way that the computed point of flow separation from the wall matched the measured one. After fitting the separation point, the ks–value in the area of the channel mouth was determined by fitting flow velocities to the measured flow field. Higher values led to under-estimated velocities in the eddy. A disadvantage of such a model construction is, that submerged floodplain and therefore flow conditions at high water discharges cannot be modelled.

TABLE II. ROUGHNESS DISTRIBUTION (K_s) FOR 2D-MODEL

Zone 1	Zone 2	Zone 3	Zone 4	Wall
River up-stream mouth	***River down-stream mouth***	***Channel mouth***	***Separation zone***	***Grid boundary***
0.15 m	0.05 m	0.01 m	0.01 m	5.0 m

VII. THE 3D-TELEMAC MODEL

A. Model description

The 3D-Telemac model is an extension of the above presented 2D-Telemac model. All numerical relevant information is given in Table 3. The model needed re-calibration.

TABLE III. NUMERICAL PARAMETERS OF THE 3D-TELEMAC MODEL

No. Of elements	**Min. edge length [m]**	**Max. edge length [m]**	**Time step [s]**	**Type of advection**
136 446	0.86	20.77	2.0	MURD
Turbulence modell	**Hor. Viscosity [m²/s]**	**Wall friction [m] (k_s-value)**	**Roughness Model**	**Telemac Version**
k-ε	0.0001	Nikuradse ($k_{s,Wall}$)	Nikuradse ($k_{s,\ Zone}$)	V6p3r2
Vertical layering	**Number of vertical layers**			
logarithmic σ-layering	10			

Table 4 gives the distribution of k_s in the sections shown in Fig. 6. A fourth zone (flow separation zone) was introduced to get a better fitting for water levels. The values in the upper part of the river model had to be increased by a factor of three and by a factor of two in the lower part for fitting the water levels. The value in the channel mouth had to be lowered distinctively. Again, the flow velocities in the eddy showed being sensitive to the k_s-value. The value for $k_{s,\ Wall}$ had to be raised to 7.0 m in order to fit the shape of the eddy.

TABLE IV. ROUGHNESS DISTRIBUTION (K_s) FOR 3D-MODEL

Zone 1	Zone 2	Zone 3	Zone 4	Wall
River up-stream mouth	***River down-stream mouth***	***Channel mouth***	***Separation zone***	***Grid boundary***
0.35 m	0.10 m	0.001 m	0.015 m	7.0 m

B. Results

The presentation of results will be restricted to the 2MQ-discharge. Fig. 7 shows the computed depth-averaged flow velocities in the channel mouth computed by the 2D- and the 3D-model.

For comparison, the measurements are also shown. Both model show good agreement with the measured data in the river stretch. The separation front is represented in both models well enough and the eddy, computed by the 3D-model fits the measurement very well. The 2D-model gives a sufficiently good representation of the flow-field in the mouth, but can certainly be further improved by varying $k_{s,Wall}$ and $k_{s,Zone3}$.

Fig. 8 shows the influence of the values for $k_{s,Wall}$ and $k_{s,Zone3}$ on the eddy computed by the 3D-model. If the wall roughness is considerably lowered to a value of 0.10 m, the flow sticks to the wall over a longer distance, as was already observed in the scaled model (see Fig. 5). A $k_{s,Wall}$=7.0 m leads to very good agreement with the measurements. The value for the bottom friction influences the flow velocities in the eddy, but not so much its spatial extent.

VIII. DISCUSSION

Both the 2D- and 3D-Telemac model were calibrated successfully to the in-situ measurements. The velocity cross profiles showed good agreement with measurements both in the river itself and in the channel mouth The calibration of the river stretch is based on fitting water-levels by adjusting the Nikuradse roughness height k_s. The values for k_s in zone 1 and zone 2 are high considering the characteristic of local soil material. For a 2D-model it can always be argued, that form drag (e.g. dunes) has to be parameterized via k_s. Following this reasoning, the k_s-values set in the 3D-model are then far too high, as form drag, in theory, is reproduced directly.

From experience we already know that the k_s-value depends on the chosen vertical turbulence model, so when the k-ε-model is used in Telmac3D, k_s-values are up to three times higher than in a 2D-model built on the same computational grid [4]. Apparently, in the friction dominated flow in the river the k-ε-model under-estimates energy dissipation to obtain the correct water levels. It has to be introduced via bottom friction. In the channel mouth (zone 3), we have to reduce the k_s-value by a factor of 10 in order to fit flow velocities. The flow in the re-circulation zone is formed by the interaction of turbulent mixing in the shear layer and the boundary layer due to the sheet pile wall. To accurately capture these processes, both an adequate advection and turbulence model are required. It appears that either the MURD advection scheme, the k-ε-model, the chosen wall roughness parameterisation, or their

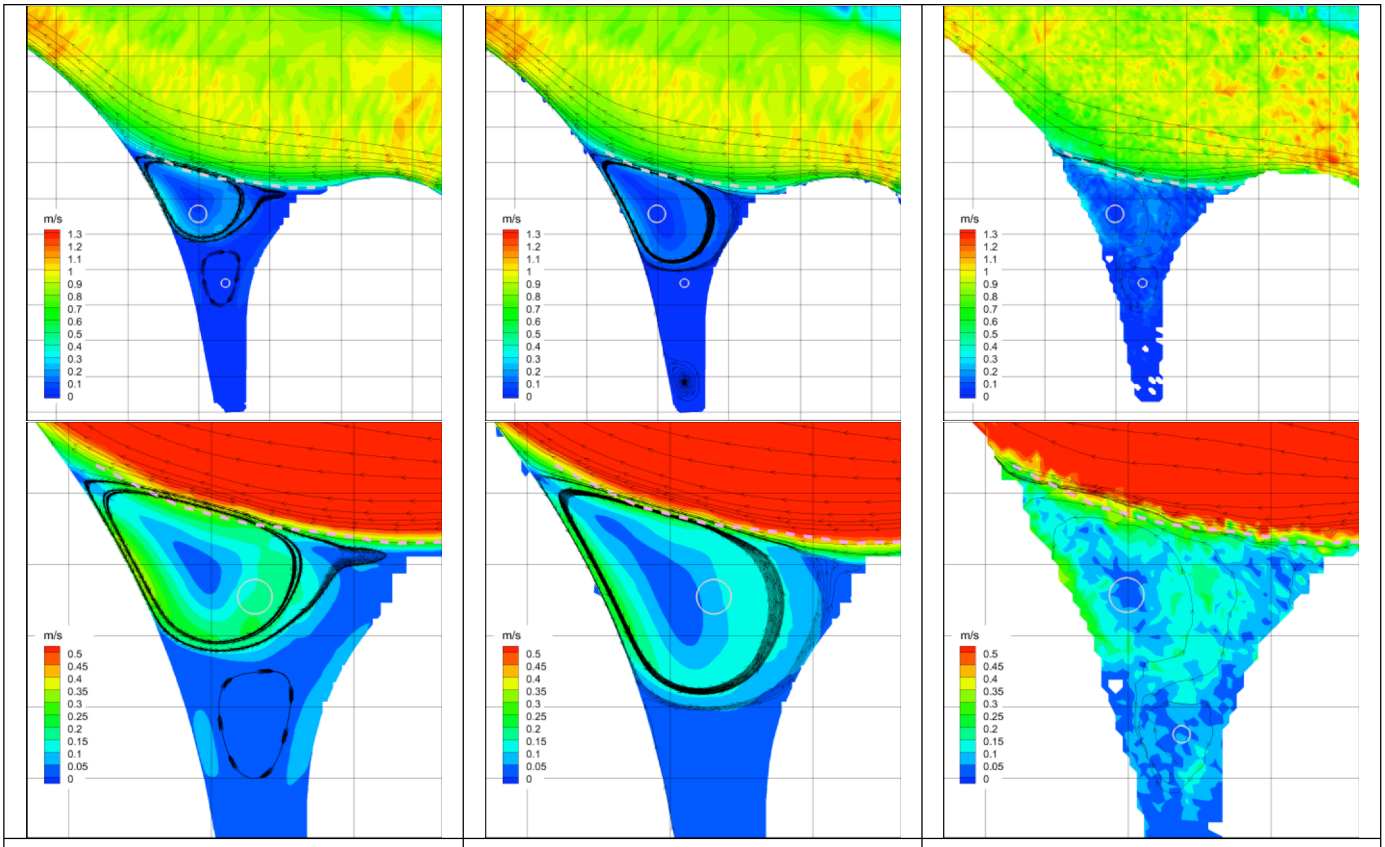

Figure 7: Computed and measured depth averaged flow velocities for 2DTelemac (left row), 3DTelemac (middle row), measurements (right row).

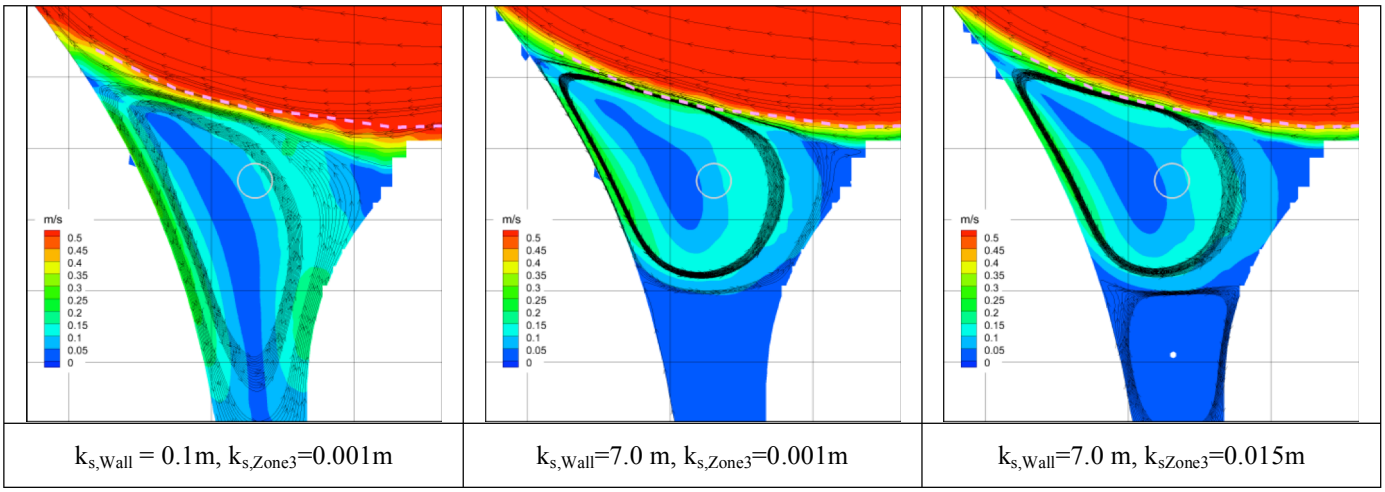

Figure 8: Influence of chosen Nikuradse Roughness height for wall and bottom on the computed flow field.

combination, over-estimates the dissipation and slows down the flow considerably. Unfortunately, tests with a combination of a constant horizontal viscosity and Prandtl's mixing length model in the vertical were not possible.

Due to these uncertainties in the calibration, a direct investigation of possible solutions to the sedimentation problem was not deemed reliable without cross-check. Fortunately, in this case, the cross-check can be supplied by the scaled model.

The most difficult part in the set-up of the numerical model, (2D or 3D) was to decide how to integrate the impact of the sheet pile wall into the numerical model. Only the measurements over a certain discharge range and experiments with the scaled model delivered the necessary information and gave the certainty needed to decide for modelling the wall via

wall friction at the grid boundary and to introduce the high - but needed - $k_{s,Wall}$-value of 7.0 m.

The $k_{s,Wall}$-value of 7.0 m seems unphysically high. If transferred to the thickness of the roughness length z_0, related to the boundary layer thickness (1/30 of k_s), a value of 0.23 m is reached. If one takes into account the geometry of a sheet pile wall (see Fig. 9), maybe such a value is not so unrealistic.

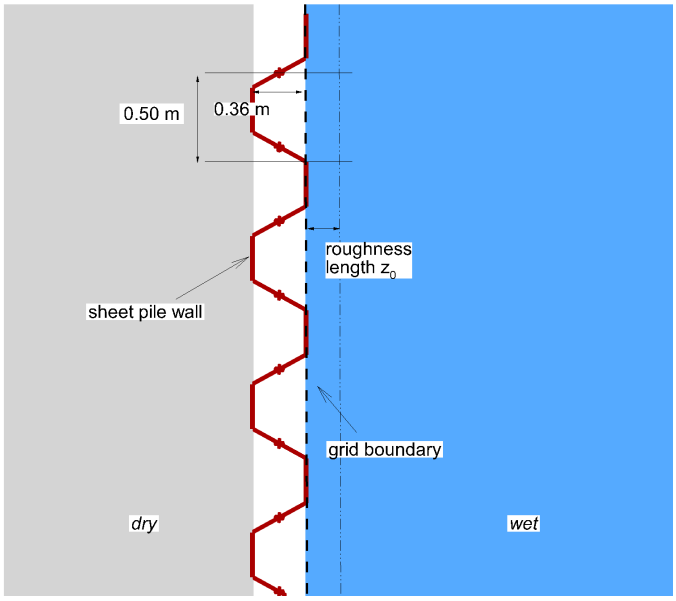

Figure 9: Sketch of sheet pile wall in context with the location of the grid boundary and the roughness length z_0

IX. Conclusion

Modelling re-circulation zones developing e.g. in channel mouths is beyond the daily-modelling routine and lacks experience. Therefore both the measurements and the data from the scaled model provided indispensable information which led to a model set-up, allowing calibration.

The significant influence of the different calibration parameters, e.g. bottom and wall friction, on the results of the applied 2D and 3D numerical models, opens the door for further investigation.

Acknowledgements

The authors want to thank all colleagues working with the scaled model for providing data, advice and discussion, in particular Bernd Hentschel, Thanks also goes to Boris Glander who made the first and important steps in the set-up of the 2D-Telemac-model presented here. The authors also want to thank Manuela Baron for sharing 3DTelemac expertise with us and Frank Platzek for discussion and numerical expertise.

References

[1] J-M. Hervouet (2007), Hydrodynamics of the free surface flows: modelling with the finite element method. Chichester: Wiley, Formerly CP

[2] www.opentelemac.org, TELEMAC-3D manual.

[3] J. Becker (2014), Sedimentablagerungen an einem Mündungstrichter, numerische und physikalische Variantenuntersuchung zur Hydraulik, Diploma Thesis, KIT, unpublished.

[4] M. Baron and R. Patzwahl (2013), Influence of numerical schemes in representing flow over and around groynes, Proceedings to the 20th Telemac-Mascaret User Conference.

Salinity in the 3D TELEMAC model Scaldis (the Scheldt Estuary): tracer diffusion, dispersion and numerical diffusion

Smolders, S. [1], Maximova, T. [1], Vanlede, J.[1]

[1]Flanders Hydraulics Research
Berchemlei 115, 2140 Antwerp- Borgerhout, Belgium
svensmolders@gmail.com

***Abstract*— This paper describes how salinity was introduced as an active tracer in the 3D TELEMAC model of the Scheldt estuary. Boundary conditions are discussed and model results are compared with measured data. The role of the parameters: velocity diffusivity, tracer diffusion coefficient and numerical diffusion and their effect on the salinity field are shown. Next to the salinity data, tracer data from the model will be used to determine dispersion coefficients for a 1D ecological box model of our project partner, the University of Antwerp.**

I. INTRODUCTION

The Scheldt estuary is located in the south-western part of the Netherlands and in Belgium. In the framework of the projects "Integral Plan for the Upper Sea Scheldt" and "Agenda for the Future", it was necessary to develop an integrated model for the Scheldt estuary. Existing models lack a high resolution in the Upper Sea Scheldt, Durme, Rupel and Nete. For this reason, the SCALDIS model, a new unstructured high resolution model of the tidal Scheldt is developed in TELEMAC 3D for the entire estuary, but with special attention to the upstream parts. The calibrated model will be used to analyse the effects of several scenarios (different morphology of the Scheldt with different ranges of boundary conditions). Because this model will also be used for other projects in the future, including projects in the coastal zone, the model domain was extended to the coastal zone of Belgium.

The model domain (figure 1) covers the entire Scheldt estuary, including the mouth area, the Belgian coastal zone and the Eastern Scheldt. Upstream, the model extends to the limits of the tidal intrusion. The use of an unstructured grid allows to combine a large model extent with a high resolution upstream. The grid resolution varies from 500 m at the offshore boundaries to 7-9 m in the Upper Sea Scheldt.

Calibration parameters are bed roughness and velocity diffusivity. The model is calibrated for one spring-neap tidal cycle in 2013 against field data: water levels, velocities (in deep and shallow zones) and discharges. The calibration process is described in further detail in [1] and with extra focus on the velocities in [2]. For a complete overview of the model and calibration process we refer to [3]. This paper will go into detail on how salinity was implemented as an active tracer in the Scaldis model.

One of the project partners, the university of Antwerp, will need tracer calculations from different regions of the estuary to calibrate the dispersion coefficients for their 1D ecosystem box model [4]. Salinity is included in the 1D model as passive tracer (only transport). Every box in their 1D model corresponds to a part of the Scaldis model. For every box a dispersion coefficient is calibrated based on the dispersion coefficients of passive tracer simulations from the 3D Scaldis model of Flanders Hydraulics.

The coupling of both models by means of the dispersion coefficient, stresses the importance of the tracer calculations in the Scaldis model.

II. THE NUMERICAL MODEL

A. *Model grid*

The TELEMAC model developed in the framework of this project covers a part of the North Sea, the entire Scheldt estuary (until the tidal border) and the Eastern Scheldt. The flood control areas (FCA's) with or without a controlled reduced tide (CRT) are included in the model grid as they are important for the storm scenarios [3].

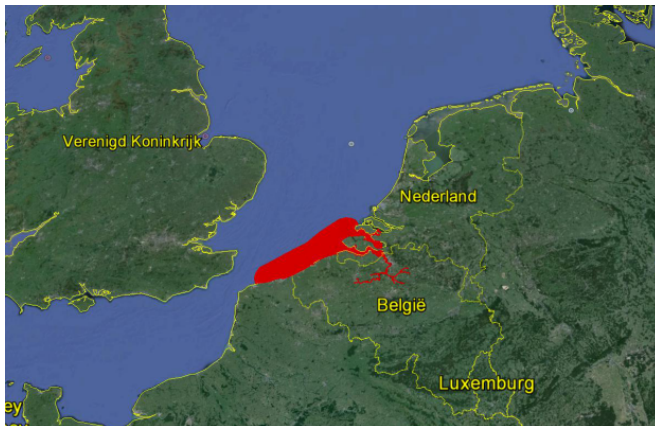

Figure 1. Scaldis model domain in red.

The model grid consists of 459,692 nodes in 2D mesh and 873,419 elements. In the 3D model we use five sigma layers, totalling 2,298,460 of nodes with the following distribution: 0D, 0.12D, 0.30D, 0.60D, 1D.

B. Bathymetry

The most recent available bathymetry is used in the model. Several datasets from different sources were pasted together.

The bathymetry for the Belgian continental shelf and the Belgian coastal zone comes from MDK-aKust (year 2007 - 2010). The bathymetry of the Dutch coast (2007-2012) was measured by Rijkswaterstaat and downloaded from Open Earth. For the ports of Zeebrugge, Blankenberge, Oostende and Nieuwpoort data from 2014 – 2015 are used. The bathymetry of the Western Scheldt (2013) and the Eastern Scheldt (2010) is available from Rijkswaterstaat. For the Lower Sea Scheldt, bathymetric data of 2011 were provided by Maritime Access division. The topographic data for the channel banks (2007) are taken from the Mercator databank.

The bathymetric data for the Upper Sea Scheldt and Rupel basin are available from Maritime Access division for the years 2013 - 2014. For the Durme bathymetry from 2012 - 2013 is defined. The data for the tributaries of Rupel are available for 2007 - 2013 (Dijle and Nete) and 2001 (Zenne and upstream part of Nete) from W&Z, Sea Scheldt division. For the Flood Control Areas along the river, the topographic data are derived from the Mercator Database.

C. Boundary conditions

The downstream model boundary is located in the North sea. The upstream boundary is located at the tidal border. The model domain includes all the tidal tributaries of the Scheldt estuary. The TELEMAC model is nested in the overall ZUNO model (figure 2) (a correction of the harmonic components is done: M2 phase +4°; M4 phase -6°; S2 phase +7° and Z_0 -0.21 m) [5]. The 10 minute time series of the water level calculated in ZUNO are defined at the downstream boundary of TELEMAC. The subroutine bord3d.f was changed to allocate a water level and a salinity value for each boundary node separately (469 nodes).

There are 8 upstream boundaries with prescribed discharge and free tracer. The measured daily average discharges are defined as upstream boundary conditions at Merelbeke (Upper Sea Scheldt), Dender, Zenne, Dijle, Kleine Nete, Grote Nete, channel Ghent – Terneuzen and channel Bath.

Wind is applied on the coastal zone through the subroutine meteo.f. To include the culvert function in TELEMAC 3D the function t3d.debsce was changed [1].

The salinity boundary conditions are generated by nesting the SCALDIS in the CSM-ZUNO model train. Model results for salinity are highly influenced by values imposed at the boundaries. Therefore, it is very important to have accurate salinity boundary conditions. Salinity boundary values in the SCALDIS model are corrected based on the comparison of the calculated and measured salinity time series at Vlakte van de Raan (located in the North sea; red dot in figure 4 in the larger mouth area of the Scheldt Estuary).

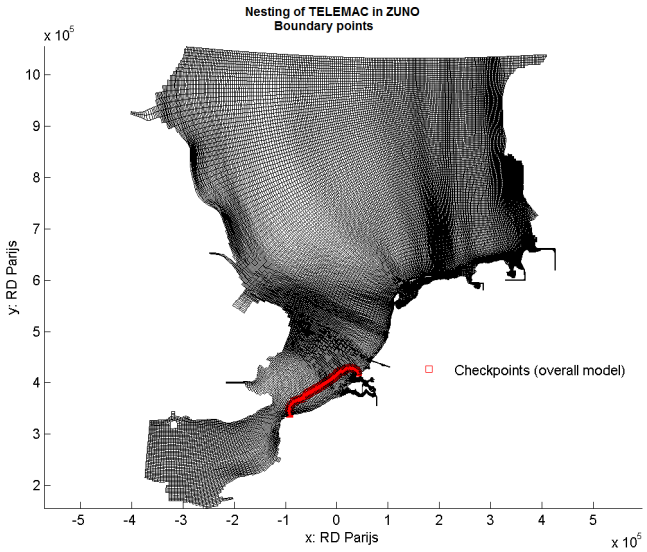

Figure 2. Nesting of Scaldis model in ZUNO. Scaldis boundary nodes given in red.

The modeled and measured salinity at Vlakte van de Raan are compared in figure 3. Thicker lines show the daily average curves. The missing values in the daily average measured salinity were filled by a linear interpolation. The ZUNO model underestimates the salinity values in the area of interest a lot. Therefore, a salinity correction at the boundaries was necessary.

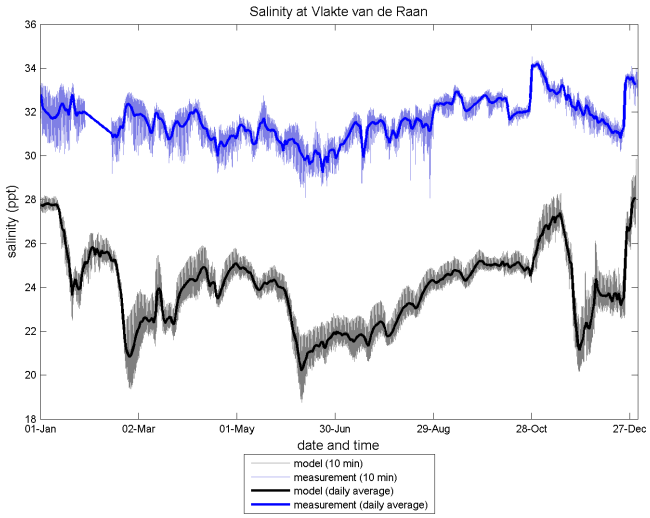

Figure 3. Comparison of modelled salinity in ZUNO and measured salinity for Vlakte van de Raan station.

The correction, the difference between the daily averaged measured and modelled values were added to the boundaries point values of the Scaldis model; the values of which were extracted from the ZUNO model. Salinity is the only active tracer in the Scaldis model.

D. Simulation period and initial condition

Salinity simulations are done with a three month simulation. The model starts from a previous computation file (a short simulation to start up the tidal motion in the model). The model runs from 17/09/2013 00:00 to 20/12/2013 00:00.

To get the salinity distribution in the estuary immediately good, the model starts from an initial salinity field: a map like the BOTTOM or BOTTOM FRICTION is made based on a combination of salinity measurements and model results from ZUNO. Figure 4 shows the outline of the model. The dots in the North Sea and Eastern Scheldt are extracted from the ZUNO model for the start date situation. All these point values are first corrected in the same way as the boundary conditions. The red dots in figure 4 give the location of stations where salinity is measured. The measured values at 17/09/2013 00:00 were interpolated using inverse distance method together with the corrected model values from ZUNO to give an initial salinity map (figure 5) that is read by a modified subroutine fonstr.f. The values of the 2D map are copied to the other four layers in the model.

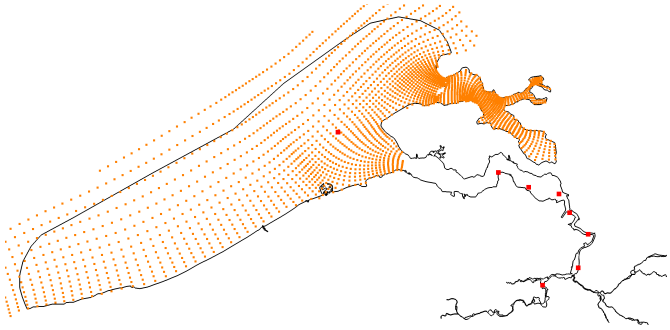

Figure 4 – Salinity values at 17/09/2013 00:00 extracted from ZUNO (orange dots) and location of the stations that measure salinity in the Scheldt Estuary (red dots). These stations are named (from downstream to upstream) Vlakte van de Raan, Overloop van Hansweert, Baalhoek, Prosperpolder, Liefkenshoek, Boei 84, Hemiksem and Driegoten.

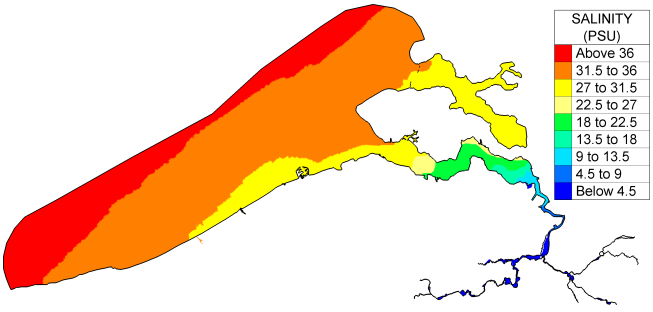

Figure 5 – Initial salinity field for start simulation at "17/09/2013 00:00"

E. Initialising tracer calculation

Salinity is the first tracer in the Scaldis model. But the salinity does not reach all the way upstream the estuary. So it is not sufficient to calculate dispersion coefficients for the 1D box model. The Scaldis model was divided into 89 parts by means of polygons. The focus lies on the Scheldt estuary itself and not on the tributaries. Figure 6 shows an example of how the model partitioning by the polygons was done. In the downstream part of the estuary, the polygons have a length of 5 km. In the upstream part the distance along the estuary axis is 1,5 km with a gradually transition. All flooding areas with controlled reduced tide [3] are also given a separate polygon.

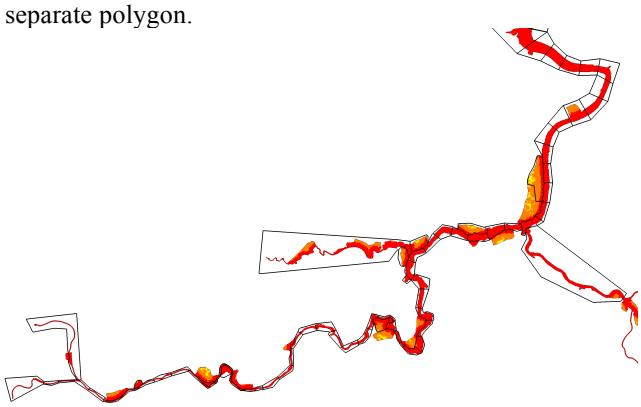

Figure 6. example of model domain divided by polygons

A concentration of 1000 kg/m³ for 19 passive tracers will be initialized in different parts of the Scheldt estuary. The simulation will start the same way as the salinity simulation, but will only simulate three days. For every tracer the concentration inside every polygon will be calculated for every graphical output time step (= 1 hour). From this data, the university of Antwerp can extract the necessary dispersion coefficients for their 1D box model.

III. Model vs Measurements

The advection scheme for tracers is scheme 13 (Leo Postma for tidal flats; necessary for combination with sinks and sources). The coefficient for vertical and horizontal diffusion of tracers was kept at the default value of 1.E-6 m²/s. The coefficient for horizontal and vertical diffusion of velocities was calibrated and found optimal at 2.E-2 m²/s [3]. When after a simulation period of three months the model results are compared with the measurements (figures 7-11), the results show that for Vlakte van de Raan (figure 7) (for location of the stations see figure 4) the comparison is not good. The model is not able to reproduce the measurements. The results of Baalhoek (figure 8), however, are much better. Despite the discrepancy between model and measurement in the Coastal area, inside the estuary results look good. The results improve going further upstream for Liefkenshoek (figure 9) and Boei 84 (results not shown). For Hemiksem (figure 10) and Driegoten (figure 11) the model seems to follow the tendencies of the measured salinity, but the average salinity level in the model is too low.

Overall the results are satisfying. Certainly knowing that the model was not "calibrated" for this tracer. No calibration was done, because the only parameter to change was the horizontal diffusivity of tracer para meter and at this moment we don't know exactly what it does. From the

comparsion of measurments and model an overestimation of the measurement by the model in the downstream part can be seen (figures 8 and 9) and a small underestimation is noticed in the downstream part (figures 10 and 11). This might be due to changes in mesh resolution going from coarse downstream to fine upstream.

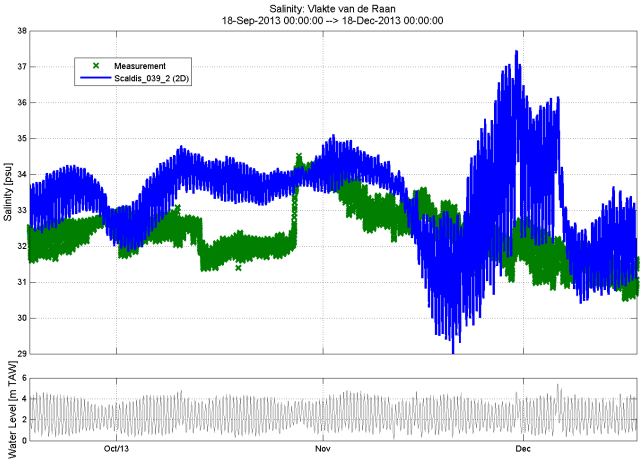

Figure 7. Salinity: model vs. measurement. Vlakte van de Raan.

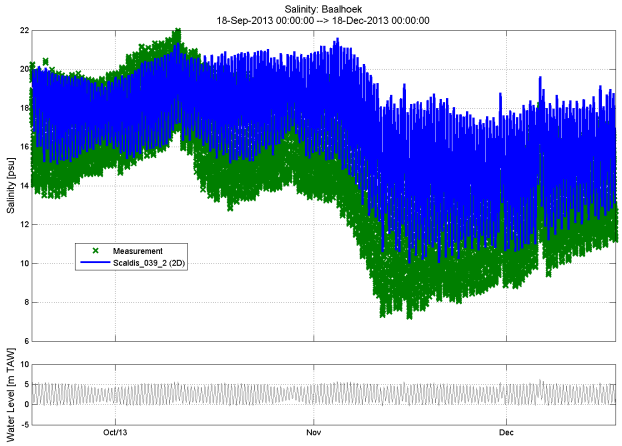

Figure 8. Salinity: model vs. measurement. Baalhoek.

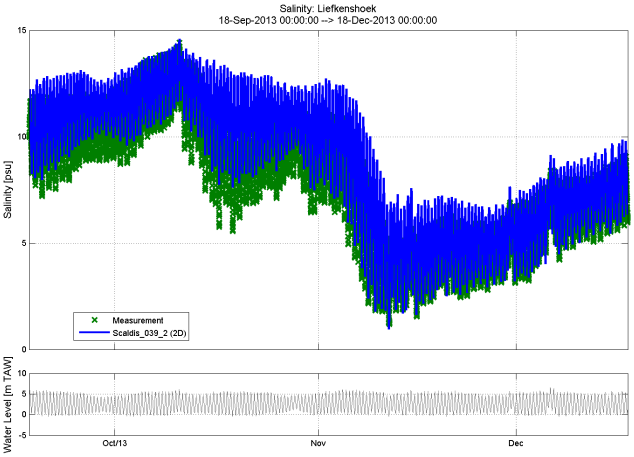

Figure 9. Salinity: model vs. measurement. Liefkenshoek.

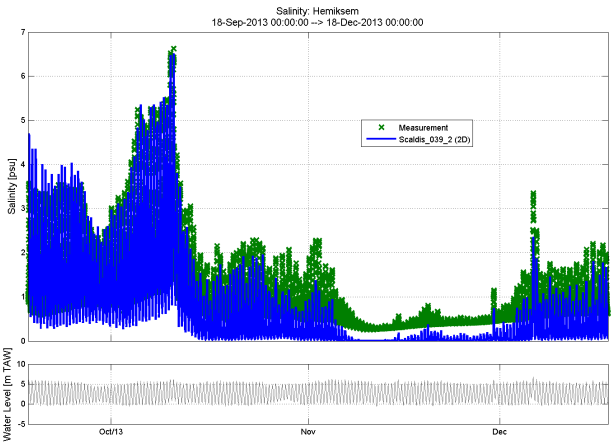

Figure 10. Salinity: model vs. measurement. Hemiksem.

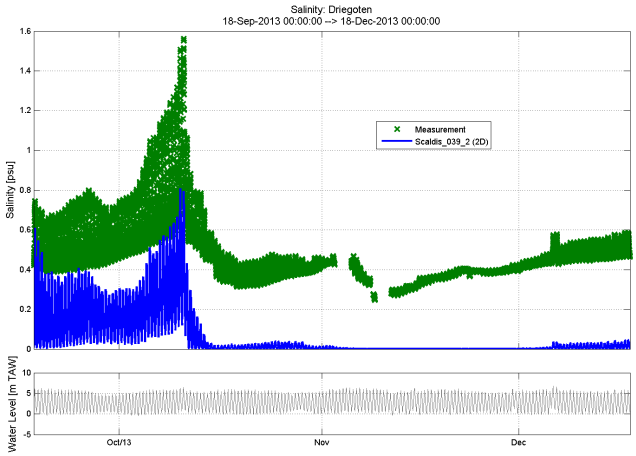

Figure 11. Salinity: model vs. measurement. Driegoten.

IV. TRACER DIFFUSION

A. Diffusion, advection and dispersion

Tracer diffusion is the mass transfer that happens because of the random thermal motion of molecules (so called Brownian motion). The salinity will move from a region of high concentration to a region of low concentration over the concentration gradient. Under the assumption of steady state this is also known as Fick's first law and is written for one dimension as follows:

$$J = -D\frac{\partial c}{\partial x} \qquad (1)$$

with J the mass flux, c the concentration of tracer, x the distance and D the diffusion coefficient or diffusivity. Dispersion is known as the mass transfer due to diffusion in non-ideal flow or turbulent flow. Diffusion helps molecules to move from one streamline to the next, and thereby transported over different distances due to the difference in velocities. The dispersive mass flux can be written with the same equation as Fick's first law (equation 1), but instead of D a dispersion coefficient E is used. The amount of

dispersion reduces with increasing diffusion coefficient, because molecules will just be moving from one streamline to another constantly. They will not spent enough time on one streamline to be transported far away from each other. In the tracer transport equation:

$$\frac{\partial T}{\partial t} + U\frac{\partial T}{\partial x} + V\frac{\partial T}{\partial y} + W\frac{\partial T}{\partial z} = \frac{\partial}{\partial x}\left(\nu_T \frac{\partial T}{\partial x}\right) + \frac{\partial}{\partial y}\left(\nu_T \frac{\partial T}{\partial y}\right) + \frac{\partial}{\partial z}\left(\nu_T \frac{\partial T}{\partial z}\right) + Q \quad (2)$$

with T, the tracer; t, the time; x,y,z, the space components; Q, the sink or source of tracer and ν_T, the tracer diffusion coefficient or diffusivity, both advective transport (left hand side of equation 2) and diffusive transport (right hand side of equation 2) are present.

In numerical models the total tracer dispersion is affected by the inherent numerical diffusion. This is an "uncontrolled" diffusion that is automatically introduced in the calculation. Numerical solver schemes can be diffusive. In the model we can choose for one or another scheme but all schemes are in some way diffusive. Another factor that affects numerical diffusion is the mesh resolution. For a 1D case the numerical diffusion can be estimated by U*dX/2. For 2D and 3D cases this formula just gives you an order of magnitude. This formula shows that the coarser your mesh, the larger the numerical diffusion will be.

The problem in the Scaldis model is that it has a very large model domain with a mesh resolution of 200-500 m in the coastal zone up to 5 m resolution at the upstream boundaries (figure 12). So the numerical diffusion will be different at different locations of the model domain. The total tracer diffusion will be a result of the tracer molecular diffusion parameter (tracer diffusivity) and the numerical diffusion. If we want to get the salinity distribution in the model as accurate as possible, we need to get an idea of the order of magnitude of the effect of the mesh resolution on the tracer transport. A second question is how to choose our tracer diffusivity parameter in order to have an effect on the total tracer transport. To test the effects of several parameters a small test case was made.

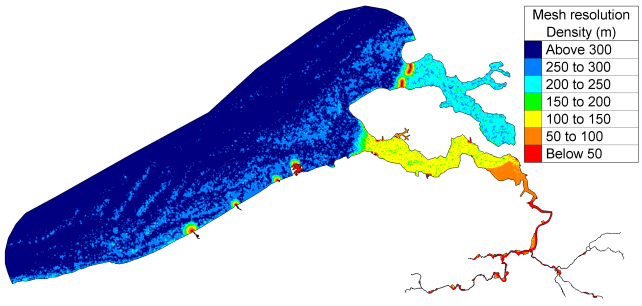

Figure 12. Scaldis 3D model mesh resolution

V. SMALL TEST CASES

We want to test two things:

1. What is the effect of the mesh resolution on the tracer movement?
2. What order of magnitude is the numerical diffusion or from which value does the parameter, horizontal diffusivity of tracer, start to play a role in the tracer movement?

A. *test case 1: the effect of mesh resolution*

1) *test model description*

A part of the estuary channel is modelled by taking a rectangular channel of 10 km long and 500 m wide. The depth is set at -10 m TAW (= the Belgian reference level, close to low water sea level). As we are only interested in the horizontal diffusion of the tracer, the model was only run in 2D. Three different mesh resolutions were applied: 5 m, 20 m and 100 m. On one side a schematic tidal water level (WL) boundary was set according to: WL = A*sin(ω*t) where A is the tidal amplitude (=2 m), t is the time and ω is the frequency (= 0,000141 for a semi diurnal tide). The simulation period was up to 90 days. On the other side a fixed discharge of 1 m³/s was set as boundary condition. The time step was 4 s and all other parameters were kept at the default values. The mesh resolution is the only parameter that changed. At the tidal boundary a fixed tracer concentration was set at 30 PSU.

2) *Results*

At 5000 m from the tidal boundary a tracer value time series was extracted for the three different mesh resolutions. The results are plotted in figure 13. It is clear that a coarse mesh has a larger effect on the tracer transport.

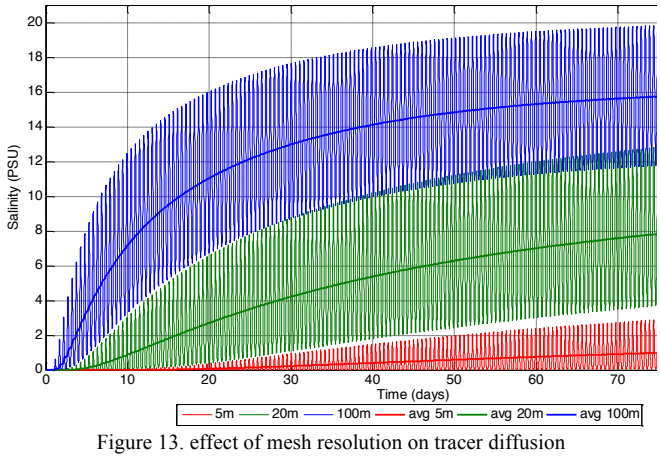

Figure 13. effect of mesh resolution on tracer diffusion

The results suggest that salt will diffuse further upstream when the mesh is coarse. In this channel test case a channel mesh of 100 m resolution in the length and 20 m in width gave the same results as the overall 100 m resolution mesh as expected since the main velocity vectors are directed along the channel axis.

B. test case 2: effect of the tracer diffusivity parameter

For a certain mesh resolution there is an amount of numerical diffusion present. We would like to know what order of magnitude this numerical diffusion has or at which parameter value of the tracer diffusivity we start to influence the tracer diffusion in the test model.

1) test model description

We used the same default parameter values and boundary conditions as the previous test case. For the 20, 50 m and 100 m mesh resolution we even used the same model domain, but for the 5 and 10 m mesh resolution we used a smaller model domain of 2000 m in length and 50 m wide. The depth was kept the at -10 m TAW. The time step was always 4 s. The tracer diffusivity was varied between 1.E-6 and 1.E3 m²/s.

2) Results

At 1000 m from the tidal and tracer boundary a tracer value time series was extracted. This was done for the small model domain with mesh resolution of 5 and 10 m.

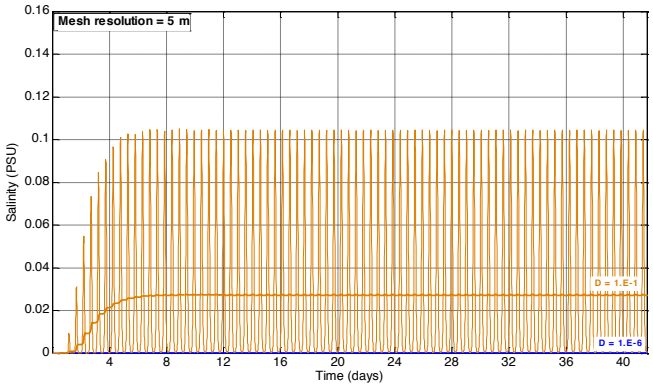

Figure 14. Mesh resolution 5 m: tracer diffusion results for D=1.E-1m²/s (orange line) and D=1.E-6 m²/s (blue line = zero)

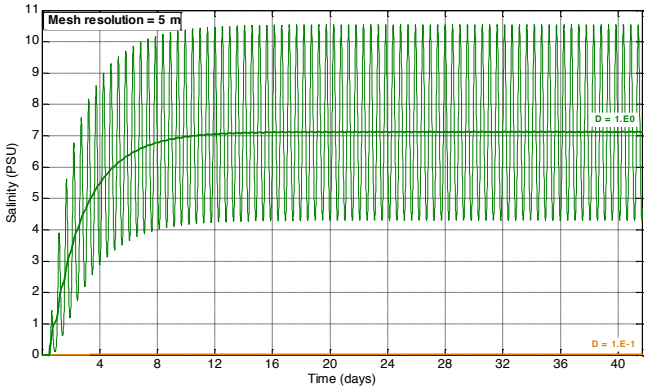

Figure 15. Mesh resolution 5 m: tracer diffusion results for D=1.E0 m²/s (green line) and D=1.E-1 m²/s (orange line = almost zero)

For the 5 m mesh a parameter value for the tracer diffusivity D of 1.E-6 m²/s gave no tracer concentration after 90 days at 1000 m from the boundary (figure 14). In the small model domain the upstream boundary discharge condition of 1m³/s has a larger effect than in the bigger model domain, because in figure 13 we see for the same diffusivity value a small tracer diffusion. If the tracer diffusivity is increased from 1.E-6 to 1.E-1 m²/s an increase of tracer diffusion to 0,025 PSU (daily averaged value) can be seen in figure 14. If the diffusivity is further increased to 1.E0 m²/s a much larger increase in tracer diffusion can be seen in figure 15.

For the mesh with 10 m resolution the diffusion is very comparable as the mesh with the 5 m resolution for the same diffusivity values. The daily averaged values just lie a little bit higher : compare results in figure 15 with results in figure 16.

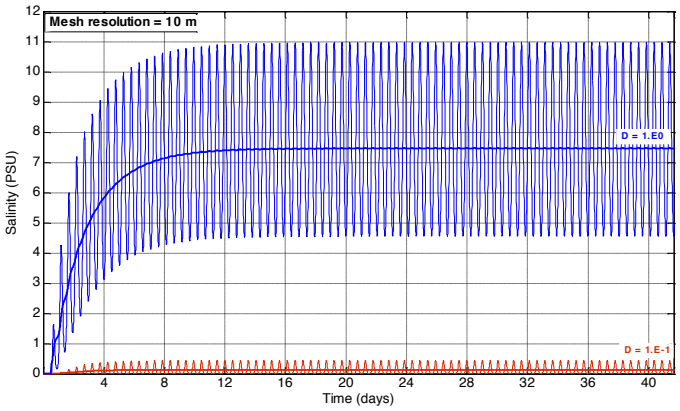

Figure 16. Mesh resolution 10 m: tracer diffusion results for D=1.E-1 m²/s (red line) and D=1.E0 m²/s (blue line)

For the mesh with 20 m resolution the diffusion of tracer increases again slightly for the same diffusivity values. A diffusivity D = 1.E1m²/s was also tested for the 20 m resolution mesh and gave a further increase in diffusion (figure 17) . It is noticed that the higher the diffusivity, the faster the tracer reacts to the concentration gradients, which is to be expected, and the faster a steady state is reached.

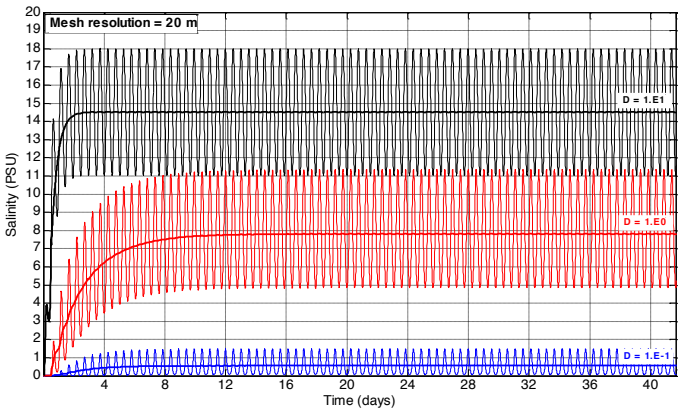

Figure 17. Mesh resolution 20 m: tracer diffusion results for D=1.E-1 m²/s (blue line), D=1.E0 m²/s (red line) and D=1.E1 m²/s (black line)

For the mesh with 50 m resolution the difference between the simulation with D=1.E-4 m²/s and D=1.E-1m²/s is small and less than 1 PSU. Increasing D with a factor ten (D=1.E0 m²/s) gives a big change in tracer transport (figure 18). Increasing the diffusivity again with a factor ten (D=1.E1 m²/s) results in the same order of magnitude increase as from D=1.E-1 m²/s to D=1.E0 m²/s (figure 19).

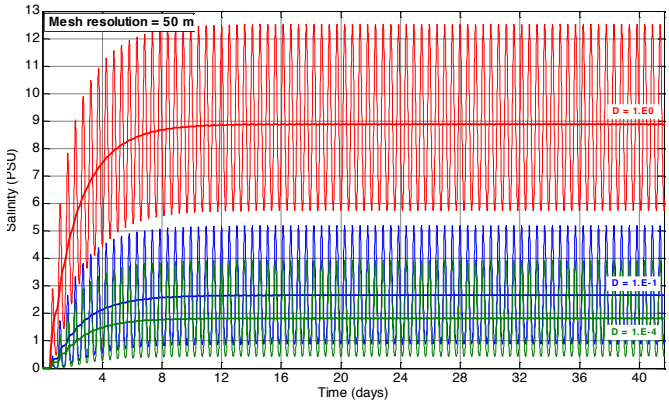

Figure 18. Mesh resolution 50 m: tracer diffusion results for D=1.E-4 m²/s (green line), D=1.E-1 m²/s (blue line) and D=1.E0 m²/s (red line)

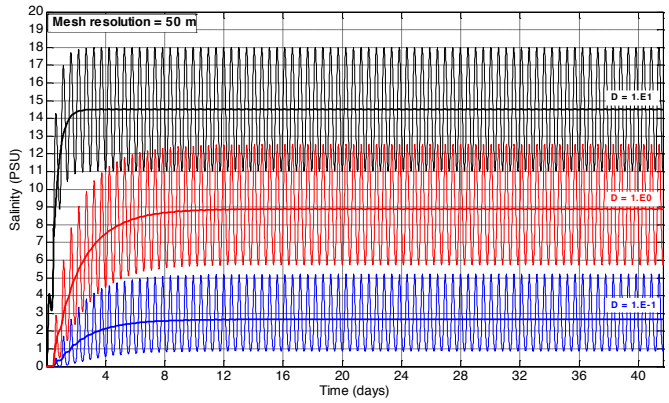

Figure 19. Mesh resolution 50 m: tracer diffusion results for D=1.E-1 m²/s (blue line), D=1.E0 m²/s (red line) and D=1.E1 m²/s (black line)

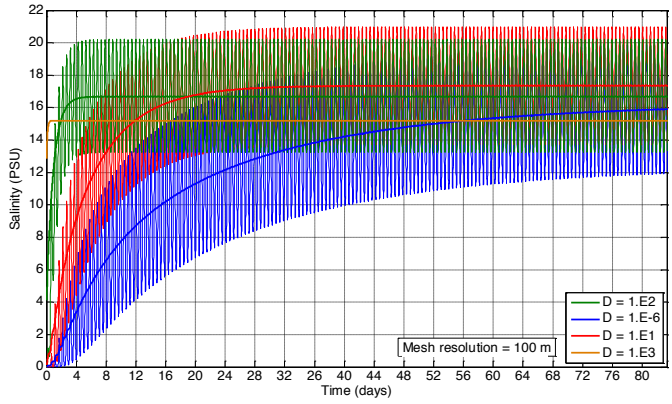

Figure 20. Mesh resolution 100 m: tracer diffusion results for D=1.E-6 m²/s (orange line), D=1.E1m²/s (red line), D=1.E2 m²/s (green line) and D=1.E3 m²/s (orange line)

For the mesh with 100 m resolution the results show that the size of the diffusivity parameter mostly influences the speed at which the steady state is reached (figure 20) and less the steady state salinity level. For D=1.E-6 m²/s (blue line in figure 20) the steady state salinity level lies even higher than for D=1.E3 m²/s, a very high diffusivity.

VI. Discussion

Even in simple test cases like the small test cases described in this paper it is very difficult to differentiate the effect on tracer transport caused by tracer advection, molecular tracer diffusion, numerical diffusion and dispersion. But the test cases show a clear and large influence of the mesh resolution on the tracer results. The test cases also show that the tracer diffusivity parameter D has a different effect at different mesh sizes. This makes it really difficult to calibrate or to improve the salinity as a tracer in our big model because of the different mesh resolutions at different locations. at least we need a place varying diffusivity parameter so we can influence tracer calculations in the model domain part where the mesh resolution is not too coarse; or in other words where the numerical diffusion is not so overwhelming that it dominates the tracer transport.

For our partner in the project, the University of Antwerp, we did some tracer calculations in the Scaldis model. Figure 21 shows the tracer concentrations of two identical tracers for seven tidal cycles. Tracer 11 (blue line) was released in the downstream part of the model (where the mesh is coarser; about 50-70 m) and tracer 17 was released in the upstream part of the model (where the mesh resolution was 7 m). Figure 21 shows that tracer 11 is more diffusive than tracer 17. But again it is difficult to differentiate and point only towards numerical diffusion. The cross sectional area downstream is much larger than upstream and so the fresh water discharge has less effect on tracer diffusion downstream than upstream. This can also be seen in the higher advective transport of the tracer upstream. This makes it very difficult to judge the models performance for tracers.

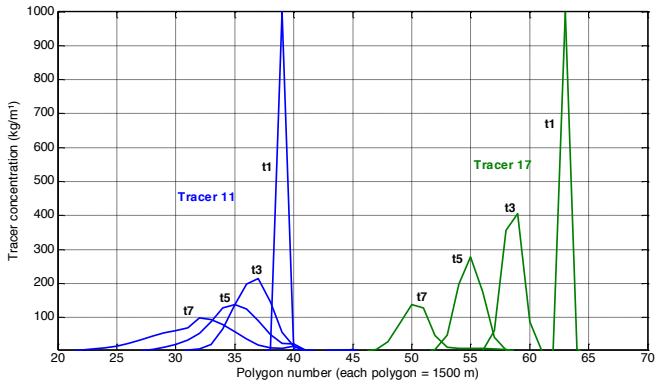

Figure 21. Tracer transport at two different locations (downstream=blue lines; and upstream= green lines) after one (t1), three (t3), five (t5) and seven (t7) tidal cycles in the Scaldis model

VII. CONCLUSIONS

For the Scaldis 3D model we do not succeed to get the salinity values right in the Coastal zone of the model. The salinity field corresponds better with the measurements inside the Scheldt Estuary. Due to the high dependency of the salinity as a tracer from the numerical diffusion (mainly due to mesh resolution) we get no grip on how to improve this salinity field in the coastal zone.

The small test cases clearly show the dependency of the tracer diffusion on the mesh resolution. If one keeps all parameters fixed, but changes only the grid resolution of his model, the whole salinity field will change, like already reported by [6].

For mesh resolution ranging from 5 to 100 m the tracer diffusivity parameter has no effect with values below 1.E-1 m^2/s. But due to the interference of tracer advection, molecular tracer diffusion, dispersion and numerical diffusion it is very difficult to estimate the real contribution of this parameter.

REFERENCES

[1] Smolders, S., Teles, M.J., Maximova, T., Vanlede J., 2014. Implementation of controlled reduced tide and flooding areas in the Telemac 3D model of the Scheldt Estuary. Conference proceedings Telemac & Mascaret User Club, 15-17 October, 2014, Grenoble, France.

[2] Maximova, T., Smolders, S., Vanlede, J., 2015. Model calibration against different types of velocity data with a dimensionless cost function: application to the Scaldis model of the Scheldt estuary. Telemac & Mascaret User Club, 15-16 October, 2015, Daresbury, UK.

[3] Smolders, S., Maximova, T., Vanlede, J., Verwaest, T., Mostaert, F., 2015. Integraal Plan Bovenzeeschelde: Subreport 1 – 3D Hydrodynamisch model Zeeschelde en Westerschelde. Version 1.0. WL Rapporten, 13_131. Flanders Hydraulics Research: Antwerp, Belgium. (in preparation)

[4] Soetaert & Herman, 1995. Nitrogen dynamics in the Westerschelde estuary (SW Netherlands) estimated by means of the ecosystem model MOSES. Hydrobiologia 311: 225 - 246.

[5] Maximova, T., Vanlede, J., Verwaest, T., Mostaert, F., 2015. Vervolgonderzoek bevaarbaarheid Bovenzeeschelde: Subreport 4 – Modellentrein CSM – ZUNO: validatie 2013. WL Rapporten, 13_131. Flanders Hydraulics Research: Antwerp, Belgium

[6] Smolders, S., Meire, P., Temmerman, S., Ides, S., Plancke Y., Cozzoli, F., 2013. A 2Dh hydrodynamic model of the Scheldt estuary in 1955 to assess the ecological past of the estuary. Telemac & Mascaret User Club, 16-18 October, 2013, Karlsruhe, Germany

Breach modelling by overflow: comparison with USDA-ARS cohesive embankment experiments

Laroche Christophe / Alquier Mathieu
Cerema / Direction Territoriale Méditerranée
Aix en Provence, France
christophe.laroche@cerema.fr

Floriani Fanny
DREAL Picardie
Amiens, France
fanny.floriani@developpement-durable.gouv.fr

Abstract— We focus on homogeneous embankment in fluvial conditions and we try to represent the flow through a breach occurred by overflow. To do this, an erosion law is coupled with TELEMAC 2D, which represents a progressive surface erosion due to the flow. This same erosion law has been used to propose a method to represent the lateral development of the breach. In the first time, we verify that the embankment erosion represented with this method is consistent with the soil resistance given by JET tests. In the second time, the effect of the lateral development of the breach method is also assess. Finally, the comparison of our results with USDA-ARS data gives a possibility to improve our implementation.

I. INTRODUCTION

To reduce flood risk, embankments are usually used, but history shows that the consequences of embankment failure can be severe. For example, a large part of 66 fatalities and 2,8 billions of Euros occurred during the flooding of the south of France in 1999, 2002 and 2003, could be affected to breaches [9].

Breaching process combine a complex interaction between hydraulic, geometric and soil property effects. For example, the compaction water content which has been identified as a key factor to assess the embankment resistance, can modify by orders of magnitude the rate of breach formation. To assess this complexity, a combination of knowledge and skills from these different disciplines is required [1].

Recent research has proposed to use in predictive breach models, the embankment erodibility [1]. Our approach is definitively pragmatic by using a hydraulic model, solving the Saint-Venant equations in 2D, in which we implement a quite simple erosion law. According with the capability of this method to predict the breach formation, the implementation of the soil property effects will be improved. During the LEVEES research project (2010-2013), we tested the first implementation of an erosion law in TELEMAC 2D. These results were presented in the XXth Telemac Mascaret User Conference in Karlsruhe. Since 2013, some field experiments were used to do a comparison with our method.

This article firstly gives a short presentation of the methodology used and results obtained before 2013. Afterwards we detail the methodology used to represent a first lateral development of the breach. Finally, we compare our results with two USDA-ARS field experiments available in the literature.

II. INCISION OF THE EMBANKMENT: FIRSTS RESULTS AVAILABLE

We focus on homogeneous embankment in fluvial conditions and we use TELEMAC 2D (*V6P1*) to represent the flow through a breach occurred by overflow. To represent the development of the breach, depending on the hydraulic conditions, we used an erosion law coupled with TELEMAC 2D. The consequence of this implementation will be that the breach shape will not be predefined unlike in most breach models [2].

In this party, the only way to have an erosion, is when the velocity of the flow is sufficient. Thereby the erosion process represented is a simple progressive surface erosion.

A. The erosion law implemented

We used the erosion law defined by Partheniades [3], which gives the erosion rate as a function of effective shear stress (τ-τ_c) and a detachment rate coefficient (k_d).

$$\varepsilon = k_d * (\tau - \tau_c) \quad (1)$$

- k_d is the detachment rate coefficient of the material (erodibility factor) (m3/N.s)

- τ_c is the shear threshold (Pa)

- τ is the shear stress (Pa)

Using the Manning formula, it is possible to calculate the shear stress and thereby the erosion rate in each node of the mesh. The erosion of a cohesive material is easily represented by this law, but the deposition of the material, downstream the erosion zone cannot be represented. For more information about the method, we recommend the reader to consult the following article [4].

It is not possible to represent the lateral development of the breach according with the conclusion in [4].

The shear stress is assessed by strong hypothesis as the using of depth-averaged velocity instead of the bed shear velocity. Moreover, turbulence effects are not taken into account in this approach.

B. Results only with the incision of the embankment

1) The study case

The erodibility classification proposed in 2009 by Wahl [5] is used to qualify the embankment resistance.

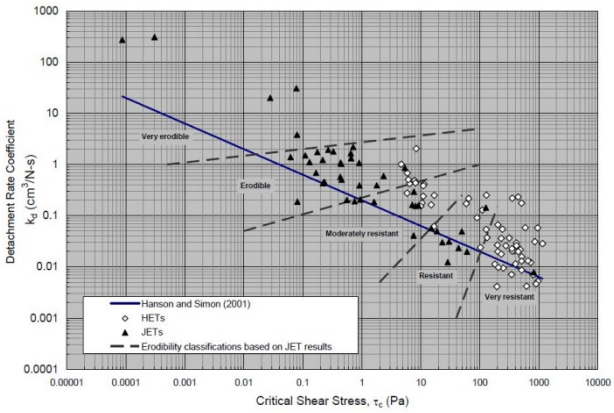

Figure 1: Erodibility classification based on k_d and τ_c according to [5]

The different embankment resistance tested are presented in table I. In each case, the resistance of the overbank is considered equal to the resistance of the embankment.

TABLE I. EMBANKMENT RESISTANCE TESTED

	Embankment resistance	**k_d m3/N.s**	**t_c Pa**
Set 1	*erodible*	10^{-5}	0,1
Set 2	*moderately erodible*	10^{-7}	10
Set 3	*resistant*	10^{-8}	50

We considered a channel with a 0,1% slope, a trapezoidal section 20 m wide at the bottom and 26 m at the surface. The dike is 6 m wide at the crest and 14 m at the base. It is placed on the left bank, 4 m back (Fig.2).

To fix the position of the breach, we cut a notch, on the crest of the dike, 20 cm deep by 18 m wide. The size of the mesh is 3 meters in the breach. Then, the mesh size increases gradually to reach 50 meters.

A constant viscosity of 0,005 m/s² is used and the Strickler friction coefficient is fixed at 20 $m^{1/3}s^{-1}$. For more information about this case, we recommend the reader to consult the following article [4].

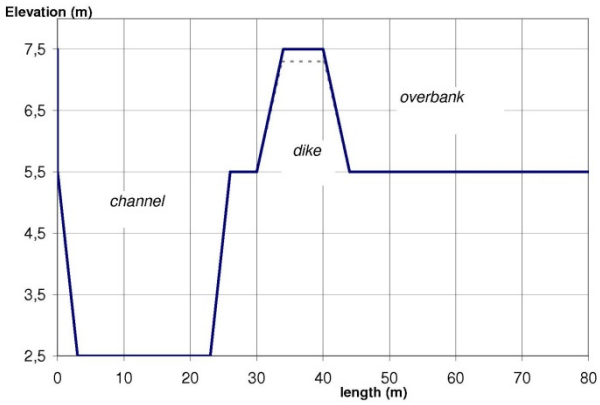

Figure 2: Cross-section of the embankment and the channel

2) Results

With the more erodible soil (set 1), the embankment is completely breached one hour after the beginning of the overflow (Fig. 3). Whereas, the more resistant soil (set 3) is not eroded despite an overflow for several dozen hours.

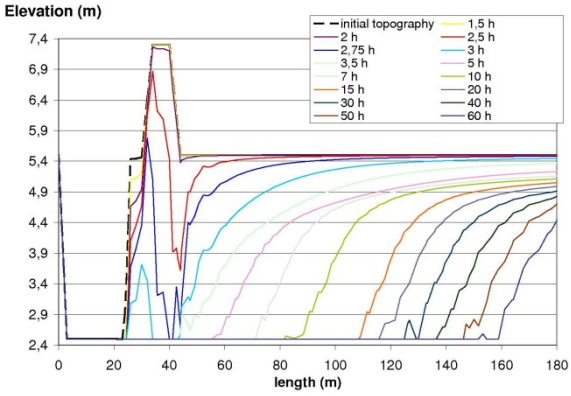

Figure 3: Time evolution of the erosion (set 1)

With the moderately erodible soil (set 2), the embankment resist several dozen hours despite an erosion on the crest and on the downstream foot of the dike (Fig.4). As indicated in [4], the mesh size have an influence of the erosion rate. Thereby, with a 1 meter size mesh, the erosion rate of the moderately erodible material is doubled.

Despite an influence of the mesh size identified in [4], the resistance of the embankment proposed with our method

seems broadly consistent with the erodibility of the materials proposed in [5] and presented in Fig. 1.

This method could be seen as a method to represent the breach formation due to surface erosion. For each case in which an erosion is observed, we can see a scour hole of the downstream foot of the embankment, which is usually saw in historical breaches. Of course, this scour hole can have an influence on the discharge calculated through the breach.

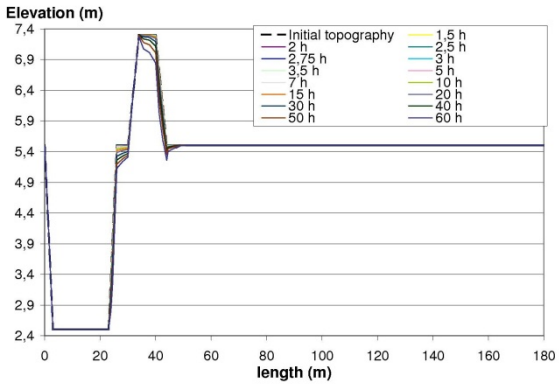

Figure 4: time evolution of the erosion (set 2)

III. COMPARISON WITH USDA-ARS DATASET

To represent the lateral development of the breach in our method, we conserve the same process as in the first part of this work: the widening of the breach is assumed given by the flow. This assumption was taken to assess the contribution of the continued surface erosion process given by the flow velocity, in the lateral development of the breach. . Of course this approach is very partial, as described in [6], other processes have a large influence on the widening of the breach, as the undercutting and the collapse of the breach sides (mass failure), or the sliding of the breach sides.

Thus, this party presents a first implementation of a lateral development method of the breach due to hydraulic conditions. In this method, we assume that all mechanical features of the embankment material are constant. Afterwards, two USDA-ARS experiments are used to do a comparison with our results.

A. Lateral development method

Here, only the partially wet elements, which have 2 nodes wet, are considered. For each wet node of this kind of element, it is possible to calculate an erosion rate, as in the incision method. The mean of these 2 erosion rates can be used to calculate an erosion rate of the wet base of the element.

All of these erosion rates are vertical erosions, and our problem is to convert them to horizontal erosion. To do this, we suppose that the erosion rate can also be applied perpendicularly on the partially wet elements. This assumption is materialized by the red dotted arrow in Fig. 5. The horizontal projection of this erosion rate (the green arrow) gives the lateral erosion rate of the partially wet element considered, during the time step *dt*.

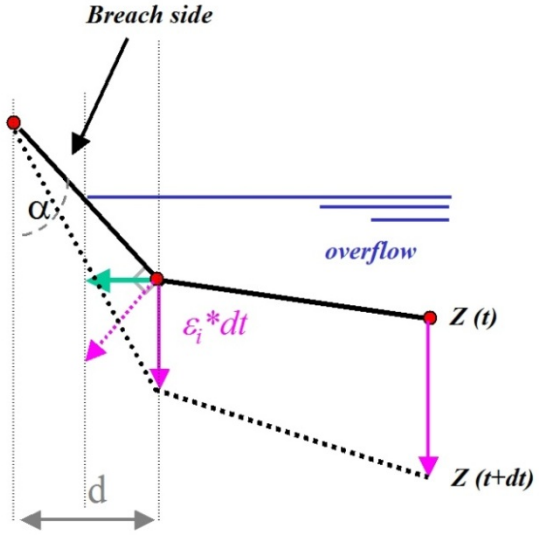

Figure 5: principle of the breach widening modelling

d is the distance between the dry node and the wet base of a partially wet element.

The cumulative lateral erosion can be stored during the simulation. When this value will be greater than *d,* the elevation of the dry node is setting to the mean altitude of the wet nodes.

B. USDA-ARS experiments used

The USDA-ARS dataset used consists of two experiments. Both experiments were performed in the same location, hence the reservoir storage is the same. The embankment was constructed 2,3 m high and with three test sections with different soils. Each test section have 7,3 m wide. To fix the position of the breach, a notch 0,46 m deep by 1,83 m wide was cut into each test section. All features of these experiments are given in [2] and [7].

As given in table II, with the erodibility classification proposed by Wahl in [5], the embankment of the first experiment can be considered as a very erodible one. For the second experiment, the embankment can be considered as a resistant one.

TABLE II. EMBANKMENT RESISTANCE TESTED

	Embankment resistance	k_d **m3/N.s**	τ_c **Pa**
Experiment 1	*very erodible*	$10{,}3.\ 10^{-6}$	0,14
Experiment 2	*resistant*	$3{,}9.\ 10^{-8}$	15

Four stages have been identified in [7] to describe the overtopping erosion processes in cohesive material:

- ***stage I***: rills erosion occur in the downstream face, one or more master rills develop into a cascade of overfalls. In the end of this stage, a large headcut is formed at the downstream crest, with a width of erosion approximately equal to the width of the flow at the downstream crest.

- ***stage II***: the headcut migrates from the downstream to the upstream crest of the embankment. The lateral development of the erosion occurred due to mass wasting of material from the sides of the gully.

- ***stage III***: this stage begins with the lowering of the upstream crest and ends when all of the upstream face is eroded. Then, the breach is completely formed.

- ***stage IV***: this stage represents the widening of the breach due to the emptying of the reservoir.

Fig. 6 gives an overview of the timing of an embankment failure using data available for the experiment 1.

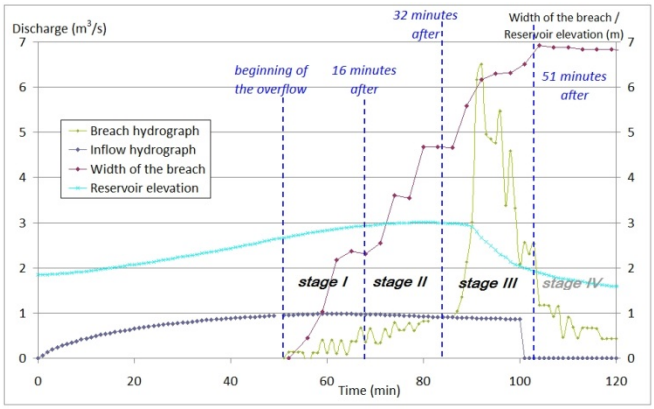

Figure 6: Time lines of observed erosion width, reservoir water surface elevation and hydrographs for experiment 1

C. *Hydraulic parameters*

According to the size of the notch and the embankment, the size mesh is 0,2 m in the erodible zone.

The Strickler friction coefficient is fixed at 25 $m^{1/3}s^{-1}$.

A model with a constant viscosity of 0,004 m²/s is used.

D. *Experiment 2 versus our method*

In the field experiment 2, despite more than 19 hours of overflow, no breach occurred during the experience due to the resistance of the soil.

Stage I lasted a little less than 3 hours (164 minutes) and because the upstream crest of the embankment did not be eroded, the stage III did not be reached.

As we can see on Fig. 7 (b)/(c), the lateral development of the breach occurred during stage II, due to mass wasting of material from the sides of the gully. The final width of the gully is given in [2] and [7] to about 4,2 m.

Inflow and outflow hydrographs are the same with a constant value about 1 m^3/s.

2 hours after the beginning of the overflow (a)

12 hours after the beginning of the overflow (b)

19 hours after the beginning of the overflow (c)

Figure 7 (a)/(b)/(c): Time evolution of the breach formation for experiment 2 according to [8]

In our results, we can see in Fig. 8, a final erosion of the downstream face of the embankment. The maximum erosion depth is 0,46 m on the foot of the downstream face. Regarding the experiment results (Fig. 7), this erosion is very limited. During the stage I, only one rill occurs without overfall and the stage II seems to be not reached in our results.

According with only the hydraulic effects taken into account, it is not possible to see in our method soil property effects as headcut or lateral development of the rill. Hence the erosion rate of the embankment is broadly underestimated.

Because the upstream crest is not eroded in our method and in the field experiment, both breach outflow hydrographs are the same.

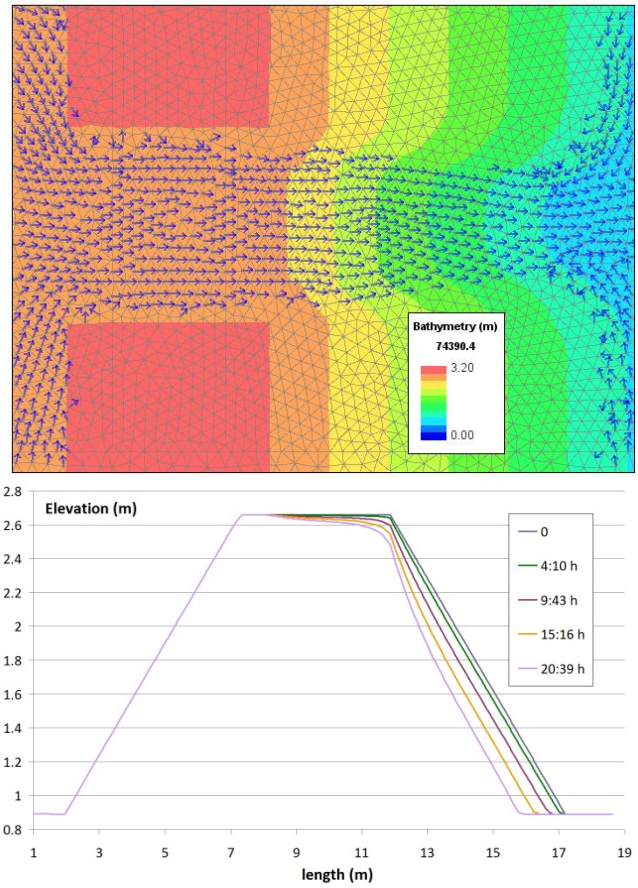

Figure 8: Comparison of our results with the field experiment.

E. Experiment 1 versus our method

In the field experiment 1, less than 50 minutes after the beginning of the overflow, the breach was formed. In the two first stages of the breach formation, the lateral development of the gully occurred due to soil property effects and also geometry and hydraulic effects. During these two stages, as we can see in Fig. 6, the outflow increased due mainly to the increasing of the water level in the reservoir. In the end of stage II, the width of the gully was a little less than 5 meters [7].

The upstream crest of the embankment began to be eroded about 32 minutes after the beginning of the overflow (stage III). During this stage, the lateral development of the breach increased a little more than 2 meters, to reach 7 meters. The failure occurred as the water elevation in the reservoir has not started to decrease (Fig. 6).

5,5 minutes after the beginning of the overflow (a)

14,5 minutes after the beginning of the overflow (b)

29,5 minutes after the beginning of the overflow (c)

38,5 minutes after the beginning of the overflow (d)

Figure 9 (a)/(b)/(c)/(d): Time evolution of the breach formation for experiment 1 according to [8]

In the field experiment 1, the outflow reached 6 m3/s. The outflow decreased rapidity because of the small reservoir size.

In our results, from the beginning of the overflow, an erosion of the embankment is observed on the downstream face as in the field experiment, but also on the crest. This second erosion which is not observed in the field experiment, comes from the very erodible material used. In our result, velocities are sufficient to erode the crest. This difference could be explained by the grass we can see on the embankment in Fig. 9(a) and which is not represented in our method. The consequence is a greater increasing of outflow discharge in our result (Fig. 10).

In our results, the erosion rate of the downstream face is not so important as in the field experiment. The stage I lasts about 24 minutes against 16 minutes in the experiment field. Soil property effects, as headcut, which are not represented in our method, but also mesh size effect, may explain a part of this difference. Due to the very erodible material, in our results the upstream crest is being eroded, the outflow increases gradually and the water elevation in the reservoir begins to decrease unlike in the field experiment.

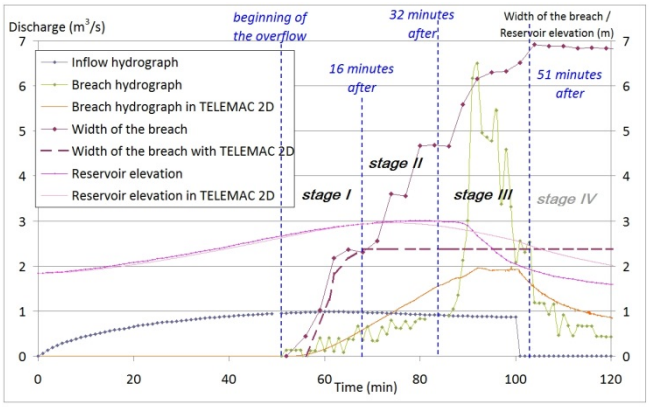

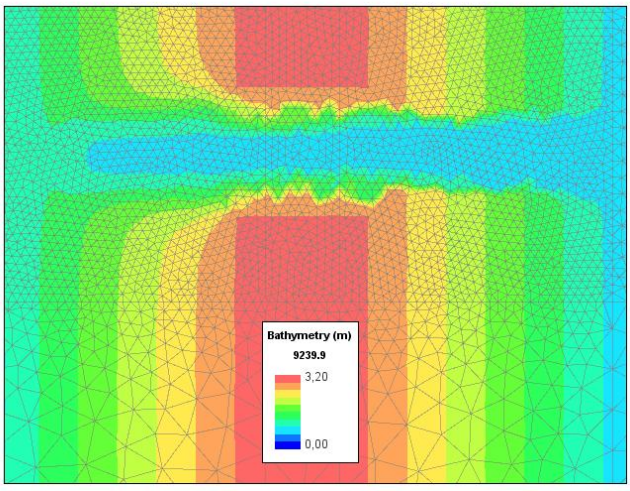

Figure 10 :TELEMAC 2D and observed data comparison

The end of the upstream face erosion (end of stage II) could be assessed broadly in the same moment as in field experiment. Until this moment, the upstream crest continues to be eroded and the outflow continues to increase gradually. The outflow in our results is greater than in field experiment. The water elevation in the reservoir continues to decrease.

Due to the erosion of the upstream face since the beginning of the overflow, the stage III is not consistent with the definition. During this stage, with 2 m^3/s in our results, the outflow reaches gradually the maximum discharge value unlike the field experiment where a very rapid increase in discharge until 6,5 m^3/s is observed.

In the end of the calculation, the upstream face is broadly eroded, but a 0,4 m high of material remains in our results (Fig. 10).

Fig. 10 presents the evolutions of the breach width from the field experiment and our method. The gap between both is clearly represented on this figure, material property effects must be implemented in our method to improve the prediction of the width of the breach.

IV. DISCUSSION

To analyse the effect of the implementation of the lateral development of the breach in our method, the experiment 1 has been used without this implementation. The comparison of both results gives some information about the lateral development of the breach effect:

- the main effect of this implementation can be seen on the cross-section of the breach (Fig. 11). The lateral sides of the breach are more vertical with the lateral development method. With minus of 0,2 m^3/s, the effect of this modification of the outflow hydrograph is insignificant.

- the eroded width on the crest of the embankment are similar in both cases. In fact, the maximum width of the erosion occurs during the first stage when the flow is not yet concentrated.

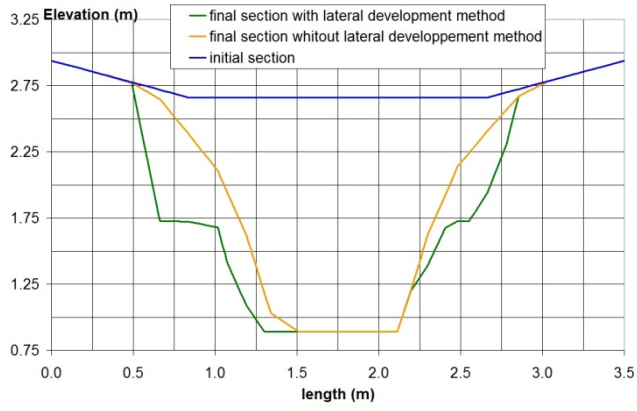

Figure 11 :comparison of the section of the breach with and without the lateral development method used

With the two experiments, even if the embankment resistance is consistent with the erodibility classification given by [5], we can observe that the erosion rate of the downstream face of the embankment given by our method is not sufficient. Furthermore, no rill and overfall are observed. The assessment of the bed velocity and hence the erosion rate could be improved by using TELEMAC 3D. But to observe rill and overfall in our results, it could be probably better to implement a no homogeneous behaviour of the material, such as a spatially variable detachment rate coefficient.

The outflow hydrograph of the experiment 1 increases more rapidly with our method, due to the erosion of the crest of the embankment. The using TELEMAC 3D to assess with more accuracy the bed velocity and hence the bed shear stress could be possible, but implementing the grass effect in our method is an other way, which could be probably a more efficient.

However, the behaviour of the outflow given by our method remains not correct because during the stage III, in field experiment, the failure seems to occur really quickly with rapid increase in discharge and decrease in water level in the reservoir. In our method such evolutions are not observed, only continuous evolutions are calculated. An implementation of a mass failure could improve the prediction of the outflow.

V. CONCLUSIONS

Despite the underestimating of the outflow maximum value and the width of the breach, TELEMAC 2D coupling with a quite simple erosion law gives some interesting results. The embankment behaviours proposed are consistent with the resistance of the soil material given by JET tests. The beginning of the evolution of the width of the breach seems correct with TELEMAC 2D. However, improvements are needed to integrate the material property effects, as the mass failure, a spatially variable detachment rate coefficient or implementing a grass layer. It could be interesting too to test this method with TELEMAC 3D.

ACKNOWLEDGEMENT

The authors would like to thank the Directorate for Research and Innovation of french Ministry of Ecology, Sustainable Development and Energy for the funding of this work.

REFERENCES

[1] Morris M.W.(2009). Breaching Processes: A state of the art review, In FLOODSite project, rep No T06-06-03, HR Wallingford UK.

[2] Van Damme M., Morris M.W., Hassan M. (2012). WP4.4 : A new approach to rapid assessment of breach driven embankment failures. Flood Risk Management Research Consortium. Research report SWP4.4.

[3] Parthéniades E. (1965). Erosion and deposition of cohesive soils.Journal of the Hydraulic Division, n°91, pp 105-139.

[4] Laroche C, Alquier M. (2013). Implementation of an erosion law in TELEMAC-2D: a way to predict the characteristics of a breach ? Proceedings of the XXth TELEMAC-MASCARET User Conference. Karlsruhe, BAW, pp 103-107.

[5] Wahl T. L., Hanson G. J., Reggazzoni P.L. (2009). Quantifying erodibility of embankment materials for the modelling of Dam breach processes. Proc. of the ASDSO Dam Safety, Hollywood, Florida, 2009, 24p.

[6] Hunt S.L., Hanson G.J., Cook K.R., Kadavy K.C. (2005). Breach widening observations from earthen embankment test. American Society of Agricultural Engineers, vol. 48(3) 1115-1120.

[7] Hanson G.J., Cook K.R., Hunt S.L. (2005). Physical Modeling of Overtopping Erosion and Breach Formation of Cohesive Embankments. American Society of Agricultural Engineers, vol. 48(5) 1783-1794.

[8] Hanson G.J. (2002). Embankment Research in the US. IMPACT Investigation of Extreme Flood. Processes & Uncertainty, Workshop at HR Wallingford, UK on 16 & 17 May 2002

[9] DREAL Languedoc Roussillon (2009). Les digues protègent...mais peuvent rompre

Wave-current interaction in the Porto di Lido entrance of the Venice Lagoon

Luca Chiapponi, Sandro Longo
Dipartimento di Ingegneria Civile, dell'Ambiente, del Territorio e Architettura (DICATeA), Università di Parma, Parco Area delle Scienze, 181/A, 43124, Parma – Italy
luca.chiapponi@unipr.it

Cesare De Piccoli
DP Consulting S.r.l., Via A. Palladio, 31021, Mogliano Veneto (TV) – Italy

Ezio Palmisani
Duferco Engineering, via Paolo Imperiale 4, 16126, Genova – Italy

Bruno Matticchio
Ipros Ingegneria Ambientale S.r.l., corso del Popolo 8, 35131 Padova – Italy

***Abstract* — The wave propagation and flow modules of the TELEMAC system have been applied to the "Porto di Lido" entrance of the Venice Lagoon. Wave-current interactions were analysed by direct coupling of the phase-averaged model TOMAWAC and of the two-dimensional depth-averaged flow TELEMAC 2D model. ARTEMIS software was separately applied to estimate the effect of refraction.**

The model includes the "Porto di Lido" entrance, one of the three channels connecting the Lagoon and the Adriatic Sea. The aim of the analysis is to evaluate the wave climate and the harbour tranquillity of a planned landing cruise, recently proposed in order to prevent the cruise ships from entering the Lagoon and mooring near San Marco. Several tests were performed and the results permit a comparison between the present condition and a future scenario including the planned terminal (landing cruise).

I. INTRODUCTION

In the past years several projects have been proposed in order to prevent large cruise ships from entering the Venice Lagoon (Venice, Italy) and, therefore, from causing environmental damage and increasing the environmental risks. One of the most promising projects (Venis Cruise 2.0) involves the construction of a terminal at the "Porto di Lido" entrance (Fig. 1). This structure would allow large ships to dock outside the Lagoon and the tourists should be fetched to the main islands by electric boats (at a reduced environmental impact). The pier (about one kilometer long and 34 meters wide) would be supported by circular pillars with a diameter of 7 meters and would be placed parallel to the North breakwater delimiting the entrance. Fig. 2 shows a rendering of the planned Venis Cruse 2.0 terminal.

The present study examines the influences of tide-induced water currents and waves at the Porto di Lido entrance in two different cases: (i) in the actual configuration (without the structure described above); (ii) in the presence of the planned pier according to the Venis Cruse 2.0 project.

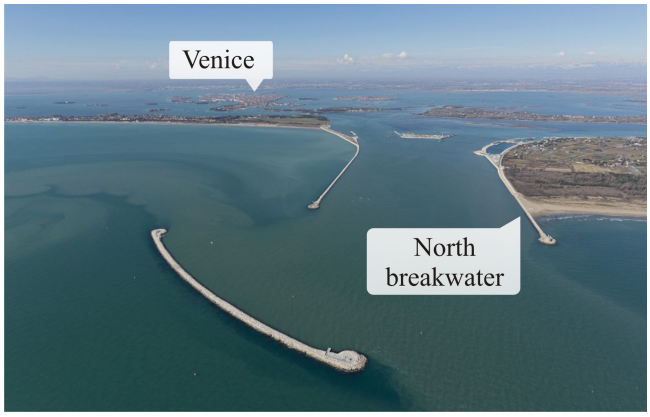

Figure 1. "Porto di Lido" entrance.

Figure 2. Rendering of the landing cruise.

Several runs were performed considering different combinations of mean wave direction and significant wave height (computed on the base of a risk analysis). Simulations were performed taking into account the effects of the different operating conditions of the MOSE gates (the Experimental Electromechanical Module intended to protect the city of Venice and the Venetian Lagoon from flooding).

The paper first describes the input data (computational domain and boundary conditions) used to launch the simulations. Then the results of all runs are compared, with particular attention to the effects of the structures described in the Venis Cruise 2.0 project (comparison between cases (i) and (ii)).

II. MODEL SETUP

A. Site characteristics and wave climate

The coastal area near the Porto Lido (Fig. 3) has been widely investigated in the past years. The studies were carried out to design the MOSE, a well-known system of mobile barriers built up to protect the Venice lagoon from the phenomenon of "high water".

Figure 3. Area of interest: the yellow line represents the planned pier.

For this reason, a detailed knowledge of the wave climate and several field measurements are available. Fig. 3 shows the area of interest and the planned layout of the landing cruise. The direction of onshore winds are in the range of 67° N and 192° N, with a fetch length up to 500 kilometres (see Fig. 4). The observation of effective fetch provides a clear and concise indication of the direction of significant waves. The stronger winds come from N-NE (Bora winds), but the limited extension of the fetch in that direction does not allow the waves to grow. Scirocco winds are not so intense, nonetheless they are characterized by a much more extended fetch length (in theory, extended along the Adriatic Sea, in practice no more than 500 km). The wave climate was determined with a statistical analysis of the data collected by wave recorder buoys and by several instruments installed on the offshore platform "CNR 3" (Lat 45°18'48''N, Long 12°30'54''E), close to the area of interest. The available data were collected from October 1987 to November 2012.

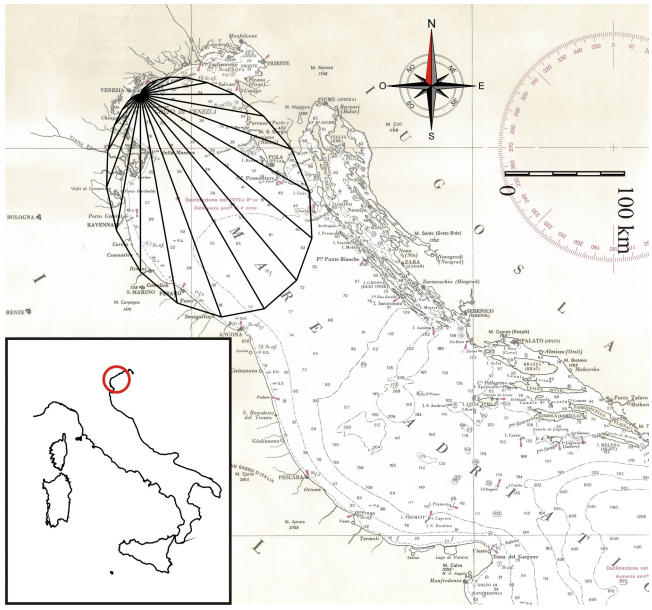

Figure 4. Effective fetch.

Fig. 5 shows the frequency of significant wave height by direction. The design wave height was calculated considering (1) the service life of the cruise terminal (L = 50 years [1]) and (2) the maximum allowable chance of exceeding the design wave (E = 0.05 [1]).

The return period of the critical event can be calculated as

$$Tr = L/-ln(1-E) \quad (1)$$

and for the assumed admissible damage, it is nearly equal to one thousand years.

The wave probability distribution function (according to Fisher-Tippet II [2]) is represented in Fig. 6 for waves from S-SE. The significant wave height corresponding to the critical event is Hs = 8.57 m. Similar analyses were carried out for waves from NE (Bora) and E-SE (Bora-Scirocco), estimating a significant wave height equal to Hs = 4.86 and Hs = 6.67, respectively.

The spectral analysis of the waves indicated a peak period of the spectrum according to the following equation [3]:

$$Tp = k\sqrt{Hs} \quad (2)$$

with k = 4.0, 4.25, 4.5 for waves from Bora, Bora-Scirocco and Scirocco. A Mitsuyasu directional distribution was assumed [4].

The sea level is locally subjected to relevant variations due to the astronomical tide and to the storm surge. The estimated highest maximum level is about 180 cm over the mean sea level (with a return period of 300 years) while the lowest minimum level is about -120 cm below the mean sea level.

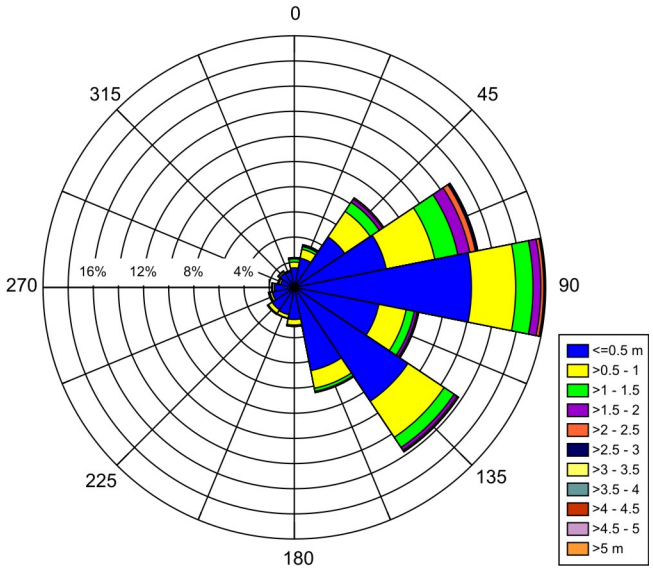

Figure 5. Frequency of significant wave height

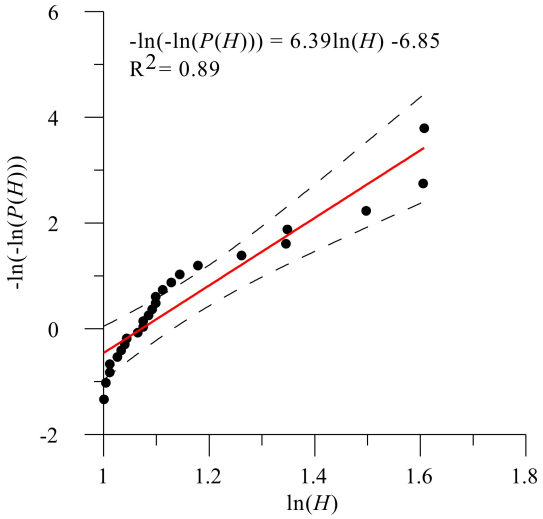

Figure 6. Wave probability distribution function (Scirocco sector, S-SE).

The typical ebb and flood current discharge through the "Porto di Lido" entrance are equal to 7150 m^3s^{-1} and 8000 m^3s^{-1}, respectively.

These values were calculated on the bases of several field measurements collected in the last years.

B. Domain contours and computational mesh

Once the domain contours were properly defined, the open source software BlueKenue was used to generate four different unstructured triangular grids. The first case (i) refers to the actual configuration (without the structure described above). The second case (ii) refers to the presence of the terminal to be built according to the Venis Cruse 2.0 project.

Two different MOSE operating conditions were analysed for each case:

- case (i.1): actual configuration, MOSE barriers off;
- case (i.2): actual configuration, MOSE barriers on;
- case (ii.1): pillars of the cruise terminal located at the design position, MOSE barriers off;
- case (ii.2): pillars of the cruise terminal located at the design position, MOSE barriers on.

Fig. 7 (1) shows the domain contour in cases (i.1) and (ii.1), while Fig. 7 (2) shows the domain limitation imposed by MOSE mobile barriers, cases (i.2) and (ii.2). Both figures provide information about the reflection coefficient, *R*, imposed in ARTEMIS simulations.

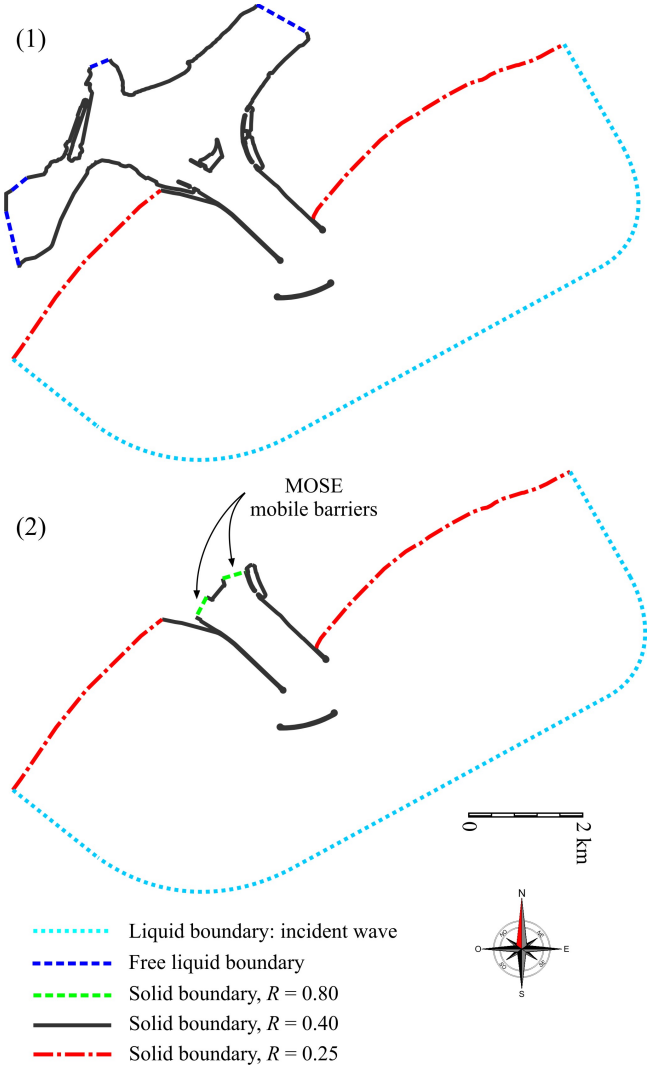

Figure 7. Domain contours. (1) MOSE barriers off and (2) domain limitation imposed by MOSE mobile barriers.

The cruise terminal pier rests on more than a hundred pillars, which are arranged in about 30 rows (each row consists of 3 or 4 pillars). Other pillars (6 units) support the access ramp at the North end of the landing cruise. Pillars represent the main interaction between the structure and the fluid domain. For this reason each pillar is represented by an island in the computational domain. Fig. 8 shows the area occupied by pillars. The grid, shown in Fig. 9, consists of more than 135 000 nodes with a minimal distance of 12 m into the "Porto di Lido" entrance. The grid size gradually increases to 50 m outside the channel. In the modified configuration (case ii) a more detailed mesh was created, with a minimal size of 2 m close to the pillars (see Fig. 10).

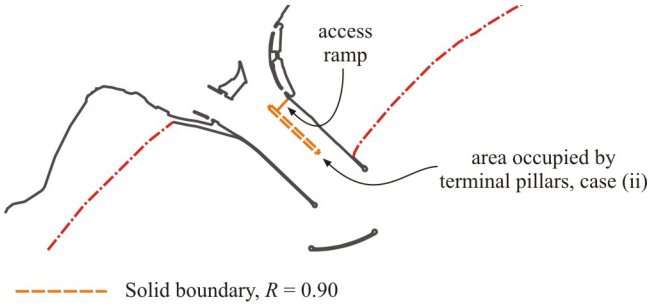

Figure 8. Domain modified according to the Venis Cruse 2.0 project.

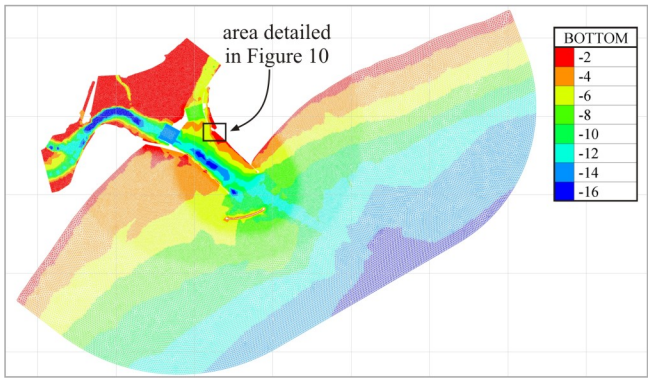

Figure 9. Bathymetry and computational grid (case i.1).

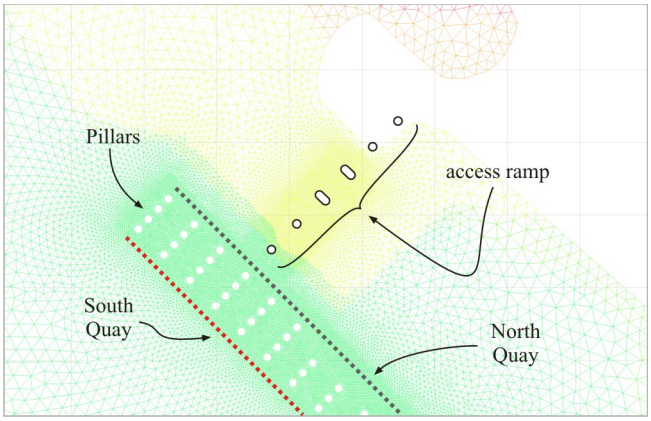

Figure 10. Detailed view of the bathymetry and computational near the North head of the pier (cases ii.1 and ii.2).

If MOSE barriers are lifted on, no flood or ebb current occurs. Therefore, the analysis of wave-current interaction (coupled TELEMAC 2D – TOMAWAC model) was limited to the condition of MOSE barriers lifted down. The mesh described above (cases i.1 and ii.1) was used for both ARTEMIS and TELEMAC 2D – TOMAWAC simulations.

III. RESULTS

A. *ARTEMIS simulations*

The first set of runs was performed without taking into account the effects of flood/ebb currents. Fig. 11 shows the results of the ARTEMIS wave modelling for case (i.1) where the incident wave travels from Scirocco (Hs = 8.57 m). A sea level equal to + 2.0 m was assumed in order to consider the toughest conditions, since it was checked that larger water depth induced higher waves near the planned pier. It is partly a consequence of the reduced wave breaking due to reduced shoaling, partly of the reduced bottom friction effect.

The pillars of the landing cruise (and the local excavation of the seabed required to guarantee a safe mooring and movement of the ships) do not increase the transformed wave height near the South Quay (see Fig. 12, case i.1). The energy propagation pattern changes according to the new local bed geometry. Near the North Quay a small reduction of the wave height is observed.

The worst condition occurs when MOSE mobile gates are lifted on and the wave energy do not propagate into the Venice Lagoon but is reflected back into the channel (see Fig. 13). The barriers reflect a relevant fraction of the energy of the incident waves which remains inside the "Porto di Lido" entrance channel, with an increment of the significant wave height up to 1.6 m (near the pier). There is no substantial difference between scenarios (i.2) and (ii.2).

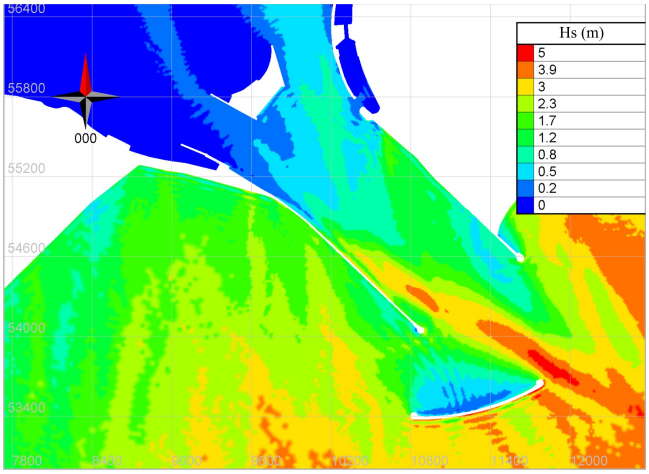

Figure 11. ARTEMIS simulations, critical wave (case i.1).

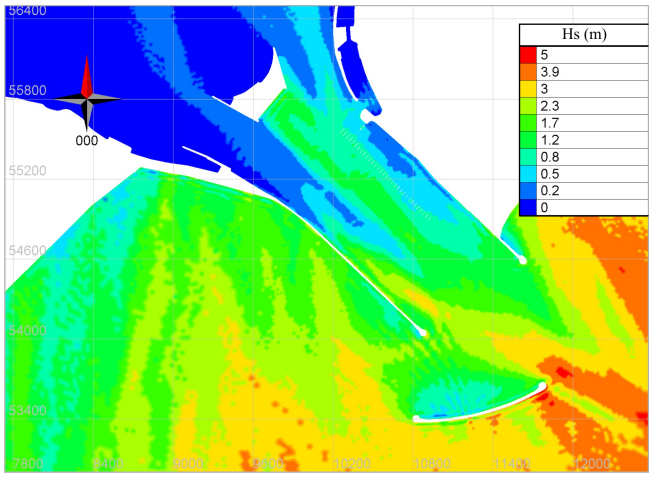

Figure 12. ARTEMIS simulations, critical wave (case ii.1).

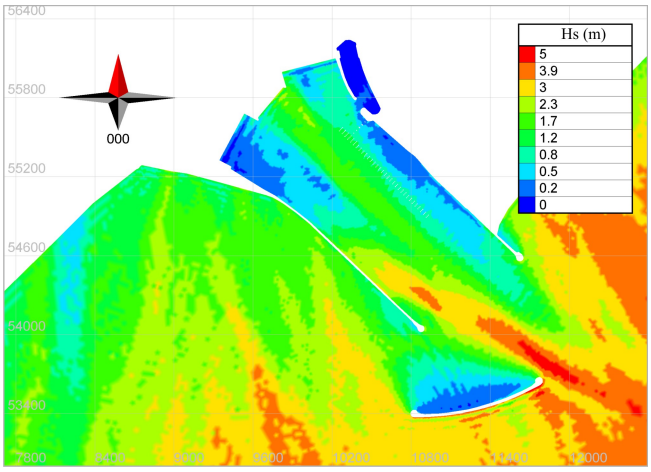

Figure 13. ARTEMIS simulations, critical wave (case i.2)

B. TELEMAC 2D – TOMAWAC simulations

Results from previous simulations were used to calibrate the input parameters of the wave–current model.

Data from TOMAWAC simulations are usually used as boundary conditions for ARTERMIS. In this case, we used experimental wave data from "CNR 3" platform close to the cost to calibrate the model. In addition, some simultaneous measurements of wave height inside the channel and offshore were also available. Hence, it was possible to compare field observations and ARTEMIS results, finding a good agreement. TOMAWAC results were not so accurate, with a systematic overestimate of the wave height. Energy losses due to wave refraction (neglected in TOMAWAC) are not negligible and that partially explains the behaviour of the phase-averaged model applied to the small domain under analysis.

We calibrated TOMAWAC parameters using ARTEMIS results, in order to obtain a more realistic and consistent wave propagation pattern. Finally, the resulting TOMAWAC model was directly coupled with a TELEMAC 2D model characterized by a constant level at the outflow section and by one of the following stationary discharge boundary conditions: flow inshore, toward the Venice Lagoon (flood current) or flow offshore (ebb current). Tide currents are modelled neglecting their time variation and considering only the peak values. In this way the effects of the interaction between waves and high velocity currents acting for a long time inside the entrance channel are verified.

Fig. 14 and 15 show the results of the TELEMAC 2D – TOMAWAC coupled modelling (case i.1, with flood and ebb current, respectively).

Wave height is increased by ebb currents (propagating in opposite directions). This phenomenon can be addressed to the Doppler shift (effect of a steady current on intrinsic relative wave frequency) [5]: waves of the same apparent absolute period have a longer intrinsic period in a favourable following current and a shorter intrinsic period in an opposing current. As a consequence, there is a steepening of waves propagating with opposite currents.

In the case of flood tide, the high velocity flow (up to 2.0 m/s, entering the channel) increases the wave height close to the head of the South breakwater. These waves propagate toward the pier. Both flood and ebb currents increase wave height up to 1.7 m (near the pier).

Fig. 16 shows the flow dynamic close to the pillars. In that region of the domain the high resolution of the mesh allows the appreciation of an interesting phenomenon that was not expected at the beginning of the present investigation, even though it is quite common in rivers. Flood and ebb currents encountering the piers pillars generate vortices that result in a periodic flow. This flow can induce local erosion and excavation, hence some further studies on physical model should be carried out to prevent erosion and possible failure of the structure.

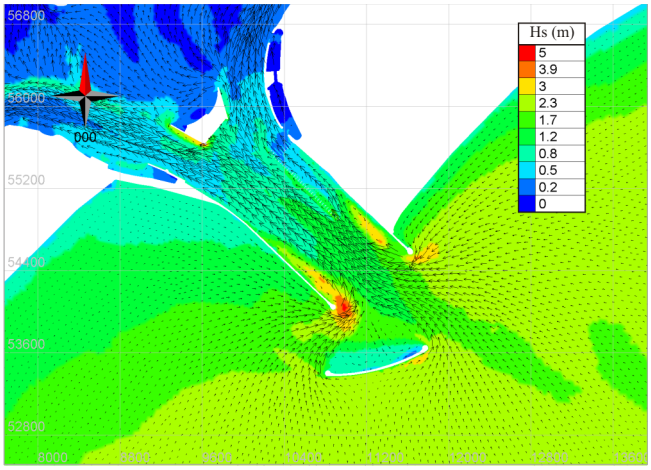

Figure 14. TELEMAC 2D – TOMAWAC simulations, critical wave and velocity field (case ii.1, maximum flood current).

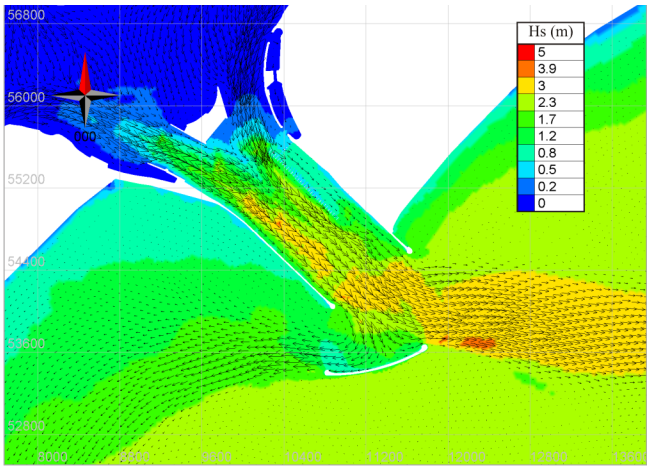

Figure 15. TELEMAC 2D – TOMAWAC simulations, critical wave and velocity field (case ii.1, maximum ebb current).

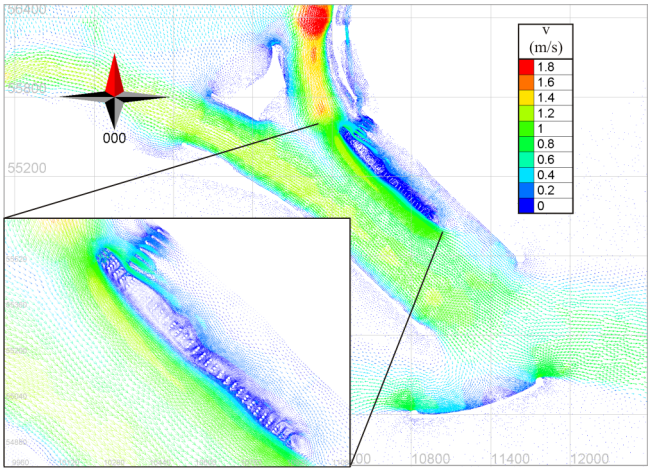

Figure 16. Velocity field (case ii.1, maximum ebb current).

IV. Conclusion

A numerical model based on hydrodynamic and wave propagation modules has been implemented at the "Porto di Lido" entrance of the Venice Lagoon. The aim of the work is to evaluate the harbour tranquillity for a planned landing cruise. The effect of tide currents on wave height was also investigated. The main outcomes of the present study are the following:

- the worst condition occurs with MOSE barriers lifted on, with the maximum water depth in the channel and with highest waves from Scirocco. The critical wave height near the pier is equal to 1.6 m;
- wave height is increased (up to 1.7 m, at project site) by the interaction between incoming waves and tide currents (occurring only with MOSE barriers lifted off); however, there is a very limited probability of occurrence of highest wave offshore and MOSE barriers lifted off, with high water depth.
- the pillars do not affect the wave field. However, flood and ebb currents interacting with the pillars generate vortices that should be further analysed in a physical model, in order to prevent local erosion and a possible failure of the structure.

References

[1] Vv.Aa, "Istruzioni tecniche per la progettazione delle dighe marittime". Assemblea Generale del Consiglio dei LL.PP., 1994.

[2] M. de St. Q. Isaacson and N.G. MacKenzie, "Long Term Distribution of Ocean Waves: A Review", Journal of The Waterways and Harbors Division, ASCE, Vol. 107, No. WW2, Proc. Paper 16277, 1981.

[3] Vv.Aa, "Relazione meteomarina e morfologica – Progetto definitivo delle opere alle Bocche", Consorzio Venezia Nuova, 2002.

[4] Y. Goda, "Random seas and design of maritime structures", University of Tokyo Press, Tokyo, Japan, 1995.

[5] J. Wolf and D. PrandleI. "Some observations of wave–current interaction", Coastal Engineering, Vol. 37, 1999, 471-485.

Modelling tides and storm surges on the European continental shelf

Olivier Gourgue[1,2], Biniyam B. Sishah[1], Joris Vanlede[2], Homayoon Komijani[3] & Margaret Chen[1]
[1] Department of Hydrology and Hydraulic Engineering, Vrije Universiteit Brussel, Brussels, Belgium
[2] Flanders Hydraulics Research, Flemish Government, Antwerp, Belgium
[3] Hydraulics Section, Katholieke Universiteit Leuven, Leuven, Belgium
ogourgue@gmail.com

***Abstract*—This paper presents an effort to simulate the propagation of tides and storm surges through the Northwestern European continental shelf using a slightly modified version of TELEMAC-2D v7p0r1. The area of interest is the Belgian Continental Shelf and the model is calibrated accordingly.**

I. INTRODUTION

A storm surge is an offshore rise of water, which is primarily caused by winds pushing on the sea surface. In shallow water areas, storm surges can be particularly damaging when they occur at the time of a high tide, potentially causing devastating coastal flooding. This phenomenon is one of the major natural threats for the Belgian coastal area and the region surrounding the tidal part of the Scheldt basin. It is therefore a subject of high interest in terms of long-term coastal protection and sustainable development in Belgium.

Studying local impacts of storm surges is a rather multi-scale problem as the latter are formed at the scale of the entire North Sea. The use of an unstructured grid model seems therefore to be a natural choice, thanks to their ability to simulate various scale processes in a rather flexible way.

Storm surges are especially damaging when occurring during a very high tide. It is therefore essential to represent accurately the tides when evaluating the impact of storm surges. In a first step, the present paper focuses on the set up of a tidal model (no influence of wind, nor waves) based on TELEMAC-2D and its calibration for best representation of tides in the area of interest. The influence of meteorological conditions (wind velocity and air pressure) to form storm surges is discussed in a second step.

II. MATERIALS AND METHODS

A. Grids

Two grid configurations are considered in this study, both covering the entire Northwestern European continental shelf. In the first configuration (Fig. 1), the open boundary offshore is located at the shelf break, which is defined as the 200 m isobath. This strategy already proved its efficiency to simulate the tides in Belgian and Dutch coastal waters with the finite element model SLIM [1]. In the second configuration (Fig. 2), the computational domain is extended to deeper parts in the Atlantic Ocean, so that the formation and propagation of very long waves can be simulated explicitly without nesting with a larger scale model or resorting to external data.

The coastlines are generated using the PUG[1] Matlab toolbox and the grids are generated using the open source application Gmsh [2,3]. In both configurations, the mesh density varies as a function of

1. the distance to the coastlines (the mesh density increases when getting closer to the coastlines, to have a good representation of them without increasing the computer cost offshore), and
2. the distance to the area of interest (the mesh density increases when getting closer to the Belgian coast and the Scheldt estuary).

B. Model setup

TELEMAC-2D v7p0r1 is used in this study, but it is slightly modified so that

1. the Coriolis parameter is evaluated as a function of the latitude, even on a Cartesian grid,
2. the tidal force is taken into account in the momentum equation, even on a Cartesian grid,
3. the wind velocity and the air pressure vary in space and time and are extracted from NetCDF files, and
4. the wind drag coefficient is a function of the wind velocity and is parameterized using Flather's formulation [4]:

$$c_d = \begin{cases} 0.565 \cdot 10^{-3} & \text{if } \|\boldsymbol{w}\| \leq 5\,, \\ (-0.12 + 0.137\|\boldsymbol{w}\|) \cdot 10^{-3} & \text{if } 5 \leq \|\boldsymbol{w}\| \leq 19.22\,, \\ 2.513 \cdot 10^{-3} & \text{if } \|\boldsymbol{w}\| \geq 19.22\,, \end{cases}$$

where $\boldsymbol{w}$ is the wind velocity vector 10 m above the water surface and is expressed in m/s in the above equation.

Manning's formulation is chosen to parameterize the bottom friction. A constant viscosity of 10^{-6} m^2/s is chosen for the turbulence model, assuming that the numerical diffusion of the model is sufficient to account for subgrid scale phenomena. The generalized wave continuity equation reformulation is

[1] http://www.oliviergourgue.net/pug

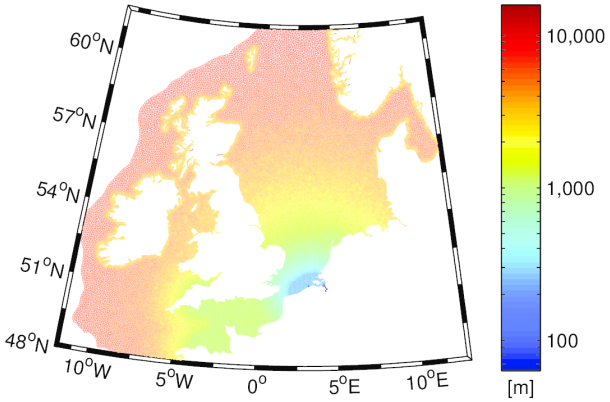

Figure 1: First grid configuration with the offshore boundary at the shelf break; the grid is made up with 320223 triangles sharing 156345 nodes; the colour scale represents the characteristic length of the triangles, ranging from 100 m in very detailed parts of the area of interest to 15 km offshore; the resolution is about 200 m in the Belgian Continental Shelf.

used to solve the primitive shallow water equations. Linear and quasi-bubble approximations are used to discretize the water depth and the horizontal depth-averaged velocity, respectively. Time integration is fully implicit and the time step is 60 s.

C. Forcing data

1) Bathymetry: Different datasets are used to describe the bathymetry of the computational domain. The main properties of the different datasets are summarized in Table 1. They are listed by decreasing order of importance. For a given dataset, all the data located inside the area of another dataset of higher importance are excluded from the final aggregated dataset. The latter is used to interpolate the bathymetry on the unstructured grid nodes.

Table 1: List of the different bathymetry datasets and their main properties, by order of importance.

	Covered area	*Spatial resolution*	*Measurement period*	*Source*
1	Belgian Continental Shelf	1-200 m	2007-2010	MDK Afdeling Kust
2	Western Scheldt	20 m	2011	Rijkswaterstaat
3	Lower Sea Scheldt	1 m	2012	Vlaamse Milieu-maatschappij
4	European seas and oceans	0.125 arc-minute	February 2015[2]	EMODnet

2) Tides in the deep ocean: The tides are the main forcing mechanism of the system. They are imposed at the offshore

[2] Date of release.

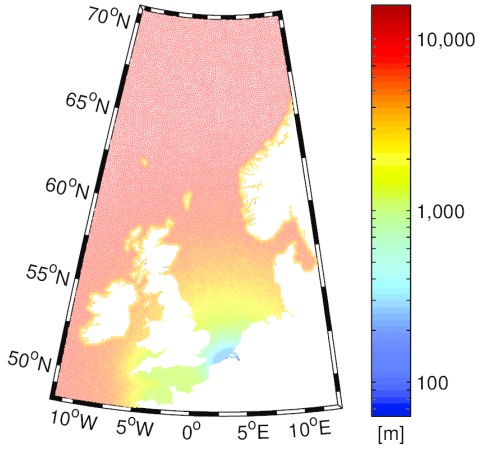

Figure 2: Second grid configuration with the offshore boundary in the Atlantic Ocean (along the 48°N, 12°W, 71°N and 13°E lines); the grid is made up with 341802 triangles sharing 166728 nodes; the colour scale represents the characteristic length of the triangles, ranging from 100 m in very detailed parts of the area of interest to 15 km offshore; the resolution is about 200 m in the Belgian Continental Shelf.

boundary of the domain using OSU Tidal Data Inversion products [5,6]. In the case of the open boundary at the shelf break (Fig. 1), the OTIS Atlantic Ocean tidal solution is used. It provides the amplitude and phase of 11 harmonic constituents over the Atlantic Ocean with a resolution of 5 arc-minutes. However, this dataset does not cover entirely the computational domain of the second configuration (Fig. 2). In that case, the OSU TOPEX/Poseidon Global Inverse Solution TPXO is used. It provides the amplitude and phase of 13 harmonic constituents over the global ocean, but with a resolution of 15 arc-minutes. The tidal signal at the offshore boundary of the domain is reconstructed by TELEMAC from these datasets, and it simply propagates through the domain, slightly nourished by the tidal force.

3) Atmospheric fields: The meteorological conditions contribute less to the movement of water masses in the region. However, the wind and the air pressure are the key factors responsible for the generation of storm surges, which can be particularly damaging when they occur at the time of a high tide, potentially causing devastating coastal flooding. In this study, the horizontal wind velocity vector 10 m above the mean sea level and the air pressure at the water surface are in used. They are extracted from the ERA-Interim global atmospheric reanalysis produced by the European Centre for Medium-Range Weather Forecasts (ECMWF), which covers the period from 1979 onwards, with a spatial resolution of 7.5 arc-minutes and a frequency of 6 hours [7].

D. Simulated periods

This study is carried out in the framework of a larger project, whose objective is to study wind waves and surge levels in the Belgian Continental Shelf during super storms, with a focus on the important storm surge event that affected the coastal margins of the southern North Sea on 5-6 December 2013 [8], as a consequence of the Cyclone Xavier, also known

ad the *Sinterklaasstorm* in Flanders and the Netherlands. For this reason, 2013 is selected as the target year for the entire project.

However, when focusing on tides, it is important to select a calm period in terms of meteorological conditions, in order to limit the influence of wind waves and surge levels on the measurements. In that case, the model is run over July 2013, as it is the month with the weakest winds in the Belgian Continental Shelf that year. On the other hand, December 2013 is selected when the influence of strong wind events is investigated. In both cases, a spin up period of 5 days is run before, to make sure that all transients effects associated with the initialization are dissipated.

E. Performance indicators

Different statistics are used to estimate the model performance. The correlation coefficient R is used to quantify pattern similarity between model results f and observations r, and is defined as

$$R = \frac{\frac{1}{N}\sum_{i=1}^{N}(f_i - \bar{f})(r_i - \bar{r})}{\sigma_f \sigma_r},$$

where f_i and r_i are the discrete values at N different times of f and r, respectively, $\bar{f}$ and $\bar{r}$ their mean values, and σ_f and σ_r their standard deviations, with

$$\bar{x} = \frac{1}{N}\sum_{i=1}^{N} x_i ,$$

$$\sigma_x = \sqrt{\frac{1}{N}\sum_{i=1}^{N}(x_i - \bar{x})^2} ,$$

where x must be replaced by either f or r. The correlation coefficient reaches a maximum value of 1 for perfectly correlated variables, i.e. when, for all i, $(f_i - \bar{f}) = \alpha(r_I - \bar{r})$, where α is a positive constant. In that case, the variables have the same centered pattern of variation, but they are not identical unless $\alpha = 1$. The correlation coefficient does not give any information about the similarity in terms of amplitude of variation [9].

The root mean square (RMS) error E is used to quantify the differences between model results and observations, and is defined as

$$E = \sqrt{\frac{1}{N}\sum_{i=1}^{N}(f_i - r_i)^2} .$$

In order to isolate the differences in the patterns from the differences in the means, the RMS error is split into the overall bias

$$\bar{E} = \bar{f} - \bar{r} ,$$

and the centered pattern RMS error

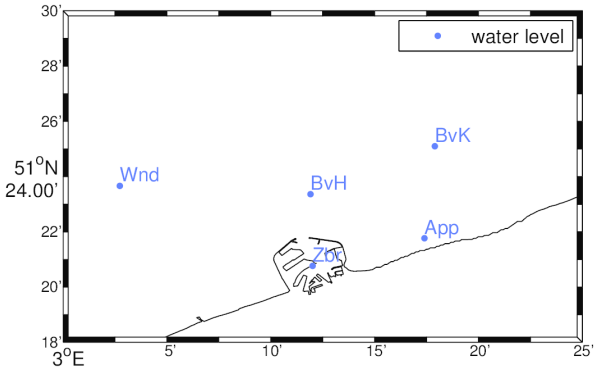

Figure 3: Flemish Banks Monitoring Network stations where observation data have been collected; the official station names are given in Table 2.

$$E' = \sqrt{\frac{1}{N}\sum_{i=1}^{N}\left((f_i - \bar{f}) - (r_i - \bar{r})\right)^2} ,$$

which tends to zero when two patterns become alike, but does not determine how much of the error is due to the structure and phase and how much is due to a difference in the amplitude of the variations [9].

The correlation coefficient and the RMS errors provide complementary statistical information about the model performance, but they must be associated with the standard deviations to include information about amplitude of pattern variation. To facilitate the analysis, those indicators are displayed in a Taylor diagram [9], as for example on the top panel of Fig. 4. In such diagram:

1. the set of observations at one location and the model results at the same location are all represented by single dots (in red in this paper),
2. the standard deviation of a given pattern is the distance between the corresponding dot and the origin (in black)
3. the centered pattern RMS error of a given simulation is the distance between the corresponding simulation dot and the observation dot (in green), and
4. the correlation coefficient between the model results of a given simulation and the observations is given by the azimuthal angle of the corresponding simulation dot (in blue).

F. Measurement stations

The observation data used to evaluate the model performance have been collected in the framework of the Flemish Banks Monitoring Network[3], which is made up of measuring pillars, wave data buoys and hydro-meteo sensors in the Belgian Continental Shelf. The measurements stations whose data are used in this study are displayed on Fig. 3 and their coordinates are given in Table 2.

[3] *Meetnet Vlaamse Banken* – http://www.meetnetvlaamsebanken.be

Table 2: Coordinates of the Flemish Banks Monitoring Network stations where observation data have been collected.

Abbreviation	*Official name*	*Latitude*	*Longitude*
App	Appelzak	51°21'46"N	3°17'24"E
BvH	Bol van Heist	51°23'22"N	3°11'55"E
BvK	Bol van Knokke[4]	51°25'6"N	3°17'54"E
Wan	Wandelaar	51°23'40"N	3°2'44"E

III. Results and Discussion

A. Influence of the offshore boundary location

As mentioned previously, two configurations are considered for the location of the offshore open boundary. In the first one, the offshore boundary is located at the shelf break (Fig. 1). In the second one, the computational domain is extended further in the Atlantic Ocean (Fig. 2). The first configuration already proved appropriate to simulate the tidal dynamics in the area of interest [1]. The second configuration could be interesting to simulate explicitly the formation of wind waves and storm surges in deep areas, together with their propagation towards the continental shore, using a single multi-scale model. The first objective of this paper is to verify that the quality of the tidal simulations is not altered when extending the computational domain. To do so, the model is roughly calibrated over July 2013 using different values of the Manning coefficient, in both grid configurations. The influence of the meteorology is not taken into account here (see simulations S1a to S2f in Table 3).

Taylor diagrams of the water elevation at Wandelaar for simulation sets S1 and S2 are displayed on the top panels of Figs. 4 and 5, respectively. The results at the other stations are very similar and are therefore not shown. Those diagrams show that the Manning coefficient has a clear effect on the standard deviation of the water surface elevation. This is due to the damping role that bottom friction has on tides: the higher the bottom friction, the lower the amplitude of the tidal variation. Also, using the second grid configuration (extended domain) instead of the first one (offshore boundary at the shelf break) seems to move the simulation dots towards the right, i.e. towards higher standard deviations of the water level. As a consequence, the optimal value of the Manning coefficient is not the same for both configurations. It is $0.022 s/m^{1/3}$ for the offshore boundary at the shelf break (simulation S1b), and $0.024 s/m^{1/3}$ in the case of the extended domain (simulation S2c).

[4] Also know as Scheur Wielingen.

Table 3: Main parameters for each simulation.

	Grid configuration	*Manning coefficient* $[s/m^{1/3}]$	*Tidal forcing shift [m]*	*Meteo*	*Period*
S1a	Shelf break (Fig. 1)	0.020	No	No	Jul. 2013
S1b		0.022			
S1c		0.024			
S1d		0.026			
S1e		0.028			
S1f		0.030			
S2a	Extended (Fig. 2)	0.020			
S2b		0.022			
S2c		0.024			
S2d		0.026			
S2e		0.028			
S2f		0.030			
S3a		0.024	-0.05		
S3b			-0.10		
S3c			-0.15		
S4			-0.10	Yes	
S5a				No	Dec. 2013
S5b				Yes	

B. Influence of the mean sea level at the open boundary

When compared to observations, the results of simulation S2c present a negative bias of the order of 0.1 m. One explanation could be that the bathymetry is defined with respect to the vertical datum NAP (*Normaal Amsterdams Peil*, or Amsterdam Ordnance Datum) while the tidal boundary conditions are defined with respect to the ocean mean sea level, which could be slightly different.

In order to neutralize this bias, a uniform vertical shift is applied at the open boundary to the mean sea level, around which the water elevation tidal forcing oscillates. A set of three simulations is run with different values of this tidal forcing shift. The rest of the setup is the same as the best extended grid simulation S2c (see Table 3). The evolution of the bias at the different measurement stations is presented on Fig. 6. The best model results are obtained with a tidal forcing shift of -0.1 m (simulation S3b), but the optimal value seems to be somewhere between -0.15 and -0.1 m.

C. Influence of the meteorological conditions

Simulation S4 is run to investigate the influence of meteorological conditions during calm weather. The setup is

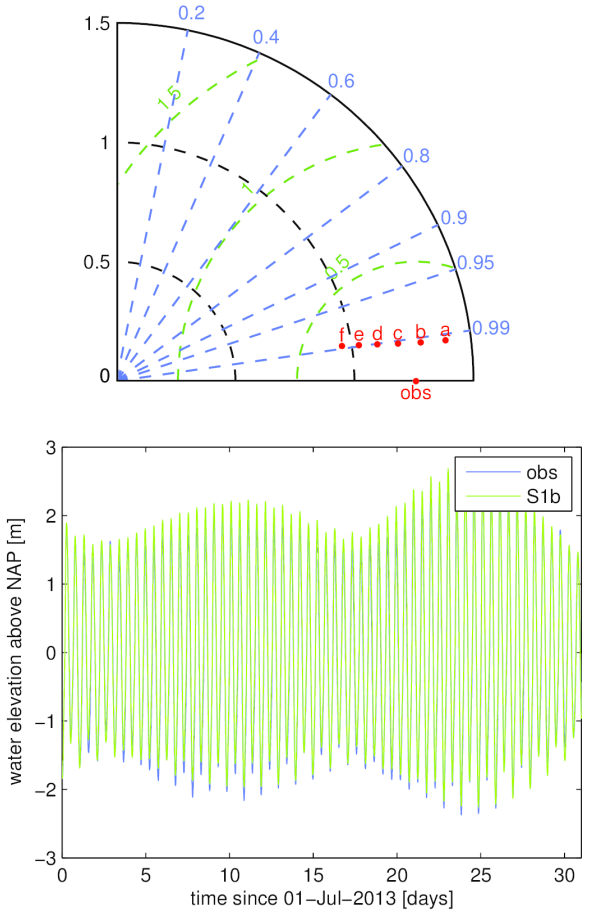

Figure 4: [Upper panel] Taylor diagram comparing water elevation from simulations S1a to S1f with observations at Wandelaar; standard deviations σ_f and σ_r are given in black, correlation coefficient R in blue, and centered pattern RMS error E' in green. [Bottom panel] Water elevation time series at Wandelaar from simulation S1b and observations.

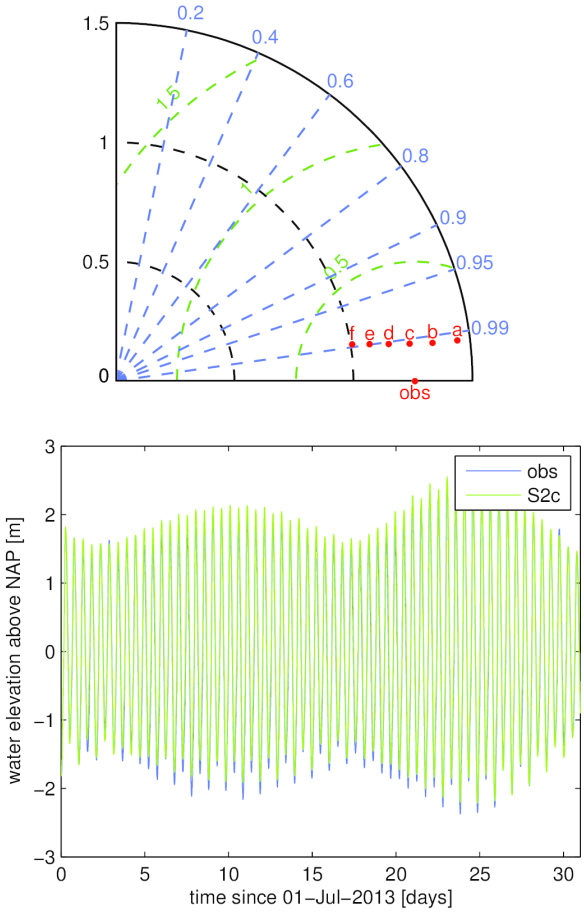

Figure 5: [Upper panel] Taylor diagram comparing water elevation from simulations S2a to S2f with observations at Wandelaar; standard deviations σ_f and σ_r are given in black, correlation coefficient R in blue, and centered pattern RMS error E' in green. [Bottom panel] Water elevation time series at Wandelaar from simulation S2c and observations.

the same as simulation S3b, except that the wind and the air pressure are now taken into account (see Table 3).

The differences between the two simulations in terms of correlation coefficient, standard deviation and centered pattern RMS error are so small that they cannot be seen on a Taylor diagram: for each station, the simulation dots cannot be distinguished (not shown). On the other hand, taking the atmospheric fields into account influences slightly the bias (Fig. 7), even though the impact is much smaller than applying a tidal forcing shift of the order of 0.1 m (Fig. 6).

Simulations S5a and S5b use the same setups as simulations S3b and S4, respectively, except that they run over December 2013 (see Table 3). Obviously, the influence of the meteorological conditions is much more important during such a windy period, as can be observed on the Taylor diagram on the top of Fig. 8. Both the correlation coefficient and the centered pattern RMS error are significantly improved when including the influence of wind and air pressure in the model. On the other hand, the standard deviation is barely influenced by the meteorological conditions. The vertical oscillations of the water surface are indeed mainly due to tides.

The time series on the bottom panel of Fig. 8 even show that the model is quite good at representing the storm surge of December 5-6 [8]. However, it also seems to overestimate slightly the water surface elevation during the first half of the month, while underestimating it during the second half, especially around December 25. The model behaviour could probably be significantly improved by using a more elaborated parameterization of the wind drag coefficient or by coupling it with a wind wave model, which is the objective of a second phase of the project. Finally, it is worth mentioning that even though Fig. 8 only presents results and observations at Wandelaar, they are very similar at the other stations, so that the above discussion about the influence of the meteorological conditions during a windy period can be assumed to stand for the entire area of interest.

IV. Conclusion

This paper presents the setup of a slightly modified version of TELEMAC-2D v7p0r1 to simulate the propagation of tides and storm surges on the Northwestern European continental shelf, as well as their influence in the Belgian coastal area.

Two grid configurations are considered. In the first one, the open boundary is located on the shelf break, which is a natural

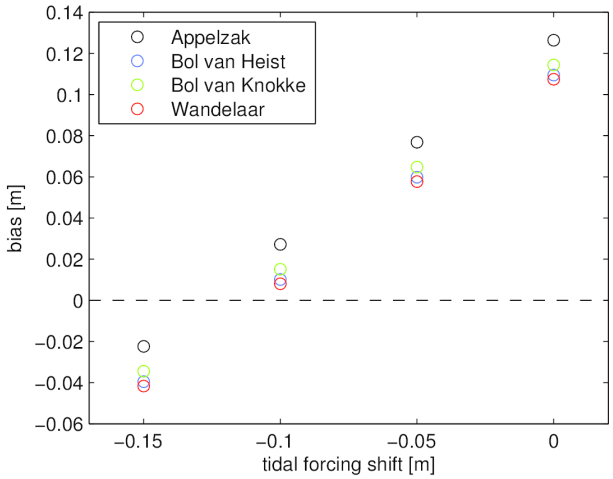

Figure 6: Evolution of the bias at the measurement stations of Fig. 3 for different values of the tidal forcing shift.

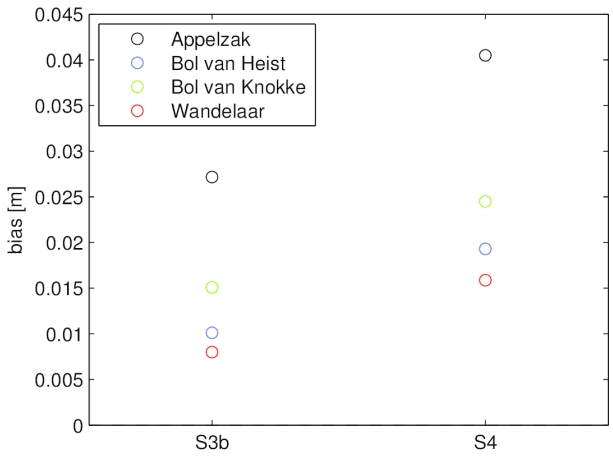

Figure 7: Bias at the measurement stations of Fig. 3 with (S4) or without (S3b) taking meteorological conditions into account.

choice since large scale tidal models that provide tidal boundary conditions are best suited for deep areas. In the second configuration, the computational domain is extended to deeper parts of the Northern Atlantic Ocean, with the aim to simulate explicitly, in a later stage of the project, the formation of storm surges and wind waves, together with their propagation toward the Belgian Continental Shelf. Both approaches lead to similar and satisfactory results in terms of tidal modelling.

Taking meteorological conditions into account do not alter the quality of the results during a calm period, and improved them significantly during a windy period. In particular, the model is able to reproduce rather satisfactorily the storm surge of December 5-6.

REFERENCES

[1] B. de Brye, A. de Brauwere, O. Gourgue, T. Kärnä, J. Lambrechts, R. Comblen, et al., A finite-element, multi-scale model of the Scheldt tributaries, river, estuary and ROFI, Coastal Engineering. 57 (2010) 850–863.

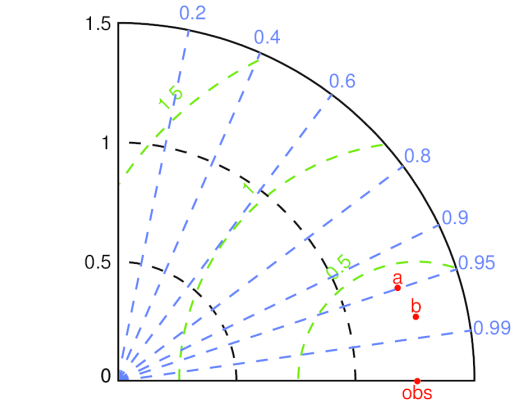

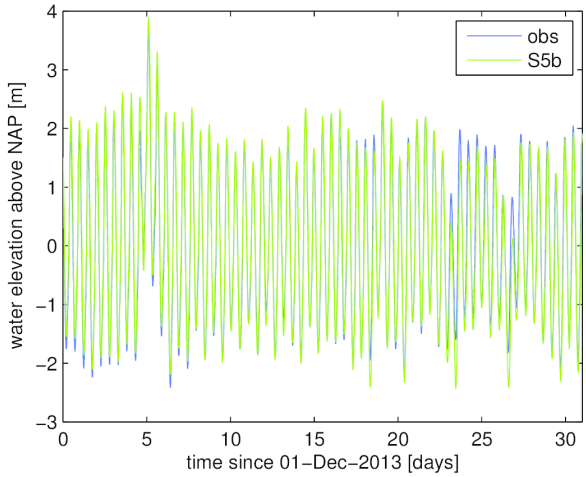

Figure 8: [Upper panel] Taylor diagram comparing water elevation from simulations S5a and S5b with observations at Wandelaar; standard deviations σ_f and σ_r are given in black, correlation coefficient R in blue, and centered pattern RMS error E' in green. [Bottom panel] Water elevation time series at Wandelaar from simulation S5b and observations.

[2] J. Lambrechts, R. Comblen, V. Legat, C. Geuzaine, J.-F. Remacle, Multiscale mesh generation on the sphere, Ocean Dynamics. 58 (2008) 461–473.

[3] C. Geuzaine, J.-F. Remacle, Gmsh: A 3-D finite element mesh generator with built-in pre- and post-processing facilities, International Journal for Numerical Methods in Engineering. 79 (2009) 1309–1331.

[4] R.A. Flather, Results from surge prediction model of the North-West European continental shelf for April, November and December 1973, United Kingdom, 1976.

[5] G.D. Egbert, A.F. Bennett, M.G.G. Foreman, TOPEX/POSEIDON tides estimated using a global inverse model, Journal of Geophysical Research. 99 (1994) 24821–24852.

[6] G.D. Egbert, S.Y. Erofeeva, Efficient inverse modeling of barotropic ocean tides, Journal of Atmospheric and Oceanic Technology. 19 (2002) 183–204.

[7] D.P. Dee, S.M. Uppala, A.J. Simmons, P. Berrisford, P. Poli, S. Kobayashi, et al., The ERA-Interim reanalysis: Configuration and performance of the data assimilation system, Quarterly Journal of the Royal Meteorological Society. 137 (2011) 553–597.

[8] T. Spencer, S.M. Brooks, B.R. Evans, J. a. Tempest, I. Möller, Southern North Sea storm surge event of 5 December 2013: Water levels, waves and coastal impacts, Earth-Science Reviews. 146 (2015) 120–145.

[9] K.E. Taylor, Summarizing multiple aspects of model performance in a single diagram, Journal of Geophysical Research. 106 (2001) 7183–7192.

Model calibration against different types of velocity data with a dimensionless cost function: application to the Scaldis model of the Scheldt estuary

Maximova, T. [1], Smolders, S. [1], Vanlede, J.[1]

[1]Flanders Hydraulics Research
Berchemlei 115, 2140 Antwerp- Borgerhout, Belgium
tatiana.maximova@mow.vlaanderen.be

***Abstract*— This paper describes the calibration of a three-dimensional hydrodynamic model of the Scheldt estuary against of different types of velocity data. The calibrated model will be used to analyse the effects of several scenarios (different morphology of the Scheldt with different ranges of boundary conditions).**

I. INTRODUCTION

The Scheldt estuary is located in the south-western part of the Netherlands and in Belgium. In the framework of the projects "Integral Plan for the Upper Sea Scheldt" and "Agenda for the Future", it was necessary to develop an integrated model for the Scheldt estuary. Existing models lack a high resolution in the Upper Sea Scheldt, Durme, Rupel and Nete. For this reason, the SCALDIS model, a new unstructured high resolution model of the tidal Scheldt is developed in TELEMAC 3D for the entire estuary, but with special attention to the upstream parts. The calibrated model will be used to analyse the effects of several scenarios (different morphology of the Scheldt with different ranges of boundary conditions).

The model domain (figure 1) covers the entire Scheldt estuary, including the mouth area, the Belgian coastal zone and the Eastern Scheldt. Upstream, the model extends to the limits of the tidal intrusion. The use of an unstructured grid allows to combine a large model extent with a high resolution upstream. The grid resolution varies from 500 m at the offshore boundaries to 7-9 m in the Upper Sea Scheldt.

The main objective of the model calibration is to improve the model performance in the upstream part of the estuary. The model is calibrated for one spring-neap tidal cycle in 2013 against field data: water levels, velocities (in deep and shallow zones) and discharges. Bed roughness and velocity diffusivity are used as the calibration parameters. This paper describes the model calibration against of different types of velocity data.

II. THE NUMERICAL MODEL

A. Model grid

The TELEMAC model developed in the framework of this project covers a large part of the North Sea, the entire

Figure 1. Model domain

Scheldt estuary (until the tidal border) and the Eastern Scheldt. The flood control areas (FCA's) with or without a controlled reduced tide (CRT) are included in the model grid as they are important for the storm scenarios (*Smolders et al.*, 2015).

The model grid consists of 459,692 nodes in 2D mesh and 873,419 elements. In the 3D model we use 5 levels totaling 2,298,460 of nodes with the following distribution of sigma layers : 0D, 0.12D, 0.30D, 0.60D, 1D.

B. Bathymetry

The most recent available bathymetry is used in the model. Several datasets from different sources were pasted together.

The bathymetry for the Belgian continental shelf and the Belgian coastal zone comes from MDK-aKust (year 2007 - 2010). The bathymetry of the Dutch coast (2007-2012) was measured by Rijkswaterstaat and downloaded from Open Earth. For the ports of Zeebrugge, Blankenberge, Oostende and Nieuwpoort data from 2014 – 2015 are used. The bathymetry of the Western Scheldt (2013) and the Eastern Scheldt (2010) is available from Rijkswaterstaat. For the Lower Sea Scheldt, bathymetric data of 2011 were provided by Maritime Access division. The topographic data for the channel banks (2007) are taken from the Mercator databank.

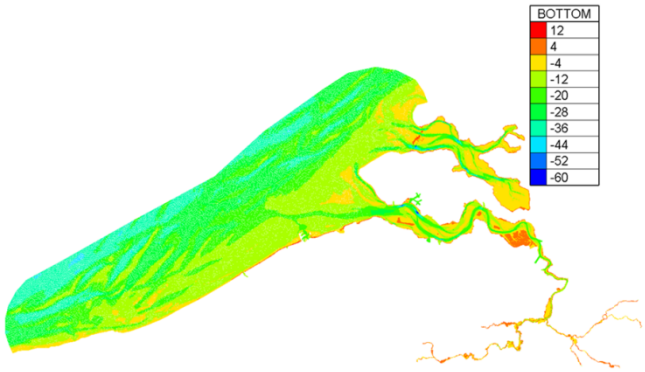

Figure 2. Model bathymetry (mTAW)

The bathymetric data for the Upper Sea Scheldt and Rupel basin are available from Maritime Access division for years 2013 - 2014. For the Durme bathymetry from 2012 - 2013 is defined. The data for the tributaries of Rupel are available for 2007 - 2013 (Dijle and Nete) and 2001 (Zenne and upstream part of Nete) from W&Z, Sea Scheldt division. For the Flood Control Areas along the river, the topographic data are derived from the Mercator Database.

C. *Boundary conditions*

The downstream model boundary is located in the North sea. The upstream boundary is located at the tidal border. The model domain includes all the tidal tributaries of the Scheldt estuary. The TELEMAC model is nested in the overall ZUNO model (a correction of the harmonic components is done). The 10 minute time series of the water level calculated in ZUNO are defined at the downstream boundary of TELEMAC. The subroutine bord3d.f was changed to allocate a water level and a salinity value for each boundary node separately.

There are 8 upstream boundaries with prescribed discharge and free tracer. The measured daily average discharges are defined as upstream boundary conditions at Merelbeke (Upper Sea Scheldt), Dender, Zenne, Dijle, Kleine Nete, Grote Nete, channel Ghent – Terneuzen and channel Bath.

Wind is applied on the coastal zone through the subroutine meteo.f. To include the culvert function in TELEMAC 3D the function t3d.debsce was changed.

The salinity boundary conditions are generated by nesting the SCALDIS in the CSM-ZUNO model train. Model results for salinity are highly influenced by values imposed at the boundaries. Therefore, it is very important to have accurate salinity boundary conditions. Salinities in the SCALDIS model are corrected based on the comparison of the calculated and measured salinity time series at Vlakte van de Raan (located in the North sea).

D. *Simulation period*

The period for the model calibration is chosen based on the analysis of the comparable tides for the available ADCP measurements. It is important that the modeled tidal conditions are similar to the ones during the measurements. The model runs from 13/09/2013 00:00 to 03/10/2013 00:00.

III. AVAILABLE VELOCITY MEASUREMENTS

Different types of velocity data are available in the Western Scheldt, Sea Scheldt and Rupel (figure 3).

A. *Sailed ADCP*

42 ADCP measurement campaigns are used for the model calibration. During such a measurement campaign, a ship-mounted ADCP measures continuously during one tidal cycle, while the ship follows a fixed transect across the river. The resulting dataset consists of velocity vectors distributed over the transect and over the water depth, during one tidal cycle.

B. *Stationary velocities in deep areas*

Stationary velocity measurements from 2013 are available in three locations in deep zones: Buoy 84 (top and bottom), Oosterweel (top and bottom) and Driegoten. In these locations velocities are measured during a long period in one point.

C. *Stationary velocities in shallow areas*

Stationary velocity measurements in the intertidal areas are available in three locations in the Western Scheldt (several measurement points per location): Hooge Platen Noord, Hooge Platen West and Plaat van Walsoorden. In the Sea Scheldt measurements are available at 13 locations.

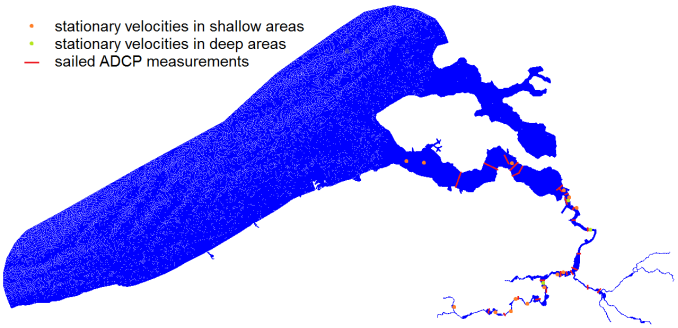

Figure 3 - Available velocity measurements

IV. MODEL CALIBRATION

A. *Methodology*

The main objective of the model calibration in this project is to improve the model performance in the upstream part of the estuary. Bed roughness is used as a calibration parameter. The model is calibrated for deep zones by comparison of the model results and measured water levels, discharges, ADCP velocities and stationary velocity measurements in deep areas. The analysis for shallow zones is done by comparison of the model results and velocity measurements (sailed ADCP and stationary) in the intertidal areas.

Comparison of modeled and measured water levels is done by comparing the time series, the high and low waters, and the harmonic components obtained from a harmonic analysis.

For sailed ADCP measurements and discharge data, comparison with the model results is done for selected modeled tides that are comparable to the tidal conditions during the measurements. This allows us to use ADCP and discharge data from different periods for the comparison with the model results. Bigger differences between the calculated and measured velocities and discharges are expected when the agreement between the measured and modeled tides is not sufficient. Differences between the model bathymetry and the actual bathymetry during the measurements can be another reason for the differences in discharges.

The magnitude and direction of the stationary velocities in deep zones are analysed. Also an analysis of the components of the currents is performed based on *Sutherland et al.,* (2003). This results in a MAE (mean absolute error), combining magnitude and direction and RMAE (relative mean absolute error).

Stationary velocity measurements in shallow zones are usually available for a long period which can be different from the modeled period. In order to compare these measurements with the model results separate tidal cycles are assembled based on concurrent water level data and given tidal amplitude boundaries.

B. Cost function

In order to select the best calibration run, a cost function is calculated for each simulation. The cost function is defined to get one objective factor that represents improvement or deterioration of the model performance. The cost function is expressed in function of the reference run, so a value lower than 1 indicates an improvement (*Vanlede et al.,* 2015*,* in preparation).

$$Cost = \sum \frac{max(Factor_i, Threshold_i)}{max(Factor_{i,ref}, Threshold_i)} * Weight_i$$

Several parameters are selected as factors for the calculation of the cost function (table 1):

- RMSE of the water level time series, RMSE of high waters, vector difference (that shows the accuracy of harmonic components in the model);
- RMAE for each location with the available ADCP measurements. The RMAE gives information about the model accuracy for both velocity magnitude and direction;
- RMSE of discharges.

An expected observation error (a threshold for different parameters) has to be taken into account to assess the accuracy of the model reference in relation to the pre-defined modelling objective (*Vos et al.,* 2000). For example, the threshold for the M2 amplitude is 2 cm. It means that if the error in M2 amplitude in both runs is smaller than 2 cm, the cost of this parameter will remain the same. This methodology helps to avoid giving too much weight to a very small improvement or deterioration of a parameter.

The threshold for the M2 amplitude was obtained from the output of the t_tide analysis for harmonic components. The thresholds for the RMSE of water levels and discharges were chosen based on the personal communication with the HIC department of Flanders Hydraulics Research. The threshold for the RMSE of discharges was calculated as 2% of RMS discharge in a certain area.

In the cost function more weight is given to the Upper Sea Scheldt because the main objective of the calibration is to improve the model accuracy there.

A small weight is given to the RMAE of sailed ADCP in shallow zones. In shallow areas a small inaccuracy in bathymetry (due to the interpolation to the grid with a certain resolution) has a strong effect on the water depth, and therefore it has a big impact on the velocities. Therefore, a limited resolution of the model grid can result in

TABLE I. WEIGHTS AND THRESHOLDS USED IN THE COST FUNCTION

	Zone	Factor	Weights [%]			Threshold
Vertical Tide (water levels)	WS*	RMSE WL time series (m)	3.50	14.00	50	0.03
		RMSE high water level (m)	3.50			0.03
		Vector difference**	3.50			0
		delta M2 amplitude (m)	3.50			0.02
	ES*	RMSE WL time series (m)	1.25	5.00		0.03
		RMSE high water level (m)	1.25			0.03
		Vector difference	1.25			0
		delta M2 amplitude (m)	1.25			0.02
	LSS*	RMSE WL time series (m)	3.50	14.00		0.03
		RMSE high water level (m)	3.50			0.03
		Vector difference	3.50			0
		delta M2 amplitude (m)	3.50			0.02
	USS*	RMSE WL time series (m)	4.25	17.00		0.03
		RMSE high water level (m)	4.25			0.03
		Vector difference	4.25			0
		delta M2 amplitude (m)	4.25			0.02
Horizontal Tide (velocities and fluxes)	WS	RMAE sailed ADCP deep	10.00	13.33	50	0
		RMSE discharges (m³/s)	3.33			738
	LSS	RMAE sailed ADCP deep	10.00	15.83		0
		RMAE sailed ADCP shallow	2.50			0
		RMSE discharges (m³/s)	3.33			87
	USS	RMAE sailed ADCP deep	15.00	20.83		0
		RMAE sailed ADCP shallow	2.50			0
		RMSE discharges (m³/s)	3.33			13
Sum			100	100	100	

*WS: Western Scheldt; ES: Eastern Scheldt; LSS: Lower Sea Scheldt; USS: Upper Sea Scheldt

** Vector difference combines the evaluation of both amplitude and phase between the observed and modeled tidal components.

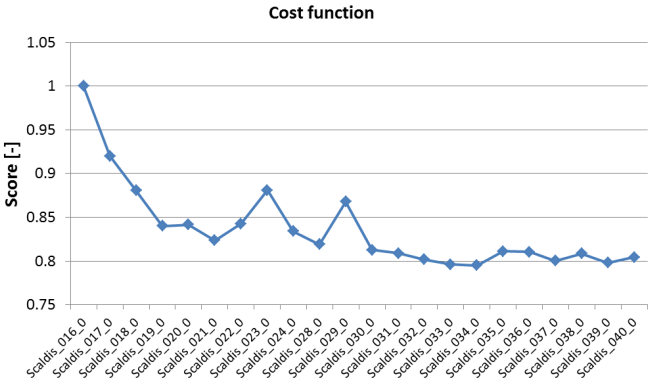

Figure 4 - Cost function

significant differences between the model results and sailed ADCP measurements in shallow zones.

The cost function for several calibration runs is shown in figure 4. During the project more recent bathymetry and contour of the flood areas became available and had to be implemented in the model (run Scaldis_035_0). This bathymetry update resulted in a slight increase of the cost function. In runs from Scaldis_036_0 to Scaldis_040_0 the bed roughness was adapted to improve the model performance. Scaldis_039_0 produced the best results.

V. QUALITY OF THE CALIBRATED MODEL

A. Sailed ADCP data

ADCP measurements at 37 locations in deep zones (from Terneuzen in the Western Scheldt to Schellebelle in the Upper Sea Scheldt) and 5 transects in shallow zones along the estuary are used for the model calibration. Bias and RMSE of velocity magnitude and direction are calculated for each location with available ADCP measurements. Furthermore, a relative mean absolute error (RMAE) is derived to identify the order of magnitude of the error compared to the observed velocities. This parameter shows the accuracy of both magnitude and direction.

1) Analysis of the complete transects

For the comparison of the model output and ADCP measurements plots of statistical parameters and plots of velocity times series are made. Velocities are plotted for each analysed transect (an example is given in figure 5) and a summary plot is made for all the analysed transects of a certain measurement campaign (figure 6). Each point on this summary plot represents an average velocity for a certain transect measured with ADCP or calculated in the model.

Average velocity magnitude and direction for each transect are calculated as the magnitude and direction of the average vector (based on the average U and V components), (average means the combination of the depth average and average over the transect). This means that both magnitude and direction of velocities are taken into account. The bias of magnitude and direction is calculated as the difference between the calculated and measured average velocity magnitude and direction.

The RMSE of velocity magnitude and direction is calculated based on the depth average velocity magnitude and direction for each point along the transect. Magnitude is not taken into account for the calculation of the RMSE of velocity direction and vice-versa. Therefore, the RMSE plots show more variation between the model and measurements than the plots of average velocity magnitude and direction for all transects (figure 7).

If the measured and modeled comparable tides have different shapes, this can have an effect on the comparison of the calculated and measured velocities. In the beginning of flood and in the end of flood (before the high water), water level increases a bit faster in the model at Liefkenshoek. The modelled velocity during this period is also higher (figure 6).

The RMSE of velocity magnitude varies between 12 and 21 cm/s for the locations with transverse ADCP measurements. For most transects it is smaller than 20 cm/s. The average RMSE of velocity magnitude for all the analysed transects in the Western Scheldt is 16 cm/s. In the Lower Sea Scheldt, Upper Sea Scheldt and Rupel the average RMSE of velocity magnitude is the same : 16 cm/s.

The RMSE of velocity magnitude of the longitudinal transects varies between 15 and 25 cm/s. The longitudinal transects are sailed in shallow areas where a limited resolution of the model grid can result in significant differences between the model results and ADCP measurements.

The RMSE of velocity direction is 16 to 43 degrees. The model accuracy for the velocity direction is good when the velocity magnitude is high. It worsens in the areas where velocity magnitude is very small (e.g., near the entrance of locks).

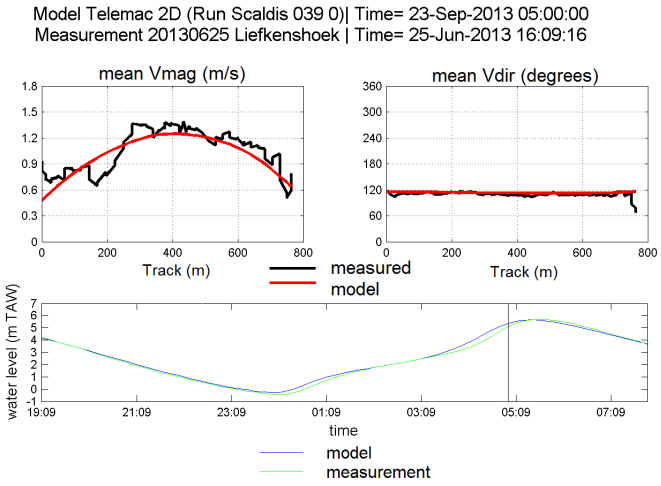

Figure 5 - Measured and modelled velocities for one of the transects at Liefkenshoek

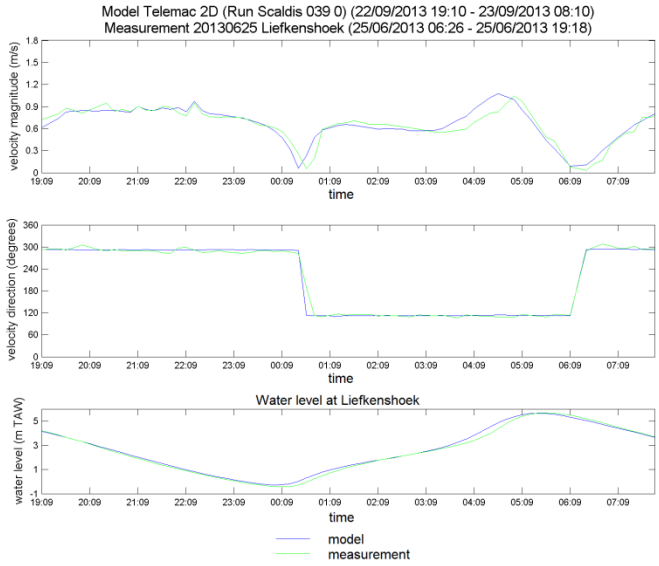

Figure 6 - Measured and modelled velocity magnitude and direction at Liefkenshoek (25/06/2013)

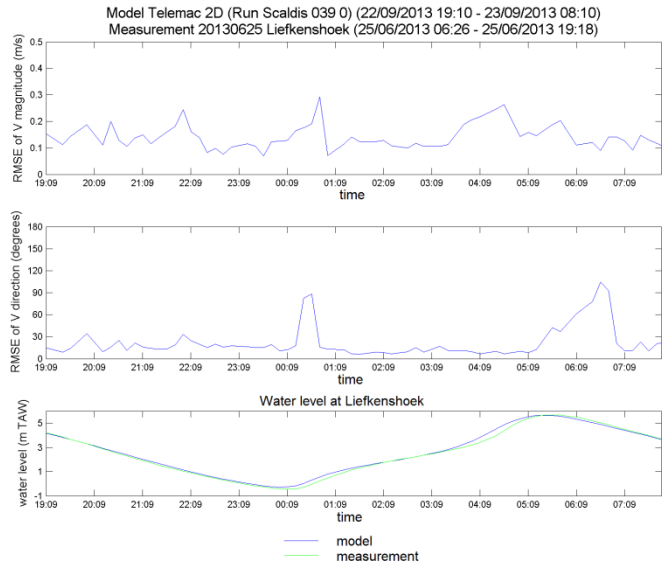

Figure 7 – RMSE of velocity magnitude and direction at Liefkenshoek (25/06/2013)

2) *Estimation of error in the intertidal zones*

To estimate an error in the intertidal zones only ADCP measurements in the intertidal areas were selected from all available transects for the comparison with the model results.

An example of the time series of the modeled and measured velocities in shallow zone is presented in figure 8. The border of the intertidal areas is defined as the average low water at a certain location during spring tide for a period from 2001 to 2010. The model results and measurements in the locations with the bathymetry deeper than the low water of spring tide are excluded from the analysis.

The velocity direction is badly defined in the areas where velocity magnitude is small. Therefore, in the intertidal zones

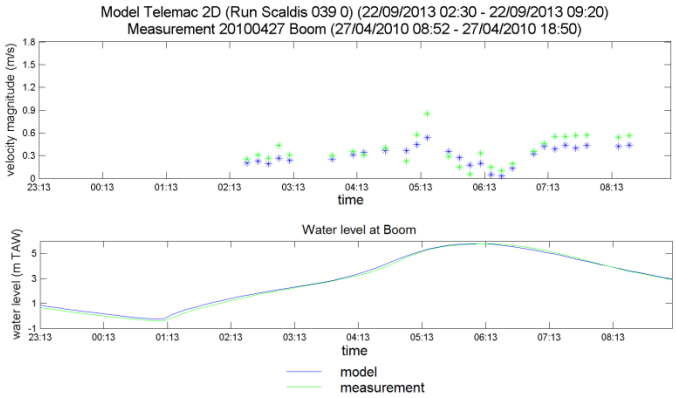

Figure 8 - Measured and modeled velocity in the intertidal area at Boom

only the model accuracy for the velocity magnitude is analysed. It is important to keep in mind that in shallow areas a small inaccuracy in bathymetry (due to the interpolation to the grid with a certain resolution) has a big effect on the water depth, and therefore it has a significant impact on the velocities. A limited resolution of the model grid can result in big differences between the model results and sailed ADCP measurements in shallow zones.

The RMSE of velocity magnitude varies between 11 and 20 cm/s at most locations. The model accuracy is worse at some transects where the grid resolution is not fine enough in the intertidal area.

B. *Stationary velocities*

1) *Deep areas*

3D modeled velocities are compared with the stationary velocity measurements at Buoy 84, Oosterweel and Driegoten at corresponding heights above the bottom. History plots are made and statistical parameters (MAE and RMAE of the velocity vector, bias and RMSE of the velocity magnitude and direction) are calculated to evaluate the model accuracy (table 2). An example of the history plot is shown in figure **9**.

At Buoy 84 and Oosterweel the bias of velocity magnitude is -7 to 5 cm/s. The RMSE of velocity magnitude is 10 to 15 cm/s. The RMAE is 0.21 to 0.29. Accordingly to *Sutherland et al.,* (2003) the model performance at these locations is good.

The differences at Driegoten are higher than at other stations. The point with the real coordinates of the measurement becomes dry in the model in the second half of ebb. If we analyze the flow velocities in a deeper point (Driegoten proxy) situated close to the location of the real point, velocities are overestimated in the model. The differences between the calculated and measured velocity can be related to the innacuracies in the bathymetry implemented in the model. The discharge through the entire cross section at Driegoten is modeled accurately.

TABLE II. STATISTICAL PARAMETERS FOR THE STATIONARY VELOCITIES IN DEEP ZONES

Location	Analysis vector		Magnitude		Direction	
	MAE TS	RMAE TS	BIAS TS	RMSE TS	BIAS TS	RMSE TS
	[m/s]	[-]	[m/s]	[m/s]	[°]	[°]
Buoy 84 bottom	0.13	0.29	0.05	0.13	1	22
Buoy 84 top	0.12	0.24	0.03	0.12	-2	22
Oosterweel bottom	0.11	0.21	0.02	0.10	4	23
Oosterweel top	0.14	0.22	-0.07	0.15	3	29
Driegoten (real)	0.15	0.33	0.03	0.16	-2	28
Driegoten (proxy)	0.27	0.60	0.25	0.32	0	17
Total	0.15		0.03	0.18	0	25

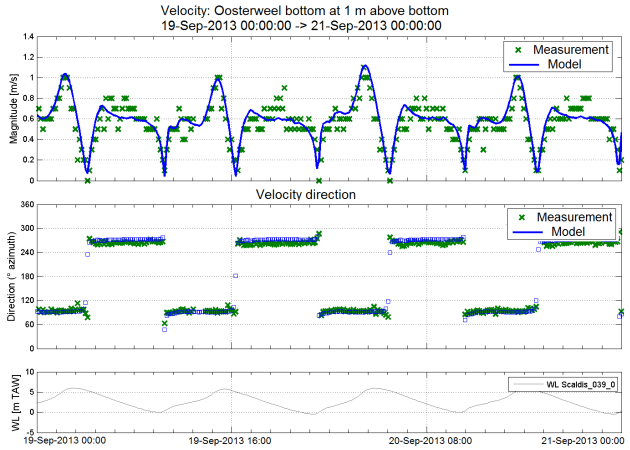

Figure 9 - Measured and modeled velocities at Oosterweel (bottom)

2) *Shallow areas*

The model results are compared with the stationary velocity measurements in shallow areas. In the Western Scheldt at Hooge Platen Noord, Hooge Platen West and Plaat van Walsoorden measurements are available at different levels. The model results at corresponding levels are compared with these measurements. Also depth average model results are compared with the depth averaged velocity measurements at these locations.

Stationary velocity measurements in shallow zones are available for a long period which is different from the modeled period. In order to compare these measurements with the model results an ensemble analysis or phase averaging are used. The measured and modelled velocities are split into individual tidal cycles and averaged out over neap, normal and spring tide.

Measured and modeled velocity ensembles for several points are presented in figure 10 to figure 15. Black and green lines in the figures represent the model result and measurement respectively. Grey and green shaded bars show the modeled and measured standard deviation. RMSE's are calculated for each analysed location for neap, average and spring tides (in case if measurements are available for these tides). Also total RMSE's are calculated.

For the analysis of flow velocities in shallow zones it is very important that the measurement point and the analysed point in the model have similar depths. It is not always possible to find a model node with a similar depth close to the measurement location. This may have resulted in differences between the calculated and measured velocities. At some locations the output in different points is analysed. The points with the real coordinates of the measurement locations have names 'real'. The bathymetry in these points in the model is sometimes very different from the real bathymetry in these locations. The points with a more similar bathymetry (located close to the real points but not in exactly the same location) have names 'a', 'b', etc.

In many locations the model results in 'real' points are similar to the output in the alternative points or slightly better. In several locations there are some differences. For example, in HPW_0311a the model results improved at some levels compared to HPW_0311_real (figure 10, figure 11). At some locations it is not possible to find a model node with the bathymetry similar to the measured bathymetry. It is important to keep this in mind while analysing the model results.

The RMSE's of the flow velocities in the shallow zones in the Sea Scheldt vary between 5 and 21 cm/s. The differences between the model and measurements can be related to the location of the measurements. The flow velocities in these points are measured at 5 cm above the bottom. The model is not suitable for the analysis so close to the bottom. At most locations in the Sea Scheldt the model overestimates the velocities (figure 12). The best results are calculated at the Lillo polder, Notelaer (figure 13) and Heusden.

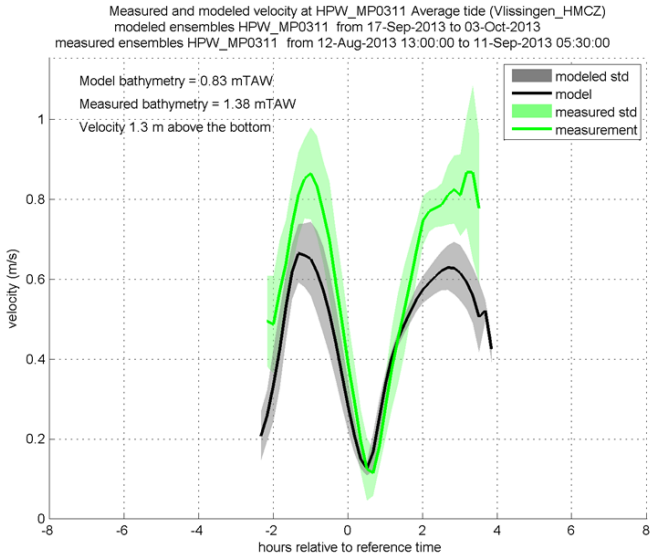

Figure 10 –Velocity at HPW_MP0311real (1.3 m above the bottom)

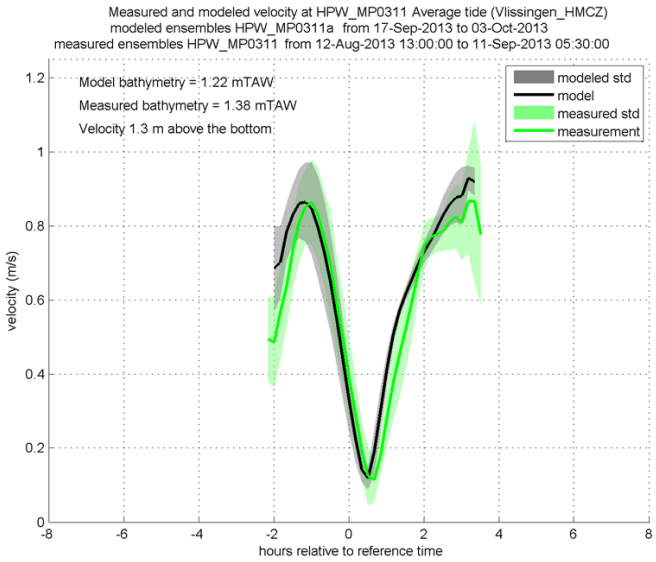

Figure 11 - Velocity at HPW_MP0311a (1.3 m above the bottom)

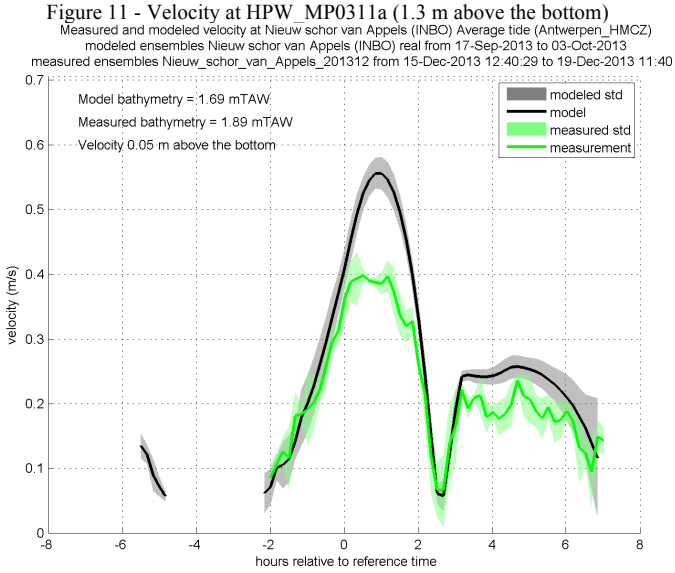

Figure 12 Velocity at Nieuw schor van Appels (at 0.05 m above the bottom)

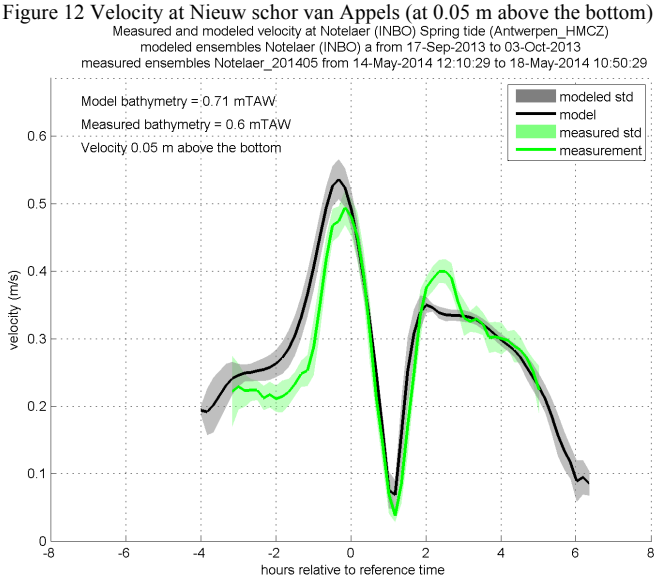

Figure 13 - Velocity at Notelaer (at 0.05 m above the bottom)

The differences between the calculated and measured velocities in shallow zones are smaller at most locations in the Western Scheldt. The model results in most points are very similar to the measurements (figure 14, figure 15). The flow velocities in the Western Scheldt are analysed at different levels and also the depth average velocities are compared.

The RMSE of velocity magnitude at Hooge Platen Noord varies between 5 and 20 cm/s. At Hooge Platen West it is 5 to 15 cm/s. At Plaat van Walsoorden the RMSE of velocity magnitude is 5 to 10 cm/s. When velocities at different levels are analysed the RMSE is higher than 20 cm/s at some levels. It may be related to the limited amount of data in these points (e.g., when measurements are available only around high water).

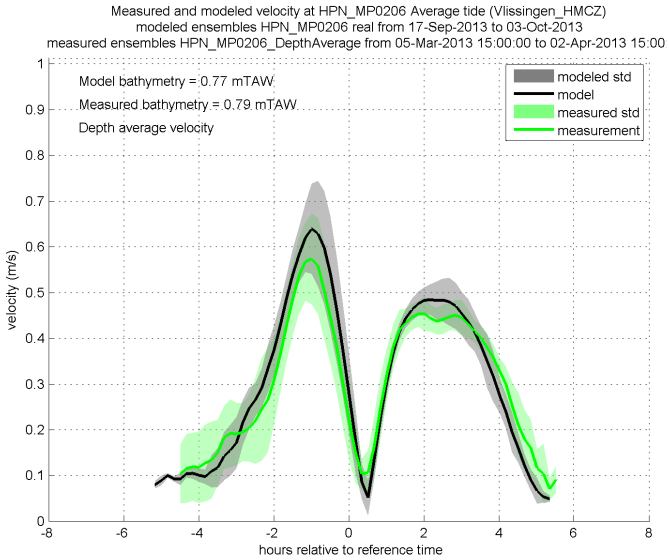

Figure 14. Depth average velocity at HPN_MP0206

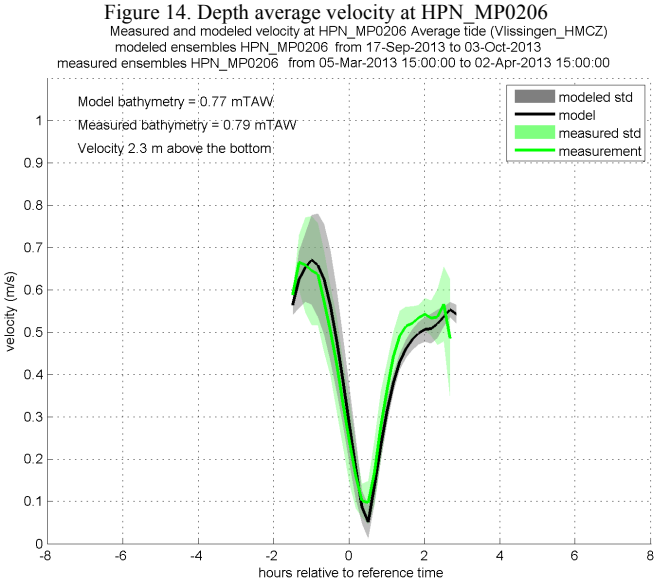

Figure 15 - Velocity at HPN_ MP0206 (at 2.3 m above the bottom)

VI. CONCLUSIONS

This paper describes the calibration of the 3D SCALDIS model against different types of velocity data. This model is developed for the tidal Scheldt in 3D TELEMAC software. A large model extent is combined with a high resolution upstream.

A weighted dimensionless cost function was used to analyse the model results. The cost function attributes equal weight to the horizontal and vertical tide. The weights are given to different parameters based on the importance of these parameters for the model calibration.

The model is calibrated against water levels, discharges and velocity measurements. This paper describes the methodology and results of the calibration against of sailed ADCP measurements and stationary velocity measurements in shallow and deep areas. The analysis of the model output shows that the model is accurate and can be used for the scenario analysis.

REFERENCES

[1] Smolders, S.; Maximova, T.; Vanlede, J.; Verwaest, T.; Mostaert, F. (2015, in prep.). Integraal Plan Bovenzeeschelde: Subreport 1 – 3D Hydrodynamisch model Zeeschelde en Westerschelde. Version 1.0. WL Rapporten, 13_131. Flanders Hydraulics Research: Antwerp, Belgium

[2] Sutherland, J., Walstra, D.J.R., Chesher, T.J., Van Rijn, L.C., Southgate, H.N. (2003) Evaluation of coastal area modelling systems at an estuary mouth. Coastal Engineering, 51 (2004), pp. 119 – 142

[3] Vanlede, J.; Delecluyse, K.; Primo, B.; Verheyen, B.; Leyssen, G.; Verwaest, T.; Mostaert, F. (2015, in preparation). Verbetering randvoorwaardenmodel: Deelrapport 7: Afregeling van het 3D Scheldemodel. WL Rapporten, 00_018. Flanders Hydraulics Research & IMDC: Antwerp, Belgium

[4] Vos, R., Brummelhuis, P. G.J., Gerritsen (2000). Integrated data-modelling approach for suspended sediment transport on a regional scale. Coastal Engineering, 41, 177–200. Available from: http://www.sciencedirect.com/science/article/pii/S0378383900000326

[Accessed 15/06/2015]

A TELEMAC-2D model for the Indian Ocean, Persian Gulf and Red Sea with a special focus on the tidal body force

Thijs Lanckriet, Alexander Breugem, Jon Kemp, Boudewijn Decrop, Gijsbert van Holland
International Marine and Dredging Consultants nv
Antwerp, Belgium
Thijs.Lanckriet@imdc.be

Abstract— **A TELEMAC-2D model is presented that incorporates the Red Sea, Persian Gulf and the northern Indian Ocean, covering an area of roughly $5 \cdot 10^6$ km^2. Due to the size of the model domain, a significant portion of the tidal forcing comes from the tidal body force that is exerted by celestial objects on the fluid mass in the model domain itself, in addition to the tidal forcing at the model domain boundaries. The formulation for the tidal body force in TELEMAC-2D is examined and improved, and the impact of the force on the M2 tidal amplitude is displayed. The model is calibrated against tidal amplitudes and phases at 29 tide gauges across the model domain using an automatic calibration procedure. Two nonlinear optimization algorithms, the Nelder-Mead simplex algorithm and the BFGS algorithm, are tested in the calibration procedure. Results from the two algorithms are comparable, although the BFGS algorithm shows a slightly faster convergence behaviour.**

I. INTRODUCTION

The flexible mesh discretization of the Telemac solver enables the modeller to compute free-surface flows over a very large domain with moderate detail in combination with highly detailed results in a smaller area of the domain. This makes it possible to speed up the development of local, site-specific models by starting from a coarser large-scale, generic model. Once such an 'off-the-shelf' model has been developed and calibrated, it can be (re)used for many projects, each time refining the mesh of the 'parent model' locally around the project site. This paper presents a large-scale TELEMAC-2D model named 'Tethys' that covers the Red Sea, Persian Gulf, and the northern section of the Indian Ocean, which has been developed for use in future projects.

The development of very large-scale models such as the Tethys model poses specific challenges. Firstly, the tide-generating force that acts on the fluid mass inside the domain becomes more important as the domain size increases. Correct treatment of the tide-generating force is therefore necessary to reproduce tidal flows. Secondly, calibrating a model across a large spatial area is non-trivial compared to calibrating the model for one or a small number of sites, and may be more labour-intensive. It is important to avoid over-fitting the model, e.g. by attempting to improve the agreement with a number of measurement stations by over-adjusting model parameters. Automating the model calibration can reduce the amount of labour needed to achieve good model accuracy. An automated calibration routine was developed for this purpose using two nonlinear optimization algorithms.

The remainder of this paper is organized as follows. Section II describes the Tethys regional model. Section III discusses the formulation of the tide-generating force in TELEMAC-2D. Section IV presents an automated calibration routine. Results are discussed in Section IV, followed by general conclusions in Section V.

II. THE TETHYS MODEL

The Tethys model was set up in TELEMAC-2D and covers the Red Sea, Persian Gulf, and the northern section of the Indian Ocean (Figure 1). The model domain has an extent of roughly 5000 km x 2600 km and an area on the order of $5 \cdot 10^6$ km^2 (roughly 6 times the size of the North Sea). It is discretized by a mesh that contains 83 000 nodes and cell sizes that range from 750 m to 90 km. The flow is forced at the southern open boundary by tidal harmonic constituents extracted from the Indian Ocean regional solution of the OSU Tidal Inversion Software (OTIS) model [1] and (optionally) by spatially and temporally varying wind fields from the NOAA-NCEP CFSR hindcast. The model was calibrated in tide-only mode by minimizing the mean vectorial difference between model and measurements for the 4 principal tidal harmonics at 29 tide gauges across the model domain.

III. THE TIDE GENERATING FORCE

Tidal flow in a basin is forced in two ways: at the basin boundaries, and as a body force exerted by astronomical bodies on the fluid mass in the basin itself. While the body force is small compared to the effect of the tide at the basin boundary for typical applications, it becomes non-negligible for very large basins or closed basins such as the Mediterranean Sea.

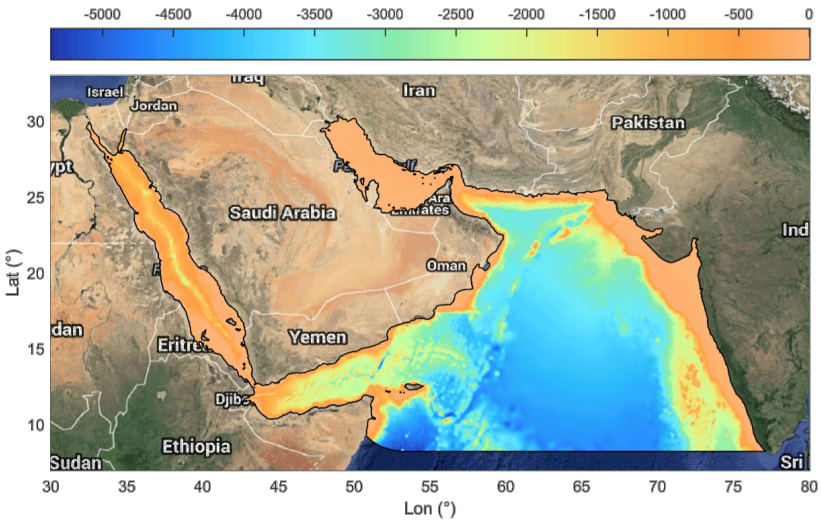

Figure 1. Illustration of the model domain.
Satellite imagery ©Google, SIO, NOAA, U.S. Navy, NGA, GEBCO, Landsat.

The tidal body force can be implemented in a numerical model either as a harmonic expansion at the tidal constituent frequencies, or explicitly as a function of the position of astronomical objects (the sun and moon). The latter approach is adopted in TELEMAC-2D. A detailed explanation of the calculation of the tidal body force based on the position of the sun and moon is given in [2] Appendix A; only a brief summary is given here.

The force $\vec{F}$ exerted by a celestial object (the sun or the moon) onto the flow at a location A on earth can be expressed as the gradient of a tide-generating potential V:

$$\vec{F} = \nabla V, \tag{1}$$

where V is expressed as

$$V = G m_M \left[\frac{1}{\Delta} - \frac{a}{r^2}\cos(\theta)\right], \tag{2}$$

where G is the constant of universal gravitation, m_M is the mass of the celestial object, Δ is the distance between the celestial object and A, a is the earth's radius, r is the distance between the center of the earth and the center of the celestial object, and θ is the angle between the celestial object, the center of the earth, and A. The west-east component of the force, F_x, is then expressed according to [2] as

$$F_x = -\frac{1}{a\cos(\phi)}\frac{\partial V}{\partial AH}, \tag{3}$$

where ϕ is the latitude of A and AH is the hour angle of A. The minus sign in (3) was explained in [2] by the fact that AH is directed toward the east-west direction, i.e. in the opposite direction as the direction of increasing longitude. However, the hour angle AH is oriented westward from the observer to the celestial object. So, at a given time, when the position of the celestial object is held constant, an increase in AH means that the observer is moving toward the east, in the same direction as F_x. In other words, ∂AH is in the same direction as F_x and the minus sign in (3) is not correct. The correct expression for F_x reads:

$$F_x = \frac{1}{a\cos(\phi)}\frac{\partial V}{\partial AH}, \tag{4}$$

The expression for the south-north component of the force according to [2] reads

$$F_y = \frac{1}{a}\frac{\partial V}{\partial \phi}, \tag{4}$$

which is correct.

The implication of this sign error for TELEMAC-2D is that F_x from the sun and moon have the wrong direction in Telemac 2D until version 7p0. The mistake was corrected in Telemac version 7p0r1.

The impact of the sign error on tidal forcing is illustrated in Figure 2, which shows the difference in the amplitude of the M2 tidal constituent between the Tethys model and the OTIS tidal inversion. In the Gulf of Aden, a TELEMAC-2D model simulation with F_x defined according to (3) (corresponding to Telemac up to v7p0; bottom panel of Figure 2) displays a strong overprediction of the M2 tidal amplitude in the Gulf of Aden compared to the OTIS model. A model run with F_x according to (4) (corresponding to Telemac v7p0r1) does not display this overprediction.

The effect of the tidal body force on the tidal flows in the model is complex and depends on the geometry and bathymetry of the (sub)-basin, the basin resonant frequencies, as well as its interactions with adjoining basins and the boundary conditions. In the example shown in Figure 2, the effect of the tidal body force is considerable in

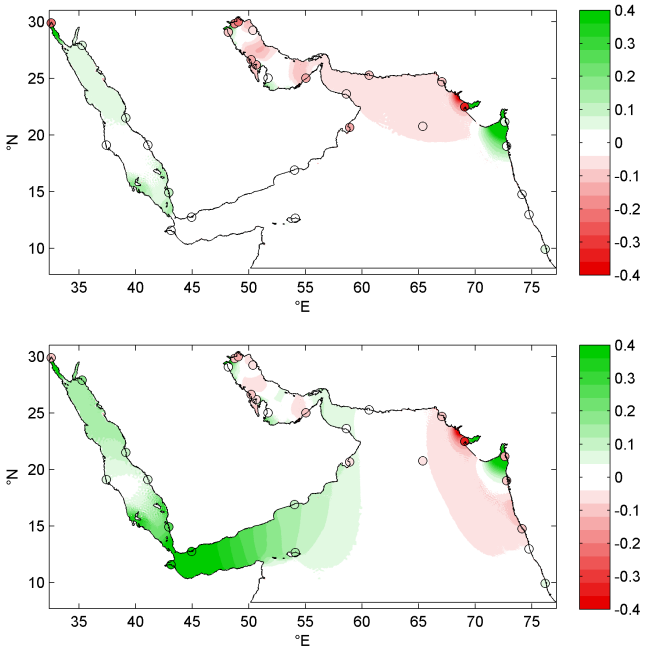

Figure 2. Amplitude difference (Tethys - OTIS) for M2 tidal constituent. Top: with F_x according to (4). Bottom: with F_x according to (3)

the Gulf of Aden and the southern Red Sea (possibly due to exchange with the Gulf of Aden), but much less so in the Persian Gulf.

IV. Automatic Model Calibration

Model parameters such as bottom roughness, tidal amplitude at the model boundary typically need to be adjusted to achieve a satisfactory agreement between model results and local measurements. This often requires a time- and labour-consuming process that involves trial and error. There is thus significant opportunity in reducing the cost of model development by (partially) automating the calibration step. One possible approach for this is as follows:

1) Define a vector of tuneable parameters $\vec{x}$ such as bottom roughness in a given area or the amplitude of tidal forcing at the model boundary.

2) Based on measured data such as water levels, velocities, or tidal harmonic amplitudes and phases, define a single-valued cost function $E(\vec{x})$ that quantifies the model error.

3) For each choice of the tuneable parameters $\vec{x}$, the cost function $E(\vec{x})$ can be evaluated by running a model simulation with the input parameter values according to $\vec{x}$ and postprocessing the model run.

4) Minimize the cost function by iteratively adjusting the tuneable parameters.

Step 4) poses a nonlinear optimization problem, for which many possible algorithms exist. When choosing which optimization algorithm to use to calibrate a flow model, the main selection criterion is that is it minimizes the number of function evaluations of the cost function, since each evaluation involves a model simulation that takes *O*(minutes - days).

The automated calibration procedure presented here was developed simultaneously with the development of the Tethys model, and the final Tethys model was calibrated using a combination of manual and automated calibration.

A toy model with the same geometry and bathymetry as the final Tethys model but different bottom roughness values is used here to demonstrate the calibration procedure (without manual calibration). The tuneable parameter vector $\vec{x}$ consists of 4 values for the Manning roughness in 4 different subsections of the model domain. Each subsection is defined a as a polygon in Figure 3:

1) The entire model domain (except for the subdomains in values 2-4).

2) The entrance of Gulf of Suez (since many reefs are present here).

3) The Strait of Hormuz, which connects the Persian Gulf to the Gulf of Oman and the Indian Ocean.

4) The Bab-el-Mandeb strait, which connects the Red Sea to the Gulf of Aden and the Indian Ocean.

The cost function $E(\vec{x})$ was defined as the mean of the summed vectorial difference (SVD) at 29 tide gauges across the model domain (indicated as circles in Figure 2) for 4 harmonic constituents. The summed vectorial difference at a station is defined as:

$$e_s = \sum_{i=1}^{N} \left| A_{c,i} e^{i\phi_{c,i}} - A_{m,i} e^{i\phi_{m,i}} \right|, \qquad (4)$$

where $A_{c,i}$ and $A_{m,i}$ are the computed (by Telemac) and measured tidal amplitudes for the i'th harmonic constituent, and $\phi_{c,i}$ and $\phi_{m,i}$ are the computed and measured tidal phases for the i'th harmonic constituent.

Using an initial guess for $\vec{x}$ that sets the Manning roughness to 0.05 s/m$^{1/3}$ in all 4 subdomains (which is deliberately too high for ocean and sea beds), the model was automatically calibrated using two nonlinear optimization algorithms: the Nelder-Mead simplex algorithm and a quasi-Newton method of Broyden, Fletcher, Goldfarb, and Shanno (BFGS).

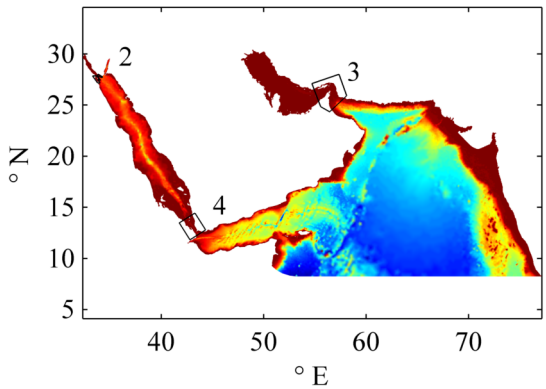

Figure 3. Location of sub-regions in the model domain where the Manning roughness is tuned.

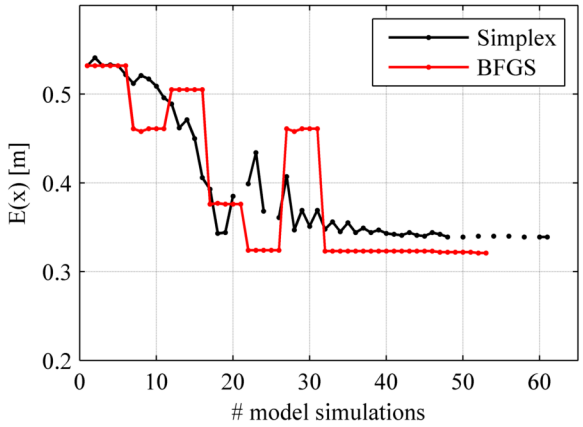

Figure 4. Results of the automatic calibration procedure.

The entire procedure of model initialization (using the selected values of $\vec{x}$), simulation submission to a Linux cluster, post-processing to evaluate $E(\vec{x})$, and nonlinear optimization was implemented in Matlab as a fully automated procedure (except for the BFGS algorithm, for which a Python implementation was used). The cost function $E(\vec{x})$ and the optimal calibration coefficients $\vec{x}$ are written to a text file after each model simulation to enable user monitoring during the optimization procedure.

Results of the procedure are shown in Figure 4. The mean summed vectorial difference (the cost function) initially equals 0.532 m. After remaining constant during the first 5 model simulations, $E(\vec{x})$ automagically decreases and reaches 0.323 for the BFGS algorithm after 32 simulations, after which it shows only marginal decrease. For the simplex algorithm, E(x) = 0.348 m after 32 simulations, and 0.339 m after 61 simulations. An automatic stopping criterion was specified for both optimization algorithms but the procedures were stopped prematurely by the user when $E(\vec{x})$ had nearly converged.

The simplex algorithm is an unconstrained optimization algorithm, meaning that no constraints on the tuning parameters (e.g. a maximum or minimum value for the friction factor) can be imposed. This was circumvented by setting the cost function equal to a very large number when a parameter constraint is exceeded (indicated as the missing dots in Figure 4). The BFGS algorithm, on the other hand, can be run as a constrained optimization algorithm, meaning that parameter constraints can be specified to the optimization algorithm.

V. Discussion

The calibration procedure presented in Section IV shows promise in reducing the labour cost of calibrating a model. The optimization algorithms may also lead to a lower final cost function than a manual calibration, resulting in more accurate model results. The procedure is also generic and can be applied to other models than TELEMAC-2D, as long as a set of tuneable parameters $\vec{x}$ and a cost function $E(\vec{x})$ are defined and implemented. The BFGS algorithm shows the fastest convergence of the two algorithms, although the convergence rate is fairly similar. The BFGS algorithm has the additional advantage that parameter constraints can be specified.

Still, there are a number of caveats. Roughly 30-40 model simulations were needed to achieve a nearly calibrated model with 4 tuneable parameters, and it is expected that the number of necessary model simulations increases with the number of tuning parameters. The procedure is thus only practically feasible for relatively simple models with run times on the order of minutes or a few hours, not days.

The two algorithms presented here may also converge to false minima. Optimization algorithms that avoid false minima exist (e.g. simulated annealing, basin-hopping) but require a larger number of model simulations. Over-training of the model is also possible and should be avoided by the user by carefully selecting the tuneable parameters and the initial values. In summary, even though the procedure may reduce developer working time, it does not replace the input of a skilled model user.

VI. Conclusions

A TELEMAC-2D model for the Red Sea, Persian Gulf, and northern Indian Ocean, named the Tethys model, was presented. Due to the large spatial extent of the model, the tidal body force becomes important for the tidal forcing. An error in the east-west component of the tide generating force was detected and corrected in TELEMAC-2D. The effect of the error on the modelled tidal amplitude depends on the resonant frequencies of each (sub-)basin but can be significant.

In addition, an automated calibration procedure for TELEMAC-2D was presented. The procedure consists of a number of tuning parameters (the Manning roughness in a number of subsections of the model domain), a cost function, defined as the mean summed vectorial difference between modelled and measured tidal constituents, and a nonlinear optimization algorithm that minimizes the cost function by adjusting the tuning parameters.

VII. Acknowledgements

The authors wish to thank Jean-Michel Hervouet for his useful contribution to the discussion on the correct calculation of the tidal body force.

VIII. References

[1] G. D. Egbert and S. Y. Erofeeva, “Efficient Inverse Modeling of Barotropic Ocean Tides,” *J. Atmos. Oceanic Technol.*, vol. 19, no. 2, pp. 183–204, Feb. 2002.

[2] J.-M. Hervouet, *Hydrodynamics of Free Surface Flows*. Chichester, UK: John Wiley & Sons, Ltd, 2007.

The hydrodynamic, sea-state and infrastructures platform developed by Saint-Venant Hydraulics Laboratory and Cerema: a special focus on the TELEMAC2D surge levels numerical model of the Atlantic Ocean, the Channel and the North Sea

Vanessya LABORIE[1,2], Philippe SERGENT[1]
Research department
[1] French Center For Studies and Expertise on Risks, Environment, Mobility, and Urban and Country planning (Cerema)
[2] Saint-Venant Hydraulics Laboratory
[1] Compiègne, France, [2] Chatou, France
contact : vanessya.laborie@cerema.fr

Florence LEVY
French National Research Agency
Paris, France

Roberto FRAU
Laboratoire d'Hydraulique de Saint-Venant
EDF R&D and Politecnico di Torino
Chatou (France) and Torino (Italy)
contact: robertofrau88@gmail.com

Jérome WEISS
Laboratoire de Biologie Halieutique
Ifremer
Brest, France

***Abstract*—Storm surges are the sea level response to meteorological conditions, such as wind effects and pressure gradients. Their evaluation is necessary in order to provide better estimates of extreme sea level for use in coastal defence and urban planning management. Inside the Saint-Venant Hydraulics Laboratory, a surge levels numerical model based on TELEMAC2D software was built in 2013 [1]. To calibrate the global signal (tide + surge levels), measurements available on 18 outputs of the Atlantic coast were used to optimize the coefficient for wind influence and for bottom friction for 11 events among which Xynthia (2010), particularly lethal in France. Maritime boundary conditions are provided by the North East Atlantic Atlas (LEGOS). Winds and pressure fields are CFSR data.**

To calibrate the surge levels numerical model, many sensitive tests have been led to determine the best parametrisation inside TELEMAC2D software concerning: the bathymetry; the wind drag force distribution; the friction distribution; the tide signal provided at the maritime boundary. It led to the choice of an optimal parametrisation for the extreme storm events selected. However, several validation tests hadn't been realised. That's why, in 2014, it was decided to go further in the evaluation of the Surge Levels Numerical model considering: some statistical parameters (mean value, standard deviation, storm surge time shift for the storm surge peak, RMSE etc.) calculated at 18 harbours of the french coastline for 11 events (from 1998 to 2010); the statistical distribution of skew surges for the slice time [1979-2010] for 31 harbours in France, United Kingdom and Spain [2]; the event validation of global water levels; the statistical distribution of skew water levels for the slice time [1979-2010] for 18 harbours on the French coastline including mean climatology and the calculation of extreme quantiles.

This surge levels numerical database has already been used in several research projects (for example, the study of the evolution of surge levels in Le Havre Harbour and the Seine Bay and of the surges/tide interactions at the Seine Mouth) [3]. It will also be used to estimate the impact of climate change on the Atlantic French coastline considering one or several IPCC5 scenarios provided by METEO-FRANCE by the end of the year (on progress). Once the numerical model evaluated and validated, it was decided to include the database provided by the surge levels numerical model into a "hydrodynamic, sea state and infrastructures platform", developed in Cerema in collaboration with Saint-Venant Hydraulics Laboratory.

INTRODUCTION

Storm surges are the sea level response to meteorological conditions, such as wind effects and pressure gradients. In a coastal defence and urban planning management's context, their evaluation is needful to provide better estimates of extreme sea levels and to obtain good estimations of the probability of occurrence of extreme sea levels in order to design suitable coastal infrastructures necessary to ensure the safety of coastal buildings and installations against extreme meteo-oceanic conditions (waves, sea levels and surges).

Within the project "Surge levels" of Saint-Venant Hydraulics Laboratory and the Cerema project "Management and Impact of Climate Change on the Coastline", a surge levels numerical model based on TELEMAC2D software was built in 2013 [1]. The aim of this study is to model surge levels along the French coastline, and particularly in the Bay of Biscay, the Channel and North Sea, using Telemac2D software.

Before using it to feed other local models with higher mesh density, it was necessary to validate the results, both in terms of tide, surge levels (instantaneous or skew surge levels) and water levels (instantaneous or skew water levels), considering that skew surges is defined as the (algebraic) difference between the maximum observed sea level around the time of theoretical (predicted) high tide and the predicted high tide level [2]. Instantaneous surge levels or water levels were validated on 11 events which occurred from 1998 to 2010 and evaluated for 6 events from 2011 to 2014, using some statistical indicators described below.

This article presents the main steps of the studies already achieved concerning this numerical surge levels model: the definition of the studied meshed area, the validation and parametrization of the modelling of tide propagation, surge levels and water levels. It concludes by the integration of this surge and water levels database in a hydrodynamic, sea-state and infrastructures platform developed by Saint-Venant Hydraulics Laboratory and Cerema.

DESCRIPTION OF THE NUMERICAL MODEL

Equations and parametrization of Telemac2D

Telemac2D solves bidimensional shallow water equations (continuity and momentum equations).

$$\frac{\partial h}{\partial t}+\left(h\vec{u}\right)=0$$

$$\frac{\partial u}{\partial t}+u\frac{\partial u}{\partial x}+v\frac{\partial u}{\partial y}=-g\frac{\partial Z_s}{\partial x}+F_x+\frac{1}{h}\div\left(h\nu_e\overrightarrow{grad}\left(u\right)\right.$$

$$\frac{\partial v}{\partial t}+u\frac{\partial v}{\partial x}+v\partial v\partial y=-g\frac{\partial Z_s}{\partial v}+F_y+\frac{1}{h}\div\left(h\nu_e\overrightarrow{grad}\left(v\right)\right.$$

where h is the water depth, u and v the horizontal components of the velocity, F_x and F_y the horizontal components of the external forcings (Coriolis force, bed friction, wind friction), Z_s is the water level and ν_e the diffusion coefficient.

Extension of numerical model, mesh and bathymetry

The numerical model extents from 9°W to 10°E and from 43°N to 62°N.

The bathymetry "North East Atlantic Europe" (30" * 30" resolution) provided by the LEGOS was used. The mesh is unstructured (finite elements) and has been built using JANET software with which the node density can depend on the bathymetry. The refinement of the mesh was defined using the criteria called "relative error on the depth". The bathymetry is linearly interpolated at the barycentre of each element, on one side, and interpolated from the digital elevation model, on the other side. If the relative error of the difference between interpolations towards the bathymetry is higher than a given value, the barycentre of the element is integrated in the mesh as a node.

The mesh is also particularly refined near the coastline, with one node per kilometer along the french coastline. Off the french coast, the highest distance between two nodes is around 40 km. The final mesh has 32644 nodes and 59159 elements (see Fig. 1). The bathymetry of the mesh has been interpolated using one of the FASP (Fast Auxiliary Space Preconditioning) package available in JANET. Fig. 2 represents mesh and bathymetry details in the Channel, in the Normano-Breton Gulf, on the south side of the English Channel, in the Atlantic coast from Vendée to Gironde.

For this study, equations have been solved using the Mercator projection [4]. The mesh is built using spheric coordinates, but it is converted into the Mercator projection during TELEMAC2D calculations.

TIDE MODELLING AND VALIDATION

Tide modelling has been realised by taking into account the astral forces generating tide inside of the studied area and also specific boundary conditions for water levels and velocities. The latter are the harmonic constants provided by the NEA (North East Atlantic atlas) consistant with the bathymetry also provided by NEA.

Some initial conditions are also imposed using the harmonic constants provided by the regional solution for the Oregon State University (similar to TPXO). This choice is explained because it is easier to use it in TELEMAC2D.

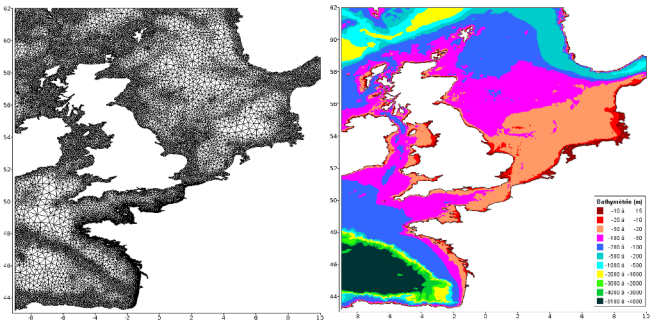

Fig. 1: Mesh and bathymetry of the numerical model

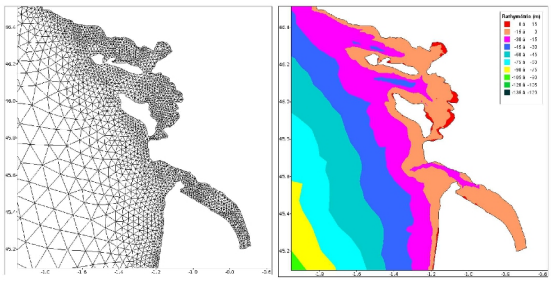

Fig. 2: Mesh and bathymetry details in the Atlantic coast from Vendée to Gironde (from (Levy, 2013))

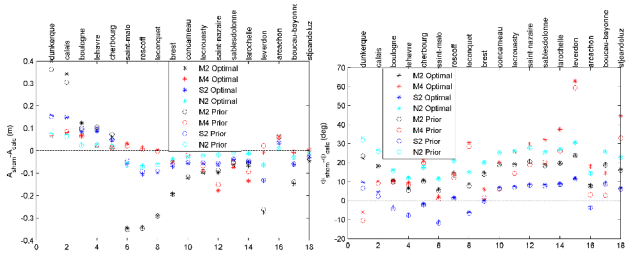

Fig. 3: comparison between results obtained with the harmonic constants provided by the "prior" and "optimal" solutions of NEA ([1]).

To perform tide modelling, the influence of several parameters have been tested: among them, boundary conditions, bed friction coefficient spatial distribution and bathymetry. The performance of the numerical model has been evaluated comparing SHOM predictions in 18 harbours represented on Fig. 1 by blue empty little rectangles (from the North to the South: Dunkerque, Calais, Boulogne-sur-Mer, Le Havre, Cherbourg, Saint-Malo, Roscoff, Le Conquet, Brest, Concarneau, Le Crouesty, Saint-Nazaire, Les Sables d'Olonne, La Rochelle, Le Verdon, Arcachon, Bayonne and Saint-Jean-de-Luz). The harmonic constants calculated at these harbours by TELEMAC2D and predicted by SHOM for tidal propagation of M2, M4, S2 and N2 are compared. The calculation of those harmonic constants was realised with Matlab T_Tide tool [5] using 10 mn time step time series lasting 1 year (from july 2011 to july 2012).

Influence of several parameters on tide modelling: boundary conditions

The North East Atlantic Atlas (NEA) resolution is between 20 to 25 km in the Atlantic Ocean and reaches 4 km at the coastline. Two sets of harmonic constants are available. The first one, called "Prior", is only based on the hydrodynamic model T-UGOm. It provides amplitudes and phases for water levels and the two horizontal velocity components for 47 tidal waves (2MK6, 2MN6, 2MS6, 2N2, 2Q1, 2SM2, 2SM6, ε2, J1, K1, K2, KJ2, L2, λ2, M1, M2, M4, M6, Mf, MK3, MK4, MKS2, Mm, MN4, MO3, MP1, MS4, MSK6, MSN2, MSN6, MSqm, Mtm, μ2, N2, ν2, O1, P1, Q1, R2, ρ1, S2, S4, σ1, SK4, SN4, T2 and Z0). The second one, called "optimal" solution, integrates at the same time the results provided by the hydrodynamic numerical model and satellite observations. It provides a solution for 15 harmonic components (2N2, K1, K2, L2, M2, M4, MS4, μ2, N2, ν2, O1, P1, Q1, S2 and T2).

Fig. 3 represents results obtained using one of the two harmonic constants sets as boundary conditions of the numerical model. For the "prior" solution, the 15 tidal waves in common for both sets have been considered. On Fig.3, each symbol (star or circle) provides the amplitude difference (on the left) or the phasis difference (on the right) between SHOM predictions and T2D simulations for M2, M4, S2 and N2 tidal waves at a given harbour. Few differences can be observed between the results obtained with "prior" or "optimal" solutions.

However, the amplitudes of the main tidal wave M2 calculated at Dunkerque, Calais and Boulogne-sur-Mer are closer to SHOM predictions with the "prior" solution than with the "optimal" solution.

That's why the harmonic constant set provided by the "prior" solution was chosen to feed the boundary conditions of the numerical model. Telemac2D permits to impose water levels and velocities at the liquid boundaries as seen before (Fig. 1) or to impose water levels and let velocities free. Fig. 4 represents results obtained for each type of boundary conditions. The tidal wave M2 amplitude calculated at Dunkerque and Cherbourg are closer to SHOM predictions when both water levels and velocities are imposed, but they are then less accurate between Saint-Malo and Brest. Considering the amplitude relative difference, results are less accurate between Dunkerque and Cherbourg than between Saint-Malo and Brest and are therefore those that should be improved in priority. Moreover, imposing both water levels and velocities generally permits to model more accurately phases for the four tidal waves. Consequently, using Prior both for water levels and velocities has been decided.

Finally, the influence of the number of harmonic constants used has been tested. Fig. 5 represents results between simulations with the 47 tidal waves available in NEA "prior" or only the 15 tidal waves which are in common between NEA "prior" and NEA "optimal". Differences are very low and negligible, except for the M4 tidal wave phases at Arcachon, which is more accurate as 15 tidal waves only are used.

Influence of several parameters on tide modelling: simulations initial conditions

Water levels and velocities provided by OSU regional Atlantic Ocean solution are imposed at each node of the mesh as initial conditions. This solution, which resolution is about 1/12 °, provides harmonic constants for 11 tidal waves (M2, S2, N2, K2, K1, O1, P1, Q1, M4, MS4 et MN4). Fig. 6 represents results obtained using this OSU solution for initial conditions and boundary condition. The main differences

obtained concern the M2 tidal wave at Dunkerque, Calais, Saint-Malo and Roscoff, as formerly obtained by the tests imposing only water levels or both water levels and velocities for NEA. This could lead to conclude that tidal propagation modelling is more sensitive to boundary conditions in the south of Roscoff. The M2, S2 and N2 tidal wave phases with boundary conditions, NEA or TPXO, are very closed. For M4 tidal wave, some differences can be observed which reach about 10° at several locations, with results obtained with TPXO more accurate than those obtained with NEA.

Influence of several parameters on tide modelling: friction coefficient

The bed friction is represented with a Chezy formulae in the numerical model:

$$F_u = \frac{-g}{hC^2} u\sqrt{u^2+v^2}\,,\; F_v = \frac{-g}{hC^2} v\sqrt{u^2+v^2}$$

where F_u and F_v are the horizontal components of the bed friction forcings and C the Chezy coefficient.

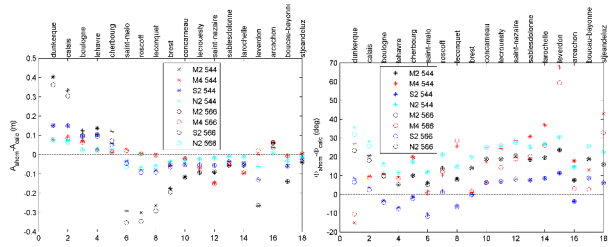

Fig. 4: comparison between results obtained imposing only water levels and letting velocities free (“544”) or imposing both water levels and velocities (“566”) (from [1]).

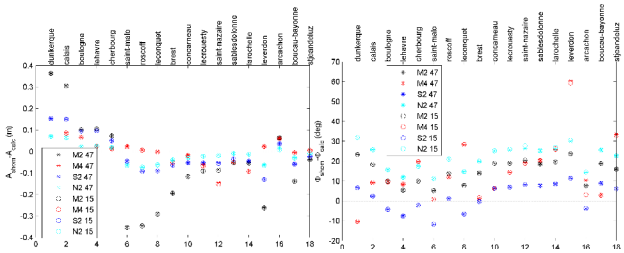

Fig. 5: comparison between results obtained taking into account as boundary conditions the 47 tidal waves harmonic constants available in NEA “prior” or using only the 15 tidal waves constants in common with NEA “optimal” (from [1]).

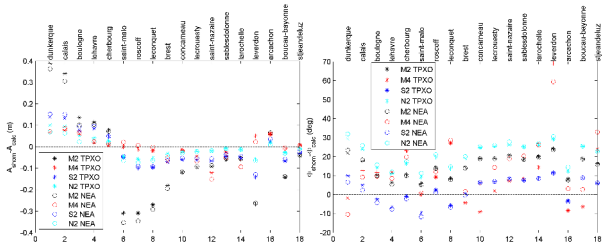

Fig. 6: comparison between results obtained using as initial conditions the harmonic constants provided by the OSU “Atlantic Ocean”

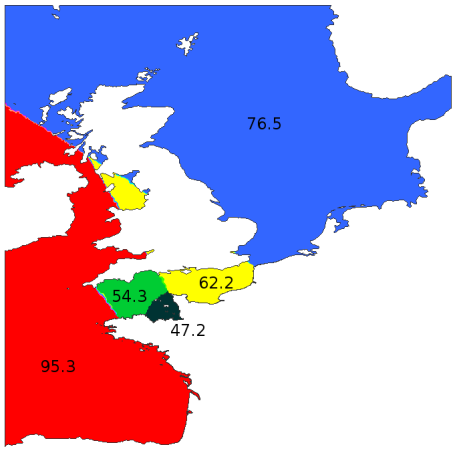

Fig. 7: Chezy friction coefficient distribution according (Barros, 1996) (in m1/2/s) (from [1]).

A variable spatial distribution of the friction coefficient has been chosen, according to [6]. Several variation around this distribution have been tested, without obtaining any significant improvement of results towards the Barros distribution shown on Fig. 7. However, better results were obtained by taking a constant friction coefficient throughout the studied area, as Fig. 8 stresses it out for M2 tidal wave. The results obtained for 3 values of Chezy coefficient are shown: 65, 70 and 75 $m^{1/2}/s$. 70 $m^{1/2}/s$ was finally chosen. Indeed, using this friction parametrization results in amplitude differences with SHOM predictions for M2 tidal wave lower than for the spatially variable distribution. Moreover, the phases are more accurate (up to 5° of improvement, except for Saint-Malo harbour).

Influence of several parameters on tide modelling: bathymetry

To be consistent with the boundary conditions, the North East Atlantic Europe (NEA) provided by LEGOS was chosen in a first step of the study. A comparison with results that could be obtained with another bathymetry is presented here. The EMODNET project grid is here used. It is built on the basis of several kind of data resulting from various methods and whose resolution is 15’’*15’’ (towards 30’’*30’’ for NEA bathymetry). The difference between EMODNET and NEA bathymetry are represented on Fig. 8. There are some significant differences, particularly in the bay of Biscay, but also in the North Sea, where water depths are low and, therefore, the relative gap high, as Fig. 9 shows it.

Fig. 10 represents differences resulting on amplitudes and phases for M2 tidal wave. Both bathymetries lead to results of comparable quality for amplitudes. By contrast, phases obtained with EMODNET bathymetry are closer to SHOM predictions than those obtained with NEA bathymetry. It means that another study should be realised to choose the right bathymetry in the future.

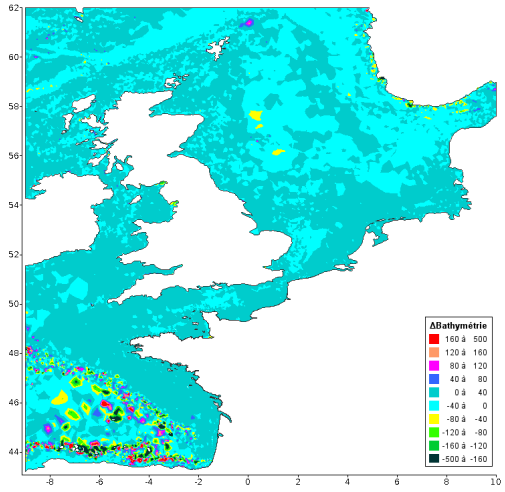

Fig. 8 : Difference between EMODNET and NEA bathymetries ([1]).

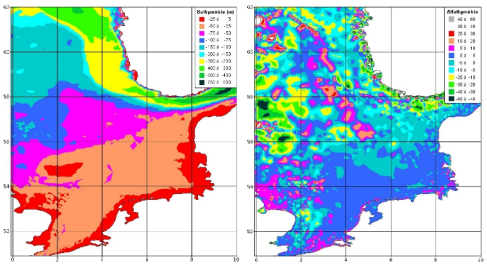

Fig. 9: NEA bathymetry in the North Sea (on the left) and difference between EMODNET and NEA bathymetry (on the right) ([1]).

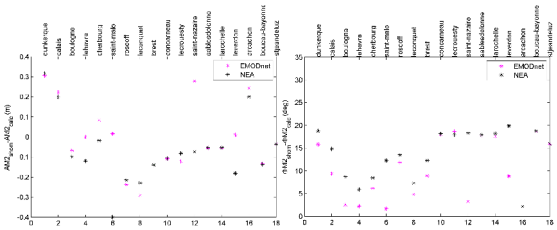

Fig. 10: Difference between EMODNET and NEA bathymetries ([1]).

Influence of several parameters on tide modelling: conclusions

The tests that have been realised have permitted to define the most suitable parameters to model tide propagation with TELEMAC2D. These parameters are kept in the following of the study. The set of harmonic constants NEA "prior" is chosen for boundary conditions using both water levels and velocities. Chezy friction coefficient is set at 70 $m^{1/2}/s$ throughout the numerical model extension.

SURGE LEVELS MODELLING AND VALIDATION

The atmospheric forcing taken into account in the calculation of surge levels includes mean level atmospheric pressure at the sea level and the horizontal components of winds (at 10 m) provided by the National Ocean and Atmospheric Administration (NOAA) (CFSR data). After having interpolated CFSR data for the time period [1979-2010] and CFSR-2 data for the time period [2011-2014] using fortran or python programs to obtain a single SELAFIN file per year containing pressures and wind velocities data, two simulations are then achieved: the first one takes into account atmospheric forcing, the second one doesn't (tide propagation only). From the TELEMAC2D result file, time series with a 10 mn time step at each harbour are extracted. Substracting water levels calculated without atmospheric forcing to water levels obtained considering CFSR pressures and winds leads to instantaneous surge levels that can, then, be compared to those observed by the SHOM. A calculation of scores, listed in Table 1, is then realised with a Fortran program provided by Meteo-France during HOMONIM project.

Fig. 11 shows several example of tidal signals calculated with this set of parameters at several harbours, compared to the tidal signal predicted by the SHOM.

TABLE 1: DEFINITION OF THE SCORES COMPUTED IN METEO-FRANCE FORTRAN PROGRAM AND OF THE ADDITIONAL SCORE ERRAPIC7

Score	*Definition*
MVA_B	Average of the biases absolute value (each variable is computed for one site and then averaged on all sites)
BIAIS	Errors average
EQM	Mean square error (and then quadratic mean on all sites)
ECT	Mean standard deviation
ERRMAX	Maximum error
ERRPIC	Error at the storm surge peak
DEPHAS	Time shift at the storm surge peak
ERRPIC_H	Skew storm surge error
DEPHAS_H	Time shift at the water level storm peak
ERRAPIC7	Average of absolute errors of storm surges peaks in 7 harbours

Noticeable effects which have to be taken into account for the numerical modelling of surge levels: the opposite barometric effect and drag coefficient

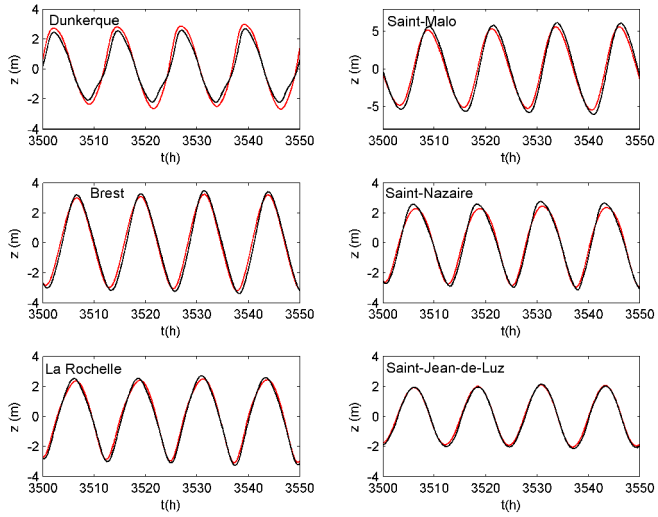

Fig. 11: tide signal calculated with TELEMAC2D (in black) and predicted by the SHOM (in red) (from [1]).

In the calculation of surge levels using TELEMAC2D, the inverse barometric effect on water levels imposed at the numerical model boundaries has been taken into account. It means that water levels provided by NEA are modulated by the increase or the decrease of the sea level due to the pressure, calculated with: $H_b = H - \frac{P - P_o}{\rho_e g}$,

where H is the water level provided by NEA, H_b the water level modulated with the inverse barometric effect (imposed as a boundary condition in the TELEMAC2D simulation), P the atmospheric pressure at the node considered, P_0 the mean atmospheric pressure (101325 Pa), g the gravity acceleration and ρ_e water density.

Simulations with and without taking into account the inverse barometric effect were realised and permitted to conclude that it is necessary to consider it in order to model surge levels properly.

Another important point to notice is the formulation of the drag coefficient that appears in the shearing force generated by wind at the sea surface. In a first step, a constant coefficient equal to $2.142.10^{-3}$ was chosen, but finally after some parametrization tests, a Flather distribution was implemented in Telemac2D.

Event validation for several storms

In this section, the scores obtained for the modelling of storm surges for one storm, Johanna among the 17 storms studied for the time period [1979, 2014], obtained at each of the harbours for which observations were available are presented in Table 2

The target period for Johanna event begins the 10th of March 2008 and ends the 11th of March 2008. Le Havre, Saint-Malo, Roscoff, le Conquet, Brest, Concarneau, La Rochelle and Saint-Jean-de-Luz harbours are concerned. The scores are computed all over the target period for each harbour.

TABLE 2: DEFINITION OF THE SCORES COMPUTED IN METEO-FRANCE FORTRAN PROGRAM

	BIAIS (cm)	BIABS (cm)	EQM (cm)	ECT (cm)	ERRMAX (cm)	ERRPIC (cm)	DEPHAS (mn)	ERRPIC_H (cm)	DEPHAS_H (mn)
Le Havre	9	**18**	**27**	**25**	**82**	**45**	30	-1	-10
Saint-Malo	10	**21**	**27**	**25**	**82**	-10	30	**22**	0
Roscoff	2	8	10	10	**23**	14	-30	-1	-10
Le Conquet	3	8	9	8	**21**	12	-10	4	-10
Brest	-2	8	10	10	**28**	**25**	-40	-5	-20
Concarneau	-4	7	9	8	**23**	2	**-90**	-13	-10
La Rochelle	0	13	**16**	**16**	**33**	-8	**70**	**16**	10
Saint-Jean de Luz	-5	**19**	**21**	**20**	**34**	**-34**	-40	-5	-10

From Table 2, it is noticeable that computed surge levels and water levels present acceptable time shifts except at Concarneau and La Rochelle. The bias is also acceptable, except at Saint-Jean de Luz and Saint-Malo. Concerning the evaluation of the storm surge peak, the difference with observations are acceptable and lower than 15 cm for all concerned harbours except Le Havre, Brest and Saint-Jean de Luz, but they are compensated in terms of skew water levels, except at La Rochelle and Saint-Malo.

Fig. 12 shows observed instantaneous storm surges and computed with TELEMAC2D instantaneous storm surges at Le Havre and La Rochelle during Johanna. The global shape of the storm surge signal is well represented, but storm surges peaks are underestimated at La Rochelle and overestimated at Le Havre.

Mean climatology validation for skew surges

A preliminary validation of the numerical surge database, before performing both local and regional statistical analysis of extremes, was achieved and described in [2]. The validation of the model is carried out to evaluate the accuracy of the simulations in order to represent observed extreme events.

Thus a comparison between simulated and observed skew surges has been carried out, using the tide gauges at 31 harbours located on the North and West French coastline, on the North of the Spanish coastline and on the South of the English coastline as shown on Fig. 13. For each site, only observed and simulated skew surges happening more or less

at the same time (more or less 2 hours) are compared. This procedure is supposed to enable the comparison between observed and simulated skew surges that occurred during the same high tide. Fig. 14 represents an example of a time skew storm surges series observed at Le Havre (in black) and the TELEMAC2D time skew surges series (in red).

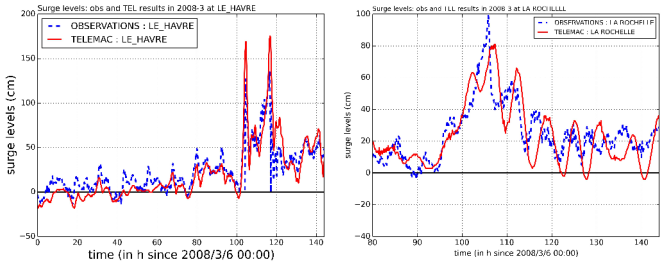

Fig. 12: storm surge signal calculated with TELEMAC2D (in red) and observed by the SHOM (in blue) at Le Havre (on the left) and La Rochelle (on the right) during Johanna storm.

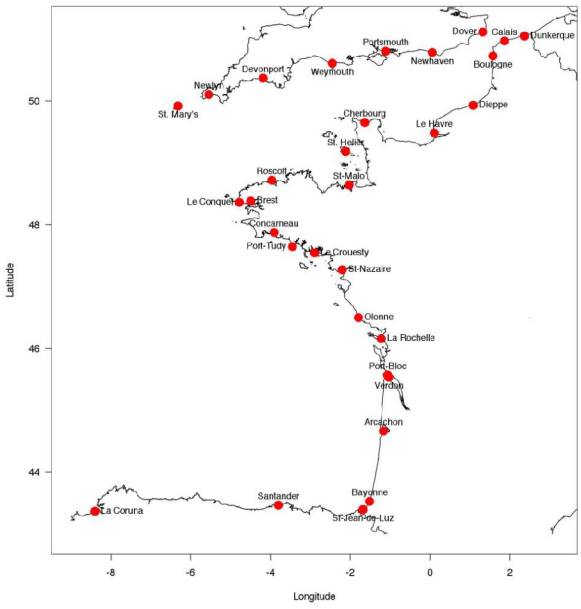

Fig. 13: Harbours used for the validation of skew surge levels (from [2])

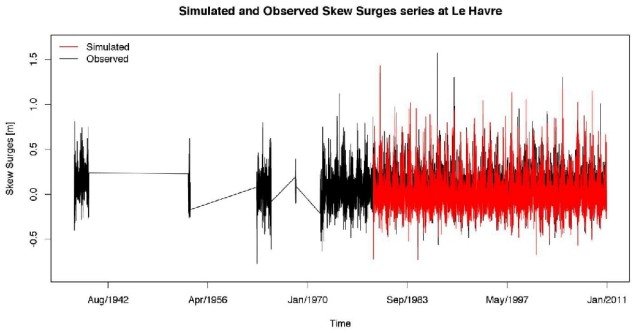

Fig. 14: skew storm surges time series at Le Havre - simulated skew storm surges (in red) and observed skew storm surges (in black) (from [2])

The methodology used to carry out the validation of the model is achieved through several statistical tests both on the overall skew surges time series compared and extreme skew surge events. The comparison is divided into two parts: a "global" comparison and a special focus on extreme skew storm surges events (storms).

The former "global" comparison has been achieved both for the single values of skew surges (Intensity of storm surges) and for the temporal structure of skew surges through the investigation of both time shifts between observed and simulated series and differences in terms of temporal correlation.

Concerning the validation of the numerical storm surge model for the intensities of skew storm surges, some statistical indicators were computed: bias, root-mean-square error (RMSE), correlation, scatterplot and QQ-plot. The results of the three former numerical criteria are displayed in Table 3 just below for each of 31 considered sites. Bias and RMSE (resp. correlation coefficient) below 15 cm (resp. 0,75) show good results. "Bad" values are in bold.

It is quite interesting to notice, that the bias values are negative nearly overall, which means that skew storm surges are underestimated by the numerical storm surge model. Globally, except at Dieppe, Dunkerque, Sables d'Olonne and Port-Tudy and Santander, La Coruna, Saint-Malo and Le Verdon where the correlation coefficient is below 0.75, biases and RMSE are below 15 cm, which shows a mean climatology for simulated skew storm surges quite in good agreement with observed skew storm surges.

Scatterplots, which shows in a cartesian graph both intensities of simulated skew storm surges series and observed skew storm surges series that happened at the same time, were displayed at each site. This analysis is useful to visualize if the extreme values are well computed or not. For example, the model seems to globally agree with observations at Dover and Le Havre, whereas it seems to underestimate skew surges at Sables d'Olonne and to overestimate low skew surges at Santander, as Fig. 15 shows it.

QQ-plot, displayed for each harbour, compares the simulated skew surges distribution and the observed skew surge distribution through the plot of empirical quantiles for both distributions. Both simulated and observed skew storm surges are similar if the points follow a straight line also represented. It is noticeable that globally the central part of the skew surges distribution is underestimated by the numerical model for each site, except at Calais and Santander. Concerning extreme values, it is difficult to carry out an overall assessment. Indeed, for example, as Fig. 16 stresses it out, the model at Le Havre seems to be good for high values, although a light underestimation of maximum extremes can be observed, whereas the model at La Rochelle is good for the high values except for the upper outlier which corresponds to Xynthia storm which occurred during 2010.

Two tests have been used to validate the temporal dynamics of the model: Auto-correlation and Cross-correlation functions. Auto-correlation function (ACF) can tell if the temporal structure of Observed and Simulated series is the same and Cross-correlation function (CCF) can

show the existence of a time shift between the two considered samples.

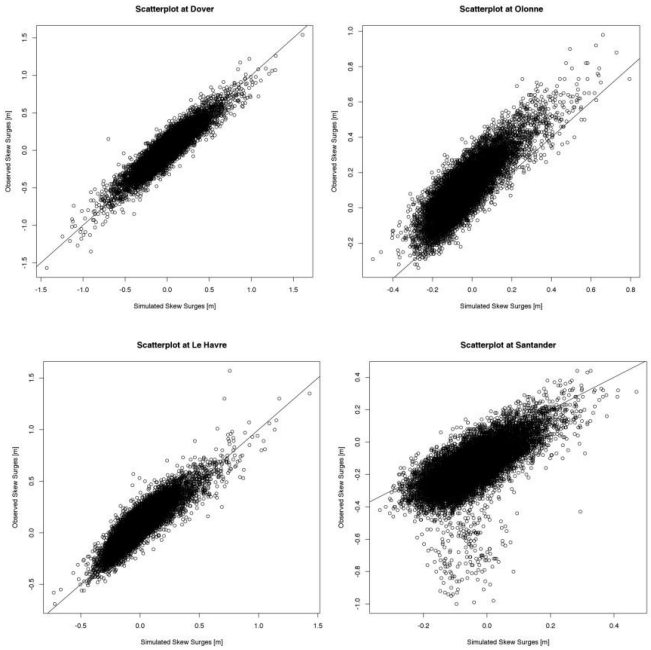

Fig. 15: scatterplots at Dover (top left), Sables d'Olonne (top right), Le Havre (bottom left) and Santander (bottom right) (from [2])

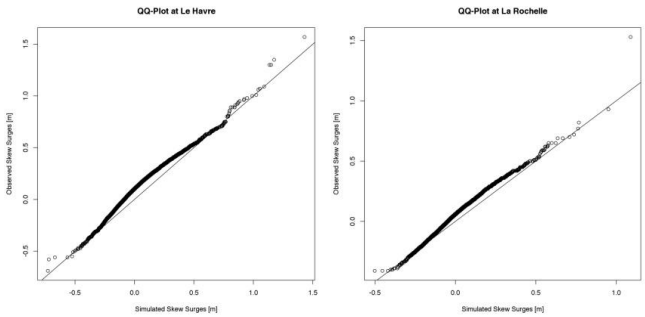

Fig. 16: QQ-plots at Le Havre (on the left) and La Rochelle (on the right) (Frau, 2014)

Concerning ACF, results obtained are very heterogeneous and don't permit to carry out an overall assessment. For example, the model shows better performances (in terms of ACF) at Arcachon than at Santander. However, the autocorrelation at Le Havre shows that the values of autocorrelation between observed skew surges and simulated skew surges are different mainly for the first time lags (except for Lag=0 where ACF value must be 1 in every sample) while the values of autocorrelation at La Rochelle between observed skew surges and simulated skew surges are different for every time lag (obviously except for Lag=0), as Fig. 17 stresses it out.

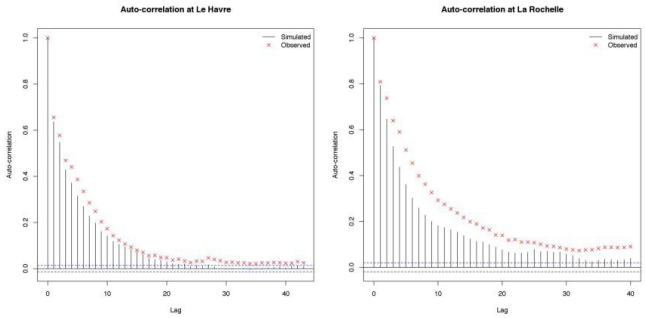

Fig. 17: autocorrelation plots at Le Havre (on the left) and La Rochelle (on the right) (Frau, 2014)

Considering cross-correlation diagrams, the model can be considered to have no time shift. Indeed, the maximum value of CCF at each site is reached for Lag=0.

A zoom on extreme events was also carried out by a comparison between model and observations for each storm in terms of storm surge peak intensity and duration, calculated for every storm occurred at each site, considering exceedances of the 99.5% quantile of observed skew surges series. Moreover, a single storm is defined as a set of observed skew surges that exceeded the harbour's threshold within 2 days.

In order to compare correctly the observations and the model during extreme events, the peak intensities are calculated for every storm that impacted each site. Thus peak intensity is here defined as the difference between the maximum simulated skew surges and the maximum observed skew surge that happened during the same storm. It can be noticed that the mean peak intensity during storms is underestimated at each site, except at Calais (slight overestimation of 2.4 cm), as Table 3 stresses it out. Globally, except for Arcachon, Bayonne, Dieppe, La Coruna, Sables d'Olonne, Port-Bloc, Roscoff, Saint-Jean de Luz, Saint-Nazaire and Le Verdon, for which the simulated mean peak intensities are more than -15 cm below the observed mean peak intensities, other harbours show good results.

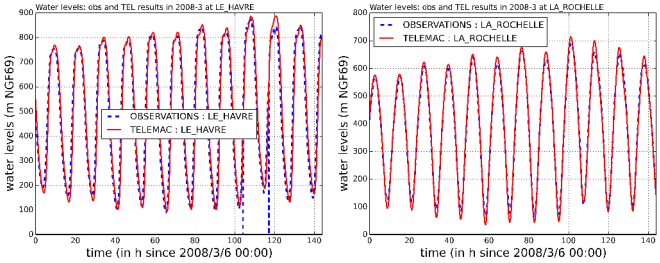

Fig. 18: water levels calculated with TELEMAC2D (in red) and observed by the SHOM (in blue) at Le Havre (on the left) and La Rochelle (on the right) during Johanna storm.

Table 3, in which "bad results" are in bold, permits more easily to do general assessments about the numerical model performance region by region and also site by site. It is

important to notice that the model trends to underestimate extremes and misses some temporal dynamics. The model provides better results in the English Channel than in Bay of Biscay and performances are globally very good in Great Britain (almost perfect in Devonport, Dover and Weymouth), in Bretagne and Basse Normandie regions. On the contrary, the model shows relatively bad performances in Pays de la Loire, Aquitaine and Spain.

TABLE 3: RESULTS OF BIAS [M], RMSE [M], CORRELATION AND MEAN PEAK INTENSITY CRITERIA FOR THE 31 SITES FOR SKEW STORM SURGES

Region/Country	Sites	Bias [m]	RMSE [m]	Correlation	Peak intensity [m]
Nord-Pas-de-Calais	Boulogne	-0.09	0.14	0.78	-0.09
	Calais	0.06	0.14	0.77	0.02
	Dunkerque	-0.12	**0.16**	0.85	-0.13
Haute-Normandie	Dieppe	**-0.16**	**0.19**	0.75	**-0.20**
	Le Havre	-0.09	0.12	0.88	-0.07
Basse-Normandie	Cherbourg	-0.06	0.08	0.87	-0.05
Bretagne (South coast)	Brest	-0.06	0.09	0.88	-0.10
	Concarneau	-0.11	0.12	0.91	-0.14
	Le Conquet	-0.05	0.08	0.88	-0.09
	Le Crouesty	-0.07	0.10	0.87	-0.10
	Port-Tudy	-0.10	0.12	0.88	-0.13
Bretagne (North coast)	Roscoff	-0.09	0.11	0.88	-0.15
	Saint-Malo	-0.01	0.10	**0.73**	-0.11
Pays de la Loire	Olonne	-0.14	**0.16**	0.84	**-0.21**
	Saint-Nazaire	-0.12	0.15	0.83	**-0.25**
Poitou-Charentes	La Rochelle	-0.04	0.09	0.83	-0.11
Aquitaine	Arcachon	0.02	0.10	0.77	**-0.23**
	Bayonne	-0.07	0.12	0.75	**-0.34**
	Port Bloc	-0.07	0.11	0.81	**-0.18**
	Saint-Jean-de-Luz	-0.09	0.11	0.79	**-0.22**
	Verdon	-0.08	0.14	**0.73**	**-0.26**
Spain	La Coruna	0.04	0.10	**0.70**	-0.20
	Santander	0.11	0.14	**0.68**	-0.06
Great Britain	Devonport	-0.03	0.06	0.91	-0.03
	Dover	-0.02	0.09	0.90	-0.03
	Newhaven	-0.02	0.08	0.88	-0.04
	Newlyn	-0.06	0.08	0.91	-0.08
	Portsmouth	-0.04	0.08	0.89	-0.06
	St. Helier	-0.02	0.08	0.83	-0.02
	St. Mary's	-0.04	0.07	0.89	-0.07
	Weymouth	-0.02	0.06	0.88	-0.06

WATER LEVELS MODELLING AND VALIDATION

Event validation for several storms

The event validation has been achieved for the same events as for storm surges (11 events during [1979; 2010] and 7 events during [2011; 2014]).

Table 4 contains for Johanna storm (2008) the minimal error at high tides, the maximal error on water levels at high tides, the mean error at high tides, the standard deviation of the error at high tides and the error for the highest water level during the storm considered.

TABLE 4: RESULTS OF MINIMAL, MAXIMAL, MEAN AND STANDARD DEVIATION OF THE DIFFERENCE AT HIGH TIDES BETWEEN TELEMAC2D AND OBSERVED WATER LEVELS AND ERROR AT HIGHEST WATER LEVEL DURING JOHANNA STORM

Region/Country	Sites	Min [cm]	Max [cm]	Mean [cm]	Standard deviation [cm]	Error at the water level peak [cm]
Nord-Pas-de-Calais	Boulogne	7	47	17	14	7
	Calais	-11	-1	-8	3	-11
	Dunkerque	-35	**-20**	-26	5	-30
Haute-Normandie	Le Havre	8	20	12	4	8
Basse-Normandie	Cherbourg	-17	-5	-11	4	-17
Bretagne (South coast)	Brest	18	32	25	5	18
	Concarneau	4	16	10	4	4
	Le Conquet	17	30	22	4	17
	Le Crouesty	7	18	12	5	7
Bretagne (North coast)	Roscoff	12	19	15	2	12
	Saint-Malo	38	53	**46**	5	38
Pays de la Loire	Olonne	-5	**10**	3	**6**	-5
	Saint-Nazaire	0	15	7	**5**	0
Poitou-Charentes	La Rochelle	7	27	17	8	7
Aquitaine	Arcachon	-3	9	3	**4**	-3
	Bayonne	21	32	26	**4**	21
	Saint-Jean-de-Luz	8	20	15	**4**	8
	Verdon	34	42	37	**2**	34

Except for harbours in red in Table 4 among which it will be necessary to check the mean water level taken into account, water levels at its highest level during Johanna are quite well evaluated by the numerical model.

Fig. 18 shows the water levels signal computed and observed at Le Havre and La Rochelle during Johanna storm.

Mean Climatology and extreme quantiles validation

The study of mean climatology and extreme should be achieved at the end of august 2015.

CONCLUSIONS AND PERSPECTIVES

A numerical storm surges model based on Telemac2D has been built in Saint-Venant Hydraulics laboratory and has been validated considering the ability of the model to represent properly tide propagation, skew surge levels and instantaneous storm surges, but also water levels at harbours mainly in France but also in Spain and Great-Britain where observations were available. The target precision of this model is 10 to 15 cm for water levels and surge levels.

This numerical model has already been used for several studies and purposes inside of several research projects (for example, the study of the evolution of surge levels in Le Havre Harvour and the Seine Bay and of the surge levels / tide interaction at the Seine Mouth) [3]. It will also be used to estimate the impact of climate change on the Atlantic French coastline considering one or several IPCC5 scenarios provided by METEO-FRANCE by the end of the year (on progress).

Once the global validation achieved, this database built for the time slice [1979; 2014] will be integrated into a hydrodynamic, sea-state and infrastructures platform, whose development is on progress and which should be available in a beta-version at the end of the year. Concerning instantaneous and skew water levels or surge levels, it should provide to the user, public institutions or engineering consultants, free data useful for urban planning or the test of the impact of future infrastructures: time series, but also mean seasonal climatology: annual and seasonal histograms, correlograms etc.

AKNOWLEDGMENTS

The sea level observations of Le Havre – Quai Meunier are the property of SHOM and GPMH and are available on the REFMAR website (refmar.shom.fr).

REFERENCES

[1] F. Lévy, “Modélisation des surcotes avec Telemac 2D”, internal report, 24 pages, April 2013.

[2] R. Frau, “Exploitation of a numerical surge database and statistic analysis of extremes”, internal report, 100 pages, August 2014.

[3] V. Laborie, P. Sergent, “Evolution of surge levels and tide/surge interactions inside of the seine bay”, IAHR E-proceedings, July 2015.

[4] J.M. Hervouet, “Hydrodynamics of free surface flows”. Ed. Wiley. 390 pages, 2006

[5] R. Pawlowicz, B. Beardsley, and S. Lentz, “Classical tidal harmonic analysis including error estimates in MATLAB using TTIDE”, Computers and Geosciences, 28, pp. 929-937, 2002.

[6] E. Barros, “Estimation des parametres dans les equations de Saint-Venant”, Ph.D. Thesis, Univ. Paris 6, 1996.

Using the DRAGFO subroutine to model Tidal Energy Converters in Telemac-2D

Antoine Joly
EDF R&D LNHE / LHSV
6 quai Watier, 78401 Chatou, France
Email: antoine.joly@edf.fr

Chi-Tuân Pham, Marc Andreewsky, Sylvain Saviot & Lauriane Fillot
EDF R&D LNHE
6 quai Watier, 78401 Chatou, France

***Abstract*—In the past few years the research on Tidal Energy Converters (TECs), or Tidal Turbines, has increased (see for example the work done at the EMEC[1]). As such a demand arose to assess the impact of potential large industrial TEC farms. This demand has also been growing in the Telemac User community, see for example Haverson *et al.* [2] or de Paula Kirinus *et al.* [1], but no clear methodology has been defined within the Telemac-Mascaret system.**

To model the hydrodynamic effects of TEC over large areas, two approaches are possible. One can either use the actuator disk method, where the influence of a TEC is modelled through a head drop [6], or it is possible to model the drag force induced by a TEC opposing the flow (this can be thought of as being similar to increasing the bed friction). This second approach has been successfully applied by EDF in Telemac-2D through the PerAWaT project[2] and its recommended implementation in Telemac-2D will be described in this article. Furthermore its implementation will be illustrated by reproducing the experiment conducted by the University of Manchester within the PerAWaT project [7].

I. Introduction

The technology used to extract tidal energy through turbines has made significant progress in recent years. As such, Tidal Energy Converters (TECs) are ready for test sites, and there is a growing need to model their hydrodynamics effects. Telemac-2D has been successfully used to model the hydrodynamic effects of such test sites scenarios, see for example [1], [2], [4]. However, no clear methodology has been defined to use Telemac-2D to model the influence of TECs on the hydrodynamics of a real site. This article is designated as guide to anyone wanting to model TECs using a tested method [4].

II. Modelling approach

To model the hydrodynamic effects of TEC over large areas, two approaches are possible. One can either use the actuator disk method, where the influence of a TEC is modelled through a head drop [6], or it is possible to model the drag force induced by a TEC opposing the flow (this can be thought of as being similar to increasing the ground friction). This second approach has been successfully applied in Telemac-2D [4] and its implementation in Telemac-2D will be described in this article.

As a reminder the drag force of a Tidal Energy Converter is defined through the following equation:

$$F_D = -\frac{1}{2}\pi R^2 \rho C_D U_r \left|U_r\right| \tag{1}$$

Where F_D is the drag force along the central axis of the TEC, ρ is the fluid density, C_D is a drag coefficient (usually given by the designer of the TEC, and checked by the manufacturer if possible), R is the radius of the TEC and U_r is a reference velocity along the central axis of the TEC ($U_r \left|U_r\right|$ is used instead of U_r^2 so that the direction of the flow is kept).

The reference velocity U_r is particularly important when modelling TECs with Telemac-2D, because when a TEC constructor calibrates the drag coefficient this velocity is usually taken at a position where the flow is not disturbed by the presence of the TEC (for example, upstream). Therefore using the velocity at the position of the TEC will usually generate the wrong drag force.

Furthermore the mechanical power extracted by a Tidal Energy Converter is given through the following formula:

$$P = \frac{1}{2}\pi R^2 C_P \rho U_r^2 \left|U_r\right| \tag{2}$$

Where P is the extracted power and C_P is power coefficient (usually given by the designer of the TEC, and also checked by the manufacturer if possible).

A. Applying the drag force as a source term

To apply (1) to the flow modelled with Telemac-2D, it needs to be slightly modified. This drag force will be applied as a stress spread out over an area representing the TEC. This will ensure a sufficient number of mesh nodes will be impacted by the turbine. The area and the mesh size at the location of the TEC will have to be chosen by the user. For more information one can refer to Joly *et al.* [5]. The stress τ can be found using (1), i.e.:

$$\begin{aligned}\tau_D =& \frac{F_D}{A} \\ =& -\frac{1}{2}\frac{\pi R^2}{A}\rho C_D U_r \left|U_r\right|\end{aligned} \tag{3}$$

Where A is the area over which the drag force will be applied.

[1] http://www.emec.org.uk/
[2] http://www.eti.co.uk/project/perawat/

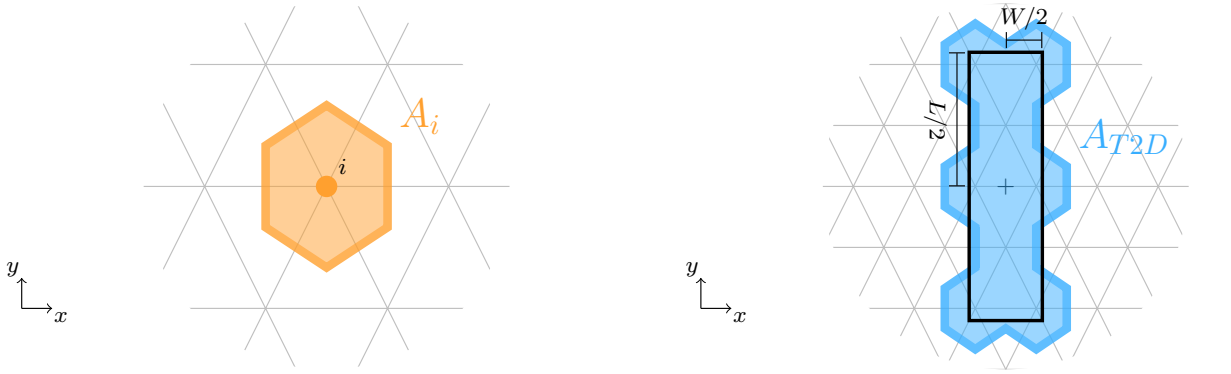

(a) Area of a node i (A_i)

(b) Area occupied by a TEC in Telemac-2D (A_{T2D})

Fig. 1: Different areas used to define a TEC in a telemac-2D simulation.

This stress can be treated as a source term in the Shallow Water Equation, in the same way that friction stresses are taken into account [3]:

$$\begin{aligned} Q_{TEC} =& \frac{\tau_D}{\rho h} \\ =& -\frac{1}{2}\frac{\pi R^2}{Ah} C_D U_r \left|U_r\right| \end{aligned} \tag{4}$$

Where h is the water depth at the position of the TEC. Finally in Telemac-2D there is a possibility for this term to be implicited, which means that it will be multiplied by the local velocity later on. Therefore, to apply the drag force of a TEC to the flow within Telemac-2D it will be necessary to divide this source term by the local velocity, i.e.:

$$\begin{aligned} \texttt{FDRAG} =& \frac{Q_{TEC}}{U_{loc}} \\ =& -\frac{1}{2}\frac{\pi R^2}{Ah} C_D \frac{U_r \left|U_r\right|}{U_{loc}} \end{aligned} \tag{5}$$

Where `FDRAG` is the source term used in Telemac-2D to model the impact of a drag force on the flow (it will later be decomposed into a horizontal and vertical components `FUDRAG` and `FVDRAG`). Variable U_{loc} is the local velocity of a node upon which the drag force is applied.

B. Taking into account the geometrical parameters in a mesh

In Telemac-2D, a TEC is defined by an area of length L and a width W. However, since the drag force is applied to nodes in a 2D mesh, the effective area (known as A_{T2D}) is the sum of the area of the nodes inside the area defined by L and W. See figure 1 for more details on the calculations of the areas.

In Telemac-2D, a TEC is also defined by the orientation of its central axis, which will be referred to as the angle θ, see figure 2 for more details. Because of this, the drag force F_D will need to be decomposed into x and y components to be applied in Telemac-2D. The components of the drag force F_D are therefore given by:

$$F_{D,x} = -\frac{1}{2}\pi R^2 C_D U_r \left|U_r\right| \cos(\theta) \tag{6a}$$

$$F_{D,y} = \frac{1}{2}\pi R^2 C_D U_r \left|U_r\right| \sin(\theta) \tag{6b}$$

As mentioned previously, the drag coefficient is usually defined for a reference velocity which is typically taken at a point where the flow is undisturbed by the TEC. This point will be assumed to be upstream, and the user will need to define its distance from the centre of the TEC (noted as D_D).

The reference velocity U_r will be calculated from the velocity vector $\boldsymbol{U_{ref}}$ taken at a distance D_D upstream of the flow going through the centre of the TEC. It is therefore necessary to calculate an angle α, which is the angle of the direction of the flow at the centre of the TEC. It will therefore be the direction of the fluid velocity vector at the centre of the TEC $\boldsymbol{U_{TEC}}$. See figure 2 for more details.

The vector $\boldsymbol{U_{ref}}$ then needs to be projected along the central axis of the TEC (given by angle θ) to calculate the reference velocity U_r. The following equations will give the steps necessary to calculate U_r:

$$\alpha = -\texttt{ATAN2}\left(U_{TEC,y}, U_{TEC,x}\right) \tag{7a}$$

$$\begin{aligned} U_r =& U_{ref,x}(D_D, \pi+\alpha)\cos(\theta) \\ & - U_{ref,y}(D_D, \pi+\alpha)\sin(\theta) \end{aligned} \tag{7b}$$

Where `ATAN2` is a function available in most Fortran compiler which gives the angle in the appropriate quadrant, $U_{TEC,x}$ and $U_{TEC,y}$ are the horizontal and vertical components of vector $\boldsymbol{U_{TEC}}$ and $U_{ref,x}(D_D, \pi+\alpha)$ and $U_{ref,y}(D_D, \pi+\alpha)$

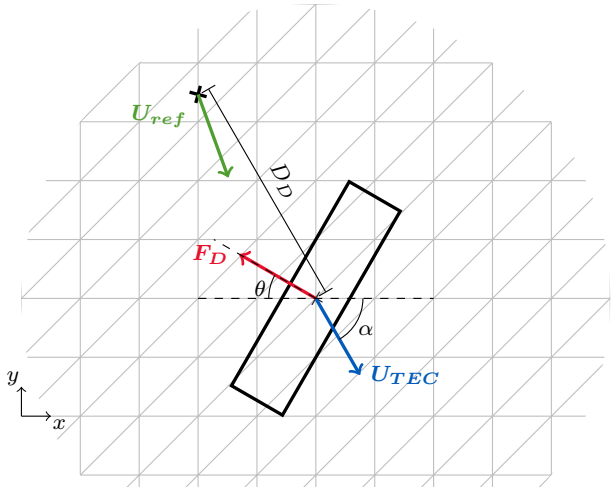

Fig. 2: Detailed geometrical parameters for a TEC in a 2D triangular mesh. Note that θ is positive in the clockwise direction and α is positive in the counter-clockwise direction.

are the horizontal and vertical components of vector $\boldsymbol{U_{ref}}$ taken at a distance D_D and an angle $\pi + \alpha$ of the TEC. In a triangular mesh it is therefore recommended to store the number of the elements that are at a distance D_D of a TEC so that U_r can be calculated fast.

C. Calculating the extracted power of the TEC

Since the extracted power by each TEC is calculated using the reference velocity U_r, equation (2) does not need to be applied to each node in a mesh. Therefore, once U_r is known for each TEC, see (7), equation (2) can be applied directly to find the extracted mechanical power of each TEC.

III. Summary of the system of equations that needs to be solved and of the parameters that need to be defined in Telemac-2D

For a TEC i and a node j in the mesh, equations (2), (5), (6) and (7) need to be solved and applied to a Telemac-2D simulation:

$$\alpha(i) = -\,\mathrm{ATAN2}\left[U_{TEC,y}(i), U_{TEC,x}(i)\right] \tag{8a}$$

$$\begin{aligned} U_r(i) =& U_{ref,x}(i, D_D, \pi+\alpha)\cos[\theta(i)] \\ & - U_{ref,y}(i, D_D, \pi+\alpha)\sin[\theta(i)] \end{aligned} \tag{8b}$$

$$A_{T2D}(i) = \sum_{j=\text{Nodes in TEC i}} A_j \tag{8c}$$

$$\mathrm{FUDRAG}(i,j) = -\frac{1}{2}\frac{\pi R(i)^2}{A_{T2D}(i)h_j} C_D(i) \frac{U_r(i)\,|U_r(i)|}{U_j}\cos[\theta(i)] \tag{8d}$$

$$\mathrm{FVDRAG}(i,j) = \frac{1}{2}\frac{\pi R(i)^2}{A_{T2D}(i)h_j} C_D(i) \frac{U_r(i)\,|U_r(i)|}{V_j}\sin[\theta(i)] \tag{8e}$$

$$P(i) = \frac{1}{2}\pi R(i)^2 C_P(i)\rho U_r(i)^2\,|U_r(i)| \tag{8f}$$

Where U_j and V_j are the horizontal and vertical components of the fluid velocity of a node j upon which the drag force will be applied.

To solve the system of equations (8) several variables will need to be defined by the user:

- R: Radius of the TEC
- C_D: Drag coefficient of the TEC
- θ: Orientation of the central axis of the TEC.
- L: Length of the 2D area covered by the TEC
- W: Width of the 2D area covered by the TEC
- D_D: Distance from the TEC for which the reference velocity will be taken
- C_P: Power coefficient of the TEC

Variables $\boldsymbol{U_{TEC}}$, $\boldsymbol{U_{ref}}$, $\boldsymbol{U_j}$ and h_j will need to be interpolated from the triangular mesh.

IV. Taking into account the influence of a TEC in Telemac-2D

A. Configuration in the steering file

Through the use of keywords in the steering file several parameters can be made easily available:

```
/-------------------------------------------------/
/                OPTIONS FOR TECS
/-------------------------------------------------/
/ USING THE DRAGFO SUBROUTINE
VERTICAL STRUCTURES     : YES
FORTRAN FILE            : './t2d_dragfo_TEC.f'
/ FILE WITH POSITIONS AND NUMBER OF THE TEC
FORMATTED DATA FILE 2   : './TEC_positions.xyz'
/ RESULT FILE TO OUTPUT THE EXTRACTED POWER
FORMATTED RESULTS FILE : './TEC_power.txt'
WATER DENSITY           : 1025.
```

Note that the keyword for the water density is only necessary for coastal simulations as the default value is 1000 kg/m^{-3}. Furthermore, the `DRAGFO` subroutine will be modified in the user Fortran code (given by the keyword `FORTRAN FILE`) to take into account TEC through the system of equations (8).

To easily define the number, the positions and physical parameters of the TECs that one wants to model it is recommended to define an external formatted file. This file will be defined in the steering file using the keyword `FORMATTED DATA FILE 2`. It should have the following format:

```
N
X1 Y1 L1 W1 THETA1 R1 DD1 CD1 CP1
X2 Y2 L2 W2 THETA2 R2 DD2 CD2 CP2
X3 Y3 L3 W3 THETA3 R3 DD3 CD3 CP3
...
XN YN LN WN THETAN RN DDN CDN CPN
```

Where `N` is the number of TEC, `X1-XN` are the x-coordinates and `Y1-YN` are the y-coordinates of the centre of the area defining each TEC. `L1-LN`, `W1-WN`, etc. are the TEC parameters defined in section III.

Finally the extracted power output per TEC will be printed in time in a file given by the keyword `FORMATTED RESULTS FILE`.

B. *Using the subroutine* DRAGFO *to model the drag force*

To apply the system of equations 8 in Telemac-2D it is possible to use the subroutine DRAGFO. This subroutine is only called in Telemac-2D if the keyword VERTICAL STRUCTURES is set to YES in the steering file. This subroutine will then need to be modified in the user FORTRAN FILE. The recommended approach to model several individual turbines in a parallel implementation of Telemac-2D will now be described. It should be noted that the line numbering, when it appears, is that of a user Fortran file containing only the modifications recommended to the user subroutine DRAGFO.

1) New variables specific to TEC simulations: It is recommended to store the simulation parameters that define the TECs in a module as it is a clean way to store values that will be accessible at all time steps. Therefore at the beginning of the Fortran user file the following lines of code will need to be added.

```
@@ -1,6 +1,36 @@
+!-----------------------------------------------------------------
+      MODULE TEC_PARAM
+!-----------------------------------------------------------------
+      ! PARAMETERS READ IN THE FORMATTED DATA FILE
+      INTEGER:: NTEC
+      DOUBLE PRECISION,DIMENSION(:),ALLOCATABLE:: XTEC
+      DOUBLE PRECISION,DIMENSION(:),ALLOCATABLE:: YTEC
+      ! PARAMETERS DEFINNING THE TEC
+      DOUBLE PRECISION,DIMENSION(:),ALLOCATABLE:: THETA
+      DOUBLE PRECISION,DIMENSION(:),ALLOCATABLE:: HDL
+      DOUBLE PRECISION,DIMENSION(:),ALLOCATABLE:: HDW
+      DOUBLE PRECISION,DIMENSION(:),ALLOCATABLE:: RTEC
+      DOUBLE PRECISION,DIMENSION(:),ALLOCATABLE:: DD
+      DOUBLE PRECISION,DIMENSION(:),ALLOCATABLE:: CDTEC
+      DOUBLE PRECISION,DIMENSION(:),ALLOCATABLE:: CPTEC
+      DOUBLE PRECISION,DIMENSION(:),ALLOCATABLE:: VCUT
+      ! PARAMETERS USED TO DEFINE THE NODES WITHIN EACH TEC
+      DOUBLE PRECISION,DIMENSION(:),ALLOCATABLE:: AREA
+      INTEGER,DIMENSION(:),ALLOCATABLE:: NNODES
+      INTEGER,DIMENSION(:,:),ALLOCATABLE:: INODES
+      ! ELEMENT AND PROCESSOR OF TEC CENTRE
+      INTEGER,DIMENSION(:),ALLOCATABLE:: TECELEM
+      INTEGER,DIMENSION(:),ALLOCATABLE:: TECPID
+      ! PARAMETERS USED TO FIND THE FAR VELOCITY
+      INTEGER,DIMENSION(:,:),ALLOCATABLE:: DDELEM
+      INTEGER,DIMENSION(:,:),ALLOCATABLE:: DDPID
+      ! EXTRACTED POWER
+      DOUBLE PRECISION,DIMENSION(:),ALLOCATABLE:: PTEC
+      END MODULE
+!-----------------------------------------------------------------
 !-----------------------------------------------------------------
                       SUBROUTINE DRAGFO
 !-----------------------------------------------------------------
 !
     &(FUDRAG,FVDRAG)
 !
```

To understand the differences shown in the line of code:

- The lines starting with "@@" give indications of the line numbers before the change. The numbers after the "-" give the line number and number of lines of the hunk of text in the original file, the number after the "+" give the line number and number of lines of the hunk of text in the modified file
- The green lines starting with a "+" show additions to the code
- The red lines starting with a "-" show deleted lines of code
- The black lines and starting with a space show unchanged code

Furthermore the memory for these variables will need to be allocated, and then they will need to be defined.

In the subroutine DRAGFO the following line is added to allow the subroutine to access the variables stored in the module TEC_PARAM:

```
@@ -43,6 +73,7 @@
 !
       USE BIEF
       USE DECLARATIONS_TELEMAC2D
+      USE TEC_PARAM
 !
       IMPLICIT NONE
       INTEGER LNG,LU
```

Finally these new variables will be used in the code:

```
@@ -64,6 +95,27 @@
       EXTERNAL         P_DSUM
 !
 !-----------------------------------------------------------------
+! ALLOCATE THE EXTRA VARIABLES FOR TEC
+!-----------------------------------------------------------------
+      DOUBLE PRECISION PI, DTR, RTD, TWOPI
+      DOUBLE PRECISION HDLCOSTHETA, HDLSINTHETA
+      DOUBLE PRECISION HDWCOSTHETA, HDWSINTHETA
+      INTEGER IPOIN,IANGLE,INODE
+      DOUBLE PRECISION ALPHA,XDD,YDD
+      DOUBLE PRECISION UTECX,UTECY,UREFX,UREFY,UR
+      INTEGER N1,N2,N3
+      DOUBLE PRECISION DET1,DET2,DET3,SURDET
+      DOUBLE PRECISION HALFCDSCOSTHETA,HALFCDSSINTHETA
+      DOUBLE PRECISION HI,UI,VI
+!-----------------------------------------------------------------
+! ALLOCATE THE EXTRA VARIABLES TO WRITE THE POWER EXTRACTED
+!-----------------------------------------------------------------
+      INTEGER POWRES
+!
+      INTEGER          P_IMAX
+      EXTERNAL         P_IMAX
+!
+!-----------------------------------------------------------------
 !
 !     COMPUTES THE MASSE INTEGRALS
 !
```

2) Defining TEC simulation parameters: Firstly, a few constants will be defined:

```
@@ -74,3 +126,13 @@
       CALL CPSTVC(VN,FVDRAG)
       CALL OS('X=C     ',FUDRAG,FUDRAG,FUDRAG,0.D0)
       CALL OS('X=C     ',FVDRAG,FVDRAG,FVDRAG,0.D0)
+
+!-----------------------------------------------------------------
+! TEC EXAMPLE
+!-----------------------------------------------------------------
+!-----------------------------------------------------------------
+! DEFINE THE CONSTANTS USED TO CALCULATE ANGLES OF TEC
+!-----------------------------------------------------------------
+      PI = 4.D0*ATAN(1.D0)
+      DTR = PI/180.D0
+      RTD = 180.D0/PI
```

Furthermore several variables need to be calculated and stored during the first time step. To do so, the variables defined in the module TEC_PARAM need to have their memory allocated:

```
@@ -77,0 +139,39 @@
+!-----------------------------------------------------------------
+! ON THE FIRST TIME STEP STORE ALL THE TEC PARAMETERS IN
+! THE MODULE
+!-----------------------------------------------------------------
+! FILE 27 IS DEFINED IN THE STEERING FILE OF TELEMAC-2D
+!  WITH THE KEYWORD:
+! FORMATTED DATA FILE 2
+      IF(LT.EQ.1) THEN
+        ! READ THE NUMBER OF TEC
+        READ(27,*) NTEC
+        WRITE(LU,*) '=========================='
```

```
+        WRITE(LU,*) 'NTEC=',NTEC
+        ! ALLOCATING THE TEC PARAMETERS
+        WRITE(LU,*) 'ALLOCATING TEC PARAMETERS'
+        !
+        ALLOCATE(XTEC(NTEC))
+        ALLOCATE(YTEC(NTEC))
+        !
+        ALLOCATE(THETA(NTEC))
+        ALLOCATE(HDL(NTEC))
+        ALLOCATE(HDW(NTEC))
+        ALLOCATE(RTEC(NTEC))
+        ALLOCATE(DD(NTEC))
+        ALLOCATE(CDTEC(NTEC))
+        ALLOCATE(CPTEC(NTEC))
+        ALLOCATE(VCUT(NTEC))
+        !
+        ALLOCATE(AREA(NTEC))
+        ALLOCATE(NNODES(NTEC))
+        ALLOCATE(INODES(NTEC,1000))
+        !
+        ALLOCATE(TECELEM(NTEC))
+        ALLOCATE(TECPID(NTEC))
+        !
+        ALLOCATE(DDELEM(NTEC,-180:180))
+        ALLOCATE(DDPID(NTEC,-180:180))
+        !
+        ALLOCATE(PTEC(NTEC))
```

The TEC parameters will need to be defined. The positions will be read from the file defined in FORMATTED DATA FILE 2, the other parameters need to be defined by the user, these will be shown as <...>.

```
@@ -77,0 +177,22 @@
+        ! SET THE VALUES OF THE TEC PARAMETERS
+        WRITE(LU,*) '=========================='
+        WRITE(LU,*) 'TEC PARAMETERS DEFINED IN FORTRAN FILE'
+        DO I = 1,NTEC
+          ! READING COORDINATES OF THE TURBINES CENTRES
+          READ(27,*) XTEC(I),YTEC(I),
+     &               HDL(I),HDW(I),THETA(I),
+     &               RTEC(I),DD(I),
+     &               CDTEC(I),CPTEC(I),
+          WRITE(LU,*) ' '
+          WRITE(LU,*) 'Turbine index : ',I
+          WRITE(LU,*) 'Position x,y of the turbine : ',
+     &                XTEC(I),YTEC(I)
+          WRITE(LU,*) ' '
+          !
+          THETA(I) = THETA(I)*PI/180.D0
+          HDL(I)   = HDL(I)/2.D0+0.05D0
+          HDW(I)   = HDW(I)/2.D0+0.05D0
+          VCUT(I)  = 0.D0
+          !
+        END DO
+        WRITE(LU,*) '=========================='
```

Then the specific simulation parameters will be calculated. Firstly, the area occupied by the TEC is calculated, $A_{T2D} =$ AREA. While this done, the list of all nodes affected by each TEC will also be stored (in INODES) to increase computation speed later on.

```
@@ -77,0 +199,60 @@
+        ! STORING THE AREA OF THE TEC
+        DO I = 1,NTEC
+          ! WIDTH AND LENGTH ALONG X AND Y COORDINATES
+          HDLCOSTHETA = HDL(I)*COS(THETA(I))
+          HDLSINTHETA = HDL(I)*SIN(THETA(I))
+          HDWCOSTHETA = HDW(I)*COS(THETA(I))
+          HDWSINTHETA = HDW(I)*SIN(THETA(I))
+          !
+          NSOM=4
+          XSOM(1) = XTEC(I) + HDWCOSTHETA + HDLSINTHETA
+          YSOM(1) = YTEC(I) + HDWSINTHETA - HDLCOSTHETA
+          XSOM(2) = XTEC(I) + HDWCOSTHETA - HDLSINTHETA
+          YSOM(2) = YTEC(I) + HDWSINTHETA + HDLCOSTHETA
+          XSOM(3) = XTEC(I) - HDWCOSTHETA - HDLSINTHETA
+          YSOM(3) = YTEC(I) - HDWSINTHETA + HDLCOSTHETA
+          XSOM(4) = XTEC(I) - HDWCOSTHETA + HDLSINTHETA
+          YSOM(4) = YTEC(I) - HDWSINTHETA - HDLCOSTHETA
+          !
+          AREA(I)=0.D0
+          NNODES(I)=0
+          DO IPOIN=1,BIEF_NBPTS(11,MESH)
+            IF(INPOLY(X(IPOIN),Y(IPOIN),
+     &         XSOM,YSOM,NSOM))THEN
+              AREA(I) = AREA(I) + T1%R(IPOIN)
+              NNODES(I) = NNODES(I) + 1
+              IF(NNODES(I).GT.1000)THEN
+                WRITE(LU,*)'DRAGFO: TOO MANY NODES IN TEC'
+                WRITE(LU,*)'       MODIFY ALLOC OF INODES'
+                CALL PLANTE(1)
+                STOP
+              ENDIF
+              INODES(I,NNODES(I)) = IPOIN
+            ENDIF
+          ENDDO
+          ! QUASI-BUBBLE POINTS
+          IF(FU%ELM.EQ.12) THEN
+            DO IELEM = 1 , NELEM
+              I4=IKLE%I(IELEM+3*NELMAX)
+              X4=(X(IKLE%I(IELEM          ))+
+     &            X(IKLE%I(IELEM+  NELMAX))+
+     &            X(IKLE%I(IELEM+2*NELMAX)))/3.D0
+              Y4=(Y(IKLE%I(IELEM          ))+
+     &            Y(IKLE%I(IELEM+  NELMAX))+
+     &            Y(IKLE%I(IELEM+2*NELMAX)))/3.D0
+              IF(INPOLY(X4,Y4,XSOM,YSOM,NSOM)) THEN
+                AREA(I) = AREA(I) + T1%R(I4)
+                NNODES(I) = NNODES(I) + 1
+                IF(NNODES(I).GT.1000)THEN
+                  WRITE(LU,*)'DRAGFO:TOO MANY NODES IN TEC'
+                  WRITE(LU,*)'       MODIFY ALLOC OF INODES'
+                  CALL PLANTE(1)
+                  STOP
+                ENDIF
+                INODES(I,NNODES(I)) = -IELEM
+              ENDIF
+            ENDDO
+          ENDIF
+          ! IN PARALLEL THE AREA MAY BE SPLIT
+          ! INTO SEVERAL SUB-DOMAINS
+          IF(NCSIZE.GT.0) AREA(I)=P_DSUM(AREA(I))
```

The second step stores all the processor and element number inside which the centre of the TEC is located as well as all the number and processors for all elements located at a distance D_D, for all angle between -180 and 180 degrees.

```
@@ -77,0 +260,74 @@
+!
+        ! LOOK FOR THE ELEM NUM FOR ALL ANGLES OF ALPHA
+        DO IANGLE=-180,180
+          XDD = XTEC(I) - DD(I)*COS(DBLE(IANGLE)*DTR)
+          YDD = YTEC(I) + DD(I)*SIN(DBLE(IANGLE)*DTR)
+          ! LOOK IN LOCAL MESH IF ELEMENT IS IN MESH
+          TECELEM(I)=0
+          TECPID(I)=0
+          DDELEM(I,IANGLE)=0
+          DDPID(I,IANGLE)=0
+          DO IELEM=1,NELEM
+            ! GET THE VERTICES
+            N1=IKLE%I(IELEM)
+            N2=IKLE%I(NELEM+IELEM)
+            N3=IKLE%I(2*NELEM+IELEM)
+            ! FIND THE ELEM AND PROC NUM OF THE TEC
+            ! FOR ALL ANGLES
+            DET1=(X(N3)-X(N2))*(YTEC(I)-Y(N2))
+     &           -(XTEC(I)-X(N2))*(Y(N3)-Y(N2))
+            DET2=(X(N1)-X(N3))*(YTEC(I)-Y(N3))
+     &           -(XTEC(I)-X(N3))*(Y(N1)-Y(N3))
+            DET3=(X(N2)-X(N1))*(YTEC(I)-Y(N1))
+     &           -(XTEC(I)-X(N1))*(Y(N2)-Y(N1))
+            IF((DET1.GE.0.D0).AND.
+     &         (DET2.GE.0.D0).AND.
+     &         (DET3.GE.0.D0)) THEN
+              TECELEM(I)=IELEM
+              IF(NCSIZE.GT.0) TECPID(I)=IPID
+            END IF
+            ! FIND THE ELEM AND PROC NUM AT DD
+            DET1=(X(N3)-X(N2))*(YDD-Y(N2))-
+     &           (XDD-X(N2))*(Y(N3)-Y(N2))
+            DET2=(X(N1)-X(N3))*(YDD-Y(N3))
```

```
+     &             -(XDD-X(N3))*(Y(N1)-Y(N3))
+               DET3=(X(N2)-X(N1))*(YDD-Y(N1))
+     &             -(XDD-X(N1))*(Y(N2)-Y(N1))
+               IF((DET1.GE.0.D0).AND.
+     &            (DET2.GE.0.D0).AND.
+     &            (DET3.GE.0.D0)) THEN
+                 DDELEM(I,IANGLE)=IELEM
+                 IF(NCSIZE.GT.0) DDPID(I,IANGLE)=IPID
+               END IF
+             END DO
+             !
+             IF(NCSIZE.GT.0)THEN
+               TECPID(I)=P_IMAX(TECPID(I))
+               TECELEM(I)=P_IMAX(TECELEM(I))
+               IF(IPID.NE.TECPID(I))THEN
+                 TECELEM(I)=-TECELEM(I)
+               END IF
+               !
+               DDPID(I,IANGLE)=P_IMAX(DDPID(I,IANGLE))
+               DDELEM(I,IANGLE)=P_IMAX(DDELEM(I,IANGLE))
+               IF(IPID.NE.DDPID(I,IANGLE))THEN
+                 DDELEM(I,IANGLE)=-DDELEM(I,IANGLE)
+               END IF
+             ENDIF
+             !
+             IF(TECELEM(I).EQ.0)THEN
+               WRITE(LU,*) 'DRAGFO:POSITION FOR TEC',I
+               WRITE(LU,*) '    IS OUTSIDE OF THE DOMAIN'
+               CALL PLANTE(1)
+               STOP
+             END IF
+             !
+             IF(DDELEM(I,IANGLE).EQ.0)THEN
+               WRITE(LU,*)'DRAGFO:POSITION FOR TEC',I
+               WRITE(LU,*)'IS TOO CLOSE TO EDGE OF DOMAIN'
+               CALL PLANTE(1)
+               STOP
+             END IF
+           END DO
+         END DO
+       END IF
```

Note that an error message will appear if the TEC is placed too close to the edge of the domain.

3) Applying the drag force: To apply the drag force a loop will be done on all TECs and on all nodes present in a TEC. The first step is to use the velocity at the centre of the TEC to find the angle of the flow α.

```
@@ -77,0 +333,34 @@
+!
+!-----------------------------------------------------------------
+! APPLY THE DRAG FORCE OF THE TEC
+!-----------------------------------------------------------------
+       DO I = 1,NTEC
+         UTECX=0.D0
+         UTECY=0.D0
+         PTEC(I) = 0.D0
+         IF(IPID.EQ.TECPID(I))THEN
+           N1=IKLE%I(TECELEM(I))
+           N2=IKLE%I(NELEM+TECELEM(I))
+           N3=IKLE%I(2*NELEM+TECELEM(I))
+           !
+           SURDET=1.D0/((X(N2)-X(N1))*(Y(N3)-Y(N1))-
+     &            (X(N3)-X(N1))*(Y(N2)-Y(N1)))
+           !
+           DET1=(X(N3)-X(N2))*(YTEC(I)-Y(N2))
+     &          -(XTEC(I)-X(N2))*(Y(N3)-Y(N2))
+           DET2=(X(N1)-X(N3))*(YTEC(I)-Y(N3))
+     &          -(XTEC(I)-X(N3))*(Y(N1)-Y(N3))
+           DET3=(X(N2)-X(N1))*(YTEC(I)-Y(N1))
+     &          -(XTEC(I)-X(N1))*(Y(N2)-Y(N1))
+           !
+           UTECX=U%R(N1)*DET1*SURDET+
+     &           U%R(N2)*DET2*SURDET+
+     &           U%R(N3)*DET3*SURDET
+           UTECY=V%R(N1)*DET1*SURDET+
+     &           V%R(N2)*DET2*SURDET+
+     &           V%R(N3)*DET3*SURDET
+
+         END IF
+         IF(NCSIZE.GT.0)UTECX=P_DSUM(UTECX)
+         IF(NCSIZE.GT.0)UTECY=P_DSUM(UTECY)
+         ALPHA=-ATAN2(UTECY,UTECX)*RTD
```

It should be noted that function $ATAN2$ might not be present in all compilers, in which case it will need to be computed by the user.

The far velocity $\boldsymbol{U_{ref}}$ will be then computed and projected along the orientation of the TEC to give U_r.

```
@@ -77,0 +367,32 @@
+         ! FIND THE FAR VELOCITY
+         IANGLE=INT(ALPHA+0.5D0)
+         XDD = XTEC(I) - DD(I)*COS(DBLE(IANGLE)*DTR)
+         YDD = YTEC(I) + DD(I)*SIN(DBLE(IANGLE)*DTR)
+         UREFX=0.D0
+         UREFY=0.D0
+         IF(IPID.EQ.DDPID(I,IANGLE))THEN
+           N1=IKLE%I(DDELEM(I,IANGLE))
+           N2=IKLE%I(NELEM+DDELEM(I,IANGLE))
+           N3=IKLE%I(2*NELEM+DDELEM(I,IANGLE))
+           !
+           SURDET=1.D0/((X(N2)-X(N1))*(Y(N3)-Y(N1))-
+     &            (X(N3)-X(N1))*(Y(N2)-Y(N1)))
+           !
+           DET1=(X(N3)-X(N2))*(YDD-Y(N2))
+     &          -(XDD-X(N2))*(Y(N3)-Y(N2))
+           DET2=(X(N1)-X(N3))*(YDD-Y(N3))
+     &          -(XDD-X(N3))*(Y(N1)-Y(N3))
+           DET3=(X(N2)-X(N1))*(YDD-Y(N1))
+     &          -(XDD-X(N1))*(Y(N2)-Y(N1))
+           !
+           UREFX=U%R(N1)*DET1*SURDET+
+     &           U%R(N2)*DET2*SURDET+
+     &           U%R(N3)*DET3*SURDET
+           UREFY=V%R(N1)*DET1*SURDET+
+     &           V%R(N2)*DET2*SURDET+
+     &           V%R(N3)*DET3*SURDET
+
+         END IF
+         IF(NCSIZE.GT.0) UREFX=P_DSUM(UREFX)
+         IF(NCSIZE.GT.0) UREFY=P_DSUM(UREFY)
+         UR=UREFX*COS(THETA(I))-UREFY*SIN(THETA(I))
```

The local nodal values will be read, i.e. U_j, V_y and h_j.

```
@@ -77,0 +399,36 @@
+         ! DO A LOOP OVER ALL THE AFFECTED NODES
+         DO INODE=1,NNODES(I)
+           IPOIN = INODES(I,INODE)
+           IF(IPOIN.LT.0)THEN !IT IS A QUASI-BUBBLE ELEMENT
+             ! FIND IELEM
+             IELEM=-IPOIN
+             N1=IKLE%I(IELEM         )
+             N2=IKLE%I(IELEM+  NELMAX)
+             N3=IKLE%I(IELEM+2*NELMAX)
+             !
+             I4=IKLE%I(IELEM+3*NELMAX)
+             X4=(X(N1)+X(N2)+X(N3))/3.D0
+             Y4=(Y(N1)+Y(N2)+Y(N3))/3.D0
+             !
+             SURDET=1.D0/((X(N2)-X(N1))*(Y(N3)-Y(N1))-
+     &            (X(N3)-X(N1))*(Y(N2)-Y(N1)))
+             !
+             DET1=(X(N3)-X(N2))*(Y4-Y(N2))
+     &            -(X4-X(N2))*(Y(N3)-Y(N2))
+             DET2=(X(N1)-X(N3))*(Y4-Y(N3))
+     &            -(X4-X(N3))*(Y(N1)-Y(N3))
+             DET3=(X(N2)-X(N1))*(Y4-Y(N1))
+     &            -(X4-X(N1))*(Y(N2)-Y(N1))
+             !
+             HI=H%R(N1)*DET1*SURDET+
+     &          H%R(N2)*DET2*SURDET+
+     &           H%R(N3)*DET3*SURDET
+             UI=U%R(I4)
+             VI=V%R(I4)
+             !
+             IPOIN=I4 ! REDEF IPOIN TO BE USED BY FUDRAG
+           ELSE
+             HI=H%R(IPOIN)
+             UI=U%R(IPOIN)
+             VI=V%R(IPOIN)
+           END IF
```

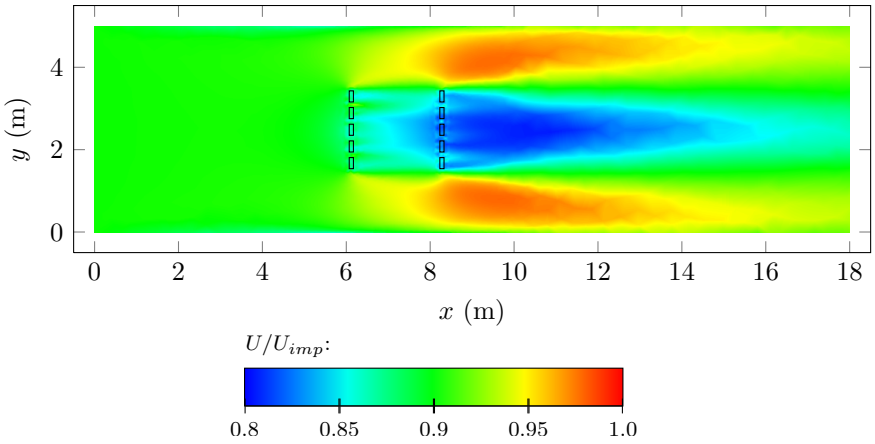

Fig. 3: Velocity contour showing the wake of 2 rows of TECs in a flume. The black rectangles show the positions of the TECs.

The two components of the source term modelling the drag force in Telemac-2D, FUDRAG and FVDRAG, can now be calculated:

```
@@ -77,0 +435,16 @@
+           !
+           IF((ABS(UR).GT.VCUT(I)).AND.(HI.GT.1.D-4))THEN
+             HALFCDSCOSTHETA=0.5D0*PI*RTEC(I)**2
+     &                       *CDTEC(I)*COS(THETA(I))
+             HALFCDSSINTHETA=0.5D0*PI*RTEC(I)**2
+     &                       *CDTEC(I)*SIN(THETA(I))
+             IF(ABS(UI).GT.1.D-4)THEN
+               FUDRAG%R(IPOIN)=FUDRAG%R(IPOIN)
+     &         -HALFCDSCOSTHETA*UR*ABS(UR)/(AREA(I)*HI*UI)
+             END IF
+             IF(ABS(VI).GT.1.D-4)THEN
+               FVDRAG%R(IPOIN)=FVDRAG%R(IPOIN)
+     &         +HALFCDSSINTHETA*UR*ABS(UR)/(AREA(I)*HI*VI)
+             END IF
+           END IF
+         END DO
```

C. Using the subroutine DRAGFO to calculate the extracted power

The subroutine DRAGFO can also be used to calculate the extracted power.

```
@@ -77,0 +451,5 @@
+!
+         PTEC(I) = CPTEC(I)*PI*RTEC(I)**2*0.5D0
+     &             *ROEAU*UR**2*ABS(UR)
+!
+       END DO
```

It can then be written in the file given by FORMATTED RESULTS FILE:

```
@@ -77, +456,41 @@
+!
+!-----------------------------------------------------------------
+! WRITING THE POWER OUTPUT
+!-----------------------------------------------------------------
+! WRITING HEADER OF FILE
+       IF((IPID.EQ.0).AND.(LT.EQ.1))THEN
+         ! FILE ID
+         POWRES = T2D_FILES(T2DRFO)%LU
+         ! HEADER
+         WRITE(POWRES,'(A)') "# TEC power result file:"
+         WRITE(POWRES,'(A)') "# Power extracted at time T"
+         WRITE(POWRES,'(A)') "# for each TEC modelled"
+         ! VARIABLE NAMES
+         WRITE(POWRES,'(A)',ADVANCE='NO') "T, "
+         DO I = 1,NTEC-1
+           WRITE(POWRES,'(A,I0.4,A)',ADVANCE='NO')"P_",I,", "
+         END DO
+         WRITE(POWRES,'(A,I0.4)') "P_",NTEC
+         ! INITIAL RESULT
+         WRITE(POWRES,'(F0.6,X)',ADVANCE='NO') 0.D0
+         DO I = 1,NTEC-1
+           WRITE(POWRES,'(F0.6,X)',ADVANCE='NO') 0.D0
+         END DO
+         WRITE(POWRES,'(F0.6)') 0.D0
+       END IF
+! WRITING RESULTS IN TIME
+       IF((IPID.EQ.0).AND.(MOD(LT,LEOPRD).EQ.0))THEN
+         ! FILE ID
+         POWRES = T2D_FILES(T2DRFO)%LU
+         ! CALCULATED RESULTS
+         WRITE(POWRES,'(F0.6,X)',ADVANCE='NO') LT*DT
+         DO I = 1,NTEC-1
+           WRITE(POWRES,'(F0.6,X)',ADVANCE='NO') PTEC(I)
+         END DO
+         WRITE(POWRES,'(F0.6)') PTEC(NTEC)
+       END IF
 !
 !-----------------------------------------------------------------
 !
       RETURN
       END
```

When using the code presented earlier, do not forget to delete the default example present in DRAGFO.

V. Example of simulations

Now that the entire user code has been given, a few illustrations of the output will be given. The simulations chosen will reproduce one of the experiment conducted during the PerAWaT project [7], for which two rows of turbines were placed in a canal. Applying a drag force in the flow will create a wake behind the TECs, see figure 3 and 4. However, the velocity close to the TEC is too high, and it is thought to be accurate at a distance greater than 10-15 diameters downstream.

VI. Concluding remarks

The code that should be used to model a group of TECs in a Telemac-2D simulation has been presented here. Nonetheless, several choices have been left to the user:

- The size of mesh elements at the position of the TEC.
- The area over which the drag force will be applied.

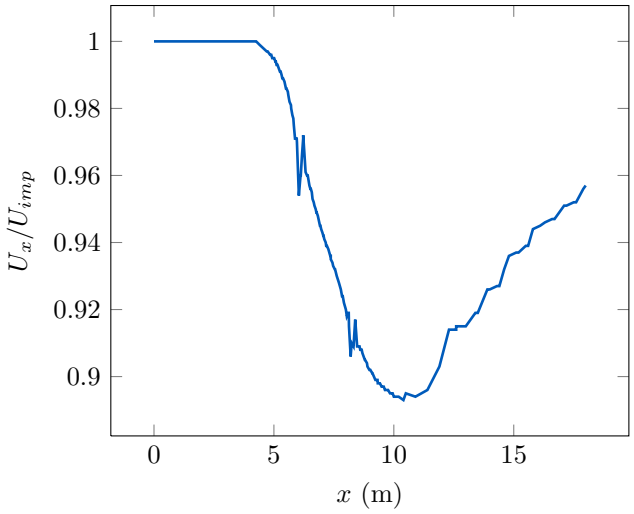

Fig. 4: Velocity profile along $y = 2.483$ m.

- The distance upstream of the TEC for which the reference velocity will be taken.

Other variables will depend on the machine modelled:

- The radius of the device.
- The orientation of the device in the flow.
- The drag coefficient.
- The power coefficient.

It should also be stated that it is not possible to get accurate velocity profiles close to the device in Telemac-2D simulations, as this would require modelling in detail each components of the TEC. The velocity modelled with this approach is thought to be valid 10-15 diameters downstream of the device.

In addition, it is recommended to use quasi-bubble elements in Telemac-2D simulations, as the presence of the TECs tend to create instabilities. It is also recommended to use an unstructured mesh around the TECs. Furthermore, the turbulence model can have an impact on the result and it should be chosen with care.

Finally, when dealing with large farms it is possible to apply the drag force of several TEC over an area covering the size of the farm (which could reduce the number of nodes in the mesh). The only modification will be to multiply surface (πR^2) used in the drag force by the number of TECs in the farm.

ACKNOWLEDGMENT

The developments presented were done and validated through the PerAWaT project, financed by the ETI.

REFERENCES

[1] E. de Paula Kirinus, C. Eadi Stringari, W. Correa Marques, and H. Barreto Matzenauer, "Harvesting the Currents Power on the Southern Brazilian Shelf," in *Proc. 20th Telemac User Conference*, Karlsruhe (Germany), 2013.

[2] D. Haverson, J. Bacon, and H. Smith, "Modelling the far field impacts of a tidal energy development at Ramsey Sound," in *Proc. 21st Telemac User Conference*, Grenoble (France), 2014.

[3] J.-M. Hervouet, *Hydrodynamics of free surface flows*. Chichester: Wyley, 2007.

[4] A. Joly, M. Andreewsky, V. Martin, S. Saviot, and C.-T. Pham, "Tidal coastal basin numerical modelling. Large scale effects of tidal energy extraction," PerAWaT WG3 WP3: EDF, Tech. Rep., 2013.

[5] A. Joly, M. Andreewsky, S. Saviot, and C.-T. Pham, "Tidal farm modelling: The Alderney Race, the Pentland Firth and the Paimpol-Bréhat sites modelled in Telemac software," PerAWaT WG3 WP3: EDF, Tech. Rep., 2013.

[6] S. Serhadlıoğlu, T. A. A. Adcock, G. T. Houlsby, S. Draper, and A. G. L. Borthwick, "Tidal stream energy resource assessment of the Anglesey Skerries," *International Journal of Marine Energy*, vol. 3-4, pp. e98–e111, 2013.

[7] T. Stallard and R. Collings, "Calibration report for Scale Model Experiments," PerAWaT WG3 WP4: University of Manchester, Tech. Rep., 2011.

The Tidal Garden concept: Numerical modelling of tidal stream turbines in channels for optimal energy extraction.

C. Cochet, D. Aelbrecht, R. Debert
Hydro Engineering Center (CIH)
Electricité de France (EDF)
Le Bourget-du-Lac, France
christophe.cochet@edf.fr

***Abstract*— The Tidal Garden concept results from the combination of existing tidal power solutions. The aim of the present article is to evaluate its performance and potential as a new cost-effective and efficient tidal energy arrangement.**

I. CONTEXT

The last decade has seen a revival of tidal power solutions development as the world is seeking cost-effective and efficient renewable power options. Today, the tidal energy landscape is formed by two main categories:

Tidal range barrages (such as La Rance tidal power plant [1]) or lagoons (such as the future Swansea Bay tidal power plant [4]); the associated technologies are mastered but require high tidal ranges to be efficient and economically feasible;

Open-sea tidal stream turbines (such as the technology developed by OpenHydro and used by EDF in the tidal demonstration project deployed off the coast of Brittany [2]); the tidal stream resource – strong tidal currents – is very localized and located on sites where offshore conditions imply heavy structural designs and difficult Operation & Maintenance access.

The idea to combine a tidal basin with tidal stream turbines fostered the proposition of the "Tidal Garden" concept – or "Marélienne" in French [5]. The concept consists in a coastal basin, outlined by breakwaters and linked with the open sea through a number of open channels equipped with arrays of tidal stream turbines; the increased flow speed in the channels allows higher energy production than with tidal turbines placed in open waters and subject to the natural tidal flow. The goal will be to maximize energy production by generating velocities as high as possible during as long as possible, while maintaining the tidal range within the basin close to the site's natural conditions to avoid or reduce the impact on the intertidal zone. The optimization parameters are: the basin geometry and equipment, the possible use of sluice gates, the dynamic control of turbines.

The Tidal Garden concept thus completes the tidal energy landscape with a solution for nearshore installations on sites with average tidal conditions.

II. GOALS

Numerical modelling is used to study the hydrodynamics of such a coastal basin and to assess tidal energy extraction possibilities by this conceptual arrangement. Note: the Tidal Garden concept also brings economical and environmental advantages [3]; however the present paper will focus on modelling and hydrodynamics.

Indeed, for a given site, hydraulic design tools are necessary to help define the best Tidal Garden layout, and simulate its energetic performance and potential impacts. EDF-CIH has thus developed a 2-level approach:

- A 0D model: the aim of this simple approach is to rapidly define a pre-optimized layout of Tidal Garden scheme, and simulate the sensitivity of hydraulic and power performance to the main controlling parameters: number of channels connecting the tidal basin and the open sea, tidal range characteristics, number of tidal stream turbines, operating mode of tidal stream turbines (dynamic control of turbines).
- A 2D numerical model based on the Telemac© software system, which is used to study hydrodynamic effects of filling and emptying the basin and the impact of tidal stream turbines in the channels and which takes into account site-specific effects (e.g. detailed bathymetry, spatial variability of tidal flows,...) on the hydraulic and generation performance of a project.

The present paper focuses on the 2D model and aims at a/ describing the work achieved so far, along with b/ the first results obtained on a generic test site and c/ presenting ongoing developments.

III. DESIGN PARAMETERS OF A TIDAL GARDEN INSTALLATION

A standard basin is basically designed as a semi-circular dyke breached with channels. The flow in and out of the channels is guided by adding converging/diverging sections at the channel extremities. Rows of tidal turbines are erected inside each channel to extract energy from the accelerated flow. The impact of this extraction is taken into account in

the simulation by adding a drag force in the surroundings of the turbines.

The main parameters that need to be defined are the following:

- Geometry: area/shape of basin (yields length of dyke), the number, orientation, length and width of channels, converging/diverging entries of channels, Strickler coefficient.
- Turbines: drag force due to each turbine, the spacing between turbines (of a same row and between rows). Note: Relation between number of turbines per row and channel width (25m per turbine), and between number of rows and channel length (100m – 5 times the turbine diameter - between 2 rows). Sensibility analyses will be needed.

A power extraction coefficient is used for computing the power output of each turbine; however it does not influence the flow calculation. All parameters related to turbine technology are based on EDF past experience and on recent studies for Paimpol-Bréhat tidal stream turbine demonstration project.

The combination of geometrical parameters and turbine spacing yields the installed capacity/total number of turbines.

Given the numerous parameters, the "right" selection of parameters is not straightforward; hence the use of the 0D model, for a multi-criteria analysis on a large number of configurations.

IV. Implementation in Telemac2D

The geometry and turbine placement are prepared using a dedicated Matlab code. The geometry is then imported in BlueKenue for the mesh generation.

Tidal conditions are imposed on the liquid boundary using TELEMAC integrated tidal model and J.-M. Janin's tidal database.

Regular head losses (in the channels and over the sea bottom) are modelled in TELEMAC2D with friction defined by a Strickler coefficient: this coefficient is defined as a function of depth and of the bottom type (e.g. the channels are assumed to be paved with concrete).

The DRAGFO routine is customized to implement turbine drag and energy extraction. Drag is a function of current speed, diameter and drag coefficient of the turbines. The classical drag force formula is encoded:

$$F_{drag} = 0.5\ \rho\ S_u\ C_d\ V^2, \quad (1)$$

with ρ the water density, S_u the sweep area of a turbine (m^2), C_d the drag coefficient and V the flow speed. In a first attempt, drag was added on each mesh nodes where turbines are installed; this resulted in diverging results. In order to avoid these numerical discrepancies, drag is allocated as density zones around the turbine rows (as shown in Fig. 2).

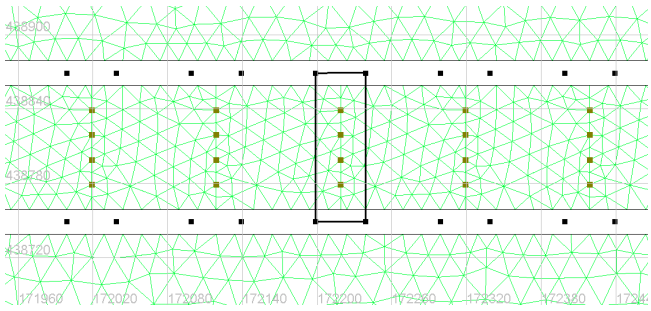

Figure 1. Mesh area around a row of turbines where drag force is applied.

The DRAGFO routine also computes the power output of each turbine, at each time step, using equation (2):

$$P = 0.5\ \rho\ S_u\ C_p\ V^3, \quad (2)$$

with C_p the turbine capacity factor which depends on turbine performance.

A result file is generated at the end of calculations to extract the time series of flow speed, water depth and power output at each turbine location (node).

It is considered that under 0.5m/s of flow speed, tidal turbines do not extract energy from the flow and drag is disregarded. Control of the turbines is important to maximize power generation. Start and stop sequences are managed during the drag calculation by adding time and flow speed constraints.

Configurations with sluice gates, temporarily isolating the basin from the sea and artificially increasing the head (and thus flow velocity) for better energy extraction are also tested. A customised CORPOR routine is used to this effect: an artificial porosity imposed on mesh zones barring the channels allows closing and opening the channels at will. The initial implementation consisted in closing the full length of the channels; however, this resulted in water filling the channels from both ends when the porosity was removed. The modified mesh zones were thus limited to a fraction of the channel length and a linear evolution of the porosity with time was implemented. Although this method results in some water flowing through the closed channels, the water level in the basin is kept sufficiently constant over the closure period. In terms of control, the sluice gates can be opened for a given head or after a given time.

The duration of simulations can be adjusted: a period of 12 hours 24 min can be simulated in order to get results during a complete semi-diurnal tidal cycle while calculations covering a 14-day period allow the study of the tide amplitude influence on the energy extraction and, by extrapolation, the evaluation of production over a complete

year. It takes around 30 min to run the first type of simulation and 150 min to run the second type (on a dual processor (3.3-GHz) standard PC configuration).

V. APPLICATION TO A TEST SITE

To test the implemented model, a Tidal Garden installation is conceived: the mesh used for this study covers a domain of 40 by 50km located on the French side of the English Channel, where the mean and spring tide amplitudes are respectively 6.3m and 9m. The dyke is a 5.6km-radius semi-circle with a changeable number of channels, forming a 50km² basin. This geometry is represented on **Error! Reference source not found.**3. Bathymetry is modelled to achieve acceptable depths in the channels: from 50m in the open ocean, a nearshore slope raises the bottom to 20m in the channels and emerged heights at the land boundaries (lower side of the mesh on the figure below). It does not exactly reproduce the real shore, so the results shall be considered theoretical. The length of finite element edges varies from approximately 3km on the open ocean boundaries to 10m in the channels.

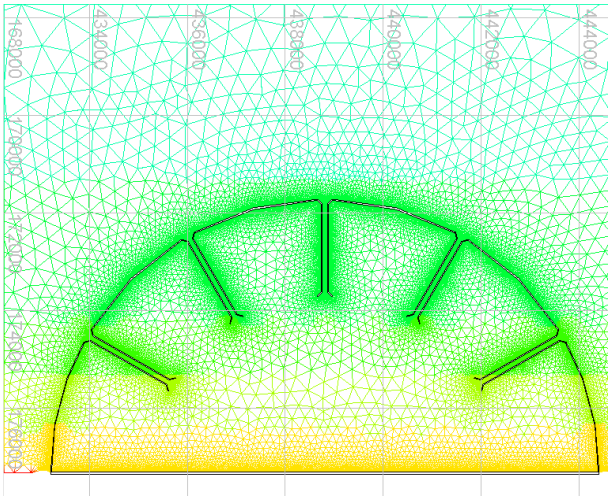

Figure 2. Modelled test site with 5.6km-radius dyke and 5 channels.

The first results show that, for a constant cumulative width of channel (600m), an installation with 5 channels generates the highest flow speeds compared to configurations with smaller numbers of channels. Because of current tidal turbine technology limitations, a flow velocity of at least 4m/s is necessary to produce more than 2MW per turbine. Without any tidal turbines, a flow speed of 4m/s is reached but energy extraction by the tidal turbines has an impact on the flow speed in the channel: speeds decrease to 3m/s during the flood and under 2m/s during the ebb; at these speeds, the energy production would drop significantly. Flow speeds in the 5-channel configuration are higher because of the smaller width of each channel. However, this flow constriction has a direct impact on the tidal amplitude in the basin, which is to be considered for environmental reasons.

According to these results, the channel width needs to be reduced in order to raise flow speeds and the energy output of the installation. A configuration with 3 channels, 10 rows of tidal turbines per channel and 3 tidal turbines per row is then tested to validate the interest of a reduced width (75m per channel). Fig. 3 shows that flow speed in the channels without the tidal turbines reaches nearly 5m/s during the flow and 3m/s during the ebb. Once the tidal turbines are in place, flow speed is maintained at 3.5m/s during the flow and 2.5m/s during the ebb.

In terms of controls, sensibility studies on the control parameters of the turbines (shut-off velocity, start sequence timing) have shown that it is more efficient to limit the number of generating tidal turbines to maintain a higher flow speed (around 4m/s) instead of working with all tidal turbines at lower flow speeds.

In order to increase the flow speed even more, a configuration with 5 channels (50m width), 20 rows per channel, 2 turbines per row and sluice gates in each channel is simulated. Once the basin is filled, the sluice gates are maintained closed until a 2-meter head between basin and sea is reached. According to Fig. 4, the water level in the basin is efficiently maintained constant during the gates closure. Flow speeds reach 5.6m/s during the flood and more than 4m/s during the ebb in the case without turbines; when turbines are activated, the velocities reach respectively 4m/s and 3m/s (see Fig. 5).

In terms of performance and energy output, 3 configurations have been compared and are presented in Table I:

- All cases are based on a 50km^2 basin with a mean tidal amplitude of 7.5m; the channels are not equipped with sluice gates;
- Cases A and B present the same total channel width (300m), but case A is equipped with twice as many turbines;
- Cases B and C present approximately the same number of turbines (respectively 90 and 72), but case C has a narrower total channel width (160m vs. 300m).

The obtained results show that a significant amount of electricity can be generated by a Tidal Garden installation; however, the load factor remains below 25% (estimated load factor for a standard tidal power plant); furthermore, the highest load factor is obtained for the site yielding the highest tidal range impact.

For all the configurations studied, the use of sluice gates allows to significantly increase the power output, up to two

fold, as well as the load factor. This higher production leads to a different evolution of the tidal range inside the basin: as with traditional tidal range plants, the high-tide slack periods will last longer, thus increasing the risk of sedimentation. Determining the balanced trade-off between power output and environmental impact will require further studies, in both hydrodynamics and sediment transport.

TABLE I

Cases		**A**	**B**	**C**
Total aperture	m	300	300	160
Number of channels & rows/channel	-	5/20	3/10	2/12
Number of tidal turbines per row	-	2	3	3
Installed power	MW	400	180	144
Annual electricity production	GWh	**424**	**245**	**290**
Load factor	-	0.12	0.16	0.23
Maximum impact on tidal range	m	3.9	1.4	5.1

VI. FUTURE WORK

The first results obtained highlight the complexity of optimising a Tidal Garden installation due to the large number of parameters. Some considerations also need to be more precisely defined (e.g. acceptable limits of the basin tidal range evolution). Economical considerations shall also be included to guide the optimisation process (e.g. should the number of turbines be reduced to achieve higher load factor?). Additional technical aspects to be studied are: optimisation of geometrical parameters (e.g. converging/diverging sections), turbine and sluice gate control methods; sediment transport modelling and siltation risk evaluation; turbine wake and turbulence dissipation.

REFERENCES

[1] Aelbrecht D., Lafon F., Gérard N. (2014-a). Tidal stream demonstration project at Paimpol-Bréhat (France). Proceedings of Marine Energy Brest 2014, Oct. 15-16, 2014.

[2] Aelbrecht D., Derlot L. (2014-b). La Rance tidal power plant (France) : past, present, and future. Proceedings of Marine Energy Brest 2014, Oct. 15-16, 2014.

[3] Aelbrecht D., Cochet C., Debert R., Lempérière F. (2015). Tidal Garden concept: development of a hydraulic operating model for optimizing its design and simulating its performance. Proceedings of HYDRO 2015, Nov. 26-28, 2015 (unpublished).

[4] Hughes M. (2015). Swansea Bay tidal lagoon. Presentation at ICOLD'2015 conference, Question 96 session. June 2015, Stavanger (Norway).

[5] Lempérière F. (2014). Utilisation innovante des hydroliennes : les maréliennes. Les Techniques de l'Ingénieur, RE-178, 4-2014.

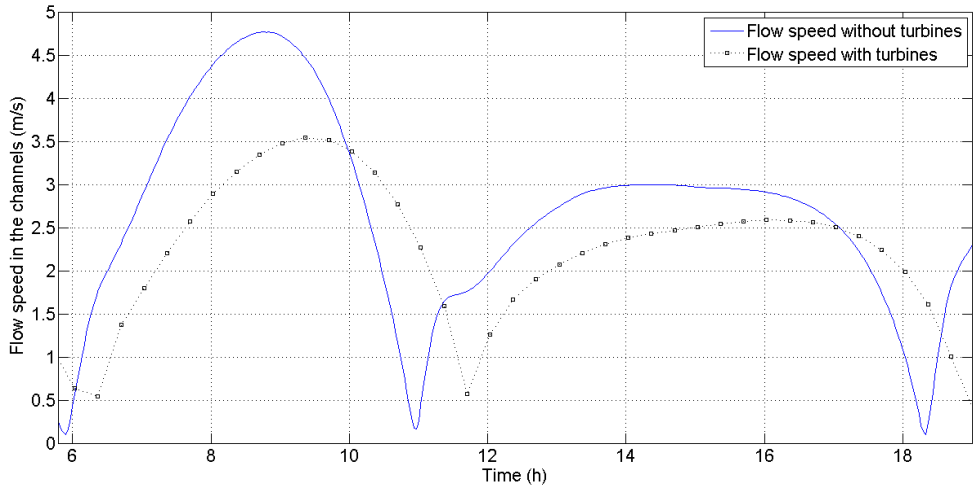

Figure 3. Flow velocity (average of the 3 channels), with and without turbines.

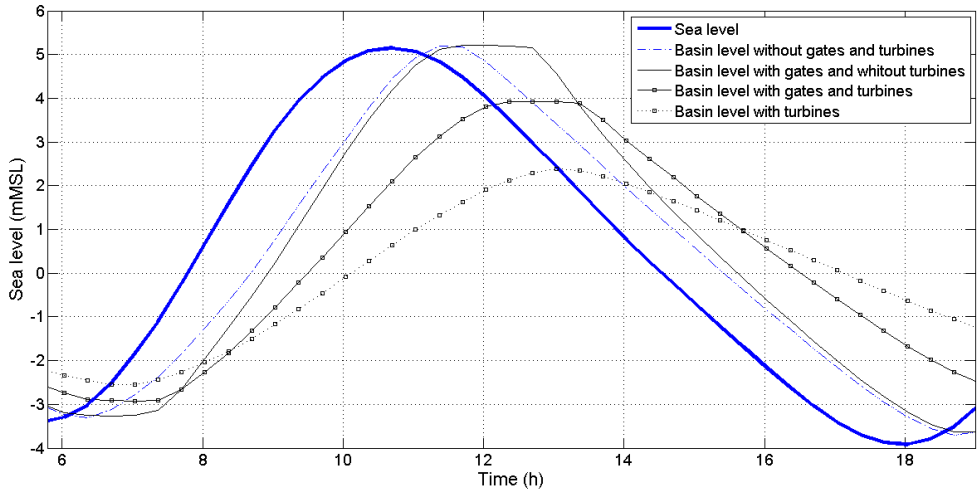

Figure 4. Achieved basin levels with different configurations.

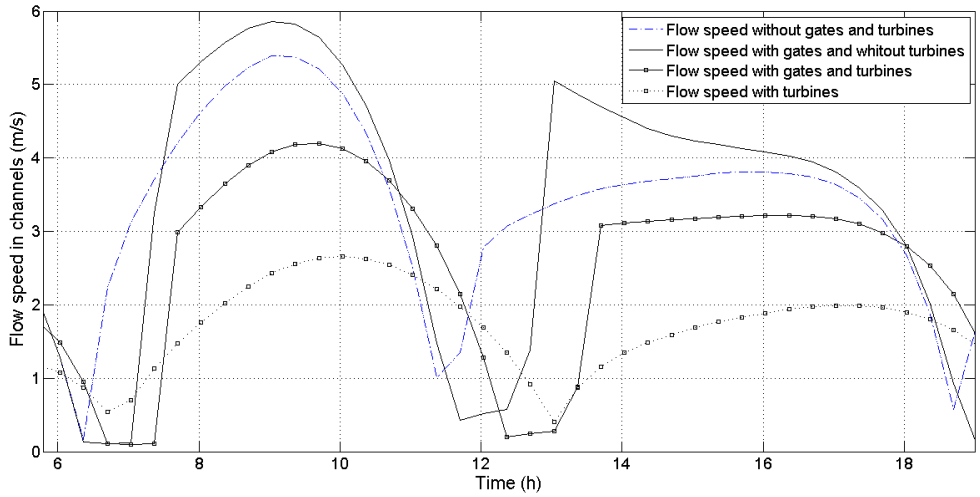

Figure 5. Achieved velocities (average of 5 channels) with different configurations.

Characterizing the tidal energy resource of the West Anglesey Demonstration Zone (UK), using TELEMAC-2D and field observations

Marco Piano, Sophie Ward, Peter Robins, Simon Neill, Matt Lewis, Alan G. Davies, Ben Powell, Aled Wyn Owen
Centre for Applied Marine Sciences (CAMS)
Bangor University, School of Ocean Sciences
Menai Bridge, UK
m.piano@bangor.ac.uk

M.Reza Hashemi
Department of Ocean Engineering and Oceanography
University of Rhode Island, Narragansett Bay Campus
Rhode Island, US

***Abstract* — A TELEMAC-2D hydrodynamic model has been applied to simulate high-resolution spatial distribution of currents in a proposed tidal stream demonstration zone. Complementary field observations provide both validation and vertical water column profile information at four sites across the region. We use the datasets to assess the theoretical power extractable from a generic tidal energy converter for deployments over the period of observation and compare these values to a typical average simulated month assessed over a 29.5 day lunar cycle. The results suggest that careful consideration should be given to micro-siting of devices within the zone as potential annual energy yield may increase by up to 180% between sites based on depth-averaged velocities of the undisturbed resource.**

I. INTRODUCTION

Strong tidal currents offer an apparent renewable and predictable resource from which we may extract energy to convert to electricity. However, the yield of a particular tidal energy converter (TEC) must be calculated relative to the overall energy cost, which includes deployment, maintenance and decommissioning. The yield will depend primarily on the resource available and the ability of a given device to convert that resource into electrical energy based on its characteristics [1]. Initial site assessments might focus on peak current flows, however attention should be given to the overall nature of the hydrodynamic resource as well as other practical constraints such as water depth, bathymetry, morphology and proximity to ports and grid infrastructure [2].

The Crown Estate (TCE), as manager of the UK seabed, announced plans in October 2013 to lease wave and tidal demonstration sites around the UK to encourage marine renewable technology developers to accelerate their efforts in UK waters. The West Anglesey Demonstration Zone (WADZ) in North Wales has been outlined for tidal stream energy development. TCE set out indicative guidelines in 2013 [3] for the principal requirements of demonstration zones - the criteria include having an appropriate energy resource, proximity to infrastructure, and the demand for opportunities to grow the marine sector. TCE constrained the resource criteria to include a mean spring peak velocity (V_{msp}) > 1.5 m s^{-1}, and a minimum water depth of 5 m (LAT).

For a tidal energy site to be considered desirable for commercial scale extraction, a number of key hydrodynamic criteria should be assessed, not least of these is the strength of the currents. However consideration should also be given to the direction of flow, as sites with rectilinear currents are generally more desirable for TEC devices, especially those without yaw capability. In this paper we use a TELEMAC-2D model to assess the WADZ region and consider the siting of a generic tidal stream energy converter at four sites where current measurements have been observed by seabed moored acoustic Doppler current profilers (ADCP). Most importantly, through this work we have significally improved the overall characterisation of the tidal energy resource for this region. Further, our assessment shows considerable spatial and temporal variability within the WADZ, suggesting that array leasing and device micro-siting requires careful consideration.

II. CASE STUDY

A. West Anglesey Demonstration Zone

The region to the west of Holy Island, Anglesey, UK (Fig. 1) has been selected for the TCE tidal stream demonstration zone project, due to strong currents experienced around this section of coast, over a relatively uniform water depth to seabed. The strong currents are created, for the most part, by a semi-diurnal Kelvin wave that propagates through the Irish Sea, generating large tidal ranges along the Welsh coast and strong tidal flows through restricted channels and around headlands and islands such as Anglesey. The WADZ can essentially be described as a headland with 'fixed' head differences in accordance with [4] The zone sea space covers an area of approximately 38 km^2, with a mean water depth of 38.4 m and V_{msp} is estimated by TCE to be 1.7 m s^{-1}. There is the potential for up to 100 MW of grid connected generating capacity [5]. Other sources estimate peak spring tide currents (V_{pk}) in excess of 2.5 m s^{-1} across large areas of the region [6] [7] [8]. Many of these studies are based on coarse resolution shelf scale models, or

analysis using a limited number of harmonic constituents with the potential for discrepancies and overestimation of the resource because energy flux within a site is related to the cube of the velocity and spatial variation will exist in flows over finer scales [7] [4]. Hence, validated high resolution regional models, simulated over a suitable time frame will provide better estimates.

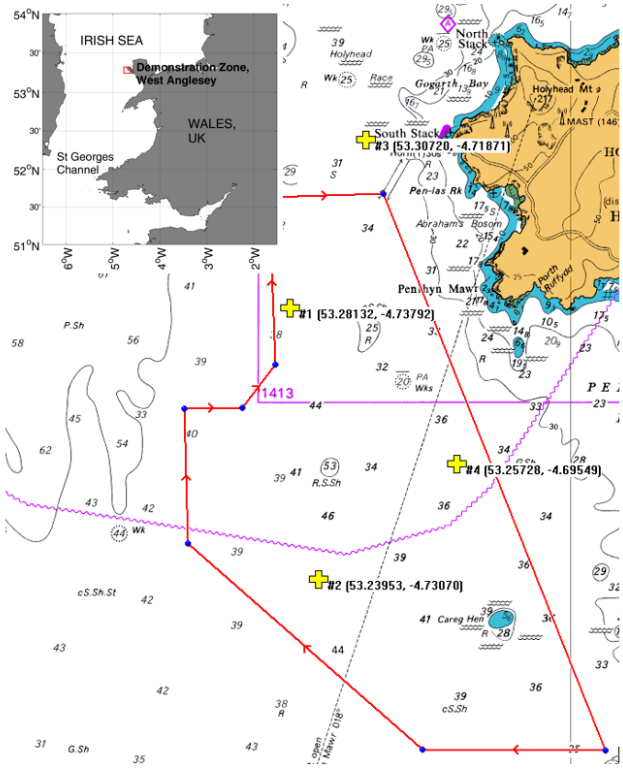

Figure 1. The region to the west of Holy Island, Anglesey with the area outlined for the tidal demonstrtion zone (red) and the position of four seabed moored ADCP stations (yellow crosses).

B. *Tides in the region*

Tidal stream currents are, in general, predictable throughout time, controlled by the movements of the earth-moon-sun system. However complexities exist when predicting currents, more so than for surface elevations, including variations in the vertical current profile as well as nonlinear and non-sinusoidal (asymmetric) behaviour in space and time: for example caused by wind-generated turbulence, eddy systems near complex bathymetry and steric or freshwater influence on density currents e.g. [2].

Tidal stream power patterns in the WADZ are dominated by a 25 h lunar day cycle created by the combination of the M_2 and S_2 semi-diurnal harmonic constituents, supplemented by smaller (diurnal and other) constituents such as O1 and P1. Some variation occurs between successive fortnightly cycles due to the influence of these smaller constituents (Fig. 2). Nevertheless, the monthly cycle of currents is relatively constant throughout the year.

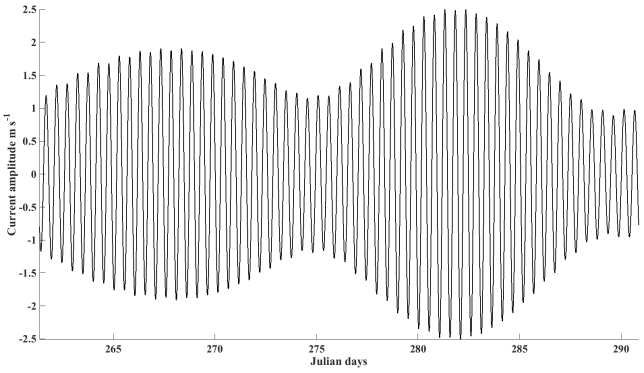

Figure 2. Amplitude and phase of depth-averaged tidal currents at ADCP station #1 in the WADZ (2014) for a complete lunar cycle as derived from five of the main harmonic constituents (M_2, S_2, N_2, O_1, K_1) using MATLAB T_TIDE analysis of observations.

C. *Site characterization*

In general, present horizontal-axis turbine technologies dictate that, for maximum rated power to be extracted, peak spring tidal velocities should exceed around 2.0 m s^{-1} in water depths of up to 50 m. However, this optimisation is driven by demand for sites that experience strong tidal flow, and severely limits the available sea space around the world where such technology can be economically deployed. Moreover, device operations in such extreme marine environments are difficult in practice, and wave-current interactions are also potentially significant (i.e., negatively affecting the available power). Present, forward-thinking research engages with the concept of lower-energy turbine optimisation, whereby available sea space is vastly increased, currents are rectilinear and less influenced by waves, and the environment is generally less harsh for engineering activity [7] [8].

The intensity of the hydrokinetic resource available for power conversion is proportional to the flow speed and for energy extraction this can be commonly defined in terms of the kinetic power (W) available, where the generated output from a turbine is calculated using:

$$P_{ki} = \frac{1}{2}\rho A \bar{U}^3 C_p \qquad (1)$$

where ρ is the density of seawater (1025 kg m^{-3}), $\bar{U}$ the depth-averaged flow velocity (m s^{-1}), A (m^2) is the swept area of the turbine blades upon which the flow acts and C_p is an overall coefficient of performance. In order to determine the best resource and likely generation rate from the turbine it is essential to understand the power available theoretically at any given location. Usually the kinetic power density available at a tidal energy site will be described in terms of its kinetic flux per unit area and an average value cited for site feasibility assessment studies. Here, we have defined this value as the average power density (W m^{-2}) that is output over the period of a complete lunar cycle (29.5 days),

which is the theoretical power available per unit area of the vertical water column:

$$APD = \frac{1}{2}\rho\frac{1}{n}\sum_{i=1}^{n}\bar{U}_i^{\,3} \qquad (2)$$

In Eq. 2, i is the index of ensembled time increments $\bar{U}_i$ is the simulated velocity at that time step and n is the total number of time intervals (over a lunar cycle in this case). The economically viable threshold for potential site development will be determined by a number of factors.

III. Methodology

We have developed a high-resolution numerical ocean model for the entire Irish Sea, and applied it to simulate the tidal currents in the Anglesey region. In this way, the tidal stream resource has been assessed, including the spatial and temporal variability. The TELEMAC software suite has been used in previous studies to assess regional coastal environments at high spatial resolution [9] [10] [11]. This method of hydrodynamic characterization was chosen here due to its relative robustness when modelling near-shore locations and for its computational efficiency over large domains (i.e. using an unstructured grid to optimize resolution). *In-situ* measurements are presented of surface elevations from fixed tide gauges and tidal currents from moored ADCP stations, collected for this study. The measurements give an accurate assessment of the flow regime at particular times and enable the accuracy of the model to be validated.

A. Observations

Two Teledyne RDI sentinel V_{50} 500kHz, 5-beam ADCP instruments, fixed in trawl-proof, seabed mounted moorings were deployed concurrently in September 2014 and again in March 2015 at the locations shown in Fig. 1. The instruments were programmed with varying temporal resolution to capture both tidal and turbulent fluctuations. The ADCP measurements provide more than 60 days of data. The initial ADCP deployments (stations #1 and #2) were to the west of the WADZ and measurements were taken at turbulence frequencies (2 Hz) and tidal frequencies (0.067 Hz). Subsequent ADCP deployments were to the east (stations #3 and #4). A precision of <1 cm s^{-1} was achieved in all cases. These data were ensembled into 10 minute (#1, #3, #4) or hourly (#2) averages, with 0.6 m vertical resolution, for subsequent analyses and comparison against model outputs. Surface data affected by boundary layer interactions was omitted. Water depths at the deployment locations are approximately 30 - 40 m at lowest astronomical tide (LAT), with a mean tidal range of approximately 5.5 m.

B. Hydrodynamic Model

TELEMAC-2D (v6.3r2) is an open source, tidal model that solves the depth-averaged Saint-Venant free surface flow equations derived from the Navier-Stokes equations, for momentum and continuity [12]. A finite-element model grid has been applied to a domain encompassing the Irish Sea (approximate latitude 50°N to 56°N, longitude 8°W to 3°W, Fig. 3).

In regions where current velocities are high and bathymetry is shallow, the water column is vertically well mixed and therefore depth-averaged velocities can provide a good approximation of the flow characteristics. The vertical acceleration caused by pressure gradients due to the sloping seabed is small in the region around Anglesey, and therefore the hydrostatic assumptions of the model remain valid [10].

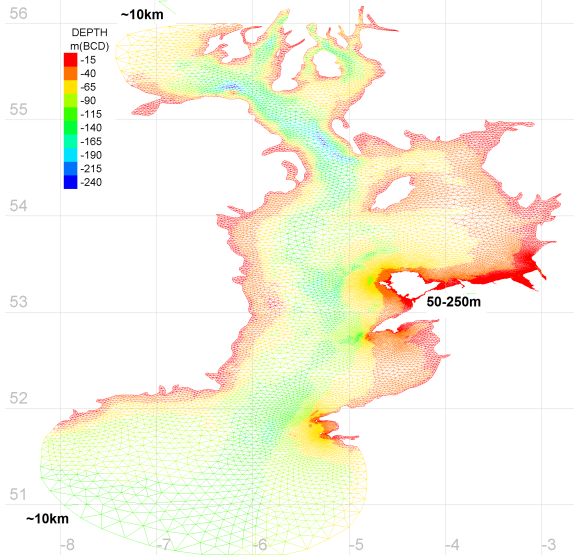

Figure 3. TELEMAC-2D Irish Sea model domain unstructured bathymetric mesh with depth profile given in metres below chart datum. Horizontal resolution at open boundaries and for the WADZ are indicated.

TELEMAC also uses an unstructured grid allowing the resolution of the mesh to be refined in areas of greater interest to the study. The mesh resolution is coarse (~10 km) at the model boundaries, increasing to 50 – 250 m around the Anglesey coast. The mesh is mapped onto gridded Admiralty Digimap bathymetry having horizontal resolution of approximately 30 m [13] and is corrected to mean sea level (MSL) using the UKHO VORF dataset [14]. TELEMAC-2D has the option of using tidal prediction boundary forcing [15]. We used the TPXO tidal database which contains up to 13 harmonic constituents (M_2, S_2, N_2, K_2, K_1, O_1, P_1, Q_1, M_4, MS_4, MN_4, M_f and M_m) on a structured grid of 0.25° resolution [16] [17]. TELEMAC utilizes both surface elevation change and the deduced horizontal component of current at the boundaries, interpolating between grid points where the mesh is less coarse. Note that only TPXO tidal forcing was applied to the model - additional forcing (e.g. wind, temperature, pressure) was omitted for this study, since astronomical tides dominate the current signal throughout the study region.

1) Simulations

The model was run for a 36 day period, discarding a 24 hour spin-up to provide 35 days of output. January 2014 was

chosen as a typical month in the year to run simulations, based on a comparison of mean predicted tide levels at Holyhead (2008 to 2026) from the British Oceanographic Data Centre (BODC) and monthly data values taken from the UK Hydrographic Office (UKHO) Admiralty Tide Tables (Table I).

TABLE I.

TIDAL RANGE PARAMETERS FOR HOLYHEAD

Values in metres above chart datum	*BODC (2008 - 2026)*	*ATT January 2014*
HAT	6.33	6.30
MHWS	5.66	5.60
MHWN	4.51	4.40
MLWN	2.02	2.00
MLWS	0.71	0.70
LAT	0.00	0.00

A water density of 1025 kg m^{-3} was used, wetting and drying of intertidal areas was included, as was the Coriolis effect. A simple approach was applied to model friction at the seabed across the whole domain using Chezy's law and a fixed friction coefficient value based on:

$$C = \frac{R^{1/6}}{n} = \frac{\left(\frac{zh}{2\sqrt{1+z^2}}\right)^{1/6}}{n} \quad (3)$$

where R is the hydraulic radius of the channel, in this case a triangular channel with approximate dimensions, 80 km wide (z) and 110 m deep (h) assuming that the largest channel into the domain has the greatest influence on dynamics, and n is the Manning roughness coefficient for a natural channel (0.030). The model time step was set at 10 s and graphical outputs were at 600 s intervals.

2) Validation

Simulated results are compared against *in-situ* observations for the amplitude and phase of the dominant harmonic constituents (M_2 and S_2) for surface elevation change at ten primary tide gauge stations and for currents using ADCP data from locations across the Irish Sea. The root mean square error (RMSE) of the model when compared with the observational data for amplitude and phase of M_2 and S_2 constituents are given in Fig. 4 together with the associated percentage variance scatter index. The normalised RMSE given by:

$$NRMSE = \frac{RMSE}{mean(obs)} \quad (4)$$

reveals a modelled error in M_2 surface elevation amplitude and phase of 4.3% and 0.9%, respectively. For S_2 the normalized errors are 6.5% (amplitude) and 2.0% (phase).

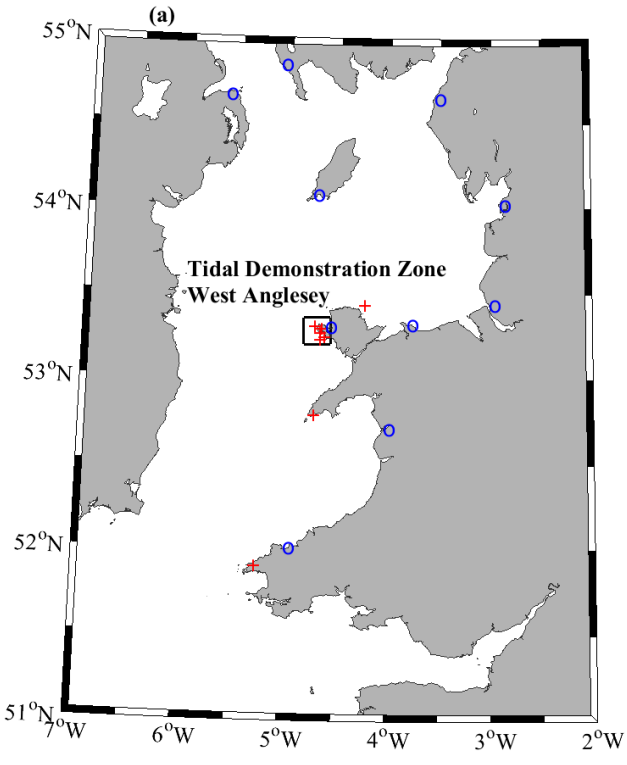

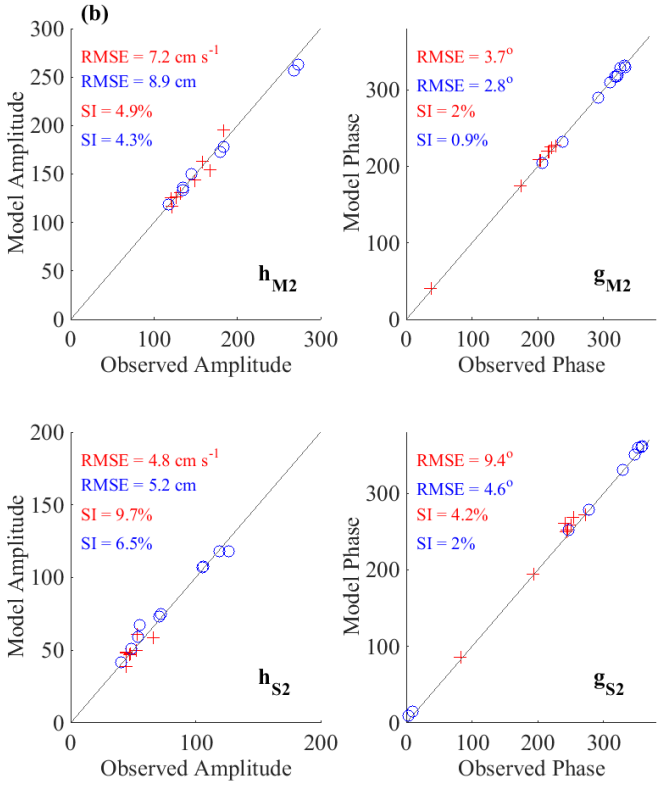

Figure 4. Map (a) indicates model validation positions of primary tide gauge stations (blue circles) for surface elevation and ADCP moorings (red crosses) for current amplitudes. Subplots (b) indicate regression analysis of amplitude, *h* and phase, *g* for M_2 and S_2 harmonic constituents derived from MATLAB T_TIDE analysis.

Similar evaluation for tidal currents reveals values of 4.9%, 2.0%, 9.7% and 4.2% respectively. Direct time series analysis of modelled velocity magnitude compared to depth-averaged observed ADCP data (Fig. 5) reveals good correlation between predicted and observed values for a 30 day time series which covers a complete lunar cycle over the duration of the observational deployment. Observed RMS current velocity (V_{rms}) for this analysis was 1.26 m s^{-1}, the simulated value for the same period was 1.29 m s^{-1}. Depth-averaged observational and modelled V_{pk} for this period were 2.52 m s^{-1} and 2.47 m s^{-1}, respectively. The extent to which flow magnitude measurements between predicted and actual regimes differs can be illustrated using regression analysis (Fig. 6), where an ideal one-to-one relationship would be identified by a line of best fit with an R^2 value equal to one. Any bias in the system is highlighted by a shift towards either the observed or predicted data. Here we see good correlation (R^2 = 0.92) between modelled values and observations with a slight over prediction by the TELEMAC-2D model.

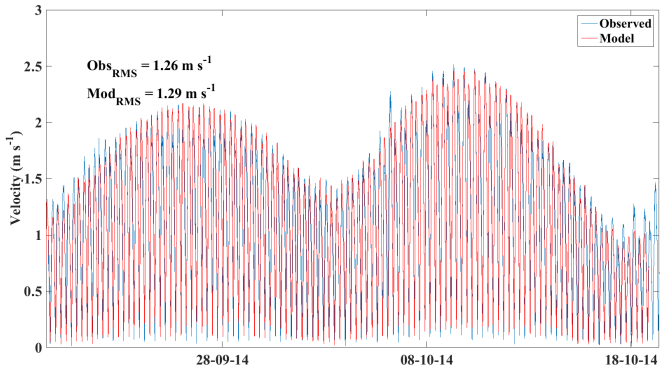

Figure 5. Simulated versus observed depth-averaged current speed for a complete lunar cycle at ADCP station #1.

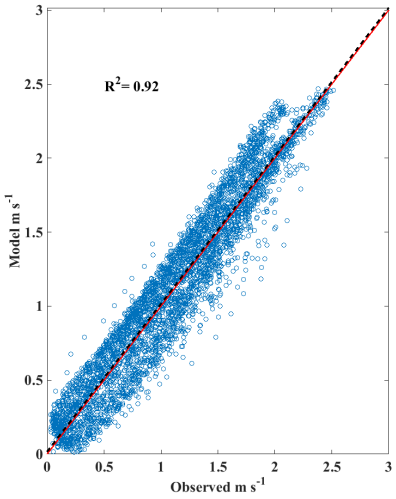

Figure 6. Regression analysis simulated versus observed current speed indicating correlation between the two datasets and any bias in the model. The red line indicates a perfect R^2 =1 fit, the black dashed line shows that 8% variance exists.

IV. RESULTS

Current speed and associated directionality, along with potential power density and annual theoretical energy yield available from the undisturbed raw resource at the four ADCP stations have been assessed and the results presented in Tables II and III.

A. Variability of flow

1) Velocity magnitude

The spatial distribution of currents is assessed using modelled outputs and plotted in Fig. 7 based on a complete lunar cycle. Significant variability across the WADZ and its surrounding area can be seen with a clear north – south divide. The strongest currents occur in the northeast close to headlands, where the tidal flow is constrained and enhanced. Mean (V_{avg}) and peak (V_{pk}) simulated velocities reach 1.6 and 3.7 m s^{-1}, respectively. For typical tidal conditions (i.e. based on M_2 and S_2 harmonics only) the flow reaches 3.1 (mean spring peak) and 1.7 m s^{-1} (mean neap peak). Across more than 50% of the WADZ V_{pk} exceeds a velocity of 2 m s^{-1}, while V_{msp} exceeds 1.7 m s^{-1}.

For micro-siting of devices to maximize potential power generation, it is important to understand where current velocities will exceed a specific threshold (e.g. device cut-in speed), and for what proportion of time this is achieved. In Fig. 8 the time that depth-averaged flow is in excess of 0.5, 1.0 and 2.0 m s^{-1} is plotted as a percentage of the total lunar cycle, with 25%, 50% and 75% exceedance times given as filled contours. Again the northeast region of the WADZ has the greatest potential for accessing highly energetic flows, which are sustained for longer periods of time.

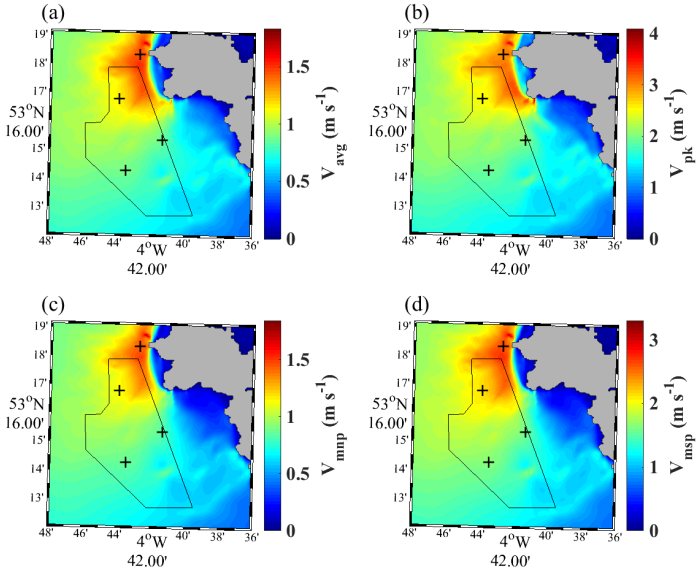

Figure 7. TELEMAC-2D simulated velocity magnitudes across the WADZ (black polygon). The four ADCP stations are marked as black crosses. A complete lunar cycle was assessed and mean (a), peak (b) mean neap peak (c) and mean spring peak (d) values are indicated.

2) Asymmetry and rectilinear misalignment

Peak current magnitude vectors (interpolated into an array of 100 vectors) are plotted in Fig. 9 (a) (as relative vector sizes), where the relative flood and ebb peak magnitude and direction from the four ADCP stations (Figs. 9 (b) to 9 (e)), show flood-dominance from station #1, #3 and #4, and ebb dominance otherwise. Even modest asymmetry between ebb and flood regimes leads to structural loading complexities, cavitation effects and cyclic loading of devices with stronger power generation occurring over one half of the tidal cycle [2] [18].

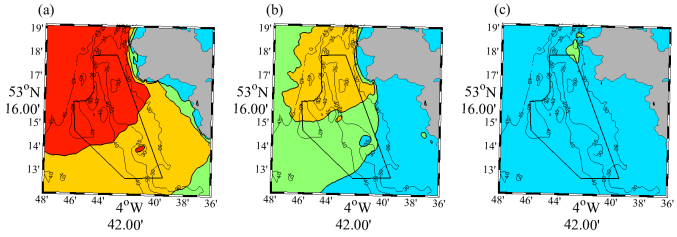

Figure 8. Contour plots indicating areas in the WADZ where time in excess of (a) 0.5 m s^{-1}, (b) 1 m s^{-1} and (c) 2 m s^{-1} occurs for >25% (green), >50% (yellow) and >75% (red) of a lunar cycle, 5 m depth contours are indicated.

Across the majority of the region, near-symmetrical, rectilinear flows exist, except in areas close to land where steep bathymetry and topographical changes combine to create turbulent eddy systems and misalignment in the ebb and flood direction. Rectilinear misalignment in ebb and flood direction in Table II is given by the absolute difference of peak direction values:

$$\theta_{assym} = \left|\left|\theta_{flood} - 180\right| - \theta_{ebb}\right| \quad (5)$$

where a perfectly rectilinear tidal regime results in an asymmetry of zero degrees. No region contains truly rectilinear currents, however turbine performance and energy yield should be greatest where currents remain more rectilinear [19]. In agreement with the model, measured currents from the ADCPs that are further offshore are more rectilinear than those closer to shore.

3) Vertical distribution of velocity

Understanding the vertical structure of water column velocity is important for resource assessment of tidal stream sites and subsequently for placement of tidal stream devices [20]. Matching the turbine rotor position to the most effective flow conditions is key to optimising power extraction as power generated is ultimately derived from the cube of the current velocity (Eq. 1). Flow analysis of the water column at the four ADCP stations (Fig. 10 (a) to (d)) again reveals much higher flows to the north and particularly in the northeast, where near bed velocities can reach sustained flows of 2 m s^{-1} at station #3 during spring tides. Again we see evidence of ebb dominance at station #2 with higher velocities during the ebbing tide.

4) Undisturbed theoretical power extraction

A simple way to visualize the available power that can be extracted at a site is to plot velocity and power histograms that indicate the percentage of time that useful power may be generated over the total time of observation. Power density is calculated by applying a time series of velocity ensembles at a specified height above the seabed to Eq. 2 prior to any averaging. Here, we have considered two hub heights (15 and 25 m) at each ADCP station for comparison of vertical distribution of the resource. As indicated by Fig. 10 (f), the apparent power density at the most energetic site (station #3), reaches almost 14 kW m^{-2} at the higher hub position, where friction effects are weaker. Also power density values greater than 3 kW m^{-2} are sustained for longer periods than is the case further south and west.

Next we consider the placement of a generic TEC in the WADZ to assess the theoretical (undisturbed) resource available, using both modelled and observed velocities. This method provides the best approach as spatial variability in energetic tidal stream locations limits the extrapolation of currents to a few tens of metres. Therefore using spatially aggregated power density plots may not be viable for site feasibility studies [7] [21]. We apply depth-averaged velocities to simulate the power generated by a theoretical generic turbine having a rotor diameter of 16 m, a cut-in speed of 0.5 m s^{-1}, a rated speed of 2.0 m s^{-1} and an efficiency of 0.38 at cut-in, linearly increasing to 0.45 at rated output. The power curve generated by such a device is shown in Fig. 11 (a). Subsequent time series of theoretical output power at each ADCP station are shown in Figs. 11(b) to 11(e) and the performance of the TEC at each site is given in Table III. We see that time in excess of cut-in and rated speeds will increase when positioned to the north of the region and that annual energy yield potential will increase by up to 180% between sites based on observed calculations.

TABLE II.

CURRENT VELOCITY, EBB/FLOOD ASSYMETRY AND APD AT THE FOUR OBSERVATION STATIONS

	ADCP #1	***ADCP #2***	***ADCP #3***	***ADCP #4***
Mean velocity magnitude (m s^{-1})	1.11	0.91	1.35	0.87
Peak velocity magnitude (m s^{-1})	2.52	2.01	2.72	2.02
Mean spring peak velocity (m s^{-1})	2.11	1.78	2.46	1.61
Mean neap peak velocity (m s^{-1})	1.05	0.86	1.28	0.82
Θassym (deg)	6.90	1.02	12.32	4.70
Apparent power density (kW m^{-2})	1.32	0.75	2.16	0.61

TABLE III.

COMPARISON OF THE UNDISTURBED DEPTH-AVERAGED THEORETICALLY AVAILABLE RESOURCE ACROSS THE WADZ REGION

	TEC theoretical performance characteristics

	Observations				*Model*			
	#1	#2	#3	#4	#1	#2	#3	#4
Time cut-in speed exceeded (%)	81	75	85	74	80	72	84	76
Time rated speed exceeded (%)	7	<1	21	<1	10	<1	24	<1
Potential annual energy yield (GWh)	1.0	0.6	1.4	0.5	1.0	0.5	1.5	0.5

	TEC theoretical performance characteristics							
	Observations				*Model*			
Capacity factor (%)	29	17	43	14	31	15	46	15

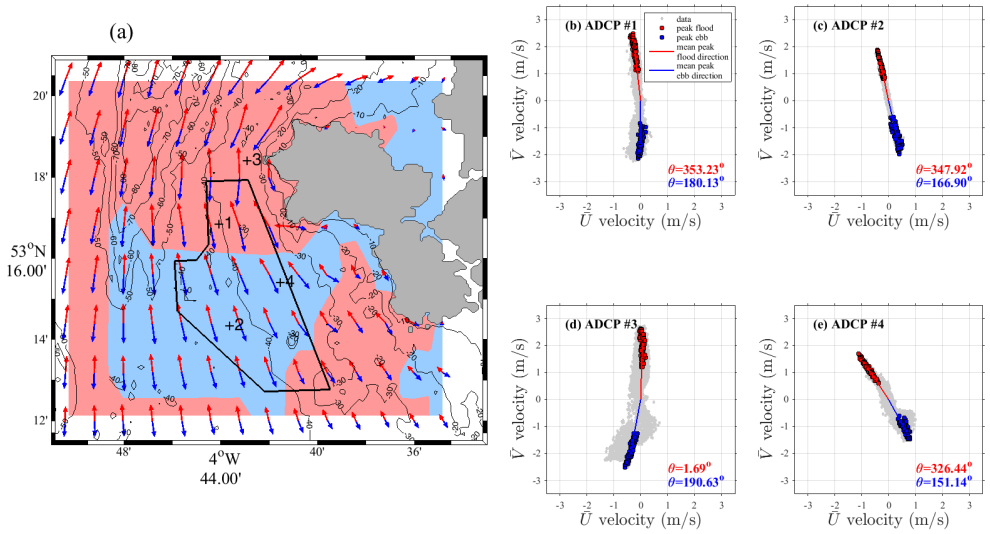

Figure 9. Simulated peak flood (red arrows) and ebb (blue arrows) flow magnitude and direction (a) with shaded areas indicating where relative flood or ebb dominance may occur. Subplots (b) to (e) show the depth averaged east and north velocity vector points (grey dots) for the four ADCP stations, with peak values highlighted accordingly and the subsequent incident angle of flow given by the mean peak values.

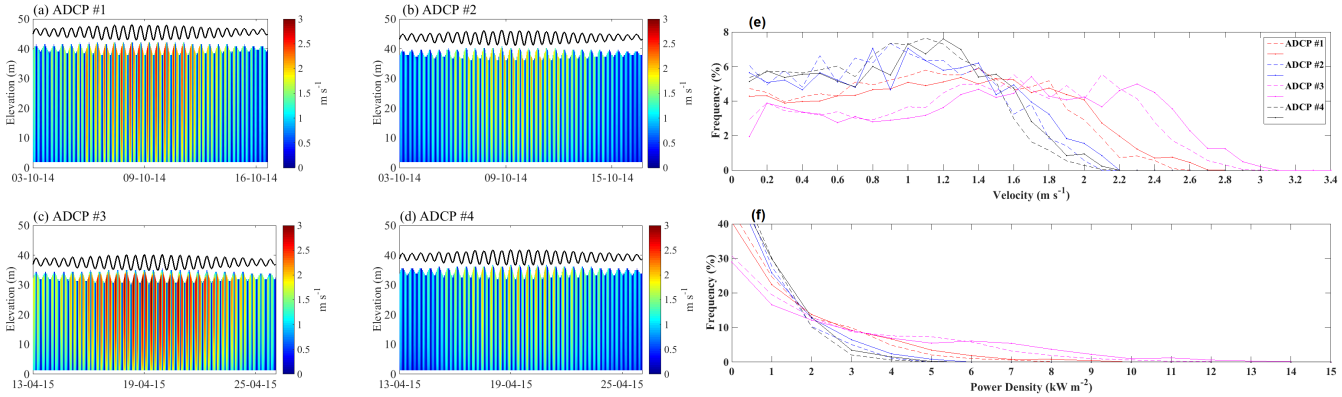

Figure 10. (a) to (d) ADCP station water column contour profiles of measured current speed interpolated between the 0.6 m vertical bin resolution and associated surface elevation change (black line) for the four ADCP stations. Surface bins (10%) have been excluded to remove side-lobe signal interference. Velocity (e) and kinetic power density (f) histograms showing occurrence as a percentage of a complete lunar cycle in 0.1 m s^{-1} and 1 kW m^{-2} bins for 15 m (dashed) and 25 m (solid) hub heights above the seabed at the four ADCP stations.

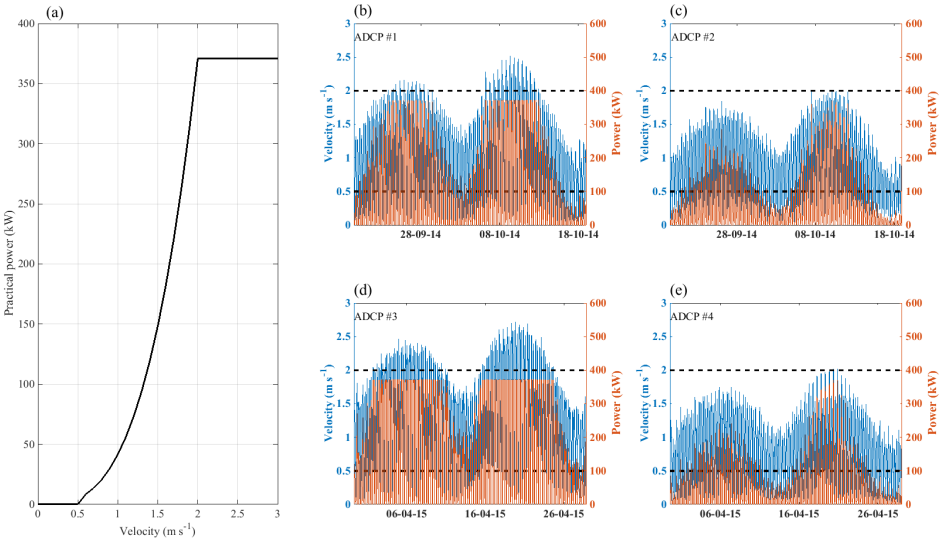

Figure 11. Generic TEC power output curve plot (a) and subsequent undisturbed power generation curves (orange) expected when depth averaged velocity (blue) from the four ADCP stations (b) to (e) is applied to the device. Dashed black lines indicate the cut-in and rated speed threshold of the device.

V. CONCLUSION

If tidal energy converters are to extract tidal energy efficiently, the resource should be assessed accurately using sophisticated models, in conjunction with *in-situ* measurements. Further the characteristics of the TEC should be tested for its suitability in the local hydrodynamic conditions. A multi-disciplinary approach to site characterisation should include an initial modelling assessment to predict, as accurately as possible, the likely spatial and temporal variation in the resource, followed by observational data collection in order to validate/calibrate the model, and to quantify the likely performance of the device under realistic conditions. High-resolution models (for example, <100 m for shelf-scale models) are desirable and these may require high performance computing (HPC) facilities that allow relatively low computational times for simulation. This is the approach that was utilised for this study.

This study reveals that areas to the north of the WADZ will yield greatest energy extraction potential, due to the higher velocities and consequent power density available. Such energetic conditions could increase loading stresses on devices, compared with calmer conditions further south. Initial site selection traditionally gives consideration to areas where the peak velocity is greatest and water depth suits the deployment of a given TEC. Consideration by developers looking to site their devices within the WADZ should also be given to the interaction of bathymetric, topographic and morphological features of the area, along with variability in the hydrodynamic regime over the year. For instance, peak flows may actually occur where asymmetric eddy systems develop, which could increase device loadings. Bottom substrate and its resultant friction coefficient will also be an important factor at the initial feasibility stage.

Although not considered here, the three-dimensional water velocity profile will vary where increased bed friction occurs and this will impact upon performance at lower hub heights. In highly energetic tidal streams, where the majority of the sea floor is bedrock, this consideration will be of lesser importance until device array deployments at a commercial scale dictate the necessity to expand to larger areas of seabed. Furthermore, surface gravity waves may propagate down the water column (wave-current interaction) and be an important factor in altering flow characteristics in these relatively shallow tidal stream regions. Further assessment of the resource should include uncertainty analysis that quantifies this interaction through coupled tide and wave modelling (preferably three-dimensional) and advanced observational techniques.

ACKNOWLEDGEMENT

This work was carried out as part of the Bangor University SEACAMS (Sustainable Expansion of the Applied Coastal and Marine Sectors) Project, part funded by the European Regional Development Fund (ERDF) by the Welsh European Funding Office (WEFO). The study formed part of a collaborative R&D project initiated by Dr Michael Roberts (SEACAMS R&D Project Manager) with the appointed WADZ third party management organization, Mentor Môn / Morlais. Data was kindly provided by the British Oceanographic Data Centre (BODC), United Kingdom Hydrographic Office (UKHO) and EDINA Marine Digimap Service.

VI. REFERENCES

VII.

[1] V. Ramos and G. Iglesias, "Performance assessment of Tidal Stream Turbines: A parametric approach," *Energy Conversion and Management,* vol. 69, pp. 49-57, 2013.

[2] S. P. Neill, R. M. Hashemi and M. J. Lewis, "The role of tidal assymetry in characterizing the tidal energy resource of Orkney," *Renewable Energy,* vol. 68, pp. 337-350, 2014.

[3] The Crown Estate, "UK wave and tidal key resource areas project," 2013.

[4] Black and Veatch, "Phase II UK tidal stream energy resource assessment," The Carbon Trust, London, 2005.

[5] The Crown Estate, "Summary report on wave and tidal demonstration zone identification process," 2013.

[6] ABPMER, "WEBvision - Renewable (tide)," [Online]. Available: http://vision.abpmer.net/renewables/map_default.phtml?config=tide&resetsession=groups,resultlayers. [Accessed 08 May 2015].

[7] M. Lewis, S. P. Neill, P. E. Robins and M. R. Hashemi, "Resource

assessment for future generations of tidal-stream energy arrays," *Energy,* vol. 83, pp. 403 - 415, 2015.

[8] P. E. Robins, S. P. Neill, M. J. Lewis and S. L. Ward, "Characterising the spatial and temporal variability of the tidal-stream energy resource over the northwest European shelf seas," *Applied Energy,* vol. 147, pp. 510-522, 2015.

[9] C. Moulinec, C. Denis, C.-T. Pham, D. Rouge, J.-M. Hervouet, E. Razafindrakoto, R. W. Barber, D. R. Emerson and X.-J. Gu, "TELEMAC: An efficient hydrodynamics suite for massively parallel architectures," *Computers and Fluids,* vol. 51, pp. 30 - 34, 2011.

[10] P. E. Robins, S. P. Neill and M. J. Lewis, "Impact of tidal-stream arrays in relation to the natural variability of sedimentary processes," *Renewable Energy,* vol. 72, pp. 311 - 321, 2014.

[11] M. R. Hashemi, S. P. Neill, P. E. Robins, A. G. Davies and M. J. Lewis, "Effect of waves on the tidal energy resource at a planned tidal stream array," *Renewable Energy,* vol. 75, pp. 626 - 639, 2015.

[12] J. M. Hervouet, Hydrodynamics of free surface flows, John Wiley and Sons, 2007.

[13] EDINA, "Marine Digimap Service," [Online]. Available: http://digimap.edina.ac.uk. [Accessed 08 05 2015].

[14] United Kingdom Hydrographic Office, "VORF model VORF-UK08," UKHO, 2008.

[15] C.-T. Pham, "Use of tidal harmonic constants databases to force open boundary conditions in TELEMAC," in *XIXth TELEMAC-MASCARET User Conference*, Oxford, 2012.

[16] G. D. Egbert, A. F. Bennett and M. G. Foreman, "TOPEX/POSEIDON tides estimated using a global inverse model," *Journal of Geophysical Research,* vol. 99, no. C12, pp. 24821-24852, 1994.

[17] G. D. Egbert and S. Y. Erofeeva, "Efficient inverse modeling of barotropic ocean tides," *Journal of Atmospheric and Oceanic Technology,* vol. 19, pp. 183 - 204, 2002.

[18] S. Gooch, J. Thomson, B. Polagye and D. Meggitt, "Site characterization for Tidal Power," in *OCEANS 2009 Marine Technology for our future: Global and Local Challenges*, Biloxi, MS, 2009.

[19] S. F. Harding and I. G. Bryden, "Directionality in prospective Northern UK tidal current energy deployment sites," *Renewable Energy,* vol. 44, pp. 474-477, 2012.

[20] M. Lewis, S. Neill, P. Robins, S. Ward, M. Piano, M. Hashemi and A. Goward-Brown, "Observation of flow characteristics at potential tidal stream energy sites," in *EWTEC*, 2015.

[21] B. L. Polagye, J. Epler and J. Thomson, "Limits to the Predictability of Tidal Current Energy," in *Oceans 2010*, Seattle, 2010.

2D numerical modelling of tracer transport and dilution in the Loire river

Nathalie Durand[1], Etienne Guerber[2], Amélie Besnard[2]
[1] Laboratoire National d'Hydraulique et Environnement, EDF R&D, 6 quai Watier, 78401 Chatou, France
[2] CIDEN, Division Environnement, EDF-DIN, 154 av. Thiers, 69458 Lyon cedex 06, France
Corresponding author: nathalie-2.durand@edf.fr

Proposed session: *Water Quality*
Keywords: tracer, transport, river, TELEMAC-2D
Speaker: Nathalie Durand

Abstract:

A TELEMAC-2D numerical model of a 50 km Loire river section has been constructed. The aim of the model is to study the downstream transport and dilution of a Nuclear Power Plant (NPP) liquid emissions. It focuses on situations from low-water to mean flow rate and thus the flood plain is not taken into account. The model is based on recent bathymetric and validation data: bottom topography, water levels, current velocities and tracer concentrations have been collected during field campaigns carried on 2014. The numerical model is based on the latest V7P0 version of Telemac-2D. Forcings of the numerical model are Loire flow rate, NPP water intake and NPP water and tracer release.

First step is simulation of several stationary situations, corresponding to different flow rates. Thus, a preliminary model calibration (based on Strickler's law) is achieved, as well as sensitivity studies (time-step, mesh size). Calibration of low-level flow is the more complex.

A field campaign, corresponding to a flow rate slightly greater than mean flow rate, has been carried out: water levels and flow currents have been measured. This situation is simulated: a finer model calibration is realised by using water level data. Model validation is achieved by comparing simulated velocities and ADCP (Acoustic Doppler Current Profiler) current data. This comparison shows the capability of the numerical model to reproduce quite well hydrodynamics in the whole study domain. Nevertheless, differences between numerical and experimental data are locally observed but can obviously be related to uncertainties of bottom representation in the model mesh.

The NPP liquid emissions transport and dilution study is based on two simulations. For these two situations, field campaigns have been achieved: a conservative and non buoyant tracer has been released by the NPP and its concentration has been measured from NPP to 30 kilometres downstream. The first situation corresponds to a mean river flow rate. The modelling results are in good agreement with field data and show the ability of the numerical model to reproduce transport and dilution in this flow range (fig. 1). Only two measured profiles show significant differences with measurements. These difficulties are not related with tracer quantification but rather with plume position and width. The low-level situation is more complex, especially within the first 5 kilometres downstream of the NPP. Plume geometry reproduction (width, position) is the main difficulty whereas downstream evolution of maximum tracer concentration is quite well represented (fig. 2). Beyond the 5 kilometres area, the plume is again rather well represented (excepting a little zone located at 12 kilometres from NPP). A moderate overestimation of lateral mixing is possibly observed but this is not problematic for model applications.

Thus, modelling difficulties are localized (from NPP to 5 km downstream and in a little area at 12 km from NPP) and especially encountered when water levels are low. The problematic zone is characterised by many sand banks separated by narrow and shallow (until 20 – 30 cm water depth when river discharge is low) channels (braided river bed) (fig. 3). In these conditions, the

flow and consequently the plume position are extremely sensitive to bathymetry; this sensitivity increases significantly when water depths decrease. Thus, modelling difficulties are doubtless due to uncertainties of bottom representation in the model mesh. Indeed, in this area, bottom data has been interpolated from bathymetric profiles separated by 200 to 300 m; data resolution does not allow a sufficiently accurate river bed representation in the model mesh with regards to the complexity of this zone. In the other areas, morphology of the river bed is less complex and water depths are more important even in low-level situations; the modelling results are thus of better quality. In order to improve modelling, a new bathymetric campaign with a higher resolution measurement technique (multibeam technique) should be realised in complex identified areas. Further work is already planned in order to estimate more precisely sensitivity of the model results in some areas of special interest to bathymetric realistic evolutions.

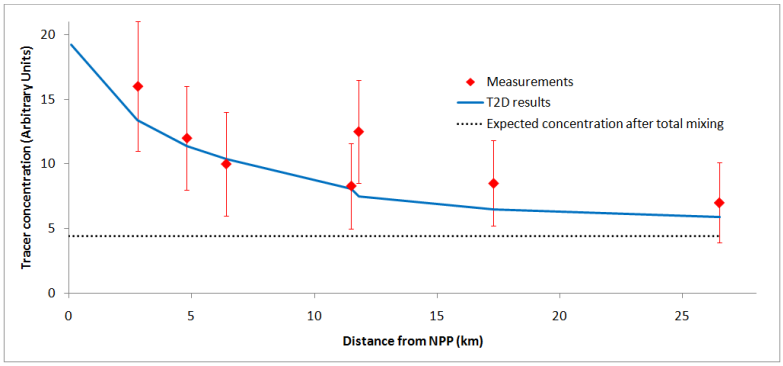

Figure 1 – Downstream evolution of the tracer concentration for mean flow rate situation.

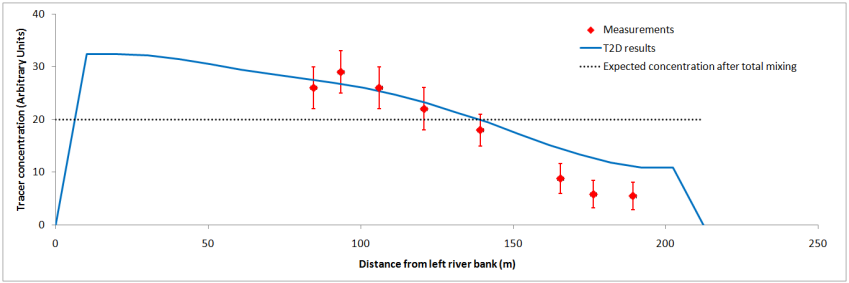

Figure 2 – Example of concentration cross-section profile for low level situation.

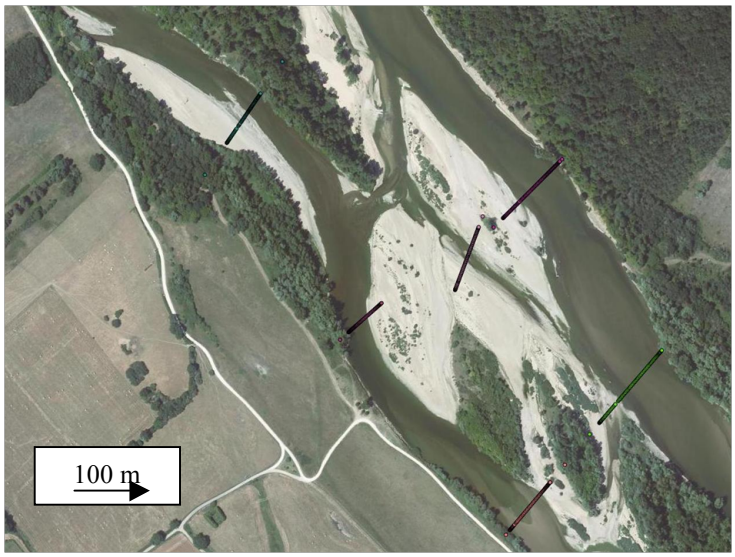

Figure 3- Example of complex river bed morphology encountered in the studied zone (position of the bathymetric data profiles is indicated).

Numerical simulations of flow around vegetation with Telemac2D: application on laboratory experiments and on the Isère river (France)

Nicolas Claude[1,2], Germain Antoine[1,2], Rabab Yassine[1], Veerle Verschoren[3], Christian Schwarz[3], Stijn Temmerman[3], Camille Jourdain[4]
[1] EDF R&D Laboratoire National d'Hydraulique et Environnement (LNHE), 78400 Chatou, France.
[2] Université Paris-Est, Laboratoire d'hydraulique Saint Venant, ENPC, EDF R&D, CEREMA, 78400 Chatou, France.
[3] University of Antwerp, Universiteitsplein 1, 2610 Antwerp, Belgium
[4] Laboratoire d'étude des Transferts en Hydrologie et Environnement (LTHE), Université de Grenoble, France
Corresponding author: nicolas-n.claude@edf.fr

Proposed session: *Water quality, ecology and environmental impact*
Keywords: Telemac2D, hydrodynamic, vegetation
Speaker: Nicolas Claude

Abstract:

Vegetation is a common feature of rivers. In these systems, the plants can significantly affect hydrodynamics and sediment transport. Indeed, vegetation deflects (blocking effect) and reduces (roughness effect) the flows, decreases the sediment transport capacity, and causes the deposition of particles within the plants. Vegetation also influences the morphological evolution of streams by controlling bank erosion, encouraging aggradation of alluvial bars and secondary channels, and by contributing to floodplain development. Thus, it is necessary to take into account the processes associated with vegetation in the numerical codes for fluvial environments.

In hydrodynamic numerical models, the effect of the vegetation is represented either by increasing the bed roughness or by adding a drag force. In this study, we propose to compare these two approaches with Telemac2D. More specifically, the ability of the friction laws of Baptist *et al.* (2007), and the drag force method to reproduce the flow velocities around vegetation patches was explored for emergent and submerged conditions, and for rigid and flexible plants. The friction law of Lindner (1982) was also evaluated for rigid emergent vegetation. For this purpose, the laboratory experiments of Pasche and Rouve (1985), Zong and Nepf (2012) and Bouma et al. (2013) were numerically simulated. A vegetated bar of the Isère river (France) was also modelled.

Preliminary results show that the friction law of Baptist and the drag force method give very similar results on the selected test cases. These methods enable to estimate correctly the flow velocities for emergent and submerged rigid plants (Figure 1). The results obtained with the friction law of Lindner (only dedicated to emergent rigid plants) are less satisfying. The vortices associated to the presence of vegetation are reproduced by the three tested methods. The flow velocity field around a flexible vegetation is estimated with a lower accuracy. This result indicates that further developments are required to incorporate the effects of the reconfiguration of flexible vegetation in the models.

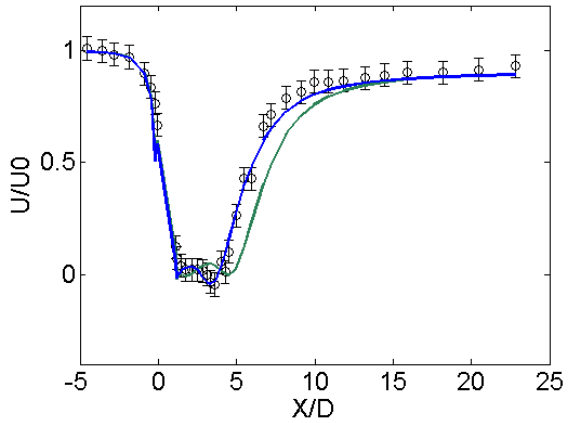

Figure 1: Longitudinal evolution of flow velocity around a circular patch of rigid emergent cylinders. The patch is located between the abscissas 0 and 0.2. The circular dots correspond to the measurements. The blue line corresponds to flow velocities estimated with the drag force method. The green line corresponds to flow velocities estimated with the friction law of Lindner.

References:

Baptist, M., V. Babovic, J. Rodríguez Uthurburu, M. Keijzer, R. Uittenbogaard, A. Mynett, and A. Verwey (2007), On inducing equations for vegetation resistance, *Journal of Hydraulic Research*, *45*(4), 435-450.

Bouma, T.J., S. Temmerman, L.A. van Duren, E. Martini, W. Vandenbruwaene, D.P. Callaghan, T. Balke, G. Biermans, P.C. Klaassen, P. van Steeg, F. Dekker, J. van de Koppel, M.B. de Vries, P.M.J. Herman (2013), Organism traits determine the strength of scale-dependent bio-geomorphic feedbacks: A flume study on three intertidal plant species, *Geomorphology*, 180-181, 57-65.

Lindner,K. (1982) Der Strömungswiderstand von Pflanzenbeständen. Mitteilungen 75. Leichtweiss-Institut fürWasserbau, Technische Universität Braunschweig.

Pasche, E., and G. Rouve (1985), Overbank flow with vegetatively roughened flood plains, *Journal of Hydraulic Engineering*, *111*(9), 1262-1278.

Zong, L., and H. Nepf (2012), Vortex development behind a finite porous obstruction in a channel, *Journal of Fluid Mechanics*, *691*, 368-391.

Development of a three-dimensional model of a vertical-axis and transverse-flow hydrokinetic turbine

Olivier BERTRAND[(1)], Adlane REBAI[(1)], Caroline GIRARD[(1)],
[(1)] Numerical Hydaulics team
Artelia Eau & Environnement
38 130 Echirolles, France,
olivier.bertrand@arteliagroup.com

Jerönimo ZANETTE[(2)] & Favio DOMINGUEZ[(3)]
[(2)] HydroQuest, Meylan, France,
jeronimo.zanette@hydroquest.net
[(3)] LEGI, Grenoble Institute of Technology, France.
favio.dominguez@legi.grenoble-inp.fr

***Abstract*—Work presented in this paper is done in the framework of the HYDROFLUV project. The hydrodynamic effects of the rotating blades are modelled without meshing the geometries under TELEMAC. Several academic studies are presented and validate the developments made.**

I. INTRODUTION

The HYDROFLUV research and development project (funded by FUI with support from the Tenerrdis, DERBI and DREAM clusters) aims at demonstrating feasibility and acceptability of vertical-axis and transverse-flow turbines. Partners of the HYDROFLUV project – Hydroquest, FOC Transmissions, ERNEO, Biotope, EDF, Artelia and the LEGI laboratory – are working both on improving the machines and on developing a more complete commercial offering (administrative authorizations, impact studies and profitability).

In order to study how well a hydrokinetic turbine is accepted by its natural environment, a geophysical model needs to be used. The incorporation of the machine's characteristics into the three-dimensional numerical model TELEMAC-3D has enabled to analyse head loss around the machine (variation in the free surface and current), interactions between machines, and hydrosedimentary impacts. Validation of these TELEMAC developments is presented in this paper.

II. MODEL DESCRIPTION

A. *Theory and concept*

Three-blade, fixed-pitch Darrieus-type turbines are used in this study. These turbines are built into a supporting structure equipped with non-symmetrical lateral diffuser-type fairings that create overspeed events in the drive areas of the turbines. Furthermore, its structure enables several turbines to be placed in two counter-rotating columns to enhance modularity and optimize productivity according to each site (Fig. 1).

Figure 1. HydroQuest hydrokinetic turbine with one level of two cross flow wheels.

This concept, which was developed under the project name "Hydrolienne à Axe de Rotation Vertical Stabilisé" (HARVEST for its acronym in French), is the result of 10 years of research started in 2001 by Professor Achard [1] at the Geophysical and Industrial Fluid Flows Laboratory (LEGI) of Grenoble University. These turbomachines are currently marketed by Hydroquest, France.

The geometric parameters of the turbine rotor are shown in table 1. Fig. 2 shows a schematic representation of a HARVEST turbine equipped with two counter-rotating three-blade rotors mounted in a ducted diffuser (the turbine stator).

TABLE I. TURBINE MODEL CARACTERISTICS

Feature	Description
Blade profile	NACA
Number of blades	3
Rotor diameter (D)	1m
Hub diameter (d)	0.06m
Solidity	1.1
TSR	Optimal
Turbine length (L_T)	4m

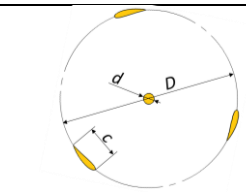

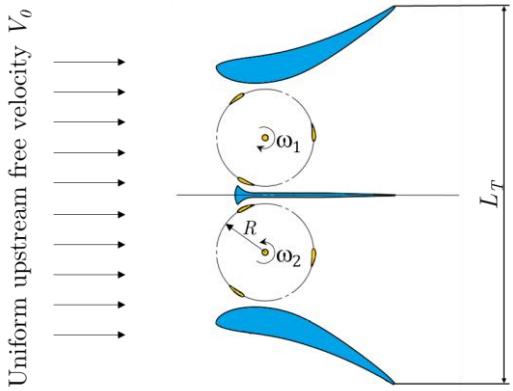

Figure 2. Schematic representation of a horizontal plane of a HARVEST turbine.

The behaviour of a hydrokinetic current turbine is subject to several parameters, including:

- Upstream infinity velocity, denoted by V_0

- Channel blockage ratio, which is the ratio of turbine length to channel width, denoted by ϕ

$$\phi = \frac{L_T}{W_c} \quad (1)$$

The Tip Speed Ratio (TSR), defined as the ratio between the tip velocity and the upstream velocity V_0:

$$TSR = \frac{\omega R}{V_0} \quad (2)$$

where R is the rotor radius and ω its rotational speed [2].

The HARVEST turbine has the ability to adjust the rotational speed of its rotors depending on the actual incident flow velocity $(\vec{V}_f)$ for maximum power extraction. All the simulation results analysed in this study hence come from a turbine operating in optimal conditions ($TSR_{optimal}$).

The actual incident flow velocity $(\vec{V}_f)$ depends on the three previously defined parameters $\vec{V}_f = f(V_0, \phi, TSR_{optimal})$.

B. Numerical implementations

TELEMAC-3D [6] developments to implement the hydrokinetic turbine are explained in this section. The TELEMAC-3D software solves the second-order partial differential equations for free-surface flows derived from the full three-dimensional turbulent Navier-Stokes equations (more precisely the Reynolds-averaged Navier-Stokes equations - RANS). This gives a system consisting of an equation for mass continuity and three force momentum equations.

The effect of a hydrokinetic turbine is introduced into the model as an extra source term in the momentum equations. The turbine imposes a drag on a flow which can be broken down into two parts: a thrust force produced by the rotor due to energy extraction, and a drag force caused by the supporting structure (the stator). Turbine operation is controlled by the pitch of the rotor blades, resulting in changes in the thrust and power coefficient. TELEMAC-3D models the hydrodynamic effects of the rotating blades averaged over time without the need to create and mesh the geometry of the blades. The source terms are distributed in an annular volume (in the case of a straight-blade turbine) corresponding to the volume swept by the blades. Specifically in 3D simulations, this is a revolution volume contained between two coaxial cylinders centred on the axis of rotation of the turbine. Other source terms are applied at elements within the stator domain.

The unstructured horizontal mesh (Fig. 3) has to describe all the elements of the turbine. Vertically, two fixed planes are located at the upper and lower part of the turbine. For a non-academic study, this is done only at the level of the turbine with a smooth region for connecting the mesh with the rest of the domain to be computed.

The source terms, which are unknown at the beginning of the iterations, evolve throughout the simulation. The relationship between the values of the source terms and the velocity of the flow passing through the turbine rotor V_f is established at each iteration. Once the source term values have been determined, the velocity of the flow passing through the turbine can be re-estimated and the new source term values can be determined for the next iteration.

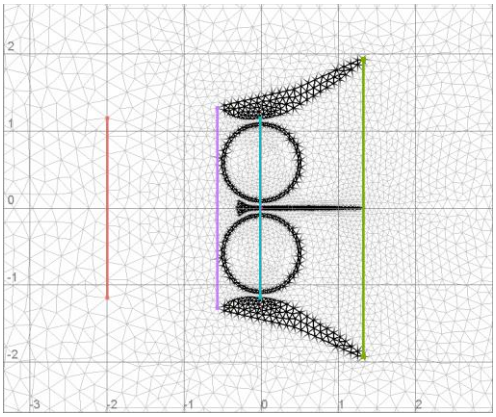

Figure 3. Horizontal fixed mesh around the turbine with identification of the sources nodes (bold) and the sections sounded.

For computing the velocity passing through the turbine rotor, we have modified both the source code and Python scripts for managing calculation of flow through control sections in parallel (previously only done for TELEMAC-2D) and the flow calculation in 3D (here also, only done in the standard version for TELEMAC-2D).

C. Source terms used to feed the TELEMAC model

Turbine is working at an optimal TSR value which is not a priori known. The laboratory LEGI with HydroQuest has previously solved the URANS equations governing the unsteady turbulent flow around the turbine [5]. This two-dimensional URANS approach is used for predicting the wake and power output for a series of numerical simulations performed at a fixed TSR. Power output is computed from

the instantaneous value of the tangential force apply on each blade. The optimal power gives the true operation conditions and the optimal TSR parameter.

The numerical simulations are then conducted for a range of channel blockage ratio ϕ and inlet flow velocity V_0. In each simulation, the reference velocity V_f varies depending on the parameters ϕ and V_0 (Fig. 4). This variation makes it possible to establish the relationship between the values of the reference velocity and the hydrodynamic force coefficient acting on the turbine blades (F_X, F_Y) in order to characterize the source terms that will feed the far-field model.

Establishing a relationship between the reference velocity V_f and the force coefficients from the instationary URANS model results, in order to feed the stationary far field model, requires the flow field to be time-averaged over one full revolution.

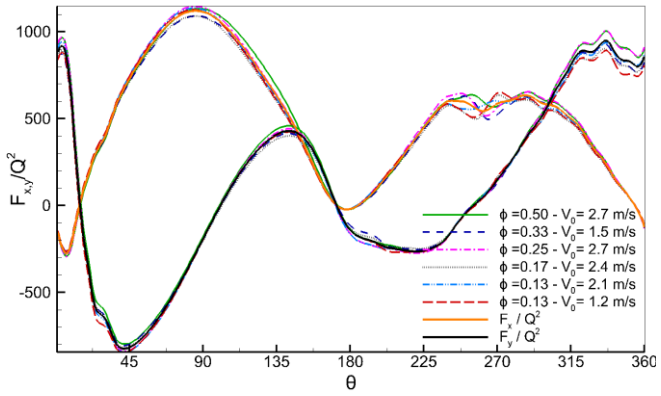

Figure 4. Computed hydrodynamic force curves $F_{x,y}$ used to feed the far-field model.

The same extraction is done for the stator part of the turbine.

III. MODEL VALIDATION

The TELEMAC model is firstly applied to a test problem of an isolated turbine in a channel. The cross flow turbine is placed inside a rectangular channel and aligned with the incoming flow direction. The isolated turbine is placed in the middle of the channel with ϕ = 0.29 and V_0 = 2.25 m/s. This configuration is simulated using both the URANS and the TELEMAC-3D approach.

Figure 5. shows the velocity contours along X calculated by the two models (for an half of the channel). The velocity profiles upstream and downstream of the turbine (traced along lines perpendicular to the main direction of flow) are also plotted in order to compare them in detail. This result shows good overall agreement between the two simulations. Differences can be explained by the 2D hypothesis under the URANS model (without free surface), and the coarse mesh without a boundary layer under the TELEMAC-3D model.

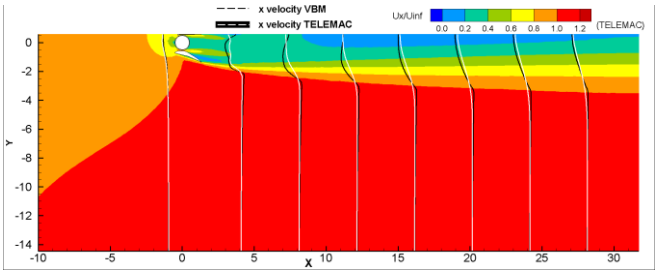

Figure 5. Horizontal fixed mesh around the turbine with identification of the sources nodes (bold) and the sections sounded.

The second validation is performed for a row of 3 turbines (6 turbine rotors). The lateral spacing between the turbines is equal to the length L_T and the channel width W_c is equal to 24 L_T. (see Figure 6. below). The uniform velocity is set to 2.1 m/s.

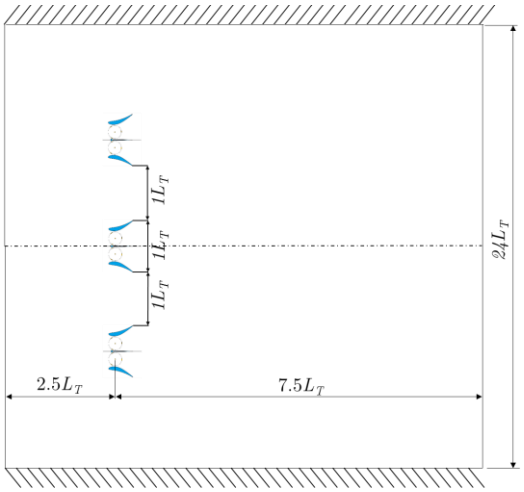

Figure 6. Overview of the channel domain with 3 turbines configuration.

With TELEMAC, the flow through the channel is defined in order to obtain the same free-stream velocity V_0. In order to compare the results with simulations conducted by the LEGI, the turbines are traversing and an arbitrary height of 7m is retained.

Computed velocities contours are compared on the Figure 7. and Figure 8. below. This comparison is just qualitative but illustrates well the variation of the flow around and through each turbine and the wakes which are significant. The TELEMAC model provides a flow more viscous but with fewer cells and lower cost. TABLE II. displays the flowrates through each rotor computed at models convergence.

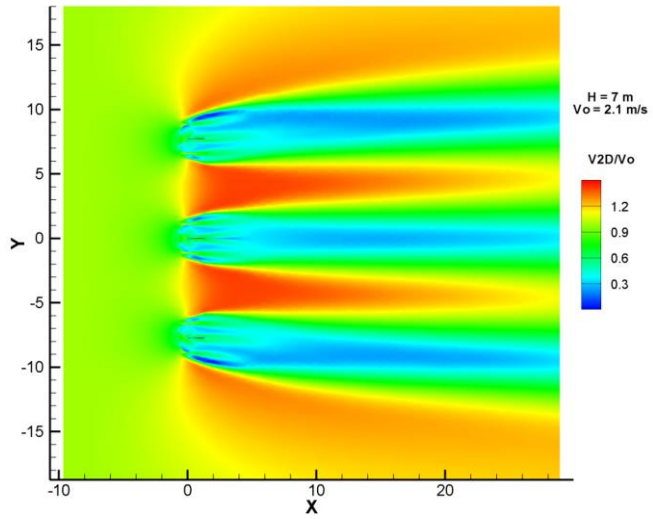

Figure 7. Computed velocity (averaged along the water depth) contours obtained by TELEMAC.

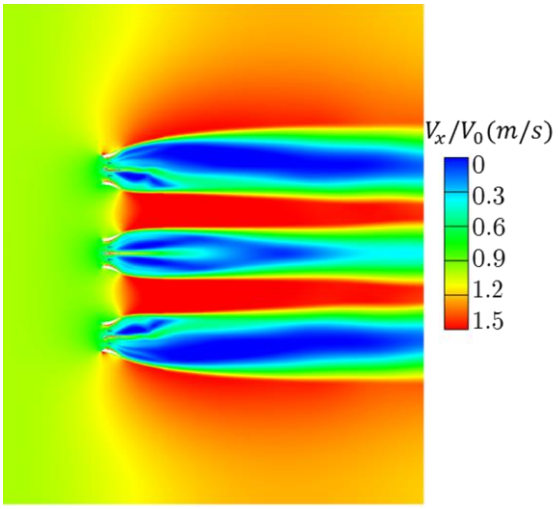

Figure 8. Computed velocity contours obtained by URANS model.

TABLE II. COMPUTED FLOWRATES AT MODELS CONVERGENCE.

Rotor	TELEMAC-3D	Fluent VBM
Left turbine, left rotor	1.70	1.73
Left turbine, right rotor	1.72	1.78
Middle turbine, left rotor	1.76	1.80
Middle turbine, right rotor	1.76	Results obtained by horizontal symmetry
Right turbine, left rotor	1.72	
Right turbine, right rotor	1.71	

The last validation is performed for an array of 5 turbines (10 turbine rotors). Turbines positions are displayed on Figure 9. Two rows of turbines are tested. In addition to model validation, the aim of this test is also to see the effect of turbines positions relatively to each other. The L_T parameter defines each turbine position.

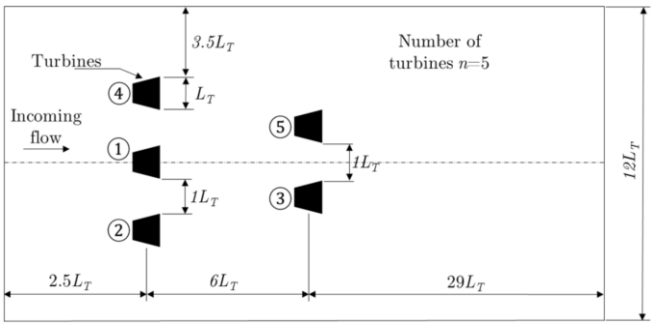

Figure 9. Overview of the channel domain with an array of 5 turbines.

Computed velocities contours are plotted on Figure 10. and spatial velocity profile is compared to the URANS model at the back of the first row or second row.

The profiles are sharper with the URANS model but here also simulations are quite different with a 3D one computed with a free surface by TELEMAC and only on 2D for the URANS model.

Moreover, turbines interaction is less when they are located close from one another. Indeed, in this case, velocity entrance in the second turbine row can be higher than velocity in the first row due to contraction between two turbines of the first row. When there is more space between turbines, it is more likely to have second row turbines in the wake/shadow zone of the first row.

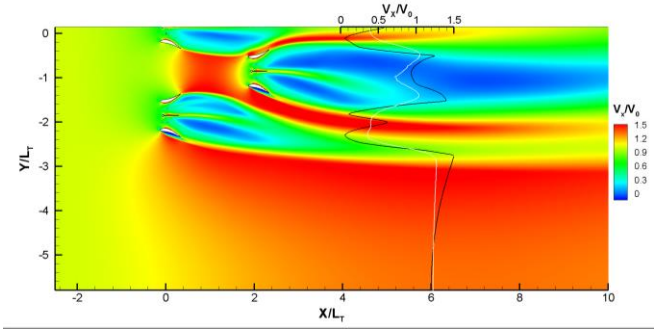

(a) $L_T = 4\ m$

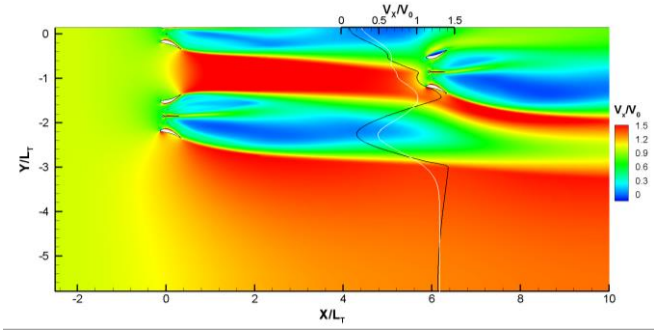

(b) $L_T = 6\ m$

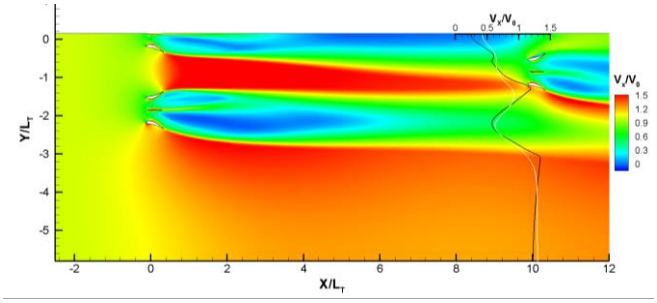

(c) $L_T = 10\ m$

Figure 10. Computed velocity contours obtained by TELEMAC and comparison of a velocity profile (URANS in black).
(a) L_T = 4 m ; (b) L_T = 6 m ; (c) L_T = 10 m

IV. CONCLUSION

The work presented in this article was carried out in the framework of the HYDROFLUV research project, which aims at developing a methodology and tools for evaluating the impacts of a river turbine at a production site.

Coupling the various modelling resources provides a means of comprehending the river turbine within its environment. By using a URANS approach, whereby the geometric surfaces of the turbine are represented in the mesh, we can determine the forces exerted on the machine's rotor and stator with a high degree of precision. The integration of these terms to the TELEMAC conservation equations without faithfully representing its geometry, larger-scale three-dimensional simulations are validated on the basis of academic cases in which the two models are compared. The modelling and simulation times are obviously much longer with the first approach.

Applying the TELEMAC model to the pilot site in the river Loire provides a means of simulating several river discharges with the turbine operating [3]. The current fields obtained and hydraulic impact maps give an indication of how well the turbine is accepted by its natural environment.

Figure 11. Picture of the hydrokinetic turbine, raised on the barge, in the river Loire at Orléans.

A river turbine has been now installed in the river Loire in Orléans since autumn 2014 (Fig. 11). This full-size prototype is used to test the various technological options on a scale of several years' operation, and provides some initial feedback.

We are currently studying resources for working backwards and calculating production capacity in order to optimize turbines location of a river turbine farm and the layout of the individual turbines.

ACKNOWLEDGEMENT

This work was carried out as part of the HYDROFLUV project approved by the Tenerrdis, DERBI and DREAM competitiveness clusters, with funding granted in the framework of the 15th Fonds Unique Interministériel (FUI) programme. The HYDROFLUV project partners are Hydroquest, FOC Transmissions, ERNEO, Biotope, EDF, Artelia and the LEGI laboratory.

REFERENCES

[1] Achard, J.-L., Projet Harvest : Hydrolienne à Axe de Rotation Vertical Stabilisé, Séminaire sur les Energies Propres et Renouvelables. 2006

[2] Aumelas, V., Modélisation des hydroliennes à axe vertical libres ou carénées : développement d'un moyen expérimental et d'un moyen numérique pour l'étude de la cavitation. Université de Grenoble, Thèse 2011

[3] O. Bertrand, L. Duron, C. Girard, J. Zanette, F. Dominguez, Numerical modelling of vertical-axis and transverse-flow hydrokinetic turbine in the river Loire, E-proceedings of the 36th IAHR World Congress 28 June – 3 July, 2015, The Hague, the NetherlandsHervouet J.-M., Hydrodynamics of Free Surface Flows – modelling with the finite element method. WILEY 2007

[4] Dellinger N., Instrumentation d'un tunnel hydrodynamique pour la caractérisation de turbines a flux transverse. Université de Grenoble, Thèse 2011

[5] F. Dominguez, J.-L. Achard, J. Zanette and Ch. Corre, A BEM-RANS approach for the fast power output prediction of ducted vertical-axis water turbines, Proceedings of the 11th European Wave and Tidal Energy Conference 6-11th sept 2015, Nantes, France

[6] Hervouet J.-M., Hydrodynamics of Free Surface Flows – modelling with the finite element method. WILEY 2007

Implementing plant growth of flexible aquatic vegetation into a hydrodynamic model (TELEMAC2D)

Veerle Verschoren[1],Christian Schwarz[1], Jonas Schoelynck[1], Kerst Buis[1], Germain Antoine[2,3], Nicolas Claude[2,3], Patrick Meire[1]; Stijn Temmerman[1]

[1] University of Antwerp, Universiteitsplein 1, 2610 Antwerp, Belgium
[2] EDF R&D, National Laboratory for Hydraulics and Environment (LNHE) & Saint Venant Laboratory for Hydraulics, Chatou, France
[3] Saint-Venant Hydraulics Laboratory, Université Paris-Est, Chatou, France
Corresponding author: Veerle Verschoren, veerle.verschoren@uantwerpen.be

Proposed session: Water quality, ecology and environmental impact
Keywords: influence of aquatic vegetation, coupling of code, hydraulic resistance
Speaker: Veerle Verschoren

Abstract:

In lowland rivers, mutual interactions between aquatic vegetation and water flow are expected to impact morphology. The presence of aquatic vegetation increases the hydraulic resistance encountered by water flow. On a local scale this results in flow deceleration within vegetation patches and in flow acceleration adjacent to vegetation patches. Reduced flow velocities within vegetation patches are beneficial for plant growth and therefore referred to as a positive feedback. While increased velocities adjacent to the vegetation patches are able to hamper plant growth, break off or uproot plants constituting a negative feedback. These two phenomena are in literature referred to as scale-dependent feedbacks (positive and negative feedbacks dependent on the spatial scale considered, i.e. in the patch or at its edges), which are further described as the mechanisms influencing heterogeneous spatial habitat structure.

A depth-averaged hydrodynamic model (TELEMAC2D) coupled with a plant model is used to investigate the importance of scale-dependent feedbacks in structuring lowland river habitats. We simulate the feedback between spatio-temporal growth of aquatic vegetation and its impact on the associated flow field. The dynamic plant growth model simulates changes in biomass of the plants. The biomass is represented as a tracer in the hydrodynamic model. The plant model itself consists of vegetation establishment-, mortality-, logistic increase of biomass- and lateral spatial expansion processes. The influence of vegetation is incorporated by schematizing vegetation as cylinders which exert a drag force to the flow, following the approach of Baptist et al. (2007). Since vegetation is flexible, the magnitude of the drag force is a function of vegetation reconfiguration and therefore dependent on the stream velocity itself.

Our preliminary results stress the importance of scale-dependent feedbacks on spatial habitat structure. We focus on three species with contrasting plant traits which due to differences in scale-dependent feedback strength lead to different spatial configurations. A dense species (*Callitriche obtusangula*) causing high hydraulic resistance instigating a strong scale-dependent feedback which results in delineated patches alternated with bare soil. An intermediate dense species (*Sparganium emersum*) forms long vegetated areas and a low density species (*Potamogeton natans)* with low hydraulic resistance, limited interaction with the water flow occupies the complete river bed. Our results underline, through a comparison between our model results and observed vegetation

patterns in lowland rivers, the importance of species-specific plant traits on spatial habitat structure.

References:

Baptist, M., V. Babovic, J. Rodríguez Uthurburu, M. Keijzer, R. Uittenbogaard, A. Mynett, and A. Verwey (2007), On inducing equations for vegetation resistance, *Journal of Hydraulic Research*, *45*(4), 435-450.